Transactions of the ASME

Technical Editor, L. B. FREUND

APPLIED MECHANICS DIVISION

Chairman, WILLIAM G. GOTTENBERG
Secretary, CHARLES R. STEELE
Associate Editors, J. D. ACHENBACH
S. T. ARIARATNAM
T. BELYTSCHKO
D. B. BOGY
R. J. CLIFTON
L. B. FREUND
MAURICE HOLT
W. D. IWAN
T. R. KANE
A. S. KOBAYASHI
S. LEIBOVICH
L. E. MALVERN
R. P. NORDGREN
R. H. PLAUT
R. T. SHIELD
C. T. SUN
J. S. WALKER
G. A. WEMPNER

BOARD ON COMMUNICATIONS
Chairman and Vice-President
M. J. RABINS

Members-at-Large
W. BEGELL
J. CALLAHAN
H. C. REEDER
D. KOENIG
M. KUTZ
F. LANDIS
J. W. LOCKE
J. E. ORTLOFF
C. PHILLIPS
K. REID

President, SERGE GRATCH
Exec. Dir.
PAUL ALLMENDINGER
Treasurer, ROBERT A. BENNETT

PUBLISHING STAFF
Mng. Dir., Pub., J. J. FREY
Dep. Mng. Dir., Pub.
JOS. SANSONE
Managing Editor,
CORNELIA MONAHAN
Production Editor, SUZANNE MAGIDA
Prod. Asst., BETH DARCHI

Journal of Applied Mechanics (ISSN 0021-8936) is edited and published quarterly at the offices of the American Society of Mechanical Engineers, United Engineering Center, 345 E. 47th St., New York, N.Y. 10017. ASME-TWX No. 710-581-5267, New York. Second Class postage paid at New York, N.Y., and at additional mailing offices.

CHANGES OF ADDRESS must be received at Society headquarters seven weeks before they are to be effective. Please send old label and new address.

PRICES: To members, $36.00, annually; to nonmembers, $72.00. Single copies, $24.00 each. Add $6.00 for postage to countries outside the United States and Canada.

STATEMENT from By-Laws. The Society shall not be responsible for statements or opinions advanced in papers or . . . printed in its publications (B7.1, Par. 3).

COPYRIGHT © 1983 by the American Society of Mechanical Engineers. Reprints from this publication may be made on condition that full credit be given the TRANSACTIONS OF THE ASME, JOURNAL OF APPLIED MECHANICS, and the author, and date of publication be stated.

INDEXED by the Engineering Index, Inc.

Journal of Applied Mechanics

Published Quarterly by The American Society of Mechanical Engineers

VOLUME 50 • NUMBER 1 • MARCH 1983

TECHNICAL PAPERS

1 **Diffusive, Electrostatic, and Gravitational Deposition of Suspensions in the Entrance of a Nozzle**
T. A. Korjack

8 **Unified Approach to the Solution of Problems of Unsteady Laminar Flow in Long Pipes** (83-APM-2)
M. F. Letelier S. and H. J. Leutheusser

13 **Buckling, Postbuckling, and the Flow Through a Tethered Elastic Cylinder Under External Pressure**
C. Y. Wang, L. T. Watson, and M. P. Kamat

19 **On the Estimation of Energy Release Rates** (83-APM-11)
R. Abeyaratne

24 **Thermal Stress in a Transversely Isotropic Medium Containing a Penny-Shaped Crack** (83-APM-8)
Y. M. Tsai

29 **The Penny-Shaped Interface Crack With Heat Flow, Part 1: Perfect Contact** (83-APM-10)
C. J. Martin-Moran, J. R. Barber, and M. Comninou

37 **Axisymmetric Singular Stresses in a Thick-Walled Spherical Shell With an Internal Edge Crack**
A. Atsumi and Y. Shindo

43 **Stress Distributions for a Quarter Plane Containing an Arbitrarily Oriented Crack**
L. M. Keer, J. C. Lee, and T. Mura

50 **Dynamic Singular Stresses for a Griffith Crack in a Soft Ferromagnetic Elastic Solid Subjected to a Uniform Magnetic Field**
Y. Shindo

57 **Dynamic Stress Concentration Around a Circular Hole in an Infinite Elastic Strip**
S. Itou

63 **Interactions of a *P*-Wave With a Laterally Stiffened Slot**
R. L. Ryan and S. Mall

67 **Nonlocal and Nonlinear Friction Laws and Variational Principles for Contact Problems in Elasticity**
J. T. Oden and E. B. Pires

77 **An Educational Elasticity Problem With Friction, Part 3: General Load Paths**
J. Dundurs and M. Comninou

85 **Stress Couple Concentrations for Cylindrically Bent Plates With Circular Holes or Rigid Inclusions** (83-APM-5)
E. Reissner

88 **Plastic Buckling of Initially Imperfect Stiffened Cylinders in Axial Compression**
G. A. Duffett and B. D. Reddy

95 **On the Unsymmetric Eigenproblem for the Buckling of Shells Under Pressure Loading**
H. A. Mang and R. H. Gallagher

101 **Analysis of Elastic Torsion in a Bar With Circular Holes by a Special Boundary Integral Method** (83-APM-15)
D. A. Caulk

109 **An Analysis of Adhesive-Bonded Single-Lap Joints** (83-APM-14)
D. Chen and S. Cheng

116 **On an Axisymmetric Coupled Thermal Stress Problem in a Finite Circular Cylinder**
Y. Takeuti, R. Ishida, and Y. Tanigawa

123 **Vibration of a Free Rectangular Parallelpiped**
J. R. Hutchinson and S. D. Zillmer

131 **Theory of Viscoplastic Shells for Dynamic Response**
R. S. Atkatch, M. P. Bieniek, and I. S. Sandler

137 **A Linear Theory for Pretwisted Elastic Beams** (83-APM-9)
S. Krenk

143 ***T*-Matrix Approach to Scattering of Elastic (*SH*-) Waves by an Inclined Surface Void** (82-APM-13)
S. J. Tsao, V. V. Varadan, and V. K. Varadan

149 **Instabilities of a Finitely Deformed Fiber-Reinforced Elastic Material**
N. Triantafyllidis and R. Abeyaratne

157 **An Effective Dispersion Theory for Layered Composites**
T. J. Delph and G. Herrmann

165 **Steady-State Point-Source Excitation of a Laminated Composite**
G. S. Beaupre and G. Herrmann

169 **The Interface Crack Between Dissimilar Anisotropic Composite Materials** (83-APM-6)
S. S. Wang and I. Choi

(Contents continued on Inside Back Cover)

Downloaded 04 May 2010 to 171.66.16.34. Redistribution subject to ASME license or copyright; see http://www.asme.org/terms/Terms_Use.cfm

CONTENTS (CONTINUED)

179 **The Interface Crack Behavior in Dissimilar Anisotropic Composites Under Mixed-Mode Loading** (83-APM-7)
S. S. Wang and I. Choi

184 **Delamination Buckling and Growth in Laminates** (83-APM-3)
W. J. Bottega and A. Maewal

190 **Experimental Determination of Stresses in Damaged Composites Using an Electric Analogue**
S. B. Batdorf

194 **Quantitative Determination of Stress and Strain Distributions During High Axial Compression of Aluminum With the Aid of Small Ruby Particles**
S. Hoekstra, M. A. Munnig Schmidt-van der Burg, H. Galenkamp, and H. van Wijngaarden

199 **Dynamics of Asymmetric Nonconservative Systems** (83-APM-4)
D. J. Inman

204 **Component Mode Analysis of Nonlinear, Nonconservative Systems** (83-APM-1)
B. H. Tongue and E. H. Dowell

BRIEF NOTES

Stability of Nonparallel Developing Flow in a Pipe to Non-axisymmetric Disturbances — 210
V. K. Garg

Stability Analysis of Systems With Finite Displacements by Means of Extremum Curves — 214
R. Parnes

Nonaxially Symmetric Thermal Stresses in Thick Cylindrical Shells — 217
D. Gamby and H. Bourdillon

Cylindrical Inclusions With Constant Transverse Eigenstrains in an Infinite Elastic Body — 218
Y. Takao

Circumferential Through-Crack in a Cylindrical Shell Under Combined Bending and Tension — 221
J. L. Sanders, Jr.

Deformation of a Thin, Elastic Plate to a Deep Parabolic Cylinder — 221
R. C. Reuter Jr. and R. K. Wilson

224 Dynamic Response of a Pulse-Loaded Ring Immersed in an Acoustic Medium
S. R. Reid and S. R. Hendry

225 On a One-Dimensional Formulation of the Problem of Torsion and Flexure of Shear Deformable Plates
E. Reissner

227 Cumulative Effect at the Soil Surface Due to Shear Wave Propagation
M. Zak

229 A Similarity Solution for a Rayleigh Flow of a Bingham Fluid
N. Phan-Thien

230 On the Stability of Large Discrete Buckling Structures
A. Maher

DISCUSSIONS

233-236 Discussions on previously published papers by **C. H. Wu** (No Closure) **K. J. Chang** (No Closure), and **K. Miza, M. Uesaka,** and **F. C. Moon** (No Closure)

BOOK REVIEWS

237 ***An Introduction to the Theory of Elasticity*** by **R. J. Atkin** and **N. Fox** . . . Reviewed by **C. O. Horgan**

Hot-Wire Anemometry by **A. E. Perry** . . . Reviewed by **P. A. Libby**

ERRATA

238 Erratum on Discussion by **M. Ziv** of **T. C. T. Ting's** "Characteristic Forms of Differential Equations for Wave Propagation in Nonlinear Media," and published in the December, 1982 issue

---

7, 28, 36	Worldwide Mechanics Meeting List
42, 49, 66, 76, 84, 94	Applied Mechanics Symposium Proceedings
122, 148, 156, 164, 178, 189	Applied Mechanics Symposium Proceedings
183	Announcement – Standard International Units
108	Special Notice – Mandatory Excess Page Charge for Transactions
56	Change of Address Form
23	ASME Applied Mechanics Division Committee on Computing in Applied Mechanics sponsors symposia

Downloaded 04 May 2010 to 171.66.16.34. Redistribution subject to ASME license or copyright; see http://www.asme.org/terms/Terms_Use.cfm

Diffusive, Electrostatic, and Gravitational Deposition of Suspensions in the Entrance of a Nozzle

T. A. Korjack
Philadelphia Electric Company,
Energy Conversion Research Section,
2301 Market Street,
Philadelphia, Pa. 19113
Assoc. Mem. ASME

An analytical investigation of the mechanics of deposition affected by gravity, electrostatic charge, and Brownian motion in an effuser from the nozzle inlet to a distance where incompressible effects are still valid has been made and a mathematical model developed for the deposition process. The analysis was restricted to laminar flow of dilute, nonreactive suspensions contained within an incompressible, viscous carrier. The results show that increasing the nozzle angle causes a decrease in deposition rate regardless of the diffusive Peclet number and gravity flow parameter. Furthermore, an increase in gravity field causes an increase in bottom deposition rate and decrease in top deposition rate.

Introduction

The mechanics of deposition rates have been dealt with by numerous investigators, particularly concerning parallel channels, tubes, or rectangular enclosures. Most of the studies have been for uniform and fully developed suspension flows. More recently, Eldighidy, et al. [1] treated the deposition process for laminar-developing electrostatic flow in both a parallel plate and diffuser configuration. Also, Chen [2] has treated the developing laminar-flow case of a parallel channel by the integral method. Chua et al. [3] and Yu et al. [4] treated the precipitation and deposition of submicron particles in human lung airways where simulated varying geometrical boundaries were considered under laminar-flow conditions. Chen and Korjack [5] analyzed the flow conditions and contamination effects under field forces of diffusers where separation of the boundary layer was considered. Since laminar suspension flows in nozzles or effusers do exist in biological systems, industrial scrubbers and cyclones, and in fluidic devices (especially in fluidic aerosol amplifiers (Comparin et al. [6])), more information is required for adequate evaluations, amplifier performances and designs, and assessments of respiratory-related afflictions. However, the case of a laminar-developing suspension flow in a nozzle has not been investigated to date. Thus, the purpose of this paper is to formulate and solve numerically the deposition of suspensions in laminar flow in the entrance of a two-dimensional straight wall nozzle where electrostatic and gravitational influences are significant. The suspension nozzle flow is considered at conditions under which a finite layer of particles is deposited at the nozzle walls due to diffusion, gravity, electrostatic charge, and wall adhesion. The electrostatic charge is generated by the collision among the solid particles themselves and also by the collision among the solid particles and the duct wall prior to their entrance into the channel. We shall treat only the case of a single species of monodispersed suspension of spherical particles of radius "a." Also, the case of a dilute suspension, $\rho_p/\rho << 1$, will be considered such that the particles have no effect on the fluid phase. Furthermore, it will be assumed that the thickness of the layer of deposit is much smaller than the channel width so that the effective reduction in channel width is not enough to appreciably change the fluid velocity distribution.

It must be noted that this investigation considers the suspension of solid particles in a gas only (air being the case) under subsonic, isothermal conditions.

Formulation

In this analysis, a rectangular Cartesian coordinate system is selected in such a way that the x-axis is the center line of the nozzle initiating from the inlet and following the direction of flow while the y-axis is normal or transverse to the flow direction (see Fig. 1). Since an incompressible carrier is assumed, the analyis will treat the flow phenomena from the inlet plane to an axial distance where the gap width is half the inlet gap width beyond which compressible effects must be considered. The discussion that ensues will consider the case of particles (suspended in an incompressible medium) each of mass "m" carrying charge "q" moving between grounded effuser plates. Hence, for incompressible, steady, two-dimensional flow of a dilute suspension, the governing equations subject to the usual boundary equations take the form (Soo [7]):

Contributed by the Applied Mechanics Division for publication in the JOURNAL OF APPLIED MECHANICS.
Discussion on this paper should be addressed to the Editorial Department, ASME, United Engineering Center, 345 East 47th Street, New York, N.Y. 10017, and will be accepted until two months after final publication of the paper itself in the JOURNAL OF APPLIED MECHANICS. Manuscript received by ASME Applied Mechanics Division, January 1981; final revision, June, 1982.

Copyright © 1983 by ASME
Downloaded 02 May 2010 to 171.66.16.246. Redistribution subject to ASME license or copyright; see http://www.asme.org/terms/Terms_Use.cfm

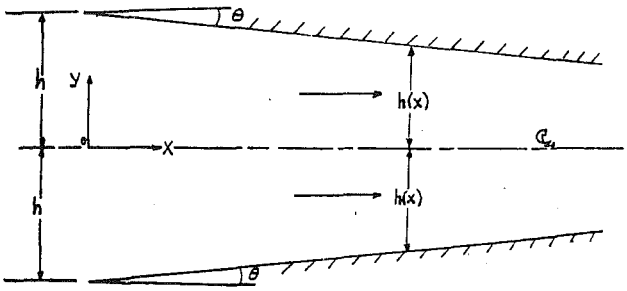

Fig. 1 Nozzle flow configuration

(a) Fluid Phase.

$$\frac{\partial u}{\partial x}+\frac{\partial v}{\partial y}=0 \tag{1}$$

$$u\frac{\partial u}{\partial x}+v\frac{\partial u}{\partial y}=-\frac{1}{\rho}\frac{dp}{dx}+\nu\frac{\partial^2 u}{\partial y^2} \tag{2}$$

The continuity equation (1) can also be expressed in integral form as:

$$\int_{-h(x)}^{h(x)} u dy=2.\ u_0\ h(x) \tag{3}$$

(b) Particulate Phase.

$$u\frac{\partial \rho_p}{\partial x}+v\frac{\partial \rho_p}{\partial y}=\frac{\partial}{\partial y}\left(\frac{q}{m_p}\frac{\rho_p}{F}\frac{\partial w}{\partial y}\right)+\frac{\partial}{\partial y}\left(D_p\frac{\partial \rho_p}{\partial y}+\frac{\rho_{pg}}{F}\right) \tag{4}$$

$$u_p\frac{\partial u_p}{\partial x}+v_p\frac{\partial u_p}{\partial y}=F\ (u-u_p)+\frac{D_p}{\rho_p}\frac{\partial}{\partial y}\left(\rho_p\frac{\partial u_p}{\partial y}\right) \tag{5}$$

$$u_p\frac{\partial v_p}{\partial x}+v_p\frac{\partial v}{\partial y}=F\ (v-v_p)-\left(\frac{g}{m_p}\right)\frac{\partial w}{\partial y}-g \tag{6}$$

$$\frac{\partial^2 w}{\partial y^2}=-\frac{\rho_p}{\epsilon_0}\frac{q}{m_p} \tag{7}$$

where $F=9\mu/2a\bar{\rho}_p$ for spherical particles in the Stokes' range, and w is the vertical component of the electrostatic potential. In these equations, the subscript p denotes properties of the particle phase. Equations (1) and (2) are simply the Prandtl boundary layer equations subject to the usual conditions as explained by Schlichting [8].

Equation (4) is the diffusion equation including the gravity and electric charge effect; it has been derived in a way done similarly by Stukel [9]. Equations (5) and (6) are the momentum particle equations for the axial and normal directions, respectively. The terms on the left-hand side account for the inertial effects; the first term on the right-hand side considers the momentum transfer between the fluid and the particle; the second part of equation (5) accounts for axial particle diffusivity, and the second and third terms of Fig. 6 accounts for electrostatic and gravitational effects, respectively.

The electrostatic potential, w, can be related to the electrostatic charge intensity, E, by the fundamental relation, $E=\partial w/\partial y$. Equation (7) is the Poisson equation neglecting the axial term and can also be expressed in terms of the electric field intensity as,

$$\frac{\partial E}{\partial y}=\frac{\rho_p}{\epsilon_0}\frac{q}{m_p} \tag{8}$$

The purpose of solving these equations is to determine the rate of deposition of the solid particles on both the bottom and top walls of the nozzle, which can be obtained from the consideration of conservation of mass of the particle phase as follows:

$$-\frac{\partial}{\partial x}\int_{-h(x)}^{h(x)}\rho_p\ u_p\ dy=[\sigma\ v_p\ \rho_p+\sigma_w f_w\ \rho_p/F]_{y=h(x)}+[\sigma_w f_w\ \rho_p/F-\sigma\ v_p\ \rho_p]_{y=-h(x)} \tag{9}$$

where the term,

$$-\frac{\partial}{\partial x}\int_{-h(x)}^{h(x)}\rho_p\ u_p\ dy$$

represents the total deposition rate; the first term on the right-hand side of equation (9) represents the deposition rate on the top wall and the second term represents the deposition rate on the bottom wall. Also, σ is the probability that the particles falling toward the wall will stick to the wall and σ_w is the sticking probability that accounts for the adhesive forces at the wall, f_w. The term $(\sigma\rho_p v_p)$ is the rate of deposition of particles per unit area due to electric charge; the term $(\sigma_w\ \rho_p f_w)$ is the rate of deposition of particles per unit area due to the surface adhesion which depends on material and surface properties.

The governing equations can be nondimensionalized as follows:

(a) Fluid Phase.

$$\frac{\partial U}{\partial X}+\frac{\partial V}{\partial Y}=0 \tag{10}$$

$$U\frac{\partial U}{\partial X}+V\frac{\partial U}{\partial Y}=-\frac{dP}{dX}+\frac{1}{N_R}\frac{\partial^2 U}{\partial Y^2} \tag{11}$$

$$\int_{-H^*}^{H^*} U\ dY=2\ H^* \tag{12}$$

(b) Particle Phase.

$$N_\beta\left[U\frac{\partial R}{\partial X}+V\frac{\partial R}{\partial Y}\right]=\frac{\partial^2 R}{\partial Y^2}+\frac{\partial R}{\partial Y}\frac{\partial W^*}{\partial Y}-4\ N_\alpha\ R^2+N_\eta\frac{\partial R}{\partial Y} \tag{13}$$

$$U_p\frac{\partial U_p}{\partial X}+V_p\frac{\partial U_p}{\partial Y}=\frac{1}{N_m}(U-U_p)+\frac{1}{N_\beta R}\frac{\partial}{\partial Y}\left(R\frac{\partial U_p}{\partial Y}\right) \tag{14}$$

$$U_p\frac{\partial V_p}{\partial x}+V_p\frac{\partial V_p}{\partial Y}=\frac{1}{N_m}(V-V_p)-\frac{1}{N_\beta N_m}\frac{\partial W^*}{\partial Y}-\frac{N_\eta}{N_\beta N_m} \tag{15}$$

$$\frac{\partial^2 W^*}{\partial Y^2}=-4\ N_\alpha\ R \tag{16}$$

$$\dot{M}^*=\underbrace{\{R\ [\sigma\ V_p+N_s/N_\beta]\}}_{\text{top wall}}+\underbrace{\{R\ [N_s/N_\beta-\sigma\ V_p]\}}_{\text{bottom wall}} \tag{17}$$

where a = radius of a particle; D_p = particle diffusivity; E = electric field intensity; E^* = dimensionless electric field intensity; f_w = adhesive force per unit mass of particles at the wall; F = inverse of relaxation time for momentum transfer; g = local acceleration of gravity; h = half the nozzle width; $h(x)$ = half the nozzle width for $x>0$; H^* = dimensionless half nozzle width; K_{np} = particle Knudsen number; L_p = fluid-particle interaction length; m_p = mass of a particle; $\dot{M}^*$ = dimensionless rate of deposition of particles; N_m = momentum transfer number (Stokes number); N_R = Reynolds number; N_s = surface adhesion parameter; p = fluid static pressure; P = dimensionless static pressure; q = electric charge per particle; R = dimensionless density of

Downloaded 02 May 2010 to 171.66.16.246. Redistribution subject to ASME license or copyright; see http://www.asme.org/terms/Terms_Use.cfm

particle cloud; u,v = axial and vertical components of fluid velocity; u_p,v_p = axial and vertical components of particle velocity; u_0 = uniform inlet velocity of fluid and particles; U,V = dimensionless axial and vertical components of fluid velocity; U_p,V_p = dimensionless axial and vertical components of particle velocities; w = electric field potential; W^* = dimensionless electric field potential; x,y = axial and vertical coordinates, respectively; X,Y = dimensionless coordinates, $X = x/h$, $Y=y/h$; θ = half the nozzle angle; Y^* = dimensionless distance, $Y/(1+X \text{ Tan } \Theta)$; N_α = electrostatic charge parameter; N_β = diffusive Peclet number; ϵ_0 = permitivity of free space; N_η = gravity flow parameter; N_λ = adhesive force parameter; $N_s = \sigma_w N_\lambda$ (surface adhesion parameter); μ = dynamic viscosity of fluid; ν = kinematic viscosity of fluid; ρ = density of fluid; ρ_p = density of particle cloud (concentration); $\tilde{\rho}_p$ = density of the material constituting the particle phase; ρ_{p0} = uniform inlet particle density; σ = sticking probability accounts for electrical and viscous forces; σ_s = distance correction factor; σ_w = sticking probability accounts for adhesive forces at the wall; and the subscript 0 denotes uniform inlet conditions.

When suspended solid particles enter a nozzle, only a fraction of these particles will be deposited on the walls. Let this fractional deposition for any given axial length of nozzle, X, be denoted by,

$$1-\frac{1}{2}\int_{-H^*}^{H^*} R\ U_p\ dY$$

The expression $1/2\int_{-H^*}^{H^*} R\ U_p\ dY$ represents the fraction of solid particles penetrating or leaving a given section of the nozzle. As depicted in Fig. 1, the width of the nozzle is $2h(x)$, the centerline is at $y = 0$, the lower wall at $y = -h(x)$, and the upper wall at $y = h(x)$. The particle velocity at each wall is, as in the case of rarefied gas flow, proportional to the velocity gradient at each wall (Stukel [9]),

$$u_p\Big|_{y=-h(x)} = L_p \frac{\partial u}{\partial y}\Big|_{y=-h(x)}$$

$$u_p\Big|_{y=h(x)} = -L_p \frac{\partial u}{\partial y}\Big|_{y=h(x)} \tag{17}$$

when the flow is laminar, L_p is the mean free path over which a particle changes its direction. When a particle phase moving at a uniform velocity u_0 enters a nozzle, particles on the walls will travel a distance u_0/F before they are retarded to a finite slip velocity as in equation (17).

For a gaseous system, when the mean free path of collision between the trace component and the principal component is large, the trace component may behave like a rarefied gas even if the principal component does not. Likewise, for a particulate suspension where the interaction length L_p of particles with fluid due to Brownian motion, wall interaction, and wake effects is large (for large particle radius) compared to X, we have a slip condition plus a finite interaction length as defined by Soo [10]. Hence, the boundary conditions for u_p at each wall are:

For $y=-h(x)$, (lower wall)

$$U_p = \sigma_s\ u_0(1-xF/u_0) + L_p \frac{\partial U_p}{\partial y}\Big|_{y=-h(x)} \quad \text{for } x < u_0/F \tag{18}$$

and

$$U_p = L_p \frac{\partial U_p}{\partial y}\Big|_{y=-h(x)} \quad \text{for } x \geq u_0/F$$

For $y=+h(x)$, (upper wall)

$$u_p = \sigma_s\ u_0(1-xF/u_0) - L_p \frac{\partial U_p}{\partial y}\Big|_{y=h(x)} \quad \text{for } x < u_0/F$$

and

$$u_p = -L_p \frac{\partial u_p}{\partial y}\Big|_{y=h(x)} \quad \text{for } x \geq u_0/F \tag{19}$$

Based on equation (4), (5), and (8), the following boundary conditions for the particle cloud density gradient at the wall are:

$$D_p \frac{\partial \rho_p}{\partial y}\Big|_{y=-h(x)} = \left(-\sigma v_p\ \rho_p + \frac{\sigma_w f_w\ \rho_p}{F} - \left(\frac{q}{m_p}\right)\frac{\rho_p}{F}\frac{\partial W}{\partial y} - \frac{g\rho_p}{F}\right)_{y=-h(x)} \tag{20}$$

$$D_p \frac{\partial \rho_p}{\partial y}\Big|_{y=h(x)} = -\left(\sigma v_{pp} + \frac{\sigma_w f_w \rho_p}{F} + \frac{q}{m_p}\frac{\rho_p}{F}\frac{\partial W}{\partial y} + \frac{g\rho_p}{F}\right)_{y=h(x)} \tag{21}$$

Equations (20) and (21) are based on the equation of conversation of mass of the particle phase. They have been obtained by direct integration of the diffusion equation taking into account Leibnitz's rule (see Eldighidy [1] and Soo [11]).

The boundary conditions can be nondimensionalized as follows:

At $X=0$ (nozzle inlet)
$U=U_p=R=1$ uniform
$V=V_p=W^*=0$
$P=0$

At $Y=-H^*$ (at the lower wall for $x > 0$)
$U=V=0$ no slip condition

$$U_p = \sigma_s(1-X/N_m) + K_{np}\frac{\partial U_p}{\partial Y} \quad \text{for } x < N_m$$

$W^*=0$

and

$$U_p = K_{np}\frac{\partial U_p}{\partial Y} \quad \text{for } X \geq N_m$$

$$\frac{\partial R}{\partial Y} = -R\left(\frac{\partial W^*}{\partial Y} + \sigma N_\beta\ V_p - N_s + N_\eta\right)$$

At $Y=H^*$ (at the upper wall for $x>0$)
$U=V=0$ no slip condition
$W^*=0$

$$U_p = \sigma_s\ (1-X/N_m) - K_{np}\frac{\partial U_p}{\partial Y} \quad \text{for } x < N_m$$

and

$$U_p = K_{np}\frac{\partial U_p}{\partial Y} \quad \text{for } X \geq N_m$$

$$\frac{\partial R}{\partial Y} = -R\left(\frac{\partial W^*}{\partial Y} + \sigma N_\beta\ V_p + N_s + N_\eta\right)$$

The equations for the particle phase can be written in the implicit finite difference form using the spatial coordinates as shown in Fig. 1. By the consideration of the Eulerian frame of reference, the governing particle phase equations are thus expressed as:

$$U_{i+1,K}\frac{\Delta Y_{i+1}R_{i+1,K} - \Delta Y_i\ R_{i,K}}{\Delta X} + V_{i+1,K}\frac{R_{i+1,K+1} - R_{i+1,K-1}}{2.0} = \frac{R_{i+1,K+1} - 2\ R_{i+1,K} + R_{i+1,K-1}}{N_\beta\ \Delta Y_{i+1}} \frac{(R_{i+1,K+1} - R_{i+1,K-1})(W^*_{i,K+1} - W^*_{i,K-1})}{4\ N_\beta\ \Delta Y_{i+1}}$$

Downloaded 02 May 2010 to 171.66.16.246. Redistribution subject to ASME license or copyright; see http://www.asme.org/terms/Terms_Use.cfm

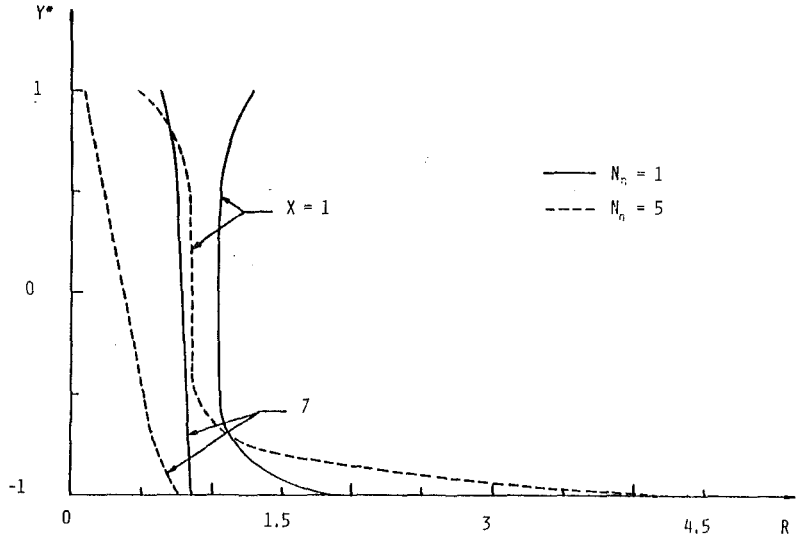

Fig. 2 Gravity effect on the axial distribution of the particle concentration ($k_{\eta p} = 0.0001$, $N_\alpha = 1$, $f\Theta = -4$ deg, $N_\beta = 40$, $N_m = 2$, $N_s = 1$, $N_R = 1000$, $\sigma = 0.5$)

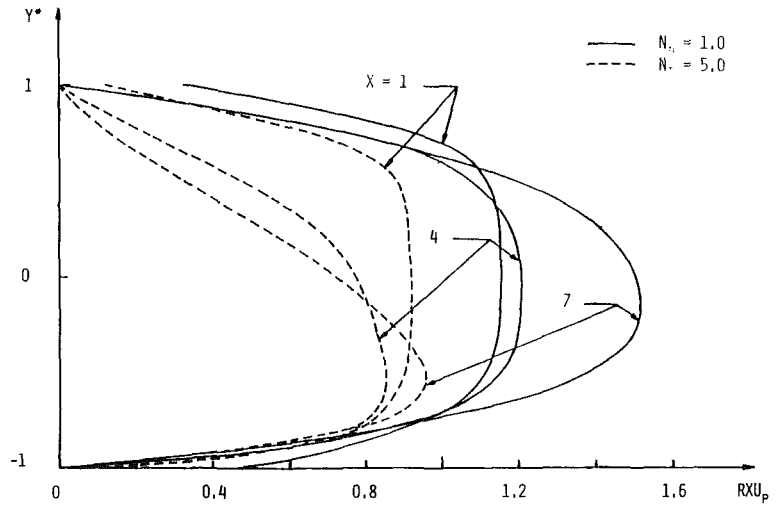

Fig. 3 Mass flux distribution with gravitational effects ($K_{\eta p} = 0.0001$, $N_\alpha = 1$, $\Theta = -4$ deg, $N_\beta = 40$, $N_m = 2$, $N_s = 1$, $N_R = 1000$, $\sigma = 0.5$)

$$- \frac{4\, N_\alpha\, \Delta Y_{i+1}\, R_{i,K}\, R_{i+1,K}}{N_\beta}$$

$$+ \frac{N_\alpha\, R_{i+1,K+1} - R_{i+1,K-1}}{N_\beta \quad 2.0} \tag{27}$$

$$U_{pi,K} \frac{\Delta Y_{i+1} U_{pi+1,K} - \Delta Y_i\, U_{pi,K}}{\Delta X}$$

$$+ V_{pi,K} \frac{U_{pi+1,K+1} - U_{pi,K}}{2}$$

$$= \frac{\Delta Y_{i+1}}{N_m} (U_{i+1,K} - U_{pi+1,K})$$

$$+ \frac{U_{pi+1,K+1} - 2\, U_{pi+1,K} + U_{pi+1,K-1}}{N_\beta\, \Delta Y_{i+1}}$$

$$+ \frac{(R_{i,K+1} - R_{i,K-1})(U_{pi+1,K+1} - U_{pi+1,K-1}}{4\, N_\beta\, \Delta Y_{i+1} R_{i,K}} \tag{28}$$

$$U_{Pi,K} \frac{\Delta Y_{i+1} V_{Pi+1,K} - \Delta Y_i\, V_{Pi,k}}{\Delta X}$$

$$+ V_{Pi,K} (V_{Pi+1,K+1} - V_{Pi+1,K})$$

$$= \frac{\Delta Y_{i+1}}{N_m} (V_{i+1,K} - V_{Pi+1,K})$$

$$- \frac{W^*_{i+1,K+1} - W^*_{i+1,K-1}}{2N_\beta\, N_m} - \frac{\Delta Y_{i+1}\, N_\eta}{N_\beta\, N_m} \tag{29}$$

$$\frac{W^*_{i+1,K+1} - 2W^*_{i+1,K} + W^*_{i+1,K-1}}{(\Delta Y_{i+1})} = -4\, N_\alpha\, R_{i+1,K} \tag{30}$$

The fluid phase equations can also be written in a similar fashion. It must be noted that the flow field was divided into converging grids of mathematical molecules. The implicit-hybrid, finite difference expressions took into consideration the variation of the vertical grid, Δ, with axial increment. A trapezoidal mesh was superimposed on the entire flow field internal to the nozzle. The flow field was discretized into 21 mesh points in the normal direction and up to 141 mesh points in the axial direction. The increments in the X-direction varied as 0.001, 0.1 while ΔY varied according to the nozzle angle (2Θ). Different values for Θ were chosen, in particular, $\Theta = -2, -4, -7.5, -9, -10$ deg. The sparse and unsymmetric matrix equation resulting from the finite difference ex-

Downloaded 02 May 2010 to 171.66.16.246. Redistribution subject to ASME license or copyright; see http://www.asme.org/terms/Terms_Use.cfm

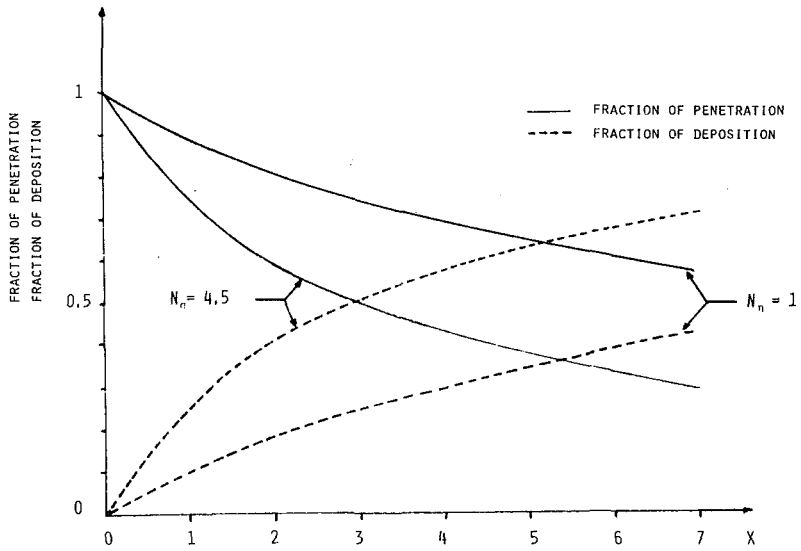

Fig. 4 Influence of the gravity parameter on the axial distribution of the fraction of penetration ($K_{\eta p} = 0.0001$, $N_\alpha = 1$, $\Theta = -4$ deg, $N_\beta = 40$, $N_m = 2$, $N_s = 1$, $N_R = 1000$, $\sigma = 0.5$)

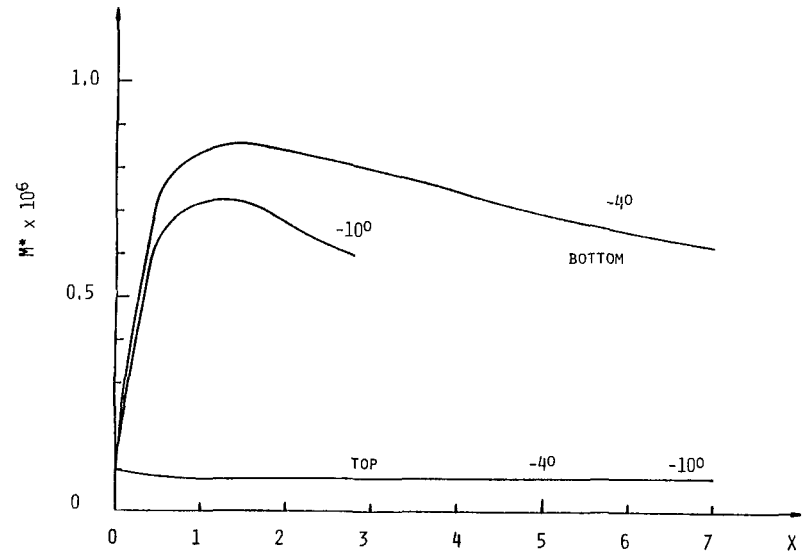

Fig. 5 Effect of nozzle angle with high diffusive peclet number on deposition rate ($K_{\eta p} = 0.0001$, $N_\alpha = 1$, $N_n = 5$, $N_\beta = 10^7$, $N_m = 2$, $N_s = 1$, $N_R = 1000$, $\sigma = 0.5$)

pressions was solved by Gaussian elimination with partial pivoting with the aid of the Crout reduction technique. Considering all variations of parameters and mesh sizes utilized in this analysis, the general condition of stability given by Quarmby [12] was completely satisfied. Hence, for all mesh sizes and angles utilized in the analysis, convergence was achieved and an accuracy of four significant figures was realized in the computations. All numerical calculations were performed on an IBM 370 digital computer.

Results and Discussion

Figure 2 illustrates the influence of the gravity parameter, N_η, on the vertical distribution of the particulate concentration, R. At $X = 1$, the higher gravity flow causes the particles to collect toward the bottom wall enabling the particle density to achieve very high values adjacent to the bottom wall itself. However, at $X = 7$, the particulate profile is much less for the high gravity flow because most of the particles have already collected on the walls of the nozzle due to electrostatic charge and, of course, gravity.

Figure 3 shows the effect of the gravity flow parameter on the vertical distribution of the mass flux of solid particles. The gravity effect is clearly discerned by the diminished magnitude of the mass flux profile for the higher gravity flow, evidencing again that a great deal of the particles are depositing on the walls not only due to gravity, but also due to electrostatic charge.

Figure 4 illustrates the gravity parameter effect on the axial distribution of the fraction of penetration or inversely, the fraction of deposition. Clearly, the higher the gravity field, the lower the penetration implying that the deposition is increased. However, as the nozzle angle increases (figure not shown) the penetration increases causing a decrease in deposition which essentially shows that deposition decreases with increasing favorable pressure fields under the influence

Downloaded 02 May 2010 to 171.66.16.246. Redistribution subject to ASME license or copyright; see http://www.asme.org/terms/Terms_Use.cfm

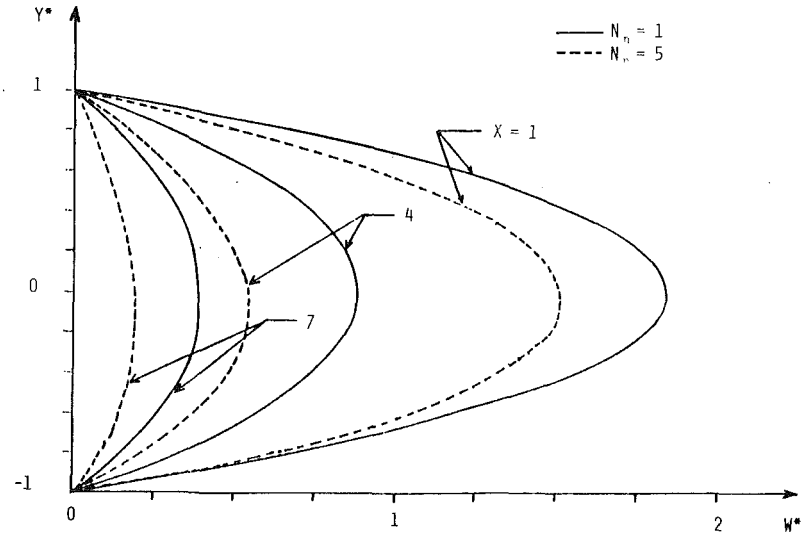

Fig. 6 Gravity effect of axial distribution of electrostatic charge potential ($K_{\eta p} = 0.00001$, $N_\alpha = 1$, $\Theta = -4$ deg, $N_\beta = 40$, $N_m = 2$, $N_S = 1$, $N_R = 1000$, $\sigma = 0.5$)

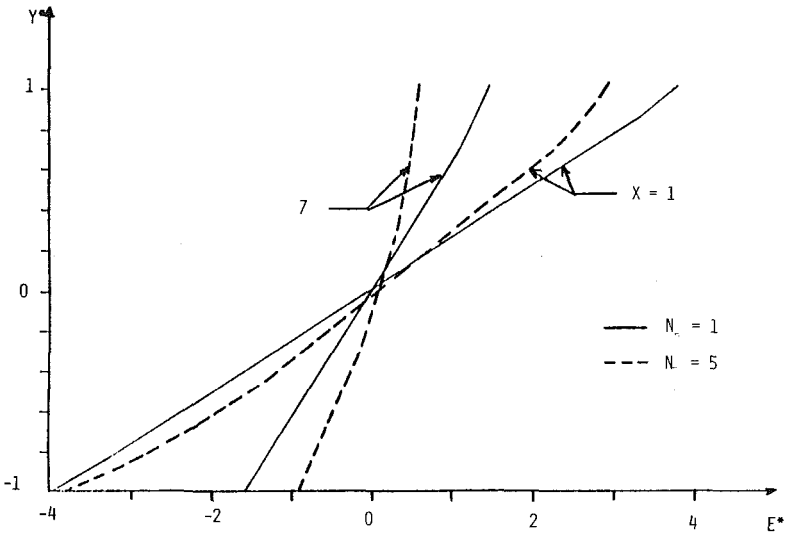

Fig. 7 Gravity effect of axial distribution of electrostatic charge intensity ($K_{\eta p} = 0.0001$, $N_\alpha = 1$, $\Theta = -4$ deg, $N_\beta = 40$, $N_m = 2$, $N_S = 1$, $N_R = 1000$, $\sigma = 0.5$)

of both gravity and electrostatic charge.

Figure 5 illustrates the effect of the nozzle angle on the top and bottom deposition rates for the case when the diffusive Peclet number is very high (shown $N_\beta = 10^7$). Again, as can be readily seen, the increase in nozzle angle causes a decrease in deposition rate particularly for the bottom rate of deposition. However, the top deposition rate difference is almost negligible due to gravity.

Figure 6 shows the axial distribution of the electrostatic potential, W^*, with gravity effect. Since the higher gravity flow causes more particles to be deposited as they travel in the positive axial direction, less particles exist in the downstream flow thereby inhibiting large electrostatic potentials. This is also witnessed when examining the axial distribution of the electrostatic intensity, E^*, in Fig. 7. Here also the intensity of the electrostatic charge of the solid particles is also diminished for the high gravity field since most of the particles are simply not present in the flow field for large axial distances.

Although not shown, the effects of increasing the Stokes number at a given particle Peclet number and given gravitational and electrostatic conditions caused an increase of deposition rate in entrance regions of $X \leq 2.5$; when gravity or electrostatic conditions increased, so did the deposition rates within the same axial interval.

Conclusions

The nozzle angle has a considerable effect on the rate of deposition of the solid particles. As the angle of convergence is increased, the rate of deposition decreases regardless of whether $N_\beta = 40$ or 10^7. The gravity flow parameter increases the bottom deposition rate and decreases the top deposition rate in the presence of an electrostatic field for all angles investigated.

The present study provides a basic understanding of the complicated flow fields existing in a monodispersed suspension flow under field forces and a straightforward procedure for a complete analysis of the effuser-nozzle channel flows. In summary, this study shows that with dilute particulate suspensions, a seemingly complicated two-phase solid-gas flow problem can be completely solved with relatively few approximations by means of a hybrid-implicit numerical technique in an efficient manner. The method can be applied to many other two-phase flow problems with great

Downloaded 02 May 2010 to 171.66.16.246. Redistribution subject to ASME license or copyright; see http://www.asme.org/terms/Terms_Use.cfm

ease to expedite unwieldly problems. An attempt is also currently being developed to formulate an experimental simulation of the aforementioned physical conditions contained in this paper, possibly to be published in a future work. It is hoped that reasonable correlation will ensue based on the works and experiments of Chen [2] and Comparin [6].

References

1 Eldighidy, S. M., Chen, R. Y., and Comparin, R. A., "Deposition of Suspensions in the Entrance of a Channel," ASME *Journal of Fluids Engineering*, June 1977.

2 Chen, R. Y., "Diffusive Deposition of Particles in a Short Channel," *Power Technology*, Vol. 16, 1977, pp. 131–135.

3 Chua, J. H., and Wang, C. S., "Deposition of Submicron Particles From Steady Flows," *J. Res. Assoc. Power Tech.*, Vol. 9, 1972, pp. 37–45.

4 Yu, C. P., and Chandra, K., "Precipitation of Submicron Charged Particles in Human Lungs," *Bulletin of Mathematical Biology*, Vol. 39, 1977, pp. 396–402.

5 Chen, R. Y., and Korjack, T. A., "Deposition of Suspensions in the Entrance of a Diffuser—Electrostatic and Gravitational Effects," *Computers and Fluids*, Vol. 7, 1979, pp. 295–304.

6 Comparin, R. A., Moses, H. L., and Rowell, E., "Contamination Effects in a Laminar Proportional Amplifier," Harry Diamond Laboratories, Report No. HDL-TR-175-1, June 1974.

7 Soo, S. L., *Fluid Dynamics of Multiphase Systems*, Blaisdell Publishing Co., Waltham, Mass., 1967.

8 Schlichting, H., *Boundary Layer Theory*, 6th Ed., McGraw-Hill, New York, 1968.

9 Stukel, J. J., and Soo, S. L., "Turbulent Flow of a Suspension into a Channel," *Power Technology*, Vol. 2, 1969, pp. 278–280.

10 Soo, S. L., "Non-Equilibrium Fluid Dynamics," *J. Appl. Math. Phys.*, Vol. 19, 1968, pp. 545–63.

11 Soo, S. L., and Tung, S. K., "Deposition and Entrainment in Pipe Flow of a Suspension," *Powder Technology*, Vol. 6, 1972, pp. 283–294.

12 Quarmby, A., "A Finite Difference Analysis of Developing Slip Flow," *Appl. Sci. Res.*, 1968, pp. 18–33.

Downloaded 02 May 2010 to 171.66.16.246. Redistribution subject to ASME license or copyright; see http://www.asme.org/terms/Terms_Use.cfm

Unified Approach to the Solution of Problems of Unsteady Laminar Flow in Long Pipes

M. F. Letelier S.
Departamento de Ingeniería Mecánica
Universidad de Santiago de Chile,
Casilla 10233,
Santiago, Chile

H. J. Leutheusser
Department of Mechanical Engineering,
University of Toronto,
Toronto, Ontario,
M5S 1A4, Canada

The paper presents a unified approach to the solution of laminar pipe-flow transients in which the forcing function may depend on the motion itself. The key to the solution procedure is a power series expansion of the local velocity in terms of radial position, involving a single time-dependent coefficient. The method of analysis is applied to the solution of two particular cases of transients, namely flow establishment, without and with inflow, respectively. It is found to yield results that are in excellent agreement with other known analytical solutions and experimental observations.

Introduction

There exists a large number of technically important cases of laminar pipe-flow transients of the surge variety [1] which are amenable to a unified analytical treatment. Problems in this group, some of which are depicted in Fig. 1, include such disparate situations as flow starting from rest [2], steady-periodic fluid motion [3], and *U*-tube oscillations [4].

Several methods of analysis have been employed in the past to treat these phenomena. These include Laplace transforms [5, 6], Fourier analysis [2], and separation of variables [2–4]. However, the classical analytical methods, while expedient for solving some specific problems (especially when the pressure gradient is explicitly time-dependent), do not offer a convenient one-dimensional approach which would be useful in the analysis of the two categories of flows which are defined in the following. Thus, it is one of the main objectives of this paper to introduce a new one-dimensional model of laminar pipe-flow transients.

CASE	FLOW SYSTEM	FORCING FUNCTION	SOLUTION	PROBLEM CLASS
1.	Flow Establishment	ϕ = constant	F. J. Szymanski 1932 Ref. 2	A $\phi=\phi(t)$
2.	Forced Oscill.Flow	$\phi = k \cos \omega t$	T. Sexl 1930 Ref. 3	
3.	Free Oscill. Flow	$\phi=\alpha_1+\alpha_2\iint u r dr dt$	C. Clarion and R.Pellisier 1975 Ref. 4	B $\phi=\phi\{u(t),t\}$
4.	q = constant Fl.Est. with Inflow	$\phi=\beta_1+\beta_2 t+\beta_3\iint u r dr dt$	(this paper)	
5.	One-armed U-tube	$\phi=\frac{\gamma_1+\gamma_2\iint u r dr dt}{\gamma_3+\gamma_4\iint u r dr dt}$		

Fig. 1 Examples of pipe-flow transients

Governing Equations

Except for the nonuniform region of flow development at the entrance, laminar flow of an incompressible Newtonian fluid in long circular pipes is wholly parallel and described by the linear forms of the Navier-Stokes and continuity equations; i.e., in cylindrical coordinates,

$$-\frac{1}{\rho}\frac{\partial P}{\partial x}=\phi=\frac{\partial u}{\partial t}-\nu\left(\frac{\partial^2 u}{\partial r^2}+\frac{1}{r}\frac{\partial u}{\partial r}\right) \tag{1}$$

$$-\frac{1}{\rho}\frac{\partial P}{\partial r}=0 \tag{2}$$

$$\frac{\partial u}{\partial x}=0 \tag{3}$$

where $u(a,t)=0$ is the no-slip boundary condition, $P=p+\rho gz$ denotes the piezometric pressure, and $\phi=\phi(t)$ represents the forcing function of the system. Furthermore, p = fluid pressure; u = local axial velocity; x,r,z = length coordinates in the axial, radial, and vertical directions, respectively; a = pipe radius; t = time; ρ = density; $\nu=\mu/\rho$ = kinematic viscosity; μ = dynamic viscosity; and g = acceleration due to gravity.

The equivalent one-dimensional forms of equations (1) and (3), preferred for engineering calculations, are obtained by averaging the equations over the cross section of the circular pipe of diameter $D=2a$ with the aid of the operator

$$\frac{2}{a^2}\int_0^a (\ldots)\, r\, dr \tag{4}$$

This process yields, respectively, for continuity

$$\frac{dU}{dx}=0 \tag{5}$$

Contributed by the Applied Mechanics Division for presentation at the 1983 ASME Applied Mechanics, Bioengineering, and Fluids Engineering Conference, Houston, Texas, June 20–22, 1983 of THE AMERICAN SOCIETY OF MECHANICAL ENGINEERS.

Discussion on this paper should be addressed to the Editorial Department, ASME, United Engineering Center, 345 East 47th Street, New York, N.Y. 10017, and will be accepted until two months after final publication of the paper itself in the JOURNAL OF APPLIED MECHANICS. Manuscript received by ASME Applied Mechanics Division, July, 1981; final revision, June, 1982. Paper No. 83-APM-2.

Copies will be available until February, 1984.

Copyright © 1983 by ASME
Downloaded 02 May 2010 to 171.66.16.246. Redistribution subject to ASME license or copyright; see http://www.asme.org/terms/Terms_Use.cfm

and for momentum

$$\phi = \frac{dU}{dt} + 4\,\frac{\tau_a}{\rho D} \tag{6}$$

in which, at any instant,

$$\tau_a = -\mu\left(\frac{\partial u}{\partial r}\right)_{r=a} = \frac{f}{4}\,\rho\,\frac{U^2}{2} \tag{7}$$

denotes the wall shear stress; U = average velocity; and f = Darcy-Weisbach friction coefficient.

Classification of Problems

The nature of the forcing function depends on the circumstances of the problem under consideration. A few typical examples, arranged vertically downward in increasing order of mathematical complexity, are schematically presented in Fig. 1. The reservoirs appearing in some of the examples are head tanks in which the motion, if any, is so slow that inertial and friction effects are negligible, and the pressure distribution in the vertical is hydrostatic; i.e., at any instant inside the tank P = constant holds.

Two classes of problems may be distinguished. First, if the elevations z of the end points of the inertially active fluid column (or the corresponding head tanks) are fixed, the length of the fluid column is also fixed and the motion is entirely controlled by an externally impressed difference in fluid pressure. Thus, in this case

$$\textbf{Class } A. \quad \phi = \phi(t). \tag{8}$$

Examples of this class of problems include the case of flow establishment, i.e., pipe flow starting from rest following the sudden opening of a downstream valve, and tending toward the steady-state; and forced oscillatory motion under the influence of a reciprocating piston (cf. Fig. 1, cases 1 and 2).

In the second, and larger class of problems, the forcing function depends on the motion itself. For instance, in the relevant examples, cases 3–5, the elevations of one or both of the column end points (or their corresponding head tanks) are not fixed, and the longitudinal extent of the inertially active fluid column may, or may not be constant. In any case, if either of these lengths is varying with time it can be expressed in terms of a time integral over the instantaneous column velocity, viz,

$$2\int_0^t \int_0^a ur\,dr\,dt' = a^2 \int_0^t U\,dt'$$

This, then, gives rise to the particular forms of the forcing functions indicated in Fig. 1 for free oscillatory flow, flow establishment with constant inflow, and motion in a one-armed U-tube, respectively.

There are many other ways in which the motion can effect the forcing function. However, in all such cases the interdependence can be expressed in terms of the instantaneous column velocity. Thus, generally, for forcing functions that depend on the motion itself, there holds

$$\textbf{Class } B. \quad \phi = \phi\{U(t),\ t\}. \tag{9}$$

It may be noted that for transient problems of this class the mathematics can become rather involved. For instance, with a functional relation between ϕ and $U(t)$ of the form implied by equation (9), equation (1) turns into an integrodifferential equation. Moreover, the occurrence of a time-varying column length will render the forcing function and, hence, the governing equation nonlinear (cf. case 5 of Fig. 1).

Method of Analysis

Introductory Considerations. In the following, it is advantageous to work in terms of nondimensional variables. Thus, defining

$$u = U_0\,u^*; \quad U = U_0\,U^*; \quad t = T_0\,t^*; \quad r = ar^* \tag{10}$$

where U_0 and T_0 represent suitable reference values of velocity and time, respectively, and asterisks denote dimensionless quantities, equation (1) and the boundary condition can be transformed into their dimensionless counterparts, viz,

$$\Omega\frac{\partial u^*}{\partial t} - \left(\frac{\partial^2 u^*}{\partial r^{*2}} + \frac{1}{r^*}\frac{\partial u^*}{\partial r^*}\right) = \phi^*; \quad u^*(1,t^*) = 0 \tag{11}$$

In these relations,

$$\phi^* = \phi\,\frac{a^2}{\nu U_0} \tag{12}$$

represents the nondimensional form of the forcing function, and

$$\Omega = \frac{a^2}{T_0\nu} \tag{13}$$

denotes an unsteadiness number, or time ratio, which measures the relative importance of a temporal inertia force against a steady viscous force [7].

With equations (11)–(13) established, there is no further need to retain special notation for dimensionless quantities and the asterisk can be dropped; i.e., henceforth the same symbols apply for the dimensionless quantities as for their dimensional counterparts.

The solution to equation (11) for the special case of steady motion, i.e., ϕ = constant = ϕ_s, and $\Omega = 0$, yields the well-known parabolic velocity distribution characteristic of Poiseuille flow, viz,

$$u_s = \frac{\phi_s}{4}\,(1 - r^2) \tag{14}$$

where subscript s identifies steady conditions.

Series Expansion of the Velocity. It is advantageous to expand the velocity as an explicit series in terms of the radial coordinate. This reduces the time dependence to a single function of time and makes it possible to develop certain general analytical relationships that hold true for all members of the vast family of flows under consideration [7].

The velocity is thus written as

$$u = A(1-r^2) + \frac{\Omega}{4^2}\frac{dA}{dt}(1-r^4) + \frac{\Omega^2}{4^2 6^2}\frac{d^2A}{dt^2}(1-r^6) + \ldots \tag{15}$$

where

$$A + \frac{\Omega}{2^2}\frac{dA}{dt} + \frac{\Omega^2}{2^2 4^2}\frac{d^2A}{dt^2} + \ldots = \frac{\phi}{4} \tag{16}$$

Equations (15) and (16) define the starting point for the method of analysis of unsteady laminar pipe-flow problems which is the subject of this paper. For given forcing function, it is first necessary to solve equation (16) for A; the velocity field is then found by substituting the result into equation (15) and by applying the initial condition.

One-Dimensional Relations. Integration of equation (15) with the aid of the operator of equation (4) yields a series expansion of the average velocity, viz,

$$U = \sum_{n=0}^{N} \beta_n \quad \Omega^n \frac{d^n A}{dt^n} \tag{17}$$

in which the upper limit of summation, N, depends on the number of derivates permitted by the forcing function; and where $\beta_0 = 1/2$, $\beta_1 = 1/24$, and, for $n \geqq 2$,

$$\beta_n = \frac{1}{4\{4^2\ 6^2\ \ldots\ (2n)^2\}\,(n+1)(n+2)} \tag{18}$$

Downloaded 02 May 2010 to 171.66.16.246. Redistribution subject to ASME license or copyright; see http://www.asme.org/terms/Terms_Use.cfm

By virtue of equation (15), the nondimensional form of equation (7) can also be written as

$$\tau_a = \sum_{n=0}^{N} \gamma_n \quad \Omega^n \frac{d^n A}{dt^n} \tag{19}$$

where $\gamma_0 = 2$, $\gamma_1 = 1/4$, and, for $n \geqq 2$,

$$\gamma_n = \frac{1}{2\{4^2 \ 6^2 \ \ldots \ (2n)^2\}(n+1)} \tag{20}$$

Expressions (16), (17), and (19) are series expansions for ϕ, U, and τ_a respectively, in terms of a single function of time, namely, A. It is readily possible to eliminate A and thus to find direct differential relationships between ϕ and U; ϕ and τ_a; and τ_a and U. These are, respectively,

$$\alpha_0 \ U + \alpha_1 \ \Omega \frac{dU}{dt} + \alpha_2 \ \Omega^2 \frac{d^2U}{dt^2} + \ \ldots$$

$$= \beta_0 \ \phi + \beta_1 \quad \Omega \frac{d\phi}{dt} + \beta_2 \ \Omega^2 \frac{d^2\phi}{dt^2} + \ \ldots \tag{21}$$

$$\gamma_0 \ U + \gamma_1 \quad \Omega \frac{dU}{dt} + \gamma_2 \ \Omega^2 \frac{d^2U}{dt^2} + \ \ldots$$

$$= \beta_0 \ \tau_a + \beta_1 \quad \Omega \frac{d\tau_a}{dt} + \beta_2 \ \Omega^2 \frac{d^2\tau_a}{dt^2} + \ \ldots \tag{22}$$

$$\alpha_0 \ \tau_a + \alpha_1 \quad \Omega \frac{d\tau_a}{dt} + \alpha_2 \ \Omega^2 \frac{d^2\tau_a}{dt^2} + \ \ldots$$

$$= \gamma_0 \ \phi + \gamma_1 \ \Omega \frac{d\phi}{dt} + \gamma_2 \ \Omega^2 \frac{d^2\phi}{dt^2} + \ \ldots \tag{23}$$

where the α_j are the coefficients in the series for ϕ (cf. equation (16)).

Equation (21) is a general form of the one-dimensional momentum equation, equivalent to (6), but with τ_a eliminated. Equation (22) is a general form of the law of friction, and equation (23) is an ordinary differential equation for τ_a in terms of ϕ and its derivatives.

Equation (21) shows that, in order to eliminate τ_a from the momentum equation, it is necessary to introduce all of the derivatives of U and ϕ. Comparison of (21) with the dimensionless form of equation (6) yields

$$\tau_a = 4\left\{U + \frac{\Omega}{8} \ \frac{dU}{dt} + \alpha_2 \ \Omega^2 \frac{d^2U}{dt^2} + \alpha_3 \ \Omega^3 \frac{d^3U}{dt^3} + \ \ldots\right\} - \left\{\Omega \ \beta_1 \frac{d\phi}{dt} + \Omega^2 \ \beta_2 \frac{d^2\phi}{dt^2} + \ \ldots\right\} \tag{24}$$

This indicates that an explicit relation for τ_a involves, in general, the sum total of the derivatives of U and of ϕ.

All of the series introduced so far are convergent under very general conditions (i.e., piecewise continuity of ϕ, no limits placed on the value of Ω, etc., cf. [7]). Simpler forms of some of these series are, however, subject to greater restrictions. Thus, combining (16) with (19) yields

$$\tau_a = 4U + \frac{\Omega}{6} \frac{dU}{dt} - \frac{\Omega^2}{288} \frac{d^2U}{dt^2} + - \ \ldots \tag{25}$$

which is an explicit form of the law of friction. The corresponding form of the one-dimensional momentum equation follows by substituting (25) into the nondimensional equivalent of equation (6), whence

$$8U + \frac{4}{3} \ \Omega \frac{dU}{dt} - \frac{\Omega^2}{144} \frac{d^2U}{dt^2} + - \ \ldots = \phi \tag{26}$$

equation (26), when applicable, is generally more simple to use than (21).

Special Considerations for Forcing Functions of Class A. Several analytical techniques are available for solving equation (1) when ϕ is a known function of time. However, the preceding relationships permit the formulation of a new and explicit method of solution for u and U, which is very convenient to use.

The particular solution of equation (16) can be obtained by inversion, viz,

$$A_p = \frac{\phi}{4} - \frac{\Omega}{16} \frac{d\phi}{dt} + \frac{3\Omega^2}{256} \frac{d^2\phi}{dt^2} - + \ \ldots \tag{27}$$

The corresponding form of u is then found to be

$$u = \sum_{j=1}^{\infty} \frac{4C_j}{b_j^2} \ J_0(b_j r) \ \exp\left(-\frac{b_j^2}{\Omega} \ t\right) + \frac{\phi}{4} \ (1 - r^2) + \frac{\Omega}{64} \frac{d\phi}{dt} \ (-3 + 4r^2 - r^4) + \frac{\Omega^2}{2304} \frac{d^2\phi}{dt^2} \ (19 - 27r^2 + 9r^4 - r^6) + \ \ldots \tag{28}$$

where C_j are arbitrary coefficients, J_0 is the Bessel function of the first kind and order zero, and b_j are the roots of J_0. The infinite sum represents the homogeneous solution, and the balance of terms corresponds to the particular solution of the problem. Integration of (28) yields the expression for the average velocity, viz,

$$U = \sum_{j=1}^{\infty} \frac{8C_j}{b_j^3} \ J_1(b_j) \ \exp\left(-\frac{b_j^2}{\Omega} \ t\right) + \frac{\phi}{8} - \frac{\Omega}{48} \frac{d\phi}{dt} + \frac{11}{3072} \Omega^2 \frac{d^2\phi}{dt^2} - + \ \ldots \tag{29}$$

where J_1 denotes the Bessel function of the first kind and order one.

Solutions (28) and (29), when applicable, have the advantage over other methods of solutions in that they can always be expressed explicitly in terms of t. This is so because the derivatives of any continuous function can always be explicitly obtained. On the other hand, existing methods of analysis usually involve integrals, or inversion of Laplace transforms, which can frequently only be numerically evaluated. Finally, it should be noted that all expressions involving Ω tend toward their steady-state counterpart when $\Omega \to 0$.

Typical Applications

Scope of Investigation. In order to demonstrate the utility of the method of analysis developed in the foregoing, it is applied in the following to two typical problems of unsteady laminar pipe flow, namely, flow establishment under constant head, and flow establishment with inflow.

The first problem, case 1 of Fig. 1, is characterized by a constant forcing function. It falls into Class A of the flow situations under discussion herein and was first solved by Szymanski in 1932 [2]. The present method of analysis is used simply to reproduce a known analytical and experimentally verified [8] result.

The second problem, case 4 of Fig. 1, has a forcing function that depends on the motion itself and, thus, belongs to the transient flow problems of Class B. This case has not been dealt with previously in the technical literature, and heretofore unpublished analytical results will be presented.

Flow Establishment Under Constant Head. The situation to be studied is schematically described by the definition diagram included in Fig. 2. A valve at the end of a long, cylindrical (but not necessarily horizontal) pipe of radius a and length L, attached to a reservoir providing a constant head H_0, is suddenly completely opened at $t = 0$. Sought is the

Downloaded 02 May 2010 to 171.66.16.246. Redistribution subject to ASME license or copyright; see http://www.asme.org/terms/Terms_Use.cfm

time history of the resulting volume rate of pipe efflux, i.e., $Q(t)$, where $Q(t) = \pi a^2 U$.

With reference to equation (12), the forcing function of the system is

$$\phi = \frac{gH_0}{L} \frac{a^2}{\nu U_0} \tag{30}$$

If the ultimate (i.e., $t \to \infty$) steady-state velocity of Poiseuille flow is chosen as a reference velocity, i.e., $U_0 = g a^2 H_0/(8\nu L)$, then $\phi = 8$. A suitable choice for the reference time is $T_0 = 2\{L\, a/(g\, H_0)\}^{1/2}$, whence, by equation (13),

$$\Omega = \frac{a}{2\nu}\sqrt{\frac{gaH_0}{L}} = \sqrt{\mathrm{I\!R}_o} \tag{31}$$

in which $\mathrm{I\!R}_o = 2a\, U_0/\nu$. Thus, in this case, Ω is the square root of the ultimate steady-state Reynolds number $\mathrm{I\!R}_o$. As such, Ω must not exceed a value of appoximately $\sqrt{2000} \approx 45$ in order for laminar flow to exist.

With ϕ and Ω established, an expression for the instantaneous local velocity follows directly from equation (28), viz,

$$u = \sum_{j=1}^{\infty} \frac{4C_j}{b_j^2}\, J_0(b_j\, r)\, \exp\left(-\frac{b_j^2}{\Omega} t\right) + 2(1 - r^2) \tag{32}$$

This is subject to the initial condition $u(r,0) = 0$ with which the Fourier-Bessel coefficients C_j can be found. The final results, i.e.,

$$u = 2\left\{1 - r^2 - \sum_{j=1}^{\infty} \frac{8J_0(b_j\, r)}{b_j^3\, J_1(b_j)} \exp\left(-\frac{b_j^2}{\Omega}\, t\right)\right\} \tag{33}$$

is exactly identical with Szymanski's original solution of the problem [2] which he obtained by the method of separation of variables.

A corresponding expression for the instantaneous average velocity follows from integration of equation (33), i.e.,

$$U = 1 - \sum_{j=1}^{\infty} \frac{32}{b_j^4} \exp\left(-\frac{b_j^2}{\Omega}\, t\right) \tag{34}$$

A plot of this equation in terms of the instantaneous volume rate of flow Q is included as curve 1 in Fig. 2.

The corresponding one-dimensional approach to the solution of this problem can proceed in at least three different forms starting from equations (21), (26), or (29), respectively. All lead to the same result. The solution based on equation (26) is, perhaps, best suited to illustrate the salient features of the present method of analysis and will be developed in the following.

The particular solution to equation (26) is $U_p = 1$, while its homogeneous solution is composed of exponential functions. Assuming the exponential argument to be $-\lambda t$, then the homogeneous version of (26) yields

$$8 - \frac{4}{3}\lambda\Omega - \frac{(\lambda\Omega)^2}{144} - \ldots = 0 \tag{35}$$

and the full solution is

$$U = 1 - \exp(-\lambda t) \tag{36}$$

The polynomial (35) can have only one positive root. It follows that the more terms considered, the better will be the accuracy of the solution. Thus, for two terms in (35), the solution is $\Omega\lambda = 6$, while for three terms, $\Omega\lambda = 5.8234$. The exact solution is $\Omega\lambda = b_1^2 \approx 5.7832$. For all practical purposes this value is approached with sufficient accuracy when the polynomial (35) is reduced to four terms. It may be noted that, in this problem, equation (35) (i.e., equation (26)), converge for any value of Ω. A plot of equation (36) in terms of the instantaneous volume rate of pipe efflux is included as curve 2 in Fig. 2. It may be mentioned that the error entailed by using equation (36) in lieu of the exact result, equation (34), amounts to less than 5 percent for $t > 8$, if $\Omega = 40$; the flow reaches $U = 0.99$ at $t \approx 35.54$ for this value of Ω.

Finally, it may be of interest to compare the present results with the predictions of a typical engineering approximation. A very common artifice is the assumption of a constant friction coefficient. Thus, with $f = 64/\mathrm{I\!R}_o$ corresponding to the ultimate, steady Poiseuille flow, there follows

$$U = \tanh\left(\frac{8}{\Omega}\, t\right) \tag{37}$$

which is plotted as curve 3 in Fig. 2. The presentation leaves little doubt about the error entailed by this crude model of transient friction.

Flow Establishment With Inflow. The flow system under discussion is schematically depicted in the definition diagram of Fig. 3. It comprises a long cylindrical (but not necessarily horizontal) pipe of radius a and length L which is attached to a finite-size tank with constant cross-sectional area A_T. Initially, steady flow prevails with tank inflow q_0 equalling

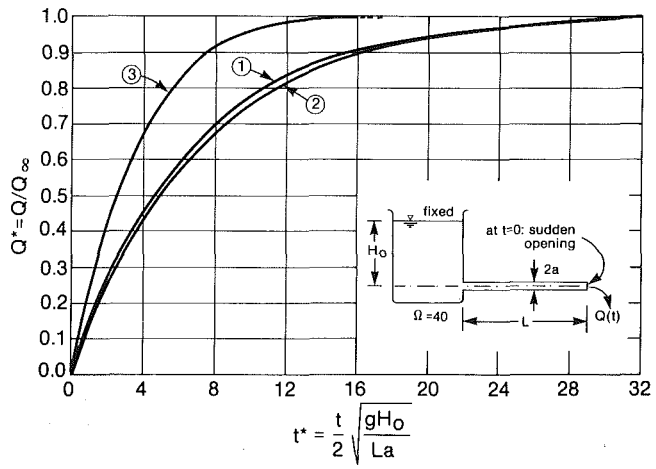

Fig. 2 Flow establishment without inflow. Curve 1: exact solution, equation (34); curve 2: approximation, equation (36); curve 3: approximation, equation (37).

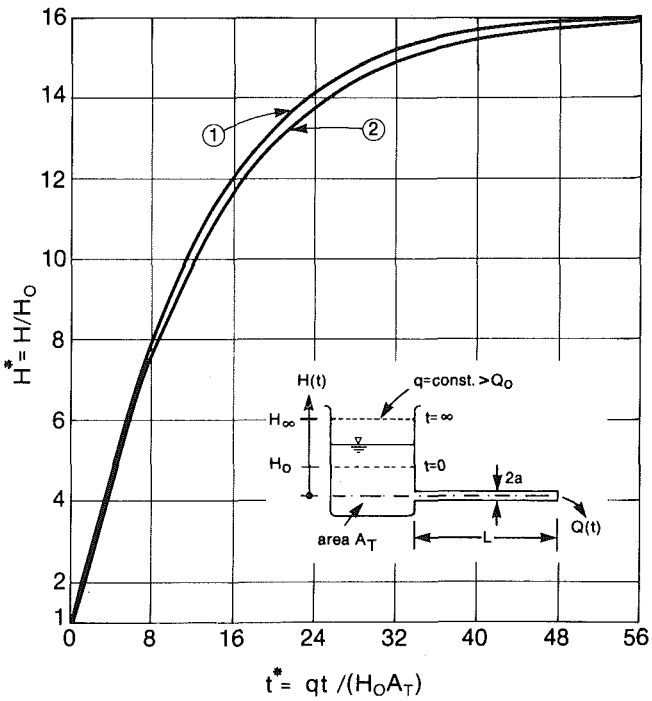

Fig. 3 Flow establishment with inflow ($\Omega = 23.4$, $\theta = 1$). Curve 1: exact solution, equation (46); curve 2: approximation, equation (50).

Downloaded 02 May 2010 to 171.66.16.246. Redistribution subject to ASME license or copyright; see http://www.asme.org/terms/Terms_Use.cfm

pipe efflux Q_0 under a constant reservoir head H_0. At time $t=0$, the volume rate of tank inflow is suddenly increased to a new constant value $q>Q_0$, thereby causing the level in the tank to rise with time. Sought is the time history of this level change, i.e., $H=H(t)$.

Taking into account the initial head H_0, and the changes in head due to constant tank inflow q and time-varying pipe efflux $Q(t)$, the dimensionless forcing function, equation (12), becomes

$$\phi = 1 + t - \theta \int_0^t \int_0^1 ur\, dr\, dt' \tag{38}$$

where

$$\Theta = \frac{2g\pi H_0 a^4}{q L \nu} = 16\frac{H_0}{H_\infty} \tag{39}$$

$$U_0 = \frac{g a^2 H_0}{\nu L}; \quad T_0 = \frac{H_0 A_T}{q}; \quad \Omega = \frac{a^2 q}{H_0 A_T \nu} \tag{40}$$

and H_∞ is the ultimate (i.e., $t\to\infty$) steady-state reservoir head for which, again, Poiseuille flow prevails in the discharge pipe. The initial condition for the local velocity is $u(r,0) = (1-r^2)/4$.

The eventually required change in dependent variable from flow velocity to reservoir head is effected with the aid of the continuity principle. Thus, in dimensionless variables, cf. Fig. 3,

$$U = \frac{2}{\Theta}\left(1 - \frac{dH}{dt}\right) \tag{41}$$

The exact solution of the problem at hand is achieved by way of the fundamental set of equations (15) and (16), whence

$$u = \frac{4}{\Theta}(1-r^2) + \sum_{j=1}^{\infty} \frac{4C_j}{\epsilon_j^2} \exp(-\lambda_j^2 t)[J_0(\epsilon_j r) - J_0(\epsilon_j)] \tag{42}$$

where

$$C_j = \frac{\kappa^2(\Theta - 16)}{8\Theta J_0(\epsilon_j)[12\kappa\epsilon_j^2 - (\epsilon_j^4 + \kappa)^2]} \tag{43}$$

in which $\kappa = \Theta\Omega/2$. The characteristic values ϵ_j are the real roots of

$$2\kappa J_1(\epsilon_j) - \epsilon_j(\epsilon_j^4 + \kappa) J_0(\epsilon_j) = 0 \tag{44}$$

and the λ_j are given by $\lambda_j = \epsilon_j/(\Omega)^{1/2}$.

Equation (44) yields complex roots for $\kappa > 11.8$; therefore oscillatory behavior must be expected to occur for values of κ in excess of 11.8. The previous solution, equation (42), is valid only for nonoscillatory motion, and the same holds true for the average velocity, which is obtained by integrating equation (42) with the aid of the operator of equation (4), viz,

$$U = \frac{2}{\Theta} + \sum_{j=1}^{\infty} \frac{4C_j \epsilon_j^2}{\kappa} J_0(\epsilon_j) \exp(-\lambda_j^2 t) \tag{45}$$

whence

$$H = 1 - \sum_{j=1}^{\infty} 4C_j J_0(\epsilon_j)[1 - \exp(-\lambda_j^2 t)] \tag{46}$$

A plot of equation (46) is included in Fig. 3 as curve 1 for $\Omega = 23.4$; $\theta = 1$. The exact expressions for the velocity, equations (42) and (45), and for the tank level, equation (46), are difficult to deal with because of the presence of the infinite series in terms of ϵ_j. In contrast, a relatively straightforward solution to the problem, albeit approximate, which avoids in part this complication, may be deduced from the one-dimensional equations of motion, equations (21) and (26), respectively. Upon substitution of equation (41) therein, these become differential equations for the nondimensional reservoir head $H(t)$, i.e.,

$$H + \left(\frac{16}{\theta} + \frac{\Omega}{12}\right)\frac{dH}{dt} + \left(\frac{4}{\theta} + \frac{\Omega}{384}\right)\Omega\frac{d^2H}{dt^2} + \ldots = \frac{16}{\theta} \tag{47}$$

and

$$H + \frac{16}{\theta}\frac{dH}{dt} + \frac{8}{3}\frac{\Omega}{\theta}\frac{d^2H}{dt^2} + \ldots = \frac{16}{\theta} \tag{48}$$

subject to the initial conditions

$$H(0) = 1; \quad \frac{dH}{dt}(0) = \frac{16-\theta}{16} \tag{49}$$

The solution for both equations (47) and (48) can be expressed as

$$H = \frac{16}{\theta} + K_1 e^{-\eta_1 t} + K_2 e^{-\eta_2 t} \tag{50}$$

The characteristic polynomial for η_1, η_2 obtained from (47) reproduces equation (44) exactly and, as such, is valid for any value of Ω [7]. The corresponding polynomial derived from (48) is an asymptotic form of (44), which is of practical use only for $\Omega < 1000$. The coefficients K_1 and K_2 are determined with the aid of equation (49). Both one-dimensional solutions yield the same results for $\Omega < 1000$. Equation (50) is an approximation of equation (46) in terms of the two leading terms in its infinite series. A plot of equation (50) is given in Fig. 3 as curve 2. The small error entailed by the one-dimensional analysis is, as in the previous problem, due to the lack of sufficient initial conditions that are necessary to determine the exact form of $H(t)$.

The use of Zielke's method [6] for this problem would lead to involved numerical calculations which would not readily yield results as simple as equation (50).

Conclusions

A method of analysis has been developed that permits a unified approach to the solution of problems of unsteady laminar flow in long pipes for which the forcing function may depend on the motion itself, i.e., of the general form $\phi = \phi\{U(t),t\}$. Application of the technique to two particular cases of laminar pipe-flow transients have demonstrated its efficacy in producing solutions that are in excellent agreement with known analytical and experimental results.

Acknowledgments

The work described herein was supported by the Natural Sciences and Engineering Research Council of Canada through Operating Grant A-1541.

References

1 Wylie, E. B., and Streeter, V. L., *Fluid Transients*, McGraw-Hill, New York, 1978.

2 Szymanski, F. J., "Quelques Solutions Exactes des Équations de l'Hydrodynamique de Fluide Visqueux dans le Cas d'un Tube Cylindrique," *Journal des Mathématiques Pures et Appliquées*, Paris, France, Vol. 11, Series 9, 1932, pp. 67-107.

3 Sexl, T., "Ueber den von E. G. Richardson Entdeckten 'Annulareffekt'," *Zeitschrift fuer Physik*, Vol. 61, 1930, pp. 349-362.

4 Clarion, C., and Pellisier, R., "A Theoretical and Experimental Study of the Velocity Distribution and Transition to Turbulence in Free Oscillatory Flow," *Journal of Fluid Mechanics*, Vol. 70, 1975, pp. 59-79.

5 D'Souza, A. F., and Oldenburger, R., "Dynamic Response of Fluid Lines," ASME *Journal of Basic Engineering*, Vol. 86, No. 3, 1964, pp. 589-598.

6 Zielke, W., "Frequency-Dependent Friction in Transient Pipe Flow," ASME *Journal of Basic Engineering*, Vol. 90, No. 1, 1968, pp. 109-115.

7 Letelier S., M. F., "An Approach to the Analysis of Unsteady Parallel Flow in Circular Pipes," Thesis presented to the University of Toronto at Toronto, Ontario, Canada, in 1979, in partial fulfillment of the requirements for the degree of Doctor of Philosophy.

8 Letelier S., M. F., and Leutheusser, H. J., "Skin Friction in Unsteady Laminar Pipe Flow," ASCE *Journal of the Hydraulics Division*, Vol. 102, No. HY1, Jan. 1976, pp. 41-56.

Downloaded 02 May 2010 to 171.66.16.246. Redistribution subject to ASME license or copyright; see http://www.asme.org/terms/Terms_Use.cfm

C. Y. Wang
Professor,
Departments of Mathematics and Physiology,
Michigan State University,
East Lansing, Mich. 48824

L. T. Watson
Associate Professor,
Department of Computer Science.

M. P. Kamat
Associate Professor,
Department of Engineering
Science and Mechanics.

Virginia Polytechnic Institute
and State University,
Blacksburg, Va. 24061

Buckling, Postbuckling, and the Flow Through a Tethered Elastic Cylinder Under External Pressure

A thin-walled elastic cylinder is tethered by numerous springs to an outer rigid cylinder. As external pressure is increased, the elastic cylinder will remain circular until a critical pressure difference is attained. The nonlinear governing equations for large deflections are formulated. The stability analysis shows the elastic cylinder may buckle with more than two circumferential waves due to the stiffness of the springs. Postbuckling shapes are integrated numerically by a quasi-Newton method. The flow through such a partially collapsed shape is then computed by a finite element method.

1 Introduction

The stability of a long, thin, circular, elastic cylinder under external pressure was first studied by Levy [1]. If the pressure difference is normalized by EI/R^3, where EI is the flexural rigidity and R is the radius of the cylinder, Levy found that the normalized critical pressure with N circumferential waves is $N^2 - 1$. Thus the lowest critical pressure is 3 with a two-fold symmetry. Using elastica theory, Greenhill [2] integrated the postbuckling shapes. Others who studied the problem include Tadjbakhsh and Odeh [3], Moreno, Katz, Gold, and Reddy [4], and Flaherty, Keller, and Rubinow [5]. The postbuckling shapes are of interest because they resemble cross sections of blood vessels collapsed by external pressure. The results compare well with observations of a *free* segment of vena cava (Moreno et al. [4]).

Similar to elastic cylinders, blood vessels collapse when the difference between the external pressure and the internal pressure reaches some critical value. The internal pressure is the hydrodynamic pressure of blood within the vessel wall. This pressure may be decreased by upstream constriction such as sphincter action. The external pressure can be increased in many normal instances: active contraction of smooth muscle tone in blood flow regulation; the increased interstitial pressure due to skeletal muscle contraction; the increase in myocardial pressure during systole; and the hydrostatic pressure affecting the upper lung and abdominal veins. Abnormal blood vessel collapse occurs when the cranial pressure is increased by inflammation or injury, when abdominal pressure is increased by ascites, and when the limbs are subjected to compression as that due to pneumatic cuffs.

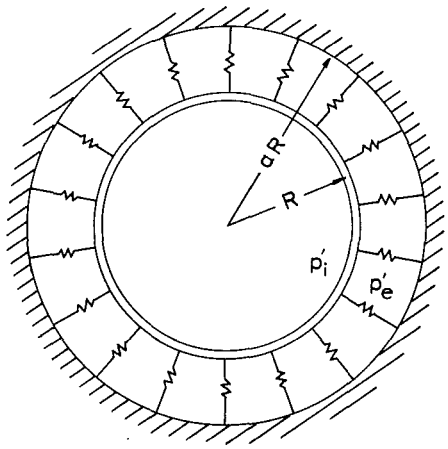

Fig. 1 The tethered elastic cylinder

Although the larger vessels (aorta, vena cava) are untethered, most blood vessels are not free. Usually they are embedded in tissue or attached to a bone matrix by collagen. This anatomical tethering prevents collapse and we may find increased buckling pressure. The postbuckling shapes may also be altered. Indeed, as we shall see later, in certain cases the lowest critical pressure no longer corresponds to the critical pressure of the untethered cylinder studied by previous authors.

2 The Basic Equations for a Tethered Elastic Cylinder

If the flow through a tethered blood vessel is slow and steady (approximately true for the venous circulation) and the cross section does not vary very much along a segment, then the internal pressure can be regarded constant locally. Thus

Contributed by the Applied Mechanics Division for publication in the JOURNAL OF APPLIED MECHANICS.

Discussion on this paper should be addressed to the Editorial Department, ASME, United Engineering Center, 345 East 47th Street, New York, N. Y. 10017, and will be accepted until two months after final publication of the paper itself in the JOURNAL OF APPLIED MECHANICS. Manuscript received by ASME Applied Mechanics Division, March, 1982; final revision, June, 1982.

Copyright © 1983 by ASME
Downloaded 02 May 2010 to 171.66.16.246. Redistribution subject to ASME license or copyright; see http://www.asme.org/terms/Terms_Use.cfm

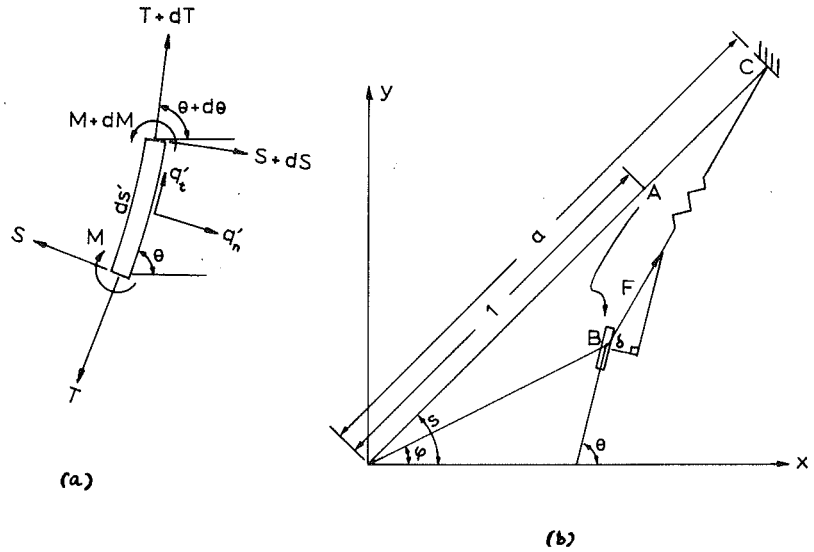

Fig. 2 (*a*) An elemental length; (*b*) element displaced from *A* to *B*

we can solve for the buckled shape first and calculate the flow rate (resistance) later.

Figure 1 shows a model of a thin-walled elastic cylinder tethered by numerous springs to a rigid outer cylinder. We assume the springs are numerous enough to be considered as continuously distributed. The elastic cylinder is subjected to constant internal pressure p_i' and constant external pressure p_e'. The cylinder will remain circular until a bifurcation buckling pressure difference is reached.

Figure 2(*a*) shows an elemental length of the cylinder. Balancing the forces in the normal and tangential directions we find

$$Td\theta - dS - q_n' ds' = 0 \tag{1}$$

$$q_t' ds' + Sd\theta + dT = 0 \tag{2}$$

Here T is the tension, S is the shear, q_n', q_t' are normal and tangential stresses on the surface, respectively, θ is the local angle of inclination, and s' is the arc length. A local moment balance gives

$$dM - Sds' = 0 \tag{3}$$

Since the wall thickness is small compared to the radius, we assume the moment M is proportional to local curvature,

$$M = EI \frac{d\theta}{ds'} \tag{4}$$

Then we eliminate T, S, and M from equations (1)–(4) to obtain the nonlinear equation

$$\frac{d\theta}{ds}\frac{d^4\theta}{ds^4} - \frac{d^2\theta}{ds^2}\frac{d^3\theta}{ds^3} + \left[\left(\frac{d\theta}{ds}\right)^3 - q_n\right] \times \frac{d^2\theta}{ds^2} + q_t\left(\frac{d\theta}{ds}\right)^2 + \frac{dq_n}{ds}\frac{d\theta}{ds} = 0 \tag{5}$$

where $s = s'/R$ is the normalized arc length and $q = q'R^3/EI$ is the normalized stress. The normalized cartesian coordinates (x,y) are related to θ by

$$\frac{dx}{ds} = \cos\theta, \quad \frac{dy}{ds} = \sin\theta \tag{6}$$

Suppose the tension per unit arc length of the springs is F_0 per unit area at a spring length of $(a-1)$. We define the normalized pressure difference p

$$p = p_e - p_i - F_0 \tag{7}$$

where $p_e = p_e'R^3/EI$ and $p_i = p_i'R^3/EI$ are external and internal pressures, respectively. The external pressure includes both active pressure due to smooth muscle and passive interstitial pressure. Figure 2(*b*) shows the cylinder surface, originally at A, deformed to a new position at B. The extra force F per unit arc length due to the spring is thus

$$F = k(\overline{BC} - \overline{AC}) \tag{8}$$

where

$$\overline{AC} = a - 1$$

$$\overline{BC} = [(a\cos s - x)^2 + (a\sin s - y)^2]^{1/2} \equiv d \tag{9}$$

and we have assumed a linear spring constant k per unit arc length. Taking normal and tangential components of F we find

$$q_t = F\cos\delta, \quad q_n = F\sin\delta - p \tag{10}$$

where

$$\tan(\theta - \delta) = \frac{a\sin s - y}{a\cos s - x} \tag{11}$$

Using equations (8)–(11) we obtain

$$q_t = k\left(\frac{d - a + 1}{d}\right)[\cos\theta(a\cos s - x) + \sin\theta(a\sin s - y)] \tag{12}$$

$$q_n = k\left(\frac{d - a + 1}{d}\right)[\sin\theta(a\cos s - x) - \cos\theta(a\sin s - y)] - p \tag{13}$$

For N circumferential waves, the boundary conditions are

$$\text{at } s = 0, \quad \theta = \frac{\pi}{2}, \quad \frac{d^2\theta}{ds^2} = 0, \quad y = 0 \tag{14}$$

$$\text{at } s = 2\pi/N, \quad \theta = \frac{\pi}{2} + \frac{2\pi}{N}, \quad \frac{d^2\theta}{ds^2} = 0 \tag{15}$$

$$(s^2 + y^2)|_{s=0} = (x^2 + y^2)|_{s=2\pi/N} \tag{16}$$

Equations (5), (6), (9), and (12–16) are nonlinear. Only when $k = 0$ is equation (5) reduced to the twice-integrable form studied by previous authors. Actually the N circumferential waves or N-fold symmetry need not be assumed a priori, since the stability problem will dictate N is an integer eigenvalue.

3 The Stability Problem

In the unbuckled state, the solution is

Downloaded 02 May 2010 to 171.66.16.246. Redistribution subject to ASME license or copyright; see http://www.asme.org/terms/Terms_Use.cfm

$$\theta = s + \frac{\pi}{2}, \quad x = \cos s, \quad y = \sin s \tag{17}$$

We shall perturb from this state

$$\theta = s + \frac{\pi}{2} + \varphi, \quad x = \cos s + \xi, \quad y = \sin s + \eta \tag{18}$$

where φ, ξ, and η are all of order $\epsilon << 1$. The leading terms of equation (9) are

$$d = a - 1 - \xi \cos s - \eta \sin s + 0(\epsilon^2) \tag{19}$$

Similarly

$$q_t = 0(\epsilon^2) \tag{20}$$

$$q_n = -p - k(\xi \cos s + \eta \sin s) + 0(\epsilon^2) \tag{21}$$

Equations (5) and (6) are then linearized to

$$\frac{d^4\varphi}{ds^4} + (p+1)\frac{d^2\varphi}{ds^2} - k\frac{d}{ds}(\xi \cos s + \eta \sin s) = 0 \tag{22}$$

$$\frac{d\xi}{ds} = -\varphi \cos s, \quad \frac{d\eta}{ds} = -\varphi \sin s \tag{23}$$

The boundary conditions become

$$\text{at } s = 0, \ \varphi = 0, \ \frac{d^2\varphi}{ds^2} = 0, \ \eta = 0 \tag{24}$$

$$\text{at } s = 2\pi/N, \ \varphi = 0, \ \frac{d^2\varphi}{ds^2} = 0 \tag{25}$$

$$\xi|_{s=0} = (\xi \cos s + \eta \sin s)|_{s=2\pi/N} \tag{26}$$

Equation (22) can be integrated twice to give

$$\frac{d^2\varphi}{ds^2} + (p+1)\varphi - k\int_0^s (\xi \cos s + \eta \sin s)ds = c_1 s + c_2 \tag{27}$$

This equation can be simplified by integration by parts using equation (23):

$$\frac{d^2\varphi}{ds^2} + (p+1)\varphi - k(\xi \sin s - \eta \cos s) = c_1 s + c_2 \tag{28}$$

The boundary condition equation (24) gives $c_2 = 0$. Equation (28) is linear with periodic coefficients. The boundary conditions suggest that φ, ξ are odd in s while η is even in s. Since φ is periodic with N circumferential waves, the general solution can be expressed as

$$\varphi = \sum_{n=1}^{\infty} b_n \sin nNs \tag{29}$$

Equations (23) give

$$\xi = \sum_{n=1}^{\infty} \frac{b_n}{2}\left[\frac{\cos(nN-1)s}{nN-1} + \frac{\cos(nN+1)s}{nN+1}\right] + c_3 \tag{30}$$

$$\eta = \sum_{n=1}^{\infty} \frac{-b_n}{2}\left[\frac{\sin(nN-1)s}{nN-1} - \frac{\sin(nN+1)s}{nN+1}\right] + c_4 \tag{31}$$

The integration constant c_4 can be set to zero since $\eta(0) = 0$. The condition equation (26) shows c_3 is also zero. We substitute equations (29)–(31) into equation (28) and obtain

$$\sum_{n=1}^{\infty} b_n \sin nNs\left(-n^2N^2 + p + 1 - \frac{k}{n^2N^2 - 1}\right) = c_1 s \tag{32}$$

This yields $c_1 = 0$ and

$$b_n\left(-n^2N^2 + p + 1 - \frac{k}{n^2N^2 - 1}\right) = 0 \tag{33}$$

For the fundamental N circumferential waves to exist, we need $b_1 \neq 0$. Thus

$$-N^2 + p + 1 - \frac{k}{N^2 - 1} = 0 \tag{34}$$

or the critical pressure is

$$p_N^* = N^2 - 1 + \frac{k}{N^2 - 1} \tag{35}$$

Under this pressure, $b_n = 0$ for $n \neq 1$. Unlike the solution to the Mathieu equation, the solution to the present problem is a single harmonic. Equation (35) agrees with the result of Seide and Weingarten [6] who used an energy method on the similar stability problem of an elastic shell with an elastic core. The critical pressure is identical for infinitesimal displacements.

Figure 3 shows the critical pressure as a function of N and k. When k is zero the critical pressure agrees with that of Levy [1]. However, there are significant differences when $k \neq 0$. Equating p_N^* and p^*_{N-1} we find N-fold collapse occurs when

$$N(N^2 - 1)(N - 2) < k < N(N^2 - 1)(N + 2) \tag{36}$$

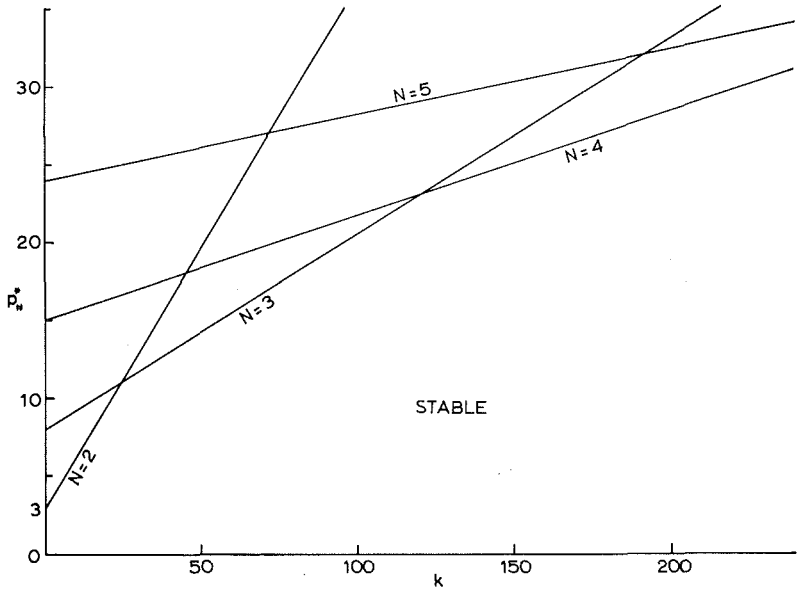

Fig. 3 Critical pressure as a function of k

Downloaded 02 May 2010 to 171.66.16.246. Redistribution subject to ASME license or copyright; see http://www.asme.org/terms/Terms_Use.cfm

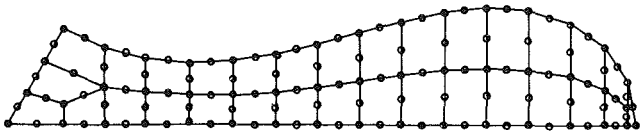

Fig. 4 A typical finite element grid

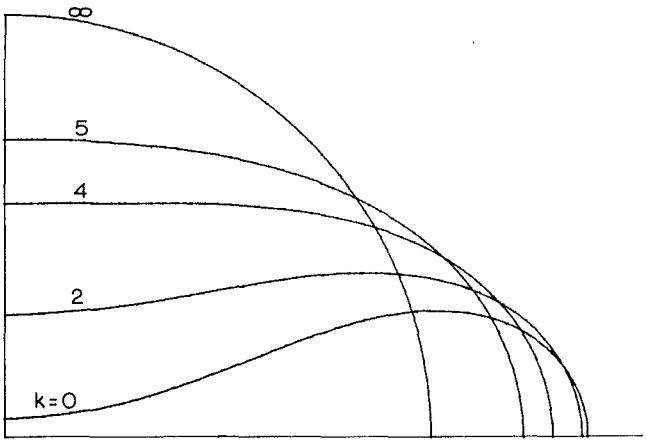

Fig. 5 Effect of spring constant k on cross section $p = 5$, $a = 2$, $N = 2$

Thus as pressure is increased, two-fold buckling occurs when $0 \le k < 24$, three-fold buckling prevails when $24 < k < 120$, and four-fold buckling will be observed when $120 < k < 360$, etc.

4 Postbuckling Shapes

For the postbuckling shapes we integrate the nonlinear equations (5), (6), (9), and (12)–(16) numerically. Let

$$\mathbf{v} = \left(x(0), \frac{d\theta}{ds}(0), \frac{d^3\theta}{ds^3}(0)\right) \tag{37}$$

and $x(s;\mathbf{v})$, $y(s;\mathbf{v})$, $\theta(s;\mathbf{v})$ be the solution to the initial value problem given by equations (5), (6), (12), and (13) with the initial conditions equations (14) and (37). Then the original two-point boundary value problem is equivalent to finding a vector $\mathbf{v}$ such that

$$\mathbf{F}(\mathbf{v}) = \begin{bmatrix} \theta\left(\frac{2\pi}{N};\mathbf{v}\right) - \left(\frac{\pi}{2} + \frac{2\pi}{N}\right) \\ \frac{d^2\theta}{ds^2}\left(\frac{2\pi}{N};\mathbf{v}\right) \\ (x^2+y^2)|_{s=0} - (x^2+y^2)|_{s=2\pi/N} \end{bmatrix} = 0 \tag{38}$$

The nonlinear system of equations $\mathbf{F}(\mathbf{v}) = 0$ is solved by a quasi-Newton method and parametric continuation. The qausi-Newton algorithm used is embodied in the computer code HYBRD, part of the MINPACK package developed at Argonne National Laboratory (Moré et al. [7]; Dennis and Moré [8]). This particular quasi-Newton algorithm is easy to use, accurate, reliable, robust, efficient, and usually does not require a good initial guess.

The quasi-Newton method, however, sometimes converges to the wrong solution (corresponding to a higher mode of symmetry) or fails to make satisfactory progress toward a solution. In these cases a parametric continuation algorithm (Davidenko [9]) is used. This method is briefly described as follows.

Since $\mathbf{F}(\mathbf{v})$ depends on p, a, k, N, as well as $\mathbf{v}$, let α denote any of the parameters p, a, k, or N and write $\mathbf{F}(\mathbf{v}) = \mathbf{F}(\mathbf{v},\alpha)$.

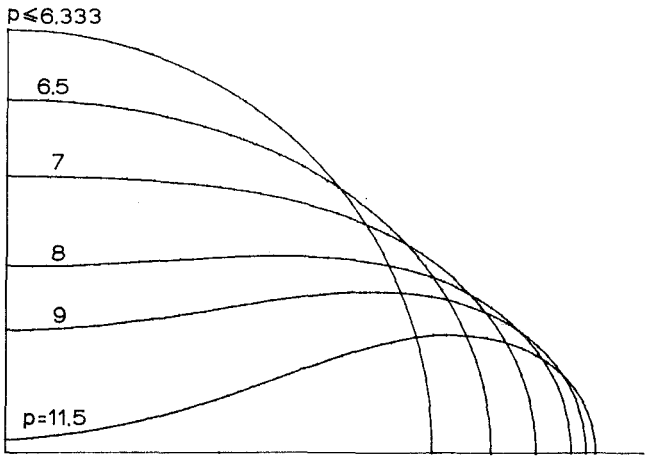

Fig. 6 Effect of pressure difference p; $k = 10$, $a = 2$, $N = 2$

Assuming that the Jacobian matrix $D_{\mathbf{v}}\mathbf{F}(\mathbf{v},\alpha)$ is invertible, by the implicit function theorem the equation

$$\mathbf{F}(\mathbf{v},\alpha) = 0 \tag{39}$$

determines $\mathbf{v}$ as a function of α. Thus

$$\mathbf{F}(\mathbf{v}(\alpha),\alpha) = 0. \tag{40}$$

Then

$$\frac{d}{d\alpha}\mathbf{F}(\mathbf{v}(\alpha),\alpha) = D_{\mathbf{v}}(\mathbf{v},\alpha)\frac{\partial \mathbf{v}}{d\alpha} + \frac{\partial \mathbf{F}}{\partial \alpha}(\mathbf{v},\alpha) = 0 \tag{41}$$

and

$$\frac{d\mathbf{v}}{d\alpha} = -[D_{\mathbf{v}}\mathbf{F}(\mathbf{v},\alpha)]^{-1}\frac{\partial \mathbf{F}}{\partial \alpha}(\mathbf{v},\alpha), \quad \mathbf{v}(\alpha_0) = \mathbf{v}_0 \tag{42}$$

(where $\mathbf{F}(\mathbf{v}_0,\alpha_0) = 0$). Thus solving the initial value problem, equation (42) gives the parametric family of solutions $\mathbf{v}(\alpha)$. This approach is efficient if a large number of points $\mathbf{v}(\alpha)$ are needed. Equation (42) is solved by the variable step, variable order ODE code in Shampine and Gordon [10].

The combination of a quasi-Newton method and parametric continuation is very successful, although many hours of CPU time on a VAX 11/780 were required to do all the calculations.

Once the initial conditions $\mathbf{v}$ is obtained, equations (5), (6), (9), (12)–(14), and (37) can be integrated to obtain the shape of the collapsed tube. This boundary curve is then used to determine the flow through the collapsed tube.

5 The Flow Rate

Let w be the velocity of the flow normalized by (pressure gradient R^2/viscosity) through a tube of given cross section. w then satisfies the Poisson equation with zero boundary condition. Although this problem can be solved by finite differences, a finite element method based on Galerkin's method of weighted residuals is more suitable (Finlayson [11]; Connor and Brebbia [12]). In brief, the cross section is divided into an appropriate number of subdomains or elements, within each, a field w^e is defined. Then w^e over each element is expressed in terms of the values of the field at n points called nodes on the boundary of the element. w^e from adjacent elements agree along interelement boundaries. Then

$$w^e = \sum_{i=1}^{n} P_i w_i^e \tag{43}$$

where P_i are specially chosen polynomials. Galerkin's criterion applied to each element reduces to

Downloaded 02 May 2010 to 171.66.16.246. Redistribution subject to ASME license or copyright; see http://www.asme.org/terms/Terms_Use.cfm

$$\int P_i[\nabla^2 w^e + 1]dA = 0 \quad i = 1,2, \ldots ,n \tag{44}$$

where A is the area of the element. Equations (43) and (44) yield linear algebraic equations that can be extended to the whole domain. These equations are then solved with $w = 0$ on the boundary.

The postbuckling shapes or the boundaries encountered in our problem are highly curved. Care must be taken in deciding the number and distribution of elements in order to maintain acceptable accuracy. The particular element used in this work has eight nodes with four parabolic sides. Figure 4 shows a finite element grid for 1/6 of an $N = 3$ case. The total flow is then simply

$$\sum_{e=1}^{m} \int w^e \, dA \tag{45}$$

where m is the total number of elements.

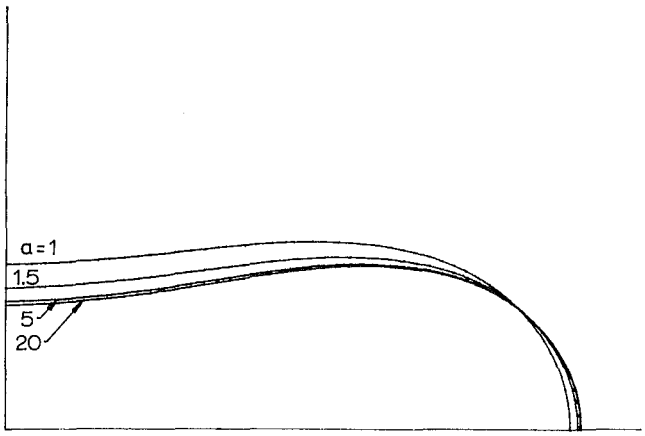

Fig. 7 Effect of radius of outer rigid cylinder a; $p = 10$, $k = 5$, $N = 2$

6 Results and Discussion

Figure 5 shows the effect of spring constant k on the cross sectional shape of the tube under external pressure, where $k = 0$ corresponds to the case where tethering is absent. When stiffness (k) increases, the tethering keeps the tube from collapsing. Figure 6 shows the effect of pressure difference p. For this particular spring constant ($k = 10$), the tube remains circular for p smaller than the critical buckling pressure of 6.333. Figure 7 shows the effect of the length of spring on the cross section is minimal. Figure 8 shows the collapse with three-fold symmetry for the same k as in Fig. 6. For this value of k, the two-fold collapse is more stable than the three-fold collapse.

We may comment that for given k, as pressure is increased, the tube will collapse in the configuration, which yields the lowest critical buckling load predicted in Fig. 3. This symmetry, being the most stable with the least potential energy, will be maintained in the postbuckling stage. However, if we start from a given-fold symmetry and decreased pressure, the tube cannot maintain the given-fold symmetry when the

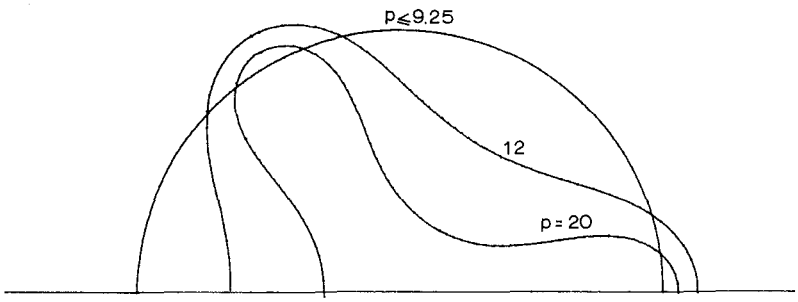

Fig. 8 Effect of pressure difference p; $k = 10$, $a = 2$, $N = 3$

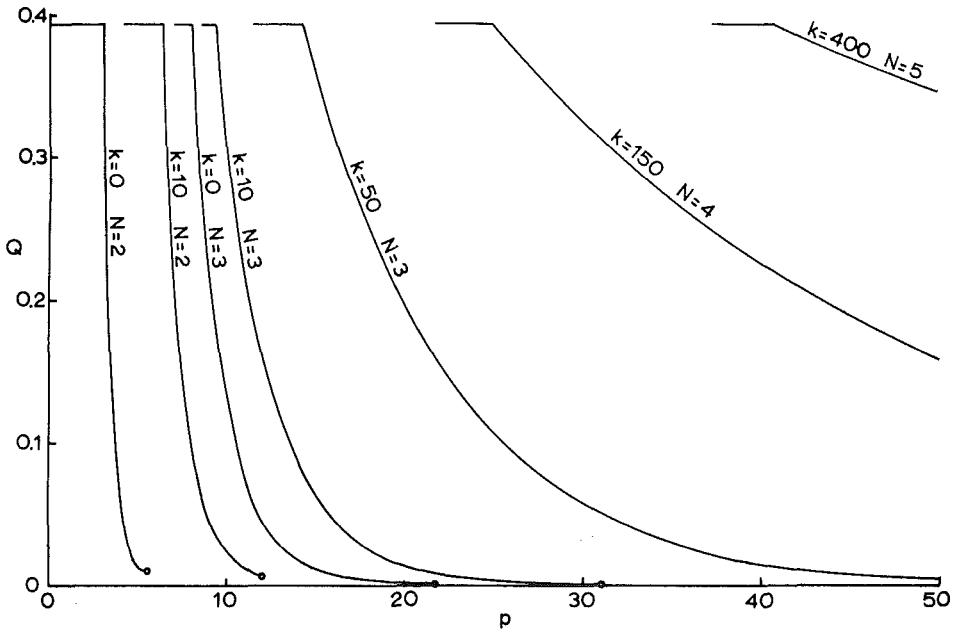

Fig. 9 The flow rate Q as a function of p for given k, N. Circle denotes when opposite walls come into contact.

Downloaded 02 May 2010 to 171.66.16.246. Redistribution subject to ASME license or copyright; see http://www.asme.org/terms/Terms_Use.cfm

pressure reaches the critical buckling pressure corresponding to a smaller N. A further decrease in p will result in a sudden change into a lower-fold symmetry.

The load-generalized deflection curves are similar to Fig. 9 which shows the flow rate Q for various k, N, and p. Our $k=0$, $N=2$ curve agrees with the results of Flaherty, Keller, and Rubinow [5]. In general, when the pressure is below the critical buckling pressure, the tube remains circular with a normalized flow rate of $\pi/8$. For small k, collapse is swift as pressure is further increased. The flow drops abruptly to almost zero. We did not continue our calculations past the small circle in Fig. 9, where opposite sides of the tube wall come into contact with each other. It is probably not worthwhile to calculate the small residual flow rate since we need to reformulate our boundary conditions and computations. The effect of nonzero k on Q is considerable. Not only are the curves shifted to the right, but also the slopes are decreased. Partial collapse becomes the prevalent phenomenon for tethered tubes if they collapse at all.

Baez et al. [13] reported that capillaries, in contrast to large vessels, appear to be quite indistensible, i.e., insensitive to pressure differences. Fung [14] and Fung et al. [15] suggested that the capillaries are embedded in a connective tissue matrix which helps to resist collapse. In fact, Fung [14] calculated that the elasticity of the surrounding tissue is the major factor in resisting the collapse of a capillary vessel. This shows that our parameter k, which models the surrounding tethering, plays quite a significant role in preventing the collapse of blood vessels, especially the smaller ones. Unfortunately there exist no published numerical data on the elastic properties of the tethering.

In this paper we have used numerous simplifications in the modeling process. Aside from representing the tethering by numerous independent springs, we have assumed the springs to be linear. The nonlinearity of biological tissues is well known (Bergel [16]). In order to take nonlinearity into account, we may replace equation (8) by a nonlinear function, for example

$$F=k(\overline{BC}-\overline{AC})+k'(\overline{BC}-\overline{AC})^3 \tag{54}$$

Although the nonlinearity does not affect the stability analysis, it will lessen the slopes of Fig. 9. The net effect is equivalent to an increase in effective k as p is increased. Also, we have not discussed inhomogeneity, anisotropy, viscoelasticity, history dependence, neural, humoral, and many other factors of biological tissues. Nevertheless, it is hoped that the present paper gives at least qualitative behavior of tethered vessels.

References

1 Levy, M., "Mémoire sur un Nouveau Cas Intégrable du Problème de l 'elastique et l 'une de Ses Applications," *J. de Math.* (Liouville), Series 3, Vol. 10, 1884, pp. 5-42.

2 Greenhill, A. G., "The Elastic Curve Under Uniform Normal Pressure," *Math Ann.*, Vol. 52, 1899, pp. 465-500.

3 Tadjbakhsh, I., and Odeh, F., "Equilibrium States of Elastic Rings," *J. Math. Anal. Appl.*, Vol. 18, 1967, pp. 59-74.

4 Moreno, A. H., Katz, A. I., Gold, L. D., and Reddy, R. V., "Mechanics of Distension of Dog Veins and Other Very Thin-Walled Tubular Structures," *Circ. Res.*, Vol. 27, 1970, pp. 1069-1080.

5 Flaherty, J. E., Keller, J. B., and Rubinow, S. I., "Post-Buckling Behavior of Elastic Tubes and Rings With Opposite Sides in Contact," *SIAM J. Appl. Math.*, Vol. 23, 1972, pp. 446-455.

6 Seide, P., and Weingarten, V. I., "Buckling of Circular Rings and Long Cylinders Enclosing an Elastic Material Under Uniform External Pressure," *Am. Rocket. Soc. J.*, Vol. 32, 1962, pp. 680-688.

7 Moré, J. J., Garbow, B. S., and Hillstrom, K. E., User Guide for MINPACK-1, ANL-80-74, Argonne National Laboratory, 1980.

8 Dennis, J. E., and Moré, J. J., "Quasi-Newton Methods-Motivation and Theory," *SIAM Rev.*, Vol. 19, 1977, pp. 46-79.

9 Davidenko, D. F., "On the Approximate Solution of Systems of Nonlinear Equations," *Ukrain. Mat. Z.*, Vol. 5, 1953, pp. 196-206.

10 Shampine, L. F., and Gordon, M. K., *Computer Solution of Ordinary Differential Equations: The Initial Value Problem*, Freeman, San Francisco, 1975.

11 Finlayson, B. A., *The Method of Weighted Residuals and Variational Principles*, Academic Press, New York, 1972.

12 Connor, J. J., and Brebbia, C. A., *Finite Element Techniques for Fluid Flow*, Butterworths, London, 1976.

13 Baez, S., Lamport, H., and Baez, A., "Pressure Effects in Living Microscopic Vessels," In: *Flow Properties of Blood*, Copley, A. L., and Stainsby, G., eds., Pergamon, London, 1960.

14 Fung, Y. C., "Microscopic Blood Vessels in the Mesentery," In: *Biomechanics*, Fung, Y. C., ed., ASME, New York, 1966.

15 Fung, Y. C., Zweifach, B. W., and Intaglietta, M., "Elastic Environment of the Capillary Bed," *Circ. Res.*, Vol. 19, 1966, pp. 441-461.

16 Bergel, D. H., "The Properties of Blood Vessels," In: *Biomechanics, Its Foundations and Objectives*, Fung, Y. C., Perrone, N., and Anliker, M., eds., Prentice-Hall, Englewood Cliffs, N.J., 1972.

Downloaded 02 May 2010 to 171.66.16.246. Redistribution subject to ASME license or copyright; see http://www.asme.org/terms/Terms_Use.cfm

On the Estimation of Energy Release Rates

R. Abeyaratne
College of Engineering,
Michigan State University,
East Lansing, Mich. 48824
Assoc. Mem. ASME

The energy release rate associated with the Mode I and Mode III crack problems for an infinite, nonlinearly elastic, incompressible body are estimated. The calculation adopts an approximation that is a natural extension of the small-scale yielding concept to problems involving moderate levels of loading. The results are compared with available exact and numerical solutions and the agreement is found to be remarkably good. The scheme used here, based on the theory of small deformations superposed on a finite deformation, can be utilized to estimate the energy release rate in many other crack problems.

1 Introduction

If a crack in a deformed solid is to propagate, it requires energy and the so-called "energy release rate" represents the rate at which energy is made available to the crack for this purpose. Experiments carried out by Begley and Landes [1] have demonstrated the potential that this parameter has for use as a fracture initiation criterion. The present study suggests an (approximate) analytical scheme for estimating the value of the energy release rate for a body composed of a nonlinearly elastic material that is subjected to moderately large loads.

The importance of the energy release rate as a fracture initiation criterion has prompted many studies to calculate its value under nonlinear conditions. These have primarily consisted of numerical and experimental investigations, for example [2–5], as well as analytical approximations based on interpolation [6, 7]. The only exact solution appears to be that due to Amazigo [8] for a pure power-law material under conditions of antiplane shear.

The small-scale yielding approximation for the energy release rate uses the argument that when the applied loads are small, the nonlinearities in the problem are confined to a small region near the crack tips and that the linear elastic solution provides a good approximation elsewhere. The approximation we use here is a natural extension of this idea and essentially, replaces the linear elastic solution in the preceding argument by an improved approximation which takes into account the nonlinearities of the problem.

Consider for example the plane strain Mode *I* crack problem. In the absence of the crack, the body is in a homogeneous state of (finite) plane-strain uniaxial tension. If one were to assume that the presence of the crack causes only a small perturbation of this homogeneous state, one can then carry out an analysis based on the theory of *small deformations superposed on a large deformation*. The results based on such an approximation would clearly be invalid in the vicinity of the crack, but one would expect it to provide a reasonable approximation at points distant from the crack tips. Since our interest here lies *solely* in estimating the energy release rate, and since this can be written in the form of a line integral J taken over a contour that is *far* from the crack tips over most of its length, Rice [9], one expects such an approximation to be suitable for our purposes, at least when confined to moderate levels of loading.

The theory of small deformations superposed on a finite deformation, as well as many of its applications, are well known. In the context of problems involving cracks, Wu [10] has adopted such a scheme to study the buckling of cracks, and more recently, He and Hutchinson [11] have used it to examine the effect of a small load, normal to the crack, in a body that is subjected to a finite load in a direction parallel to the crack.

In this paper we carry out such an analysis in order to determine the energy release rate associated with the Mode *I* and Mode *III* crack problems. The results obtained in the antiplane shear case are compared with Amazigo's exact solution [8] in the particular case of a pure power-law material. The plane-strain solution is similarly compared with the finite element results given by He and Hutchinson [11]. In both cases, the agreement is found to be remarkably good.

2 Antiplane Shear: Mode *III*

2.1 Formulation. Consider a nonlinearly elastic body occupying a cylindrical region in its unstressed state. The X_3-axis is chosen parallel to the generators of the cylinder and $\mathcal{R}_0$ denotes its cross section in the (X_1,X_2)-plane. Suppose that $\mathcal{R}_0$ is infinite in extent except for a traction-free crack of length $2a$ in the plane $X_2 = 0$. The body is loaded by a remotely applied simple shear parallel to the crack faces.

We assume that the material is homogeneous, isotropic, incompressible, and admits a nontrivial state of antiplane shear, Knowles [12]. Let $\tau = \tau(k)$ denote the response function of this material in simple shear, so that its secant, tangent, and infinitesimal shear moduli (all >0) are

Contributed by the Applied Mechanics Division for presentation at the 1983 Applied Mechanics, Bioengineering, and Fluids Engineering Conference, Houston, Texas, June 20–22, 1983, of THE AMERICAN SOCIETY OF MECHANICAL ENGINEERS.

Discussion on this paper should be addressed to the Editorial Department, ASME, United Engineering Center, 345 East 47th Street, New York, N.Y. 10017, and will be accepted until two months after final publication of the paper itself in the JOURNAL OF APPLIED MECHANICS. Manuscript received by ASME Applied Mechanics Division, June, 1982. Paper No. 83-APM-11.

Copies will be available until February, 1984.

Copyright © 1983 by ASME
Downloaded 02 May 2010 to 171.66.16.246. Redistribution subject to ASME license or copyright; see http://www.asme.org/terms/Terms_Use.cfm

$$\mu(k)=\frac{\tau(k)}{k},\quad \tau'(k)=\frac{d\tau}{dk}(k),\quad \mu_0=\tau'(0), \tag{2.1}$$

respectively. The shear components σ_{31}, σ_{32} of the Cauchy (true) stress accompanying an antiplane deformation are given in terms of the out-of-plane displacement u_3 by

$$\sigma_{3\alpha}=\mu(k_e)u_{3,\alpha},\quad k_e^2=u_{3,\alpha}u_{3,\alpha}. \tag{2.2}$$

In Section 2, a comma followed by a subscript denotes partial differentiation with respect to the corresponding X-coordinate. Thus the equilibrium condition $\sigma_{3\alpha,\alpha}=0$ requires that

$$\left[\mu(k_e)u_{3,1}\right]_{,1}+\left[\mu(k_e)u_{3,2}\right]_{,2}=0 \quad \text{on} \quad \mathcal{R}_0, \tag{2.3}$$

whereas the boundary conditions of the present problem demand that

$$\sigma_{32}=\mu(k_e)u_{3,2}=0 \quad \text{on} \quad X_2=0\pm,\ |X_1|<a, \tag{2.4}$$
$$u_3\sim k_\infty X_2 \quad \text{as} \quad |\mathbf{X}|\to\infty.$$

Here k_∞ is the amount of shear applied at infinity and k_e is given by (2.2).

The energy release rate J associated with this problem is

$$J=\int_C\left[W(k_e)n_1-\sigma_{3\alpha}\,n_\alpha\,u_{3,1}\right]ds_X \tag{2.5}$$

Rice [9], where C is any simple closed curve which encloses the right crack tip in its interior but does not include the left one and n_α are the components of the unit outward normal to C. Here W denotes the strain energy density per unit undeformed volume so that

$$\tau(k)=\frac{d}{dk}W(k). \tag{2.6}$$

Our aim here is to estimate the value of J.

2.2 Estimation of Energy Release Rate. In the absence of the crack the deformation of the body is one of simple shear and the associated displacement field is $u_3=k_\infty X_2$. If we assume that the presence of the crack causes only a small disturbance of this crack-free equilibrium state, we would have

$$u_3(X_1,X_2)=k_\infty X_2+\tilde{u}(X_1,X_2),\ |\nabla\tilde{u}|<<1 \quad \text{on} \quad \mathcal{R}_0. \tag{2.7}$$

While such a hypothesis is undoubtedly invalid in the vicinity of the crack, it seems reasonable to assume that it would be true at points distant from the crack tips. Since our interest here lies solely in the computation of the path-independent integral J, and since for this purpose we may consider a path that is essentially far removed from the crack tips, the errors introduced by such an assumption are probably small, at least when confined to moderate levels of loading.

Accordingly, we now assume that the displacement field u_3 is of the form given by (2.7). Linearization of (2.2) based on a small displacement gradient $\nabla\tilde{u}$ leads to

$$\sigma_{31}=\mu(k_\infty)\tilde{u}_{,1},\quad \sigma_{32}=\tau_\infty+\tau'(k_\infty)\tilde{u}_{,2}, \tag{2.8}$$

where τ_∞ is the shear stress σ_{32} at infinity, $\tau_\infty=\tau(k_\infty)$. The nonlinear boundary-value problem (2.3), (2.4) may now be replaced by the linear problem

$$\mu(k_\infty)\tilde{u}_{,11}+\tau'(k_\infty)\tilde{u}_{,22}=0 \quad \text{on} \quad \mathcal{R}_0,$$
$$\tilde{u}_{,2}=-\frac{\tau_\infty}{\tau'(k_\infty)} \quad \text{on} \quad X_2=0\pm,\ |X_1|<a, \tag{2.9}$$
$$\tilde{u}\to 0 \quad \text{as} \quad |X|\to\infty.$$

Similarly, the linearization of the integrand of the J-integral (2.5) yields

$$J=\int_C\frac{1}{2}\Big\{-\mu(k_\infty)\tilde{u}_{,1}^2n_1+\tau'(k_\infty)\tilde{u}_{,2}^2\,n_1-2\tau'(k_\infty)\tilde{u}_{,1}\tilde{u}_{,2}n_2\Big\}\,ds_X, \tag{2.10}$$

to leading order. Solution of the linear boundary-value problem (2.9) gives $\tilde{u}$, which then permits the computation of J according to (2.10).

This end is most conveniently achieved by a rescaling that transforms the first of (2.9) into Laplace's equation. The resulting problem is now similar to that according to the linearized theory of elasticity whence [13]

$$\tilde{u}(X_1,X_2)=\frac{\tau_\infty}{\sqrt{\mu\tau'}}\,Im\left\{\sqrt{Z^2-a^2}-Z\right\} \tag{2.11}$$

where $Z=X_1+sX_2$, $s=i\,(\mu/\tau')^{1/2}$. The value of J is then readily calculated from (2.10) to be

$$J=\frac{\pi a}{2}\,\frac{\tau_\infty^2}{\left\{\tau'(k_\infty)\mu(k_\infty)\right\}^{1/2}}. \tag{2.12}$$

3 Plane Strain: Mode *I*

3.1 Formulation. Consider again the body and coordinate system described in Section (2.1), with the body now loaded by a remotely applied tensile (true) stress σ_∞ normal to the crack faces. The resulting deformation is assumed to be one of plane strain. Let $\mathbf{X}$ and $\mathbf{y}$ denote the position vectors of a typical material point before and after deformation. The deformation gradient tensor $\mathbf{F}$ has components

$$F_{\alpha\beta}=\partial y_\alpha/\partial X_\beta,\quad \det\mathbf{F}=1. \tag{3.1}$$

A plane strain deformation of an incompressible material can always be decomposed locally into a rigid rotation followed, or preceded, by a simple shear. The amount of this *local shear* is

$$k_e=(F_{\alpha\beta}\,F_{\alpha\beta}-2)^{1/2}=|\lambda-\lambda^{-1}|, \tag{3.2}$$

[14], where λ,λ^{-1} are the principle stretches of the deformation at that point. The in-plane behavior of the material is therefore essentially determined by its response in simple shear, $\tau=\tau(k)$. For an isotropic, incompressible, nonlinearly elastic material, the components of true stress in an arbitrary plane deformation are

$$\sigma_{\alpha\beta}=\mu(k_e)F_{\alpha\gamma}F_{\beta\gamma}-p\delta_{\alpha\beta},\ k_e=(F_{\alpha\beta}\,F_{\alpha\beta}-2)^{1/2}, \tag{3.3}$$

where μ is the secant modulus of shear, equation (2.1).

In the absence of the crack, the deformation gradient, stress, and pressure fields resulting in the body describe a homogeneous state of plane-strain uniaxial tension,

$$F^0_{\alpha\beta}=\lambda_\infty^{-1}\delta_{1\alpha}\delta_{1\beta}+\lambda_\infty\delta_{2\alpha}\delta_{2\beta},\quad \sigma^0_{\alpha\beta}$$
$$=\sigma_\infty\delta_{2\alpha}\delta_{2\beta},\quad p^0=\mu(k_\infty)\lambda_\infty^{-2}, \tag{3.4}$$

where

$$\sigma_\infty=\mu(k_\infty)\,(\lambda_\infty^2-\lambda_\infty^{-2}),\quad k_\infty=\lambda_\infty-\lambda_\infty^{-1}. \tag{3.5}$$

The argument presented in the Introduction suggests that for our purposes here we might suppose that the presence of the crack causes only a small disturbance of this crack-free state. Thus we assume that

$$y_\alpha=x_\alpha+\tilde{u}_\alpha(x_1,x_2),p=p^0+\tilde{p}(x_1,x_2) \tag{3.6}$$

where we have set $x_\alpha\equiv F^0_{\alpha\beta}X_\beta$ and $|\tilde{u}_{\alpha,\beta}|$, $|\tilde{p}_{,\alpha}|$ are assumed to be small compared with unity. Here, a comma followed by a subscript denotes partial differentiation with respect to the corresponding x-coordinate.

Linearization of the incompressibility condition $\det\mathbf{F}=1$ based on the small displacement gradient $\tilde{u}_{\alpha,\beta}$ gives

$$\tilde{u}_{\alpha,\alpha}=0 \quad \text{on} \quad \mathcal{R}, \tag{3.7}$$

where $\mathcal{R}$ is the two-dimensional region exterior to the line

Downloaded 02 May 2010 to 171.66.16.246. Redistribution subject to ASME license or copyright; see http://www.asme.org/terms/Terms_Use.cfm

segment $|x_1| \le a\lambda_\infty^{-1}$, $x_2 = 0$. Similarly, linearization of the constitutive relation (3.3) leads to

$$\tilde{\sigma}_{\alpha\beta} \equiv \sigma_{\alpha\beta} - \sigma^0_{\alpha\beta} = \mathcal{L}_{\alpha\beta}\tilde{u}_{\alpha,\beta} + \mathcal{L}_{\beta\alpha}(\delta_{1\alpha}\delta_{2\beta} + \delta_{1\beta}\delta_{2\alpha})\tilde{u}_{\beta,\alpha} - \tilde{p}\delta_{\alpha\beta} \quad \text{(no sum)} \tag{3.8}$$

where the (constant) incremental moduli $\mathcal{L}_{\alpha\beta}$ ($\neq \mathcal{L}_{\beta\alpha}$) are

$$\mathcal{L}_{11} = \left\{(3\lambda_\infty - \lambda_\infty^{-1})\mu - (\lambda_\infty + \lambda_\infty^{-1})\tau'\right\}\frac{\lambda_\infty^{-2}}{k_\infty}, \mathcal{L}_{12} = \lambda_\infty^2\mu, \tag{3.9}$$

$$\mathcal{L}_{22} = \left\{(\lambda_\infty - 3\lambda_\infty^{-1})\mu + (\lambda_\infty + \lambda_\infty^{-1})\tau'\right\}\frac{\lambda_\infty^{2}}{k_\infty}, \mathcal{L}_{21} = \lambda_\infty^{-2}\mu.$$

Here, and in the remainder of this paper, the tangent and secant moduli of shear τ', μ, (2.1), are evaluated at $k_\infty = \lambda_\infty - \lambda_\infty^{-1}$.

The equilibrium equations $\tilde{\sigma}_{\alpha\beta,\beta} = 0$ on $\mathcal{R}$ hold if and only if the stress is expressed in terms of an Airy stress function $\Phi(x_1, x_2)$

$$\tilde{\sigma}_{11} = \Phi_{,22}, \tilde{\sigma}_{22} = \Phi_{,11}, \tilde{\sigma}_{12} = \tilde{\sigma}_{21} = -\Phi_{,12}. \tag{3.10}$$

If a single-valued displacement field $\mathbf{u}(\mathbf{x})$ conforming to (3.7), (3.8), and (3.10) is to exist, it is clear that the components of stress should satisfy a certain compatibility condition. This is readily derived from (3.7), (3.8), and (3.10) to be

$$\mathcal{L}_{21}\Phi_{,1111} + (\mathcal{L}_{11} + \mathcal{L}_{22} - \mathcal{L}_{12} - \mathcal{L}_{21})\Phi_{,1122} + \mathcal{L}_{12}\Phi_{,2222} = 0 \quad \text{on} \quad \mathcal{R}. \tag{3.11}$$

Turning next to the traction-free condition on the deformed crack faces, one requires that the first Piola-Kirchoff stress $P_{\alpha\beta} = \sigma_{\alpha\gamma}F^{-1}_{\beta\gamma}$ obey $P_{12} = P_{22} = 0$ on $|X_1| < a$, $X_2 = 0\pm$. The linearized expressions for $\sigma_{\alpha\beta}$ and $F_{\alpha\beta}$ may be used to linearize $P_{\alpha\beta}$,

$$\begin{aligned} &P_{\alpha\beta} = P^0_{\alpha\beta} + \tilde{P}_{\alpha\beta}, P^0_{\alpha\beta} = \sigma_\infty\lambda_\infty^{-1}\delta_{2\alpha}\delta_{2\beta}, \\ &\tilde{P}_{11} = \lambda_\infty\tilde{\sigma}_{11}, \tilde{P}_{22} = \lambda_\infty^{-1}(\tilde{\sigma}_{22} + \sigma_\infty\tilde{u}_{1,1}), \\ &\tilde{P}_{12} = \lambda_\infty^{-1}\tilde{\sigma}_{12}, \tilde{P}_{21} = \lambda_\infty(\tilde{\sigma}_{21} - \sigma_\infty\tilde{u}_{1,2}). \end{aligned} \tag{3.12}$$

The traction-free condition then approximates to $\tilde{\sigma}_{12} = 0$, $\tilde{\sigma}_{22} + \sigma_\infty\tilde{u}_{1,1} = -\sigma_\infty$. Finally, on using (3.10), (3.8), and (3.7), this may be written in terms of the stress function Φ as

$$\Phi_{,12} = 0, \sigma_\infty\Phi_{,22} + (\mathcal{L}_{11} + \mathcal{L}_{22} - \sigma_\infty)\Phi_{,11} = -\sigma_\infty(\mathcal{L}_{11} + \mathcal{L}_{22}) \quad \text{on} \quad |x_1| < a\lambda_\infty^{-1}, x_2 = 0\pm. \tag{3.13}$$

The boundary-value problem (3.11) and (3.13), subject to the decay condition $\Phi_{,\alpha\beta} \to 0$ as $|\mathbf{x}| \to \infty$, may now be solved for the stress function Φ which can in turn be then used to calculate the energy release rate.

To prepare for this, we next derive the appropriate approximation to the potential energy within the present scheme. Since the region occupied by the body is unbounded, we use the "excess potential energy" V,

$$V = \int_{\mathcal{R}_0}\left[W(k_e) - W(k_\infty) - P^0_{\alpha\beta}\frac{\partial\tilde{u}_\alpha}{\partial X_\beta}\right]dA_X - \int_{\mathcal{L}_+ U\mathcal{L}_-} P^0_{\alpha\beta}n_\beta\tilde{u}_\alpha dS_X \tag{3.14}$$

in our discussion. Here W is the strain energy density per unit undeformed volume, k_e is the amount of local shear defined by (3.2), $\mathcal{L}_+, \mathcal{L}_-$ are the undeformed upper and lower crack faces, and the unit normal $\mathbf{n}$ is directed *into* $\mathcal{R}_0$. Roughly, this represents the difference in potential energy between two bodies that are identical except for the presence of a crack in one of them. We wish to calculate the energy release rate $-\partial V/\partial(2a)$. As in Section 2, one could of course alternatively utilize the equivalent representation for the energy release rate in the J-integral form in order to calculate its value.

A straightforward power series expansion of the strain energy W, after some simplification, gives

$$W(k_e) - W(k_\infty) - P^0_{\alpha\beta}\frac{\partial\tilde{u}_\alpha}{\partial X_\beta} = \frac{1}{2}\tilde{P}_{\alpha\beta}\frac{\partial\tilde{u}_\alpha}{\partial X_\beta} \tag{3.15}$$

to leading order. On using (3.15) and the divergence theorem, one may write the excess potential energy (3.14) as

$$V = -\int_{\mathcal{L}_+ U\mathcal{L}_-}(P^0_{\alpha\beta} + \frac{1}{2}\tilde{P}_{\alpha\beta})\tilde{u}_\alpha n_\beta\, dS_X. \tag{3.16}$$

The stress and displacement components $\tilde{P}_{\alpha\beta}$, $\tilde{u}_\alpha$ appearing here are those yielded by the solution to the boundary-value problem derived previously. The solution to this problem, presented in the following section, indicates that $\tilde{P}_{\alpha\beta}$, $\tilde{u}_\alpha$ are, respectively, of order r^{-2}, r^{-1} at infinity and of order $r^{-1/2}$, $r^{1/2}$ near the crack tips ($r = |\mathbf{x}|$). This fact has of course been used in deriving (3.16). Finally, use of the traction-free boundary condition $(P^0_{\alpha\beta} + \tilde{P}_{\alpha\beta})n_\beta = 0$ on $\mathcal{L}_+, \mathcal{L}_-$, together with (3.12), (3.16) gives

$$V = -\frac{1}{2}\sigma_\infty\lambda_\infty^{-1}\int_{-a}^{a}(\overset{+}{u}_2 - \overset{-}{u}_2)dX_1 \tag{3.17}$$

where $\overset{+}{u}_2$, $\overset{-}{u}_2$ are the limiting values of the displacement $\tilde{u}_2$ on $\mathcal{L}_+$ and $\mathcal{L}_-$, respectively.

3.2 Solution. Energy Release Rate. Here we solve the boundary-value problem (3.11) and (3.13), $\Phi_{,\alpha\beta} \to 0$ as $r \to \infty$, for the stress function Φ and then calculate the energy release rate from (3.17). Differential equations of the form (3.11) are commonly encountered in the study of plane anisotropic linear elasticity and the complex variable solution techniques developed there may be readily utilized in the present context. We refer the reader to Sih and Liebowitz [15] for details.

Here we will only be concerned with the case wherein the applied loading (and constitutive equation) obeys the condition $\tau'(k_\infty) > 0$, (2.1), i.e., when the partial differential equation (3.11) is elliptic. Then the polynomial

$$\mathcal{L}_{12}z^4 + (\mathcal{L}_{11} + \mathcal{L}_{22} - \mathcal{L}_{12} - \mathcal{L}_{21})z^2 + \mathcal{L}_{21} = 0 \tag{3.18}$$

has four (nonreal) complex roots $z = S_1, S_2, \bar{S}_1, \bar{S}_2$ and it may be easily shown that the roots S_1, S_2 with positive imaginary part obey

$$S_1S_2 = -\left\{\frac{\mathcal{L}_{21}}{\mathcal{L}_{12}}\right\}^{1/2}, \quad S_1 + S_2 = i\sqrt{2}\left\{-S_1S_2 + \frac{\mathcal{L}_{11} + \mathcal{L}_{22} - \mathcal{L}_{12} - \mathcal{L}_{21}}{2\mathcal{L}_{12}}\right\}^{1/2}. \tag{3.19}$$

If $(k_\infty^2 + 4)\tau' = 4\mu$ the roots of (3.18) are equal ($S_1 = S_2$, $\bar{S}_1 = \bar{S}_2$), and a rescaling transforms (3.11) into the biharmonic equation. Otherwise, the roots are distinct and the solution to (3.11) is

$$\Phi(x_1, x_2) = 2\mathcal{R}e\left\{\Phi_1(z_1) + \Phi_2(z_2)\right\} \tag{3.20}$$

where Φ_1, Φ_2 are arbitrary holomorphic functions of the complex variables z_1, z_2, respectively, $z_1 = x_1 + S_1x_2$, $z_2 = x_1 + S_2x_2$. The components of stress are now given in terms of the complex stress functions Φ_1, Φ_2 by (3.20) and (3.10), while the corresponding pressure field $\tilde{p}$ may be obtained from (3.8). Furthermore, integration of the displacement gradients in (3.7) and (3.8) yields expressions for the associated displacement field,

$$\begin{aligned} \tilde{u}_1 &= 2\mathcal{R}e\left\{p_1\Phi_1'(z_1) + p_2\Phi_2'(z_2)\right\}, \\ \tilde{u}_2 &= -2\mathcal{R}e\left\{\frac{p_1}{S_1}\Phi_1'(z_1) + \frac{p_2}{S_2}\Phi_2'(z_2)\right\}, \end{aligned} \tag{3.21}$$

where

$$p_\alpha = (S_\alpha^2 - 1)/(\mathcal{L}_{11} + \mathcal{L}_{22}). \tag{3.22}$$

Downloaded 02 May 2010 to 171.66.16.246. Redistribution subject to ASME license or copyright; see http://www.asme.org/terms/Terms_Use.cfm

Enforcement of the boundary conditions (3.13), using (3.10), (3.20), and (3.21) leads to a classical Riemann-Hilbert problem for Φ_1, Φ_2, the solution to which is

$$\Phi_\alpha'(z_\alpha) = \epsilon_{\beta\alpha} S_\beta D(z_\alpha - \sqrt{z_\alpha^2 - a^2\lambda_\infty^{-2}}), \quad \text{(no sum on } \alpha\text{)}$$

$$D = \frac{\sigma_\infty}{2}\left\{(1+\sigma_\infty p_1)S_2 - (1+\sigma_\infty p_2)S_1\right\}^{-1}. \tag{3.23}$$

Here $\epsilon_{\alpha\beta}$ is the two-dimensional alternator, and in view of (3.19) and (3.22), D is a real constant. We omit the derivation of this result since it is fairly standard (see for example Section IV*B* of [15]).

The limiting values of $\tilde{u}_2$ on $\mathcal{L}_+$ and $\mathcal{L}_-$ are given by (3.21)–(3.23), from which one obtains

$$\overset{+}{u}_2 - \overset{-}{u}_2 = -4\,\frac{\sqrt{\lambda_\infty^{-2}a^2 - x_1^2}}{\mathcal{L}_{11}+\mathcal{L}_{22}}\,\mathrm{Re}\left\{i\left[\frac{S_1^2 - S_2^2}{S_1 S_2}\right]D\right\}. \tag{3.24}$$

The potential energy V may now be evaluated from (3.17), (3.22), and (3.24) so that the energy release rate, $J = -1/2\,\partial V/\partial a$, is

$$J = \frac{\pi a}{2}\sigma_\infty^2\,\lambda_\infty^{-2}\,\mathrm{Re}\left\{\frac{i\,(S_1+S_2)}{S_1S_2[\mathcal{L}_{11}+\mathcal{L}_{22}-\sigma_\infty(S_1S_2+1)]}\right\}. \tag{3.25}$$

Finally, substituting for S_1, S_2, $\mathcal{L}_{11}$, $\mathcal{L}_{22}$, and σ_∞ from (3.19), (3.9), and (3.5) gives

$$J = \frac{\pi a}{2}\,\frac{\sigma_\infty^2}{\{\tau'(k_\infty)\mu(k_\infty)\}^{1/2}}\cdot\frac{1}{(1+\lambda_\infty^2)} \cdot\left\{1-\left[\frac{1-\lambda_\infty^{-2}}{\lambda_\infty+\lambda_\infty^{-1}}\right]^2\frac{\mu(k_\infty)}{\tau'(k_\infty)}\right\}^{-1}. \tag{3.26}$$

4 Discussion

In this paper we have examined a two-dimensional problem for an infinite nonlinearly elastic body containing a crack of undeformed length $2a$. Both Mode *I* and Mode *III* loadings have been considered and the corresponding values of the energy release rates have been calculated. The results are displayed in equations (3.26) and (2.12), respectively (see also (4.4)), and are expected to be suitable at moderate levels of loading. In both cases $\tau(k)$ represents the response function of the material in simple shear and $\mu(k)$, $\tau'(k)$, are the corresponding secant and tangent moduli of shear. In the Mode *III* case, k_∞ is the amount of shear applied at infinity. On the other hand, in Mode *I*, $k_\infty \equiv \lambda_\infty - \lambda_\infty^{-1}$ where λ_∞ is the principal stretch (>1) corresponding to the remotely applied true stress σ_∞, (3.5).

In the particular case when the applied load is small, the tangent and secant moduli coincide with the infinitesimal shear modulus μ_0 and (2.12) and (3.26) reduce to

$$J = \frac{\pi a}{2\mu_0}\tau_\infty^2 \quad (\text{Mode } III), \qquad J = \frac{\pi a}{4\mu_0}\sigma_\infty^2 \quad (\text{Mode } I), \tag{4.1}$$

which are of course identical to the results for J according to the small-scale yielding approximation of fracture mechanics [16].

Next consider the pure power-law material studied by Amazigo [8],

$$\tau(k) = \tau_0\left\{\frac{k}{\alpha k_0}\right\}^{1/n}. \tag{4.2}$$

In this case (2.12) yields

$$J = \frac{\pi a}{2}\tau_\infty k_\infty\sqrt{n}. \tag{4.3}$$

Figure 1 shows the variation of J with the material hardening exponent n according to (4.3). The exact values shown there are taken from Table 1 of Amazigo [8]. The comparison is seen to be remarkably good over a wide range of values of the material exponent n, with the formula (4.3) becoming less

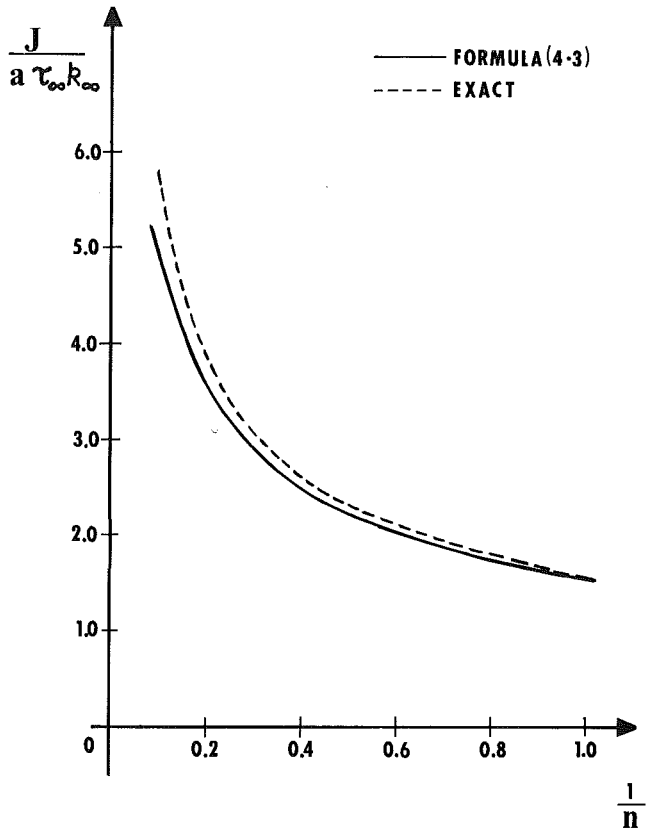

Fig. 1 Variation of energy release rate J with material hardening exponent n in antiplane shear. Comparison of formula (4.3) with exact result [8].

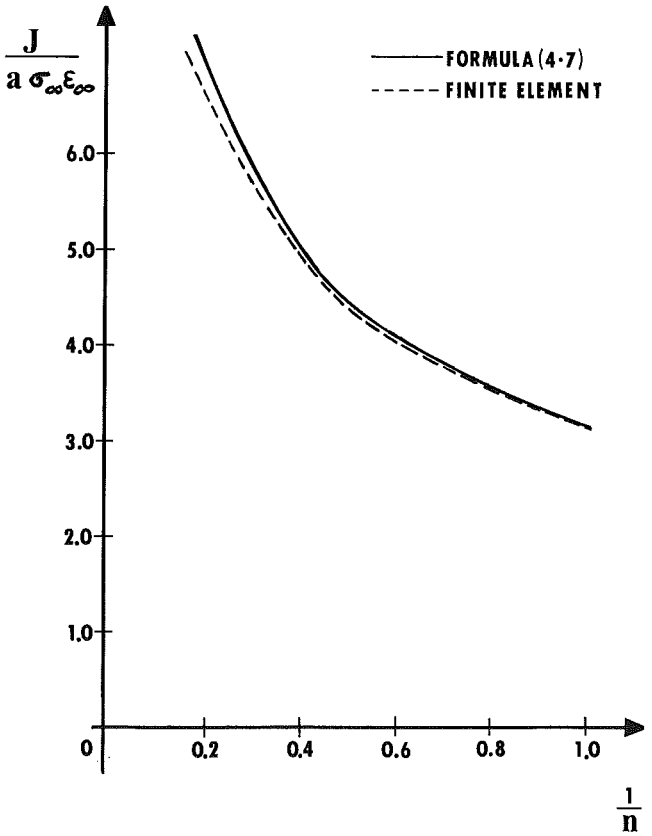

Fig. 2 Variation of energy release rate J with material hardening exponent n in plane strain mode *I*. Comparison of formula (4.7) with finite element results [11].

Downloaded 02 May 2010 to 171.66.16.246. Redistribution subject to ASME license or copyright; see http://www.asme.org/terms/Terms_Use.cfm

accurate as the shear response curve becomes "flatter," $n \to \infty$. It should be noted that the comparison made here is in fact for *all* values of the applied load and not merely for moderate ones.

Finally, consider the plane-strain result (3.26) and suppose that the load applied at infinity is sufficiently small so as to allow a *small strain nonlinear theory* to adequately describe the field far from the crack. Then, equation (3.26) may be further approximated to read

$$J = \frac{\pi a}{4} \frac{\sigma_\infty^2}{\{\tau'(k_\infty)\mu(k_\infty)\}^{1/2}} \tag{4.4}$$

with $k_\infty \simeq 2(\lambda_\infty - 1) \equiv 2\epsilon_\infty$, provided $\epsilon_\infty^2 \mu(k_\infty)/\tau'(k_\infty) << 1$. Consider now the small strain description of a nonlinearly elastic, pure power-law material

$$\frac{\epsilon_{ij}}{\epsilon_0} = \frac{3}{2} \alpha \left\{ \frac{\sigma_e}{\sigma_0} \right\}^{n-1} \frac{S_{ij}}{\sigma_0}, \quad \epsilon_{ij} = \frac{1}{2}(u_{i,j} + u_{j,i}), \tag{4.5}$$

He and Hutchinson [11]. Here S_{ij} is the stress deviator and σ_e is the effective stress $\sigma_e = (3\, S_{ij} S_{ij}/2)^{1/2}$. The response of this material in simple shear is described by

$$\tau(k) = \left\{ \frac{\sigma_0{}^n}{\alpha \epsilon_0 (\sqrt{3})^{n+1}} \right\}^{\frac{1}{n}} k^{\frac{1}{n}}, \tag{4.6}$$

so that in this case (4.4) reduces to

$$J = \pi a\, \sigma_\infty \epsilon_\infty \sqrt{n}, \tag{4.7}$$

where $\epsilon_\infty = \lambda_\infty - 1$. This agrees with the result obtained in [11]. Figure 2 displays the variation of J with n according to (4.7). The finite element solution shown there is taken from Table 3 of He and Hutchinson [11]. Again, the agreement is striking.

Acknowledgments

The author wishes to express his appreciation to Professor John W. Hutchinson of Harvard University; the work described here was initiated as a result of discussions with him. The support provided by the National Science Foundation through Grant CME 81-06581 is gratefully acknowledged.

References

1 Begley, J. A., and Landes, J. D., "The J Integral as a Fracture Criterion," in: *Fracture Toughness*, ASTM STP 514, 1972, pp. 1–23.

2 Ranaweera, M. P., and Leckie, F. A., "J Integrals for Some Crack and Notch Geometries," *International Journal of Fracture*, Vol. 18, 1982, pp. 3–18.

3 McMeeking, R. M., "Path Dependence of the J Integral and the Role of J as a Parameter Characterizing the Near Tip Field," in: *Flaw Growth and Fracture*, ASTM STP 631, 1977, pp. 28–41.

4 Griffis, C. A., and Yoder, G. R., "Initial Crack Extension in Two Intermediate Strength Aluminum Alloys," ASME *Journal of Engineering Materials and Technology*, Vol. 98, 1976, pp. 152–158.

5 Clarke, G. A., Andrews, W. R., Paris, P. C., and Schmidt, D. W., "Single Specimen Tests for J_{IC} Determination," in: *Mechanics of Crack Growth*, ASTM STP 590, 1976, pp. 27–42.

6 Shih, C. F., "J Integral Estimates for Strain Hardening Materials in Antiplane Shear Using Fully Plastic Solutions," in: *Mechanics of Crack Growth*, ASTM STP 590, 1976, pp. 3–22.

7 Shih, C. F., and Hutchinson, J. W., "Fully Plastic Solutions and Large Scale Yielding Estimates for Plane Stress Crack Problems," ASME *Journal of Engineering Materials and Technology*, Vol. 98, 1976, pp. 289–295.

8 Amazigo, J. C., "Fully Plastic Crack in an Infinite Body Under Anti-Plane Shear," *International Journal of Solids and Structures*, Vol. 10, 1974, pp. 1003–1015.

9 Rice, J. R., "Mathematical Analysis in the Mechanics of Fracture," in: *Fracture: An Advanced Treatise*, Liebowitz, H., ed., Vol. 2, Academic Press, New York, 1968, pp. 191–311.

10 Wu, C. H., "Plain Strain Buckling of Cracks in Incompressible Elastic Solids," *Journal of Elasticity*, Vol. 10, 1980, pp. 163–177.

11 He, M. Y., and Hutchinson, J. W., "The Penny-Shaped Crack and the Plane Strain Crack in an Infinite Body of Power-Law Material," ASME JOURNAL OF APPLIED MECHANICS, Vol. 48, 1981, pp. 830–840.

12 Knowles, J. K., "On Finite Anti-Plane Shear for Incompressible Elastic Materials," *The Journal of the Australian Mathematical Society*, Series B, Vol. 19, 1976, pp. 400–415.

13 Sneddon, I., and Lowengrub, M., *Crack Problems in the Classical Theory of Elasticity*, Wiley, New York, 1969.

14 Abeyaratne, R., "Discontinuous Deformation Gradients in Plane Finite Elastostatics of Incompressible Materials," *Journal of Elasticity*, Vol. 10, 1980, pp. 255–293.

15 Sih, G. C., and Liebowitz, H., "Mathematical Theories of Brittle Fracture," in: *Fracture: An Advanced Treatise*, Liebowitz, H., ed., Vol. 2, Academic Press, New York, 1968, pp. 67–190.

16 Hutchinson, J. W., *Nonlinear Fracture Mechanics*, Technical University of Denmark, 1979.

Downloaded 02 May 2010 to 171.66.16.246. Redistribution subject to ASME license or copyright; see http://www.asme.org/terms/Terms_Use.cfm

Thermal Stress in a Transversely Isotropic Medium Containing a Penny-Shaped Crack

Y. M. Tsai
Professor,
Department of Engineering Science and Mechanics,
Engineering Research Institute,
Iowa State University,
Ames, Iowa 50011

The thermal stress problem for a penny-shaped crack contained in a transversely isotropic medium is investigated using the techniques of Hankel transforms and double integrations. Symmetrical thermal loadings are applied over the crack surfaces. For constant temperature and heat flux over the crack surfaces, expressions for the crack shapes and the thermal stresses in the crack plane are obtained in closed forms. The stress intensity factors are also obtained and shown to be dependent on the material properties.

Introduction

The stresses set up by the application of heat to the surfaces of a penny-shaped crack in an infinite elastic isotropic material were investigated using the techniques of dual integral equations [1]. The thermal conditions on the upper surface of the crack were identical to those on the lower surface. Therefore, the problem was symmetrical with respect to the crack plane [1]. Any problem of an infinite isotropic medium can be resolved in two ways: one symmetrical and the other antisymmetrical [2]. The features of antisymmetry were presented in the linear thermoelastic problem of uniform heat flow disturbed by a penny-shaped insulated crack [2].

The anisotropic thermal and elastic properties of materials were presented in [3] for metallic substances and in [4] for composite materials. The thermal stress problem for a penny-shaped crack contained in a transversely isotropic medium [5–7] is investigated in the present work. The thermal conditions considered are symmetrical with respect to the crack plane [1]. The anisotropic properties of materials satisfy the requirement for nonvanishing value of a characteristic determinant obtained in the present problem whereas an isotropic medium makes the determinant vanishing. Therefore, the functions of solution required for the current anisotropic problem are different from those for an isotropic medium [1]. Crack shapes and thermal stresses in the crack plane are presented in closed forms, using the techniques of Hankel transforms and double integrations [7].

Formal Solution

The Duhamel-Neumann equations for a transversely isotropic medium can be written in terms of cylindrical coordinates (r,ϕ,z) as follows [3]:

$$\begin{aligned}
\sigma_{rr} &= c_{11}e_{rr} + c_{12}e_{\phi\phi} + c_{13}e_{zz} - \beta_1\theta \\
\sigma_{\phi\phi} &= c_{12}e_{rr} + c_{11}e_{\phi\phi} + c_{13}e_{zz} - \beta_1\theta \\
\sigma_{zz} &= c_{13}e_{rr} + c_{13}e_{\phi\phi} + c_{33}e_{zz} - \beta_2\theta \\
\sigma_{rz} &= c_{44}e_{rz},\ \sigma_{\phi z} = c_{44}e_{\phi z} \\
\sigma_{r\phi} &= \frac{1}{2}(c_{11} - c_{12})e_{r\phi}
\end{aligned} \tag{1}$$

where the thermal moduli are

$$\begin{aligned}
\beta_1 &= (c_{11} + c_{12})\alpha_1 + c_{13}\alpha_2 \\
\beta_2 &= 2c_{13}\alpha_1 + c_{33}\alpha_2
\end{aligned} \tag{2}$$

In the foregoing equations, the z-axis is along the axis of symmetry of the material that has five elastic constants c_{ij}. θ is the deviation of the absolute temperature from the temperature of the medium in a state of zero stress and strain. α_1 is the thermal expansion coefficient in the planes of isotropy and α_2 is the thermal expansion coefficient along the z-axis. The strain-displacement relationships and the equilibrium equations are the same as those for an isotropic solid [5, 7]. For symmetrical deformations, the equilibrium equations can be written in terms of the displacement components $(u_r,0,u_z)$ as follows:

$$c_{11}\frac{\partial}{\partial r}\left[\frac{1}{r}\frac{\partial}{\partial r}(ru_r)\right] + (c_{13} + c_{44})\frac{\partial^2 u_z}{\partial r \partial z} + c_{44}\frac{\partial^2 u_r}{\partial z^2} - \beta_1\frac{\partial\theta}{\partial r} = 0 \tag{3}$$

$$c_{44}\frac{1}{r}\frac{\partial}{\partial r}\left(r\frac{\partial u_z}{\partial r}\right) + (c_{13} + c_{44})\frac{\partial}{\partial z}\left[\frac{1}{r}\frac{\partial}{\partial r}(ru_r)\right] + c_{33}\frac{\partial^2 u_z}{\partial z^2} - \beta_2\frac{\partial\theta}{\partial z} = 0 \tag{4}$$

Contributed by the Applied Mechanics Division for presentation at the 1983 ASME Applied Mechanics, Bioengineering, and Fluids Engineering Conference, Houston, Texas, June 20–22, 1983 of the AMERICAN SOCIETY OF MECHANICAL ENGINEERS.

Discussion on this paper should be addressed to the Editorial Department, ASME, United Engineering Center, 345 East 47th Street, New York, N.Y. 10017, and will be accepted until two months after final publication of the paper itself in the JOURNAL OF APPLIED MECHANICS. Manuscript received by ASME Applied Mechanics Division, May, 1982; final revision, July, 1982. Paper No. 83-APM-8.

Copies will be available until February, 1984.

Copyright © 1983 by ASME
Downloaded 02 May 2010 to 171.66.16.246. Redistribution subject to ASME license or copyright; see http://www.asme.org/terms/Terms_Use.cfm

The temperature field in the medium in a steady state is governed by the following equation:

$$\frac{1}{r}\frac{\partial}{\partial r}\left(r\frac{\partial\theta}{\partial r}\right)+k^2\frac{\partial^2\theta}{\partial z^2}=0 \tag{5}$$

where $k=k_2/k_1$. k_1 is the coefficient of thermal conductivity in the planes of isotropy and k_2 the coefficient of thermal conductivity in the z-direction.

To solve the foregoing system of three partial differential equations, the first-order Hankel transforms are applied to equation (3), while the zeroth-order Hankel transforms are applied to equations (4) and (5) over the variable r. The transformed equations in terms of the parameter s are obtained as follows:

$$c_{44}\frac{\partial^2\hat{u}_r^1}{\partial z^2}-c_{11}s^2\hat{u}_r^1-(c_{13}+c_{44})s\frac{\partial\hat{u}_z^0}{\partial z}=-\beta_1 s\hat{\theta}^0 \tag{6}$$

$$c_{33}\frac{\partial^2\hat{u}_z^0}{\partial z^2}-c_{44}s^2\hat{u}_z^0+(c_{13}+c_{44})s\frac{\partial\hat{u}_r^1}{\partial z}=\beta_2\frac{\partial\hat{\theta}^0}{\partial z} \tag{7}$$

$$k^2\frac{\partial^2\hat{\theta}^0}{\partial z^2}-s^2\hat{\theta}^0=0 \tag{8}$$

Since the problem is symmetrical with respect to the plane $z=0$, it is sufficient to consider only the solution for the upper portion of the infinite solid. Therefore, the solution of equation (8) is readily obtained as

$$\hat{\theta}^0=C\,se^{-sz/k} \tag{9}$$

where C is an unknown constant to be determined later using the prescribed thermal boundary conditions.

Equations (6) and (7) can now be regarded as a system of inhomogeneous ordinary differential equations. In terms of equation (9), the particular solutions can be written as

$${}_p\hat{u}_r^1=A_3e^{-sz/k},\quad {}_p\hat{u}_z^0=B_3e^{-sz/k} \tag{10}$$

where the coefficients are obtained as

$$A_3=[\beta_2(c_{13}+c_{44})-\beta_1(c_{33}-k^2c_{44})]C/\Delta \tag{11}$$

$$B_3=-[\beta_2(c_{44}-k^2c_{11})+\beta_1k^2(c_{13}+c_{44})]C/(k\Delta) \tag{12}$$

$$\Delta=(c_{13}+c_{44})^2-(c_{44}-k^2c_{11})(c_{44}-c_{33}/k^2) \tag{13}$$

The characteristic determinant Δ in the denominators was also obtained in [6]. It is assumed here that the value of Δ does not vanish. This condition is generally satisfied for anisotropic solids. For an isotropic solid, Δ is equal to zero. Therefore, different functions of solution are required for an isotropic solid as presented in [1].

To solve the homogeneous equations of the system of equations (6) and (7), the solutions can be chosen as

$${}_h\hat{u}_r^1=A\,e^{-\lambda sz} \tag{14}$$

$${}_h\hat{u}_z^0=B\,e^{-\lambda sz} \tag{15}$$

The homogeneous equations are satisfied if the parameter satisfies the following characteristic equation:

$$(c_{44}\lambda^2-c_{11})(c_{33}\lambda^2-c_{44})+(c_{13}+c_{44})^2\lambda^2=0 \tag{16}$$

The preceding quadratic equation for λ^2 has two roots, λ_1^2 and λ_2^2, which are either both real or a pair of complex conjugates, depending on the values of the material constants. Obviously the square roots of λ_1^2 and λ_2^2 can be positive and negative. For the infinite solid considered, the roots λ_1 and λ_2 are selected to have positive real parts. For the first root, λ_1, the constants in equations (14) and (15) are written as A_1 and B_1. The homogeneous equation of equation (7) gives the following relationship:

$$(c_{13}+c_{44})\lambda_1A_1=(c_{33}\lambda_1^2-c_{44})B_1 \tag{17}$$

If all of the foregoing subscript 1's are replaced by 2's, the resulting equation becomes a new relationship for the similar constants A_2 and B_2 for the second root λ_2. The formal solutions have thus been obtained in terms of the five constants A_1, A_2, B_1, B_2, and C, which are to be determined in terms of the prescribed thermal and stress boundary conditions.

Thermal Crack Shape

A penny-shaped crack with radius a is assumed to be located in the interior of the transversely isotropic medium. The z-axis is normal to the crack surfaces which are located at $z=0$. The crack is opened up by the application of heat to its flat surfaces. Two cases of axisymmetrical thermal loadings are to be considered. The first case concerns an axisymmetrical temperature applied over the crack surfaces. The thermal boundary conditions at $z=0$ can be written as

$$\theta=\theta_0(r),\quad 0\le r\le a \tag{18}$$

$$\frac{\partial\theta}{\partial z}=0,\quad r>a \tag{19}$$

To satisfy the foregoing equations, the temperature gradient in the crack surface is first assumed to be Q', which will later be determined in terms of θ_0.

Using equation (19), the constant in equation (9) is determined as follows:

$$C=-k/s^2\int_0^a Q'\lambda\,J_0(s\lambda)\,d\lambda \tag{20}$$

The condition in equation (18) gives the integral equation obtained from equation (9) in terms of equation (20) at $z=0$ for $r\le a$ as follows:

$$\int_0^\infty\int_0^a Q'\lambda J_0(s\lambda)d\lambda J_0(sr)\,ds=-\theta_0/k \tag{21}$$

If the double integrations on the right-hand side of the following equations are operated over the preceding equation, the integral equation is integrated [8] out into the form

$$Q'=\frac{2}{\pi k}\frac{1}{r}\frac{\partial}{\partial r}\int_r^a\frac{\xi}{\sqrt{\xi^2-r^2}}\frac{\partial}{\partial\xi}\int_0^\xi\frac{\theta_0\lambda d\lambda}{\sqrt{\xi^2-\lambda^2}}\,d\xi \tag{22}$$

For the case of constant temperature $\theta_0=T$, the preceding equation is readily integrated out as

$$Q'=-2T(a^2-r^2)^{-1/2}/(\pi k) \tag{23}$$

Substituting equation (23) into equation (20) gives, after integrations [8], the following results:

$$C=2T\sin(as)/(\pi s^3) \tag{24}$$

In terms of the preceding equation, the temperature that is the inversion of $\hat{\theta}^0$ in equation (9) at $z=0$ recovers its prescribed crack surface value in equation (18). Outside the crack surface at $z=0$, the temperature is found from equations (9) and (24) as

$$\theta=(2T/\pi)\sin^{-1}(a/r),\quad r>a \tag{25}$$

The stress boundary conditions due to the foregoing thermal loadings can be written at $z=0$ as

$$\sigma_{rz}=0\quad \text{for all}\quad r \tag{26}$$

$$u_z=\begin{cases}w(r), & 0\le r\le a\\ 0, & a<r\end{cases} \tag{27}$$

The unknown crack shape function $w(r)$ is to be determined later, using the stress-free condition at the crack surfaces.

To satisfy the stress boundary conditions, the transformed forms of the two related stress components can be written from equation (1) as follows:

Downloaded 02 May 2010 to 171.66.16.246. Redistribution subject to ASME license or copyright; see http://www.asme.org/terms/Terms_Use.cfm

$$\hat{\sigma}^1_{rz} = c_{44}\left(\frac{\partial \hat{u}^1_r}{\partial z} - s\,\hat{u}^0_z\right) \tag{28}$$

$$\hat{\sigma}^0_{zz} = c_{13}s\,\hat{u}^1_r + c_{33}\frac{\partial \hat{u}^0_z}{\partial z} - \beta_2\hat{\theta}^0 \tag{29}$$

The foregoing transformed displacements are the sums of the particular solutions in equation (10) and the homogeneous solutions in equations (14) and (15) in terms of the characteristic roots and their associated constants. In terms of equations (28) and (17), and the related equation for λ_2, the condition in equation (26) gives

$$(c_{33}\lambda_1^2 + c_{13})B_1 + (c_{33}\lambda_2^2 + c_{13})B_2 = -(A_3/k + B_3)/(c_{13} + c_{44}) \tag{30}$$

In terms of equation (30), the condition in equation (27) gives

$$B_2 = \frac{(c_{33}\lambda_1^2 + c_{13})\hat{w}^0 + (c_{44} - c_{33}\lambda_1^2)B_3 + (c_{13} + c_{44})A_3/k}{c_{33}(\lambda_1^2 - \lambda_2^2)} \tag{31}$$

where the transform in terms of the zeroth-order Bessel function $J_0(x)$ is

$$\hat{w}^0 = \int_0^a J_0(s\lambda)\,\lambda\, w(\lambda)\,d\lambda \tag{32}$$

The transformed normal stress in equation (29) can be calculated in terms of equations (9), (17), (20), (30), and (31); and its inverse transform at $z = 0$ is found as follows:

$$\sigma_{zz} = -K\,I_1 + M\,I_2 \tag{33}$$

where

$$I_1 = \int_0^\infty J_0(sr)\,s^2\,\hat{w}^0\,ds \tag{34}$$

$$I_2 = \int_0^\infty C\,J_0(sr)\,s^2\,ds \tag{35}$$

K and M are functions of material constants as defined in the Appendix.

The surfaces of the crack are free from stresses. Therefore, σ_{zz} in equation (33) is equal to zero for $r \le a$. This gives an integral equation for determining the crack-shape function w caused by the thermal loading. The double-integration techniques used in the previous work [7] can be used here to invert the integral equation. The operation of the double integrations over I_1 in equation (34) gives, as in [7], the following results:

$$\frac{\partial}{\partial r}\int_r^a \sqrt{\xi^2 - r^2}\int_0^\xi \frac{mI_1\,dm}{\sqrt{\xi^2 - m^2}}\,d\xi = -\pi w(r)\,r/2 \tag{36}$$

I_2 in equation (35) can first be integrated in terms of equation (24) as follows:

$$I_2 = \frac{2T}{\pi}\int_0^\infty \frac{J_0(sr)\sin(as)}{s}\,ds = \begin{cases} T, & r \le a \\ \dfrac{2T}{\pi}\sin^{-1}\dfrac{a}{r}, & r > a \end{cases} \tag{37}$$

The integration was carried out using an identity in [8]. The double integrations on the left-hand side of equation (36) are now applied over I_2 for $r \le a$, and the integrations are carried out exactly. The integrated results and equation (36) are substituted into equation (33), and the condition $\sigma_{zz} = 0$ for $r \le a$ gives the following thermal crack shape

$$w = 2TM/(\pi k)\int_r^a \xi(\xi^2 - r^2)^{-1/2}\,d\xi = 2TM(a^2 - r^2)^{1/2}/(\pi k) \tag{38}$$

The second case of thermal loading considered is that an axisymmetrical flux of heat across the upper surface of the crack is the same as that across lower surfaces. The thermal boundary condition at $z = 0$ can be written as

$$\frac{\partial \theta}{\partial z} = \begin{cases} Q(r), & 0 \le r \le a \\ 0, & a < r \end{cases} \tag{39}$$

The coefficient in equation (9) can readily be determined in terms of equation (39) as

$$C = -k/s^2\int_0^a Q\lambda J_0(s\lambda)\,d\lambda \tag{40}$$

The boundary conditions in equations (26) and (27) also apply for the current heat flux condition, and so does the normal stress in equation (33). In the present case, I_2 replaces I_1 in the inner integral of equation (36) and yields an expression similar to equation (37). After integrations by parts, the results can be written for $\xi \le a$ as

$$F(\xi) = \int_0^\xi \frac{mI_2\,dm}{\sqrt{\xi^2 - m^2}} = -k\left[\frac{\pi}{2}q(0) - \xi\int_\xi^a \frac{q\,d\lambda}{\lambda\sqrt{\lambda^2 - \xi^2}}\right] \tag{41}$$

where

$$q(\lambda) = \int_\lambda^a Q\eta\,d\eta \tag{42}$$

The outer integration and differentiation in equation (36) are applied over $F(\xi)$ in equation (41). The results and equation (36) are substituted into equation (33). The stress-free condition at the crack surfaces, i.e., $\sigma_{zz} = 0$ for $r \le a$, yields the following expression:

$$w = \frac{2M}{\pi K}\int_r^a \frac{F(\xi)\,d\xi}{\sqrt{\xi^2 - r^2}} \tag{43}$$

For the case of constant heat flux $Q = -Q_0$, the preceding equation can readily be integrated out into the following thermal crack shape:

$$w = MQ_0a^2/4\{1 - r^2/a^2 + 2ln(1 + \sqrt{1 - r^2/a^2})\} \tag{44}$$

Thermal Stress Distribution

The normal stress in equation (33) involves singularities. To determine the stress for the first case of constant temperature, the transform in equation (32) is calculated for w given in equation (38) as follows:

$$\hat{w}^0 = \frac{2TM}{\pi K}\int_0^a \frac{\xi\sin(\xi s)}{s}\,d\xi \tag{45}$$

Substituting equation (45) into equation (34) yields the following integral:

$$I_1 = \frac{2MT}{\pi K}\frac{1}{r}\frac{\partial}{\partial r}\,r\int_0^a \xi\int_0^\infty J_1(sr)\sin(\xi s)\,ds\,d\xi \tag{46}$$

The foregoing integration over s can be carried out using an identity in [8], and the double integrations are explicitly carried out as follows:

$$I_1 = \begin{cases} MT/K, & r \le a \\ \dfrac{2MT}{\pi K}\left[\sin^{-1}\dfrac{a}{r} - \dfrac{a}{\sqrt{r^2 - a^2}}\right], & r > a \end{cases} \tag{47}$$

Downloaded 02 May 2010 to 171.66.16.246. Redistribution subject to ASME license or copyright; see http://www.asme.org/terms/Terms_Use.cfm

Employing equations (37) and (47) in equation (33), we note that σ_{zz} vanishes for $r \le a$, while for $r > a$ we obtain:

$$\sigma_{zz} = 2TMa\pi^{-1}(r^2 - a^2)^{-1/2} \tag{48}$$

The preceding equation gives the stress intensity factor of $K_I = 2TM(a/\pi)^{1/2}$.

The radial component of stress σ_{rr} can be calculated from equation (1) with procedures similar to those for σ_{zz}. The results at $\dot{z} = 0$ can be written as

$$\sigma_{rr} = K_2 I_1 - K_3 I_3 + M_2 I_2 - M_3 I_4 \tag{49}$$

where

$$I_3 = \int_0^\infty \frac{sJ_1(sr)}{r}\,\hat{w}^0 ds; \quad I_4 = \int_0^\infty \frac{sJ_1(sr)}{r}\,C ds \tag{50}$$

K_2, K_3, M_2, and M_3 are functions of material constants and defined in the Appendix. In terms of equation (45), I_3 is explicitly integrated out [8] as follows:

$$I_3 = \begin{cases} MT/(2K), & r \le a \\ MT/(\pi K)[\sin^{-1}(a/r) - ar^{-2}(r^2 - a^2)^{1/2}], & r > a \end{cases} \tag{51}$$

I_4 is integrated out [8] in terms of equations (24) as follows:

$$I_4 = \begin{cases} T/2, & r \le a \\ T/\pi[\sin^{-1}(a/r) + ar^{-2}(r^2 - a^2)^{1/2}], & r > a \end{cases} \tag{52}$$

If the material constants c_{11} and c_{12} in K_2, K_3, M_2, and M_3 are exchanged, the stress in equation (49) becomes the circumferential stress $\sigma_{\phi\phi}$. The inverse square-root singularity in equation (49) results only from I_1 in equation (47). This is the same as σ_{zz}. However, the intensities of the singularities are different, depending on the values of K and K_2.

The thermal stress distribution for the second case of heat flux condition can also be determined by means of procedures similar to those for the first case. The only required modifications are to delete T and replace $\xi \sin(\xi s)$ by $F(\xi) \sin(\xi s)$ in equations (45) and (46). I_1 in equation (46) is integrated [8] as

$$I_1 = \begin{cases} \dfrac{2M}{\pi K}\dfrac{1}{r}\dfrac{\partial f}{\partial r}; \quad f(r) = \displaystyle\int_0^r \frac{\xi F(\xi)}{\sqrt{r^2 - \xi^2}}\,d\xi, & r \le a \\ \dfrac{2M}{\pi K}\dfrac{1}{r}\dfrac{\partial g}{\partial r}; \quad g(r) = \displaystyle\int_0^a \frac{\xi F(\xi)}{\sqrt{r^2 - \xi^2}}\,d\xi, & r > a \end{cases} \tag{53}$$

The Abel transform of I_2 in equation (35) is identical with $F(\xi)$ in equation (41) for $\xi \le a$. For $\xi > a$, the transform is equal to $-k\pi q(0)/2$. The inverse transform of the Abel transform of I_2 gives

$$I_2 = \begin{cases} 2(\pi r)^{-1}\partial f/\partial r, & r \le a \\ 2(\pi r)^{-1}\partial g/\partial r - k\,q(0)(r^2 - a^2)^{-1/2}, & r > a \end{cases} \tag{54}$$

In terms of equations (53) and (54), σ_{zz} in equation (33) recovers the prescribed condition of vanishing normal stress on the crack surfaces for $r \le a$. For $r > a$, the normal stress takes the following form:

$$\sigma_{zz} = -kMq(0)(r^2 - a^2)^{-1/2} \tag{55}$$

For the special case of constant heat flux $Q = -Q_0$, $q(0)$ is equal to $-Q_0 a^2/2$. The stress intensity factor is equal to $K_I = kMQ_0(a^3\pi)^{1/2}/2$.

The radial stress σ_{rr} in equation (49) also holds for the second case. Using procedures similar to those for I_1, I_3 in equation (50) is integrated into the following form:

$$I_3 = \begin{cases} 2M(\pi K)^{-1} r^{-2} f, & r \le a \\ 2M(\pi K)^{-1} r^{-2} g, & r > a \end{cases} \tag{56}$$

I_4 in equation (50) can be integrated by means of the following identities, which are used in [9]:

$$L\frac{J_1(sm)}{m} = \frac{\partial}{\partial \xi}\int_0^\xi \frac{J_1(sm)}{m} \cdot \frac{m^3 dm}{(\xi^2 - m^2)^{1/2}} = \xi \sin(s\xi) \tag{57}$$

$$h(r) = \frac{2}{\pi}\frac{1}{r^2}\int_0^r \frac{d\xi}{(r^2 - \xi^2)^{1/2}}\frac{\partial}{\partial \xi}\int_0^\xi \frac{h(m)m^3 dm}{(\xi^2 - m^2)^{1/2}} \tag{58}$$

The operator L in equation (57) which is the same as the inner differentiation and integration in equation (58) is first applied over the variable r in I_4. The resulting integral is then integrated over s using the expression for C in equation (40). These two calculations give $LI_4 = \xi F(\xi)$ for $r \le a$. For $r > a$, LI_4 is equal to $-k\pi q(0)/2$. LI_4 can now be recognized as a resulting quantity of the inner differentiation and integration of equation (58). The outer integration and multiplication in equation (58) are applied to LI_4 to recover the value of I_4, which can be written as

$$I_4 = \begin{cases} 2\pi^{-1} r^{-2} f(r), & r \le a \\ 2\pi^{-1} r^{-2} g(r) - kq(0)(r^2 - a^2)^{-1/2}, & r > a \end{cases} \tag{59}$$

The stress $\sigma_{\phi\phi}$ can be obtained from σ_{rr} using the same procedures of exchanging material constants as those for the first case.

For the special case of constant heat flux $Q = -Q_0$, the integrations concerning f and g are obtained [10] as follows:

$$r^{-1}\partial f/\partial r = kQ_0 a\,E(r/a) \tag{60}$$

$$r^{-2} f = kQ_0 a[(1 + a^2/r^2)E(r/a) + (1 - a^2/r^2)K(r/a)]/3 \tag{61}$$

$$r^{-1}\partial g/\partial r = kQ_0[a^2(r^2 - a^2)^{-1/2}\pi/4 - rE(a/r) + (r^2 - a^2)K(a/r)/r] \tag{62}$$

$$r^{-2} g = kQ_0[a^2(r^2 - a^2)^{1/2}\pi/(4r) - E(a/r) + (1 - a^2/r^2)K(a/r)]/r \tag{63}$$

$K(y)$ and $E(y)$ are the complete elliptic integrals of the first and second kinds [10], respectively. Equation (61) has the value of $kQ_0 a\pi/4$ at $r = 0$.

The radial stress σ_{rr} can be calculated in terms of equations (60)–(63), and has the inverse square-root singularity that results from both I_1 and I_4. The intensity of the singular term is different from that of σ_{zz} and depends on material properties.

The characteristic roots of equation (16) are calculated for typical glass-epoxy and graphite-epoxy composites. Complete definite values of the elastic constants for these two materials are listed in the fourth columns of Tables 1 and 2 in [11]. The roots for the glass-epoxy composite are $\lambda_1 = 1.638$ and $\lambda_2 = 0.343$, and for the graphite-epoxy composite are $\lambda_1 = 1.393$ and $\lambda_2 = 0.222$. For typical metallic substances, magnesium gave real roots whereas the roots for zinc were a pair of complex conjugates [5].

Acknowledgment

This research was supported by the Engineering Research Institute of Iowa State University.

References

1 Olesiak, Z., and Sneddon, I. N., "This Distribution of Thermal Stress in an Infinite Elastic Solid Containing a Penny-Shaped Crack," *Arch. Rat. Mech. Anal.*, Vol. 4, 1960, pp. 238–254.

2 Florence, A. L., and Goodier, J. N., "The Linear Thermoelastic Problem of Uniform Heat Flow Disturbed by a Penny-Shaped Insulated Crack," *Int. J. Eng. Sci.*, Vol. 1, 1963, pp. 533–540.

3 Nowinski, J. L., *Theory of Thermoelasticity With Applications*, Sijthoff & Noordhoff, Alphen ann den Rijn, The Netherlands, 1978, p. 118.

4 Christensen, R. M., *Mechanics of Composite Materials*, Wiley, New York, 1979, p. 311.

5 Elliott, H. A., "Three-Dimensional Stress Distributions in Hexagonal

Downloaded 02 May 2010 to 171.66.16.246. Redistribution subject to ASME license or copyright; see http://www.asme.org/terms/Terms_Use.cfm

Aeolotropic Crystals," *Proceedings of the Cambridge Philosophical Society*, Vol. 44, 1948, pp. 522–533.

6 Sharma, B., and Pradesh, M., "Thermal Stresses in Transversely Isotropic Semi-Infinite Elastic Solids," ASME JOURNAL OF APPLIED MECHANICS, Vol. 25, 1958, pp. 86–88.

7 Tsai, Y. M., "Penny-Shaped Crack in a Transversely Isotropic Plate of Finite Thickness," Iowa State University, Engineering Research Institute Preprint, ERI-81233, 1981 (To appear in *Int. J. Fracture)*.

8 Watson, G. N., *Theory of Bessel Functions*, 2nd Ed,, Cambridge University Press, London, 1966, p. 405.

9 Tsai, Y. M., "Dynamic Contact Stresses Produced by the Impact of an Axisymmetrical Projectile on an Elastic Half-Space," *Int. J. Solids & Structures*, Vol. 7, 1971, pp. 543–558.

10 Gradshteyn, I. S., and Ryshik, I. M., *Table of Integrals, Series, and Products*, 4th Ed., Academic Press, New York, 1965, pp. 249, 276, and 277.

11 Behrens, E., "Elastic Constants of Fiber-Reinforced Composites With Transversely Isotropic Constituents," ASME JOURNAL OF APPLIED MECHANICS, Vol. 38, 1971, pp. 1062–1065.

APPENDIX

$$K=\frac{c_{13}c_{44}[c_{33}(\lambda_1^2+\lambda_2^2)+c_{13}+c_{33}^2\lambda_1^2\lambda_2^2/c_{13}]}{c_{33}(c_{13}+c_{44})(\lambda_1+\lambda_2)\lambda_1\lambda_2}$$

$$a_3=[\beta_2(c_{13}+c_{44})-\beta_1(c_{33}-k^2c_{44})]/\Delta$$

$$b_3=-[\beta_2(c_{44}-k^2c_{11})+\beta_1k^2(c_{13}+c_{44})]/(k\Delta)$$

$$m_2=c_{44}-(\lambda_2^2+\lambda_1\lambda_2+\lambda_1^2)c_{33}-\lambda_1\lambda_2c_{33}(c_{44}+\lambda_1\lambda_2c_{33})/c_{13}$$

$$m_3=(c_{13}+c_{44})(1-\lambda_1\lambda_2c_{33}/c_{13})$$

$$M=c_{13}a_3-c_{33}b_3/k-\beta_2-c_{13}c_{44}(m_2b_3+m_3a_3/k)/[\lambda_1\lambda_2(\lambda_1+\lambda_2)c_{33}(c_{13}+c_{44})]$$

$$m_4=[c_{33}\lambda_1\lambda_2-c_{13}-(\lambda_2^2+\lambda_1\lambda_2+\lambda_1^2+c_{13}/c_{44})c_{44}/\lambda_1\lambda_2]/(c_{13}+c_{44})$$

$$m_5=[c_{44}(\lambda_1^2+\lambda_1\lambda_2+\lambda_2^2-1)-\lambda_1\lambda_2c_{33}-c_{44}^2/c_{33}]b_3/(c_{13}+c_{44})+[(\lambda_1+\lambda_2)k-1-c_{44}/(\lambda_1\lambda_2c_{33})]a_3/k$$

$$K_2=[c_{11}m_4+c_{13}(\lambda_1\lambda_2+c_{13}/c_{33})]/(\lambda_1+\lambda_2)$$

$$K_3=(c_{11}-c_{12})m_4/(\lambda_1+\lambda_2),\quad M_3=(c_{11}-c_{12})m_5/(\lambda_1+\lambda_2)$$

$$M_2=[c_{11}m_5+(\lambda_1\lambda_2+c_{44}/c_{33})c_{13}b_3+(c_{13}+c_{44})c_{13}a_3/(kc_{33})]/(\lambda_1+\lambda_2)+b_3/k-\beta_1$$

Downloaded 02 May 2010 to 171.66.16.246. Redistribution subject to ASME license or copyright; see http://www.asme.org/terms/Terms_Use.cfm

The Penny-Shaped Interface Crack With Heat Flow

Part 1: Perfect Contact

C. J. Martin-Moran
Department of Mechanical Engineering, University of Newcastle-Upon-Tyne, NE1 7RU, England

J. R. Barber
Department of Mechanical Engineering and Applied Mechanics.

M. Comninou
Department of Civil Engineering. Mem. ASME

University of Michigan, Ann Arbor, Mich. 48109

A solution is given for the thermal stresses due to a penny-shaped crack at the interface between dissimilar materials loaded in tension for the case where the heat flux is into the material with higher distortivity. Regions of separation and perfect thermal contact are developed at the crack faces. A harmonic potential function representation is used to reduce the problem to a three-part boundary value problem which is formulated as a pair of coupled Abel integral equations using the method of Green and Collins. These equations are further reduced to a single Fredholm equation which is solved numerically. Results are presented illustrating the effect of heat flux and applied tractions on the contact radius and the stress intensity factors for various combinations of material constants. The effect of heat flux is profoundly influenced by the relative signs of Dundurs constant β and a constant γ describing the mismatch of distortivities. If the more distortive material is also the more rigid, the contact region at the crack face is reduced by heat flow; otherwise it is increased. In the latter case, solutions involving separation are obtained even for applied compressive tractions if the latter is within a certain range. The solution also exhibits nonuniqueness in this range.

Introduction

If a body conducting heat contains a crack, the crack will act as an obstruction to the heat flux, producing a local perturbation in the temperature field [1, 2]. Thermal stresses will therefore be developed, the stress field being influenced by the inability of the crack to transmit noncompressive tractions [3–7].

If the crack occurs at an interface between dissimilar materials, further complications are introduced – we anticipate the development of contact regions between the crack faces [8] and for one direction of heat flow, regions of "imperfect contact" may be required [9, 10]. In certain circumstances, these contact regions are small, but they have a substantial influence on the stress intensity factor at the crack tip and hence on the mechanics of fracture.

The only thermoelastic interface crack problem that has been treated to date is the axisymmetric external crack [11] which may be regarded as two dissimilar semi-infinite bodies bonded over a circular region of their common plane. In this paper we consider the related problem of the penny-shaped crack in which the two bodies are bonded throughout the plane *except* in a circular region.

Contributed by the Applied Mechanics Division for presentation at the 1983 Applied Mechanics, Bioengineering, and Fluids Engineering Conference, Houston, Texas, June 20–22, 1983 of THE AMERICAN SOCIETY OF MECHANICAL ENGINEERS.

Discussion on this paper should be addressed to the Editorial Department, ASME, United Engineering Center, 345 East 47th Street, New York, N.Y. 10017, and will be accepted until two months after final publication of the paper itself in the JOURNAL OF APPLIED MECHANICS. Manuscript received by ASME Applied Mechanics Division, May 1982. Paper No. 83-APM-10.

Copies will be available until February, 1984.

Statement of the Problem

The penny-shaped interface crack in a uniform tension field was treated by Keer et al. [12], who showed that the crack opens except for a small annular region of contact adjacent to the crack tip. If the crack is first loaded in tension and then subjected to a heat flux, it seems reasonable to anticipate that a similar configuration would be maintained with a possible change in the extent of the contact region.

The geometry is illustrated in Fig. 1. The interface is taken as the plane $z=0$ in cylindrical polar coordinates, the crack extending over the region $0 \le r \le b$. We assume that separation occurs in a central circular region $0 \le r \le a$ and that the faces of the crack are in frictionless contact in the annulus $a \le r \le b$. The significant material properties of the two half spaces are coefficients of thermal expansion α, thermal conductivity k, modulus of rigidity μ, and Poisson's ratio ν and we use subscripts 1, and 2 to refer to half spaces $z>0$, $z<0$, respectively. A uniform heat flux, $q_z = q_0$, and a uniform tension, $\sigma_{zz} = \sigma_0$, are imposed distant from the crack.

From an asymptotic analysis [10], we know that the transition from perfect thermal contact to separation is only possible if the heat flows into the more distortive material – i.e.,

$$q_0(\delta_1 - \delta_2) > 0 \tag{1}$$

where the distortivity δ is defined by [13]

$$\delta = \frac{\alpha(1+\nu)}{k} \tag{2}$$

For the opposite direction of heat flow, we anticipate that an annulus of imperfect contact will be interposed between

Copyright © 1983 by ASME
Downloaded 02 May 2010 to 171.66.16.246. Redistribution subject to ASME license or copyright; see http://www.asme.org/terms/Terms_Use.cfm

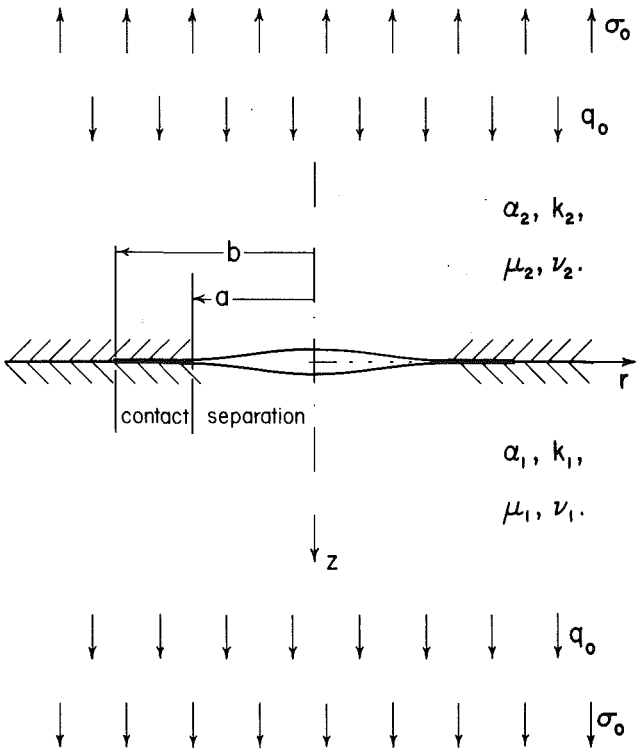

Fig. 1 Geometry of the problem

separation and perfect contact regions [9, 10]. In the present paper we restrict attention to the simpler case of perfect contact where condition (1) is satisfied. The solution with imperfect contact will form the subject of a second paper.

Mathematical Formulation

Following Keer et al. [12], we construct the solution as the sum of two parts – a state of uniform tension and heat flux and a perturbation stress and temperature field due to the crack that tends to zero at large distances from the origin. We note that even without the crack, a uniform tension and heat flux will generally require nonzero radial and circumferential stresses $(\sigma_{rr}, \sigma_{\theta\theta})$ because of differential thermal expansion and a difference of Poisson's ratio.

As in [11], we represent the perturbation field in each half space in terms of three harmonic functions, ϕ, ψ, ω, the displacement and temperature being

$$\mathbf{u} = \frac{(1-\nu)}{\mu}\nabla\phi + \frac{z}{2\mu}\nabla\frac{\partial\phi}{\partial z} - \frac{(3-4\nu)}{2\mu}\mathbf{k}\frac{\partial\phi}{\partial z} + 2\delta\mathbf{k}\frac{\partial\psi}{\partial z} - \delta\nabla\psi + \frac{(1-2\nu)}{2\mu}\nabla\omega + \frac{z}{2\mu}\nabla\frac{\partial\omega}{\partial z} - \frac{(3-4\nu)}{2\mu}\mathbf{k}\frac{\partial\omega}{\partial z} \tag{3}$$

$$T = \frac{1}{k}\frac{\partial^2\psi}{\partial z^2}. \tag{4}$$

The perturbations in stress and heat flux at the plane $z=0$ are

$$\sigma_{zz} = -\frac{\partial^2\omega}{\partial z^2}; \quad \sigma_{rz}\frac{\partial^2\phi}{\partial r\partial z} \tag{5}$$

$$q_z = -\frac{\partial^3\psi}{\partial z^3} \tag{6}$$

and continuity of these quantities at the interface is satisfied by imposing the symmetry conditions

$$\begin{aligned} \omega(r,z) &\equiv \omega_1(r,z) = \omega_2(r,-z), \\ \phi(r,z) &\equiv \phi_1(r,z) = -\phi_2(r,-z), \\ \psi(r,z) &\equiv \psi_1(r,z) = -\psi_2(r,-z). \end{aligned} \tag{7}$$

The remaining conditions at the interface define a mixed boundary value problem for the functions ω, ϕ, ψ, in the half space $z>0$.

Boundary Conditions

In the separation region $(0\le r\le a)$, the heat flux and the normal stress both contain a component from the uniform solution that must be cancelled by the perturbation. We therefore require

$$\frac{\partial^2\omega}{\partial z^2} = \sigma_0;\ 0\le r\le a,\ z=0, \tag{8}$$

$$\frac{\partial^3\psi}{\partial z^3} = q_0;\ 0\le r\le a,\ z=0, \tag{9}$$

from equations (5) and (6).

The crack surfaces must also be free of shear tractions giving

$$\frac{\partial^2\phi}{\partial r\partial z} = 0;\ 0\le r\le b,\ z=0, \tag{10}$$

or

$$\frac{\partial\phi}{\partial z} = C_1;\ 0\le r\le b,\ z=0, \tag{11}$$

where C_1 is an arbitrary constant of integration. Notice that this condition extends to $r=b$ because we assume that the contact in $a<r\le b$ is frictionless.

The normal displacement u_z must be continuous (i.e., no gap is opened) in both the bonded region $(r>b)$ and the contact region $(a<r\le b)$, while radial displacements are continuous in the bond only. Following the same procedure as in [11], we find that this requires

$$-B\frac{\partial\phi}{\partial z} - A\frac{\partial\omega}{\partial z} + (\delta_1-\delta_2)\frac{\partial\psi}{\partial z} = 0;\ r>a,\ z=0, \tag{12}$$

$$A\frac{\partial\phi}{\partial r} + B\frac{\partial\omega}{\partial r} - (\delta_1+\delta_2)\frac{\partial\psi}{\partial r} = 0;\ r>b,\ z=0, \tag{13}$$

where

$$A = \frac{(1-\nu_1)}{\mu_1} + \frac{(1-\nu_2)}{\mu_2} \tag{14}$$

$$B = \frac{(1-2\nu_1)}{2\mu_1} - \frac{(1-2\nu_2)}{2\mu_2}. \tag{15}$$

Finally, we assume that neither the bond nor the contact region offer any resistance to heat flow – i.e., there is "perfect thermal contact" [10]. This region of the interface is therefore an isothermal surface that must be the zero of temperature in the perturbation solution, i.e.,

$$\frac{\partial^2\psi}{\partial z^2} = 0;\ r>a,\ z=0, \tag{16}$$

from equation (4).

The Temperature Field

The solution for ψ and hence T can be obtained independently of ϕ, ω from equations (9) and (16). The problem is of standard form and we merely record the solution which can be written

Downloaded 02 May 2010 to 171.66.16.246. Redistribution subject to ASME license or copyright; see http://www.asme.org/terms/Terms_Use.cfm

$$\frac{\partial^2\psi}{\partial z^2} = \frac{2q_0}{\pi}\, Im[-\sqrt{r^2+(z+ia)^2}$$

$$+ z\log(\sqrt{r^2+(z+ia)^2}+z+ia)]. \tag{17}$$

We also record expressions for certain derivatives at the surface,

$$\frac{\partial\psi}{\partial r} = \frac{2q_0a^3}{3\pi r};\ r>a,\ z=0 \tag{18}$$

$$\frac{\partial^2\psi}{\partial z^2} = \frac{-2q_0\sqrt{a^2-r^2}}{\pi};\ 0<r<a,\ z=0 \tag{19}$$

which are required in subsequent calculations. We note that (18) is obtained from (17) by integration, arbitrary constants being assigned to ensure continuity of derivatives at $r=0$, a.

Development of Two Integral Equations

We anticipate that the stress field will contain discontinuities at both $r=a$ (due to the discontinuous heat flux) and at $r=b$ (due to the crack tip). It is convenient to isolate these discontinuities in separate functions and this can be achieved by making the change of variable

$$\chi=\omega+\beta\phi-\frac{(\delta_1-\delta_2)}{A}\psi,\ \text{all } r,z, \tag{20}$$

where

$$\beta=B/A \tag{21}$$

is Dundurs constant [14].

Using equation (20) to eliminate ω in the conditions (8), (12), and (13) we obtain, respectively,

$$\frac{\partial^2\chi}{\partial z^2}-\beta\frac{\partial^2\phi}{\partial z^2}=\sigma_0-\frac{(\delta_1-\delta_2)}{A}\frac{\partial^2\psi}{\partial z^2};$$

$$0<r<a,\ z=0, \tag{22}$$

$$\frac{\partial\chi}{\partial z}=0;\ r>a,\ z=0, \tag{23}$$

$$(1-\beta^2)\frac{\partial\phi}{\partial r}+\beta\frac{\partial\chi}{\partial r}=-\frac{(\delta_1-\delta_2)}{A}(\beta-1/\gamma)\frac{\partial\psi}{\partial r};$$

$$r>b,\ z=0, \tag{24}$$

where

$$\gamma=\left(\frac{\delta_1-\delta_2}{\delta_1+\delta_2}\right) \tag{25}$$

Following Green [15] and Collins [16], we now satisfy the conditions (11) and (12) identically by the representations

$$\frac{\partial\chi}{\partial z}=Im\int_0^a\frac{g_1(t)dt}{\sqrt{r^2+(z+it)^2}} \tag{26}$$

$$\frac{\partial\phi}{\partial z}=\frac{2C_1}{\pi}Im[\log(\sqrt{r^2+(z+ia)^2}+z+ia)]$$

$$+R_e\int_b^\infty\frac{g_2(t)dt}{\sqrt{r^2+(z+it)^2}} \tag{27}$$

where g_1, g_2 are real functions of t to be determined.

Differentiating with respect to z and interpreting the square roots in accordance with references [15, 16], we find

$$\frac{\partial^2\chi}{\partial x^2}=\frac{1}{r}\frac{d}{dr}\int_0^{\min(r,a)}\frac{tg_1(t)dt}{\sqrt{r^2-t^2}};\ z=0, \tag{28}$$

$$\frac{\partial^2\phi}{\partial z^2}=-\frac{2C_1}{\pi\sqrt{b^2-r^2}}+\frac{1}{r}\frac{d}{dr}\int_b^\infty$$

$$\frac{tg_2(t)dt}{\sqrt{t^2-r^2}};\ 0\le r\le b,\ z=0$$

$$=\frac{1}{r}\frac{d}{dr}\int_r^\infty\frac{tg_2(t)dt}{\sqrt{t^2-r^2}};\ r>b;\ z=0 \tag{29}$$

Hence, on substituting (19), (28), and (29) into (22)

$$\frac{d}{dr}\int_0^r\frac{tg_1(t)dt}{\sqrt{r^2-t^2}}=\frac{\beta d}{dr}\int_b^\infty\frac{tg_2(t)dt}{\sqrt{t^2-r^2}}-\frac{2\beta C_1 r}{\pi\sqrt{b^2-r^2}}$$

$$+\sigma_0 r+\frac{2q_0(\delta_1-\delta_2)r\sqrt{a^2-r^2}}{\pi A};\ 0\le r\le a. \tag{30}$$

We integrate this equation from zero to r obtaining

$$\int_0^r\frac{tg_1(t)dt}{\sqrt{r^2-t^2}}=\beta\int_b^\infty\left\{\frac{t}{\sqrt{t^2-r^2}}-1\right\}g_2(t)dt$$

$$-\frac{2\beta C_1}{\pi}(\sqrt{b^2-r^2}-b)+\frac{\sigma_0 r^2}{2}$$

$$+\frac{2q_0(\delta_1-\delta_2)}{3\pi A}[a^3-(a^2-r^2)^{3/2}];\ 0\le r\le a \tag{31}$$

which can be treated as an Abel equation for g_1 in terms of g_2 and known functions.

A similar equation for g_2 in terms g_1 is obtained by applying the same procedure to equation (24). Expressions for $\partial\chi/\partial r$, $\partial\phi/\partial r$ are obtained from (26) and (27) by integration as

$$\frac{\partial\chi}{\partial r}=-\frac{1}{r}\int_0^{\min(r,a)}\frac{tg_1(t)dt}{\sqrt{r^2-t^2}};\ z=0 \tag{32}$$

$$\frac{\partial\phi}{\partial r}=\frac{2C_1b}{\pi}+\frac{1}{r}\int_b^\infty g_2(t)dt$$

$$-\frac{1}{r}\int_r^\infty\frac{tg_2(t)dt}{\sqrt{t^2-r^2}};\ r>b,\ z=0 \tag{33}$$

where constants of integration have been assigned to ensure continuity of derivatives of the harmonic functions (and hence of displacements) at $r=0$, a, b. The resulting Abel equation is

$$\int_r^\infty\frac{tg_2(t)dt}{\sqrt{t^2-r^2}}=\int_b^\infty g_2(t)dt+\frac{2q_0(\delta_1-\delta_2)(\beta-1/\gamma)a^3}{3\pi A(1-\beta^2)}$$

$$+\frac{2C_1b}{\pi}-\frac{\beta}{(1-\beta^2)}\int_0^a\frac{tg_1(t)dt}{\sqrt{r^2-t^2}};\ r>b. \tag{34}$$

Solution of the Integral Equations

Equations (31) and (34) can be inverted by standard methods (see e.g. (15)), but a bounded solution for g_2 is obtained only if the right-hand side of (34) tends to zero at large r, i.e., if

$$\int_b^\infty g_2(t)dt+\frac{2q_0(\delta_1-\delta_2)(\beta-1/\gamma)a^3}{3\pi A(1-\beta^2)}$$

$$+\frac{2C_1b}{\pi}=0 \tag{35}$$

If this condition is satisfied, we obtain after some manipulations

$$g_2(x)=\frac{2\beta}{\pi(1-\beta^2)}\int_0^a\frac{tg_1(t)dt}{(t^2-x^2)};\ x>b \tag{36}$$

from (34) and

Downloaded 02 May 2010 to 171.66.16.246. Redistribution subject to ASME license or copyright; see http://www.asme.org/terms/Terms_Use.cfm

$$g_1(x)=\frac{2\beta x}{\pi}\int_b^\infty \frac{g_2(t)\,dt}{(t^2-x^2)}+\frac{2\sigma_0 x}{\pi}$$

$$+\frac{q_0(\delta_1-\delta_2)}{\pi^2 A}\left[2ax+(a^2-x^2)\log\left(\frac{a+x}{a-x}\right)\right]$$

$$-\frac{2\beta C_1}{\pi^2}\log\left(\frac{b+x}{b-x}\right);\quad 0\le x\le a \tag{37}$$

from (31).

We can now obtain a single Fredholm equation for g_1 by substituting (36) into (37) and reversing the order of the double integral. Notice that the ranges of the integrals in (36) and (37) do not overlap and hence no singularities will occur in the range of the Fredholm equation except perhaps at the end points. This is a consequence of change of variable (equation (20)). It will also be observed from equation (36) that g_1 is an odd function of x, and some simplification can be achieved both at this stage and in the subsequent numerical solution by using this fact to extend the range of the integral equation to $-a\le x\le +a$. We then obtain the equation

$$g_1(x)+\frac{\beta^2}{\pi^2(1-\beta^2)}\int_{-a}^{+a}\log\left[\left(\frac{b+x}{b-x}\right)\left(\frac{b-s}{b+s}\right)\right]\frac{g_1(s)}{(x-s)}\,ds$$

$$=\frac{2\sigma_0 x}{\pi}+\frac{q_0(\delta_1-\delta_2)}{\pi^2 A}\left[2ax+(a^2-x^2)\log\left(\frac{a+x}{a-x}\right)\right]$$

$$-\frac{2\beta C_1}{\pi^2}\log\left(\frac{b+x}{b-x}\right);\quad -a\le x\le +a \tag{38}$$

Auxilary Conditions

To complete the solution, we need two auxiliary conditions to find the unknown constant C_1 and the inside radius of the contact zone a. One condition (35) has already been found as a requirement for the regular inversion of the Abel equation (34). We write (35) as a condition on g_1 by substituting for g_2 from (36) obtaining

$$\beta\int_{-a}^{+a} g_1(t)\log\left(\frac{b+t}{b-t}\right)dt=4\,C_1 b(1-\beta^2)$$

$$+\frac{4q_0(\delta_1-\delta_2)(\beta-1/\gamma)a^3}{3A} \tag{39}$$

The second condition follows from the inequalities at the transition from contact to separation ($r=a$) and can be imposed by demanding that the contact traction tend to zero at $r\to a^+$. (The condition that the gap close smoothly at $r\to a^-$, used by Keer et al. [12] is equivalent.)

From equations (5) and (20), we note that a discontinuity of contact tractions at $r=a$, $z=0$ could only arise through the term $\partial^2\chi/\partial z^2$, since equations (17) and (29) guarantee continuity of $\partial^2\psi/\partial z^2, \partial^2\phi/\partial z^2$, respectively. Further, it can be shown that (28) will define an expression that is discontinuous at $r=a$ *unless*

$$g_1(a)=0. \tag{40}$$

and hence

$$\frac{\beta^2}{\pi^2(1-\beta^2)}\int_{-a}^{+a}\log\left[\left(\frac{b+a}{b-a}\right)\left(\frac{b-s}{b+s}\right)\right]\frac{g_1(s)}{(a-s)}\,ds=\frac{2\sigma_0 a}{\pi}$$

$$+2\frac{q_0(\delta_1-\delta_2)a^2}{\pi^2 A}-\frac{2\beta C_1}{\pi^2}\log\left(\frac{b+a}{b-a}\right), \tag{41}$$

from (38) with $x=a$. This is the required additional condition.

Solution Procedure

We first use (39) to eliminate C_1 in (41) obtaining

$$SQ=\frac{\sigma_0 A}{q_0(\delta_1-\delta_2)b}=\frac{\beta^2}{\pi^2(1-\beta^2)}$$

$$\int_{-a}^{+a}\left[\frac{b}{2a}\frac{\log\left[\left(\frac{b+a}{b-a}\right)\left(\frac{B-s}{b+s}\right)\right]}{(a-s)}\right.$$

$$\left.+\frac{1}{4a}\log\left(\frac{b+a}{b-a}\right)\log\left(\frac{b+s}{b-s}\right)\right]g(s)\,ds$$

$$-\frac{a}{\pi b}-\frac{\beta(\beta-1/\gamma)a^2/b^2\,\log\left(\frac{b+a}{b-a}\right)}{3\pi(1-\beta^2)} \tag{42}$$

where

$$g(x)=\frac{Ag_1(x)}{q_0(\delta_1-\delta_2)b^2}. \tag{43}$$

This equation and (39) are then used to eliminate σ_0, C_1, respectively, in (38) which becomes

$$g(x)+\frac{\beta^2}{\pi^2(1-\beta^2)}\int_{-a}^{+a}K(x,s)\;g(s)\,ds$$

$$=h(x),\quad -a\le x\le +a \tag{44}$$

where

$$K(x,s)=$$

$$\frac{\log\left[\left(\frac{b+x}{b-x}\right)\left(\frac{b-s}{b+s}\right)\right]}{(x-s)}-\frac{\frac{x}{a}\log\left[\left(\frac{b+a}{b-a}\right)\left(\frac{b-s}{b+s}\right)\right]}{(a-s)}$$

$$+\frac{1}{2b}\left[\log\left(\frac{b+x}{b-x}\right)-\frac{x}{a}\log\left(\frac{b+a}{b-a}\right)\right]\log\left(\frac{b+s}{b-s}\right) \tag{45}$$

and

$$h(x)=\frac{(a^2-x^2)}{\pi^2 b^2}\log\left(\frac{a+x}{a-x}\right)$$

$$+\frac{2\beta(\beta-1/\gamma)}{3\pi^2(1-\beta^2)}\frac{a^3}{b^3}\left[\log\left(\frac{b+x}{b-x}\right)\right.$$

$$\left.-\frac{x}{a}\log\left(\frac{b+a}{b-a}\right)\right]. \tag{46}$$

In practice, SQ would be given while the contact radius a would be unknown. However, it is numerically more convenient to solve (43) for various values of a and the compute appropriate values of SQ from (41). Note that SQ can be regarded as a dimensionless ratio of mechanical and thermal loading.

Interface Tractions and Stress Intensity Factors

The interface tractions can be obtained from equations (5) and (20) by substituting for the appropriate derivatives and using (36) and (43) to express the results in terms of $g(x)$. The calculations are routine but tedious and only the final expressions are given here which are

$$\sigma_{zz}/\sigma_0=1-\frac{2C_1\beta}{\sigma_0\pi\sqrt{b^2-r^2}}$$

Downloaded 02 May 2010 to 171.66.16.246. Redistribution subject to ASME license or copyright; see http://www.asme.org/terms/Terms_Use.cfm

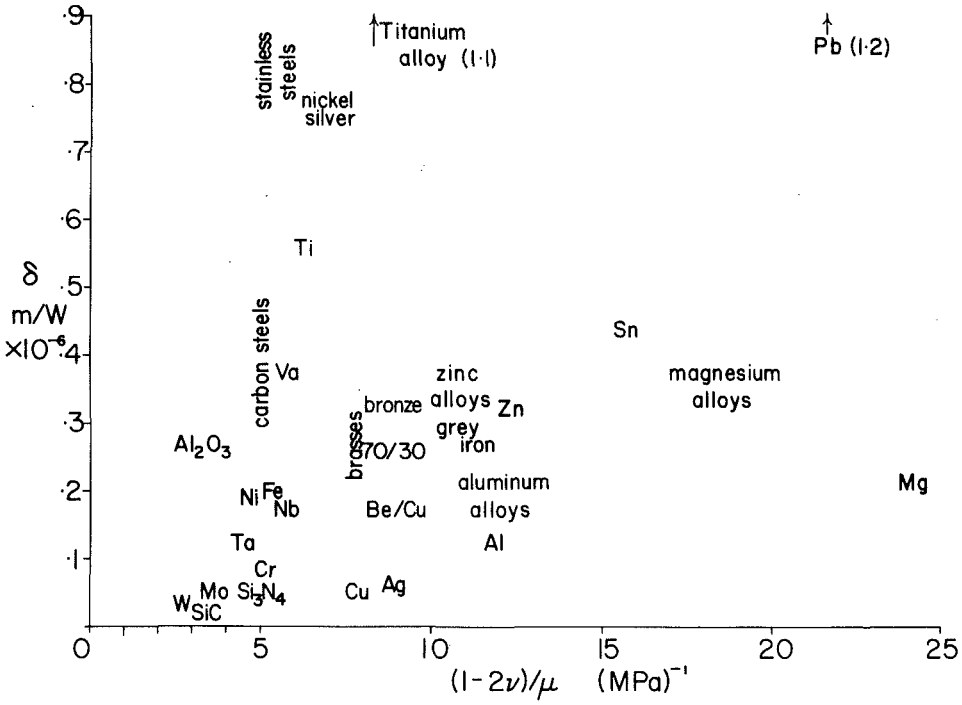

Fig. 2 Distortivity (δ) and $(1\cdot2\nu)/\mu$ for a range of common structural materials. The slope of a straight line joining any two points will have the same sign as the product $\beta\gamma$ for the corresponding interface.

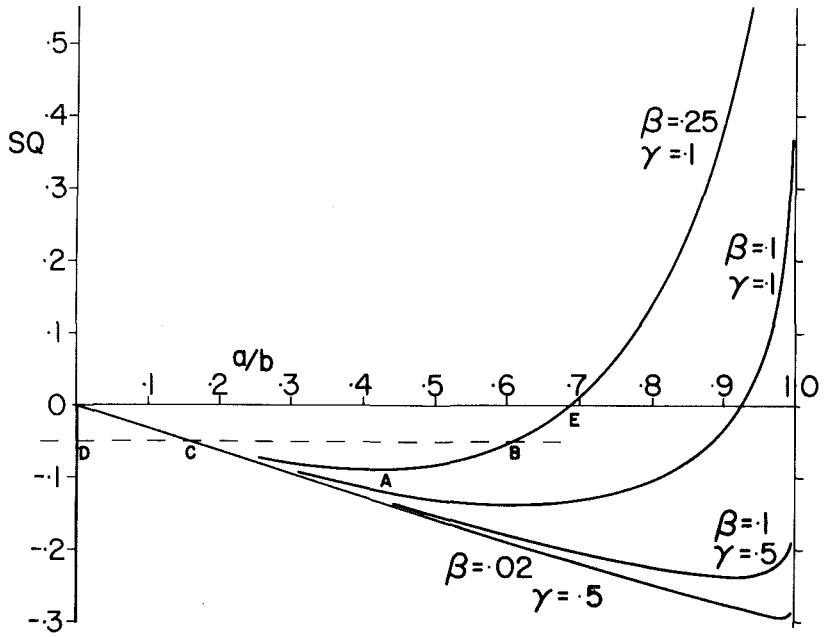

Fig. 3 Variation of the contact radius a/b with $SQ=\sigma_0 Al\{q_0(\delta_1-\delta_2)b\}$ for various material combinations

$$-\frac{1}{2(1-\beta^2)SQ}\int_{-a}^{+a}\left[\frac{2\beta^2}{\pi\sqrt{b^2-r^2}}+\frac{2\beta^2}{\pi\sqrt{r^2-s^2}}\arctan\sqrt{\frac{b^2-r^2}{r^2-s^2}}-\frac{1}{\sqrt{r^2-s^2}}\right]\frac{g(s)\,ds}{(r-s)};\quad a\le r\le b,\ z=0 \tag{47}$$

$$\sigma_{zz}/\sigma_0=1+\frac{b}{2(1-\beta^2)SQ}\int_{-a}^{+a}\frac{g(s)\,ds}{(r-s)\sqrt{r^2-s^2}};\quad r>b; \tag{48}$$

$$\sigma_{rz}/\sigma_0=\frac{-2C_1 b}{\sigma_0\pi r\sqrt{r^2-b^2}}-\frac{\beta b}{\pi(1-\beta^2)SQ}\int_{-a}^{+a}\left\{\frac{b}{r(r-s)\sqrt{r^2-b^2}}+\frac{r}{(r^2-s^2)^{3/2}}\log[b\sqrt{r^2-s^2}-s\sqrt{r^2-b^2}]\right\}g(s)ds\ ;\ r>b,\ z=0. \tag{49}$$

The normal traction is bounded at $r=b^+$, but singular at $r=b^-$ with dimensionless stress intensity factor

Downloaded 02 May 2010 to 171.66.16.246. Redistribution subject to ASME license or copyright; see http://www.asme.org/terms/Terms_Use.cfm

$$K_1 = \lim_{r\to b^-}\left(\frac{\sigma_{zz}\sqrt{1-r^2/b^2}}{\sigma_0}\right) = -\frac{2C_1\beta}{\sigma_0\pi b} - \frac{\beta^2}{\pi(1-\beta^2)SQ} \times$$

$$\times \int_{-a}^{+a} \frac{g(s)\,ds}{(b-s)}, \tag{50}$$

from equation (47). Notice that $a<r\le b$ is a region of contact and hence for a physically meaningful result (50) must define a compressive traction, i.e.,

$$\sigma_0 K_1 < 0. \tag{51}$$

From the definition of SQ (equation (42)), it can be seen that the inequalities (1) and (51) are compatible if and only if

$$SQ\,K_1 < 0, \tag{52}$$

since A, b are necessarily positive.

The stress intensity factor in shear at $r=b^+$ can be obtained from equation (49) and is related to K_1 by

$$K_2 = \lim_{r\to b^+} \frac{\sigma_{rz}\sqrt{r^2/b^2-1}}{\sigma_0} = K_1/\beta \tag{53}$$

as required by the asymptotic stress field at the crack tip.

Results and Discussion

The solution of the Fredholm equation (44) depends on the material properties of the two half spaces only through the dimensionless ratios β and γ defined by equations (21) and (25). This is also the case for SQ, the dimensionless tractions, and the stress intensity factors.

In discussing the numerical results, it is convenient to take as a point of reference the solution due to Keer et al. [12] for the penny-shaped interface crack without heat flow, which is essentially the present solution in the limiting case where $q_0\to 0$ and hence $SQ\to\infty$.

We can recover Keer's solution if we choose a/b to be an eigenvalue (C_0) of the homogeneous Fredholm equation corresponding to (44). At such a value, the nonhomogeneous equation will give an unbounded solution for $g(x)$ and hence for SQ. In practice, this means that SQ increases without limit as a/b approaches C_0 from either side.

The eigenvalue C_0 depends on the kernel of the integral equation and hence on $|\beta|$ only, and the values obtained agree with those given by Keer et al. [12] within limits of numerical accuracy. For all physically possible values of β ($-0.5\le\beta\le+0.5$), C_0 is very close to 1, the minimum being $C_0=0.99991$ for $\beta=\pm 0.5$.

For given values of β and γ, equation (44) can be solved numerically for any value of a/b in the range $0<a/b<1$, but we find that the inequality (52) is always violated for values of a/b on one or the other side of the eigenvalue C_0. If β and γ have the same sign, physically possible solutions are obtained if and only if $0\le a/b<C_0$, whereas if β and γ have opposite signs they are obtained only for $C_0<a/b<1$.

Thus, if we apply a uniform tension σ_0 and gradually increase the heat flux q_0 from zero, the contact region will get larger if $\beta\gamma>0$ and smaller if $\beta\gamma<0$.

In view of this striking dependence on the sign of $\beta\gamma$, it is pertinent to ask whether there is sufficient correlation between the properties of real materials to make one sign more common than the other. The product $\beta\gamma$ will be positive if the material with the higher distortivity has also the higher value of $(1-2\nu)/\mu$. We therefore plot δ against $(1-2\nu)/\mu$ for a range of materials in Fig. 2. If we join the points corresponding to the two materials of the interface by a straight line, $\beta\gamma$ will have the same sign as the slope of this line. For example, an interface between copper and zinc gives $\beta\gamma>0$, while one between copper and mild steel gives $\beta\gamma<0$. It is clear from Fig. 2 that many practical examples of each kind occur.

Examples With $\beta\gamma>0$

We next consider in more detail the behavior when $\beta\gamma>0$. It is convenient to choose the material of higher distortivity to occupy the region $z>0$ (half space 1) in which case β and γ are

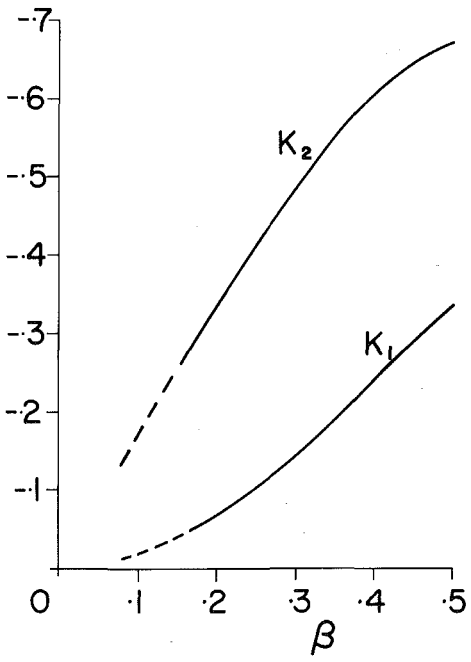

Fig. 4 Stress intensity factors for purely mechanical loading ($q_0=0$) as a function of β

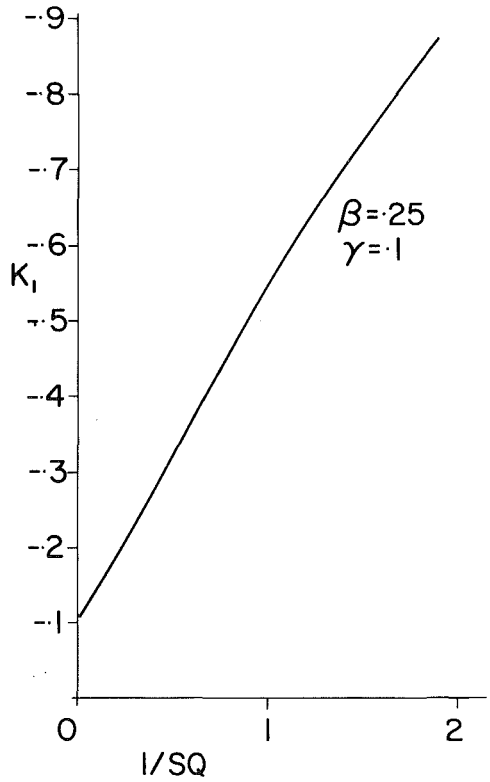

Fig. 5 Effect of heat flux on K_1 for $\beta=0.25$ and $\gamma=0.1$

Downloaded 02 May 2010 to 171.66.16.246. Redistribution subject to ASME license or copyright; see http://www.asme.org/terms/Terms_Use.cfm

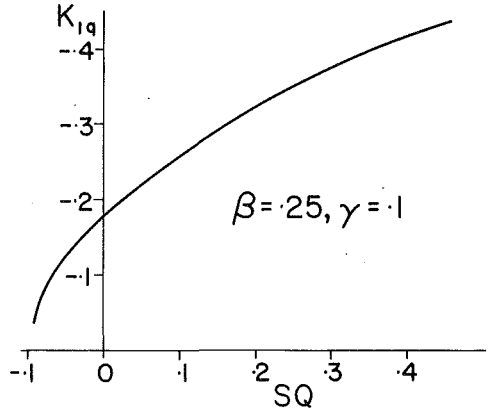

Fig. 6 Effect of applied traction σ_0 on the thermal stress intensity factor K_{1q} for $\beta = 0.25$ and $\gamma = 0.1$

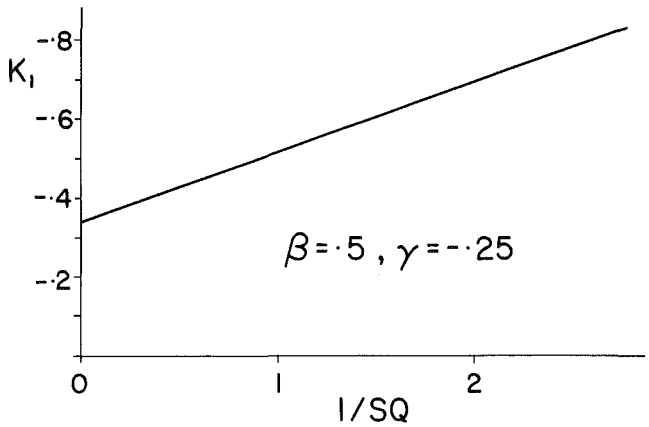

Fig. 7 Effect of heat flux on K_1 for $\beta = 0.5$ and $\gamma = -0.25$, for which $\beta\gamma < 0$ and the contact area is reduced by heat flux

both positive. The inequality (1) then requires that $q_0 > 0$ if imperfect contact is not to occur.

Figure 3 shows the relation between SQ and a/b for various combinations of β and γ. The ratio SQ falls continuously with a/b from the eigenvalue C_0, reaching zero at $a/b = 0.688$ for $\beta = 0.25$, $\gamma = 0.1$. This point corresponds to the crack with thermal loading only (i.e., $\sigma_0 = 0$). For $a/b > 0.688$, *negative* values of SQ are obtained corresponding to $\sigma_0 < 0$—in other words, the contact region $a < r \leq b$ can be further extended by applying compressive tractions at infinity up to the limiting point A where $SQ = -0.090$.

The crack loaded by a uniform compressive traction presents some interesting features. If there is no heat flow ($q_0 = 0$), it will close completely, since the crack is able to transmit compressive tractions. If we now superpose a flow of heat and assume as in the foregoing analysis that the contact region does not impose a resistance to heat flow between the faces of the crack, there is no reason to anticipate any perturbation in either temperature or stress field. Thus, $a/b = 0$ is always a solution of the problem if $\sigma_0 < 0$. We show this in Fig. 3 by continuing the SQ curve down the axis $a/b = 0$ for negative values of SQ.

However, it follows that, in the range $-0.09 < SQ < 0$, there are three solutions to the problem, for $\beta = 0.25$, $\gamma = 0.1$ corresponding to the points B, C, and D in the Fig. 3. All these solutions satisfy the boundary conditions and inequalities of the problem.

There are precedents for the existence of multiple solutions in thermoleastic contact problems where, as here, the heat flows into the more distortive material [17-20]. In simple one-dimensional cases, for which a stability analysis can be completed by perturbation methods [17, 20], it is found that, if several steady-state solutions exist, at least two of them are stable and hence the configuration achieved in practice depends on the history of heating and loading.

In the present problem, we should anticipate that the point D, with the crack fully closed, could be reached by starting with $\sigma_0 < 0$, $q_0 = 0$ and slowly increasing the heat flux. On the other hand, point B should be obtainable by first loading the crack in tension and then slowly changing σ_0 to the desired compressive value. If the compressive stress were increased beyond this point, presumably the solution would proceed to A in Fig. 3 and then change discontinuously to the state with $a/b = 0$. A similar jump from 0 to E must occur if σ_0 is increased from compressive to tensile values at $a/b = 0$.

It is not clear what if any sequence of heating and loading could cause solution C to be established and it is tempting to label it unstable. However, we should remark that the only unstable solutions discovered in [17, 20] were those involving states resembling imperfect contact.

In Fig. 3 we also show results for other combinations of β and γ from which it is clear that if β is reduced or γ is increased, the extent of the contact region for a given SQ is reduced. All the curves are asymptotic to the straight line

$$SQ = -0.366\, a/b \tag{54}$$

as $a/b \to 0$.

Stress Intensity Factor

In discussing the stress intensity factor at the crack tip, it is helpful to distinguish cases where the mechanical loading is dominant (SQ large) and those where thermal loading is dominant (SQ small). In the former case, the stress intensity factor is best presented in the dimensionless form of equation (50). Values for purely mechanical loading ($q_0 = 0$) are shown in Fig. 4. For $\beta < 0.3$, the eigenvalue C_0 is very close to unity and the numerical accuracy of the limiting solution is questionable. However, the stress intensity factor is a smooth function of $1/SQ$ (see Fig. 5) which tends to a limit as a/b approaches C_0. Values for $\beta < 0.3$ were therefore obtained by extrapolation from the more reliable solutions with $a/b < C_0$. This extrapolation procedure was tested on the established points for $\beta > 0.3$ and was very precise.

The effect of heat flux superposed on mechanical loading is illustrated in Fig. 5 where K_1 is plotted against $1/SQ$ for $\beta = 0.25$ and $\gamma = 0.1$. Notice that the heat flux has a very substantial effect in increasing the stress intensity factor above the mechanical value.

When thermal loading is dominant, it is more meaningful to relate the stress intensity factor to the heat flux defining a "thermal" stress intensity factor.

$$K_{1q} = \lim_{r \to b^-} \frac{\sigma_{zz}\sqrt{1 - r^2/b^2}}{[q_0(\delta_1 - \delta_2)b/A]} = SQ\, K_1 \tag{55}$$

We plot $K_1 q$ against SQ in Fig. 6 for $\beta = 0.25$, and $\gamma = 0.1$. In the limit $SQ = 0$ (no applied tractions) $K_{1q} = 0.17$. Superposition of compressive traction reduces the stress intensity factor, but tensile traction exacerbates it.

Example With $\beta\gamma < 0$

When $\beta\gamma < 0$, the contact region decreases with increasing heat flux q_0 and is always small, a/b being in the range $C_0 < a/b < 1$. This presents problems of numerical accuracy, particularly when β is small and C_0 is very close to unity. We therefore give results for the case $\beta = 0.5$ and $\gamma = -0.25$, in Fig. 7 where K_1 is plotted against $1/SQ$. The results obtained are closely approximated by the relation

$$K_1 = 0.341 + 0.18/SQ \tag{56}$$

Downloaded 02 May 2010 to 171.66.16.246. Redistribution subject to ASME license or copyright; see http://www.asme.org/terms/Terms_Use.cfm

It follows from the definition (55) that

$$K_{1q} = 0.18 + 0.341\ SQ \tag{57}$$

It is interesting to note that with $\beta\gamma < 0$ an increase of the tensile traction σ_0 causes an *increase* in the extent of the contact region.

Results for small values of SQ correspond to a/b very close to unity – e.g., $SQ = 0.5$. is obtained with $a/b = 1 - 10^{-8}$. All calculations were performed with double precision, but results for lower values of SQ must be treated with caution.

Acknowledgments

The authors gratefully acknowledge support from the U.S. Army under contract DAAG29-82-K-0001.

References

1 Karush, W., and Young, G., "Temperature Rise in a Heat Producing Solid Behind a Surface Defect," *J. Appl. Phys.* Vol. 23, 1952, pp. 1191–1193.

2 Barber, J. R., "The Disturbance of a Uniform Steady-State Heat Flux by a Partially Conducting Plane Crack," *Int. J. Heat Mass Transfer*, Vol. 19, 1976, pp. 956–958.

3 Florence, A. L., and Goodier, J. N., "The Linear Thermoelastic Problem of Uniform Heat Flow Disturbed by a Penny-Shaped Insulated Crack," *Int. J. Eng. Sci.*, Vol. 1, 1963, pp. 533–540.

4 Shail, R., "Some Steady-State Thermoelastic Stress Distributions in the Vicinity of an External Crack in an Infinite Solid," *Int. J. Eng. Sci.*, Vol. 6, 1968, pp. 685–694.

5 Rubenfeld, L., "Non-Axisymmetric Thermoelastic Stress Distribution in a Solid Containing an External Crack," *Int. J. Eng. Sci.*, Vol. 8, 1970, pp. 499–509.

6 Barber, J. R., "Steady-State Thermal Stresses in an Elastic Solid Containing an Insulated Penny-Shaped Crack," *J. Strain Analysis*, Vol. 10, 1975, pp. 19–24.

7 Barber, J. R., "Steady-State Thermal Stresses Caused by an Imperfectly Conducting Penny-Shaped Crack in an Elastic Solid," *J. Thermal Stresses*, Vol. 3, 1979, pp. 77–83.

8 Comninou, M., "The Interface Crack," ASME JOURNAL OF APPLIED MECHANICS, Vol. 44, 1977, pp. 631–636.

9 Barber, J. R., "Contact Problems Involving a Cooled Punch," *J. Elasticity*, Vol. 8, 1978, pp. 409–423.

10 Comninou, M., and Dundurs, J., "On the Barber Boundary Conditions for Thermoelastic Contact," ASME JOURNAL OF APPLIED MECHANICS, Vol. 46, 1979, pp. 849–853.

11 Barber, J. R., and Comninou, M., "The External Axisymmetric Interface Crack With Heat Flow," *Q. J. Mech. Appl. Math.*, Vol. 35, 1982, pp. 403–417.

12 Keer, L. M., Chen, S. H., and Comninou, M., "The Interface Penny-Shaped Crack Reconsidered," *Int. J. Eng. Sci.*, Vol. 16, 1978, pp. 765–772.

13 Dundurs, J., and Panek, C., "Heat Conduction Between Bodies With Wavy Surfaces," *Int. J. Heat Mass Transfer*, Vol. 19, 1976, pp. 731–736.

14 Dundurs, J., "Discussion on Edge-Bonded Dissimilar Orthogonal Elastic Wedges Under Normal and Shear Loading," ASME JOURNAL OF APPLIED MECHANICS, Vol. 36, 1969, pp. 650–652.

15 Green, A. E., and Zerna, W., *Theoretical Elasticity*, Clarendon Press, Oxford, 1954, pp. 174–178.

16 Collins, W. D., "On the Solution of Some Axisymmetric Boundary Value Problems by Means of Integral Equations. VIII: Potential Problems for a Circular Annulus," *Proc. Edin. Math. Soc.*, Vol. 13, 1963, pp. 235–246.

17 Barber, J. R., Dundurs, J., and Comninou, M., "Stability Considerations in Thermoelastic Contact," ASME JOURNAL OF APPLIED MECHANICS, Vol. 47, 1980, pp. 871–874.

18 Comninou, M., and Dundurs, J., "On Lack of Uniqueness in Heat Conduction Through a Solid to Solid Interface," ASME *Journal of Heat Transfer*, Vol. 102, 1980, pp. 319–323.

19 Comninou, M., and Dundurs, J., "On the Possibility of History Dependence and Instabilities in Thermoelastic Contact," *J. Thermal Stresses*, Vol. 3, 1980, pp. 427–433.

20 Barber, J. R., "Stability of Thermoelastic Contact for the Aldo Model," ASME, JOURNAL OF APPLIED MECHANICS, Vol. 48, 1981, pp. 555–558.

Downloaded 02 May 2010 to 171.66.16.246. Redistribution subject to ASME license or copyright; see http://www.asme.org/terms/Terms_Use.cfm

A. Atsumi
Professor.

Y. Shindo
Associate Professor.

Department of Mechanical Engineering II,
Faculty of Engineering,
Tohoku University,
Sendai 980, Japan

Axisymmetric Singular Stresses in a Thick-Walled Spherical Shell With an Internal Edge Crack

The paper considers the elastostatic axisymmetric problem for a thick-walled spherical shell containing a circumferential edge crack on the inner surface. The ring-shaped edge crack and the inner surface of the spherical shell are subjected to internal pressure. Using an integral transform technique we obtain a singular integral equation of the first kind which has a generalized Cauchy kernel as the dominant part. The integral equation is solved numerically, and the influence of the geometrical configuration on the stress-intensity factor and the crack-opening displacement is shown graphically in detail.

Introduction

In recent years, the fracture problem in pressure vessels has developed rapidly because of various technical applications. If the wall thickness relative to the mean radius is sufficiently small, the related crack problem may be solved by assuming the structure to be a shallow shell. Erdogan and Ratwani [1] have investigated a problem of fatigue and fracture of cylindrical and spherical shells containing a through crack and subjected to internal pressure or torsion. For thick-walled pressure vessels, Erdol and Erdogan [2] have solved an elastostatic axisymmetric problem for a long thick-walled cylinder containing a ring-shaped internal or edge crack. The corresponding problem for the solid cylinder with a circumferential edge crack was treated in [3], and for the cylindrical cavity in [4]. Keer and Watts [5] have solved a torsion problem for a cylindrical shell containing a circumferential edge crack. Their technique has been applied with success to investigate the axially symmetrical problem of an elastic sphere with a circumferential edge crack [6]. More recently, the authors [7] have analyzed singular stresses near a circumferential edge crack in a spherical cavity.

Thus the present analysis considers the linear-elastic fracture analysis of a thick-walled spherical shell having an internal circumferential edge crack that is subjected to an axisymmetrical loading. The outer surface of the spherical shell is traction free, and the inner surface and the surface of the crack are subjected to an internal pressure. By suitable definition of integral transforms [7], the problem is reduced to a singular integral equation of the first kind. By expanding the unknown function in the integral equation in terms of Jacobi polynomials, we derive an infinite set of linear algebraic equations. Results are presented by the stress-intensity factor and the crack-opening displacement and are shown graphically to demonstrate the influence of the geometric parameters. Calculations are also carried out for the case of the inner surface being stress-free.

Formulation of the Problem

Consider a thick-walled spherical shell of inner radius a and outer radius ad having a circumferential edge crack of depth $ca = (b-1)a$ on the inner surface of the spherical shell. The center of the spherical shell is taken as the origin O, and cylindrical and spherical coordinates $(R,\varphi,z),(r,\theta,\varphi)$ are used with the z-axis coinciding with the axis of symmetry, as shown in Fig. 1. For convenience, R, z, and r will be regarded as dimensionless quantities referring to a typical length a. They are connected with each other by

$$\left.\begin{aligned} z &= r\cos\theta \\ R &= r\sin\theta \end{aligned}\right\} \tag{1}$$

The crack is in a plane perpendicular to the z-axis and occupies the region, $z=0$, $1 \le r < b$. The crack surface is stressed by a uniform pressure p_0, the inner spherical surface is subjected to a uniform internal pressure q_0, and the outer spherical surface is stress-free. The boundary conditions, expressed in terms of spherical coordinates, can be written in the following form:

$$\sigma_{r\theta}(r,\pi/2) = 0, \quad 1 \le r \le d \tag{2}$$

$$\left.\begin{aligned} \sigma_{\theta\theta}(r,\pi/2) &= -p_0 \ , \quad 1 \le r < b \\ u_\theta(r,\pi/2) &= 0 \ , \quad b \le r \le d \end{aligned}\right\} \tag{3}$$

$$\left.\begin{aligned} \sigma_{rr}(1,\theta) &= -q_0 \\ \sigma_{r\theta}(1,\theta) &= 0 \end{aligned}\right\} \tag{4}$$

$$\sigma_{rr}(d,\theta) = \sigma_{r\theta}(d,\theta) = 0 \tag{5}$$

Contributed by the Applied Mechanics for publication in the JOURNAL OF APPLIED MECHANICS.

Discussion on this paper should be addressed to the Editorial Department, ASME, United Engineering Center, 345 East 47th Street, New York, N.Y. 10017, and will be accepted until two months after final publication of the paper itself in the JOURNAL OF APPLIED MECHANICS. Manuscript received by ASME Applied Mechanics Division, November, 1981; final revision, July, 1982.

Copyright © 1983 by ASME
Downloaded 02 May 2010 to 171.66.16.246. Redistribution subject to ASME license or copyright; see http://www.asme.org/terms/Terms_Use.cfm

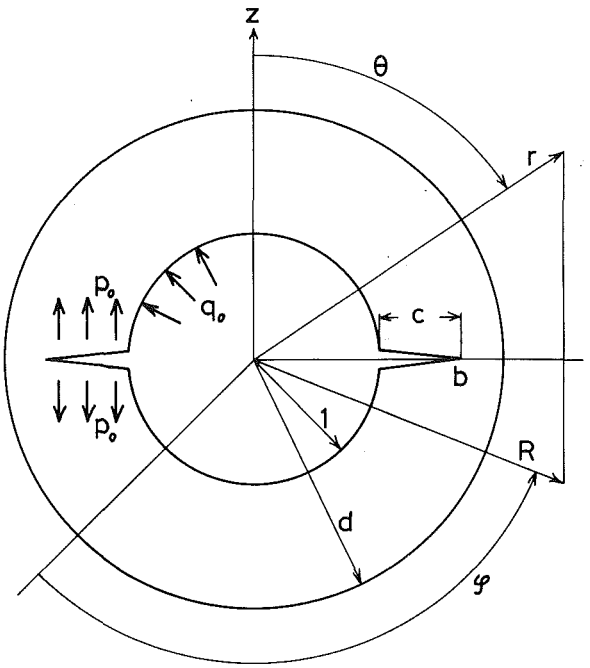

Fig. 1 Geometry of a thick-walled spherical shell containing a circumferential edge crack

Analysis

The displacement field is expressed in the following forms [8,9].

$$2\mu u_r(r,\theta) = \int_0^\infty A(\xi)e^{-\xi r\cos\theta}[J_1(\xi r\sin\theta)(\xi r\cos\theta - 1 + 2\nu)\sin\theta + J_0(\xi r\sin\theta)(\xi r\cos\theta + 2 - 2\nu)\cos\theta]d\xi + \sum_{n=0}^{\infty}\{a_{2n}2n(2n+3-4\nu)r^{-2n} - b_{2n}(2n+1)r^{-2n-2}\}P_{2n}(\cos\theta) - 2c_0(1-2\nu)r + \sum_{n=1}^{\infty}\{c_{2n}(2n+1)(2n-2+4\nu)r^{2n+1} + d_{2n}2nr^{2n-1}\}P_{2n}(\cos\theta)$$

$$2\mu u_\theta(r,\theta) = \int_0^\infty A(\xi)e^{-\xi r\cos\theta}[J_1(\xi r\sin\theta)(\xi r\cos\theta - 1 + 2\nu)\cos\theta - J_0(\xi r\sin\theta)(\xi r\cos\theta + 2 - 2\nu)\sin\theta]d\xi + \sum_{n=1}^{\infty}\{a_{2n}(4-2n-4\nu)r^{-2n} + b_{2n}r^{-2n-2}\}\frac{d}{d\theta}P_{2n}(\cos\theta) + \sum_{n=1}^{\infty}\{c_{2n}(2n+5-4\nu)r^{2n+1} + d_{2n}r^{2n-1}\}\frac{d}{d\theta}P_{2n}(\cos\theta) \quad (6)$$

where ν is Poisson's ratio, μ is the shear modulus of elasticity, $J_n(\ )$, $P_{2n}(\ )$ are the n-order Bessel function of the first kind and the $2n$-order Legendre's polynomial, respectively, and $A(\xi)$, a_{2n}, b_{2n}, c_{2n}, d_{2n} are unknown function and coefficients to be determined later.

The stresses obtained from the displacement field (6) are

$$\sigma_{rr}(r,\theta) = \int_0^\infty A(\xi)\frac{e^{-\xi r\sin\theta}}{r}\{J_1(\xi r\sin\theta)(1-2\nu - \xi r\cos\theta - 2\xi^2r^2\cos^2\theta)\sin\theta - J_0(\xi r\sin\theta)(1+\xi r\cos\theta\cos2\theta)\xi r\}d\xi + \sum_{n=0}^{\infty}\{a_{2n}2n(2\nu-6n-4n^2)r^{-2n-1} + b_{2n}(2n+1)(2n+2)r^{-2n-3}\}P_{2n}(\cos\theta) - 2(1+\nu)c_0 + \sum_{n=1}^{\infty}\{c_{2n}(2n+1)(4n^2-2n-2-2\nu)r^{2n} + d_{2n}2n(2n-1)r^{2n-2}\}P_{2n}(\cos\theta)$$

$$\sigma_{\theta\theta}(r,\theta) = \int_0^\infty \xi A(\xi)e^{-\xi r\cos\theta}\left\{\frac{J_1(\xi r\sin\theta)}{\xi r\sin\theta}\cos^2\theta(1-2\nu - \xi r\cos\theta + 2\xi^2r^2\sin^2\theta) - J_0(\xi r\sin\theta)(1 - \xi r\cos\theta\cos2\theta)\right\}d\xi - b_0r^{-3} + \sum_{n=1}^{\infty}[\{a_{2n}2n(4n^2-4n+2\nu-1)r^{-2n-1} - b_{2n}(2n+1)^2r^{-2n-3}\}P_{2n}(\cos\theta) + \{a_{2n}(2n-4+4\nu)r^{-2n-1} + b_{2n}r^{-2n-3}\}\cot\theta\frac{d}{d\theta}P_{2n}(\cos\theta)] - 2c_0(1+\nu) - \sum_{n=1}^{\infty}[\{c_{2n}(2n+1)(4n^2+8n+2+2\nu)r^{2n} + d_{2n}4n^2r^{-2n-2}\}P_{2n}(\cos\theta) + \{c_{2n}(2n+5-4\nu)r^{2n} - d_{2n}r^{2n-2}\}\cot\theta\frac{d}{d\theta}P_{2n}(\cos\theta)]$$

$$\sigma_{r\theta}(r,\theta) = \int_0^\infty A(\xi)\frac{e^{-\xi r\cos\theta}}{r}\cos\theta\{J_0(\xi r\sin\theta)\xi^2r^2\sin2\theta + J_1(\xi r\sin\theta)(1-2\nu-\xi r\cos\theta-\xi^2r^2\cos2\theta)\}d\xi + \sum_{n=1}^{\infty}\{a_{2n}(4n^2+2\nu-2)r^{-2n-1} - b_{2n}(2n+2)r^{-2n-3}\}\frac{d}{d\theta}P_{2n}(\cos\theta) + \sum_{n=1}^{\infty}\{c_{2n}(4n^2+4n-1+2\nu)r^{2n} + d_{2n}(2n-1)r^{2n-2}\}\frac{d}{d\theta}P_{2n}(\cos\theta) \quad (7)$$

Note that $\sigma_{r\theta}$ satisfies the boundary condition (2) automatically.

If the following definition is made on the crack-opening displacement,

$$\frac{\mu}{1-\nu}\frac{\partial}{\partial r}u_\theta(r,\pi/2) = \begin{cases}\phi(r), & 1\le r<b\\ 0, & b\le r\le d\end{cases} \quad (8)$$

$A(\xi)$ is determined as

$$A(\xi) = \int_1^b t\phi(t)J_1(\xi t)\,dt \quad (9)$$

which satisfies the second equation of (3) automatically. From boundary condition (4) with the help of results from [7], one can easily derive the following equations:

Downloaded 02 May 2010 to 171.66.16.246. Redistribution subject to ASME license or copyright; see http://www.asme.org/terms/Terms_Use.cfm

$$\sigma_{rr}(1,\theta)=\int_1^b t\phi(t)\sum_{n=0}^{\infty}(-1)^n t^{-2n}\left\{-\frac{2n(4n^2-4n-1+2\nu)}{4n-1}\right.$$

$$\left.+\frac{(2n+1)(4n^2-2n-2-2\nu)}{t^2(4n+3)}\right\}\frac{(2n-1)!!}{(2n)!!}P_{2n}(\cos\theta)dt$$

$$+2b_0+\sum_{n=1}^{\infty}\{a_{2n}2n(2\nu-6n-4n^2)+b_{2n}(2n+1)(2n$$

$$+2)\}P_{2n}(\cos\theta)-2(1+\nu)c_0+\sum_{n=1}^{\infty}\{c_{2n}(2n+1)(4n^2$$

$$-2n-2-2\nu)+d_{2n}2n(2n-1)\}P_{2n}(\cos\theta)=-q_0$$

$$\frac{d}{d\theta}\sin\theta[\sigma_{r\theta}(1,\theta)]$$

$$=\int_1^b t\phi(t)\sum_{n=1}^{\infty}(-1)^n t^{-2n}\left\{\frac{2n(2n+1)(4n^2-4n-1+2\nu)}{(4n-1)}\right.$$

$$\left.-\frac{2n(2n+1)(4n^2+4n-1+2\nu)}{t^2(4n+3)}\right\}\frac{(2n-1)!!}{(2n)!!}\sin\theta P_{2n}(\cos\theta)dt$$

$$-\sum_{n=1}^{\infty}2n(2n+1)\{a_{2n}(4n^2+2\nu-2)-(2n+2)b_{2n}\}\sin\theta P_{2n}(\cos\theta)$$

$$-\sum_{n=1}^{\infty}2n(2n+1)\{c_{2n}(4n^2+4n-1+2\nu)$$

$$+d_{2n}(2n-1)\}\sin\theta P_{2n}(\cos\theta) \tag{10}$$

With the help of results from [6], we obtain the following equations from boundary condition (5):

$$\sigma_{rr}(d,\theta)=\frac{1}{d^2}\int_1^b t\phi(t)\left[-\frac{2(1+\nu)}{3}(t/d)\right.$$

$$+\sum_{n=1}^{\infty}(-1)^n(t/d)^{2n-1}\left\{\frac{2n(4n^2+6n-2\nu)}{4n-1}\right.$$

$$\left.\left.-(t/d)^2\frac{(2n+1)(4n^2+8n+2+2\nu)}{4n+3}\right\}\frac{(2n-1)!!}{(2n)!!}P_{2n}(\cos\theta)\right]dt$$

$$+2b_0/d^3+\sum_{n=1}^{\infty}\{a_{2n}2n(2\nu-6n-4n^2)d^{-2n-1}$$

$$+b_{2n}(2n+1)(2n+2)d^{-2n-3}\}P_{2n}(\cos\theta)$$

$$-2(1+\nu)c_0+\sum_{n=1}^{\infty}\{c_{2n}(2n+1)(4n^2-2n-2-2\nu)d^{2n}$$

$$+d_{2n}2n(2n-1)d^{2n-2}\}P_{2n}(\cos\theta)=0$$

$$\frac{d}{d\theta}\sin\theta[\sigma_{r\theta}(d,\theta)]$$

$$=\frac{1}{d^2}\int_1^b t\phi(t)\sum_{n=1}^{\infty}(-1)^n(t/d)^{2n-1}\left\{\frac{2n(2n+1)(4n^2+2\nu-2)}{4n-1}\right.$$

$$\left.-(t/d)^2\frac{2n(2n+1)(4n^2+8n+2+2\nu)}{4n+3}\right\}$$

$$\times\frac{(2n-1)!!}{(2n)!!}\sin\theta P_{2n}(\cos\theta)dt$$

$$-\sum_{n=1}^{\infty}2n(2n+1)\{a_{2n}(4n^2+2\nu-2)d^{-2n-1}$$

$$-b_{2n}(2n+2)d^{-2n-3}\}\sin\theta P_{2n}(\cos\theta)$$

$$-\sum_{n=1}^{\infty}2n(2n+1)\{c_{2n}(4n^2+4n-1+2\nu)d^{2n}$$

$$+d_{2n}(2n-1)d^{2n-2}\}\sin\theta P_{2n}(\cos\theta)=0 \tag{11}$$

From equations (10) and (11), the unknown coefficients a_{2n}, b_{2n}, c_{2n}, and d_{2n} are determined and are given in the Appendix. For the sake of convenience, we perform the following change of variables and function:

$$r=\frac{c}{2}(1+s)+1,\quad t=\frac{c}{2}(1+\tau)+1 \tag{12}$$

$$\phi(t)=p_0\Phi(\tau) \tag{13}$$

Finally, boundary condition (3) gives the equation:

$$\frac{1}{\pi}\int_{-1}^{1}\Phi(\tau)\left[\frac{1}{s-\tau}+\frac{c}{4r}\log|\tau-s|+\frac{c}{2}\left\{M_0(s,\tau)\right.\right.$$

$$\left.\left.+\pi tS_0(s,\tau)\right\}\right]d\tau=-1-\frac{(q_0/p_0)}{1-d^3}\left\{1+\frac{1}{2}(d/r)^3\right\} \tag{14}$$

where

$$M_0(s,\tau)=-\frac{1}{r+t}E(r/t)+L_0(s,\tau);\quad s<\tau$$

$$=\frac{1}{r+t}E(t/r)+L_0(s,\tau),\quad s>\tau \tag{15}$$

$$L_0(s,\tau)=\frac{E(r/t)-1}{r-t}-\frac{1}{2r}\log|\tau-s|;\quad s<\tau$$

$$=\frac{E(t/r)-1}{r-t}-\frac{2K(t/r)}{r}-\frac{1}{2r}\log|\tau-s|;\quad s>\tau \tag{16}$$

$$S_0(s,\tau)=\frac{(1+\nu)d^3}{3(1-d^3)}\left\{\frac{1}{r^3t^2}-\frac{t}{r^3d^3}+\frac{2}{d^3}\left(\frac{1}{t^2}-t\right)\right\}$$

$$+\sum_{n=1}^{\infty}\left[\frac{1}{D_{\alpha n}(rt)^{2n}r}[2n(4n^2-4n+2\nu\right.$$

$$-1)\{\alpha_{dn}L_{an}(t)-\alpha_{bn}L_{bn}(t)\}$$

$$-\frac{1}{r^2}(2n+1)^2\{\alpha_{an}L_{bn}(t)-\alpha_{cn}L_{an}(t)\}$$

$$-\frac{(rt/d^2)^{2n}}{D_{\beta n}}\left[(2n+1)(4n^2+8n+2+2\nu)\{\beta_{8n}L_{cn}(t)\right.$$

$$-\beta_{4n}L_{dn}(t)\}+\frac{1}{r^2}4n^2\{\beta_{3n}L_{dn}(t)$$

$$\left.\left.-\beta_{7n}L_{cn}(t)\}\right]\right\}\left\{\frac{(2n-1)!!}{(2n)!!}\right\}^2 \tag{17}$$

In equation (17), K and E are complete elliptic integrals of the first and second kind, respectively.

The solution of equation (17) is as given as in [7] by the form

$$\Phi(\tau)=\left(\frac{1+\tau}{1-\tau}\right)^{1/2}\sum_{n=0}^{\infty}B_nP_n^{(-1/2,1/2)}(\tau) \tag{18}$$

where $P_n^{(-1/2,1/2)}(\tau)$ are the Jacobi polynomials. B_n are unknown constants and are governed by the following infinite system of linear algebraic equations:

$$\theta_k^{(1/2,-1/2)}B_k+\sum_{n=0}^{\infty}(\gamma_{kn}+c_{kn})B_n$$

Downloaded 02 May 2010 to 171.66.16.246. Redistribution subject to ASME license or copyright; see http://www.asme.org/terms/Terms_Use.cfm

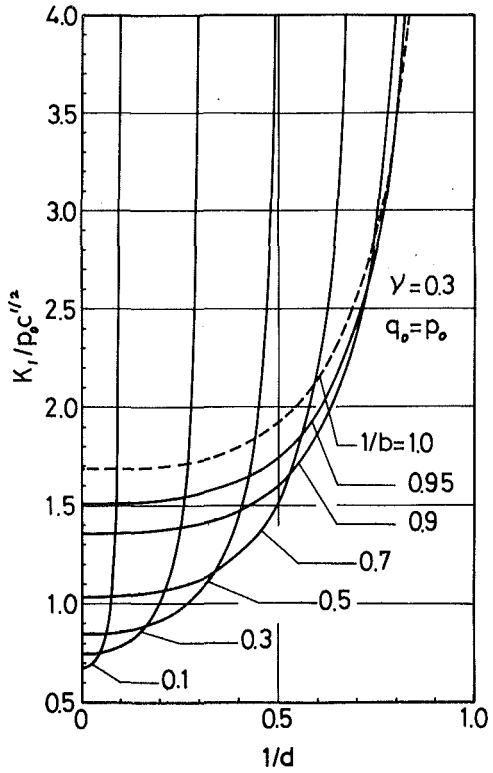

Fig. 2 Normalized stress-intensity factor $K_1/p_0c^{1/2}$ versus $1/d$ $(q_0=p_0)$

$$= (q_0/p_0)dk + \pi\left\{1 + \frac{(q_0/p_0)}{d^3-1}\right\}\delta_{k0}, \quad (k=0,1,\ldots) \tag{19}$$

where δ_{k0} is the Kronecker delta and $\theta_k^{(1/2,-1/2)}$, γ_{kn}, c_{kn}, and d_k are

$$\theta_k^{(1/2,-1/2)} = \frac{2(2k)!(2k+2)!\pi}{(1+2k)(k!)^3(k+1)!2^{2(2k+1)}}$$

$$\gamma_{kn} = \int_{-1}^{1} P_k^{(1/2,-1/2)}(s)\, w_n(s)\left(\frac{1-s}{1+s}\right)^{1/2} ds$$

$$c_{kn} = \int_{-1}^{1} P_k^{(1/2,-1/2)}(s) p_n(s)\left(\frac{1-s}{1+s}\right)^{1/2} ds$$

$$d_k = \frac{d^3}{2(d^3-1)}\int_{-1}^{1} P_k^{(1/2,-1/2)}(s)\frac{1}{r^3}\left(\frac{1-s}{1+s}\right)^{1/2} ds \tag{20}$$

In equations (20), $w_n(s)$ and $p_n(s)$ are

$$w_n(s) = \frac{c}{4r}(s+\log 2) \quad (n=0)$$

$$= \frac{c(2n)!}{4r(n!)^2 2^{2n}}\left\{\frac{1}{n}T_n(s) + \frac{1}{n+1}T_{n+1}(s)\right\}$$

$$(n=1,2,\ldots)$$

$$p_n(s) = -\frac{c}{2\pi}\int_{-1}^{1}\{M_0(s,\tau)$$

$$+ \pi t S_0(s,\tau)\}P_n^{(-1/2,1/2)}(\tau)\left(\frac{1+\tau}{1-\tau}\right)^{1/2} d\tau \tag{21}$$

where $T_n(s)$ are the n-order Chebyshev polynomials of the first kind.

The Stress-Intensity Factor and the Crack-Opening Displacement

Following the same procedure as in [7], the stress-intensity factor can be found as

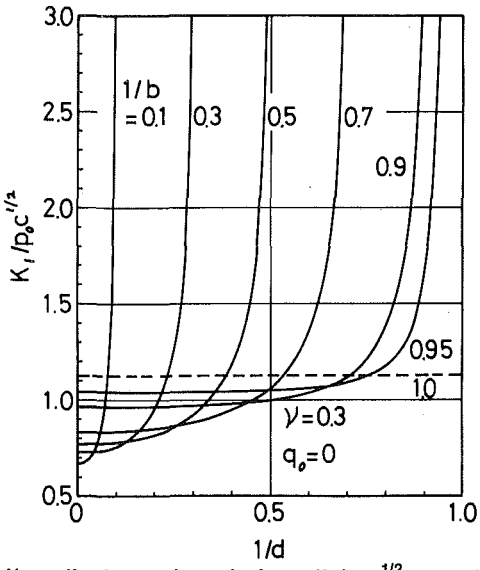

Fig. 3 Normalized stress-intensity factor $K_1/p_0c^{1/2}$ versus $1/d$ $(q_0=0)$

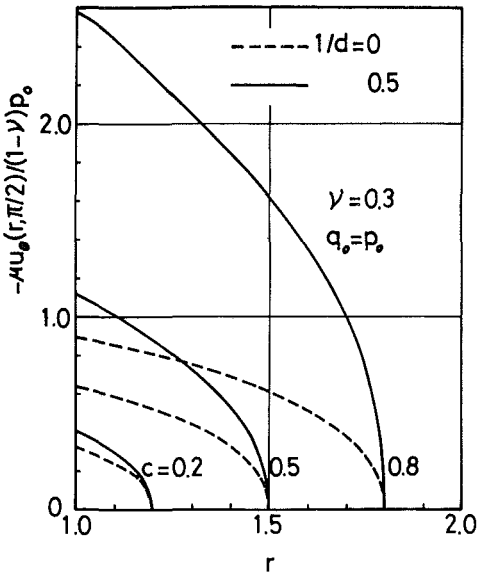

Fig. 4 Normalized crack-opening displacement $-\mu u_\theta(r,\pi/2)/(1-\nu)p_0$ for $1/d=0, 0.5$ $(q_0=p_0)$

$$K_1/p_0c^{1/2} = 2^{1/2}\sum_{n=0}^{\infty}\frac{(2n)!}{2^{2n}(n!)^2}B_n \tag{22}$$

The crack-opening displacement is also obtained in a similar way. The result is as follows:

$$-\frac{\mu}{(1-\nu)p_0}u_\theta(r,\pi/2) = \frac{c}{2}\sum_{n=0}^{\infty}B_nI_{ns} \tag{23}$$

where

$$I_{ns} = \{(1-s)(1+s)\}^{1/2} + 2\sin^{-1}\left(\frac{1-s}{2}\right)^{1/2} \quad (n=0)$$

$$= \frac{\Gamma(n+1/2)}{n!\pi^{1/2}}(1-s^2)\left\{\frac{1}{n}U_{n-1}(s)\right.$$

$$\left. + \frac{1}{n+1}U_n(s)\right\}, \quad (n=1,2,\ldots) \tag{24}$$

Here, $U_n(s)$ denote the n-order Chebyshev polynomials of the second kind.

Downloaded 02 May 2010 to 171.66.16.246. Redistribution subject to ASME license or copyright; see http://www.asme.org/terms/Terms_Use.cfm

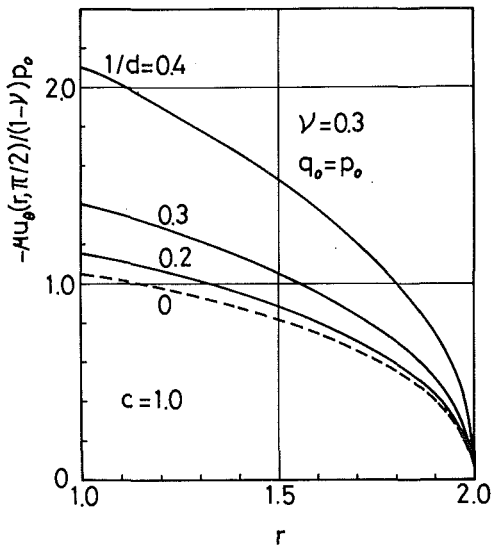

Fig. 5 Normalized crack-opening displacement $-\mu u_\theta(r,\pi/2)/(1-\nu)p_0$ for $c=1.0$ $(q_0=p_0)$

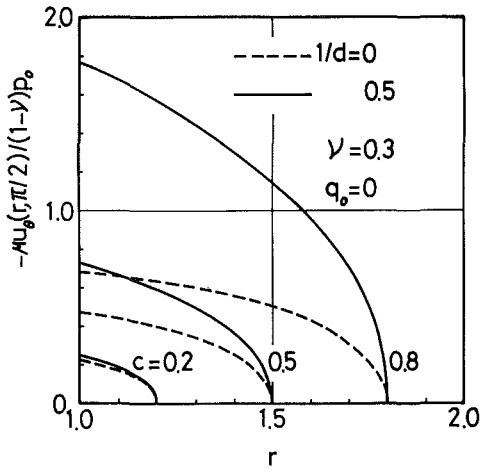

Fig. 6 Normalized crack-opening displacement $-\mu u_\theta(r,\pi/2)/(1-\nu)p_0$ for $1/d=0, 0.5$ $(q_0=0)$

Numerical Results and Considerations

Solving the infinite system of linear algebraic equations (19) numerically, we have examined the effect of geometrical parameters on the stress-intensity factors and crack-opening displacements. Numerical calculations have been carried out for $\nu=0.3$. The value of normalized stress-intensity factor $K_1/p_0\,c^{1/2}$ versus $1/d$ are shown in Fig. 2, for various ratios of $1/b$ in the case of $p_0=q_0$. The dotted line for $1/b=1.0$, which means $c=0$, shows the values of $K_1/p_0c^{1/2} \fallingdotseq 1.122\{1-(1+d^3/2)/(1-d^3)\}$ which is the stress-intensity factor of the plane-strain problem. $K_1/p_0c^{1/2}$ tends to $1.122\{1-(1+d^3/2)/(1-d^3)\}$ as $c\to 0$ and increases monotonically with the increase of $1/d$ and becomes infinity as $1/d\to 1/b$.

The same kind of results for $q_0=0$ is shown in Fig. 3. The dotted line shows the value of the stress-intensity factor $K_1/p_0c^{1/2}\fallingdotseq 1.122$ which is the similar solution of the plane-strain problem. It is observed that, regardless of the crack length, the stress-intensity factor is relatively constant for thin shells. Both results for $q_0=0$ and $q_0=p_0$ become the solution in reference [7] as $1/d\to 0$.

Figure 4 shows the crack-opening displacement $-\mu u_\theta(r,\pi/2)/(1-\nu)p_0$ versus r for the case of $q_0=p_0$. The dotted lines show the results in reference [7]. The values of the maximal crack-opening displacement for $1/d=0.5$ are $0.410(c=0.2)$, 1.118 $(c=0.5)$, and $2.578(c=0.8)$, which are larger than the corresponding values 0.324, 0.640, and 0.895 for the infinite solid of $1/d=0$. Figure 5 shows the same kind of results for $c=1.0$. The values of the maximal crack-opening displacement for $1/d=0$, 0.2, 0.3, and 0.4 are 1.050, 1.151, 1.406, and 2.098, respectively. Figures 6 and 7 show the results for $q_0=0$. The corresponding maximal values are $0.227(c=0.2)$, $0.472(c=0.5)$, $0.684(c=0.8)$, for $1/d=0$ and 0.252, 0.730, 1.768 for $1/d=0.5$, respectively. These values become 0.822, 0.898, 1.086, 1.579, for $c=1.0$ when $1/d=0$, 0.2, 0.3, 0.4, respectively.

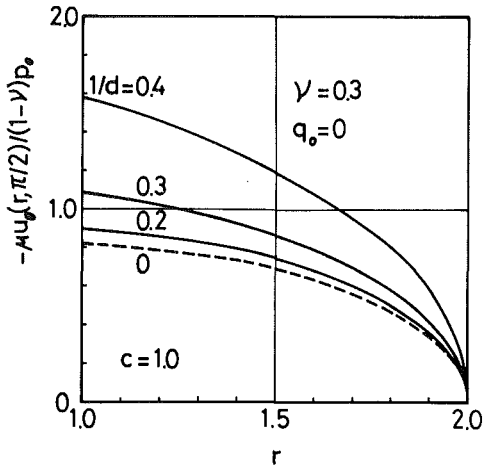

Fig. 7 Normalized crack-opening displacement $-\mu u_\theta(r,\pi/2)/(1-\nu)p_0$ for $c=1.0$ $(q_0=0)$

Acknowledgment

It should be acknowledged that the expense for this study has been appropriated from the Scientific Research Fund of the Ministry of Education for the fiscal year 1980.

References

1 Erdogan, F., and Ratwani, M., "Fracture of Cylindrical and Spherical Shells Containing a Crack," *Nuclear Engineering and Design*, Vol. 20, 1972, pp. 265–286.

2 Erdol, R., and Erdogan, F., "A Thick-Walled Cylinder With an Axisymmetric Internal or Edge Crack," ASME JOURNAL OF APPLIED MECHANICS, Vol. 45, 1978, pp. 281–286.

3 Keer, L. M., Freedman, J. M., and Watts, H. A., "Infinite Tensile Cylinder With Circumferential Edge Crack," *Letters in Applied and Engineering Sciences*, Vol. 5, 1977, pp. 129–139.

4 Keer, L. M., Luk, V. K., and Freedman, J. M., "Circumferential Edge Crack in a Cylindrical Cavity," ASME JOURNAL OF APPLIED MECHANICS, Vol. 44, 1977, pp. 250–254.

5 Keer, L. M., and Watts, H. A., "Mixed Boundary Value Problems for a Cylindrical Shell," *International Journal of Solids and Structures*, Vol. 12, 1976, pp. 723–729.

6 Atsumi, A., and Shindo, Y., "Axially Symmetrical Stress Problem of an Elastic Sphere With Peripheral Edge Crack" (in Japanese), *Trans. JSME*, Series *A*, Vol. 47, 1981, pp. 1006–1011.

7 Atsumi, A., and Shindo, Y., "Singular Stresses Near a Peripheral Edge Crack in a Spherical Cavity" (in Japanese), *Trans. JSME*, Series *A*, Vol. 48, 1982, pp. 627–632.

8 Lure, A. I., *Three-Dimensional Problems of the Theory of Elasticity*, Interscience, New York, 1964.

9 Sneddon, I. N., *Fourier Transforms*, McGraw-Hill, New York, 1951.

APPENDIX

$$a_{2n} = \frac{1}{D_{\alpha n}}\int_1^b t\phi(t)[\alpha_{dn}L_{an}(t) - \alpha_{bn}L_{bn}(t)](-1)^n\left\{\frac{(2n-1)!!}{(2n)!!}\right\}(1/t)^{2n}dt$$

Downloaded 02 May 2010 to 171.66.16.246. Redistribution subject to ASME license or copyright; see http://www.asme.org/terms/Terms_Use.cfm

$$
\begin{aligned}
b_0 &= -\frac{d^3}{1-d^3}\left[\frac{1+\nu}{3}\int_1^b \phi(t)\left\{\frac{1}{t}-\frac{1}{d}\,(t/d)^2\right\}dt - q_0/2\right] \\
b_{2n} &= \frac{1}{D_{\alpha n}}\int_1^b t\phi(t)\,[\alpha_{an}L_{bn}(t) \\
&\quad - \alpha_{cn}L_{an}(t)](-1)^n\left\{\frac{(2n-1)!!}{(2n)!!}\right\}(1/t)^{2n}dt \\
c_0 &= -\frac{1}{1-d^3}\left[\frac{1}{3}\int_1^b \phi(t)\left(\frac{1}{t}-t^2\right)dt - \frac{q_0}{2(1+\nu)}\right] \\
c_{2n} &= \frac{1}{D_{\beta n}d^{2n}}\int_1^b t\phi(t)\,[\beta_{8n}L_{cn}(t) \\
&\quad - \beta_{4n}L_{dn}(t)](-1)^n\left\{\frac{(2n-1)!!}{(2n)!!}\right\}(t/d)^{2n}dt \\
d_{2n} &= \frac{1}{D_{\beta n}d^{2n}}\int_1^b t\phi(t)\,[\beta_{3n}L_{dn}(t) \\
&\quad - \beta_{7n}L_{cn}(t)](-1)^n\left\{\frac{(2n-1)!!}{(2n)!!}\right\}(t/d)^{2n}dt
\end{aligned}
\qquad (a)
$$

where

$$
\begin{aligned}
D_{\alpha n} &= \alpha_{an}\alpha_{dn} - \alpha_{bn}\alpha_{cn} \\
D_{\beta n} &= \beta_{3n}\beta_{8n} - \beta_{4n}\beta_{7n}
\end{aligned}
\qquad (b)
$$

$$
\begin{aligned}
\alpha_{an} &= (\beta_{3n}\alpha_{8n} - \alpha_{7n}\beta_{4n})\,(\alpha_{7n}\alpha_{1n} - \alpha_{3n}\alpha_{5n}) \\
&\quad - (\alpha_{7n}\alpha_{4n} - \alpha_{3n}\alpha_{8n})\,(\beta_{3n}\alpha_{5n} - \alpha_{7n}\beta_{1n}d^{-4n-1}) \\
\alpha_{bn} &= (\beta_{3n}\alpha_{8n} - \alpha_{7n}\beta_{4n})\,(\alpha_{7n}\alpha_{2n} - \alpha_{3n}\alpha_{6n}) \\
&\quad - (\alpha_{7n}\alpha_{4n} - \alpha_{3n}\alpha_{8n})(\beta_{3n}\alpha_{6n} - \alpha_{7n}\beta_{2n}d^{-4n-1}) \\
\alpha_{cn} &= (\beta_{7n}\beta_{4n} - \beta_{3n}\beta_{8n})\,(\beta_{3n}\alpha_{5n} - \alpha_{7n}\beta_{1n}d^{-4n-1}) \\
&\quad - (\beta_{3n}\alpha_{8n} - \alpha_{7n}\beta_{4n})\,(\beta_{7n}\beta_{1n} - \beta_{3n}\beta_{5n})d^{-4n-1} \\
\alpha_{dn} &= (\beta_{7n}\beta_{4n} - \beta_{3n}\beta_{8n})\,(\beta_{3n}\alpha_{6n} - \alpha_{7n}\beta_{2n}d^{-4n-1}) \\
&\quad - (\beta_{3n}\alpha_{8n} - \alpha_{7n}\beta_{4n})\,(\beta_{7n}\beta_{2n} - \beta_{3n}\beta_{6n})\,d^{-4n-1}
\end{aligned}
\qquad (c)
$$

$$
\begin{aligned}
\alpha_{1n} &= \frac{2\nu - 6n - 4n^2}{2n+1}\,, \quad \alpha_{2n} = \frac{n+1}{n} \\
\alpha_{3n} &= \frac{2n^2 - n - 1 - \nu}{n}\,, \quad \alpha_{4n} = \frac{2n-1}{2n+1} \\
\alpha_{5n} &= \frac{2n^2 + \nu - 1}{n+1}\,, \quad \alpha_{6n} = -1 \\
\alpha_{7n} &= \frac{4n^2 + 4n - 1 + 2\nu}{2n+2}\,, \quad \alpha_{8n} = \frac{2n-1}{2n+1} \\
\beta_{1n} &= \frac{2\nu - 6n - 4n^2}{2n+1}\,, \quad \beta_{2n} = \frac{n+1}{nd^2} \\
\beta_{3n} &= \frac{2n^2 - n - 1 - \nu}{n}\,, \quad \beta_{4n} = \frac{2n-1}{(2n+1)d^2} \\
\beta_{5n} &= \frac{4n^2 + 2\nu - 2}{2n-1}\,, \quad \beta_{6n} = -\frac{2n+2}{(2n-1)d^2}
\end{aligned}
\qquad (d)
$$

Downloaded 02 May 2010 to 171.66.16.246. Redistribution subject to ASME license or copyright; see http://www.asme.org/terms/Terms_Use.cfm

L. M. Keer
Mem. ASME

J. C. Lee

T. Mura
Fellow ASME

Department of Civil Engineering,
Northwestern University,
Technological Institute,
Evanston, Ill. 60201

Stress Distributions for a Quarter Plane Containing an Arbitrarily Oriented Crack

A solution for an elastic quarter plane containing an arbitrarily oriented crack is presented. The problem is formulated by means of Mellin integral transforms and reduced to a system of two coupled singular integral equations where the unknown quantities are the dislocation densities that characterize the crack. Numerical solutions are investigated for various orientations of the cracks. In each case the stress intensity factors are computed for the different parameters.

Introduction

We consider here the problem when an electric quarter plane containing an interior or surface crack is loaded by tractions on its surface. Although there are many solutions for the surface-loaded quarter plane, the simplest ones given are those by Hetenyi [1], who based his solution on the superposition and subsequent iteration of the Flamant solution for the half plane, and Sneddon [2], who gives, in addition to a comprehensive survey, a formal solution by means of the Mellin transform. Having a formal solution, one can use a numerical integration scheme to solve the resulting integrals.

Our objective is to first deduce the solution for a quarter plane containing a single dislocation. By using one of the fundamental solutions such as that given by Dundurs and Mura [3], suitable superposition solutions can be used to establish the equivalent loading on the quarter plane surface. The problem then becomes one for the formal application of the Mellin transform to determine the interior stress field. Thus, a Green's functions will be developed for the field of a dislocation in a quarter plane.

The next step is to use this solution to establish boundary conditions for a crack problem by writing the dislocation solution as a distribution of dislocations, thereby obtaining pairs of coupled singular integral equations. Through this rather elementary procedure, an efficient scheme is developed for determining the stress field for a quarter plane containing an interior crack. The integral equations are solved approximately by numerical techniques and crack-tip stress intensity factors are developed for certain cases.

Method of Solution—Dislocations $\mathbf{b}_x$ and $\mathbf{b}_y$ in Quarter Plane

Normal Loading. The problem in which the positive quadrant $x \geq 0$, $y \geq 0$ is loaded by the application of surface pressure has been formulated in references [1] and [2]. The latter reference gives a formal solution by means of the Mellin transform, which is an essential technique accepted herein. The integral equations for normal loading on the plane, $y = 0$, stress free on the plane $x = 0$, are given by (see Fig. 1 and references [1, 2])

$$p_B(x) + \frac{4}{\pi}\int_0^\infty \frac{x\zeta^2}{(x^2+\zeta^2)} q_B(\zeta)\,d\zeta = \sigma_{yy}^B(x,0), \quad y=0, \quad 0<x<\infty \tag{1}$$

$$q_B(y) + \frac{4}{\pi}\int_0^\infty \frac{y\zeta^2}{(y^2+\zeta^2)^2} p_B(\zeta)\,d\zeta = 0, \quad x=0, \quad 0<y<\infty \tag{2}$$

where p_B nd q_B are the normal tractions applied to the half planes $y = 0$ and $x = 0$, respectively, with the properties that $p_B(x) = p_B(-x)$, $q_B(y) = q_B(-y)$.

If one uses the dislocation solutions in the manner of Fig. 1, then the stress $\sigma_{yy}^B(x,0)$ corresponding to dislocation $\mathbf{b}_x$ is given as

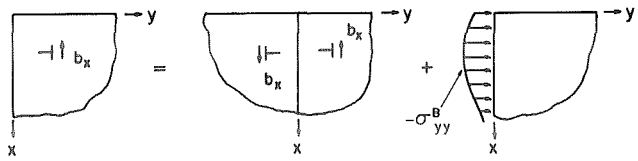

Fig. 1 Geometry and coordinate system for quarter plane with dislocation b_x

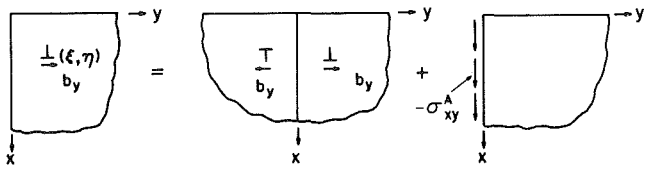

Fig. 2 Geometry and coordinate system for quarter plane with dislocation b_y

Contributed by the Applied Mechanics Division for publication in the JOURNAL OF APPLIED MECHANICS.

Discussion on this paper should be addressed to the Editorial Department, ASME, United Engineering Center, 345 East 47th Street, New York, N.Y. 10017, and will be accepted until two months after final publication of the paper itself in the JOURNAL OF APPLIED MECHANICS. Manuscript received by ASME Applied Mechanics Division, December, 1981.

Copyright © 1983 by ASME
Downloaded 02 May 2010 to 171.66.16.246. Redistribution subject to ASME license or copyright; see http://www.asme.org/terms/Terms_Use.cfm

$$\sigma_{yy}^{B}(x,0)=\frac{4\mu}{\pi(\kappa+1)}\left\{\frac{(x-\xi)^2\eta-\eta^3}{[(x-\xi)^2+\eta^2]^2}-\frac{(x+\xi)^2\eta-\eta^3}{[(x+\xi)^2+\eta^2]^2}\right.$$
$$\left.+\frac{4\xi\eta(-x+2\xi)}{[(x+\xi)^2+\eta^2]^2}+\frac{16\,x\xi\eta^3}{[(x+\xi)^2+\eta^2]^3}\right\} \tag{3}$$

where $(\xi, \pm\eta)$ are the locations of the two dislocations in the half plane, μ and ν are the shear modulus and Poisson's ratio, respectively, and $\kappa = 3 - 4\nu$ for the plane strain. The shear stress vanishes on the boundary $y = 0$ because of symmetry.

In the form given by equation (3) for $\sigma_{yy}^{B}(x,0)$, the Mellin transform can be applied to equations (1) and (2) as in reference [2] to give the following equations:

$$p_B^*(s)=\frac{\cos^2(\pi s/2)}{\cos^2(\pi s/2)-(s-1)^2}\sigma_{yy}^{B*}(s)\equiv\frac{2\mu}{\kappa+1}P_B^*(s) \tag{4}$$

$$q_B^*(s)=\frac{(s-1)\cos(\pi s/2)}{\cos^2(\pi s/2)-(s-1)^2}\sigma_{yy}^{B*}(s)\equiv\frac{2\mu}{\kappa+1}Q_B^*(s) \tag{5}$$

where we have

$$\sigma_{yy}^{B*}(s)=\frac{4\mu}{\kappa+1}\frac{(\xi^2+\eta^2)^{s/2-2}}{\cos(\pi s/2)}\{-(s-1)\eta(\eta^2-\xi^2)\sin(\phi s)$$
$$+2\xi\eta^2(s-1)\cos(\phi s)\}$$
$$+\frac{4\mu}{\kappa+1}\frac{(\xi^2+\eta^2)^{s/2-2}}{\sin(\pi s)}\left\{(s^2-3s+2)\left[4\xi^2\eta\cos\left\{\left(\frac{\pi}{2}-\phi\right)s\right\}\right.\right.$$
$$\left.\left.+2\xi(\eta^2-\xi^2)\cdot\sin\left\{\left(\frac{\pi}{2}-\phi\right)s\right\}\right]\right\} \tag{6}$$

and

$$\phi=\tan^{-1}(\xi/\eta). \tag{7}$$

$p_B(x)$ and $q_N(x)$ can be obtained by the inverse Mellin transforms of $p_B^*(s)$ and $q_B^*(s)$. The corresponding stress components are given by

$$\sigma_{xx}(x,y)=-\frac{2}{\pi}\int_{-\infty}^{\infty}\frac{(x-\zeta)^2y}{[(x-\zeta)^2+y^2]^2}p_B(\zeta)\,d\zeta$$
$$-\frac{2}{\pi}\int_{-\infty}^{\infty}\frac{x^3}{[x^2+(y-\zeta)^2]^2}q_B(\zeta)\,d\zeta$$
$$\sigma_{yy}(x,y)=-\frac{2}{\pi}\int_{-\infty}^{\infty}\frac{y^3}{[(x-\zeta)^2+y^2]^2}p_B(\zeta)\,d\zeta$$
$$-\frac{2}{\pi}\int_{-\infty}^{\infty}\frac{x(y-\zeta)^2}{[x^2+(y-\zeta)^2]^2}q_B(\zeta)\,d\zeta$$
$$\sigma_{xy}(x,y)=-\frac{2}{\pi}\int_{-\infty}^{\infty}\frac{(x-\zeta)y^2}{[(x-\zeta)^2+y^2]^2}p_B(\xi)\,d\zeta$$
$$-\frac{2}{\pi}\int_{-\infty}^{\infty}\frac{x^2(y-\zeta)}{[x^2+(y-\zeta)^2]^2}q_B(\zeta)\,d\zeta. \tag{7'}$$

Tangential Loading. In the same spirit as in the preceding case the solution for tangential tractions on a quarter plane can be developed. The problem of the quadrant subjected to tangential tractions can be reduced to the solution of the following coupled integral equations:

$$p_A(x)+\frac{4}{\pi}\int_0^{\infty}\frac{x\zeta^2}{(x^2+\zeta^2)^2}q_A(\zeta)\,d\zeta=\sigma_{xy}^{A}(x,0),$$
$$y=0,\quad 0<x<\infty \tag{8}$$
$$q_A(y)+\frac{4}{\pi}\int_0^{\infty}\frac{y\zeta^2}{(y^2+\zeta^2)^2}p_A(\zeta)\,d\zeta=0,\quad x=0,$$
$$0<y<\infty \tag{9}$$

where $p_A(x)$, $q_A(y)$ are the shearing tractions applied to the half planes $y = 0$ and $x = 0$, respectively, with the properties that $p_A(x) = p_A(-x)$, $q_A(y) = q_A(-y)$.

If one uses the dislocation solutions in the manner of Fig. 2, then the stress $\sigma_{xy}^{A}(x,0)$ corresponding to dislocation $\mathbf{b}_y$ is given by

$$\sigma_{xy}^{A}(x,0)=\frac{4\mu}{\pi(\kappa+1)}\left\{\frac{-(x-\xi)^2\eta+\eta^3}{[(x-\xi)^2+\eta^2]^2}+\frac{(x+\xi)^2\eta-\eta^3}{[(x+\xi)^2+\eta^2]^2}\right.$$
$$\left.-\frac{12\,x\xi\eta}{[(x+\xi)^2+\eta^2]^2}+\frac{16\,x\xi\eta^3}{[(x+\xi)^2+\eta^2]^3}\right\}. \tag{10}$$

The σ_{yy}^{A} component vanishes on the boundary $y = 0$ because of antisymmetry. In the form given by equation (10) for $\sigma_{xy}^{A}(x,0)$ the Mellin transform can be applied to equations (8) and (9) to give the following equations:

$$p_A^*(s)=\frac{\cos^2(\pi s/2)}{\cos^2(\pi s/2)-(s-1)^2}\sigma_{xy}^{A*}(s)\equiv\frac{2\mu}{\kappa+1}P_A^*(s) \tag{11}$$

$$q_A^*(s)=\frac{(s-1)\cos(\pi s/2)}{\cos^2(\pi s/2)-(s-1)^2}\sigma_{xy}^{A*}(s)\equiv\frac{2\mu}{\kappa+1}Q_A^*(s) \tag{12}$$

where we have

$$\sigma_{xy}^{A*}(s)=\frac{4\mu}{\kappa+1}\frac{(\xi^2+\eta^2)^{s/2-2}}{\cos(\pi s/2)}\{(s-1)\eta(\eta^2-\xi^2)\sin(\phi s)$$
$$-2\xi\eta^2(s-1)\cos(\phi s)\}$$
$$+\frac{4\mu}{\kappa+1}\frac{(\xi^2+\eta^2)^{s/2-2}}{\sin(\pi s)}\left[4s(s-1)\xi^2\eta\cos\left\{\left(\frac{\pi}{2}-\phi\right)s\right\}+\right.$$
$$\left.+2s(s-1)\xi(\eta^2-\xi^2)\sin\left\{\left(\frac{\pi}{2}-\phi\right)s\right\}\right] \tag{13}$$

and

$$\phi=\tan^{-1}(\xi/\eta). \tag{14}$$

The corresponding stress components are

$$\sigma_{xx}(x,y)=-\frac{2}{\pi}\int_{-\infty}^{\infty}\frac{(x-\zeta)^3}{[(x-\zeta)^2+y^2]^2}p_A(\zeta)\,d\zeta$$
$$-\frac{2}{\pi}\int_{-\infty}^{\infty}\frac{x^3}{[(x^2+(y-\zeta)^2]^2}q_A(\zeta)\,d\zeta$$
$$\sigma_{yy}(x,y)=-\frac{2}{\pi}\int_{-\infty}^{\infty}\frac{(x-\zeta)y^2}{[(x-\zeta)^2+y^2]^2}p_A(\zeta)\,d\zeta$$
$$-\frac{2}{\pi}\int_{-\infty}^{\infty}\frac{(y-\zeta)^3}{[(x^2+(y-\zeta)^2]^2}q_A(\zeta)\,d\zeta$$
$$\sigma_{xy}(x,y)=-\frac{2}{\pi}\int_{-\infty}^{\infty}\frac{(x-\zeta)^2y}{[(x-\zeta)^2+y^2]^2}p_A(\zeta)\,d\zeta$$
$$-\frac{2}{\pi}\int_{-\infty}^{\infty}\frac{x(y-\zeta)^2}{[x^2+(y-\zeta)^2]^2}q_A(\zeta)\,d\zeta. \tag{14'}$$

Dislocation Arbitrarily Oriented in Quarter Plane

To determine the solution to the problem of a dislocation located arbitrarily in a quarter plane, use will be made of the solutions developed in the preceding section. The stress distribution for the dislocation located in a quarter plane with a geometry as shown in Fig. 3 can be given as

$$\sigma_{xy}=\cos\alpha\,K_{11}(x,y;\xi,\eta)+\sin\alpha\,K_{12}(x,y;\xi,\eta) \tag{15}$$
$$\sigma_{yy}=\cos\alpha\,K_{21}(x,y;\xi,\eta)+\sin\alpha\,K_{22}(x,y;\xi,\eta) \tag{16}$$
$$\sigma_{xx}=\cos\alpha\,K_{31}(x,y;\xi,\eta)+\sin\alpha\,K_{32}(x,y;\xi,\eta) \tag{17}$$

where

Downloaded 02 May 2010 to 171.66.16.246. Redistribution subject to ASME license or copyright; see http://www.asme.org/terms/Terms_Use.cfm

$$K_{11}(x,y;\xi,\eta)=\frac{2\mu}{\pi(\kappa+1)}\left\{\frac{(y-\eta)[(x-\xi)^2-(y-\eta)^2]}{[(x-\xi)^2+(y-\eta)^2]^2}-\frac{(y-\eta)[(x+\xi)^2-(y-\eta)^2]}{[(x+\xi)^2+(y-\eta)^2]^2}\right.$$
$$\left.+\frac{12x\xi(y-\eta)}{[(x+\xi)^2+(y-\eta)^2]^2}-\frac{16x\xi(y-\eta)^3}{[(x+\xi)^2+(y-\eta)^2]^3}\right\}-\frac{2\mu}{\pi(\kappa+1)}\left\{\frac{(y+\eta)[(x-\xi)^2-(y+\eta)^2]}{[(x-\xi)^2+(y+\eta)^2]^2}\right.$$
$$\left.-\frac{(y+\eta)[(x+\xi)^2-(y+\eta)^2]}{[(x+\xi)^2+(y+\eta)^2]^2}+\frac{12x\xi(y+\eta)}{[(x+\xi)^2+(y+\eta)^2]^2}-\frac{16x\xi(y+\eta)^3}{[(x+\xi)^2+(y+\eta)^2]^3}\right\}$$
$$-\frac{2\mu}{\kappa+1}\frac{1}{2\pi i}\int_{c-i\infty}^{c+i\infty}\frac{(x^2+y^2)^{-s/2-1}}{\cos(\pi s/2)}\left\{sxy\sin\left\{\left(\frac{\pi}{2}-\theta\right)s\right\}+(x^2+y^2-sx^2)\right.$$
$$\left.\cdot\cos\left\{\left(\frac{\pi}{2}-\theta\right)s\right\}\right\}Q_A^*(s)\,ds-\frac{2\mu}{\kappa+1}\frac{1}{2\pi i}\int_{c-i\infty}^{c+i\infty}\frac{(x^2+y^2)^{-s/2-1}}{\cos(\pi s/2)}\{sxy\sin(\theta s)$$
$$+(x^2+y^2-sy^2)\cos(\theta s)\}P_A^*(s)\,ds \tag{18}$$

where $\theta=\tan^{-1}(x/y)$;

$$K_{12}(x,y;\xi,\eta)=\frac{2\mu}{\pi(\kappa+1)}\left\{\frac{(x-\xi)[-(x-\xi)^2+(y-\eta)^2]}{[(x-\xi)^2+(y-\eta)^2]^2}+\frac{(x+\xi)[(x+\xi)^2-(y-\eta)^2]}{[(x+\xi)^2+(y-\eta)^2]^2}\right.$$
$$\left.+\frac{2\xi(x^2-\xi^2)+2\xi(y-\eta)^2}{[(x+\xi)^2+(y-\eta)^2]^2}-\frac{16x\xi(x+\xi)(y-\eta)^2}{[(x+\xi)^2+(y-\eta)^2]^3}\right\}-\frac{2\mu}{\pi(\kappa+1)}\left\{\frac{(x-\xi)[-(x-\xi)^2+(y+\eta)^2]}{[(x-\xi)^2+(y+\eta)^2]^2}\right.$$
$$\left.+\frac{(x+\xi)[(x+\xi)^2-(y+\eta)^2]}{[(x+\xi)^2+(y+\eta)^2]^2}+\frac{2\xi(x^2-\xi^2)+2\xi(y+\eta)^2}{[(x+\xi)^2+(y+\eta)^2]^2}-\frac{16x\xi(x+\xi)(y+\eta)^2}{[(x+\xi)^2+(y+\eta)^2]^3}\right\}$$
$$-\frac{2\mu}{\kappa+1}\frac{1}{2\pi i}\int_{c-i\infty}^{c+i\infty}\frac{(x^2+y^2)^{-s/2-1}}{\cos(\pi s/2)}\left\{sx^2\sin\left\{\left(\frac{\pi}{2}-\theta\right)s\right\}+sxy\cos\left\{\left(\frac{\pi}{2}-\theta\right)s\right\}\right\}Q_B^*(s)\,ds$$
$$-\frac{2\mu}{\kappa+1}\frac{1}{2\pi i}\int_{c-i\infty}^{c+i\infty}\frac{(x^2+y^2)^{-s/2-1}}{\cos(\pi s/2)}\{sy^2\sin(\theta s)+sxy\cos(\theta s)\}P_B^*(s)\,ds; \tag{19}$$

$$K_{21}(x,y;\xi,\eta)=\frac{2\mu}{\pi(\kappa+1)}\left\{\frac{(x-\xi)[(x-\xi)^2+3(y-\eta)^2]}{[(x-\xi)^2+(y-\eta)^2]^2}-\frac{(x+\xi)[(x+\xi)^2+3(y-\eta)^2]}{[(x+\xi)^2+(y-\eta)^2]^2}\right.$$
$$\left.-\frac{2\xi(x^2-\xi^2)+2\xi(7-\eta)}{[(x+\xi)^2+(y-\eta)^2]^2}+\frac{16x\xi(x+\xi)(y-\eta)^2}{[(x+\xi)^2+(y-\eta)^2]^3}\right\}-\frac{2\mu}{\pi(\kappa+1)}\left\{\frac{(x-\xi)[(x-\xi)^2+3(y+\eta)^2]}{(x-\xi)^2+(y+\eta)^2]^2}\right.$$
$$\left.-\frac{(x+\xi)[(x+\xi)^2+3(y+\eta)^2]}{[(x+\xi)^2+(y+\eta)^2]^2}-\frac{2\xi(x^2-\xi^2)+2\xi(y+\eta)}{[(x+\xi)^2+(y+\eta)^2]^2}+\frac{16x\xi(x+\xi)(y+\eta)^2}{[(x+\xi)^2+(y+\eta)^2]^3}\right\}$$
$$-\frac{2\mu}{\kappa+1}\frac{1}{2\pi i}\int_{c-i\infty}^{c+i\infty}\frac{(x^2+y^2)^{-s/2-1}}{\cos(\pi s/2)}\left\{(2x^2+2y^2-sx^2)\sin\left\{\left(\frac{\pi}{2}-\theta\right)s\right\}\right.$$
$$\left.-sxy\cos\left\{\left(\frac{\pi}{2}-\theta\right)s\right\}\right\}Q_A^*(s)\,ds-\frac{2\mu}{\kappa+1}\frac{1}{2\pi i}\int_{c-i\infty}^{c+i\infty}\frac{(x^2+y^2)^{-s/2-1}}{\cos(\pi s/2)}\{sy^2\sin(\theta s)$$
$$+sxy\cos(\theta s)\}P_A^*(s)\,ds; \tag{20}$$

$$K_{22}(x,y;\xi,\eta)=\frac{2\mu}{\pi(\kappa+1)}\left\{\frac{(y-\eta)[-(x-\xi)^2+(y-\eta)^2]}{[(x-\xi)^2+(y-\eta)^2]^2}+\frac{(y-\eta)[(x+\xi)^2-(y-\eta)^2}{[(x+\xi)^2+(y-\eta)^2]^2}\right.$$
$$\left.-\frac{12x\xi(y-\eta)+8\xi^2(y-\eta)}{[(x+\xi)^2+(y-\eta)^2]^2}+\frac{16x\xi(x+\xi)^2(y-\eta)}{[(x+\xi)^2+(y-\eta)^2]^3}\right\}-\frac{2\mu}{\pi(\kappa+1)}\left\{\frac{(y+\eta)[-(x-\xi)^2+(y+\eta)^2]}{[(x-\xi)^2+(y+\eta)^2]^2}\right.$$
$$\left.+\frac{(y+\eta)[(x+\xi)^2-(y+\eta)^2]}{[(x+\xi)^2+(y+\eta)^2]^2}-\frac{12x\xi(y+\eta)+8\xi^2(y+\eta)}{[(x+\xi)^2+(y+\eta)^2]^2}+\frac{16x\xi(x+\xi)^2(y+\eta)}{[(x+\xi)^2+(y+\eta)^2]^3}\right\}$$
$$-\frac{2\mu}{\kappa+1}\frac{1}{2\pi i}\int_{c-i\infty}^{c+i\infty}\frac{(x^2+y^2)^{-s/2-1}}{\cos(\pi s/2)}\left\{sxy\sin\left\{\left(\frac{\pi}{2}-\theta\right)s\right\}\right.$$
$$\left.+(x^2+y^2-sx^2)\cos\left\{\left(\frac{\pi}{2}-\theta\right)s\right\}\right\}Q_B^*(s)\,ds-\frac{2\mu}{\kappa+1}\frac{1}{2\pi i}\int_{c-i\infty}^{c+i\infty}\frac{(x^2+y^2)^{-s/2-1}}{\cos(\pi s/2)}\right\}$$
$$\{-sxy\sin(\theta s)+(x^2+y^2+sy^2)\cos(\theta s)\}P_B^*(s)\,ds; \tag{21}$$

$$K_{31}(x,y;\xi,\eta)=\frac{2\mu}{\pi(\kappa+1)}\left\{\frac{(x-\xi)[(x-\xi)^2-(y-\eta)^2]}{[(x-\xi)^2+(y-\eta)^2]^2}-\frac{(x+\xi)](x+\xi)^2-(y-\eta)^2]}{[(x+\xi)^2+(y-\eta)^2]^2}\right.$$

Downloaded 02 May 2010 to 171.66.16.246. Redistribution subject to ASME license or copyright; see http://www.asme.org/terms/Terms_Use.cfm

$$+\frac{6x^2\xi+8x\xi^2+2\xi^3-2\xi(y-\eta)^2}{[(x+\xi)^2+(y-\eta)^2]^2}-\frac{16x\xi(x+\xi)(y-\eta)^2}{[(x+\xi)^2+(y-\eta)^2]^3}\Big\}-\frac{2\mu}{\pi(\kappa+1)}\Big\{\frac{(x-\xi)[(x-\xi)^2-(y+\eta)^2]}{[(x-\xi)^2+(y-\eta)^2]^2}$$

$$-\frac{(x+\xi)[(x+\xi)^2-(y+\eta)^2]}{[(x+\xi)^2+(y-\eta)^2]^2}+\frac{6x^2\xi+8x\xi^2+2\xi^3-2\xi(y+\eta)^2}{[(x+\xi)^2+(y+\eta)^2]^2}-\frac{16x\xi(x+\xi)(y+\eta)^2}{[(x+\xi)^2+(y+\eta)^2]^3}\Big\}$$

$$-\frac{12\mu}{\kappa+1}\frac{1}{2\pi i}\int_{c-i\infty}^{c+i\infty}\frac{(x^2+y^2)^{-s/2-1}}{\cos(\pi s/2)}\Big\{sx^2\sin\Big\{\Big(\frac{\pi}{2}-\theta\Big)s\Big\}+sxy\cos\Big\{\Big(\frac{\pi}{2}-\theta\Big)s\Big\}\Big\}Q_A^*(s)\,ds$$

$$-\frac{2\mu}{\kappa+1}\frac{1}{2\pi i}\int_{c-i\infty}^{c+i\infty}\frac{(x^2+y^2)^{-s/2-1}}{\cos(\pi s/2)}\{(2x^2+2y^2-sy^2)\sin(\theta s)-sxy\cos(\theta s)\}P_A^*(s)\,ds; \tag{22}$$

$$K_{32}(x,y;\xi,\eta)=\frac{2\mu}{\pi(\kappa+1)}\Big\{\frac{(y-\eta)[3(x-\xi)^2+(y-\eta)^2]}{[(x-\xi)^2+(y-\eta)^2]^2}-\frac{(y-\eta)[3(x+\xi)^2+(y-\eta)^2]}{[(x+\xi)^2+(y-\eta)^2]^2}$$

$$-\frac{12x\xi(y-\eta)}{[(x+\xi)^2+(y-\eta)^2]^2}+\frac{16x\xi(y-\eta)^3}{[(x+\xi)^2+(y-\eta)^2]^3}\Big\}-\frac{2\mu}{\pi(\kappa+1)}\Big\{\frac{(y+\eta)[3(x-\xi)^2+(y+\eta)^2}{[(x-\xi)^2+(y+\eta)^2]^2}$$

$$-\frac{(y+\eta)[3(x+\xi)^2+(y+\eta)^2]}{[(x+\xi)^2+(y+\eta)^2]^2}-\frac{12x\xi(y+\eta)}{[(x+\xi)^2+(y+\eta)^2]^2}+\frac{16x\xi(y+\eta)^3}{[(x+\xi)^2+(y+\eta)^2]^3}$$

$$-\frac{2\mu}{\kappa+1}\frac{1}{2\pi i}\int_{c-i\infty}^{c+i\infty}\frac{(x^2+y^2)^{-s/2-1}}{\cos(\pi s/2)}\Big\{-sxy\sin\Big\{\Big(\frac{\pi}{2}-\theta\Big)s\Big\}+(sx^2+x^2+y^2)$$

$$\cdot\cos\Big\{\Big(\frac{\pi}{2}-\theta\Big)s\Big\}\Big\}Q_B^*(s)\,ds-\frac{2\mu}{\kappa+1}\frac{1}{2\pi i}\int_{c-i\infty}^{c+i\infty}\frac{(x^2+y^2)^{-s/2-1}}{\cos(\pi s/2)}\{sxy\sin(\theta s)$$

$$+(x^2+y^2-sy^2)\cos(\theta s)\}P_B^*(s)\,ds. \tag{23}$$

The last two integrals in equations (18)–(23) arise from the clearing of the stresses on the free surfaces. We note that equations (18)–(23) contain complex integrals to evaluate. However, this evaluation poses no problems in practice. Once the equations in the foregoing have been obtained, then they can be used to solve the problem of a crack embedded in a quarter plane.

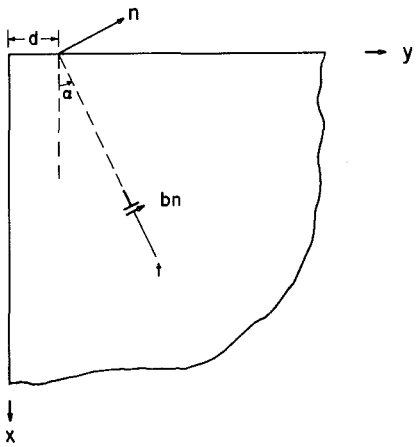

Fig. 3 Geometry for dislocation at (ξ, η)

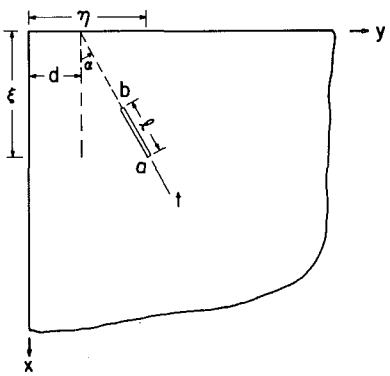

Fig. 4 Coordinate for crack

Crack in a Quarter Plane

In terms of the Green's functions developed in the preceding section the stress components due to $\mathbf{b}_n$ and $\mathbf{b}_t$ are given, respectively, as

$$\sigma_{nt}^{bn}=\sin\alpha\cos^2\alpha(K_{21}-K_{31})+\sin^2\alpha\cos\alpha(K_{22}-K_{32})$$

$$+\cos 2\alpha\cos\alpha K_{11}+\cos 2\alpha\sin\alpha K_{12} \tag{24}$$

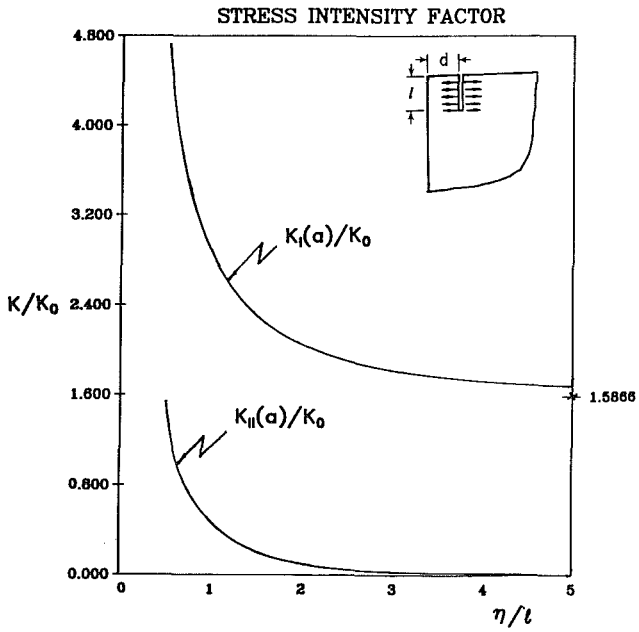

Fig. 5 Stress intensity factor for edge crack ($\alpha = 0$) as a function of η/l (1.58666 is case when $\eta/l \to \infty$[5], $K_0 = \sigma_{nn}^A \sqrt{l}$)

Downloaded 02 May 2010 to 171.66.16.246. Redistribution subject to ASME license or copyright; see http://www.asme.org/terms/Terms_Use.cfm

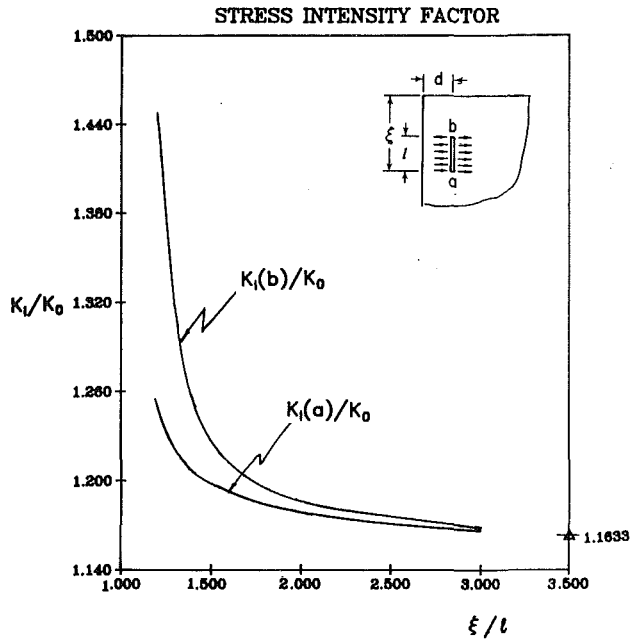

Fig. 6 Mode *I* component of the stress intensity factor (K_1) for a vertical crack ($\alpha = 0$, $\eta/l = 1$) under uniform internal pressure as a function of ξ/l, $K_0 = \sigma^A_{nn}\sqrt{l}$

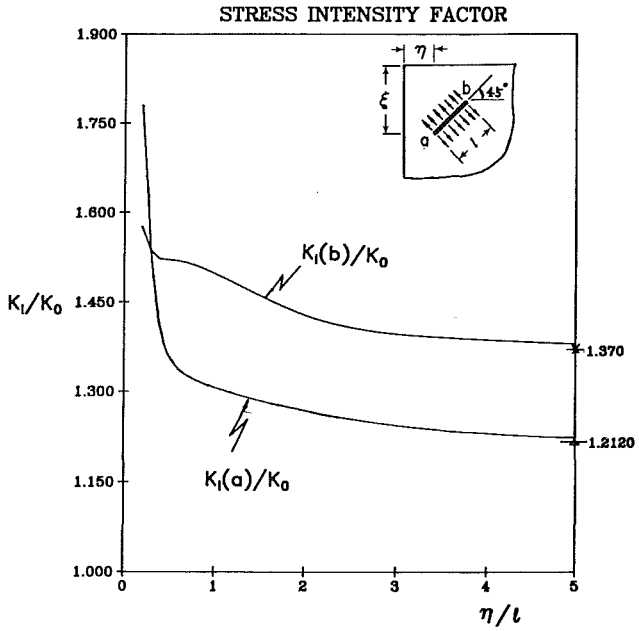

Fig. 8 Mode *I* component of the stress intensity factor (K_I) for an inclined crack ($\alpha = -45$ deg, $\xi/l = 1$) under uniform internal pressure as a function of η/l, $K_0 = \sigma^A_{nn}\sqrt{l}$

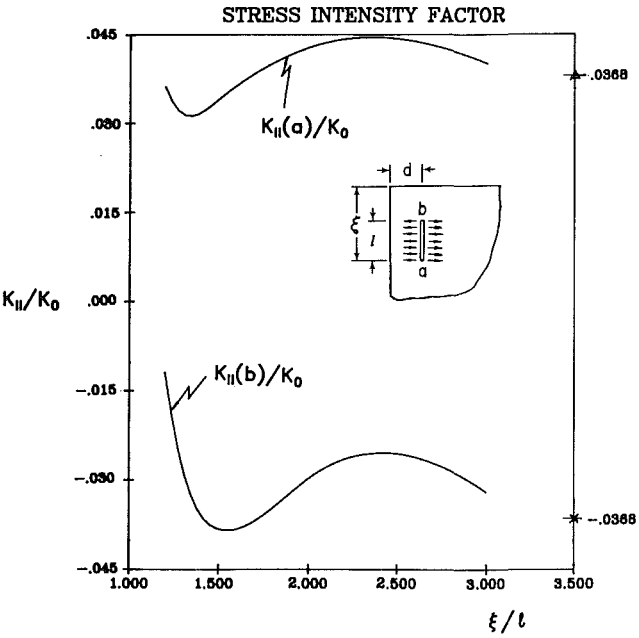

Fig. 7 Mode *II* component of the stress intensity factor (K_{II}) for a vertical crack ($\alpha = 0$, $\eta/l = 1$) under uniform internal pressure as a function of ξ/l, $K_0 = \sigma^A_{nn}\sqrt{l}$

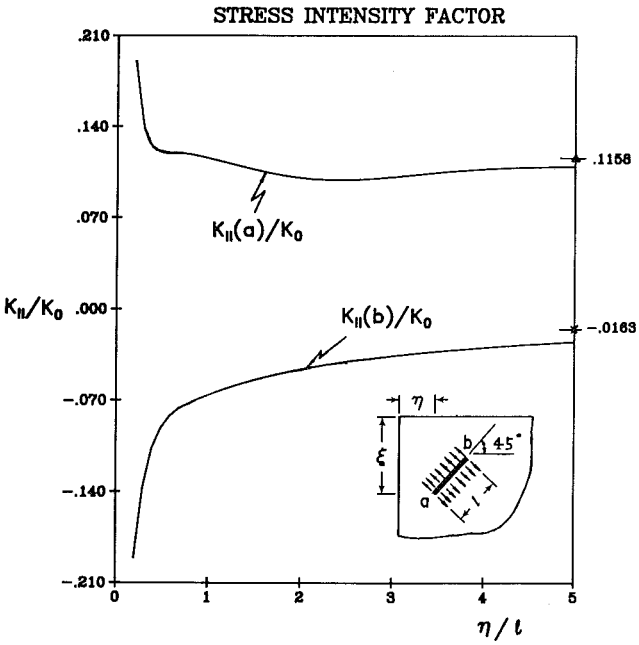

Fig. 9 Mode *II* component of the stress intensity factor (K_{II}) for an inclined crack ($\alpha = 45$ deg, $\xi/l = 1$) under uniform internal pressure as a function of η/l, where $K_0 = \sigma^A_{nn}\sqrt{l}$

$$\sigma^{bn}_{nn} = \sin\alpha\cos^2\alpha(K_{22} - 2K_{11}) + \sin^2\alpha\cos\alpha\,(K_{31} - 2K_{12}) + \cos^3\alpha\,K_{21} + \sin^3\alpha\,K_{32} \tag{25}$$

$$\sigma^{bt}_{nt} = \sin\alpha\cos^2\alpha(K_{22} - K_{32}) + \sin^2\alpha\cos\alpha\,(K_{31} - K_{21}) + \cos 2\alpha\cos\alpha\,K_{12} - \cos 2\alpha\sin\alpha\,K_{11} \tag{26}$$

$$\sigma^{bt}_{nn} = -\sin\alpha\cos^2\alpha(2K_{12} + K_{21}) + \sin^2\alpha\cos\alpha(K_{32} + 2K_{11}) + \cos^3\alpha\,K_{22} - \sin^3\alpha\,K_{31}. \tag{27}$$

where subscripts represent tangential or normal components due to dislocation indicated by superscripts. The geometry and coordinate system for the quarter plane containing a crack is shown in Fig. 4, where ξ, η locates the end of the crack at a, d is the intersection of the crack line with the $x = 0$ surface, and x is the inclination from the vertical.

On the crack surface, $n = 0$, $b < t < a$, the total traction is prescribed. Thus, if the contribution of the dislocations is considered as a distribution over the crack surface, the following coupled integral equations are obtained:

$$\int_b^a K^{bn}_{11}(t,t')\,b_n(t')\,dt' + \int_b^a K^{bt}_{12}(t,t')\,b_t(t')\,dt' = \sigma^A_{nt}(t), \quad b < t < a \tag{28}$$

Downloaded 02 May 2010 to 171.66.16.246. Redistribution subject to ASME license or copyright; see http://www.asme.org/terms/Terms_Use.cfm

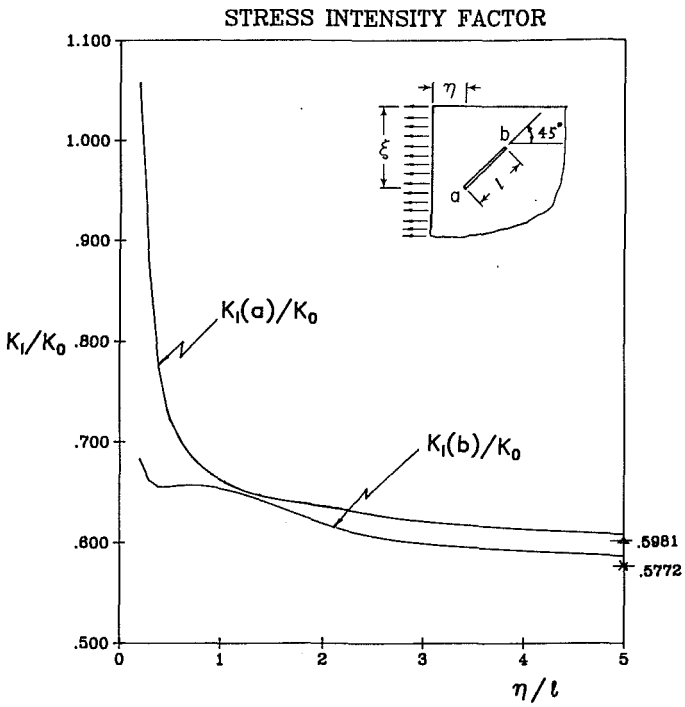

Fig. 10 Mode I component of the stress intensity factor (K_I) for an inclined crack ($\alpha = -45$ deg, $\xi/l = 1$) under uniform tension on side plane as a function of η/l, where $K_0 = \sigma^A \sqrt{l}$

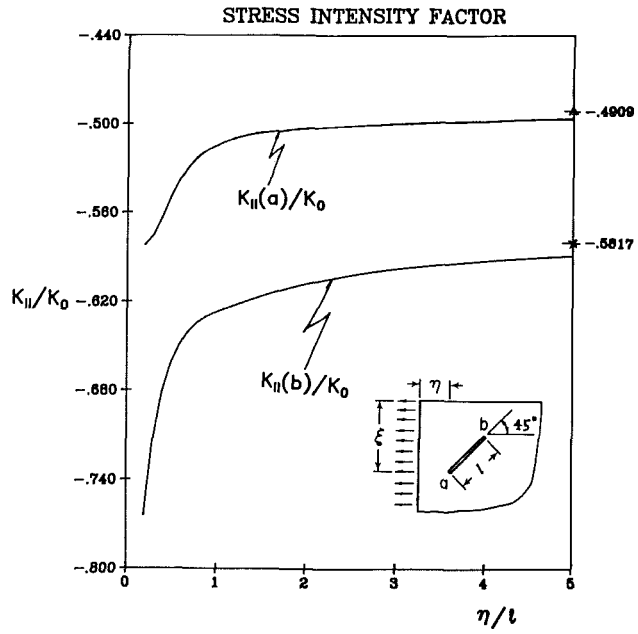

Fig. 11 Mode I component of the stress intensity factor (K_{II}) for an inclined crack ($\alpha = -45$ deg, $\xi/l = 1$) under uniform tension on side plane as a function of η/l, where $K_0 = \sigma^A \sqrt{l}$

$$\int_b^a K_{21}^{bn}(t,t')\,b_n(t')\,dt' + \int_b^a K_{22}^{bt}(t,t')\,b_t(t')\,dt' = \sigma_{nn}^A(t), \quad b<t<a \tag{29}$$

where

$$K_{11}^{bn}(t,t') = \sigma_{nt}^{bn}(t\cos\alpha,\ t\sin\alpha + d;\ t'\cos\alpha,\ t'\sin\alpha + d) \tag{30}$$

$$K_{12}^{bt}(t,t') = \sigma_{nt}^{bt}(t\cos\alpha,\ t\sin\alpha + d;\ t'\cos\alpha,\ t'\sin\alpha + d) \tag{31}$$

$$K_{21}^{bn}(t,t') = \sigma_{nn}^{bn}(t\cos\alpha,\ t\sin\alpha + d;\ t'\cos\alpha,\ t'\sin\alpha + d) \tag{32}$$

$$K_{22}^{bt}(t,t') = \sigma_{nn}^{bt}(t\cos\alpha,\ t\sin\alpha + d;\ t'\cos\alpha,\ t'\sin\alpha + d). \tag{33}$$

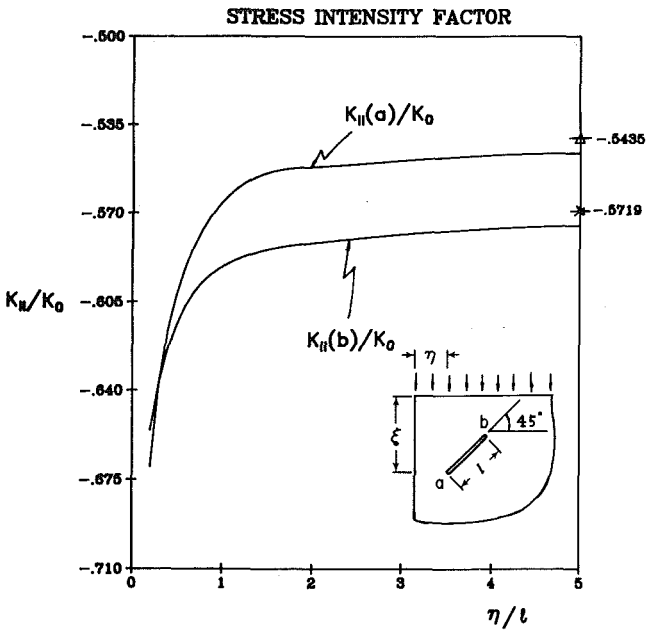

Fig. 12 Mode II component of the stress intensity factor (K_{II}) for an inclined crack ($\alpha = -45$ deg, $\xi/l = 1$) under uniform compression on top plane as a function of η/l, where $K_0 = \sigma^A \sqrt{l}$

By inspection, it can be seen that $K_{12}^{bt}(t,t')$ and $K_{21}^{bn}(t,t')$ contain Cauchy-type singularities in their structure.

Numerical Procedure and Discussion

The pair of integral equations, equations (28) and (29), is solved by using the Gauss-Chebyshev integration formula [4]. For the interior crack cases two additional equations,

$$\int_b^a b_n(t)\,dt = 0 \tag{34}$$

$$\int_b^a b_t(t)\,dt = 0 \tag{35}$$

are required, which represent the continuity of displacements outside the crack. Once $b_n(t)$ and $b_t(t)$ are obtained, then the stress intensity factors can be calculated as follows [4]:

$$K_I(a) = -\lim_{t\to a^+}[2(t-a)]^{1/2}\sigma_{nn}(0,t)$$

$$= \frac{2\mu}{\kappa+1}\lim_{t\to a^-}[2(a-t)]^{1/2}b_n(t) = \frac{2\mu}{\kappa+1}\sqrt{(a-b)/2}B_n(1) \tag{36}$$

$$K_I(b) = -\lim_{t\to b^-}[2(b-t)]^{1/2}\sigma_{nn}(0,t)$$

$$= -\frac{2\mu}{\kappa+1}\lim_{t\to b^+}[2(t-b)]^{1/2}b_n(t) = -\frac{2\mu}{\kappa+1}\sqrt{(a-b)/2}B_n(-1) \tag{37}$$

$$K_{II}(a) = \lim_{t\to a^+}[2(t-a)]^{1/2}\sigma_{nt}(0,t)$$

$$= -\frac{2\mu}{\kappa+1}\lim_{t\to a^-}[2(a-t)]^{1/2}b_t(t) = -\frac{2\mu}{\kappa+1}\sqrt{(a-b)/2}B_t(1) \tag{38}$$

$$K_{II}(b) = \lim_{t\to a^-}[2(b-t)]^{1/2}\sigma_{nt}(0,t)$$

$$= \frac{2\mu}{\kappa+1}\lim_{t\to b^+}[2(t-b)]^{1/2}b_t(t) = \frac{2\mu}{\kappa+1}\sqrt{(a-b)/2}B_t(1) \tag{39}$$

where

Downloaded 02 May 2010 to 171.66.16.246. Redistribution subject to ASME license or copyright; see http://www.asme.org/terms/Terms_Use.cfm

$$b_n(t) = B_n(u)(1-u^2)^{-1/2} \tag{40}$$

$$b_t(t) = B_t(u)(1-u^2)^{-1/2} \tag{41}$$

with

$$u = 2t/(a-b) - (b+a)/(a-b).$$

As a first example problem the elastic quarter plane with a vertical edge crack is considered. The result for uniform normal traction of the crack surface is given in Fig. 5, where $K_0 = \sigma_{nn}^A\sqrt{l}$. As expected, the stress intensity factors decrease with increasing distance of the crack to the other free boundary and they converge to the values corresponding to the edge crack for a half plane as given by Sneddon and Das [5].

The stress intensity factors for the interior crack perpendicular to one free boundary are given in Figs. 6 and 7. The limiting case is given by Erdogan, Gupta, and Cook [4]. We note here that the stress intensity factor for the vertical edge crack or interior crack due to uniform tension loaded on the surface parallel to the crack is equivalent to a uniform internal pressure on the crack surface.

Figures 8–12 depict the stress intensity factors for the inclined interior crack with $\alpha = -45$ deg subjected to various kinds of loading. In Fig. 8, $K_I(a) = K_I(b)$ corresponds to the geometry that is symmetric with respect to the line bisecting the angle of the corner and at that point $K_{II}(a) = -K_{II}(b)$ in Fig. 9. the limiting case here is obtained from Erdogan and Arin [6].

Acknowledgment

The authors are grateful for support from the National Science Foundation Grant CME 7918015.

References

1 Hetenyi, M., "A Method of Solution for the Elastic Quarter-Plane," ASME JOURNAL OF APPLIED MECHANICS, Vol. 27, 1961, pp. 289–296.

2 Sneddon, I. N., *Fourier Transform Solution of the Quarter-Plane Problem in Elasticity*, File No. PSR-99/6, Applied Mathematical Research Group, North Carolina State University, May 1971.

3 Dundurs, J., and Mura, T., "Interaction Between An Edge Dislocation and a Circular Inclusion," *Journal of the Mechanics and Physics of Solids*, Vol. 12, 1964, p. 177.

4 Erdogan, F., Gupta, G. D., and Cook, T. S., "Numerical Solution of Singular Integral Equations," in: *Mechanics of Fracture*, Vol. 1, G. C. Sih, Ed., Noordhoff, Leyden, 1973.

5 Sneddon, I. N., and Das, S. C., "The Stress-Intensity Factor at the Tip of an Edge Crack in an Elastic Half-Plane," *International Journal of Engineering Science*, Vol. 9, 1971, pp. 25–36.

6 Erdogan, F., and Arin, K., "A Half-Plane and a Strip With an Arbitrarily Located Crack," *International Journal of Fracture*, Vol. 11, 1975, pp. 191–204.

Downloaded 02 May 2010 to 171.66.16.246. Redistribution subject to ASME license or copyright; see http://www.asme.org/terms/Terms_Use.cfm

Dynamic Singular Stresses for a Griffith Crack in a Soft Ferromagnetic Elastic Solid Subjected to a Uniform Magnetic Field

Y. Shindo
Associate Professor,
Department of Mechanical Engineering II,
Faculty of Engineering,
Tohoku University,
Sendai 980, Japan

The problem of the diffraction of normally incident longitudinal waves on a Griffith crack located in an infinite soft ferromagnetic elastic solid is considered. It is assumed that the solid is a homogeneous and isotropic one and is permeated by a uniform magnetostatic field normal to the crack surfaces. Fourier transforms are used to reduce the problem to two simultaneous dual integral equations. The solution to the integral equations is expressed in terms of a Fredholm integral equation of the second kind having the kernel that is a finite integral. The dynamic singular stress field near the crack tip is obtained and the influence of the magnetic field on the dynamic stress intensity factor is shown graphically in detail. Approximate analytical expressions valid at low frequencies are also obtained and the range of validity of these expressions is examined.

Introduction

The interaction of electromagnetic fields with deformable continua has been a subject of recent interest. These investigations have been fastly developed in the past decades because of the possibilities of their extensive practical applications to problems that have appeared in fields of optics, acoustics, geophysics, and so on [1, 2]. If an electromagnetic elastic material is used in a magnetic field, the effects of induced current and magnetization should be considered. Following a linear theory for soft ferromagnetic elastic solids by Pao and Yeh [3], the author [4] has investigated the effect of induced magnetization on a soft ferromagnetic elastic solid with a Griffith crack, which has numerous applications in the field of fracture machanics. The results in the paper have been extended to the problems of two coplanar cracks [5] and a penny-shaped crack [6] in an infinite medium. However, these solutions are limited to static problems and few results on the dynamic analysis have been reported. Hutter and Pao [7] have developed a linear theory of magnetoelastic interactions for a magnetizable conductor. Thus to exactly examine dynamic stresses in a solid in a magnetic field requires the simultaneous solutions to the full set of the basic equations of magnetoelasticity of Hutter and Pao [7]. It is indeed a very difficult task. If we consider only a slowly moving body in a stationary magnetic field, the coupling of the induced current and the deformation will not be considered. This is certainly valid for a magnetic insulator. For soft ferromagnetic materials, we may, as a first approximation, omit the induced current effect as the effect of induced magnetization is more pronounced than that of induced current. Based on this approximation, Moon [8] has investigated the stability and vibration of two-dimensional ferroelastic plates in a uniform, static, oblique, magnetic field.

In this paper, the diffraction of normally incident longitudinal waves by a Griffith crack located in the interior of a homogeneous, isotropic, soft ferromagnetic, linearly elastic, infinite solid is investigated. A soft ferromagnetic material is characterized by small hysteresis loss in one complete cycle of increasing and decreasing magnetic field strength. Many nickel-iron alloys used widely as core materials for motors, generators, inductors, and transformers are of this type. The problem is considered for a uniform magnetostatic field normal to the crack surfaces. The analysis is based on a quasi-static model of the magnetoelastic interactions, which is an extension of a static problem presented in reference [4]. Conduction currents are neglected but magnetization forces are included. It is assumed that the separation of the crack faces is such that the resulting force, due to the applied compressive wave, will not be large enough to cause crack closure. Fourier transforms are used to reduce the mixed boundary value problem to two simultaneous dual integral equations. The solution is then expressed in terms of a Fredholm integral equation of the second kind. The integral

Contributed by the Applied Mechanics Division for publication in the JOURNAL OF APPLIED MECHANICS.
Discussion of this paper should be addressed to the Editorial Department, ASME, United Engineering Center, 345 East 47th Street, New York, N.Y. 10017, and will be accepted until two months after final publication of the paper itself in the JOURNAL OF APPLIED MECHANICS. Manuscript received by ASME Applied Mechanics Division, January, 1982; final revision, August, 1982.

Copyright © 1983 by ASME
Downloaded 02 May 2010 to 171.66.16.246. Redistribution subject to ASME license or copyright; see http://www.asme.org/terms/Terms_Use.cfm

in the kernel is converted into integrals with finite limits by means of contour integration. The magnetoelastic stresses and the Maxwell stresses are expressed and the dynamic stress intensity factor is computed. The method of solution is such that numerical results can be obtained at any desired finite frequency. Approximate analytical expressions at low frequencies are also obtained. Allowing the magnetic field to tend to zero, we have the purely elastic problem, which has been studied by Sih and Loeber [9] for the low and intermediate frequencies and Mal [10] for any given finite frequencies. The object of the present paper is to show the effect of the magnetic field on the dynamic singular stresses near the crack tip.

Basic Equations

In rectangular cartesian coordinates x_i and time t, the linearized field equations in the perturbation state associated with linear theory for soft ferromagnetic elastic solids are [3]

$$t_{ji,j} + \mu_0(M_{0j}H_{0i,j} + M_{0j}h_{i,j} + m_jH_{0i,j}) = \rho u_{i,tt} \tag{1}$$

$$e_{ijk}h_{k,j} = 0 \tag{2}$$

$$b_{i,i} = 0 \tag{3}$$

where the usual summation convention over repeated indices is applied, a comma denotes partial differentiation with respect to the coordinate, t_{ij} is the magnetoelastic stress tensor, M_{0i} and H_{0i} are the magnetization and the magnetic intensity in the rigid body state, m_i, h_i are magnetic quantities in the perturbation state, u_i is the displacement vector, e_{ijk} is the permutation symbol and b_i is the magnetic induction in the perturbation state. The last three terms on the left-hand side of equation (1) are due to the effect of magnetic field which is represented by using a dipole model for magnetization.

The linearized constitutive equations are also obtained as

$$t_{ij} = \sigma_{ij} + \frac{\mu_0}{\chi}M_{0i}M_{0j} + \frac{\mu_0}{\chi}(M_{0i}m_j + M_{0j}m_i)$$

$$\sigma_{ij} = \lambda\delta_{ij}u_{k,k} + \mu(u_{i,j} + u_{j,i})$$

$$t_{ij}^M = \mu_0(1+\chi)H_{0i}H_{0j} - \frac{1}{2}\mu_0H_{0k}H_{0k}\delta_{ij} + \mu_0(1+\chi)$$

$$(H_{0i}h_j + h_iH_{0j}) - \mu_0H_{0k}h_k\delta_{ij} \tag{4}$$

$$h_i = \frac{m_i}{\chi}, \quad b_i = \mu_0(h_i + m_i) = \mu_0\mu_r h_i \tag{5}$$

where σ_{ij} is the elastic stress tensor, t_{ij}^M is the Maxwell stress tensor, and δ_{ij} is the Kronecker delta.

It should be noted that for dynamic problems, eddy currents will be induced in the solid, proportional to the electrical conductivity. These eddy currents will dampen the motion. In this paper, we neglect this effect of conduction currents and assume that the magnetic field in the vibrating solid at any instant is given by that for a stationary solid for the instantaneous solid configuration. Some justification for neglecting dynamic effects in an elastically dynamic problem has been discussed by Moon and Pao [11].

If we consider plane strain perpendicular to the z-axis in a rectangular cartesian coordinate system (x,y,z) and assume that the applied magnetic induction B_{0i} is of the form $B_{0y} = B_0$ where B_0 is constant, then we have the solution for the rigid body state

$$B_{0y} = B_0, \quad H_{0y} = B_0/\mu_0\mu_r, \quad M_{0y} = \chi B_0/\mu_0\mu_r \tag{6}$$

and the linearized field equations in the perturbation state

$$\nabla_1^2 u_x + \frac{1}{1-2\nu}(u_{x,x} + u_{y,y})_{,x} + \frac{2\chi B_0}{\mu\mu_r}h_{x,y} = \frac{1}{c_2^2}u_{x,tt}$$

$$\nabla_1^2 u_y + \frac{1}{1-2\nu}(u_{x,x} + u_{y,y})_{,y} + \frac{2\chi B_0}{\mu\mu_r}h_{y,y} = \frac{1}{c_2^2}u_{y,tt} \tag{7}$$

$$h_{x,y} - h_{y,x} = 0, \quad h_{x,x} + h_{y,y} = 0 \tag{8}$$

where $\nabla_1^2 = \partial^2/\partial x^2 + \partial^2/\partial y^2$ is the two-dimensional Laplace operator in the variables x and y.

The two magnetic equations (8) for the perturbation field are satisfied by introducing a magnetic potential ϕ such that

$$h_x = \phi_{,x}, \quad h_y = \phi_{,y} \tag{9}$$

and

$$\nabla_1^2\phi = 0 \tag{10}$$

The displacements can be expressed in terms of two scalar functions φ_h and ψ_h each of which depends on x, y, and t. The rectangular components of the displacement vector are

$$u_x = \varphi_{h,x} + \psi_{h,y}, \quad u_y = \varphi_{h,y} - \psi_{h,x} \tag{11}$$

Substituting equations (9) and (11) into the equations of equilibrium (7), we find

$$\nabla_1^2\varphi_h + (2\chi B_0/\mu\mu_r)(c_2/c_1)^2\phi_{,y} = \frac{1}{c_1^2}\varphi_{h,tt},$$

$$\nabla_1^2\psi_h = \frac{1}{c_2^2}\psi_{h,tt} \tag{12}$$

Statement and Solution of the Problem

We consider an infinite soft ferromagnetic elastic solid with a Griffith crack located on the line $y = 0$, $|x| < a$ as shown in Fig. 1. A uniform magnetic field B_0 is applied perpendicularly to the crack surfaces. For convenience, all magnetic quantities outside the solid will be denoted by the superscript (e). The solutions for the rigid body state outside the solid are

$$B_{0y}^{(e)} = B_0, \quad H_{0y}^{(e)} = B_0/\mu_0, \quad M_{0y}^{(e)} = 0 \tag{13}$$

Nondimensional Quantities

$$c_0 = (c_2/c_1)^2 - 1, \quad y_0 = 1 + \frac{1}{2}\{1 - 2\nu - 2(1-\nu)\chi\}(\chi b_c/\mu_r)^2$$

$$b_c^2 = \frac{B_0^2}{\mu_0\mu}, \quad P = ap/c_2, \quad \sigma = c_2/c_1, \quad \alpha_1 = P\sigma, \quad \alpha_2 = P$$

$$y_1 = 2 + (1-2\nu)(\chi b_c/\mu_r)^2, \quad y_2 = 2 + (3-4\nu)(\chi b_c/\mu_r)^2$$

$$y_3 = 2 + (3-4\nu)(\chi b_c/\mu_r)^2$$

$$z_0 = 1 + \frac{1}{2}\{2(1-\nu) + (5-6\nu)\chi\}(\chi b_c^2/\mu_r^2)$$

Nomenclature

- $2a$ = width of a Griffith crack
- ρ = mass density
- ν = Poisson's ratio
- λ, μ = Lamé constants $\left(\lambda = \frac{2\mu\nu}{1-2\nu}\right)$
- c_1 = compression wave velocity $(c_1 = \{(\lambda+2\mu)/\rho\}^{1/2})$
- c_2 = shear wave velocity $(c_2 = (\mu/\rho)^{1/2})$
- μ_0 = magnetic permeability of free space $(\mu_0 = 4\pi \times 10^{-7}$ $(H/m))$
- x = magnetic susceptibility
- μ_r = specific magnetic permeability $(\mu_r = 1 + \chi)$
- B_0 = strength of external magnetic induction
- p = circular frequency

Downloaded 02 May 2010 to 171.66.16.246. Redistribution subject to ASME license or copyright; see http://www.asme.org/terms/Terms_Use.cfm

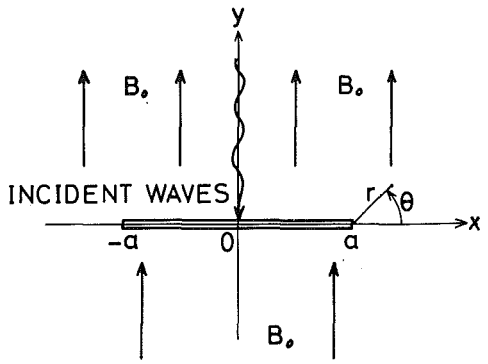

Fig. 1 A Griffith crack in a soft ferromagnetic elastic solid and incident waves

Let an incident plane, harmonic compression wave be directed at an angle $\pi/2$ with the x-axis so that

$$\varphi_h^{(i)} = \varphi_{h0}\exp\left[-ip\left(t+\frac{y}{c_1}\right)\right], \quad \psi_h^{(i)} = 0 \tag{14}$$

in which φ_{h0} is a measure of the wave amplitude and a superscript (i) stands for the incident component. All other incident waves are zero. In view of the harmonic time variation of the input wave given by equations (14), the field quantities will all contain the time factor $\exp(-ipt)$ which will henceforth be dropped. These waves automatically satisfy the field equations (7) and (8) and produce a stress component $\sigma_{zz}^{(i)}$ on the crack surfaces. Hence, it suffices to determine the scattered portion of the solution fulfilling the next boundary conditions:

$$h_x^{(es)}(x,0) - h_x^{(s)}(\chi,0) = -(\chi B_0/\mu_0\mu_r)u_{y,x}^{(s)}(x,0)$$
$$(|x|<a), \quad \phi^{(s)}(x,0) = 0 \quad (a \le |x|) \tag{15}$$

$$b_y^{(es)}(x,0) - b_y^{(s)}(x,0) = 0 \quad (|x|<a),$$
$$\phi^{(es)}(x,0) = 0 \quad (|x|<a) \tag{16}$$

$$t_{yx}^{(s)}(x,0) = 0 \quad (|x|<\infty) \tag{17}$$

$$t_{yy}^{(s)}(x,0) = (\chi^2/\mu_r)B_0 h_y^{(s)}(x,0) - p_0 \quad (|x|<a),$$
$$u_y^{(s)}(x,0) = 0 \quad (a \le |x|) \tag{18}$$

where $p_0 = -\mu(p/c_2)^2\varphi_{h0}$, and superscripts (es), (s) stand for a scattered component of the magnetic quantities outside the solid and a scattered component of the field quantities, respectively.

It can be shown that solutions satisfying equations (10) and (12) for $y \ge 0$ are given by

$$\phi^{(s)} = \frac{2}{\pi}\int_0^\infty a(\alpha)e^{-\alpha y}\cos(\alpha x)\,d\alpha \tag{19}$$

$$\varphi_h^{(s)} = \frac{2}{\pi}\int_0^\infty \left\{A(\alpha)e^{-\gamma_1(\alpha)y} + \frac{1}{(p/c_2)^2}(2\chi B_0/\mu\mu_r) \times \alpha a(\alpha)e^{-\alpha y}\right\}\cos(\alpha x)\,d\alpha$$

$$\psi_h^{(s)} = \frac{2}{\pi}\int_0^\infty B(\alpha)e^{-\gamma_2(\alpha)y}\sin(\alpha x)\,d\alpha \tag{20}$$

$$\phi^{(es)} = \frac{2}{\pi}\int_0^\infty a_e(\alpha)\sinh(\alpha y)\cos(\alpha x)\,d\alpha \tag{21}$$

where $A(\alpha)$, $B(\alpha)$, $a(\alpha)$, and $a_e(\alpha)$ are unknown functions, and $\gamma_1(\alpha)$ and $\gamma_2(\alpha)$ are represented as

$$\gamma_1(\alpha) = \{\alpha^2 - (p/c_1)^2\}^{1/2}, \quad \gamma_2(\alpha) = \{\alpha^2 - (p/c_2)^2\}^{1/2} \tag{22}$$

The functions $\gamma_1(\alpha)$, $\gamma_2(\alpha)$ should be restricted as

$$Re\gamma_j(\alpha) > 0, \quad Im\gamma_j(\alpha) < 0 \quad (j=1,2) \tag{23}$$

in the upper half space $y \ge 0$, because of a radiation condition at infinity and an edge condition near the crack tips [12]. A simple calculation leads to the magnetic intensity and displacement expressions:

$$h_x^{(s)} = -\frac{2}{\pi}\int_0^\infty \alpha a(\alpha)e^{-\alpha y}\sin(\alpha x)\,d\alpha, \quad h_y^{(s)} = -\frac{2}{\pi}\int_0^\infty \alpha a(\alpha)e^{-\alpha y}\cos(\alpha x)\,d\alpha \tag{24}$$

$$u_x^{(s)} = -\frac{2}{\pi}\int_0^\infty \left\{\alpha A(\alpha)e^{-\gamma_1(\alpha)y} + \gamma_2(\alpha)B(\alpha)e^{-\gamma_2(\alpha)y} + \frac{1}{(p/c_2)^2}(2\chi B_0/\mu\mu_r)\alpha^2 a(\alpha)e^{-\alpha y}\right\}\sin(\alpha x)\,d5q$$

$$u_y^{(s)} = -\frac{2}{\pi}\int_0^\infty \left\{\gamma_1(\alpha)A(\alpha)e^{-\gamma_1(\alpha)y} + \alpha B(\alpha)e^{-\gamma_2(\alpha)y} + \frac{1}{(p/c_2)^2}(2\chi B_0/\mu\mu_r)\alpha^2 a(\alpha)e^{-\alpha y}\right\}\cos(\alpha x)\,d\alpha \tag{25}$$

$$h_x^{(es)} = -\frac{2}{\pi}\int_0^\infty \alpha a_e(\alpha)\sinh(\alpha y)\sin(\alpha x)\,d\alpha,$$

$$h_y^{(es)} = \frac{2}{\pi}\int_0^\infty \alpha a_e(\alpha)\cosh(\alpha y)\cos(\alpha x)\,d\alpha \tag{26}$$

The dynamic magnetoelastic and Maxwell stresses $t_{ij}^{(s)}$, $t_{ij}^{M(s)}$ may be obtained readily from equations (4). That is,

$$t_{xx}^{(s)} = \sigma_{xx}^{(s)}, \quad t_{yy}^{(s)} = \sigma_{yy}^{(s)} + \frac{2\chi B_0}{\mu_r}h_y^{(s)},$$

$$t_{xy}^{(s)} = t_{yx}^{(s)} = \sigma_{xy}^{(s)} + \frac{\chi B_0}{\mu_r}h_x^{(s)} \tag{27}$$

$$t_{xx}^{M(s)} = -\frac{B_0}{\mu_r}h_y^{(s)}, \quad t_{yy}^{M(s)} = \frac{(1+2\chi)B_0}{\mu_r}h_y^{(s)},$$

$$t_{xy}^{M(s)} = t_{yx}^{M(s)} = B_0 h_x^{(s)} \tag{28}$$

where

$$\sigma_{xx}^{(s)} = -\frac{2\mu}{\pi}\int_0^\infty \left[\{2\alpha^2 + (p/c_2)^2 - 2(p/c_1)^2\}A(\alpha)e^{-\gamma_1(\alpha)y} + 2\alpha\gamma_2(\alpha)B(\alpha)e^{-\gamma_2(\alpha)y} + \frac{1}{(p/c_2)^2}(4\chi B_0/\mu\mu_r)\alpha^3 a(\alpha)e^{-\alpha y}\right]\cos(\alpha x)\,d\alpha$$

$$\sigma_{yy}^{(s)} = \frac{2\mu}{\pi}\int_0^\infty \left[\{2\alpha^2 - (p/c_2)^2\}A(\alpha)e^{-\gamma_1(\alpha)y} + 2\alpha\gamma_2(\alpha)B(\alpha)e^{-\gamma_2(\alpha)y} + \frac{1}{(p/c_2)^2}(4\chi B_0/\mu\mu_r)\alpha^3 a(\alpha)e^{-\alpha y}\right]\cos(\alpha x)\,d\alpha$$

$$\sigma_{xy}^{(s)} = \frac{2\mu}{\pi}\int_0^\infty \left[2\alpha\gamma_1(\alpha)A(\alpha)e^{-\gamma_1(\alpha)y} + \{2\alpha^2 - (p/c_2)^2\}B(\alpha)e^{-\gamma_2(\alpha)y} + \frac{1}{(p/c_2)^2}(4\chi B_0/\mu\mu_r)\alpha^3 a(\alpha)e^{-\alpha y}\right]\sin(\alpha x)\,d\alpha \tag{29}$$

Downloaded 02 May 2010 to 171.66.16.246. Redistribution subject to ASME license or copyright; see http://www.asme.org/terms/Terms_Use.cfm

The boundary condition of equation (17) leads to the following relation between unknown functions:

$$2\alpha\gamma_1(\alpha)A(\alpha)+\{2\alpha^2-(p/c_2)^2\}B(\alpha)+\left\{\frac{4\alpha^2}{(p/c_2)^2}-1\right\}\times(\chi B_0/\mu\mu_r)\alpha a(\alpha)=0 \tag{30}$$

The satisfaction of the two mixed boundary conditions (15) and (18) leads to two simultaneous dual integral equations of the following form:

$$\int_0^\infty \alpha\{a(\alpha)+(\chi B_0/\mu_0\mu_r)C(\alpha)\}\sin(\alpha x)\,d\alpha=0 \quad (|x|<a)$$
$$\int_0^\infty a(\alpha)\cos(\alpha x)\,d\alpha=0 \quad (a\le|x|) \tag{31}$$

$$\frac{2}{\pi}\int_0^\infty \alpha[f_e(\alpha)C(\alpha)+f_m(\alpha)(\chi B_0/\mu\mu_r)a(\alpha)]\cos(\alpha x)\,d\alpha=-p_0/2\mu \quad (|x|<a)$$
$$\int_0^\infty C(\alpha)\cos(\alpha x)\,d\alpha=0 \quad (a\le|x|) \tag{32}$$

in which $f_e(\alpha)$ and $f_m(\alpha)$ are known functions given by

$$f_e(\alpha)=\frac{1}{(p/c_2)^2\gamma_1(\alpha)}[-\{2\alpha^2-(p/c_2)^2\}^2+4\alpha^2\gamma_1(\alpha)\gamma_2(\alpha)]\frac{1}{2\alpha}$$

$$f_m(\alpha)=\frac{1}{(p/c_2)^2\gamma_1(\alpha)}\left[-\{2\alpha^2-(p/c_2)^2\}-2\gamma_1(\alpha)\gamma_2(\alpha)+4\alpha\gamma_1(\alpha)+(p/c_2)^2\gamma_1(\alpha)\frac{1}{\alpha}(\chi-2)\right]\frac{1}{2}\alpha \tag{33}$$

and the original unknowns $A(\alpha)$, $B(\alpha)$, $a(\alpha)$ are related to the new one $C(\alpha)$ through

$$A(\alpha)=-\frac{1}{\gamma_1(\alpha)(p/c_2)^2}[\{2\alpha^2-(p/c_2)^2\}C(\alpha)+(\chi B_0/\mu\mu_r)\alpha^2 a(\alpha)]$$

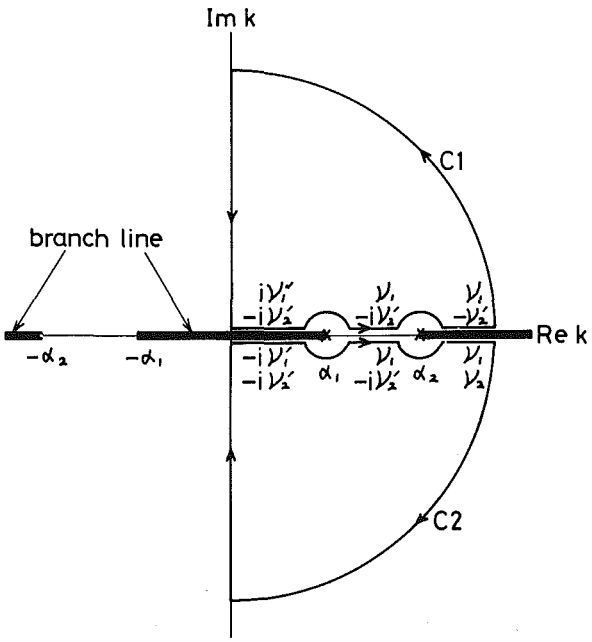

Fig. 2 Contours of integration for integrals in equations (39)

$$B(\alpha)=\frac{1}{(p/c_2)^2}[2\alpha C(\alpha)-(\chi B_0/\mu\mu_r)\alpha a(\alpha)] \tag{34}$$

Following a procedure developed by the author [4], a solution to equations (31) and (32) is

$$a(\alpha)=-\frac{\pi\chi B_0 p_0 a^{1/2}}{4\mu_0\mu_r\mu c_0 y_0}\int_0^1 u^{1/2}\Phi(u)J_0(\alpha a u)\,du$$

$$C(\alpha)=\frac{\pi p_0 a^2}{4\mu c_0 y_0}\int_0^1 u^{1/2}\Phi(u)J_0(\alpha a u)\,du \tag{35}$$

where J_0 is the zero-order Bessel function of the first kind. The unknown function $\Phi(u)$ is governed by a Fredholm integral equation of the second kind:

$$\Phi(u)-\int_0^1 \Phi(s)(su)^{1/2}K_h(u,s)\,ds=u^{1/2} \tag{36}$$

where the kernel $K_h(u,s)$ is given by the equation:

$$K_h(u,s)=\int_0^\infty[\alpha+\frac{1}{c_0 y_0 P^2}\{f_e^*(\alpha)-(\chi b_c/\mu_r)^2 f_m^*(\alpha)\}]J_0(\alpha u)J_0(\alpha s)\,d\alpha \tag{37}$$

In equation (37), the functions $f_e^*(\alpha)$, $f_m^*(\alpha)$ are

$$f_e^*(\alpha)=\frac{1}{2\gamma_1{}^*(\alpha)}[-(2\alpha^2-P^2)^2+4\alpha^2\gamma_1{}^*(\alpha)\gamma_2{}^*(\alpha)]$$

$$f_m^*(\alpha)=\frac{1}{2\gamma_1{}^*(\alpha)}[-\alpha^2(2\alpha^2-P^2)-2\alpha^2\gamma_1{}^*(\alpha)\gamma_2{}^*(\alpha)+4\alpha^3\gamma_1{}^*(\alpha)+P^2\gamma_1{}^*(\alpha)\alpha(\chi-2)] \tag{38}$$

where $\gamma_1{}^*(\alpha)=(\alpha^2-\alpha_1^2)^{1/2}$, $\gamma_2^*(\alpha)=(\alpha^2-\alpha_2^2)^{1/2}$

We note that the kernel function $K_h(u,s)$, equation (37), is an infinite integral that has a rather slow rate of convergence. To improve this problem the infinite integral is converted into integrals with finite limits. Thus for the calculation of the integral we consider the contour integrals:

$$I_{h1}=\oint_{C1} L_h(k,\gamma_1^*,-\gamma_2^*)J_0(ks)H_0^{(1)}(ku)\,dk \quad (u>s)$$

$$I_{h2}=\oint_{C_2} L_h(k,\gamma_1^*,\gamma_2^*)J_0(ks)H_0^{(2)}(ku)\,dk \quad (u>s) \tag{39}$$

where

$$L_h(k,\gamma_1^*,\gamma_2^*)=k+\frac{1}{c_0 y_0 P^2}\{f_e^*(k)-(\chi b_c/\mu_r)^2 f_m^*(k)\} \tag{40}$$

In equations (39), $C1$ and $C2$ are defined in Fig. 2 and $H_0^{(1)}$, $H_0^{(2)}$ are, respectively, the zero-order Hankel functions of the first and second kind. Since the integrals satisfy Jordan's Lemma on infinite quarter circles, we get

$$\begin{aligned}I_{h1}+I_{h2}=&\int_0^{\alpha_1}\{L_h(\alpha,i\nu_1',i\nu_2')H_0^{(1)}(\alpha u)+L_h(\alpha_1-i\nu_1',-i\nu_2')H_0^{(2)}(\alpha u)\}J_0(\alpha s)\,d\alpha\\&+\int_{\alpha_1}^{\alpha_2}\{L_h(\alpha,\nu_1,i\nu_2')H_0^{(1)}(\alpha u)+L_h(\alpha,\nu_1,-i\nu_2')H_0^{(2)}(\alpha u)\}J_0(\alpha s)\,d\alpha\\&+2\int_{\alpha_2}^{\infty}L_h(\alpha,\nu_1,\nu_2)J_0(\alpha s)J_0(\alpha u)\,d\alpha\\&+\int_{\infty}^{0}\{L_h(i\alpha,i\nu_1',i\nu_2')+L_h(-i\alpha,-i\nu_1',-i\nu_2')\}J_0(e^{i\pi/2}\alpha s)H_0^{(1)}(e^{i\pi/2}\alpha u)\,id\alpha=0\end{aligned} \tag{41}$$

where

Downloaded 02 May 2010 to 171.66.16.246. Redistribution subject to ASME license or copyright; see http://www.asme.org/terms/Terms_Use.cfm

$$\nu_1=(\alpha^2-P^2\sigma^2)^{1/2},\quad \nu_2=(\alpha^2-P^2)^{1/2}$$
$$\nu_1'=(P^2\sigma^2-\alpha^2)^{1/2},\quad \nu_2'=(P^2-\alpha^2)^{1/2} \tag{42}$$

Because of the second equation of (23), the integral in equation (37) must be taken along a path located slightly below the real k-axis as in $C2$. Therefore $K_h(u,s)$ for $u>s$ can be finally written as

$$K_h(u,s)=iP^2\int_0^1 \{M_{h1}(\alpha)J_0(\alpha Ps)H_0^{(1)}(\alpha Pu) + M_{h2}(\alpha)J_0(\alpha\sigma Ps)H_0^{(1)}(\alpha\sigma Pu)\}d\alpha \tag{43}$$

where

$$M_{h1}(\alpha)=-\frac{1}{c_0y_0}\{2+(\chi b_c/\mu_r)^2\}\alpha^2(1-\alpha^2)^{1/2}$$

$$M_{h2}(\alpha)=-\frac{1}{c_0y_0}\cdot\frac{1}{2(1-\alpha^2)^{1/2}}\{(2\alpha^2\sigma^2-1)^2 - (\chi b_c/\mu_r)^2\sigma^2(2\alpha^2\sigma^2-1)\alpha^2\} \tag{44}$$

The kernel $K_h(u,s)$ is symmetric in u and s and the value of this kernel for $u<s$ is obtained by interchanging u and s in equation (43).

Dynamic Singular Stresses Near the Crack Tip

The complete dynamic stresses t_{cij} are obtained in the form:

$$t_{cij}=t_{ij}^{(i)}+t_{ij}^{(s)}+t_{ij}^{M(i)}+t_{ij}^{M(s)} \tag{45}$$

The dynamic magnetoelastic stresses $t_{ij}^{(i)}$ and the dynamic Maxwell stresses $t_{ij}^{M(i)}$ of incident waves possess no singularities. The singular parts of the dynamic magnetoelastic stresses $t_{ij}^{(s)}$ and dynamic Maxwell stresses $t_{ij}^{M(s)}$ near the crack tip can be derived in terms of the polar coordinates (r,θ) defined in Fig. 1 for very small r. Considering the behavior as $\alpha\to\infty$ in the expressions of stresses, we obtain the final results as follows;

$$t_{xx}^{(s)}\sim\frac{K_{h1}}{2z_0}\{y_1-y_2\sin(\theta/2)\sin(3\theta/2)\}\cos(\theta/2)\frac{1}{(2r)^{1/2}}$$
$$t_{xy}^{(s)}=t_{yx}^{(s)}\sim\frac{K_{h1}}{2z_0}y_3\sin(\theta/2)\cos(\theta/2)\cos(3\theta/2)\frac{1}{(2r)^{1/2}}$$
$$t_{yy}^{(s)}\sim\frac{k_{h1}}{2z_0}\{y_1+y_2\sin(\theta/2)\sin(3\theta/2)\}\cos(\theta/2)\frac{1}{(2r)^{1/2}} \tag{46}$$

$$t_{xx}^{M(s)}\sim-\frac{K_{h1}}{Z_0}(1-\nu)(\chi b_c^2/\mu_r^2)\cos(\theta/2)\frac{1}{(2r)^{1/2}}$$
$$t_{xy}^{M(s)}=t_{yx}^{M(s)}\sim-\frac{K_{h1}}{z_0}(1-\nu)(\chi b_c^2/\mu_r)\sin(\theta/2)\frac{1}{(2r)^{1/2}}$$
$$t_{yy}^{M(s)}\sim\frac{K_{h1}}{z_0}(1-\nu)(1+\mu_r)(\chi b_c^2/\mu_r^2)\cos(\theta/2)\frac{1}{(2r)^{1/2}} \tag{47}$$

where K_{h1} stands for the dynamic stress intensity factor and is defined by

$$K_{h1}=\lim_{x\to a+}\{2(x-a)\}^{1/2}t_{cyy}(x,0)=\frac{p_0a^{1/2}}{y_0}z_0\Phi(1) \tag{48}$$

Approximate Solution at Low Frequency

For sufficiently small values of the normalized frequency P, the iterative solution can be obtained in series of ascending powers of P. The form of the kernel equation (43) is suitable for expanding the kernel $K_h(u,s)$ in powers such P that $P<<1$. Using the series expansions for the Bessel and Hankel functions J_0, $H_0^{(1)}$ in the equation (43), we get

$$K_h(u,s)=-\frac{2}{\pi}E_{h0}P^2\log P+\{(i-\frac{2}{\pi}\gamma+\frac{2}{\pi}\log 2)E_{h0} - \frac{2}{\pi}F_{h0}-\frac{2}{\pi}E_{h0}\log u\}P^2+\frac{E_{h2}}{2\pi}(u^2+s^2)P^4\log P+O(P^4) \quad (u>s) \tag{49}$$

where γ is Euler's constant and

$$E_{hn}=\int_0^1\alpha^n\{M_{h1}(\alpha)+\sigma^nM_{h2}(\alpha)\}d\alpha \quad (n=0,1,2,\ldots)$$
$$F_{hn}=\int_0^1\alpha^n\{(\log\alpha)M_{h1}(\alpha)+\sigma^n(\log\alpha\sigma)M_{h2}(\alpha)\}d\alpha \quad (n=1,2,\ldots) \tag{50}$$

Assuming that the solution $\Phi(u)$ can be expanded in the form:

$$\Phi(u)=u^{1/2}+\Phi_{h1}(u)P^2\log P+\Phi_{h2}(u)P^2 + \Phi_{h3}(u)(P^2\log P)^2+\Phi_{h4}(u)P^4\log P+O(P^4) \tag{51}$$

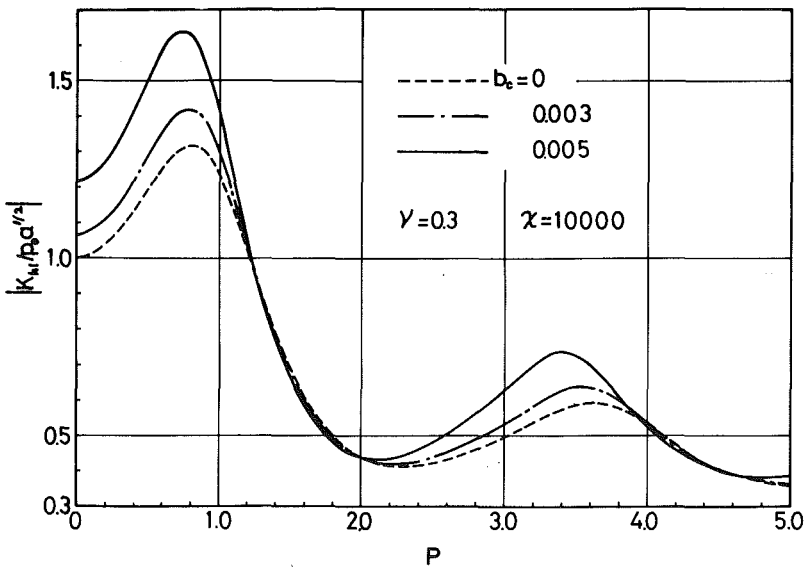

Fig. 3 Effect of magnetic field on normalized dynamic stress intensity factor $|K_{h1}/p_0a^{1/2}|$ with P for $\nu=0.3$

Downloaded 02 May 2010 to 171.66.16.246. Redistribution subject to ASME license or copyright; see http://www.asme.org/terms/Terms_Use.cfm

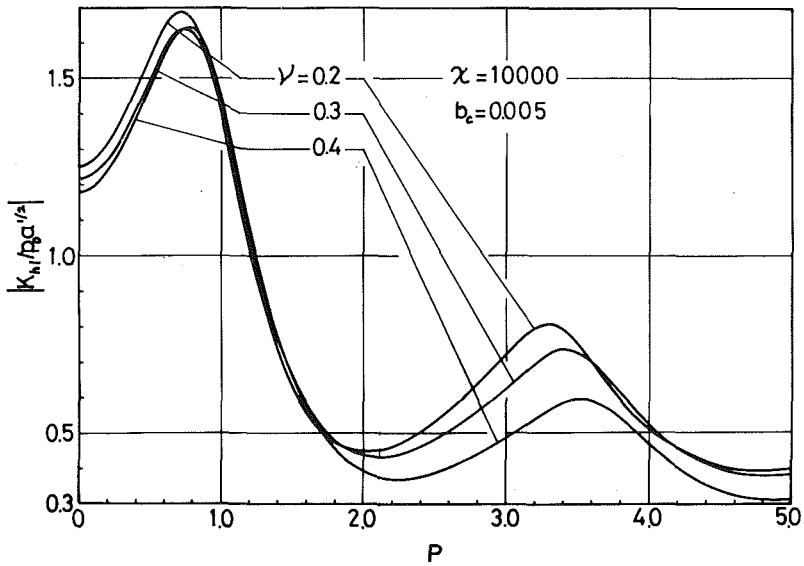

Fig. 4 Poisson's ratio effect on normalized dynamic stress intensity factor $|K_{h1}/p_0a^{1/2}|$ with P for $b_c = 0.005$

and substituting it into the integral equation (36), we obtain the following iteration scheme:

$$\Phi_{h1}(u) = -\frac{1}{\pi}E_{h0}u^{1/2}$$

$$\Phi_{h2}(u) = \left\{\frac{1}{2}\left(i - \frac{2}{\pi}\gamma + \frac{2}{\pi}\log 2\right)E_{h0} - \frac{1}{\pi}F_{h0} - \frac{1}{2\pi}E_{h0}(1-u^2)\right\}u^{1/2}$$

$$\Phi_{h3}(u) = \frac{1}{\pi^2}u^{1/2}$$

$$\Phi_{h4}(u) = \frac{1}{16}\left[-\frac{2}{\pi}E_{h0}\left\{8\left(i - \frac{2}{\pi}\gamma + \frac{2}{\pi}\log 2\right)E_{h0} - \frac{16}{\pi}F_{h0} - \frac{6}{\pi}E_{h0}\right\} + \frac{2}{\pi}E_{h2} + \left(\frac{8}{\pi^2}E_{h0}^2 + \frac{4}{\pi}E_{h2}\right)u^2\right]u^{1/2} \quad (52)$$

Numerical Results and Discussions

To examine the effect of the magnetic field on the dynamic stress intensity factor as a function of the normalized frequency P, the solution of the Fredholm integral equation of the second kind (36) has been computed numerically by the use of Gaussian quadrature formulas. As $P \to 0$, the dynamic stress intensity factor tends to the static solution by the author [4]. In the absence of the magnetic field, $b_c = 0$, the static stress intensity factor becomes $K_{h1} = p_0 a^{1/2}$. First, we examine the effect of the magnetic field on the dynamic stress intensity factor. Figure 3 shows the variation of absolute value of the normalized dynamic stress intensity factor $|K_{h1}/p_0a^{1/2}|$ with P for the normalized magnetic induction $b_c = 0$, 0.003, 0.005, a Poisson's ratio $\nu = 0.3$, and a magnetic susceptibility $\chi = 10000$. Most of the ferromagnetic materials become magnetically saturated in a field of 2-3 (T). The numerical results are based on $b_c = 0.003$, and 0.005. For $\mu = 10^{11}$ (Pa), $b_c = 0.003$, 0.005 corresponds to an induction of $B_0 \doteqdot 1.1$, 1.8 (T), respectively. The magnetic susceptibility for most ferromagnetic materials used in electromechanical devices are of the order of 10^4. The dynamic stress-intensity factor curves have increasing peaks at smaller frequencies as b_c increases. The same trend is observed for secondary peaks. The effect of the magnetic field on $|K_{h1}/p_0a^{1/2}|$ is pronounced in the neighborhood of P reaching the peaks. The same kind of results for $b_c = 0.005$ and $\nu = 0.2$, 0.3, 0.4 is also shown in Fig. 4. For $b_c = 0.005$, the peaks of the curves shift to higher P as

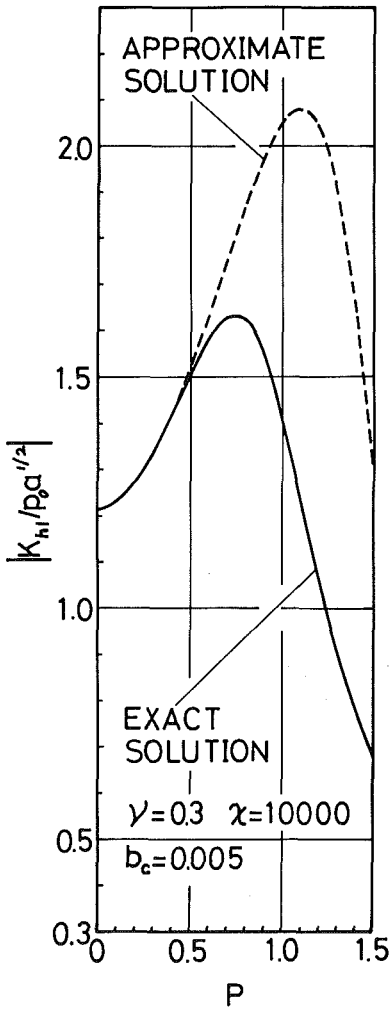

Fig. 5 Comparison between the exact and approximate solutions of normalized dynamic stress intensity factor $|K_{h1}/p_0a^{1/2}|$

Downloaded 02 May 2010 to 171.66.16.246. Redistribution subject to ASME license or copyright; see http://www.asme.org/terms/Terms_Use.cfm

the values of the extremes first fall and then rise as ν increases. However, secondary peaks decrease in magnitude as ν increases.

In Figs. 3 and 4 the integral equation (36) has been solved numerically by the use of Gaussian quadrature formulas. The computation in Fig. 5 is based on the approximate solution (51), and the result for $b_c = 0.005$, $\nu = 0.3$, and $\chi = 10000$ is shown in it together with the exact numerical one. The figure indicates that the approximate solution quite accurately predicts the behavior of the interaction phenomena in the range $0 \leq P < 0.6$.

Acknowledgment

The author would like to acknowledge the continuing direction and encouragement of Prof. Dr. A. Atsumi, Tohoku University and Prof. Dr. S. Mito, Hachinohe Institute of Technology. This work was supported by the Scientific Research Fund of the Ministry of Education for the fiscal year 1981, for which the author is grateful.

References

1 Parkus, H., ed., *Electromagnetic Interactions in Elastic Solids*, Springer-Verlag, Wien, New York, 1979.

2 Moon, F. C., "Problems in Magneto-Solid Mechanics," *Mechanics Today*, Vol. 4, Nemat-Nasser, S., ed., Pergamon Press, New York, 1978, pp. 307–390.

3 Pao, Y.-H., and Yeh, C.-S., "A Linear Theory for Soft Ferromagnetic Elastic Solids," *International Journal of Engineering Science*, Vol. 11, 1973, pp. 415–436.

4 Shindo, Y., "The Linear Magnetoelastic Problem for a Soft Ferromagnetic Elastic Solid With a Finite Crack," ASME JOURNAL OF APPLIED MECHANICS, Vol. 44, 1977, pp. 47–51.

5 Shindo, Y., "Singular Stresses in a Soft Ferromagnetic Elastic Solid With Two Coplanar Griffith Cracks," *International Journal of Solids and Structures*, Vol. 16, 1980, pp. 537–543.

6 Shindo, Y., "Magnetoelastic Interaction of a Soft Ferromagnetic Elastic Solid With a Penny-Shaped Crack in a Constant Axial Magnetic Field," ASME JOURNAL OF APPLIED MECHANICS, Vol. 45, 1978, pp. 291–296.

7 Hutter, K., and Pao, Y.-H., "A Dynamic Theory for Magnetizable Elastic Solids With Thermal and Electrical Conductor," *Journal of Elasticity*, Vol. 4, 1974, pp. 89–114.

8 Moon, F. C., "The Mechanics of Ferroelastic Plates in a Uniform Magnetic Field," ASME JOURNAL OF APPLIED MECHANICS, Vol. 37, 1970, pp. 153–158.

9 Sih, G. C., and Loeber, J. F., "Wave Propagation in an Elastic Solid With a Line of Discontinuity or Finite Crack," *Quarterly of Applied Mathematics*, Vol. 27, 1969, pp. 193–213.

10 Mal, A. K., "Interaction of Elastic Waves With a Griffith Crack," *International Journal of Engineering Science*, Vol. 8, 1970, pp. 763–776.

11 Moon, F. C., and Pao, Y.-H., "Vibration and Dynamic Instability of a Beam-Plate in a Transverse Magnetic Field," ASME JOURNAL OF APPLIED MECHANICS, Vol. 36, 1969, pp. 92–100.

12 Noble, B., *Methods Based on the Wiener-Hopf Technique*, Pergamon Press, New York, 1958.

Downloaded 02 May 2010 to 171.66.16.246. Redistribution subject to ASME license or copyright; see http://www.asme.org/terms/Terms_Use.cfm

S. Itou
Associate Professor,
Department of Mechanical Engineering and Energy,
Hachinohe Institute of Technology,
Hachinohe 031,
Japan

Dynamic Stress Concentration Around a Circular Hole in an Infinite Elastic Strip

Transient response of an infinite elastic strip with a circular hole is investigated in this study. A normal stress is suddenly applied and maintained at the hole. The boundary condition equations are satisfied in the Laplace transformed domain. A numerical Laplace inversion technique is then used to recover the time dependence of the solution.

Introduction

The transient response of a circular hole under the action of impact loads has been studied by Kromm [1] and Selberg [2]. They considered an infinite elastic medium weakened by a circular cavity. Therefore, their solutions were limited to specimens of very large dimensions compared with that of the cavity such that boundary effects may be neglected in the analysis.

If the cavity is situated at a little distance from the other surface(s) such as a plane boundary, the effect of the waves reflected from the surface(s) must be considered. However, it is very difficult to solve such problems because the separation of the variable on the circular hole cannot be achieved. To bypass the inherent difficulty of the problems the Schmidt orthogonalization method [3, 4] is useful.

In the present paper, the transient dynamic stress concentration around a cylindrical cavity in an infinite elastic strip is investigated. Internal pressure is applied to the circular hole with the Heaviside-function time dependence. In the Laplace transformed domain, first, the boundary conditions at the plane surfaces are satisfied with the aid of the Fourier transformation. Then, the Schmidt orthogonalization method is used to satisfy the boundary condition equations on the circular hole. The transformed solutions are inverted numerically in the physical space by means of the Miller and Guy's technique [5].

Formulation

Consider a strip bounded in the x, y plane by the lines $y = \pm h$. The circular hole is supposed to have its center at the origin with "a" being the radius of the cavity as shown in Fig. 1. A polar coordinate system (r,θ) is brought into relation with (x,y) as

$$x = r\cos\theta, \quad y = r\sin\theta. \tag{1}$$

Displacement potential functions ϕ and ψ are introduced by the following relations

$$\begin{aligned} u &= \partial\phi/\partial x + \partial\psi/\partial y, \\ v &= -\partial\psi/\partial x + \partial\phi/\partial y, \end{aligned} \tag{2}$$

where u and v are defined as the x and y components of the displacement, respectively. Substituting equation (2) into the equation of motion reduces to

$$\begin{aligned} \partial^2\phi/\partial x^2 + \partial^2\phi/\partial y^2 &= 1/c_L^2 \quad \partial^2\phi/\partial t^2, \\ \partial^2\psi/\partial x^2 + \partial^2\psi/\partial y^2 &= 1/c_T^2 \quad \partial^2\psi/\partial t^2, \end{aligned} \tag{3}$$

where the medium is assumed to be homogeneous and isotropic and $c_L = \{(\lambda+2\mu)/\rho\}^{1/2}$, $c_T = (\mu/\rho)^{1/2}$ are the dilatational and shear wave velocities with λ and μ being the Lamé constants, and ρ being the density of the material. Equation (3) can be expressed in polar coordinate (r, θ) as

$$\begin{aligned} &\partial^2\phi/\partial r^2 + 1/r\partial\phi/\partial r + 1/r^2\partial^2\phi/\partial\theta^2 = 1/c_L^2\partial^2\phi/\partial t^2, \\ &\partial^2\psi/\partial r^2 + 1/r\partial\psi/\partial r + 1/r^2\partial^2\psi/\partial\theta^2 = 1/c_T^2\partial^2\psi/\partial t^2. \end{aligned} \tag{4}$$

The stresses are written in terms of ϕ and ψ as

$$\tau_{xx}/(2\mu) = -\partial^2\phi/\partial y^2 + \frac{1}{2}\kappa^2(\partial^2\phi/\partial x^2 + \partial^2\phi/\partial y^2) + \partial^2\psi/\partial x\partial y,$$

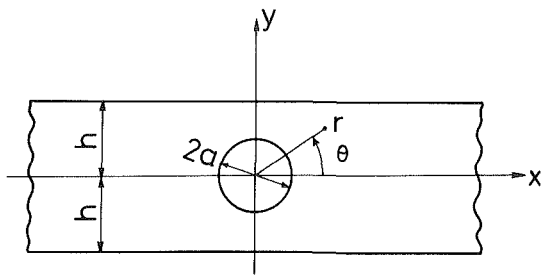

Fig. 1 Geometry and coordinate system

Contributed by the Applied Mechanics Division for publication in the JOURNAL OF APPLIED MECHANICS.
Discussion on this paper should be addressed to the Editorial Department, ASME, United Engineering Center, 345 East 47th Street, New York, N.Y. 10017, and will be accepted until two months after final publication of the paper itself in the JOURNAL OF APPLIED MECHANICS. Manuscript received by ASME Applied Mechanics Division June, 1982; final revision, September, 1982.

Copyright © 1983 by ASME
Downloaded 02 May 2010 to 171.66.16.246. Redistribution subject to ASME license or copyright; see http://www.asme.org/terms/Terms_Use.cfm

$$\tau_{yy}/(2\mu) = -\partial^2\phi/\partial x^2 + \frac{1}{2}\kappa^2(\partial^2\phi/\partial x^2 + \partial^2\phi/\partial y^2) - \partial^2\psi/\partial x\partial y,$$

$$\tau_{xy}/(2\mu) = \partial^2\phi/\partial x\partial y - \partial^2\psi/\partial x^2 + \frac{1}{2}(\partial^2\psi/\partial x^2 + \partial^2\psi/\partial y^2), \quad (5)$$

where the elastic constant κ^2 takes the value

$$\kappa^2 = 2(1-\nu)/(1-2\nu) \quad (6)$$

in the state of plane strain with ν being Poisson's ratio. The stresses relative to the polar coordinate are given by the equations

$$\begin{aligned}\tau_{rr} &= \tau_{xx}\cos^2\theta + \tau_{yy}\sin^2\theta + \tau_{xy}\sin(2\theta),\\ \tau_{\theta\theta} &= \tau_{xx}\sin^2\theta + \tau_{yy}\cos^2\theta - \tau_{xy}\sin(2\theta),\\ \tau_{r\theta} &= \frac{1}{2}(\tau_{yy}-\tau_{xx})\sin(2\theta) + \tau_{xy}\cos(2\theta). \quad (7)\end{aligned}$$

The boundary conditions to be studied are as follows:

$$\tau_{rr} = -P\,H(t), \quad \tau_{r\theta} = 0, \quad \text{on } r = a, \quad (8)$$

$$\tau_{yy} = \tau_{xy} = 0, \quad \text{on } y = \pm h, \quad (9)$$

where P is a constant and $H(t)$ is the Heaviside unit step function.

Analysis

Define a Laplace transform pair by

$$f^*(s) = \int_0^\infty f(t)\exp(-st)dt,$$

$$f(t) = \frac{1}{2\pi i}\int_{Br} f^*(s)\exp(st)ds, \quad (10)$$

in which Br stands for the Bromwich path of integration. Applying equation (10) to equations (3) and (4) results in

$$\partial^2\phi^*/\partial x^2 + \partial^2\phi^*/\partial y^2 - s^2/c_L^2\phi^* = 0,$$

$$\partial^2\psi^*/\partial x^2 + \partial^2\psi^*/\partial y^2 - s^2/c_T^2\psi^* = 0, \quad (11)$$

$$\partial^2\phi^*/\partial r^2 + 1/r\partial\phi^*/\partial r + 1/r^2\partial^2\phi^*/\partial\theta^2 - s^2/c_L^2\phi^* = 0,$$

$$\partial^2\psi^*/\partial r^2 + 1/r\partial\psi^*/\partial r + 1/r^2\partial^2\psi^*/\partial\theta^2 - s^2/c_T^2\psi^* = 0. \quad (12)$$

The Laplace transforms of the boundary conditions (8) and (9) are

$$\tau_{rr}^* = -P/s, \quad \tau_{r\theta}^* = 0, \quad \text{on } r = a, \quad (13)$$

$$\tau_{yy}^* = \tau_{xy}^* = 0, \quad \text{on } y = \pm h. \quad (14)$$

The solutions of the transformed wave equations will be in the following forms

$$\phi^* = 2\int_0^\infty B_1(\xi)\cosh(\gamma_1 y)\cos(\xi\,x)d\xi + \sum_{n=1}^\infty C_n K_{2n-2}(sr/c_L)\cos\{2(n-1)\theta\}, \quad (15)$$

$$\psi^* = 2\int_0^\infty B_2(\xi)\sinh(\gamma_2 y)\sin(\xi\,x)d\xi + \sum_{n=1}^\infty D_n K_{2n}(\kappa\,sr/c_L)\sin(2n\theta), \quad (16)$$

with

$$\gamma_1 = (\xi^2 + s^2/c_L^2)^{1/2}, \quad \gamma_2 = (\xi^2 + \kappa^2 s^2/c_L^2)^{1/2}, \quad (17)$$

where $K_n(\ \ )$ are the modified Bessel function of the second kind and $B_1(\xi)$, $B_2(\xi)$, C_n, and D_n are the unknowns to be solved.

By substituting equations (15) and (16) into the transformed equations of stresses, we obtain

$$\begin{aligned}\tau_{xx}^*/(2\mu) &= \int_0^\infty [B_1(\xi)\{-\kappa^2\xi^2 + 2(\kappa^2/2-1)\gamma_1^2\}\cosh(\gamma_1 y) + B_2(\xi)\\ &\quad\times\{2\xi\gamma_2\cosh(\gamma_2 y)\}]\cos(\xi\,x)d\xi\\ &\quad+\sum_{n=1}^\infty C_n\{\kappa^2/2 f_1^n(r,\theta,s) + (\kappa^2/2-1)f_2^n(r,\theta,s)\}\\ &\quad+\sum_{n=1}^\infty D_n\{g_3^n(r,\theta,s)\},\\ \tau_{yy}^*/(2\mu) &= \int_0^\infty [B_1(\xi)\{2(1-\kappa^2/2)\xi^2 + \kappa^2\gamma_1^2\}\cosh(\gamma_1 y) + B_2(\xi)\\ &\quad\times\{-2\gamma_2\xi\cosh(\gamma_2 y)\}]\cos(\xi\,x)d\xi\\ &\quad+\sum_{n=1}^\infty C_n\{(\kappa^2/2-1)f_1^n(r,\theta,s) + \kappa^2/2 f_2^n(r,\theta,s)\}\\ &\quad+\sum_{n=1}^\infty D_n\{-g_3^n(r,\theta,s)\},\\ \tau_{xy}^*/(2\mu) &= \int_0^\infty [B_1(\xi)\{-2\gamma_1\xi\sinh(\gamma_1 y)\} + B_2(\xi)\{(\xi^2+\gamma_2^2)\\ &\quad\times\sinh(\gamma_2 y)\}]\sin(\xi\,x)d\xi\\ &\quad+\sum_{n=1}^\infty C_n\{f_3^n(r,\theta,s)\} + \sum_{n=1}^\infty D_n\{g_2^n(r,\theta,s)/2\\ &\quad-g_1^n(r,\theta,s)/2\}, \quad (18)\end{aligned}$$

with

$$\begin{aligned}f_1^n(r,\theta,s) &= (s/c_L)^2/4\{K_{2n-4}(sr/c_L) + 2K_{2n-2}(sr/c_L) + K_{2n}(sr/c_L)\}\\ &\quad\times\cos\{2(n-1)\theta\}\cos^2\theta - 2(n-1)(s/c_L)\{K_{2n-3}(sr/c_L)\\ &\quad+K_{2n-1}(sr/c_L)\}\sin\{2(n-1)\theta\}\sin\theta\cos\theta/r - (s/c_L)/2\\ &\quad\times\{K_{2n-3}(sr/c_L) + K_{2n-1}(sr/c_L)\}\cos\{2(n-1)\theta\}\sin^2\theta/r\\ &\quad-4(n-1)K_{2n-2}(sr/c_L)\sin\{2(n-1)\theta\}\sin\theta\cos\theta/r^2\\ &\quad-4(n-1)^2K_{2n-2}(sr/c_L)\cos\{2(n-1)\theta\}\sin^2\theta/r^2,\end{aligned}$$

$$\begin{aligned}f_2^n(r,\theta,s) &= (s/c_L)^2/4\{K_{2n-4}(sr/c_L) + 2K_{2n-2}(sr/c_L) + K_{2n}(sr/c_L)\}\\ &\quad\times\cos\{2(n-1)\theta\}\sin^2\theta + 2(n-1)(s/c_L)\{K_{2n-3}(sr/c_L)\\ &\quad+K_{2n-1}(sr/c_L)\}\sin\theta\cos\theta/r - (s/c_L)/2\{K_{2n-3}(sr/c_L)\\ &\quad+K_{2n-1}(sr/c_L)\}\cos\{2(n-1)\theta\}\cos^2\theta/r - 4(n-1)^2\\ &\quad\times K_{2n-2}(sr/c_L)\cos\{2(n-1)\theta\}\cos^2\theta/r^2 + 4(n-1)\\ &\quad\times K_{2n-2}(sr/c_L)\sin\{2(n-1)\theta\}\sin\theta\cos\theta/r^2,\end{aligned}$$

$$\begin{aligned}f_3^n(r,\theta,s) &= (s/c_L)^2/4\{K_{2n-4}(sr/c_L) + 2K_{2n-2}(sr/c_L) + K_{2n}(sr/c_L)\}\\ &\quad\times\cos\{2(n-1)\theta\}\sin\theta\cos\theta - (n-1)(s/c_L)\{K_{2n-3}(sr/c_L)\\ &\quad+K_{2n-1}(sr/c_L)\}\sin\{2(n-1)\theta\}(\sin^2\theta - \cos^2\theta)/r\end{aligned}$$

Downloaded 02 May 2010 to 171.66.16.246. Redistribution subject to ASME license or copyright; see http://www.asme.org/terms/Terms_Use.cfm

$$+(s/c_L)/2\{K_{2n-3}(sr/c_L)+K_{2n-1}(sr/c_L)\}\cos\{2(n-1)\theta\}$$
$$\times\sin\theta\cos\theta/r+4(n-1)^2K_{2n-2}(sr/c_L)\cos\{2(n-1)\theta\}$$
$$\times\sin\theta\cos\theta/r^2-2(n-1)K_{2n-2}(sr/c_L)\sin\{2(n-1)\theta\}$$
$$\times(\sin^2\theta-\cos^2\theta)/r^2,$$

$$g_1^n(r,\theta,s) = f_1^{n+1}(r,\theta,\kappa s)\,|\{\cos(2n\theta)\to\sin(2n\theta),\ \sin(2n\theta\to)\cos(2n\theta)\},$$

$$g_2^n(r,\theta,s) = f_2^{n+1}(r,\theta,\kappa s)\,|\{\cos(2n\theta)\to\sin(2n\theta),\ \sin(2n\theta)\to\cos(2n\theta)\},$$

$$g_3(r,\theta,s) = f_3^{n+1}(r,\theta,\kappa s)\,|\{\cos(2n\theta)\to\sin(2n\theta),\ \sin(2n\theta)\to\cos(2n\theta)\}. \tag{19}$$

To satisfy equation (14), the functions $B_1(\xi)$ and $B_2(\xi)$ are represented by the coefficients C_n and D_n using Fourier transformation,

$$B_1(\xi) = \sum_{n=1}^{\infty} C_n p_1^n(\xi)+\sum_{n=1}^{\infty} D_n p_2^n(\xi),$$
$$B_2(\xi) = \sum_{n=1}^{\infty} C_n p_3^n(\xi)+\sum_{n=1}^{\infty} D_n p_4^n(\xi), \tag{20}$$

with

$$p_1^n(\xi) = \{q_1^n(\xi)a_{22}-q_3^n(\xi)a_{12}\}/(a_{11}a_{22}-a_{12}a_{21}),$$
$$p_2^n(\xi) = \{q_2^n(\xi)a_{22}-q_4^n(\xi)a_{12}\}/(a_{11}a_{22}-a_{12}a_{21}),$$
$$p_3^n(\xi) = \{q_3^n(\xi)a_{11}-q_1^n(\xi)a_{21}\}/(a_{11}a_{22}-a_{12}a_{21}),$$
$$p_4^n(\xi) = \{q_4^n(\xi)a_{11}-q_2^n(\xi)a_{21}\}/(a_{11}a_{22}-a_{12}a_{21}), \tag{21}$$
$$a_{11} = \{2(1-\kappa^2/2)\xi^2+\kappa^2\gamma_1^2\}\cosh(\gamma_1 h),$$
$$a_{12} = -2\gamma_2\xi\cosh(\gamma_2 h),$$
$$a_{21} = -2\gamma_1\xi\sinh(\gamma_1 h),\quad a_{22}=(\xi^2+\gamma_2^2)\sinh(\gamma_2 h), \tag{22}$$

$$g_1^n(\xi) = 2/\pi\int_0^{\infty}\{(1-\kappa^2/2)f_1^n(r_h,\theta_h,s)$$
$$-\kappa^2/2f_2^n(r_h,\theta_h,s)\}\cos(\xi\,x)dx,$$

$$q_2^n(\xi) = 2/\pi\int_0^{\infty} g_3^n(r_h,\theta_h,s)\cos(\xi\,x)dx$$

$$q_3^n(\xi) = -2/\pi\int_0^{\infty} f_3^n(r_h,\theta_h,s)\sin(\xi\,x)dx,$$

$$q_4^n(\xi) = 1/\pi\int_0^{\infty}\{g_1^n(r_h,\theta_h,s)-g_2^n(r_h,\theta_h,s)\}\sin(\xi\,x)dx, \tag{23}$$

$$r_h=(h^2+x^2)^{1/2},\quad \theta_h=\tan^{-1}(h/x). \tag{24}$$

Then, using equations (7), (18), and (20) we obtain the stresses that satisfy the boundary conditions on the plane boundaries $y=\pm h$ as follows,

$$\tau_{rr}^*/(2\mu) = \sum_{n=1}^{\infty} C_n Q_1^n(r,\theta)+\sum_{n=1}^{\infty} D_n Q_2^n(r,\theta),$$
$$\tau_{\theta\theta}^*/(2\mu) = \sum_{n=1}^{\infty} C_n Q_3^n(r,\theta)+\sum_{n=1}^{\infty} D_n Q_4^n(r,\theta),$$
$$\tau_{r\theta}^*/(2\mu) = \sum_{n=1}^{\infty} C_n Q_5^n(r,\theta)+\sum_{n=1}^{\infty} D_n Q_6^n(r,\theta), \tag{25}$$

with

$$Q_1^n(r,\theta) = (\kappa^2/2-\sin^2\theta)f_1^n(r,\theta,s)+(\kappa^2/2-\cos^2\theta)f_2^n(r,\theta,s)$$
$$+\sin(2\theta)f_3^n(r,\theta,s)$$
$$+\int_0^{\infty}\{p_1^n(\xi)h_1(\xi)+p_3^n(\xi)h_2(\xi)\}\cos(\xi\,x)d\xi$$
$$+\int_0^{\infty}\{p_1^n(\xi)h_3(\xi)+p_3^n(\xi)h_4(\xi)\}\sin(\xi\,x)d\xi,$$

$$Q_2^n(r,\theta) = (\cos^2\theta-\sin^2\theta)g_3^n(r,\theta,s)-\sin(2\theta)/2\{g_1^n(r,\theta,s)$$
$$-g_2^n(r,\theta,s)\}$$
$$+\int_0^{\infty}\{p_2^n(\xi)h_1(\xi)+p_4^n(\xi)h_2(\xi)\}\cos(\xi\,x)d\xi$$
$$+\int_0^{\infty}\{p_2^n(\xi)h_3(\xi)+p_4^n(\xi)h_4(\xi)\}\sin(\xi\,x)d\xi,$$

$$Q_3^n(r,\theta) = (\kappa^2/2-\cos^2\theta)f_1^n(r,\theta,s)+(\kappa^2/2-\sin^2\theta)f_2^n(r,\theta,s)$$
$$-\sin(2\theta)f_3^n(r,\theta,s)$$
$$+\int_0^{\infty}\{p_1^n(\xi)h_5(\xi)+p_3^n(\xi)h_6(\xi)\}\cos(\xi\,x)d\xi$$
$$+\int_0^{\infty}\{p_1^n(\xi)h_7(\xi)+p_3^n(\xi)h_8(\xi)\}\sin(\xi\,x)d\xi,$$

$$Q_4^n(r,\theta) = (\sin^2\theta-\cos^2\theta)g_3^n(r,\theta,s)+\sin(2\theta)/2\{g_1^n(r,\theta,s)$$
$$-g_2^n(r,\theta,s)\}$$
$$+\int_0^{\infty}\{p_2^n(\xi)h_5(\xi)+p_4^n(\xi)h_6(\xi)\}\cos(\xi\,x)d\xi$$
$$+\int_0^{\infty}\{p_2^n(\xi)h_7(\xi)+p_4^n(\xi)h_8(\xi)\}\sin(\xi\,x)d\xi,$$

$$Q_5^n(r,\theta) = \sin(2\theta)/2\{f_2^n(r,\theta,s)-f_1^n(r,\theta,s)\}+\cos(2\theta)f_3^n(r,\theta,s)$$
$$+\int_0^{\infty}\{p_1^n(\xi)h_9(\xi)+p_3^n(\xi)h_{10}(\xi)\}\cos(\xi\,x)d\xi$$
$$+\int_0^{\infty}\{p_1^n(\xi)h_{11}(\xi)+p_3^n(\xi)h_{12}(\xi)\}\sin(\xi\,x)d\xi,$$

$$Q_6^n(r,\theta) = -\sin(2\theta)g_3^n(r,\theta,s)-\cos(2\theta)/2\{g_1^n(r,\theta,s)$$
$$-g_2^n(r,\theta,s)\}$$
$$+\int_0^{\infty}\{p_2^n(\xi)h_9(\xi)+p_4^n(\xi)h_{10}(\xi)\}\cos(\xi\,x)d\xi$$
$$+\int_0^{\infty}\{p_2^n(\xi)h_{11}(\xi)+p_4^n(\xi)h_{12}(\xi)\}\sin(\xi\,x)d\xi, \tag{26}$$

$$h_1(\xi) = \{\kappa^2(\gamma_1^2-\xi^2)-2\gamma_1^2\cos^2\theta+2\xi^2\sin^2\theta\}\cosh(\gamma_1 y),$$
$$h_2(\xi) = 2\gamma_2\xi(\cos^2\theta-\sin^2\theta)\cosh(\gamma_2 y),$$
$$h_3(\xi) = -2\gamma_1\xi\sin(2\theta)\sinh(\gamma_1 y),$$
$$h_4(\xi) = (\xi^2+\gamma_2^2)\sin(2\theta)\sinh(\gamma_2 y),$$
$$h_5(\xi) = \{\kappa^2(\gamma_1^2-\xi^2)-2\gamma_1^2\sin^2\theta+2\xi^2\cos^2\theta\}\cosh(\gamma_1 y),$$
$$h_6(\xi) = 2\gamma_2\xi(\sin^2\theta-\cos^2\theta)\cosh(\gamma_2 y),$$
$$h_7(\xi) = 2\gamma_1\xi\sin(2\theta)\sinh(\gamma_1 y),$$
$$h_8(\xi) = -(\xi^2+\gamma_2^2)\sin(2\theta)\sinh(\gamma_2 y),$$
$$h_9(\xi) = \sin(2\theta)(\xi^2+\gamma_1^2)\cosh(\gamma_1 y),$$
$$h_{10}(\xi) = -2\sin(2\theta)\gamma_2\xi\cosh(\gamma_2 y),$$
$$h_{11}(\xi) = -2\cos(2\theta)\gamma_1\xi\sinh(\gamma_1 y),$$
$$h_{12}(\xi) = \cos(2\theta)(\xi^2+\gamma_2^2)\sinh(\gamma_2 y). \tag{27}$$

Downloaded 02 May 2010 to 171.66.16.246. Redistribution subject to ASME license or copyright; see http://www.asme.org/terms/Terms_Use.cfm

The remaining boundary conditions at the cavity surface $r = a$ give the following form

$$\sum_{n=1}^{\infty} C_n Q_1^n(a,\theta) + \sum_{n=1}^{\infty} D_n Q_2^n(a,\theta) = -P/(2\mu s),$$

$$\sum_{n=1}^{\infty} C_n Q_5^n(a,\theta) + \sum_{n=1}^{\infty} D_n Q_6^n(a,\theta) = 0, \tag{28}$$

where $Q_1^n(a,\theta)$, $Q_2^n(a,\theta)$, $Q_5^n(a,\theta)$, and $Q_6^n(a,\theta)$ are considered to be the function of only y because on $r = a$,

$$x = (a^2 - y^2)^{1/2}, \quad \theta = \tan^{-1}(y/x). \tag{29}$$

Equation (28) can be solved for the coefficients C_n and D_n by a modified version of the Schmidt orthogonalization method [4]. For convenience sake, we rewrite equation (28) as

$$\sum_{n=1}^{\infty} C_n E_n(y) + \sum_{n=1}^{\infty} D_n F_n(y) = -w(y), \tag{30a}$$

$$\text{for} \quad 0 \leqq y \leqq a,$$

$$\sum_{n=1}^{\infty} C_n G_n(y) + \sum_{n=1}^{\infty} D_n H_n(y) = 0, \tag{30b}$$

with

$$E_n(y) = Q_1^n(a,\theta), \quad F_n(y) = Q_2^n(a,\theta), \quad G_n(y) = Q_5^n(a,\theta),$$
$$H_n(y) = Q_6^n(a,\theta), \quad w(y) = P/(2\mu s). \tag{31}$$

A set of functions $P_n(y)$ that satisfies the orthogonality condition

$$\int_0^a P_m(y) P_n(y)\,dy = N_n \delta_{mn}, \quad N_n = \int_0^a P_n^2(y)\,dy, \tag{32}$$

can be constructed from a given set of the arbitrary function, say $G_n(y)$, such that

$$P_n(y) = \sum_{i=1}^{n} M_{in}/M_{nn} G_i(y), \tag{33}$$

where M_{in} is the cofactor of the element d_{in} of Δ_n, which is defined as

$$\Delta_n = \begin{vmatrix} d_{11} & d_{12} & \cdots & d_{1n} \\ d_{21} & & & \cdot \\ \cdot & & & \cdot \\ \cdot & & & \cdot \\ d_{n1} & \cdots & \cdots & d_{nn} \end{vmatrix}, \tag{34}$$

$$d_{in} = \int_0^a G_i(y) G_n(y)\,dy.$$

Representing the first series in equation (30*b*) by the orthogonal series $P_n(y)$ with the coefficients ϵ_n, the following relationships are derived

$$\sum_{n=1}^{\infty} C_n G_n(y) = \sum_{n=1}^{\infty} \epsilon_n P_n(y) = -\sum_{n=1}^{\infty} D_n H_n(y). \tag{35}$$

The second equality gives

$$\epsilon_n = \sum_{i=1}^{\infty} \alpha_{ni} D_i, \quad \alpha_{ni} = -1' N_n \int_0^a P_n(y) H_i(y)\,dy, \tag{36}$$

and considering equation (33) the first equality shows,

$$C_n = \sum_{n=1}^{\infty} \gamma_{ni} D_i, \quad \gamma_{ni} = -\sum_{j=n}^{\infty} M'_{nj}/(N_j M_{jj}) \int_0^a P_j(y) H_i(y)\,dy. \tag{37}$$

Substituting equation (37) into equation (30*a*), it becomes

$$\sum_{n=1}^{\infty} D_n Y_n(y) = -w(y), \quad Y_n(y) = F_n(y) + \sum_{i=1}^{\infty} \gamma_{in} E_i(y). \tag{38}$$

Following the same procedure to orthogonalize the series in equation (38) by $Q_n(y)$ satisfies

$$\int_0^a Q_m(y) Q_n(y)\,dy = K_n \delta_{mn}, \quad K_n = \int_0^a Q_n^2(y)\,dy. \tag{39}$$

The coefficient D_n can be obtained by

$$D_n = \sum_{j=n}^{\infty} q_j L_{nj}/L_{jj}, \tag{40}$$

with

$$q_j = -1/K_j \int_0^a w(y) Q_j(y)\,dy, \quad Q_j(y) = \sum_{i=1}^{j} L_{ij}/L_{jj}\, Y_i(y), \tag{41}$$

where L_{jn} is the cofactor of the element e_{jn} of the determinant Δ'_n,

$$\Delta'_n = \begin{vmatrix} e_{11} & \mathbf{e}_{12} & \cdots & e_{1n} \\ e_{21} & & & \cdot \\ \cdot & & & \cdot \\ \cdot & & & \cdot \\ e_{n1} & \cdots & \cdots & e_{nn} \end{vmatrix}, \tag{42}$$

$$e_{jn} = \int_0^a Y_j(y) Y_n(y)\,dy.$$

Circumferential Stress at Boundary of Cavity

The coefficients C_n and D_n are now known, so that the entire stress field is obtainable. An important quantity is the stress $\tau_{\theta\theta}$ at $r = a$ and it is given as

$$\tau^*_{\theta\theta}/(2\mu) = \sum_{n=1}^{\infty} C_n Q_3^n(a,\theta) + \sum_{n=1}^{\infty} D_n Q_4^n(a,\theta). \tag{43}$$

The Laplace inverse transformation in equation (43) is carried out by the numerical method given by Miller and Guy [5]. When the Laplace transform $f^*(s)$ can be evaluated at discrete points given by

$$s = (\beta + 1 + p), \quad p = 0,1,2,3, \ldots\ldots\ldots, \tag{44}$$

we may then determine coefficients C'_q from the following set of equations

$$\delta' f^*\left\{(\beta+1+p)\delta'\right\} = \sum_{q=1}^{p} C'_q p!/\{(p+\beta+1)(p+\beta+2)$$
$$\cdots (p+\beta+1+q)(p-q)!\}, \tag{45}$$

where $\delta' > 0$, $\beta > -1.0$. If the first Q coefficients are calculated, an approximate value of $f(t)$ can be found as

$$f(t) = \sum_{q=0}^{Q-1} C'_q P_q^{(0,\beta)} \{2\exp(-\delta' t) - 1\}, \tag{46}$$

where $P_q^{(0,\beta)}(x)$ is a Jacobi polynomial and Q is the number of terms employed. The parameters δ', β, and Q are selected such that $f(t)$ can be best described within a particular time t.

Numerical Examples and Results

The dynamic stress concentration factor is calculated numerically for $\nu = 0.25$. The semi-infinite integrals in equations (23) and (26) can be easily evaluated numerically by using Filon's method [6], because those integrands almost decrease exponentially. To perform the Schmidt procedure the first five terms of the infinite series to equation (30) are retained. For a check of the accuracy, the values of

$$\left\{\sum_{n=1}^{\infty} C_n E_n(y) + \sum_{n=1}^{\infty} D_n F_n(y)\right\},$$

$$\left\{\sum_{n=1}^{\infty} C_n G_n(y) + \sum_{n=1}^{\infty} D_n H_n(y)\right\}$$

Downloaded 02 May 2010 to 171.66.16.246. Redistribution subject to ASME license or copyright; see http://www.asme.org/terms/Terms_Use.cfm

Table 1 Values of equation (30*a*) and (30*b*) for $h/a = 2.0$, $sa/c_L = 1.6$

y/a	$\left\{\sum_{n=1}^{5} C_n E_n(y) + \sum_{n=1}^{5} D_n F_n(y)\right\}$ $\times\{2\mu c_L/(Pa)\}$	$\left\{\sum_{n=1}^{5} C_n G_n(y) + \sum_{n=1}^{5} D_n H_n(y)\right\}$ $\times\{2\mu c_L/(Pa)\}$	$-w(y)$ $\times\{2\mu c_L/(Pa)\}$
0.999	-0.6250011	-0.1830049×10^{-5}	
0.900	-0.6250013	0.2996530×10^{-6}	
0.500	-0.6250024	-0.1862645×10^{-8}	-0.6250000
0.100	-0.6250013	-0.3543682×10^{-6}	
0.001	-0.6250021	-0.3856258×10^{-8}	

Table 2 Values of coefficients C_n and D_n for $h/a = 2.0$, $sa/c_L = 1.6$

n	$C_n\times2\mu c_L/(Pa^3)$	$D_n\times2\mu c_L/(Pa^3)$
1	-0.5699237×10^{0}	0.1986548×10^{-1}
2	0.4354805×10^{-2}	-0.2533868×10^{-2}
3	-0.2107955×10^{-3}	0.4245820×10^{-4}
4	0.1282509×10^{-5}	-0.1864181×10^{-6}
5	-0.1969322×10^{-8}	-0.1253006×10^{-11}

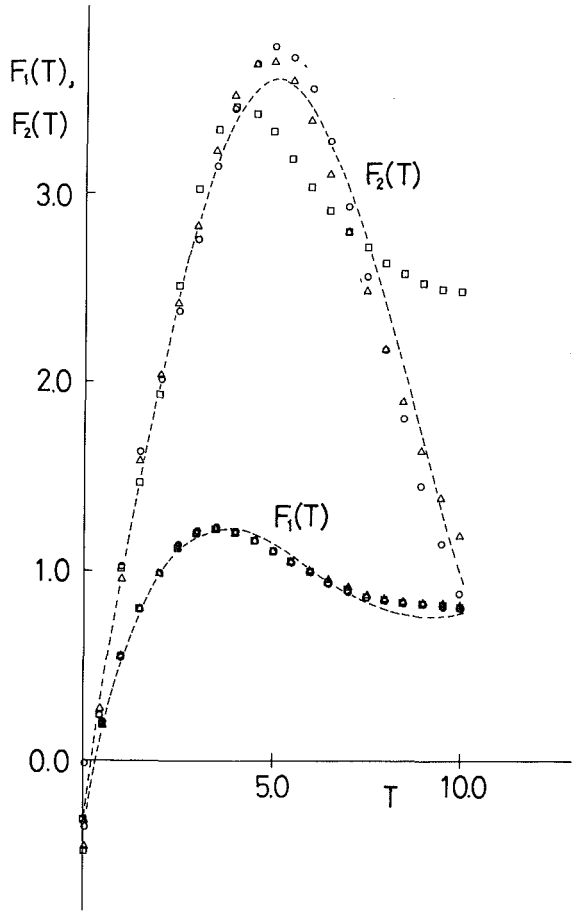

Fig. 2 Numerical Laplace inversions of known functions $F_1(T)$ and $F_2(T)$ (○ .... $\delta' = 0.2$, Δ .... $\delta' = 0.4$, □ .... $\delta' = 0.6$)

and $w(y)$ are given in Table 1 for $a/h = 0.5$ and $sa/c_L = 1.6$. In Table 2, the values of the coefficients C_n and D_n are also given for $a/h = 0.5$, $sa/c_L = 1.6$. From these it is clear that the Schmidt method is carried out completely.

To invert the Laplace transforms numerically, we must select the values β, δ', and Q. However, there is no optimum way of selecting these values. Here, we consider two functions $F_1(T)$ and $F_2(T)$ which are defined as

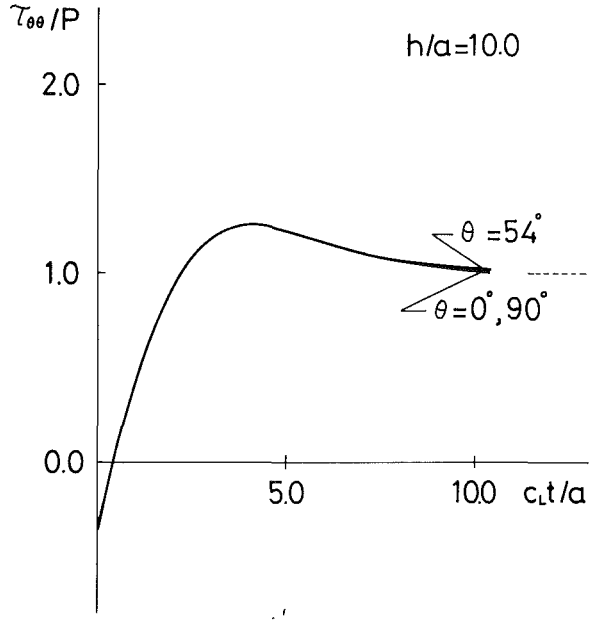

Fig. 3 $\tau_{\theta\theta}/P$ at $r = a$ for $h/a = 10.0$

$$
\begin{aligned}
F_1(T) &= -0.3333 + 1.1[1.0 - \exp(-0.889T) + 0.9 \\
&\quad \times \{1.0 - \cos(0.7T)\}/T], \\
F_2(T) &= -0.3333 + 1.9\{1.0 - \exp(-0.2T) + 2.5 \\
&\quad \times J_1(0.4T)\},
\end{aligned} \tag{47}
$$

where $J_1(T)$ is a Bessel function and T is a dimensionless time variable. The Laplace transforms of equations (47) are

$$
\begin{aligned}
F_1^*(s) &= -0.3333/s + 1.1[1.0/s - 1.0/(s+0.889) \\
&\quad + 0.9\log\{(s^2+0.72)/s^2\}2.0], \\
F_2^*(s) &= -0.3333/s + 1.9[1.0/s - 1.0/(s+0.2) \\
&\quad + 2.5\{(\sqrt{s^2+0.4^2} - s)/(0.4\sqrt{s^2+0.4^2})\}].
\end{aligned} \tag{48}
$$

$F_1^*(s)$ and $F_2^*(s)$ in equation (48) are inverted numerically by using the values of $\delta' = 0.2$, 0.4, and 0.6 with the fixed values of $\beta = 0.0$, $Q = 7$. The results are shown in Fig. 2, in which the broken lines are those calculated from equation (47). The numerical inversions of $F_1^*(s)$ are carried out satisfactorily for every combinations of β, δ', and Q. On the contrary, the inversions of $F_2^*(s)$ are affected by the values of (β, δ', Q). Therefore, the numerical Laplace inversion for the function that varies rapidly with time must be done very carefully.

In Figs. 3 and 4, the dynamic stress concentrations, which are inverted numerically with the values $\beta = 0.0$, $\delta' = 0.4$, $Q = 7$, are shown for $h/a = 10.0$, 2.0, and $\theta = 0$ deg, 54 deg, 90 deg. From Fig. 2, it is considered that there may be a difference of about 5 percent between the curve for $h/a = 2.0$, θ

Downloaded 02 May 2010 to 171.66.16.246. Redistribution subject to ASME license or copyright; see http://www.asme.org/terms/Terms_Use.cfm

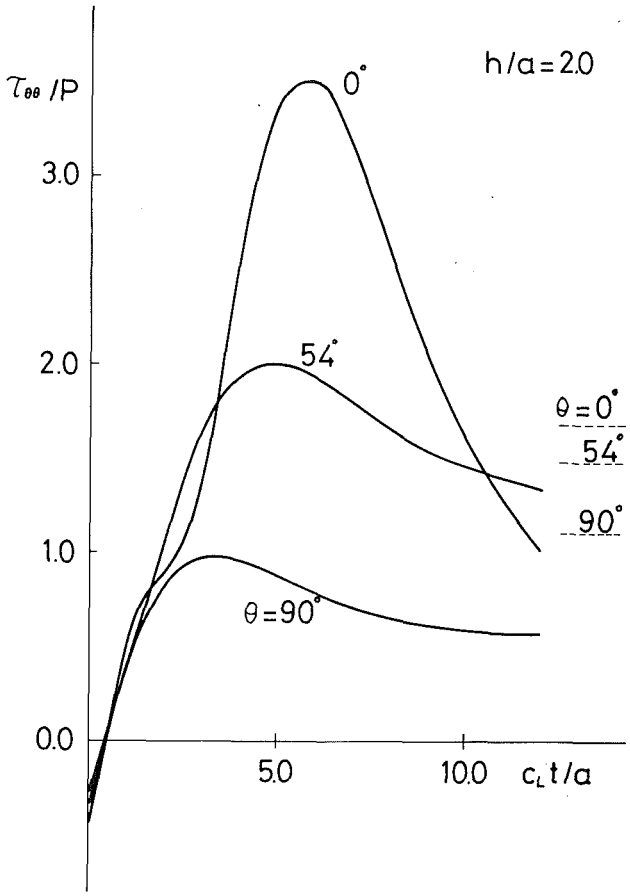

Fig. 4 $\tau_{\theta\theta}/P$ at $r = a$ for $h/a = 2.0$

= 0 deg and the true one. However, as pointed out by Chen [7], such a difference may be admissible because the present solution is based on the numerical analysis. The corresponding static values are calculated by using the Fortan program from reference [8] and those are shown by the broken lines in Figs. 3 and 4.

The curves for $h/a = 10.0$ are similar with that for an infinite medium given by Selberg [2]. The effect of the boundaries on the dynamic stress concentrations are significant for $h/a = 2.0$. The peak value of $\tau_{\theta\theta}$ at $\theta = 0$ deg is increased by about two times over its static values. For $\theta = 90$ deg, the first value is smaller than the corresponding static value, and thereby, the second peak value or the third may exceed the first.

Acknowledgment

The author wishes to thank Prof. A. Atsumi of Tohoku University for his encouragement and support and Asst. Prof. K. Watanabe of Yamagata University for his helpful discussion.

References

1 Kromm, A., "Zur Ausbreitung von Stosswellen in Kreislochscheiben," *Zeitschrift für Angewandte Mathematik und Mechanik*, Bd. 28, 1948, pp. 297–303.

2 Selberg, H. L., "Transient Compression Waves From Spherical and Cylindrical Cavities," Arkiv för Fysik, Bd. 5, 1952, pp. 97–108.

3 Morse, P. M., and Feshback, H., *Methods of Theoretical Physics*, Vol. 1, McGraw-Hill, New York, 1958.

4 Yau, W. F., "Axisymmetric Slipless Indentation of an Infinite Elastic Cylinder," *SIAM Journal of Applied Mathematics*, Vol. 15, 1967, pp. 219–227.

5 Miller, M. K., and Guy, W. T., "Numerical Inversion of the Laplace Transform by Use of Jacobi Polynomials," *SIAM Journal of Numerical Analysis*, Vol. 3, 1966, pp. 624–635.

6 Amemiya, A., and Taguchi, T., *Numerical Analysis and Fortran*, Maruzen, Tokyo, 1969.

7 Chen, E. P., "Transient Response of a Finite Crack in a Strip With Stress-Free Edges," ASME JOURNAL OF APPLIED MECHANICS, Vol. 48, 1981, pp. 681–682.

8 Itou, S., "The Effect of Couple-Stresses on Stress Concentrations Around a Circular Hole in a Strip Under Tension," *International Journal of Engineering Science*, Vol. 14, 1976, pp. 861–867.

Downloaded 02 May 2010 to 171.66.16.246. Redistribution subject to ASME license or copyright; see http://www.asme.org/terms/Terms_Use.cfm

R. L. Ryan

S. Mall

Department of Mechanical Engineering,
University of Maine at Orono,
Orono, Me. 04469

Interaction of a *P*-Wave With a Laterally Stiffened Slot

The interaction of a longitudinal wave with a narrow cavity or slot that contains an inclusion is considered. A singular integral equation is derived for the scattered field and the integral equation is solved numerically by a Gauss-Chebyshev technique. The stress intensity at the ends of the slot is obtained as a function of frequency and inclusion stiffness for both a continuous and discrete element inclusion.

Introduction

The effect of frequency on the stress intensity at the ends of a crack due to the interaction of a *P*-wave has been determined by Mal [1]. Later, Jain and Kanwal [2] conducted a similar study for a rigid inclusion, and obtained results valid for low frequencies. The present study concerns the related problem of *P*-wave interaction with a narrow cavity or slot that contains an inclusion. The inclusion is modeled both as a continuous element and as a series of discrete elements. In each model the inclusion is assumed to possess a lateral stiffness only. That is, the longitudinal and flexural stiffness, as well as the inertia of the inclusion, are neglected. The discrete element model may be regarded, for example, as a series of lateral braces set in a long, narrow tunnel.

In the present study the stress intensity at the ends of the slot is determined by means of a singular integral equation formulation, coupled with a Gauss-Chebyshev numerical technique. This approach has been applied recently to various elastodynamic crack problems (e.g. [3–5]). The influence of frequency and stiffness on the stress intensity is determined for a moderate frequency range and a wide stiffness range, and the results are compared with those of [1] and [2].

Formulation

Consider an infinite elastic medium of density ρ and Lamé constants λ and μ. The medium contains a narrow cavity or slot with dimension h and $2l$ as shown in Fig. 1. It is assumed that $h/l << 1$, and that as $h \to 0$ the slot is equivalent to a line crack. For convenience the unit of length is taken as the half-length of the slot, so that $l = 1$.

Let the medium be excited by a harmonic *P*-wave of frequency ω, and suppose the wave is at normal incidence to the slot. If $u_j e^{-i\omega t}$, $j = 1,2$ denote the displacement components of the scattered waves, then the associated stress components may be expressed as

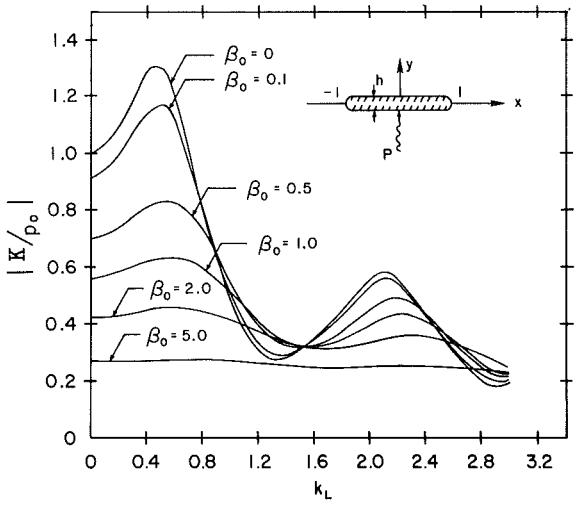

Fig. 1 Stress intensity versus frequency: continuous stiffener

$$\tau_{jk} = \mu^{-1}\sigma_{jk} = (\kappa^2 - 2)\delta_{jk}u_{l,l} + u_{j,k} + u_{k,j}\ , \quad j,k,l = 1,2 \tag{1}$$

where $\kappa^2 = (\lambda + 2\mu)/\mu$, and the time factor is understood. The scattered field, of course, must obey the equations

$$u_{j,ll} + (\kappa^2 - 1)u_{l,lj} + k_T{}^2 u_j = 0 \tag{2}$$

in which $k_T = \kappa k_L = \omega/c_T$, and $c_T = (\mu/\rho)^{12}$. Henceforth the notation (u,v) and the usual notation for stress components will be employed. Thus, if the incident wave is described as

$$u^{(i)} = 0, \quad v^{(i)} = ik_L \phi_0 e^{i(k_L y - \omega t)}, \tag{3}$$

where ϕ_0 is a constant, then the incident normal stress is

$$\tau_y{}^{(i)} = p_0 = -\kappa^2 k_L{}^2 \phi_0, \quad y = 0 \tag{4}$$

On account of symmetry with respect to the plane $y = 0$ it is sufficient to obtain the scattered field for $y \geq 0$. Further, since $h << 1$ the conditions in the contact region may be applied on $y = 0$. Thus, if the inertia of the inclusion is neglected, the normal stress in the contact region may be expressed as

$$\tau_{ys} = \frac{1}{2}(v_+ - v_-)\ \beta(x), \quad |x| < 1, \tag{5}$$

where $(v_+ - v_-)$ is the jump in vertical displacement across the slot, and $\beta(x)$ is a stiffness factor. The shear stress in the contact region, however, is assumed absent.

Contributed by the Applied Mechanics Division for publication in the JOURNAL OF APPLIED MECHANICS.

Discussion on this paper should be addressed to the Editorial Department, ASME, United Engineering Center, 345 East 47th Street, New York, N.Y. 10017, and will be accepted until two months after final publication of the paper itself in the JOURNAL OF APPLIED MECHANICS. Manuscript received by ASME Applied Mechanics Division, February, 1982; final revision, June, 1982.

Copyright © 1983 by ASME
Downloaded 02 May 2010 to 171.66.16.246. Redistribution subject to ASME license or copyright; see http://www.asme.org/terms/Terms_Use.cfm

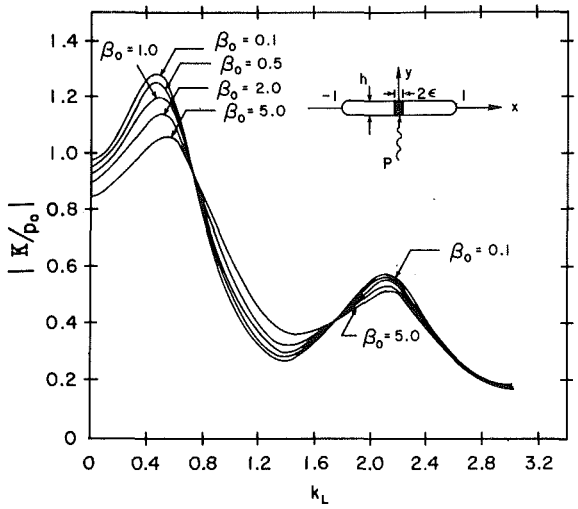

Fig. 2 Stress intensity versus frequency: discrete stiffener, $n = 0$

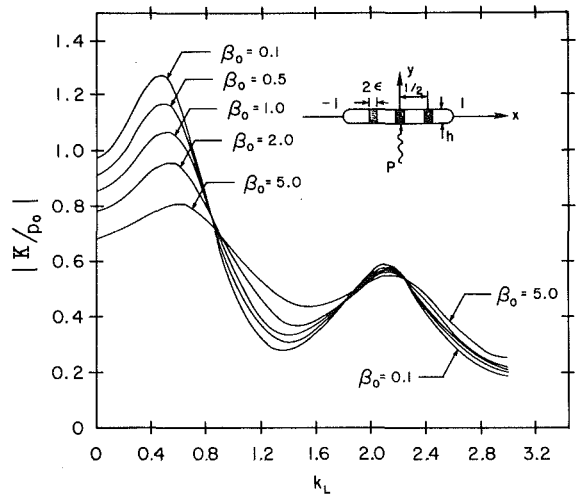

Fig. 3 Stress intensity versus frequency: discrete stiffener, $n = 1$

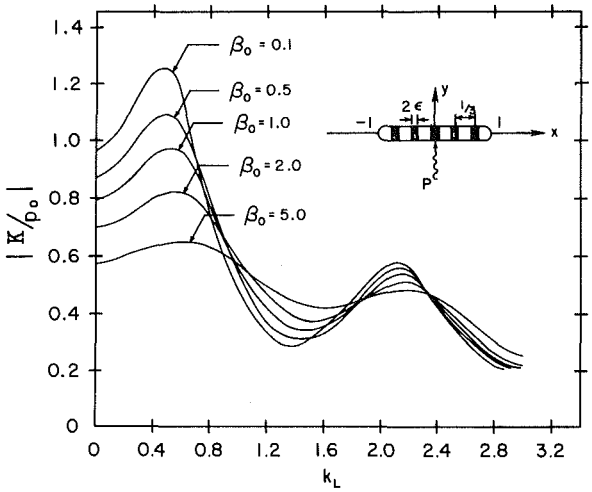

Fig. 4 Stress intensity versus frequency: discrete stiffener, $n = 2$

The stiffness factor for the continuous inclusion, based on a unit contact area, is simply $\beta(x) = \beta_0 = 2E/\mu h$, where E is Young's modulus of the inclusion. For the discrete element model we consider n elements, each of width 2ϵ, placed symmetrically with respect to $x=0$ at equal intervals $d = 1/n+1$. The inserts in Figs. 2-4 correspond to the models in which $n=0$, 1, 2, respectively. It is noted that the maximum number of elements depends on the half-element width ϵ. We express the stiffness factor for the discrete element model as $\beta(x) = \beta_0 r_n(x)$, where

$$r_n(x) = H(\epsilon - |x|), \quad n=0$$

$$r_n(x) = H(\epsilon - |x|) + \frac{1}{2}\sum_{m=1}^{n} [\mathrm{sgn}(md+\epsilon-|x|) + \mathrm{sgn}(|x|-md+\epsilon)], \quad n \geq 1. \tag{6}$$

In (6) $H(\cdot)$ and $\mathrm{sgn}(\cdot)$ designate the unit step and signum functions, respectively.

Inserting the appropriate stiffness factor in (5), the conditions on $y=0$ are as follows

$$\tau_{xy} = 0, \quad |x| \geq 0, \tag{7}$$

$$\tau_y = -\tau_y^{(i)} + \tau_{ys}, \quad |x| < 1, \tag{8}$$

$$v = 0, \quad |x| \geq 0, \tag{9}$$

where $v = 1/2\,(v_+ - v_-) = v_+$, and $\tau_y^{(i)}$ is defined by (4). Apart from satisfying equations (2) and conditions (7)-(9), the scattered field is expected to give rise to a crack-like stress singularity at the ends of the slot.

Through the use of the conventional Fourier transform approach, equations (2) and conditions (7)-(9) may be shown to reduce to a singular integral equation. Omitting the lengthy but straightforward calculations, the following equation is obtained.

$$i\int_{-1}^{1} v'(s)\, Q(s-x)\, ds = \tau_{ys}(x) - \tau_y^{(i)}(x), \quad |x| < 1, \tag{10}$$

where $v'(s)$ denotes $\partial/\partial s\, v(s,0)$, and

$$Q(s-x) = P_L(s-x) - P_T(s-x), \tag{11}$$

$$2\pi i\, k_T^2\, P_L(s-x) = -\left(2\frac{\partial^2}{\partial x^2} + k_T^2\right)^2 \int_0^\infty (\xi\alpha_L)^{-1} \sin[(s-x)\xi]\, d\xi, \tag{12}$$

$$2\pi i\, k_T^2\, P_T(s-x) = -4\,\frac{\partial^2}{\partial x^2}\left(\frac{\partial^2}{\partial x^2} + k_T^2\right)\int_0^\infty (\xi\alpha_T)^{-1}\sin[(s-x)\xi]\, d\xi. \tag{13}$$

In (12) and (13) $\alpha_L = (\xi^2 - k_L^2)^{1/2}$ and $\alpha_T = (\xi^2 - k_T^2)^{1/2}$ are the usual attenuation functions for elastic waves, and the integrals are indented at the branch points $\xi = k_L$ and $\xi = k_T$, respectively. Closed-form expressions are obtained by writing the integral in (12) as

$$\int_0^\infty (\xi\alpha_L)^{-1}\sin u\xi\, d\xi = \int_0^u dt \int_0^\infty \alpha_L^{-1}\cos t\xi\, d\xi,$$

and likewise for the integral in (13). Next, performing the indicated operations and using the tabulated results [10]

$$\int_0^\infty \alpha_L^{-1}\cos u\xi\, d\xi = i\pi/2\, H_0^{(1)}(k_L|u|), \tag{14}$$

$$\int_0^u H_0^{(1)}(k_L|t|)\, dt = u\, F(k_L|u|) \tag{15}$$

gives

$$P_L(u) = (1-\kappa^{-2})k_L\, H_1^{(1)}(k_L|u|)\,\mathrm{sgn}\,u + (\kappa^2 u)^{-1} H_2^{(1)}(k_L|u|) - 1/4\kappa^2 k_L^2\, uF(k_L|u|),$$

$$P_T(u) = u^{-1}H_2^{(1)}(\kappa k_L|u|), \tag{17}$$

where

$$F(k_L|u|) = H_0^{(1)}(k_L|u|) + \pi/2G(k_L|u|),$$

Downloaded 02 May 2010 to 171.66.16.246. Redistribution subject to ASME license or copyright; see http://www.asme.org/terms/Terms_Use.cfm

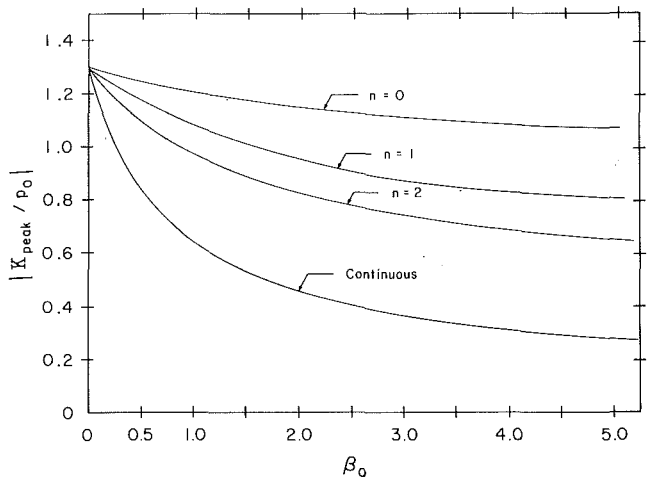

Fig. 5 Peak stress intensity versus stiffness parameter

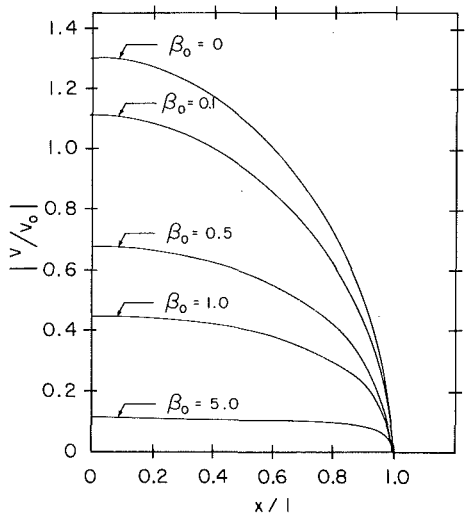

Fig. 6 Slot displacement: continuous stiffener, $k_L = 0.4$

$$G(k_L|u|) = S_0(k_L|u|)H_1^{(1)}(k_L|u|) - S_1(k_L|u|)H_0^{(1)}(k_L|u|), \quad (18)$$

and $S_0(\cdot)$ and $S_1(\cdot)$ denote Struve functions. From (16) and (17) it can be shown that $Q(s-x)$ has a Cauchy-type singularity. Hence the integral in (10) is a principal value.

In addition to equation (10), the constraint condition

$$\int_{-1}^{1} v'(s)\, ds = 0 \quad (19)$$

is required to ensure a single-valued solution.

On account of the expected crack-like singularity at $x = \pm 1$, we set

$$v'(x) = p_0/\mu\pi\, u(x)(1-x^2)^{-1/2}, \quad |x|<1, \quad (20)$$

and assume $u(x)$ is bounded. Then putting (20) into (10) and (19), and using (4) and (5) gives

$$\frac{1}{\pi}\int_{-1}^{1}(1-s^2)^{-1/2}\, u(s)\, [i\, Q(s-x) - \beta(x)\, H(x-s)]\, ds = 1, \quad |x|<1, \quad (21)$$

$$\frac{1}{\pi}\int_{-1}^{1}(1-s^2)^{-1/2}\, u(s)\, ds = 0. \quad (22)$$

Once the solution of (21) and (22) is obtained, the slot displacement is computed as

$$v(x) = p_0/\mu\pi\int_{-1}^{x} u(s)\,(1-s^2)^{-1/2}\, ds. \quad (23)$$

Numerical Solution

Equations (21) and (22) can be solved numerically by the Gauss-Chebyshev collocation scheme developed by Erdogan and Gupta [6]. This technique, although relatively inefficient compared to some alternative techniques (see, e.g. [7-9]), has the advantage of simplicity. Following the procedure described in [6] leads to the algebraic system

$$\frac{1}{N}\sum_{1}^{N} u_p(i\, Q_{p_q} - \beta_q\, H_{P_q}) = 1, \quad q = 1,2,\ldots N-1, \quad (24)$$

$$\frac{1}{N}\sum_{1}^{N} u_p = 0, \quad (25)$$

where Q_{pq} denotes $Q(s_p, x_q)$, etc., $s_p = \cos(2p-1)\pi/2N$, and $x_q = \cos q\pi/N$. The solution of the algebraic system can be made to approximate the exact solution to any degree of accuracy by choosing N sufficiently large. To maintain a given degree of accuracy, however, N must increase with frequency.

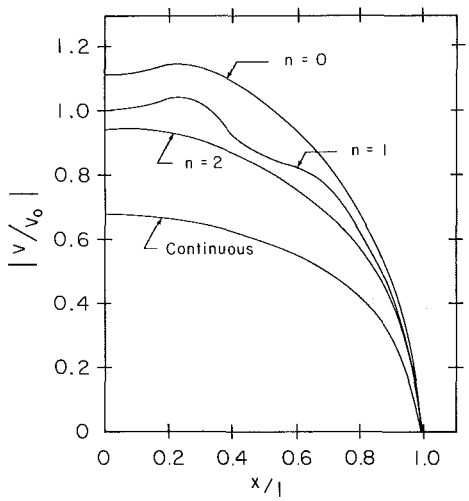

Fig. 7 Slot displacement: discrete stiffener, $n = 0, 1, 2., \beta_0 = 0.5$, $k_L = 0.4$

Stress Intensity

The left side of equation (10) represents the normal stress on $y = 0$ for $|x| > 1$ as well as for $|x| < 1$. As $|x| \to 1+$, the normal stress follows by extracting the singular part of the kernel and integrating the result. In terms of the replacement function $u(x)$, we get

$$\tau_y = \frac{p_0}{\mu\pi}\left(\frac{\kappa^2-1}{\kappa^2}\right)\frac{u(1)}{\sqrt{2(x-1)}}, \quad x \to 1+. \quad (26)$$

Defining the stress intensity as

$$K = \lim_{x\to 1+} \mu\, \tau_y\sqrt{2(x-1)} \quad (27)$$

supplies the result

$$K = \frac{p_0}{\pi}\left(\frac{\kappa^2-1}{\kappa^2}\right) u(1). \quad (28)$$

Results

Equations (24) and (25) were solved by a complex computer program using $N = 20$ and Poisson's ratio equal to 1/4 ($\kappa^2 = 3$). On the basis of random check using $N = 40$, it is

Downloaded 02 May 2010 to 171.66.16.246. Redistribution subject to ASME license or copyright; see http://www.asme.org/terms/Terms_Use.cfm

estimated that the results are accurate to within about 3 percent for the frequency range considered. The stress intensity and slot displacement were computed for a moderate range of frequencies and for various values of the stiffness factor $\beta(x)$. The results for the continuous stiffener model are illustrated in Fig. 1. The curve marked $\beta_0 = 0$ represents an unstiffened slot or crack. This curve agrees well with that given by Mal [1]. By comparison, the remaining curves show the stiffening effect of the inclusion. It is observed that as the stiffness increases the stress intensity decreases, and the oscillations are essentially eliminated. Additionally, a gradual increase occurs in the frequency of the peak intensity. Now from reference [2] the stress intensity for a rigid inclusion is of the order $(\log k_L)^{-1}$ for $k_L << 1$. A rigid inclusion, of course, would be approximated by our model as $\beta_0 \to \infty$. Thus our results are consistent, albeit loosely, with those of [2].

Figures 2–4 illustrate the corresponding results for a discrete stiffener model in which $\epsilon = 0.05$ and $n = 0, 1, 2$. As shown, the stiffening effect becomes more pronounced as n increases. The effect on the peak intensity is illustrated more clearly in Fig. 5.

The slot displacement is shown in Figs. 6 and 7 for the continuous and discrete models, respectively. These figures were arrived at by a numerical evaluation of the integral in (23), using $k_L = 0.4$. The results in Fig. (7) correspond to $\beta_0 = 0.5$, and in each figure $v_0 = P_0/\mu(\kappa^2/\kappa^2 - 1)$. As shown, the results exhibit a similar trend as those for the stress intensity. In particular, it is noticed in Fig. 7 that the perturbations due to the stiffeners become quickly suppressed as the number of elements is increased.

References

1 Mal, A. K., "Interaction of Elastic Waves With a Griffith Crack," *International Journal of Engineering Science*, Vol. 8, 1970, pp. 763–776.

2 Jain, D. L., and Kanwal, R. P., "Diffraction of Elastic Waves by Two Coplanar and Parallel Rigid Strips," *International Journal of Engineering Science*, Vol. 10, 1972, pp. 925–937.

3 Stone, S. F., Ghosh, M. L., and Mal, A. K., "Diffraction of Antiplane Shear Waves by an Edge Crack," ASME JOURNAL OF APPLIED MECHANICS, Vol. 47, 1980, pp. 359–362.

4 Achenbach, J. D., Keer, L. M., and Mendelsohn, D. A., "Elastodynamic Analysis of an Edge Crack," ASME JOURNAL OF APPLIED MECHANICS, Vol. 47, 1980, pp. 551–556.

5 Achenbach, J. D., and Brind, R. J., "Scattering of Surface Waves by a Subsurface Crack," *Journal of Sound and Vibration*, Vol. 76, 1981, pp. 43–56.

6 Erdogan, F., and Gupta, G. D., "On the Numerical Solution of Singular Integral Equations," *Quarterly of Applied Mathematics*, Vol. 30, 1972, pp. 525–534.

7 Theocaris, P. S., and Ioakimidis, N. I., "Stress Intensity Factors at Crack Tips Near Boundaries or Other Geometrical Discontinuities," *International Journal of Fracture*, Vol. 15, 1979, pp. 419–428.

8 Gerasoulis, A., and Srivastav, R. P., "A Method for the Numerical Solution of Singular Integral Equations With a Principal Value Integral," *International Journal of Engineering Science*, Vol. 19, 1981, pp. 1293–1298.

9 Gerasoulis, A., "Piecewise Polynomial Approximations in the Solution of Singular Integral Equations," *Advances in Computer Methods for Partial Differential Equations, IV*, Vichnevetsky, R., and Stepleman, R. S., eds., I.M.A.C.S., 1981, pp. 386–390.

10 Abramowitz, M., and Stegun, I. A., *Handbook of Mathematical Functions*, Dover, New York, 1965, p. 480.

Downloaded 02 May 2010 to 171.66.16.246. Redistribution subject to ASME license or copyright; see http://www.asme.org/terms/Terms_Use.cfm

Nonlocal and Nonlinear Friction Laws and Variational Principles for Contact Problems in Elasticity

J. T. Oden
Mem. ASME

E. B. Pires

Texas Institute for Computational Mechanics,
Department of Aerospace Engineering
and Engineering Mechanics,
The University of Texas at Austin,
Austin, Texas 78712

The use of the classical Coulomb law of friction in the formulation of contact problems in elasticity leads to both physical and mathematical difficulties; the former arises from the fact that this law provides a poor model of frictional stresses at points on metallic surfaces in contact, and the latter is due to the fact that the existence of solutions of the governing equations can be proved only for very special situations. In the present paper, nonclassical friction laws are proposed in an attempt to overcome both of these difficulties. We consider a class of contact problems involving the equilibrium of linearly elastic bodies in contact on surfaces on which nonlocal and nonlinear friction laws are assumed to hold. The physics of friction between metallic bodies in contact is discussed and arguments in support of the theory are presented. Variational principles for boundary-value problems in elasticity in which such nonlinear nonlocal laws hold are then developed. A brief discussion of the questions of existence and uniqueness of solutions to the nonlocal and nonlinear problems is given.

Introduction

In 1781, the French engineer C. A. Coulomb published his "Théorie des Machines Simples" in which he presented his celebrated law of friction. This work earned him a double prize from the French Royal Academy of Sciences in 1785. The classical Coulomb law of static dry friction, of course, asserts that *relative sliding between two bodies in contact along plane surfaces will occur when the net shear force parallel to the plane reaches a critical value proportional to the net normal force pressing the two bodies together. The constant of proportionality is called the coefficient of friction.*

It can be argued that as a basis for contact problems in the theory of elasticity, Coulomb's law is not acceptable from either a physical or a mathematical point of view. From the purely physical side, it has been recognized for many years that Coulomb's law is capable of describing only friction effects between effectively rigid bodies and gross sliding of one body relative to another. Indeed, it is clear that Coulomb himself never intended that his law be applied pointwise in boundary-value problems in elasticity; the foundations of continuum mechanics, particularly the concept of stress and the equations of linear elastostatics, were only fully developed many decades after Coulomb proposed his law, and the first successful formulation of a contact problem in elasticity came over a full century after Coulomb's work. From the mathematical point of view, it is known (see Duvaut [4] and also Duvaut and Lions [5]) that if Coulomb's law is applied pointwise in contact problems involving linearly elastic bodies, then the contact stress σ_n developed normal to the contact surface is ill defined. Except for some very special cases (e.g., Nečas, Jarušek, and Haslinger [10]) the fundamental question of existence of solutions of the friction problem is open (for other related open questions, see Duvaut and Lions [5]).

There are several aspects of actual friction phenomena between metallic bodies that suggest alternative friction laws which represent a marked departure from the classical formulations. First, we mention the obvious nonlocal character of the mechanism by which normal stresses are distributed on machined contact surfaces. These stresses are transmitted over junctions formed by deformed asperities and are not concentrated at isolated points on the contact surface. Second, we note that upon the application of loads, experiments show that there always exists a small tangential displacement of points on the contact surfaces due to the elastic and elastoplastic deformation of these junctions; "sliding" occurs when these junctions are actually fractured. Since these junctions can be recovered upon a quasi-static reversal of loads, the actual "adhesion-sliding" friction mechanism is highly nonlinear and depends on the elastoplastic properties of the metal oxide and contaminant film on the contact surfaces.

Independent of the nonlinear character of local friction phenomena, there are also mathematical reasons to expect that a nonlocal friction law might lead to a more tractable theory. Recently, Duvaut [4] published a brief note in which he observed that the source of difficulties in establishing an

Contributed by the Applied Mechanics Division for publication in the JOURNAL OF APPLIED MECHANICS.

Discussion on this paper should be addressed to the Editorial Department, ASME, United Engineering Center, 345 East 47th Street, New York, N.Y. 10017, and will be accepted until two months after fianl publication of the paper itself in the JOURNAL OF APPLIED MECHANICS. Manuscript received by ASME Applied Mechanics Division April, 1982.

Copyright © 1983 by ASME
Downloaded 02 May 2010 to 171.66.16.246. Redistribution subject to ASME license or copyright; see http://www.asme.org/terms/Terms_Use.cfm

existence theory for Signorini's problem with Coulomb friction was the lack of smoothness of the normal contact pressure σ_n. Therefore, by considering, instead, a proper mollification of the normal stresses on the contact boundary he was able to state that the principal obstacles in the way of deriving an existence and uniqueness theory for contact problems with friction could be overcome. One interpretation of such a smoothing of the contact pressure is as a result of nonlocal effects arising from micromechanical phenomena taking place on the contact regions.

In the present study, we propose nonlinear, nonlocal friction laws for contact problems involving linearly elastic bodies and we present variational principles for contact problems in elastostatics in which these laws hold. Roughly speaking, a nonlocal friction law proposes that *impending motion at a point of contact between two deformable bodies will occur when the shear stress at that point reaches a value proportional to a weighted measure of the normal stresses in a neighborhood of the point*. The character of the effective local neighborhood and the manner in which neighborhood stresses contribute to the sliding condition depends on features of the microstructure of the materials.

While such nonlocal laws do lead to a mathematically tractable theory, they still do not capture the effects of the tangential elastic-plastic deformations of the contact junctions mentioned earlier. To accommodate such effects, we present a further amendment which provides for small but nonzero, elastic tangential displacements at the contact surface for tangential stresses below a certain critical level. For shear stresses at or near this critical level, substantially larger motions can occur which effectively represent large tangential motions such as sliding. This critical value may be proportional to a weighted measure of the normal stresses in a neighborhood of the point on the contact surface.

An interesting feature of our results is that these nonconventional friction laws are given in terms of three positive material parameters: ν, ρ, and ϵ. The parameter ν is the coefficient of friction, although its actual interpretation is somewhat more complex than that of classical mechanics. The

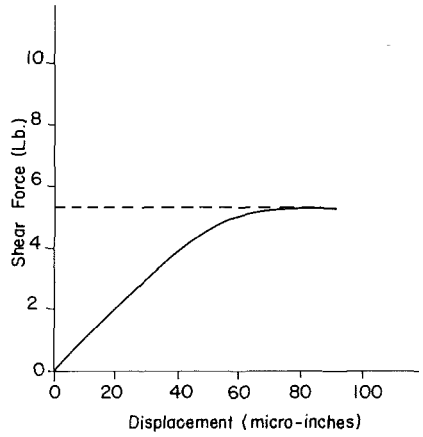

Fig. 1 Measured shear-tangential displacement variations after the experiments of Johnson [8]

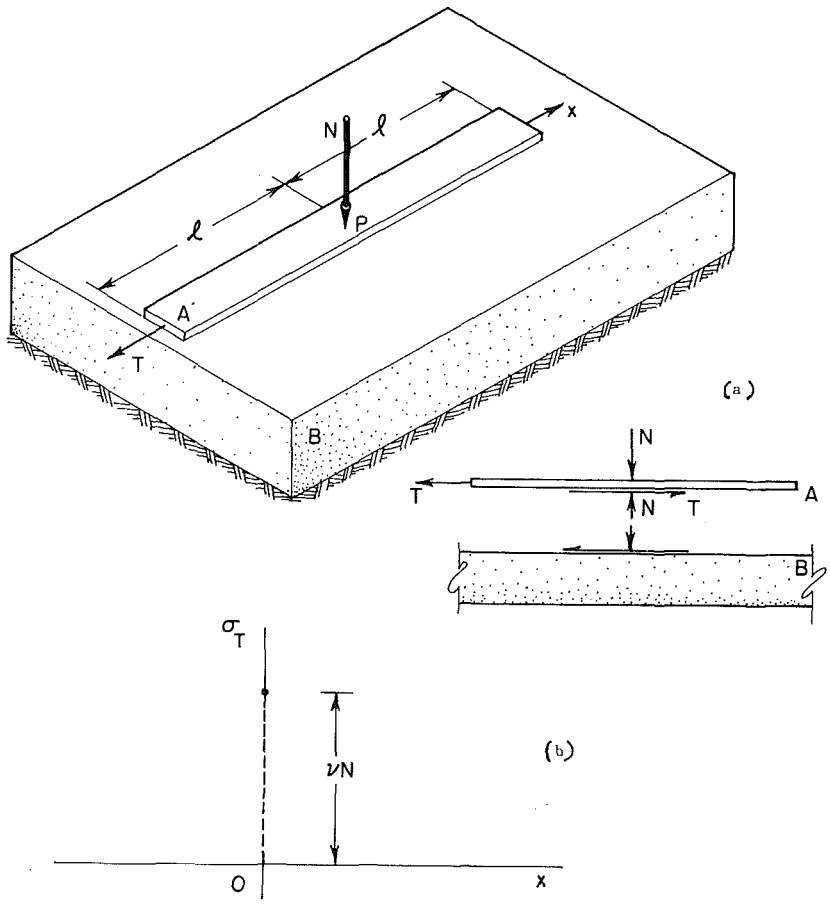

Fig. 2 (*a*)A thin strip *A* pressed on an elastic block *B*; (*b*) shear stress distribution (symbolic) assuming a pointwise Coulomb law of friction

Downloaded 02 May 2010 to 171.66.16.246. Redistribution subject to ASME license or copyright; see http://www.asme.org/terms/Terms_Use.cfm

parameter ρ quantifies the nonlocal character of the response; for $\rho = 0$ a fully local law is obtained. Finally, ϵ is a measure of the tangential stiffness of the elastic-plastic junctions on the contact surface; the case $\epsilon = 0$ corresponds to a fully rigid response – full adhesion or full sliding of contact surfaces. Thus, by allowing ρ and ϵ to approach zero, we can recover the classical, local, pointwise formulation of contact problems in elastostatics based on Coulomb's law.

Following this introduction, we give a brief account of the physics of friction as well as a justification of specific friction models. Several variational principles for boundary-value problems in elasticity in which nonlocal and nonlinear laws are assumed to hold are derived in Section 3. The results of some theoretical studies of these principles are summarized in Section 4. Our results include conditions sufficient to guarantee the existence and uniqueness of solutions to the variational problems as well as results that establish the asymptotic behavior of solutions as parameters ρ and ϵ tend to zero.

2 A Basis for Nonlocal and Nonlinear Friction Laws

2.1 Micromechanics of Friction. Friction phenomena have been the subject of considerable experimental and theoretical research over the last 30 years and its study is a popular and important aspect of modern mechanical engineering design. A standard reference is the monumental two-volume treatise by Bowden and Tabor [2, 3]; more concise accounts can be found in standard texts on the subject (e.g. Rabinowicz [12]).

To understand friction, one must first appreciate the role of the microstructure of the materials involved. Consider an experiment in which two metallic bodies are placed in contact along two apparently machined flat surfaces. At microscopic levels, specifically at magnifications of 1000x to 5000x, machined metal surfaces are seen to be not smooth homogeneous planes, but rough contours with numerous irregularities which are large compared with molecular dimensions. We refer to these deviations from the plane as *asperities*.

When we press together two surfaces, actual contact initially occurs only at the peaks or summits of the asperities. Large areas of the surfaces are separated by a distance that is large compared with the range of molecular action, so that these gaps in the surfaces are completely separated and have no interaction with one another. The load is, therefore, initially supported at the tips of the asperities; the area of contact is extremely small, and the pressure at the points of contact, even for lightly loaded surfaces, is high. Plastic deformation of the tip of the asperities occurs at small loads while the bulk of the underlying metal deforms elastically. As the normal load is further increased, the asperities deform and fracture with the result that the local load is distributed over an area surrounding each deformed asperity. At this stage, each asperity has been flattened and the local contact forces are distributed over a neighborhood of the asperity. The *real area of contact* A_r (as opposed to the *apparent* area) is

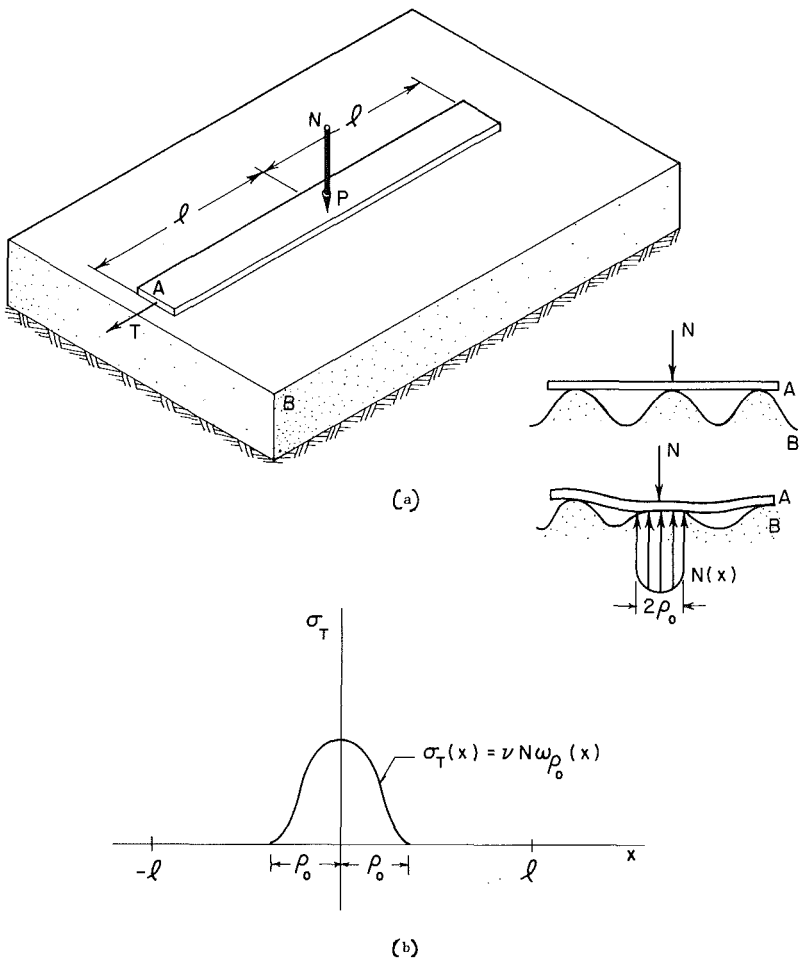

Fig. 3 (*a*)A thin strip *A* pressed onto an elastic block *B* with surface asperities; (*b*) the shear stress distribution at the point of impending motion

Downloaded 02 May 2010 to 171.66.16.246. Redistribution subject to ASME license or copyright; see http://www.asme.org/terms/Terms_Use.cfm

therefore the sum of the areas of all the surface irregularities that are touching and that support the load.

It is often assumed that the local plastic yield pressure p_0 is nearly constant and is comparable to the indentation hardness of the metal. Under these circumstances, the real area of contact for any one asperity bearing a load N_i is $A_i = N_i/p_0$; for the assembly of the asperities, the real contact area is

$$A_r = A_1 + A_2 + \ldots = \frac{N_1}{p_0} + \frac{N_2}{p_0} \ldots = \frac{N}{p_0} \tag{2.1}$$

where N is the total normal force pressing the surfaces together. The real area of contact is, thus, proportional to the load and independent of the size of the surfaces. Over these regions where intimate contact occurs, strong adhesion and welding of the metal surfaces takes place and the specimens become, in effect, a continuous solid. We refer to these regions as *junctions*.

Under most working conditions, metal surfaces are covered by a thin film of oxide, water vapor, and other absorbed impurities. The shear strength of these junctions can be strongly dependent on the shear strength of these surface films. In particular, it is the shear strength of this layer of oxide and impurities that determines the coefficient of friction and not, in general, the shear strength of the parent metals.

The application of a tangential force T creates a tendency for the two bodies to slide relative to each other. The contact pressure must then decrease (since it was near or equal the plastic yield stress). Some microscopic motion will occur (junction growth) even when T is small. If T is steadily increased, a value of sufficient magnitude to fracture the contaminant films is eventually reached and gross sliding occurs. It is customary to set the ratio of the magnitude of T at which sliding occurs to the net normal force N equal to the coefficient of friction ν. If s is the average shear strength of the interface, it follows that approximately

$$T = A_r s \tag{2.2}$$

i.e., T is independent of the apparent area of contact (since A_r is). Then substituting for A_r, we obtain

$$T = \frac{s}{p_0} N \quad \text{or} \quad \nu = \frac{s}{p_0} \tag{2.3}$$

i.e., T is directly proportional to the load (or ν is independent of the load).

As an idealization of the contact surfaces, one may assume that the asperities are superposed on the surface of spherical protuberances with a larger radius of curvature. It is then possible to consider that although each individual asperity at the interface will deform plastically, the deformation of each spherical protuberance will be elastic. This idealization has two purposes: first, the area of real contact still remains approximately proportional to the load, although the overall deformation is elastic (see Archard [1]); second, it allows us to treat each region of contact as being roughly circular (see microphotographs in Bowden and Tabor [3, p 71]) and to regard the contact pressure as being essentially symmetric, attaining its maximum magnitude at the center of the circle of contact, in a manner consistent with the well-known analysis of Mindlin [9].

We emphasize that the junctions through which loads are transmitted from one body to another are not rigid; indeed, they are composed of a deformable composite of metal, metal oxide, and surface contaminant which, for our purposes, can be assumed to be elastoplastic or nonlinearly elastic. Several researchers have actually measured the tangential microdisplacements that occur in friction experiments on metals, prior to gross sliding of the surfaces, and we mention as examples the works of Johnson [8], Bowden and Tabor [3], and Rabinowicz [12]. Figure 1 reproduces a typical result of static displacement tests of Johnson [8] which involved the contact of hard steel balls with the flat end of a hard steel roller. Microdisplacements are produced by an applied shear force varying progressively from zero to the value necessary to produce slip.

2.2 A Nonlocal Friction Law. In order to develop a basis for a nonlocal friction law we consider here the two simple physical models shown in Figs. 2 and 3. Figure 2, a thin weightless strip A of length $2l$ is pressed against a fixed elastic block B by a concentrated normal force N applied at its midpoint P; then a force T is applied to the strip and is increased slowly in magnitude until motion (sliding) of the strip relative to the block occurs. For this idealized situation, designed to emphasize the local character of the classical Coulomb law of friction, we are interested in calculating the distribution of frictional (shear) stresses between the strip and the block assuming that Coulomb's law holds and that the coefficient of friction ν is given.

We consider the origin of a coordinate axis x along the length of the strip to coincide with the midpoint P of the strip. Then, the only point on the contact surfaces between bodies A and B at which a resistive force can be developed is at an isolated point beneath P. Thus, impending sliding is reached when the resisting shear σ_T is formally given by

$$\sigma_T(x) = \nu N \delta(x); \quad -l < x < l \tag{2.4}$$

where δ is the Dirac delta corresponding to the point source at the origin. Of course, equation (2.4) is merely the symbolic representation of the distribution

$$<\sigma_T, \phi> = \nu N <\delta, \phi> = \nu N \phi(0) \tag{2.5}$$

for all test functions ϕ in the class $\mathfrak{D}(-l,l)$ of infinitely differentiable functions with support in the interval $(-l,l)$, where $<\ ,\ .>$ denotes duality pairing on distributions and test functions (i.e., the action of a distribution q on a test function ϕ is denoted $q(\phi) \equiv <q,\phi>$). Alternatively, δ can be interpreted as the limit of a δ-sequence, $\{\omega_\rho\}_{0<\rho}$, ω_ρ in $\mathfrak{D}(-l,l)$:

$$\phi(0) = \delta(\phi) = \lim_{\rho \to 0} \int_{-l}^{l} \omega_\rho \phi \, dx \quad \text{for all } \phi \text{ in } \mathfrak{D}(-l,l) \tag{2.6}$$

Then we have, instead of (2.5)

$$<\sigma_T, \phi> = \nu \lim_{\rho \to 0} <N\omega_\rho, \phi> \quad \text{for all } \phi \text{ in } \mathfrak{D}(-l,l) \tag{2.7}$$

We see that the classical pointwise version of Coulomb's law must be interpreted in the sense of distributions for this situation. As a typical δ-sequence, we mention:

$$\omega_\rho(x) = \begin{cases} c \exp[\rho^2/(x^2 - \rho^2)] & , |x| \le \rho \\ 0 & , |x| \ge \rho \end{cases} \tag{2.8}$$

A more realistic model of friction from the physical point of view is obtained if we take into account the microscopic aspects of the physics of friction described earlier. Specifically, the contact surface of body B will present asperities deviating from a smooth plane. As the normal force N is gradually applied, these asperities are gradually deformed and broken down until equilibrium of normal forces is reached. The normal force reaching body B through the strip A must then be distributed over the contact area of the deformed asperity as indicated in Fig. 3. We shall now assume that the asperity's finite transmission area is accounted for by using the δ-sequence $\{\omega_\rho\}$ of (2.8) keeping $\rho = \rho_0$, ρ_0 being the radius of the contact area of the deformed asperity. Since $N = N(x)$ is now a function, we have instead of (2.7),

$$\sigma_T(x) = \nu N(y) * \omega_{\rho_0}(x - y) \tag{2.9}$$

Downloaded 02 May 2010 to 171.66.16.246. Redistribution subject to ASME license or copyright; see http://www.asme.org/terms/Terms_Use.cfm

where * denotes the convolution of the two functions. Thus, we have arrived at a friction law in which impending motion occurs at a point x on the contact surface when the shear stress at that point reaches a value proportional to the weighed average of the normal stress in a neighborhood of the point. If ω_{ρ_0} is used to characterize this weighting function, then the neighborhood is a circular disk of radius ρ_0 centered at x, the maximum weight is given to the stress intensity at the center of the disk (the contact area of the deformed asperity), and exponentially decreasing weights are assigned to stress intensities as one moves from the center of the neighborhood outward to the periphery of the disk.

We can now generalize these results to the three-dimensional case: let $\mathbf{u}_T$ denote the relative tangential component of displacement of a point $\mathbf{x}=(x_1,x_2,x_3)$ on the contact surface between two deformable bodies and let $\sigma_n(\mathbf{u})$ and $\sigma_T(\mathbf{u})$ denote the normal and tangential stresses on the contact surface corresponding to the displacement field $\mathbf{u}$. Then

$$\left.\begin{array}{ll} |\sigma_T(\mathbf{u})| < \nu S_{\rho_0}(\sigma_n(\mathbf{u})) & \text{implies } \mathbf{u}_T = \mathbf{0} \\ |\sigma_T(\mathbf{u})| = \nu S_{\rho_0}(\sigma_n(\mathbf{u})) & \text{implies that there exists } \lambda \geq 0 \text{ such that } \mathbf{u}_T = -\lambda \sigma_T \end{array}\right\} \tag{2.10}$$

where S_{ρ_0} is an operator mollifying the normal stress distribution; e.g.,

$$S_{\rho_0}(\sigma_n(\mathbf{u}))(\mathbf{x}) = \int_{\Gamma_C} \omega_{\rho_0}(|\mathbf{x}-\mathbf{y}|)(-\sigma_n(\mathbf{u}(\mathbf{y})))dy \tag{2.11}$$

where $\mathbf{x}$ and $\mathbf{y}$ are points on the contact surface Γ_C.

We mention that nonlocal theories for other classes of problems in solid and fluid mechanics have been put forth by Eringen and Edelen [7]; a detailed account of this work can be found in Eringen [6].

2.3 Model of Nonlinear Friction. Both Coulomb's law and the nonlocal law given in (2.10) depict perfect rigid-adhesion-sliding conditions on the contact surface: they assert that there is absolutely no motion of points of one body relative to those of another if the tangential stress on the contact surface remains below some critical value τ; but when this limit is reached, unbounded motions can occur, the ensuing tangential displacement being directed opposite to the tangential stress vector. It was pointed out in the Introduction and in Section 2.1 that in physical experiments on contact, tangential displacements are produced by any nonzero tangential force developed on the contact surface since elastic-plastic deformations of the junctions will always accompany the application of tangential forces (recall Fig. 1).

To model this phenomenon, we shall consider a family of nonlinear friction laws of the form

$$\sigma_T(\mathbf{u}) = -\tau \phi_\epsilon(|\mathbf{u}_T|)\frac{\mathbf{u}_T}{|\mathbf{u}_T|} \tag{2.12}$$

where the function $\phi_\epsilon(\cdot)$ satisfies the following conditions:

$$\left.\begin{array}{l} (i)\ \phi_\epsilon \text{ is a continuous, monotone, real-valued function of the non-negative real numbers } r, \text{ depending on a parameter } \epsilon>0, \text{ such that} \\ \qquad 0 \leq \phi_\epsilon(r) \leq 1, \quad r \geq 0 \\ (ii)\ \lim_{\epsilon \to 0} \phi_\epsilon(r) = 1 \text{ for all } r>0 \\ (iii)\ \lim_{r \to \infty} \phi_\epsilon(r) = 1 \text{ for all } \epsilon>0 \end{array}\right\} \tag{2.13}$$

In (2.12), τ is a non-negative function of the displacement vector $\mathbf{u}$ representing the critical value that the tangential stress cannot exceed, i.e., $\tau = \nu|\sigma_n(\mathbf{u})|$ for the local case and $\tau = \nu S_\rho(\sigma_n(\mathbf{u}))$ for the nonlocal case. It will also be of interest, as will be seen later, to consider the case in which τ is a given (known) function of the position vector $\mathbf{x}$, thus no longer dependent on the displacement $\mathbf{u}$.

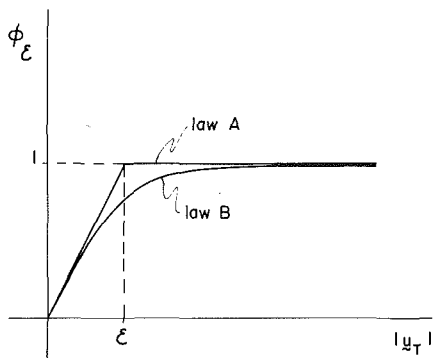

Fig. 4 Graphs of functions (2.14) and (2.15)

As specific examples, we select for ϕ_ϵ the following two functions:

$$(A)\ \phi_\epsilon(|u_T|) = \begin{cases} 1 & \text{if } |\mathbf{u}_T| > \epsilon \\ |\mathbf{u}_T|/\epsilon & \text{if } |\mathbf{u}_T| \leq \epsilon \end{cases} \tag{2.14}$$

$$(B)\ \phi_\epsilon(|\mathbf{u}_T|) = \tanh\frac{|\mathbf{u}_T|}{\epsilon} \tag{2.15}$$

It is readily seen that both of these functions satisfy (2.13). The first example represents an "elastic-perfectly plastic" type response in which slipping can occur only after a tangential displacement $|\mathbf{u}_T| > \epsilon$. On the other hand, the second example describes a situation in which the critical stress is approximated asymptotically as $|\mathbf{u}_T| \to \infty$. Both curves are depicted in Fig. 4. We notice that these are not the only possible choices and that several others can also be considered (e.g. arctan, etc.). Also, we observe that the slope of ϕ_ϵ at the origin, i.e., the derivative of ϕ_ϵ at zero displacement equals $1/\epsilon$. Thus ϵ provides a measure of the rigidity or stiffness of the elastic-plastic or nonlinear elastic junctions.

Finally, we wish to comment on the combination of a nonlocal law with a nonlinear law. A nonlocal-nonlinear law of friction will be of the form (2.12) with τ replaced by $\nu S_\rho(\sigma_n(\mathbf{u}))$, i.e.,

$$\sigma_T(\mathbf{u}) = -\nu S_\rho(\sigma_n(\mathbf{u}))\phi_\epsilon(|\mathbf{u}_T|)\frac{\mathbf{u}_T}{|\mathbf{u}_T|} \tag{2.16}$$

where S_ρ is of the form given in (2.11). If we allow $\rho \to 0$ maintaining $\epsilon > 0$ fixed we obtain a local nonlinear law, i.e.,

$$\sigma_T(\mathbf{u}) = -\nu|\sigma_n(\mathbf{u})|\phi_\epsilon(|\mathbf{u}_T|)\frac{\mathbf{u}_T}{|\mathbf{u}_T|} \tag{2.17}$$

On the other hand, if we allow $\epsilon \to 0$ for a given positive ρ we recover the perfect rigid-adhesion-sliding nonlocal law given in (2.10). Finally if both $\epsilon \to 0$ and $\rho \to 0$ the static Coulomb's law (local) for unilateral contact in the contact surface Γ_C is obtained:

$$\left.\begin{array}{ll} |\sigma_T|(\mathbf{u})| < \nu|\sigma_n(\mathbf{u})| & \text{implies } \mathbf{u}_T = \mathbf{0} \\ |\sigma_T(\mathbf{u})| = \nu|\sigma_n(\mathbf{u})| & \text{implies the existence of } \lambda \geq 0 \\ & \text{such that } \mathbf{u}_T = -\lambda\sigma_T \end{array}\right\} \tag{2.18}$$

Downloaded 02 May 2010 to 171.66.16.246. Redistribution subject to ASME license or copyright; see http://www.asme.org/terms/Terms_Use.cfm

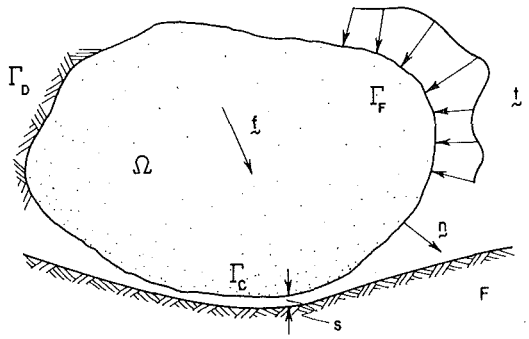

Fig. 5 An elastic body in contact with a rigid rough foundation

3 Variational Principles for Nonlocal-Nonlinear Friction

3.1 Signorini Problems With Nonlocal Nonlinear Friction. We consider here the Signorini problem of contact of a linearly elastic body with a rigid foundation on which nonlocal, nonlinear friction laws hold.

We begin our analysis by considering a linearly elastic body the particles of which occupy a smooth bounded domain $\bar{\Omega}$ in $\mathbb{R}^N$, $N=2,3$, with open interior Ω. The boundary Γ of the body is assumed to consist of three disjoint parts, Γ_D, Γ_F, and Γ_C, where Γ_D and Γ_F are the portions of the boundary on which the displacements and forces (tractions) are prescribed, respectively, and Γ_C is the candidate contact area; i.e. Γ_C is a portion of the boundary that contains the material surface which comes in unilateral contact with a rigid foundation $\mathcal{F}$ upon the application of loads (see Fig. 5). The external forces on the body consist of a prescribed body force field intensity $\mathbf{f}$ per unit volume and of surface tractions of intensity $\mathbf{t}$ per unit surface area.

We shall assume that Γ_D is perfectly fixed, so that

$$\mathbf{u}=\mathbf{0} \text{ on } \Gamma_D$$

$\mathbf{u}$ being the displacement field. On Γ_F we will have

$$\sigma_{ij}(\mathbf{u})n_i = t_j$$

where σ_{ij} $(\mathbf{u})$ is the stress produced by $\mathbf{u}$ and n_i are the components of the unit outward normal $\mathbf{n}$ to Γ. Here and throughout our presentation Cartesian index notation and the summation convention are employed. Since the body is assumed to be linearly elastic, Hooke's law holds so that

$$\sigma_{ij}(\mathbf{u}) = E_{ijkl}u_{k,l}$$

where E_{ijkl} are the usual elastic constants of the material, $u_{k,l} \equiv \partial u_k/\partial x_l$ and

$$E_{ijkl} = E_{jikl} = E_{klij} = E_{ijkl}$$
$$1 \le i, j, k, l \le N$$

Of course, particles within Ω are assumed to be in static equilibrium so that

$$\sigma_{ij}(\mathbf{u}),_j + f_i = 0 \text{ in } \Omega$$

The unilateral motion of particles of the body on the material surface Γ_C is constrained by the presence of a rigid foundation which is a given distance s from the body prior to the application of loads. Mathematically, this constraint is represented by the requirement that the normal displacement of boundary points cannot exceed s:

$$\mathbf{u}\cdot\mathbf{n} \le s \quad \text{on} \quad \Gamma_C \tag{3.1}$$

If $\mathbf{u}\cdot\mathbf{n}=s$ then contact is established, while $\mathbf{u}\cdot\mathbf{n}<s$ indicates the existence of a gap between the support and the body. Thus (3.1) represents a nonpenetration condition. If contact is not made (i.e., if $\mathbf{u}\cdot\mathbf{n}<s$) then the normal contact pressure $\sigma_n(\mathbf{u})=0$, where

$$\sigma_n(\mathbf{u}) = E_{ijkl}u_{k,l}n_in_j$$

Alternatively, if $\mathbf{u}\cdot\mathbf{n}=s$ at a point on Γ_C, then σ_n must be nonpositive:

$$\mathbf{u}\cdot\mathbf{n}=s \text{ implies } \sigma_n(\mathbf{u}) \le 0$$

Thus, the unilateral contact conditions on the contact surface Γ_C are:

$$\left.\begin{aligned} &\mathbf{u}\cdot\mathbf{n}-s\le 0, \quad \sigma_n(\mathbf{u})\le 0 \\ &\sigma_n(\mathbf{u})(\mathbf{u}\cdot\mathbf{n}-s)=0 \end{aligned}\right\} \text{on } \Gamma_C$$

Condition $\sigma_n(\mathbf{u})$ $(\mathbf{u}\cdot\mathbf{n}-s)=0$ signifies that the pressure can only be nonzero when there is contact.

There remains the characterization of friction on the contact surface Γ_C. In agreement with the nonlinear and nonlocal friction laws described in the preceding section, we will have

$$\left.\begin{aligned} &\text{If } \mathbf{u}\cdot\mathbf{n}<s, \quad \boldsymbol{\sigma}_T(\mathbf{u})=\mathbf{0} \\ &\text{If } \mathbf{u}\cdot\mathbf{n}=s, \\ &\boldsymbol{\sigma}_T(\mathbf{u}) = -\nu S_\rho(\sigma_n(\mathbf{u}))\phi_\epsilon(|\mathbf{u}_T|)\frac{\mathbf{u}_T}{|\mathbf{u}_T|} \end{aligned}\right\} \text{on } \Gamma_C \tag{3.2}$$

where S_ρ is of the form (2.11) and ϕ_ϵ is a nonlinear function of the type in (2.13) or (2.14). It is important to note that always

$$|\boldsymbol{\sigma}_T(\mathbf{u})| \le \nu S_\rho(\sigma_n(\mathbf{u}))$$

since $\phi_\epsilon(|\mathbf{u}_T|)\le 1$ for every $\epsilon>0$ and any $\mathbf{u}_T(\mathbf{x})$, $\mathbf{x}$ in Γ_C. By computing the inner product of both sides of the second equation (3.2) with $\mathbf{u}_T$, we can write, equivalently,

$$\boldsymbol{\sigma}_T(\mathbf{u})\cdot\mathbf{u}_T + \nu S_\rho(\sigma_n(\mathbf{u}))\phi_\epsilon(|\mathbf{u}_T|)|\mathbf{u}_T| = 0$$

Summarizing, the Signorini problem with nonlocal, nonlinear friction consists of seeking a displacement field $\mathbf{u}$, which satisfies the following system of equations and inequalities:

(1) Equilibrium equations

$$(E_{ijkl}u_{k,l}),_j + f_i = 0 \text{ in } \Omega \tag{3.3}$$

(2) Boundary conditions

(*a*) Prescribed displacements

$$u_i = 0 \quad \text{on} \quad \Gamma_D \tag{3.4}$$

(*b*) Prescribed traction

$$E_{ijkl}u_{k,l}n_j = t_i \text{ on } \Gamma_F \tag{3.5}$$

(*c*) Unilateral constraint

$$\mathbf{u}\cdot\mathbf{n}\le s, \ \sigma_n(\mathbf{u})\le 0,$$
$$\sigma_n(\mathbf{u})(\mathbf{u}\cdot\mathbf{n}-s)=0 \text{ on } \Gamma_C \tag{3.6}$$

(*d*) Friction condition

$$\boldsymbol{\sigma}_T(\mathbf{u}) = -\nu S_\rho(\sigma_n(\mathbf{u}))\phi_\epsilon(|\mathbf{u}_T|)\frac{\mathbf{u}_T}{|\mathbf{u}_T|} \quad \text{on } \Gamma_C \tag{3.7}$$

where

$$S_\rho(\sigma_n(\mathbf{u}))(\mathbf{x}) = \int_{\Gamma_C} \omega_\rho(|\mathbf{x}-\mathbf{y}|)(-\sigma_n(\mathbf{u}(\mathbf{y})))ds$$

and ω_ρ and ϕ_ϵ are given, respectively, by (2.8) and (2.14) or (2.15).

Downloaded 02 May 2010 to 171.66.16.246. Redistribution subject to ASME license or copyright; see http://www.asme.org/terms/Terms_Use.cfm

3.2 Variational Principles for Nonlocal, Nonlinear Friction. Relationship With the Classical Problems. We now introduce variational principles for the nonlocal, nonlinear Signorini problem and establish the relationship between the variational and the classical formulations.

Using the notation introduced previously, we define

V = space of admissible displacements. A displacement vector $\mathbf{v}$ will belong to V if and only if

(1) $\mathbf{v}=\mathbf{0}$ on Γ_C

(2) $\mathbf{v}$ produces finite (normalized) strain energy in the sense that the norm

$$\|\mathbf{v}\|_V=\left\{\int_\Omega v_{i,j}v_{i,j}dx\right\}^{1/2} \tag{3.8}$$

is finite, where $dx=dx_1dx_2\ldots dx_N$.

K = subset of V consisting of all admissible displacements $\mathbf{v}$ in V for which $\mathbf{v}\cdot\mathbf{n}\le s$ at all points on the contact surface Γ_C.

$a(\mathbf{u},\mathbf{v})$ = virtual work produced by the action of stresses $\sigma_{ij}(u)$ on strains caused by the displacement $\mathbf{v}$

$$=\int_\Omega E_{ijkl}u_{k,l}v_{i,j}dx$$

$j_{\rho,\epsilon}(\mathbf{u},\mathbf{v})$ = virtual work done by the frictional forces on the displacement $\mathbf{v}$

$$=\int_{\Gamma_C}\nu S_\rho(\sigma_n(\mathbf{u}))\psi_\epsilon(|\mathbf{v}_T|)ds$$

Here ds is an element of surface area on Γ_C and ψ_ϵ is the primitive of ϕ_ϵ: $\phi_\epsilon=\psi_\epsilon'$. For example,

$$\psi_\epsilon(|\mathbf{v}_T|)=\begin{cases}|\mathbf{v}_T|-\epsilon/2 & \text{if } |\mathbf{v}_T|>\epsilon\\ |\mathbf{v}_T|^2/2\epsilon & \text{if } |\mathbf{v}_T|\le\epsilon\end{cases} \tag{3.9}$$

when $\phi_\epsilon(|\mathbf{v}_T|)$ is given by (2.14) or

$$\psi_\epsilon(|\mathbf{v}_T|)=\epsilon\, ln\cosh\frac{|\mathbf{v}_T|}{\epsilon} \tag{3.10}$$

$f(\mathbf{v})$ = virtual work done by the external forces on the displacement $\mathbf{v}$

$$=\int_\Omega \mathbf{f}\cdot\mathbf{v}\,dx+\int_{\Gamma_F}\mathbf{t}\cdot\mathbf{v}\,ds$$

With the foregoing definitions and notations now established, we consider the following variational boundary-value problem:

Find an admissible displacement vector $\mathbf{u}$ in the set K such that

$$a(\mathbf{u},\mathbf{v}-\mathbf{u})+j_{\rho,\epsilon}(\mathbf{u},\mathbf{v})-j_{\rho,\epsilon}(\mathbf{u},\mathbf{u})\ge f(\mathbf{v}-\mathbf{u}) \tag{3.11}$$

for all admissible displacements $\mathbf{v}$ in K.

Inequality (3.11) is a statement of the principle of virtual work for an elastic body restrained by frictional forces of the type in (3.2). Note that this characterizes equilibrium configurations by an inequality rather than an equality because of the presence of the unilateral contact constraint $\mathbf{u}\cdot\mathbf{n}\le s$ on Γ_C. We also notice that the actual contact surface depends on the solution $\mathbf{u}$ and is, therefore, not known in advance.

Our first major result is stated in the following proposition, the proof of which is given in the Appendix.

Proposition 3.1: Let $\mathbf{u}$ be a sufficiently smooth solution of the Signorini problem with nonlocal, nonlinear friction (3.3)–(3.7). Then $\mathbf{u}$ is also a solution of the variational inequality (3.11). Conversely, if $\mathbf{u}$ is a solution of (3.11), then $\mathbf{u}$ also satisfies the system (3.3)–(3.7) if these relations are interpreted in a weak or distributional sense.

3.3 Other Related Friction Problems. Several friction problems can be obtained as special cases of the nonlocal, nonlinear problem discussed in the previous sections by allowing $\rho\to 0$ or $\epsilon\to 0$ or both $\rho,\epsilon\to 0$ or by restricting the dependence of the friction functional to its second variable. Results similar to those established in Proposition 3.1 can also be stated. Moreover, if $\nu S_\rho(\sigma_n(\mathbf{u}))$ is prescribed on Γ_C, and, hence, is independent of the displacement $\mathbf{u}$, the static friction problem thus obtained becomes equivalent to a constrained minimization problem involving a functional representing the associated potential energy. Thus, we have the following cases:

Case 1 ($\rho=0$). The friction law, which is now of a local type, is given by (2.17). Thus the system (3.3)–(3.6) together with condition (2.17) will produce a Signorini problem with local-nonlinear friction, which can be shown to be equivalent to the variational principle (3.11) with the functional $j_{\rho,\epsilon}(\cdot,\cdot)$ replaced by

$$j_\epsilon(\mathbf{u},\mathbf{v})=\int_{\Gamma_C}\nu|\sigma_n(\mathbf{u})|\psi_\epsilon(|\mathbf{v}_T|)ds$$

Case 2 ($\epsilon=0$). For this case, the friction law is given by (2.10). If we add this condition to the system (3.3)–(3.6) we will obtain a Signorini problem with nonlocal friction which may be seen to be equivalent to the variational inequality (3.11) if we replace $j_{\rho,\epsilon}(\cdot,\cdot)$ in (3.11) by the functional

$$j_\rho(\mathbf{u},\mathbf{v})=\int_{\Gamma_C}\nu S_\rho(\sigma_n(\mathbf{u}))|\mathbf{v}_T|ds$$

The proof of this equivalence differs in some aspects from the one given in the Appendix; it can be found in the unpublished report by Oden and Pires [11].

Case 3 ($\rho=\epsilon=0$). When both $\rho=0$ and $\epsilon=0$, the corresponding friction law is given by the conditions (2.18). The system (3.3)–(3.6) and (2.18) will then correspond to the Signorini problem with Coulomb friction. Duvaut and Lions [5] derived a variational principle characterizing this problem which is given by (3.11) if we replace the functional $j_{\rho,\epsilon}(\cdot,\cdot)$ by the functional

$$j(\mathbf{u},\mathbf{v})=\int_{\Gamma_C}|\sigma_n(\mathbf{u})|\,|\mathbf{v}_T|\,ds$$

Finally we mention as a last special case, an auxiliary problem which proves to be useful in the next section when we establish the conditions for the existence of solutions to the nonlocal, nonlinear friction problem. This auxiliary problem involves a friction law for which the critical or limiting value of the tangential stress is prescribed rather than being determined by the equilibrium displacement field $\mathbf{u}$. We will then have in the nonlinear case ($\epsilon>0$), a law of friction of type (2.12) where now τ is given on the contact surface Γ_C. In the case $\epsilon=0$, this friction law assumes the form:

$$\left.\begin{array}{l}|\boldsymbol{\sigma}_T(\mathbf{u})|<\tau \text{ implies } \mathbf{u}_T=\mathbf{0}\\ |\boldsymbol{\sigma}_T(\mathbf{u})|=\tau \text{ implies the existence of } \lambda\ge 0 \text{ such that}\\ \qquad\qquad \mathbf{u}_T=-\boldsymbol{\sigma}_T\end{array}\right\}\text{on } \Gamma_C \tag{3.12}$$

Thus, depending on ϵ being strictly positive or zero, we have the following cases.

Case 4 (τ *fixed,* $\epsilon>0$). The corresponding Signorini problem now consists of (3.3)–(3.6) together with the friction

Downloaded 02 May 2010 to 171.66.16.246. Redistribution subject to ASME license or copyright; see http://www.asme.org/terms/Terms_Use.cfm

condition (2.12) (τ given on Γ_C). The equivalent variational formulation of this problem is:

Find a displacement field $\mathbf{u}$ in K such that

$$a(\mathbf{u},\mathbf{v}-\mathbf{u})+j_{0_\epsilon}(\mathbf{v})-j_{0_\epsilon}(\mathbf{u})\geq f(\mathbf{v}-\mathbf{u}) \tag{3.13}$$

for all $\mathbf{v}$ in K

where

$$j_{0_\epsilon}=\int_{\Gamma_C}\tau\psi_\epsilon(|\mathbf{v}_T|)ds \tag{3.14}$$

Also, it is not difficult to show that in this case (3.13) is equivalent to the constrained minimization problem of finding $\mathbf{u}$ in K such that

$$I_\epsilon(\mathbf{u})\leq I_\epsilon(\mathbf{v}) \tag{3.15}$$

for all $\mathbf{v}$ in K, where the energy functional $I_\epsilon(\cdot)$ is defined by

$$I_\epsilon(\mathbf{v})=\frac{1}{2}a(\mathbf{v},\mathbf{v})-f(\mathbf{v})+j_{0_\epsilon}(\mathbf{v}) \tag{3.16}$$

Case 5 (τ fixed, $\epsilon=0$). The law of friction is now of the form (3.12) which, when added to the system (3.3)–(3.6), gives the corresponding Signorini problem. We emphasize here that condition (3.12) represents a law of friction different from Coulomb's law. It is easy to establish the equivalence between (3.3)–(3.6) together with (3.12) and (3.13) if we replace in (3.13) $j_{0_\epsilon}(\cdot)$ by the functional

$$j_0(v)=\int_{\Gamma_C}\tau|\mathbf{v}_T|ds \tag{3.17}$$

The energy functional for this case is defined by

$$I(\mathbf{v})=\frac{1}{2}a(\mathbf{v},\mathbf{v})-f(\mathbf{v})+j_0(\mathbf{v}),\quad \mathbf{v}\text{ in }K \tag{3.18}$$

Then problem (3.13) with $j_{0_\epsilon}(\cdot)$ replaced by $j_0(\cdot)$ is equivalent to the problem of seeking minimizers of the functional in (3.18) which satisfies the unilateral constraints.

Remark 3.1: It is interesting to note that when $\epsilon=0$ the functional $j_0(\cdot)$ defined in (3.16) in nondifferentiable while the nonlinear functional $j_{0_\epsilon}(\cdot)$ given by (3.14) is differentiable on all of V. Its derivative $Dj_{0_\epsilon}(\cdot)$ at the point $\mathbf{u}$, in the direction $\mathbf{v}$ is given by

$$Dj_{0_\epsilon}(\mathbf{u})\cdot\mathbf{v}=\int_{\Gamma_C}\tau\phi_\epsilon(|\mathbf{u}_T|)\frac{\mathbf{u}_T\cdot\mathbf{v}_T}{|\mathbf{u}_T|}ds \tag{3.19}$$

It is then possible to show that the variational inequality (3.13) is equivalent to the variational inequality

$$a(\mathbf{u},\mathbf{v}-\mathbf{u})+Dj_{0_\epsilon}(\mathbf{u})\cdot(\mathbf{v}-\mathbf{u})\geq f(\mathbf{v}-\mathbf{u}),\text{for all }\mathbf{v}\text{ in }K \tag{3.20}$$

The differentiability of the functional $j_{0_\epsilon}(\cdot)$ has important implications when we wish to consider finite element approximations of the friction problems discussed so far. In fact, the direct approximation of the variational problem considered in Case 5 ($\epsilon=0$) by finite elements through the minimization of the functional defined in (3.18) leads to a discrete system for which the most popular methods for solving nonlinear variational inequalities do not apply, owing to the nondifferentiability of $j_0(\cdot)$.

3.4 Estimate of the Difference Between the Solutions of the Friction Problems With $\epsilon<0$ (Nonlinear) and $\epsilon=0$. We wish to record here an estimate of the difference between the solutions of problem (3.11) and of the problem considered in Case 2 ($\epsilon=0$) of the preceding section, as a function of ϵ. The first result is concerned with the approximation of the functional $j_\rho(\cdot,\cdot)$ by the functional $j_{\rho,\epsilon}(\cdot,\cdot)$.

Proposition 3.2: For a given element $\mathbf{u}$ in K for which $\sigma_n(\mathbf{u})$ is well defined there exists a constant $c>0$ independent of ϵ, such that

$$|j_{\rho,\epsilon}(\mathbf{u},\mathbf{v})-j_\rho(\mathbf{u},\mathbf{v})|\leq c\,\epsilon \tag{3.21}$$

for all $\mathbf{v}$ in K. Thus, $j_{\rho,\epsilon}$ approximates j_ρ arbitrarily closely as $\epsilon\to 0$.

This result constitutes the basis for the proof of the following estimate:

Proposition 3.3: Let $\mathbf{u}_\epsilon$ denote a solution of (3.11) for fixed $\epsilon>0$ and let $\mathbf{u}$ be a solution of the corresponding variational inequality obtained by setting $\epsilon=0$ in (3.11). Then, for a sufficiently small coefficient of friction ν, there exists a constant $k>0$, independent of ϵ, such that

$$\|\mathbf{u}_\epsilon-\mathbf{u}\|\leq k\sqrt{\epsilon} \tag{3.22}$$

where $\|\cdot\|$ is the norm given in (3.8).

Results similar to (3.21) and (3.22) can be easily derived for the cases $\rho=0$ and τ fixed (given) on Γ_C.

4 Existence and Uniqueness of Solutions to the Nonlocal-Nonlinear Friction Problem

We shall now establish conditions sufficient to guarantee the existence of solutions to the nonlocal, nonlinear problem (3.11) as well as additional requirements that provide for uniqueness of solutions.

We begin by considering an important preliminary result concerning the auxiliary problem (3.13) introduced in the preceding section.

Proposition 4.1: Given $\tau\geq 0$ on Γ_C, τ smooth enough,

(*i*) there exists a unique solution $\mathbf{u}$ to (3.13);

(*ii*) the correspondence that gives for each τ the corresponding solution $\mathbf{u}$ of (3.13) defines a continuous, nonlinear map B, $B(\tau)=\mathbf{u}$;

(*iii*) the normal contact stress produced by the displacement $\mathbf{u}$, $\sigma_n(\mathbf{u})=E_{ijkl}u_{k,l}\,n_in_j$ is well defined, and is continuous as a function of $\mathbf{u}$.

We next state our second major result which concerns the existence of solutions to the nonlocal, nonlinear friction problem:

Proposition 4.2: For the smoothing operator S_ρ defined in (2.11) which transforms the normal contact stresses σ_n into regularized ones, there exists at least one solution $\mathbf{u}$ in K of the nonlocal, nonlinear friction problem (3.11) for each choice of smooth enough data $\mathbf{f}$ and $\mathbf{t}$.

One method of proof of this proposition was suggested by Duvaut [4]. A complete proof for the nonlocal friction problem ($\epsilon=0$) is given in Oden and Pires [11]. Only the general structure of the proof is of interest here since it suggests a means for actually calculating solutions of the Signorini problem. The key steps in the proof are outlined as follows:

1. Pick an arbitrary smooth enough $\tau\geq 0$ on Γ_C.
2. By Proposition 4.1, for each such τ, there exists a unique solution to

$$a(\mathbf{u},\mathbf{v}-\mathbf{u})+\int_{\Gamma_C}\tau(\psi_\epsilon(|\mathbf{v}_T|)-\psi_\epsilon(|\mathbf{u}_T|))ds \geq f(\mathbf{v}-\mathbf{u}) \tag{4.1}$$

for every $\mathbf{v}$ in K.

3. Let $\mathbf{u}=B(\tau)$, where B is defined in Proposition 4.1.
4. Compute $\sigma_n(\mathbf{u})$.
5. Calculate $\nu S_\rho(\sigma_n(B(\tau))$ and check if it is equal to τ. If so, we can write

$$a(\mathbf{u},\mathbf{v}-\mathbf{u})+\int_{\Gamma_C}\nu S_\rho(\sigma_n(\mathbf{u}))(\psi_\epsilon(|\mathbf{v}_T|)-\psi_\epsilon(|\mathbf{u}_T|))ds\geq f(\mathbf{v}-\mathbf{u})$$

Downloaded 02 May 2010 to 171.66.16.246. Redistribution subject to ASME license or copyright; see http://www.asme.org/terms/Terms_Use.cfm

for every $\mathbf{v}$ in K. If not, we go back to Step 2 and replace in (4.1) τ by the new value $\nu S_\rho(\sigma_n(B(\tau)))$. An iterative scheme is therefore obtained by repeating in this way, Steps 2–5.

6. Obviously, Step 5 describes a fixed point problem for the operator

$$T = \nu S_\rho \circ \sigma_n \circ B$$

We must therefore show that there exists at least one element τ^* such that $T(\tau^*) = \tau^*$. Then $\mathbf{u}^* \equiv B(\tau^*)$ will be a solution of the contact problem with nonlocal, nonlinear, friction.

For small ν, the composition T defined in the foregoing, becomes a contraction and the fixed point is unique. Hence, we can state the uniqueness result:

Proposition 4.3: If the coefficient of friction is sufficiently small, the nonlocal, nonlinear friction problem (3.11) possesses a unique solution.

Future Work

Numerical solutions of the nonlocal, nonlinear friction problems considered in this paper are currently under investigation. These include studies of behavior of the solution for various values of the major parameters; the coefficient of friction ν, the nonlocal contact parameter ρ, and the tangential stiffness of the junctions ϵ. This work is to be the subject of a forthcoming paper.

Acknowledgment

This work was completed during the course of research supported by the U.S. Air Force Office of Scientific Research under Contract No. F-49620-79-C-0083.

References

1 Archard, J. F., "Elastic Deformation and the Laws of Friction," *Proc. Roy. Soc.* Series A, Vol. 243, 1957, pp. 190–205.

2 Bowden, F. P., and Tabor, D., *The Friction and Lubrication of Solids, Part I* Clarendon Press, Oxford, 1950.

3 Bowden, F. P., and Tabor, D., *The Friction and Lubrication of Solids, Part II*, Clarendon Press, Oxford, 1964.

4 Duvaut, G., "Problemes Mathematiques de la Mecanique—Equilibre d' un Solide elastique Avec Contact Unilateral et Frottement de Coulomb," *C. R. Acad. Sc.*, Paris, t. 290, Serie A, 1980, pp. 263–265.

5 Duvaut, G., and Lions, J. L., *Inequalities in Mechanics and Physics*, Springer-Verlag, Berlin, Heidelberg, New York, 1976.

6 Eringen, A. C., (Ed.), *Continuum Physics, Vol. IV—Polar and Nonlocal Field Theories*, Part II by D. G. B. Edelen, "Nonlocal Field Theories," Academic Press, New York, 1976.

7 Eringen, A. C., and Edelen, D. G. B., "On Nonlocal Elasticity," *Int. J. Eng. Sci.*, Vol. 10, 1972, p. 233.

8 Johnson, K. L., "Surface Interaction Between Elastically Loaded Bodies Under Tangential Forces," *Proc. Roy. Soc.* Series A, Vol. 230, 1955, pp. 531–548.

9 Mindlin, R. D., "Compliance of Elastic Bodies in Contact," ASME *Journal of Applied Mechanics*, Vol. 16, 1949, pp. 259–268.

10 Necas, J., Jarusek, J., and Haslinger, J., "On the Solution of the Variational Inequality to the Signorini Problem with Small Friction," *Boll. U. M. I.* Vol. 5, 17-B, 1980, pp. 796–811.

11 Oden, J. T., and Pires, E. B., "*Contact Problems in Elastostatics With Nonlocal Friction Laws*," TICOM Report 81-12, The University of Texas at Austin, 1981.

12 Rabinowicz, E., *Friction and Wear of Materials*, J. Wiley, New York, 1965.

APPENDIX

Proof of Proposition 1

Let $\mathbf{u}$ be a sufficiently smooth solution of the Signorini problem with nonlocal, nonlinear friction (3.3)–(3.7). Then, the following inequality holds for every admissible displacement $\mathbf{v}$:

$$\sigma_T(\mathbf{u})\cdot(\mathbf{v}_T - \mathbf{u}_T) + \nu S_\rho(\sigma_n(\mathbf{u}))(\psi_\epsilon(|\mathbf{v}_T|) - \psi_\epsilon(|\mathbf{u}_T|) \geq 0 \text{ on } \Gamma_C \tag{A.1}$$

In fact, since the function $\psi_\epsilon(\cdot)$ is convex and differentiable,

$$\psi_\epsilon'(|\mathbf{u}_T|)\cdot(\mathbf{v}_T - \mathbf{u}_T) \leq \psi_\epsilon(|\mathbf{v}_T|) - \psi_\epsilon(|\mathbf{u}_T|)$$

or

$$\phi_\epsilon(|\mathbf{u}_T|)\frac{\mathbf{u}_T}{|\mathbf{u}_T|}\cdot(\mathbf{v}_T - \mathbf{u}_T) \leq \psi_\epsilon(|\mathbf{v}_T|) - \psi_\epsilon(|\mathbf{u}_T|)$$

Hence, since $\mathbf{u}$ is such that (3.7) holds

$$\sigma_T(\mathbf{u})\cdot(\mathbf{v}_T - \mathbf{u}_T) = -\nu S_\rho(\sigma_n(\mathbf{u}))\phi_\epsilon(|\mathbf{u}_T|)\frac{\mathbf{u}_T}{|\mathbf{u}_T|}\cdot(\mathbf{v}_T - \mathbf{u}_T)$$
$$\geq -\nu S_\rho(\sigma_n(\mathbf{u}))[\psi_\epsilon(|\mathbf{v}_T|) - \psi_\epsilon(|\mathbf{u}_T|)]$$

or

$$\sigma_T(\mathbf{u})\cdot(\mathbf{v}_T - \mathbf{u}_T) + \nu S_\rho(\sigma_n(\mathbf{u}))\psi_\epsilon(|\mathbf{v}_T|) - \psi_\epsilon(|\mathbf{u}_T|) \geq 0$$

Since we assume $\mathbf{u}$ to be sufficiently regular (e.g., $\mathbf{u} \in \mathbf{H}^2(\Omega) \cap K^1$), the following Green's formula holds for every $\mathbf{v}$ in K:

$$a(\mathbf{u},\mathbf{v}-\mathbf{u}) \equiv \int_\Omega \sigma_{ij}(\mathbf{u})(v_{i,j} - u_{i,j})dx$$
$$= -\int_\Omega \sigma_{ij}(\mathbf{u})_{,j}(v_i - u_i)dx + \int_\Gamma \sigma_{ij}(\mathbf{u})n_j(v_i - u_i)ds$$

But $\sigma_{ij}(\mathbf{u})_{,j} = -f_i$ in Ω by (3.3) and

$$\int_\Gamma \sigma_{ij}(\mathbf{u})n_j(v_i - u_i)ds = \int_{\Gamma_F} t_i(v_i - u_i)ds + \int_{\Gamma_C} \sigma_{ij}(\mathbf{u})n_j(v_i - u_i)ds$$

for any $\mathbf{v}$ in K since $\mathbf{u} = \mathbf{0}$ on Γ_D by (3.4) and $\sigma_{ij}(\mathbf{u})n_j = t_i$ on Γ_F by (3.5). Therefore

$$a(\mathbf{u},\mathbf{v}-\mathbf{u}) - f(\mathbf{v}-\mathbf{u}) = \int_{\Gamma_C} \sigma_{ij}(\mathbf{u})n_j(v_i - u_i)ds$$
$$= \int_{\Gamma_C} [\sigma_T(\mathbf{u})\cdot(\mathbf{v}_T - \mathbf{u}_T) + \sigma_n(\mathbf{u})(v_n - u_n)]ds$$

Here $v_n = \mathbf{v}\cdot\mathbf{n}$ and similarly for u_n. Hence for every $\mathbf{v}$ in K

$$a(\mathbf{u},\mathbf{v}-\mathbf{u}) + \int_{\Gamma_C} \nu S_\rho(\sigma_n(\mathbf{u}))(\psi_\epsilon(|\mathbf{v}_T|) - \psi_\epsilon(|\mathbf{u}_T|))ds - f(\mathbf{v}-\mathbf{u}) =$$
$$= \int_{\Gamma_C} [\sigma_T(\mathbf{u})\cdot(\mathbf{v}_T - \mathbf{u}_T) + \nu S_\rho(\sigma_n(\mathbf{u}))(\psi_\epsilon(|\mathbf{v}_T|) - \psi_\epsilon(|\mathbf{u}_T|)) + \sigma_n(\mathbf{u})(v_n - u_n)]ds$$

But

$$\sigma_n(\mathbf{u})(v_n - u_n) = \sigma_n(\mathbf{u})[v_n - s - (u_n - s)] = \sigma_n(\mathbf{u})(v_n - s) \geq 0$$

[1] $H^2(\Omega) \cap K$ = intersection of the Sobolev space $H^2(\Omega) = (H^2(\Omega))^N = H^2(\Omega) \times H^2(\Omega) \times \ldots \times H^2(\Omega)$ with the set K. For the definition of the space $H^2(\Omega)$ see Adams, R. A., *Sobolev Spaces*, Academic Press, New York, 1975.

Downloaded 02 May 2010 to 171.66.16.246. Redistribution subject to ASME license or copyright; see http://www.asme.org/terms/Terms_Use.cfm

by (3.6) and the definition of the set K. Hence applying inequality $(A.1)$ we finally obtain

$$a(\mathbf{u},\mathbf{v}-\mathbf{u})+j_{\rho,\epsilon}(\mathbf{u},\mathbf{v})-j_{\rho,\epsilon}(\mathbf{u},\mathbf{u})\geq f(\mathbf{v}-\mathbf{u})$$

for every $\mathbf{v}$ in K, i.e., variational inequality (3.11) and the first part of the proposition is proved.

Conversely, let $\mathbf{u}$ in K be a solution of the variational inequality (3.11). Following the proof given Oden and Pires [11, pp. 20–22] for the case $\epsilon=0$ and omitting algebraic manipulations, we are led to conditions (3.3)–(3.6) if we interpret them in the sense of distributions. Then, variational inequality (3.11) will be reduced to

$$\int_{\Gamma_C}[\sigma_T(\mathbf{u})\cdot(\mathbf{v}_T-\mathbf{u}_T)+\nu S_\rho(\sigma_n(\mathbf{u}))(\psi_\epsilon(|\mathbf{v}_T|)-$$
$$-\psi_\epsilon(|\mathbf{u}_T|))]ds\geq 0$$

for every $\mathbf{v}$ in K. If we let $\mathbf{v}_T$ to be of the form

$$\mathbf{v}_T=\mathbf{u}_T+\theta(\mathbf{w}_T-\mathbf{u}_T)$$

where θ belongs to the open interval $(0,1)$ and $\mathbf{w}_T$ is the tangential component on Γ_C of an arbitrary displacement $\mathbf{w}$ in K, we obtain

$$\int_{\Gamma_C}[\theta\sigma_T(\mathbf{u})\cdot(\mathbf{w}_T-\mathbf{u}_T)+\nu S_\rho(\sigma_n(\mathbf{u}))$$
$$(\psi_\epsilon(|\mathbf{u}_T+\theta(\mathbf{w}_T-\mathbf{u}_T)|)$$
$$-\psi_\epsilon(|\mathbf{u}_T|))]ds\geq 0$$

Dividing through by θ, taking the limit as $\theta\to 0$ and noticing that ψ_ϵ is differentiable gives

$$\int_{\Gamma_C}[\sigma_T(\mathbf{u})\cdot(\mathbf{w}_T-\mathbf{u}_T)+\nu S_\rho(\sigma_n(\mathbf{u}))$$
$$\phi_\epsilon(|\mathbf{u}_T|)\frac{\mathbf{u}_T}{|\mathbf{u}_T|}\cdot(\mathbf{w}_T-\mathbf{u}_T)]ds\geq 0$$

for every $\mathbf{w}$ in K. Finally taking first $\mathbf{w}_T=-\mathbf{u}_T$ and then $\mathbf{w}_T=2\mathbf{u}_T$ produces

$$\sigma_T(\mathbf{u})\cdot\mathbf{u}_T+\nu S_\rho(\sigma_n(\mathbf{u}))\phi_\epsilon(|\mathbf{u}_T|)|\mathbf{u}_T|=0 \text{ on } \Gamma_C$$

which we have seen in Section 3.1 to be equivalent to the law of friction (3.7).

Downloaded 02 May 2010 to 171.66.16.246. Redistribution subject to ASME license or copyright; see http://www.asme.org/terms/Terms_Use.cfm

J. Dundurs
Professor,
Department of Civil Engineering,
Northwestern University,
Evanston, Il. 60201
Fellow ASME

M. Comninou
Associate Professor,
Department of Civil Engineering,
University of Michigan,
Ann Arbor, Mich. 48109
Mem. ASME

An Educational Elasticity Problem With Friction

Part 3: General Load Paths

This concluding paper treats general load paths when the two components of the concentrated force are allowed to change independently with time. It is shown that there are two kinds of dependence on the load path. For certain directions of the forward tangent, the dependence is strict in that the deformations depend on the full details of the path. For other directions, however, the dependence is loose, and the deformations do not depend on the exact nature of the path as long as the forward tangent falls within given bounds. The problem also shows that, given an initial state, the load space can be subdivided into different regions each corresponding to a certain mode of deformations.

Introduction

To conclude the discussion of the example for friction in elasticity, which was treated earlier for a constant direction of the applied force [1, 2], we consider the more general case when the two components of the force can change independently. This will illustrate the dependence of deformations on the load path. A particularly interesting aspect of friction in elasticity, which emerges from the analysis, is that there are two types of dependence. For certain directions of the load path the dependence is *strict* in that the deformations depend on the exact nature of the path. For other directions, however, the dependence is *loose*, and the slip process does not depend on the detailed nature of the path, as long as the forward tangent of the path falls within certain bounds.

The geometry of the problem is shown in Fig. 1. The two components of the force $P(t)$ and $Q(t)$ can vary independently, but the restriction $P(t) \geq 0$ is imposed to avoid singular normal and shear tractions on the cut because they require separate considerations [1]. The extent of the separation zone $0 < x < a$ and the distribution of normal tractions on the cut do not depend on the slip process, and from [1]

$$a = \frac{\kappa - 1}{\pi(\kappa + 1)} \frac{P}{p^\infty} \tag{1}$$

$$N(x) = -p^\infty \left(\frac{x-a}{x}\right)^{1/2} H(x-a), \quad 0 < x < \infty \tag{2}$$

Suppose that there are initial shear tractions $S_i(x)$ on the cut due to some previous loading. The solution for the next segment of the load path can be constructed by distributing additional dislocations with the density $B_x^c(x)$ on a finite interval. This dislocation distribution gives the corrective shear tractions

$$S_c(x) = -\frac{2\mu}{\pi(\kappa+1)} \int_0^{\max(b)} \frac{B_x^c(\xi)d\xi}{\xi - x}, \quad 0 < x < \infty \tag{3}$$

and the total shear tractions, which must satisfy the appropriate boundary conditions on the separation and slip zones, are then

$$S(x) = S_i(x) + S_c(x) \tag{4}$$

The upper limit of integration in (3) denoted symbolically by $\max(b)$ must be chosen so that all of the new dislocations are included, even if they become locked into a stick zone in case a slip zone shrinks or there is no slip zone [2].

The friction law can be written as

$$S(x) = -fN(x)\operatorname{sng} V(x), \quad 0 < x < b \tag{5}$$

valid in both the separation and slip zones. Substituting from (2),

$$S(x) = fp^\infty \left(\frac{x-a}{x}\right)^{1/2} H(x-a)\operatorname{sgn} V(x), \quad 0 < x < b \tag{6}$$

and consequently

$$\int_0^{\max(b)} \frac{B_x^c(\xi)d\xi}{\xi - x} = \frac{\pi(\kappa+1)}{2\mu} \left\{ S_i(x) - fp^\infty \left(\frac{x-a}{x}\right)^{1/2} H(x-a)\operatorname{sgn} V(x) \right\}, \quad 0 < x < b \tag{7}$$

where $0 < x < a$ is the separation zone and $a < x < b$ is the active slipe zone.

Expanding Slip Zone

We take for the first initial state that reached by loading with a force in a constant direction to the point (P_1, Q_1) in the P,Q plane. It can be assumed without loss of generality that $Q_1 > 0$. Then the extents of the initial separation and slip zones, and the normal and shearing tractions are given by [1]

Contributed by the Applied Mechanics Division for publication in the JOURNAL OF APPLIED MECHANICS.

Discussion on this paper should be addressed to the Editorial Department, ASME, United Engineering Center, 345 East 47th Street, New York, N.Y. 10017, and will be accepted until two months after final publication of the paper itself in the JOURNAL OF APPLIED MECHANICS. Manuscript received by ASME Applied Mechanics Division, February, 1982.

Copyright © 1983 by ASME
Downloaded 02 May 2010 to 171.66.16.246. Redistribution subject to ASME license or copyright; see http://www.asme.org/terms/Terms_Use.cfm

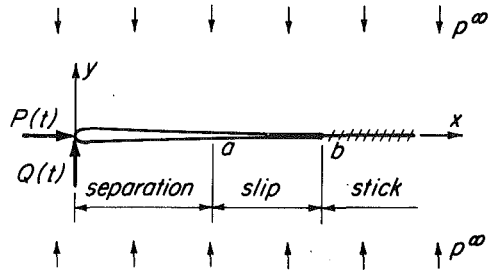

Fig. 1 Geometry of the problem

$$a_1 = \frac{\kappa-1}{\pi(\kappa+1)}\frac{P_1}{p^\infty} \tag{8}$$

$$b_1 = a_1 + \frac{\kappa-1}{\pi(\kappa+1)}\frac{Q_1}{fp^\infty} = \frac{\kappa-1}{\pi(\kappa+1)}\frac{fP_1+Q_1}{fp^\infty} \tag{9}$$

$$N_1(x) = -p^\infty\left(\frac{x-a_1}{x}\right)^{1/2} H(x-a_1), \quad 0<x<\infty \tag{10}$$

$$S_1(x) = fp^\infty\left\{-\left(\frac{x-a_1}{x}\right)^{1/2} H(x-a_1) + \left(\frac{x-b_1}{x}\right)^{1/2} H(x-b_1)\right\}, \quad 0<x<\infty \tag{11}$$

It will be seen that the same initial state can be reached by other quite different load paths.

For an expanding slip zone

$$\frac{db}{dt} > 0 \tag{12}$$

and the upper limit of the integral in (7) can be taken as b. It is not known, however, where b falls in relation to a_1 and b_1, and the right side of (7) must be modified by introducing the Heaviside step functions $H(b-a_1)$ and $H(b-b_1)$ to obtain the governing integral equation. Thus,

$$\int_0^b \frac{B_x^c(\xi)d\xi}{\xi-x} = \frac{\pi(\kappa+1)}{2\mu} fp^\infty\left\{-\left(\frac{x-a}{x}\right)^{1/2} H(x-a)\operatorname{sgn} V - \left(\frac{x-a_1}{x}\right)^{1/2} H(x-a_1)H(b-a_1) + \left(\frac{x-b_1}{x}\right)^{1/2} H(x-b_1)H(b-b_1)\right\}, \quad 0<x<b \tag{13}$$

The solution of the integral equation that is singular at $x = 0$ but bounded at $x = b$ is

$$B_x^c(x) = \frac{\kappa+1}{2\mu} fp^\infty\left\{-\left(\frac{a-x}{x}\right)^{1/2} H(a-x)\operatorname{sng} V + \left(\frac{b-x}{x}\right)^{1/2} [\operatorname{sgn} V + H(b-a_1) - H(b-b_1)] - \left(\frac{a_1-x}{x}\right)^{1/2} H(a_1-x)H(b-a_1) + \left(\frac{b_1-x}{x}\right)^{1/2} H(b_1-x)H(b-b_1)\right\}, \quad 0<x<b \tag{14}$$

The corrective shear tractions computed from (3) are in turn

$$S_c(x) = fp^\infty\left\{\left(\frac{x-a}{x}\right)^{1/2} H(x-a)\operatorname{sgn} V + \left(\frac{x-b}{x}\right)^{1/2} H(x-b)[-\operatorname{sgn} V - H(b-a_1) + H(b-b_1)] + \left(\frac{x-a_1}{x}\right)^{1/2} H(x-a_1)H(b-a_1) - \left(\frac{x-b_1}{x}\right)^{1/2} H(x-b_1)H(b-b_1)\right\}, \quad 0<x<\infty \tag{15}$$

yielding the total shear tractions

$$S(x) = fp^\infty\left\{\left(\frac{x-a}{x}\right)^{1/2} H(x-a)\operatorname{sgn} V + \left(\frac{x-b}{x}\right)^{1/2} H(x-b)[\operatorname{sgn} V + H(b-a_1) - H(b-b_1)] - \left(\frac{x-a_1}{x}\right)^{1/2} H(x-a_1)[1-H(b-a_1)] + \left(\frac{x-b_1}{x}\right)^{1/2} H(x-b_1)[1-H(b-b_1)]\right\}, \quad 0<x<\infty \tag{16}$$

The conditions remaining to be enforced are that the slip velocity derived from the dislocation distribution as

$$V(x) = -\frac{\kappa-1}{4\mu}\dot{Q} - \int_0^x \dot{B}_x^c(\xi)d\xi \tag{17}$$

should not be inconsistent because of the $\operatorname{sgn} V$ term in $B_x^c(x)$, and that the tangential shift corresponding to $B_x^c(x)$ vanishes at the end of the active slip zone, or

$$h_c(b) = \frac{\kappa-1}{4\mu}(Q_1 - Q) - \int_0^b B_x^c(\xi)d\xi = 0 \tag{18}$$

The time derivative of the dislocation distribution is

$$\dot{B}_x^c(x) = \frac{\kappa+1}{4\mu} fp^\infty\left\{-\frac{\dot{a}}{(ax-x^2)^{1/2}} H(a-x)\operatorname{sgn} V + \frac{\dot{b}}{(ax-x^2)^{1/2}}[\operatorname{sgn} V + H(b-a_1) - H(b-b_1)]\right\}, \quad 0<x<b \tag{19}$$

which from (17) yields the slip velocity

$$V(x) = -\frac{\kappa-1}{4\mu}\dot{Q} - \frac{\kappa+1}{4\mu} fp^\infty\left\{-\pi\dot{a}\operatorname{sgn} V + \dot{b}[\operatorname{sgn} V + H(b-a_1) - H(b-b_1)]\cos^{-1}\left(1-\frac{2x}{b}\right)\right\}, \quad a<x<b \tag{20}$$

Since $V(b) = 0$, we can express $\dot{b}$ in terms of $\dot{a}$ and $\dot{Q}$, and substituting for $\dot{a}$ from (1),

$$V(x) = \frac{\kappa-1}{4\pi\mu}(f\dot{P}\operatorname{sgn} V - \dot{Q})\left\{\pi - \cos^{-1}\left(1-\frac{2x}{b}\right)\right\}, \quad a<x<b \tag{21}$$

It is seen from (21) that $V(x)$ is of the same algebraic sign over the whole slip zone, and that for its sign to be consistent with the previous relations we must have

$$\operatorname{sgn}(f\dot{P}\operatorname{sgn} V - \dot{Q}) = \operatorname{sgn} V \tag{22}$$

Thus

$$V(x) > 0 \text{ requires } f\dot{P} - \dot{Q} > 0 \quad \text{or} \quad dQ < f\,dP \tag{23}$$

$$V(x) < 0 \text{ requires } f\dot{P} + \dot{Q} > 0 \quad \text{or} \quad dQ > -f\,dP \tag{24}$$

These are conditions on the forward tangent of the load path, and they are shown graphically in Fig. 2. It is seen that the conditions for $V(x) > 0$ and $V(x) < 0$ overlap in the right sector, and that the left sector remains empty.

The condition (18) that the tangential shift vanishes at $x = b$ gives upon substitution of (14) and (9)

Downloaded 02 May 2010 to 171.66.16.246. Redistribution subject to ASME license or copyright; see http://www.asme.org/terms/Terms_Use.cfm

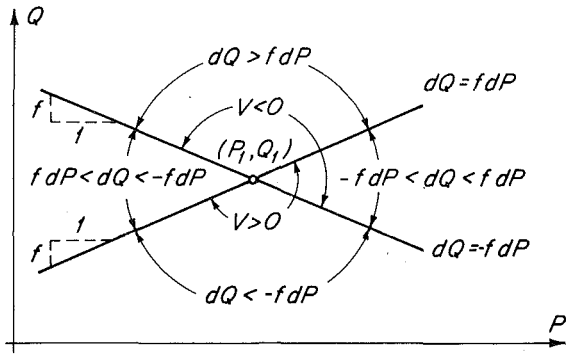

Fig. 2 Conditions on the directions of the forward tangent for loading from the initial state

$$b[\operatorname{sgn}V + H(b-a_1) - H(b-b_1)] = -\frac{\kappa-1}{\pi(\kappa+1)}\frac{Q}{fp^\infty} + a\operatorname{sgn}V$$

$$-a_1[1-H(b-a_1)] + b_1[1-H(b-b_1)] \tag{25}$$

The evaluation of this relation is tedious because a large number of cases must considered individually. Most of them lead to contradictions and are not possible. Consider, for instance, the possibility $V(x)<0$ and $a<b<a_1<b_1$, for which (25) gives

$$b = \frac{\kappa-1}{\pi(\kappa+1)}\frac{Q}{fp^\infty} + a + a_1 - b_1$$

Then using (1), (8) and (9), it is seen that

$a<b$ requires $Q>Q_1$

$b<a_1$ requires $Q<Q_1+f(P-P_1)$

$a<a_1$ requires $P<P_1$

which makes the point (P, Q) fall in the empty sector, so that it cannot be reached under the restriction (24) for $V(x)<0$.

A full investigation of the various possibilities reveals that only two cases can be realized under the assumption of $db/dt>0$. They will be called regimes *I* and *II* and are described in the next section.

Regimes *I* and *II*

Regime *I* corresponds to the choice $V(x) < 0$, which requires $dQ > -fdP$, and $b_1 < b$ with $\max(a_1,a) < b$. Relation (25) then yields

$$b = \frac{\kappa-1}{\pi(\kappa+1)}\frac{Q}{fp^\infty} + a \tag{26}$$

and

$$b_1<b \text{ requires } Q>Q_1-f(P-P_1) \tag{27}$$

$$a_1<b \text{ requires } Q>-f(P-P_1) \tag{28}$$

$$a<b \text{ requires } Q>0 \tag{29}$$

These inequalities contain no contradictions and regime *I* is achieved if the load path starting at (P_1, Q_1) satisfies (24) at all points. The extent of regime *I* in the P, Q plane determined by (27) and (29) is shown in Fig. 3. Using the inequalities that describe regime *I* in (14)–(16), we obtain

$$B_x^c(x) = \frac{\kappa+1}{2\mu}fp^\infty\left\{\left(\frac{a-x}{x}\right)^{1/2}H(a-x) - \left(\frac{a_1-x}{x}\right)^{1/2}H(a_1-x) + \left(\frac{b_1-x}{x}\right)^{1/2}H(b_1-x) - \left(\frac{b-x}{x}\right)^{1/2}\right\}, \quad 0<x<b \tag{30}$$

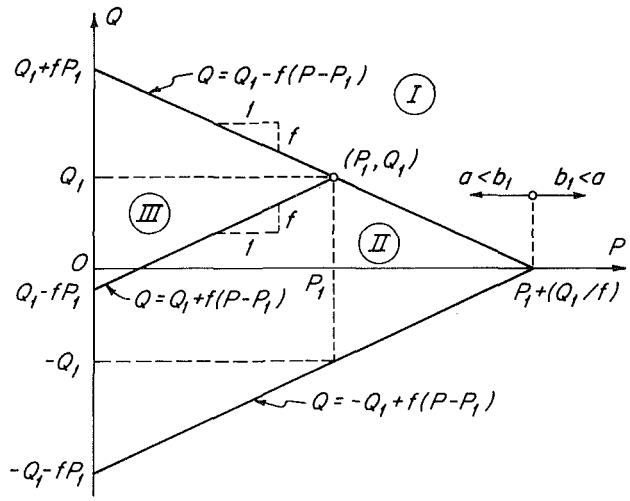

Fig. 3 Regimes achieved by loading from the point (P_1, Q_1)

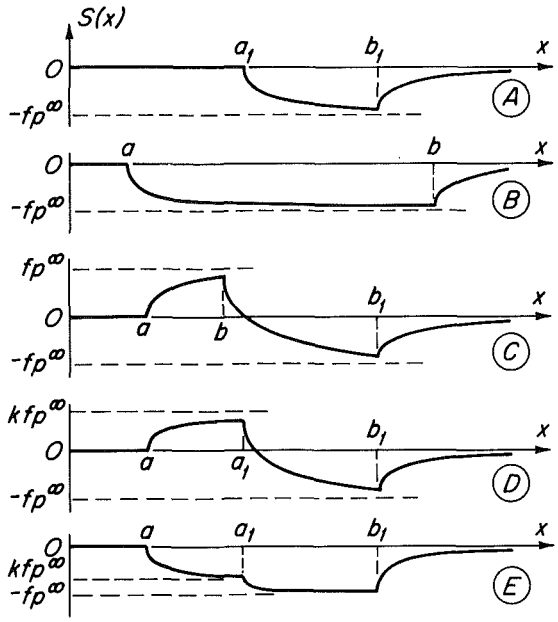

Fig. 4 Distributions of shear tractions for loading from (P_1, Q_1): *(A)*–initial distribution; *(B)*–regime *I*; *(C)*–regime *II*; *(D)*–regime *III* with $k > 0$; *(E)* regime *III* with $k < 0$

$$S_c(x) = fp^\infty\left\{-\left(\frac{x-a}{x}\right)^{1/2}H(x-a) + \left(\frac{x-a_1}{x}\right)^{1/2}H(x-a_1) - \left(\frac{x-b_1}{x}\right)^{1/2}H(x-b_1) + \left(\frac{x-b}{x}\right)^{1/2}H(x-b)\right\},$$

$$0<x<\infty \tag{31}$$

$$S(x) = fp^\infty\left\{-\left(\frac{x-a}{x}\right)^{1/2}H(x-a) + \left(\frac{x-b}{x}\right)^{1/2}H(x-b)\right\},$$

$$0<x<\infty \tag{32}$$

The distribution of the shear tractions for regime *I* is shown schematically in Fig. 4. Loading from (P_1,Q_1) to the boundary $P=0$, $Q > Q_1 + fp_1$ leads to

$$a=0, \quad b = \frac{\kappa-1}{\pi(\kappa+1)}\frac{Q}{fp^\infty} \tag{33}$$

Downloaded 02 May 2010 to 171.66.16.246. Redistribution subject to ASME license or copyright; see http://www.asme.org/terms/Terms_Use.cfm

$$S(x)=fp^{\infty}\left\{-1+\left(\frac{x-b}{x}\right)^{1/2}H(x-b)\right\},\quad 0<x<\infty \tag{34}$$

Similarly, loading to the boundary $Q = 0$, $P > P_1 + Q_1/f$ gives

$$b=a=\frac{\kappa-1}{\pi(\kappa+1)}\frac{P}{p^{\infty}}>b_1 \tag{35}$$

$$S(x)=0,\quad 0<x<\infty \tag{36}$$

thus erasing all shear tractions.

Comparing (11) with (32) it is clear that the initial state corresponding to (P_1,Q_1) can be reached from the origin along any path that satisfies (24).

Regime *II* corresponds to $V(x) > 0$, requiring $dQ < fdP$, and $\max(a_1,a) < b < b_1$. These conditions reduce (25) to

$$2b=-\frac{\kappa-1}{\pi(\kappa+1)}\frac{Q}{fp^{\infty}}+a+b_1 \tag{37}$$

and

$$a_1<b \quad \text{requires} \quad Q<Q_1+f(P-P_1) \tag{38}$$

$$a<b \quad \text{requires} \quad Q<Q_1-f(P-P_1) \tag{39}$$

$$b<b_1 \quad \text{requires} \quad Q>-Q_1+f(P-P_1) \tag{40}$$

Again, these inequalities contain no contradictions if the load path starting at (P_1,Q_1) falls within the three boundaries given by (38)–(40). The extent of regime *II* in the P,Q plane is shown in Fig. 3. The results obtained from (14)–(16) are for this regime

$$B_x^c(x)=\frac{\kappa+1}{2\mu}fp^{\infty}\left\{-\left(\frac{a-x}{x}\right)^{1/2}H(a-x)\right.$$

$$\left.-\left(\frac{a_1-x}{x}\right)^{1/2}H(a_1-x)+2\left(\frac{b-x}{x}\right)^{1/2}\right\},\quad 0<x<b \tag{41}$$

$$S_c(x)=fp^{\infty}\left\{\left(\frac{x-a}{x}\right)^{1/2}H(x-a)+\left(\frac{x-a_1}{x}\right)^{1/2}H(x-a_1)\right.$$

$$\left.-2\left(\frac{x-b}{x}\right)^{1/2}H(x-b)\right\},\quad 0<x<\infty \tag{42}$$

$$S(x)=fp^{\infty}\left\{\left(\frac{x-a}{x}\right)^{1/2}H(x-a)-2\left(\frac{x-b}{x}\right)^{1/2}H(x-b)\right.$$

$$\left.+\left(\frac{x-b_1}{x}\right)^{1/2}H(x-b_1)\right\},\quad 0<x<\infty \tag{43}$$

The distribution of the shear tractions for regime *II* is shown in Fig. 4. Loading from (P_1,Q_1) to the boundary $P = 0$, $-Q_1 - fP_1 < Q < Q_1 - fP_1$ of the regime *II* gives

$$a=0,\quad 2b=\frac{\kappa-1}{\pi(\kappa+1)}\frac{(-Q+fP_1+Q_1)}{fp^{\infty}} \tag{44}$$

$$S(x)=fp^{\infty}\left\{1-2\left(\frac{x-b}{x}\right)^{1/2}H(x-b)\right.$$

$$\left.+\left(\frac{x-b_1}{x}\right)^{1/2}H(x-b_1)\right\},\quad 0<x<\infty \tag{45}$$

Loading to the bottom boundary $Q = -Q_1 + f(P-P_1)$, $P < P_1 + Q_1/f$ leads to

$$b=b_1=\frac{\kappa-1}{\pi(\kappa+1)}\frac{fP_1+Q_1}{fp^{\infty}} \tag{46}$$

$$S(x)=fp^{\infty}\left\{\left(\frac{x-a}{x}\right)^{1/2}H(x-a)\right.$$

$$\left.-\left(\frac{x-b}{x}\right)^{1/2}H(x-b)\right\},\quad 0<x<\infty \tag{47}$$

The shearing tractions then are the same as for loading from the origin to the point (P,Q) on the bottom boundary using a force with a constant direction. Consequently, consideration of the points below the bottom boundary can be omitted without loss of generality.

It is seen from (32) and (43) that the distributions of the shear tractions for regimes *I* and *II* are of the same general nature as for loading and weak friction unloading, respectively, using a force with a constant direction [1]. Moreover, the dependence on the load path for both regimes *I* and *II* is loose, in that the exact nature of the path does not matter as long as the inequalities (23) and (24) are satisfied at every point of the path. A rather interesting aspect of the problem arises also from the fact that the inequalities (23) and (24) partially overlap (see Fig. 2), and that the condition $-fdP < dQ < fdP$ on the forward tangent of the path is allowable for regime *I* ($V < 0$) as well as for regime *II* ($V > 0$). Comparing Figs. 2 and 3 it is seen that we can have $-fdP < dQ < fdP$ immediately upon departure from (P_1,Q_1) in regime *I*, but that some point under the restriction $dQ < fdP$ must be reached in regime *II* before $-fdP < dQ < fdP$ becomes compatible with the conditions under this regime.

Loading from (P_1,Q_1) along the common boundary $Q = Q_1 - f(P-P_1)$ between regimes *I* and *II* corresponds to $V(x) = 0$. Substituting this value of Q into (26) gives $b = b_1$ while (37) yields $b = a$. There is no contradiction, however, as (32) with $b = b_1$ and (43) with $b = a$ lead to the same result for the shear tractions:

$$S(x)=fp^{\infty}\left\{-\left(\frac{x-a}{x}\right)^{1/2}H(x-a)\right.$$

$$\left.+\left(\frac{x-b_1}{x}\right)^{1/2}H(x-b_1)\right\},\quad 0<x<\infty \tag{48}$$

It is seen from (48) that, in this case, the separation zone simply propagates into the old slip zone $a_1 < x < b_1$ and there is no new slip.

No Slip Zone and Regime *III*

To complete the study of load paths originating from the point (P_1,Q_1) what remains is dealing with the triangle left between regimes *I* and *II* in the P,Q plane (see Fig. 3). The two possibilities are either a shrinking slip zone, which implies

$$\frac{db}{dt}<0 \tag{49}$$

or no slip zone.

Considering the possibility of a shrinking slip zone first, we assume that the initial extent of the slip zone is $a_1 < x < b_0$, and that the extent of the slip zone at some later time is a $a < x < b$, with $a < a_1$ because $P < P_1$ in the empty triangle. From (7) we have

$$\int_0^{b_0}\frac{B_x^c(\xi)d\xi}{\xi-x}=\frac{\pi(\kappa+1)}{2\mu}fp^{\infty}\left\{-\left(\frac{x-a}{x}\right)^{1/2}H(x-a)\operatorname{sgn}V\right.$$

$$-\left(\frac{x-a_1}{x}\right)^{1/2}H(x-a_1)H(b-a_1)$$

$$\left.+\left(\frac{x-b_1}{x}\right)^{1/2}H(x-b_1)H(b-b_1)\right\},\quad 0<x<b<b_0 \tag{50}$$

Since the interval $b < x < b_0$ is a stick zone, the dislocations in this interval are locked in and do not change with time. Consequently, differentiating (50) with respect to time we obtain

$$\int_0^{b}\frac{\dot{B}_x^c(\xi)d\xi}{\xi-x}=\frac{\pi(\kappa+1)}{4\mu}fp^{\infty}\frac{\dot{a}}{(x^2-ax)^{1/2}}H(x-a)\operatorname{sgn}V,$$

$$0<x<b \tag{51}$$

Downloaded 02 May 2010 to 171.66.16.246. Redistribution subject to ASME license or copyright; see http://www.asme.org/terms/Terms_Use.cfm

The most general result is obtained by taking the solution of (51) that is unbounded at $x = b$. Thus

$$\dot{B}_x^c(x) = \frac{c}{(bx-x^2)^{1/2}} + \frac{\kappa+1}{4\mu} fp^\infty \dot{a}\,\mathrm{sgn}\,V\left\{ -\frac{1}{(ax-x^2)^{1/2}} H(a-x) + \frac{1}{(bx-x^2)^{1/2}} \right\}, \quad 0<x<b \tag{52}$$

The slip velocity is computed from (17), and imposing the condition that $V(b) = 0$, the result is identical with (21). Consequently (22)–(24) must be satisfied, and the empty region cannot be entered from (P_1,Q_1) with a shrinking slip zone.

Consider next the possibility of no slip zone for which (7) yields upon differentiation with respect to time

$$\int_0^a \frac{\dot{B}_x^c(\xi)d\xi}{\xi - x} = 0, \quad 0<x<a \tag{53}$$

Hence

$$\dot{B}_x^c(x) = \frac{C}{(ax-x^2)^{1/2}}, \quad 0<x<a \tag{54}$$

Evaluating C from the requirement that $V(a) = 0$ with the aid of (17),

$$\dot{B}_x^c(x) = -\frac{\kappa-1}{4\pi\mu} \frac{\dot{Q}}{(ax-x^2)^{1/2}} \tag{55}$$

Since $\dot{Q} = \dot{P}(dQ/dP)$ and $\dot{P}$ is related to $\dot{a}$ through (1),

$$\dot{B}_x^c(x) = -\frac{p^\infty(\kappa+1)}{4\mu} \frac{\dot{a}(dQ/dP)}{(ax-x^2)^{1/2}}, \quad 0<x<a \tag{56}$$

It is seen from (56) that, because of the term dQ/dP, the solution cannot be carried further without specifying the actual path in the P,Q plane. This means that the distribution of shear tractions left on the cut as the separation zone closes without slip depends on the full details of the load path.

As an example we consider loading along a straight line, or

$$\frac{dQ}{dP} = kf = \text{const}, \quad -1<k<1 \tag{57}$$

which is called regime *III*. The problem then is identical to unloading with strong friction in [2], and

$$B_x^c(x) = \frac{\kappa+1}{2\mu} kfp^\infty \left\{ -\left(\frac{a-x}{x}\right)^{1/2} H(a-x) + \left(\frac{a_1-x}{x}\right)^{1/2} \right\}, \quad 0<x<a \tag{58}$$

$$S(x) = fp^\infty \left\{ k\left(\frac{x-a}{x}\right)^{1/2} H(x-a) - (1+k)\left(\frac{x-a_1}{x}\right)^{1/2} H(x-a_1) + \left(\frac{x-b_1}{x}\right)^{1/2} H(x-b_1) \right\}, \quad 0<x<\infty \tag{59}$$

The distribution of the shear tractions for positive and negative k are shown schematically in Fig. 4.

Loading along the common boundary $Q = Q_1 - f(P-P_1)$ between the regimes *I* and *III* corresponds to $V(x) = 0$, and the distribution of the shear tractions is given by (48). In contrast, loading from (P_1,Q_1) along the common boundary $Q = Q_1 + f(P-P_1)$ between regimes *II* and *III* corresponds to $b = a_1 = \text{const}$ and $V(x) > 0$, and

$$S(x) = fp^\infty \left\{ \left(\frac{x-a}{x}\right)^{1/2} H(x-a) - 2\left(\frac{x-a_1}{x}\right)^{1/2} H(x-a_1) + \left(\frac{x-b_1}{x}\right)^{1/2} H(x-b_1) \right\}, \quad 0<x<\infty \tag{60}$$

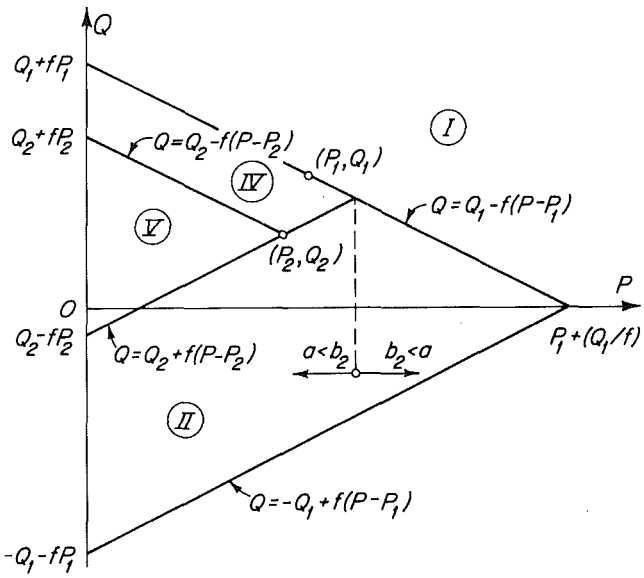

Fig. 5 Regimes achieved by loading from the point (P_2, Q_2) that belongs to regime *II*

Loading From Regimes *I* and *III*

Suppose that loading is carried on from (P_1,Q_1) to some point (P_2,Q_2) under the conditions of regime *I*, but that beyond (P_2,Q_2) condition (24) is violated. Comparing (32) with (11) is it clear that the shear tractions at (P_2,Q_2) are of the same nature as those at (P_1,Q_1). Consequently the transition to new regimes beyond (P_2,Q_2) is the same as that analyzed at (P_1,Q_1). New transitions must be studied, however, if the point (P_2,Q_2) is reached by loading under the conditions of regime *II*. From (1), (37), and (43)

$$a_2 = \frac{\kappa-1}{\pi(\kappa+1)} \frac{P_2}{p^\infty} \tag{61}$$

$$b_2 = \frac{\kappa-1}{\pi(\kappa+1)} \frac{f(P_1+P_2)+Q_1-Q_2}{2fp^\infty} \tag{62}$$

$$S_2(x) = fp^\infty \left\{ \left(\frac{x-a_2}{x}\right)^{1/2} H(x-a_2) - 2\left(\frac{x-b_2}{x}\right)^{1/2} H(x-b_2) + \left(\frac{x-b_1}{x}\right)^{1/2} H(x-b_1) \right\}, \quad 0<x<\infty \tag{63}$$

Taking $S_2(x)$ as $S_i(x)$ in (7), the investigation of the different cases is quite similar to that for loading from (P_1,Q_1) and, consequently, the derivations are omitted and only the results presented.

The general situation is shown in Fig. 5. Regime *II* is of course continued at (P_2,Q_2) if (23) is not violated. Otherwise the two regimes *IV* and *V* are encountered.

Regime *IV* is characterized by $db/dt > 0$, $V(x) > 0$ (so that $dQ > -fdP$ must be satisfied at all points), and $a_2 < b < b_2$. The extent of the slip zone is given by

$$b = \frac{\kappa-1}{\pi(\kappa+1)} \frac{f(P+P_2)+Q-Q_2}{2fp^\infty} \tag{64}$$

The shear tractions

$$S(x) = fp^\infty \left\{ -\left(\frac{x-a}{x}\right)^{1/2} H(x-u) + 2\left(\frac{x-b}{x}\right)^{1/2} H(x-b) - 2\left(\frac{x-b_2}{x}\right)^{1/2} H(x-b_2) + \left(\frac{x-b_1}{x}\right)^{1/2} H(x-b_1) \right\}, \quad 0<x<\infty \tag{65}$$

Downloaded 02 May 2010 to 171.66.16.246. Redistribution subject to ASME license or copyright; see http://www.asme.org/terms/Terms_Use.cfm

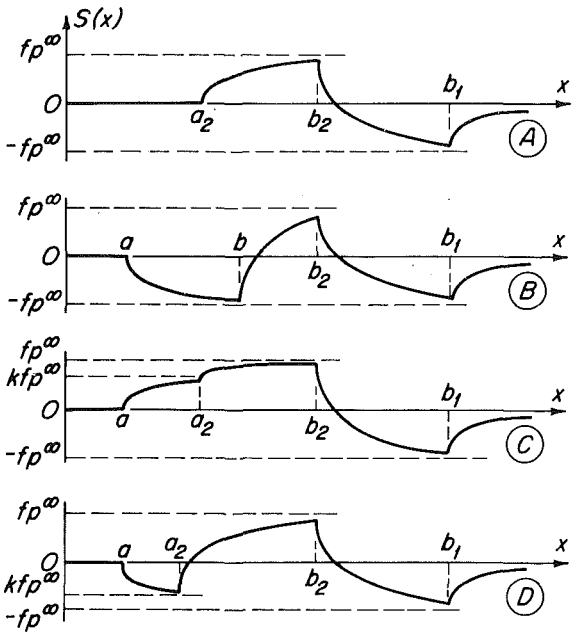

Fig. 6 Distributions of shear tractions for loading from (P_2, Q_2) that belong to regime *II*: (*A*)-initial distribution; (*B*)-regime *IV*; (*C*)-regime *V* for $k > 0$; (*D*)-regime *V* for $k < 0$

are shown in Fig. 6. Loading under regime *IV* to the boundary $Q = Q_1 - f(P - P_1)$ leads to

$$b = b_2 \tag{66}$$

$$S(x) = fp^\infty \left\{ -\left(\frac{x-a}{x}\right)^{1/2} H(x-a) + \left(\frac{x-b_1}{x}\right)^{1/2} H(x-b_1) \right\},$$

$$0 < x < \infty \tag{67}$$

and loading slightly beyond this boundary returns the slip process to regime *I*, while involving a sudden jump in the slip zone from b_2 to b_1.

Regime *V* is similar to regime *III* in that the separation zone recedes, and there is no new slip. Again a strict dependence on the load path is involved as

$$\dot{B}_x^c(x) = -\frac{p^\infty(\kappa+1)}{4\mu} \frac{\dot{a}(dQ/dP)}{(ax-x^2)^{1/2}}, \quad 0 < x < a \tag{68}$$

For the example considered before, or $dQ/dP = k$,

$$S(x) = fp^\infty \left\{ k\left(\frac{x-a}{x}\right)^{1/2} H(x-a) \right.$$

$$+ (1-k)\left(\frac{x-a_2}{x}\right)^{1/2} H(x-a_2) - 2\left(\frac{x-b_2}{x}\right)^{1/2} H(x-b_2)$$

$$\left. + \left(\frac{x-b_1}{x}\right)^{1/2} H(x-b_1) \right\}, \quad 0 < x < \infty \tag{69}$$

The shear tractions are shown schematically in Fig. 6 for positive and negative values of k.

Loading From Regime *III*

We can only continue to consider the example $dQ/dP = k$ because the shear tractions at (P_2, Q_2) need to be known to do a full analysis. Using

$$a_2 = b_2 = \frac{\kappa-1}{\pi(\kappa+1)} \frac{P_2}{p^\infty} \tag{70}$$

$$S_2(x) = fp^\infty \left\{ k\left(\frac{x-a_2}{x}\right)^{1/2} H(x-a_2) \right.$$

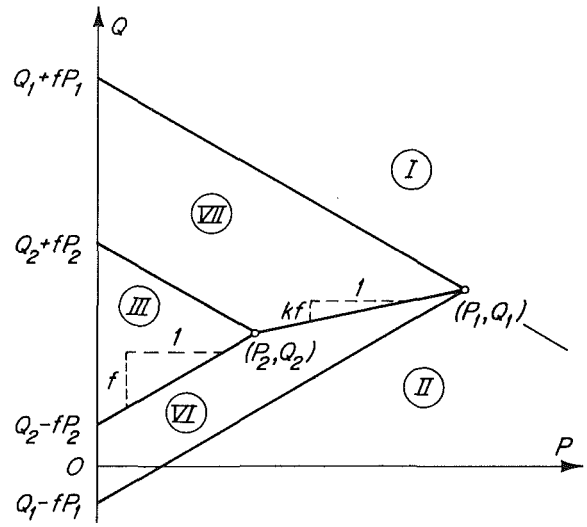

Fig. 7 Regimes achieved by loading from the point (P_2, Q_2) that belongs to regime *III*

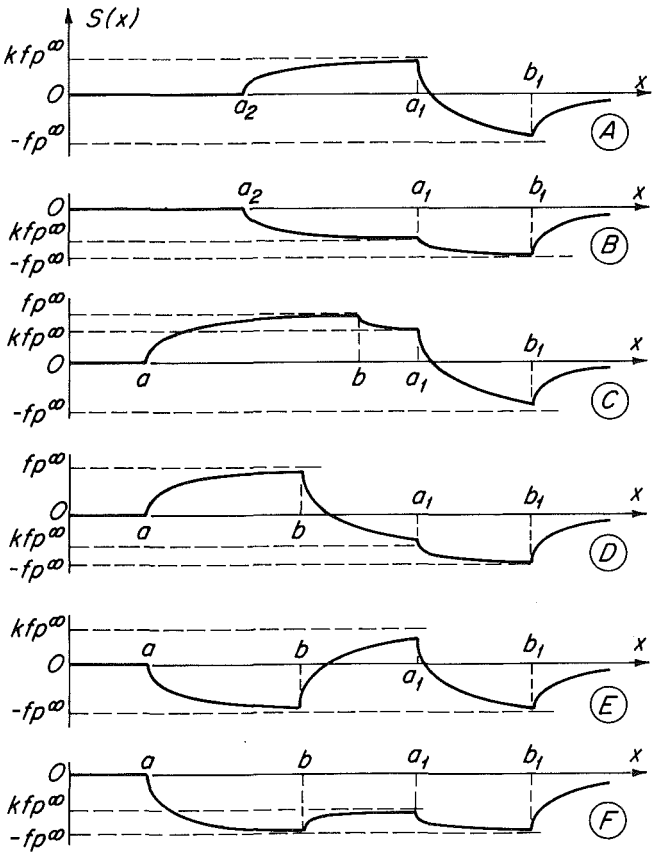

Fig. 8 Distributions of shear tractions for loading from (P_2, Q_2) that belongs to regime *III*: (*A*)-initial distribution for $k > 0$; (*B*)-initial distribution for $k < 0$; (*C*)-regime *VI* for $k > 0$; (*D*)-regime *VI* for $k < 0$; (*E*)-regime *VII* for $k > 0$; (*F*)-regime *VII* for $k < 0$.

$$-(1+k)\left(\frac{x-a_1}{x}\right)^{1/2} H(x-a_1)$$

$$\left. + \left(\frac{x-b_1}{x}\right)^{1/2} H(x-b_1) \right\}, \quad 0 < x < \infty \tag{71}$$

The analysis leads to the general situation shown in Fig. 7, which indicates the possibility of continuing under regime *III* if $dQ < -f dP$ and $dQ > f dP$, and also shows two new regimes.

Downloaded 02 May 2010 to 171.66.16.246. Redistribution subject to ASME license or copyright; see http://www.asme.org/terms/Terms_Use.cfm

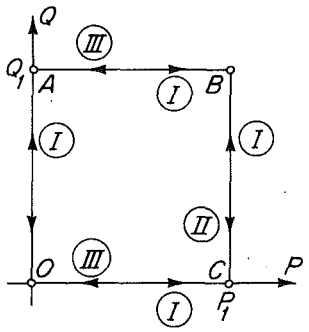

Fig. 9 Load path used in the example

Regime *VI* involves $db/dt > 0$, $V(x) > 0$, and $\max(a,a_2) < b < a_1$. The extent of the slip zone is given by

$$b = \frac{\kappa-1}{\pi(\kappa+1)} \frac{f(P-kP_2)-Q+Q_2}{(1-k)fp^\infty} \tag{72}$$

and the shear tractions are

$$S(x) = fp^\infty \left\{ \left(\frac{x-a}{x}\right)^{1/2} H(x-a) - (1-k)\left(\frac{x-b}{x}\right)^{1/2} H(x-b) - (1+k)\left(\frac{x-a_1}{x}\right)^{1/2} H(x-a_1) + \left(\frac{x-b_1}{x}\right)^{1/2} H(x-b_1) \right\},$$

$$0 < x < \infty \tag{73}$$

They are shown in Fig. 8. If the load path crosses the boundary $Q = Q_1 + f(P-P_1)$ the slip process returns to regime *II*.

Regime *VII* is characterized by $db/dt > 0$, $V(x) < 0$, and $\max(a,a_2) < b < a_1 < b_1$. The results are

$$b = \frac{\kappa-1}{\pi(\kappa+1)} \frac{f(P+kP_2)+Q-Q_2}{(1+k)fp^\infty} \tag{74}$$

$$S(x) = fp^\infty \left\{ -\left(\frac{x-a}{x}\right)^{1/2} H(x-a) + (1+k)\left(\frac{x-b}{x}\right)^{1/2} H(x-b) - (1+k)\left(\frac{x-a_1}{x}\right)^{1/2} H(x-a_1) + \left(\frac{x-b_1}{x}\right)^{1/2} H(x-b_1) \right\},$$

$$0 < x < \infty \tag{75}$$

The shear tractions are shown schematically in Fig. 8. If the load path crosses the boundary $Q = Q_1 - f(P-P_1)$, the slip process returns to regime *I*.

Example

As an example consider a closed rectangular load path starting and terminating at the origin, as shown in Fig. 9. Regardless of whether the load path is followed in a clockwise or counterclockwise direction, the first two legs correspond to regime *I* and, consequently from (8), (26), and (32), we have at point *B*

$$a_B = \frac{\kappa-1}{\pi(\kappa+1)} \frac{P_1}{p^\infty} \tag{76}$$

$$b_B = \frac{\kappa-1}{\pi(\kappa+1)} \frac{fP_1+Q_1}{fp^\infty} \tag{77}$$

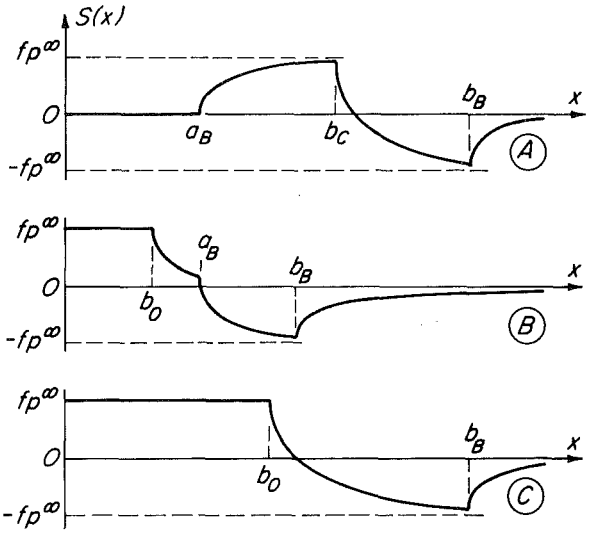

Fig. 10 Residual shear tractions left on the cut when the loads are removed: (*A*)-clockwise traverse; (*B*)-counterclockwise traverse for $f > Q_1/P_1$; (*C*)-counterclockwise traverse for $f < Q_1/P_1$.

$$S_B(x) = fp^\infty \left\{ -\left(\frac{x-a_B}{x}\right)^{1/2} H(x-a_B) + \left(\frac{x-b_B}{x}\right)^{1/2} H(x-b_B) \right\}, \quad 0 < x < \infty \tag{78}$$

Clockwise Traverse. The leg *BC* corresponds to regime *II*. It follows then from (37) and (43) that at point *C*

$$b_C = \frac{\kappa-1}{\pi(\kappa+1)} \frac{2fP_1+Q_1}{2fp^\infty} \tag{79}$$

$$S_C(x) = fp^\infty \left\{ \left(\frac{x-a_B}{x}\right)^{1/2} H(x-a_B) - 2\left(\frac{x-b_C}{x}\right)^{1/2} H(x-b_C) + \left(\frac{x-b_B}{x}\right)^{1/2} H(x-b_B) \right\},$$

$$0 < x < \infty \tag{80}$$

The segment *CO* belongs to regime *V* with $k = 0$. Consequently on the basis of (69), the residual shear stress left upon removal of the loads is

$$S_0(x) = fp^\infty \left\{ \left(\frac{x-a_B}{x}\right)^{1/2} H(x-a_B) - 2\left(\frac{x-b_C}{x}\right)^{1/2} H(x-b_C) + \left(\frac{x-b_B}{x}\right)^{1/2} H(x-b_B) \right\}, \quad 0 < x < \infty \tag{81}$$

Counterclockwise Traverse. The part *BA* of the counterclockwise load path corresponds to regime *III* with $k = 0$ and $a_A = 0$. Thus from (59)

$$S_A(x) = fp^\infty \left\{ -\left(\frac{x-a_B}{x}\right)^{1/2} H(x-a_B) + \left(\frac{x-b_B}{x}\right)^{1/2} H(x-b_B) \right\}, \quad 0 < x < \infty \tag{82}$$

For loading along the last segment *AO* of the counterclockwise circuit, it is necessary to distinguish between two cases. If $f > Q_1/P_1$, the whole segment *AO* corresponds to regime *VI*. Then noting that $a_A = 0$, it follows from (72) and (73) with $k = 0$ that

$$b_0 = \frac{\kappa-1}{\pi(\kappa+1)} \frac{Q_1}{fp^\infty} \tag{83}$$

Downloaded 02 May 2010 to 171.66.16.246. Redistribution subject to ASME license or copyright; see http://www.asme.org/terms/Terms_Use.cfm

$$S_0(x)=fp^\infty\left\{1-\left(\frac{x-b_0}{x}\right)^{1/2}H(x-b_0)\right.$$

$$\left.-\left(\frac{x-a_B}{x}\right)^{1/2}H(x-a_B)+\left(\frac{x-b_B}{x}\right)^{1/2}H(x-b_B)\right\},$$

$$0<x<\infty \tag{84}$$

In case of $f < Q_1/P_1$, only the first part of the segment AO belongs to regime *VI*. It is seen from Fig. 7 that the point on AO at which a transition to a different regime takes place is $Q = Q_1 - fP_1$. At this point,

$$b=\frac{\kappa-1}{\pi(\kappa-1)}\frac{P_1}{p^\infty}=a_B \tag{85}$$

$$S(x)=fp^\infty\left\{1-2\left(\frac{x-a_B}{x}\right)^{1/2}H(x-a_B)\right.$$

$$\left.+\left(\frac{x-b_B}{x}\right)^{1/2}H(x-b_B)\right\},\quad 0<x<\infty \tag{86}$$

from (72) and (73). Although loading from regime *VI* has not been considered, there is no need to do new mathematics. Comparing (86) with (63) for $a_2 = 0$, $b_2 = a_B$ and $b_1 = b_B$, it is seen that loading along the bottom part of AO is the same as loading that starts and stays in regime *II*. Consequently

$$b_0=\frac{1}{2}b_B \tag{87}$$

from (37), and (43) yields

$$S_0(x)=fp^\infty\left\{1-2\left(\frac{x-b_0}{x}\right)^{1/2}H(x-b_0)\right.$$

$$\left.+\left(\frac{x-b_B}{x}\right)^{1/2}H(x-b_B)\right\},\quad 0<x<\infty \tag{88}$$

for the residual shear tractions left when the concentrated load is completely removed.

The residual shear tractions given by (81), (84), and (88) are shown schematically in Fig. 10. It is seen that the residual tractions are quite different not only for the two directions of traverse, but that also their qualitative features may be affected by the value of the friction coefficient.

Acknowledgment

Support by the Office of Naval Research under contract N00 014-81-K-0626 is gratefully acknowledged.

References

1 Dundurs, J., and Comninou, M., "An Educational Elasticity Problem With Friction. Part 1: Loading, and Unloading for Weak Friction," ASME JOURNAL OF APPLIED MECHANICS, Vol. 48, 1981, pp. 841–845.

2 Comninou, M., and Dundurs, J., "An Educational Elasticity Problem With Friction. Part 2: Unloading for Strong Friction and Reloading," ASME JOURNAL OF APPLIED MECHANICS, Vol. 49, 1982, pp. 47–51.

Downloaded 02 May 2010 to 171.66.16.246. Redistribution subject to ASME license or copyright; see http://www.asme.org/terms/Terms_Use.cfm

Stress Couple Concentrations for Cylindrically Bent Plates With Circular Holes or Rigid Inclusions

E. Reissner
Department of Applied Mechanics and Engineering Sciences, University of California, San Diego, La Jolla, Calif. 92093
Fellow ASME

We obtain explicit solutions for the two problems considered, in terms of Poisson's ratio ν and in terms of a parameter μ which is of the order of the ratio of hole radius a to plate thickness h, through application of a sixth-order theory of shear deformable plates, with this solution involving distinct edge zone and interior solution contributions when $1 << \mu$. It is shown that in this range some relevant asymptotic Bessel function formulas furnish explicit examples concerning the distinction between first-order shear corrections and second-order (Timoshenko-type) shear corrections which have been established in a recent general analysis.

Introduction

In what follows we supplement a recent consideration of the distinction between first and second-order shear deformation effects, and their dependence on edge zone and/or interior solution contributions in the linear two-dimensional theory of transverse bending of two-dimensionally isotropic homogeneous plates [4], by the consideration of two specific examples. The first example complements earlier results for *plain* bending of a plate with circular hole [3] by providing analogous results for *cylindrical* bending. The second example represents a modified derivation of an unpublished result by C. C. Pai [2] for the problem of cylindrical bending of a plate with rigid circular inclusion.

In regard to the results obtained, it is of particular interest to observe that while for the problem of the plate with a hole both first and second-order shear corrections come from the edge zone solution contribution, the opposite state of affairs prevails for the problem of the plate with a rigid inclusion, for which there are no first-order corrections and for which the second-order corrections come from the interior solution contribution.

Differential Equations, Boundary Conditions, and Particular Solutions

We have as expressions for stress couples M, stress resultants Q, and angular displacements ϕ with reference to polar coordinates r, θ in the plane of a uniform isotropic shear deformable plate acted upon by edge loads [4]

$$M_{rr} = -D\left(v_{,rr} + \nu\frac{v_{,r}}{r} + \nu\frac{v_{,\theta\theta}}{r^2}\right) + \frac{2}{\lambda^2}\left(\frac{\chi_{,\theta r}}{r} - \frac{\chi_{,\theta}}{r^2}\right), \quad (1)$$

$$M_{\theta\theta} = -D\left(\frac{v_{,r}}{r} + \frac{v_{,\theta\theta}}{r^2} + \nu\, v_{,rr}\right) - \frac{2}{\lambda^2}\left(\frac{\chi_{,\theta r}}{r} - \frac{\chi_{,\theta}}{r^2}\right), \quad (2)$$

$$M_{r\theta} = -(1-\nu)D\left(\frac{v_{,\theta r}}{r} - \frac{v_{,\theta}}{r^2}\right) - \chi + \frac{2}{\lambda^2}\left(\frac{\chi_{,r}}{r} + \frac{\chi_{,\theta\theta}}{r^2}\right), \quad (3)$$

$$Q_r = -D(\nabla^2 v)_{,r} + \frac{\chi_{,\theta}}{r}, \quad Q_\theta = -D\frac{(\nabla^2 v)_{,\theta}}{r} - \chi_{,r}, \quad (4a,b)$$

$$D\,\phi_r = -D\,v_{,r} + \frac{2\lambda^{-2}}{1-\nu}\frac{\chi_{,\theta}}{r}, \quad D\,\phi_\theta = -D\frac{v_{,\theta}}{r} - \frac{2\lambda^{-2}}{1-\nu}\chi_{,r}. \quad (5a,b)$$

In this

$$v = w + \frac{2}{\lambda^2}\frac{\nabla^2 w}{1-\nu}, \quad \frac{1}{\lambda^2} = \frac{1-\nu}{2}B\,D, \quad (6a,b)$$

with D and B being transverse bending stiffness and transverse shear deformability factors[1] and with w and χ being solutions of the differential equations

$$\nabla^2\nabla^2 w = 0, \quad \nabla^2\chi - \lambda^2\chi = 0. \quad (7a,b)$$

Given the sixth-order differential equation system (7a,b) we have for the case of cylindrical bending at distances large compared with the radius of a circular hole or rigid inclusion the stipulations

$$r \to \infty; \quad w \to -\frac{M_0 x^2}{2D} = -\frac{M_0 r^2}{2D}\frac{1+\cos 2\theta}{2}, \quad \chi \to 0. \quad (8a,b)$$

At the same time we have as conditions at the edge of a hole of radius a,

[1] In the original approximate three-dimensional analysis of transversely homogeneous plates [3] $D = Eh^3/12(1-\nu^2)$ and $B = 12(1+\nu)/5\,Eh$, and therewith $1/\lambda = h/\sqrt{10}$.

Contributed by the Applied Mechanics Division for presentation at the 1983 ASME Applied Mechanics, Bioengineering, and Fluids Engineering Conference, Houston, Texas, June 20–22, 1983 of THE AMERICAN SOCIETY OF MECHANICAL ENGINEERS.

Discussion on this paper should be addressed to the Editorial Department, ASME, United Engineering Center, 345 East 47th Street, New York, N.Y. 10017, and will be accepted until two months after final publication of the paper itself in the JOURNAL OF APPLIED MECHANICS. Manuscript received by ASME Mechanics Division, April 1982. Paper No. 83-APM-5.

Copies will be available until February, 1984.

Copyright © 1983 by ASME
Downloaded 02 May 2010 to 171.66.16.246. Redistribution subject to ASME license or copyright; see http://www.asme.org/terms/Terms_Use.cfm

$$r = a\,; \quad Q_r = 0\,, \quad M_{rr} = 0\,, \quad M_{r\theta} = 0\,, \qquad (9a,b,c)$$

and at the edge of a rigid circular inclusion

$$r = a\,; \quad w = 0\,, \quad \phi_r = 0\,, \quad \phi_\theta = 0\,. \qquad (10a,b,c)$$

Given the behavior of the solutions w and χ at infinity as in (8), in conjunction with the *homogeneous* boundary conditions (9) or (10), we have that appropriate particular solutions of (7) are of the form

$$w = -\frac{M_0 a^2}{2D}\left[\frac{1}{2}\frac{r^2}{a^2} + C_0 + C_1 \ln\frac{r}{a} + \left(\frac{1}{2}\frac{r^2}{a^2} + C_2\frac{a^2}{r^2} + C_3\right)\cos 2\theta\right], \qquad (11)$$

$$\chi = M_0\, C_4 \frac{K_2(\lambda r)}{K_2(\mu)} \sin 2\theta, \quad \mu = \lambda a\,, \qquad (12)$$

with K_2 being the appropriate modified Bessel function of order two [1], with the constants of integration C_n having to be determined by means of (9) or (10), and with the Laplacian $\nabla^2 w$ given by

$$\nabla^2 w = -\frac{M_0}{D}\left(1 - 2\,C_3\frac{a^2}{r^2}\cos 2\theta\right). \qquad (13)$$

Remarkably, the boundary condition $M_{rr}(a,\theta) = 0$ for the problem of the hole implies as expression for the *circumferential* edge bending moment

$$M_{\theta\theta}(a,\theta) = -(1+\nu)D\nabla^2 w(a,\theta)\,, \qquad (14)$$

while the boundary conditions $\phi_r(a,\theta) = \phi_\theta(a,\theta) = 0$ for the problem of the rigid inclusion imply as expression for the *radial* edge bending moment

$$M_{rr}(a,\theta) = -D\nabla^2 w(a,\theta)\,, \qquad (15)$$

with these two formulas being the basis of the wanted expressions for stress couple concentration factors.

Stress Couple Concentration Factor for Plate With Circular Hole

The introduction of (11)–(13) in (6*a*), (1), and (3) gives, as a consequence of the boundary conditions (9*a*,*b*,*c*), the relation $(1-\nu)C_1 = 1 + \nu$ as well as the system of three simultaneous equations

C_2	C_3	C_4	*RHS*	
0	4	2	0	(17*a*)
$3(1-\nu)$	$-2\nu - \dfrac{24}{\mu^2}$	$\dfrac{4K_2'(\mu)}{\mu K_2(\mu)} - \dfrac{4}{\mu^2}$	$-\dfrac{1-\nu}{2}$	(17*b*)
$3(1-\nu)$	$1-\nu-\dfrac{24}{\mu^2}$	$-1+\dfrac{2K_2'(\mu)}{\mu K_2(\mu)} - \dfrac{8}{\mu^2}$	$\dfrac{1-\nu}{2}$	(17*c*)

For the interpretation of this system we need, in particular, the asymptotic Bessel function relation [1]

$$1 << \mu: \quad \frac{K_2'(\mu)}{K_2(\mu)} \approx -\frac{1+19/8\mu}{1+15/8\mu} \approx -1 - \frac{1}{2\mu}\,, \qquad (18)$$

but before undertaking this interpretation we note, as part of the explicit solution of (17*a*,*b*,*c*), that

$$\left(3 + \nu + \frac{4K_2'}{\mu K_2} + \frac{8}{\mu^2}\right)C_3 = (1-\nu)\,. \qquad (19)$$

The introduction of (19) into the circumferential edge bending-moment formula (15) then gives as the value of the associated stress couple concentration factor

$$k_H = \frac{M_{\theta\theta}(a,\pi/2)}{M_0} = (1+\nu)\left[1 + \frac{2-2\nu}{3+\nu+\dfrac{4K_2'(\mu)}{\mu K_2(\mu)} + \dfrac{8}{\mu^2}}\right]. \qquad (20)$$

Equation (20), in conjunction with (18), implies the approximate relation

$$k_H(\mu) \approx \frac{5+4\nu-\nu^2}{3+\nu}\left[1 + \frac{8-8\nu}{15+2\nu-\nu^2}\frac{1}{\mu}\left(1 - \frac{1+3\nu}{6+2\nu}\frac{1}{\mu}\right)\right], \qquad (21a)$$

for $1 << \mu$. At the same time it also follows from (20) that

$$k_H(0) = 3 - \nu\,, \qquad (21b)$$

with this latter result being a consequence of the formula

$$K_2' = -K_1 - 2\mu^{-1}K_2, \qquad (22)$$

in conjunction with the approximation $K_1(\mu)/K_2(\mu) \approx \mu/2$ for $\mu << 1$.[2]

First and Second-Order Transverse Shear Corrections for Large μ. As far as equation (21*a*) for the values of the stress couple concentration factor k_H is concerned the correction of first order is represented by the term with $1/\mu$ inside the bracket on the right, and the corresponding correction of the second order by the term with $1/\mu^2$.

As regards the origin of these correction terms we take account of the fact, which follows here directly from the form of the solution contributions (11) and (12), that in the range $1 << \mu$ it is appropriate to designate χ as the *edge zone* solution contribution and w as the *interior* solution contribution. It is then further appropriate to raise the question to what extent first and second-order shear corrections are associated with edge zone and/or interior contributions to the solution of the given boundary value problem. The answer to this question may be deduced from the form of the simultaneous equation system (17*a*,*b*,*c*), in which, it is recalled, C_2 and C_3 come from the interior solution contribution and C_4 from the edge zone contribution. Upon writing in (17*b*,*c*)

$$\frac{4K_2'}{\mu K_2} - \frac{4}{\mu^2} \approx -\frac{4}{\mu} - \frac{6}{\mu^2}\,,$$

$$-1 + \frac{2K_2'}{\mu K_2} - \frac{8}{\mu^2} \approx -1 - \frac{2}{\mu} - \frac{9}{\mu^2}\,, \qquad (23)$$

[2] It is recalled that the corresponding results for the problem of *plain* bending [3] have a factor $5 + 3\nu$ in place of $5 + 4\nu - \nu^2$ in (21*a*), and a value of 3 in place of $3 - \nu$ in (21*b*).

Downloaded 02 May 2010 to 171.66.16.246. Redistribution subject to ASME license or copyright; see http://www.asme.org/terms/Terms_Use.cfm

we see that first *and* second-order shear corrections come from the edge zone solution contribution, while only second-order corrections come from the interior solution contribution.

Going beyond this, two further conclusions may be established on the basis of (17) in conjunction with (23). The first of these is that for the given specific problem both the first and the second-order corrections in the stress couple concentration formula (21*a*) come *exclusively* from the edge zone solution contribution. The second conclusion, which for the present specific problem is not of technical importance, is as follows. As long as second-order effects are disregarded systematically, by deletion of all $0(\mu^{-2})$ terms in (17), the given three-by-three system of equations may be reduced to a two-by-two system for the determination of the interior contribution coefficients C_2 and C_3 alone by considering the combinations (17*a*) + 2 $(1-\mu^{-1})$ (17*c*) and (17*b*) − 4 μ^{-1} (17*c*), as follows,

C_2	C_3	RHS	
$6(1-\nu)(1-\mu^{-1})$	$4+(1-\nu)(1-\mu^{-1})$	$(1-\nu)(1-\mu^{-1})$	(24*a*)
$3(1-\nu)(1-4\mu^{-1})$	$-2\nu-4(1-\nu)\mu^{-1}$	$-\frac{1}{2}(1-\nu)(1+4\mu^{-1})$	(24*b*)

Equations (24*a*) and (24*b*) are consistent with a set of *two contracted boundary conditions, including first-order shear correction terms, for the determination of the interior solution contribution*, as given in [4].[3]

Stress Couple Concentration Factor for Plate With Rigid Circular Inclusion

In satisfying the boundary conditions (10*a*,*b*,*c*) on the basis of (5*a*,*b*), (6*a*), (11), and (12) it is convenient, as may be surmised from the asymptotic considerations in [4], to introduce a modified coefficient $C_4{}^*$ by means of the relation

$$C_4 = \mu C_4{}^* . \tag{25}$$

When this is done there follows from (10*a*,*b*,*c*) as a system of simultaneous equations for C_2, C_3, and $C_4{}^*$,

C_2	C_3	$C_4{}^*$	RHS	
2	2	0	−1	(26*a*)
−2	$\frac{1}{1-\nu}\frac{16}{\mu^2}$	$\frac{1}{1-\nu}\frac{8}{\mu}$	−1	(26*b*)
0	$\frac{1}{1-\nu}\frac{16}{\mu^2}$	$-\frac{4}{1-\nu}\frac{K_2'(\mu)}{K_2(\mu)}$	0	(26*c*)

and therewith, in place of (19), as equation for C_3,

$$\left(1-\nu+\frac{16}{\mu^3}\frac{K_2}{K_2'}+\frac{8}{\mu^2}\right)C_3 = -(1-\nu). \tag{27}$$

The introduction of (27) in conjunction with (22) into (16) then gives as expression for the stress couple concentration factor of the present problem

$$k_1 = \frac{M_{rr}(a,0)}{M_0} = 1 + \frac{2-2\nu}{1-\nu+\frac{8}{\mu^2}+\frac{16}{\mu^3}\frac{K_2(\mu)}{K_2'(\mu)}}, \tag{28}$$

with this formula being equivalent to an earlier unpublished result, of a somewhat more complex appearance, by Pai [2]. Equation (28) implies the approximate relation

$$k_1(\mu) \approx 3 - \frac{16}{1-\nu}\frac{1}{\mu^2}\left(1-\frac{2}{\mu}\right), \tag{29a}$$

for $1 << \mu$, as well as that

$$k_1(0) = \frac{5-3\nu}{3-\nu} . \tag{29b}$$

First and Second-Order Transverse Shear Corrections for Large μ. Equation (29*a*) indicates that there are *no* first-order shear corrections insofar as the values of k_1 are concerned. Furthermore, for this problem, in contrast to the corresponding result for the problem of the circular hole, the *entire* second-order shear correction for k_1 comes from the effect of transverse shear deformability on the *interior* solution contribution. To see this without making use of the explicit solution (27) introduce (18) into (26*c*), so as to have $C_4{}^* \approx -4\mu^{-2} C_3$, with (26*a*,*b*) then giving in turn

$$\left(2+\frac{16}{1-\nu}\frac{1}{\mu^2}-\frac{32}{1-\nu}\frac{1}{\mu^3}\right)C_3 \approx -2, \tag{30}$$

and with the edge-zone solution contribution evidently being responsible for a *third*-order transverse shear deformation effect.

We observe finally that equations (26*b*,*c*) are consistent with the previously established result [4] that up to terms of relative order $1/\mu$ the coefficients C_2 and C_3 of the interior solution contribution may be determined without explicit reference to the edge zone contribution, by means of the system of contracted boundary conditions $w(a,\theta) = \bar{w}(a,\theta)$ and $w_{,r}(a,\theta) - (1/\mu)(w_{,\theta}/a) = \bar{\phi}_r - (1/\mu)(\bar{\phi}_{\theta,\theta}/a)$.

[3] Equations (23*b*,*a*) in [4] correspond to the present equations (24*a*,*b*).

References

1 Abramovich, M., and Stegun, I. A., *Handbook of Mathematical Functions*, 1964.

2 Pai, C. C., "Some Applications of a Theory of Plates Which Include the Effect of Transverse Shear Deformation," M.S. Thesis, Massachusetts Institute of Technology, Cambridge, Mass., Sept. 1946.

3 Reissner, E., "The Effect of Transverse Shear Deformation on the Bending of Elastic Plates," ASME JOURNAL OF APPLIED MECHANICS, Vol. 12, 1945, pp. A69–A77; Vol. 13, 1946, p. A252.

4 Reissner, E., "On the Analysis of First and Second-Order Shear Deformation Effects for Isotropic Elastic Plates," ASME JOURNAL OF APPLIED MECHANICS, Vol. 47, 1980, pp. 959–961.

Downloaded 02 May 2010 to 171.66.16.246. Redistribution subject to ASME license or copyright; see http://www.asme.org/terms/Terms_Use.cfm

Plastic Buckling of Initially Imperfect Stiffened Cylinders in Axial Compression

G. A. Duffett
Graduate Student,
Department of Civil Engineering.

B. D. Reddy
Senior Lecturer,
Department of Applied Mathematics and
Department of Civil Engineering.

University of Cape Town,
Private Bag Rondebosch,
7700,
Republic of South Africa

The behavior in the plastic range of axially compressed stringer-stiffened cylinders is investigated. The shell under consideration is assumed to have an initial imperfection in the form of sinusoidal deviation both axially and circumferentially. The constitutive relation employed here is J_2 deformation theory of plasticity. This relation, as well as kinematic assumptions regarding the behavior of the panels and stiffeners that constitute the stiffened shell, is used in the principle of virtual work to obtain a set of nonlinear algebraic equations whose solution provides complete information about the prebuckling equilibrium path. Bifurcation from the primary path is examined by making use of a functional whose first variation is zero when two solutions to the problem are possible. This leads to an eigenvalue problem, the eigenvalue being the critical compressive load and the eigenfunction being the corresponding buckling mode. Results are presented for shells of different geometries and material properties, and a comparison of results is made with results obtained by others. The imperfect shells analyzed all exhibit stable behavior, with sufficiently large imperfections having a beneficial effect. Results for bifurcation from these paths are also discussed.

1 Introduction

Interest in the behavior of stiffened cylinders in axial compression has been generated by their use as components of large offshore structures and also for aerospace structures. The latter generally comprise relatively thin shells with closely spaced stiffeners, and tend to buckle into an overall mode in which one half-wave in the circumferential direction may extend across a number of stiffeners. Critical stresses are generally calculated by "smearing-out" the stiffener properties to obtain an equivalent orthotropic cylinder of uniform thickness [1].

In contrast, offshore structures are usually sparsely stiffened, and the stiffeners are sufficiently flexible torsionally to be able to twist along their length. These marine structures are very susceptible to geometric imperfections which may arise during fabrication and as a result of damage during transportation. Such imperfections can alter the behavior of stiffened cylinders in service and their consequences are thus of particular interest, with regard to buckling in axial compression.

In this paper we investigate the effects of initial imperfections on the behavior of longitudinally stiffened cylinders, which are subjected to axial compression. Elastic-plastic behavior is considered, and the material model we use is J_2 deformation theory. We consider sparsely stiffened cylinders that have an imperfection in the form of a sinusoidal deviation from the perfect geometry of the shell, both longitudinally and circumferentially. Deformation along the primary path then amounts to a growth of the imperfection with increase in load, and we subsequently investigate the possibility of bifurcation from this equilibrium path.

Koiter [2] considered the buckling and postbuckling behavior of a cylindrical elastic panel, and found that sufficiently flat panels had stable postbuckling behavior, while less flat panels had unstable postbuckling behavior. Koiter's analysis was extended by Stephens [3], who included the effects of torsional rigidity along the edge generators of the panel. It was found that this torsional rigidity reduced the sensitivity to imperfections.

Wang and Lin [4] approached the buckling problem of an elastic discretely stiffened cylinder in axial compression by treating the stiffeners, and the panels between adjacent stiffeners, as separate structural components. Donnell's shell theory was used for the panels and Vlasov's thin-walled beam theory was used for the stiffeners. Critical load obtained by this analysis were lower than those obtained using the "smeared" analysis.

Syngellakis and Walker [5] approached the problem of buckling of elastic stiffened cylinders by treating the stiffeners as long narrow plates. It was shown that these stiffened cylinders had several critical loads in close proximity, which could result in a coupling of modes in the post critical range and thus lead to an increase in imperfection-sensitivity.

In a subsequent paper Syngellakis and Walker [6] con-

Contributed by the Applied Mechanics Division for publication in the JOURNAL OF APPLIED MECHANICS.

Discussion on this paper should be addressed to the Editorial Department, ASME, United Engineering Center, 345 East 47 Street, New York, N.Y. 10017, and will be accepted until two months after final publication of the paper itself in the JOURNAL OF APPLIED MECHANICS. Manuscript received by ASME Applied Mechanics Division, December, 1981; final revision, July, 1982.

Copyright © 1983 by ASME
Downloaded 02 May 2010 to 171.66.16.246. Redistribution subject to ASME license or copyright; see http://www.asme.org/terms/Terms_Use.cfm

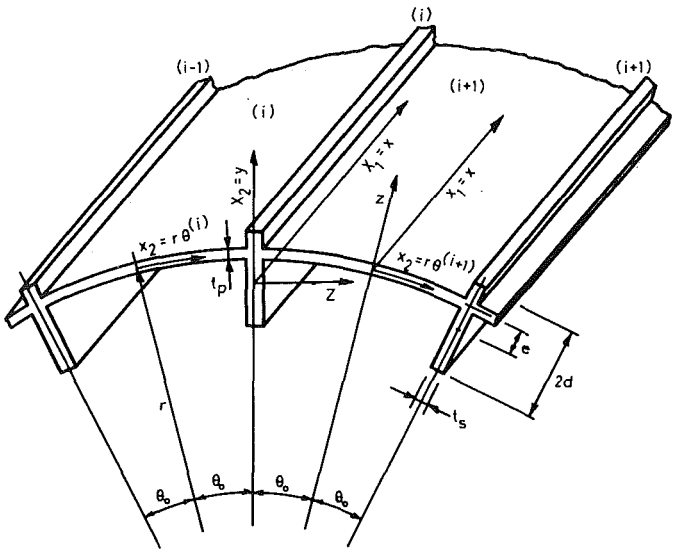

Fig. 1 Geometry of stiffened cylinder

sidered the effects of initial imperfections on the bifurcation of stiffened cylinders. The imperfection chosen had the approximate shape of the symmetric buckling mode in [5], and bifurcation into a mode that was antisymmetric with respect to the panel midgenerators was considered. The critical loads for this antisymmetric mode were found to be higher than those obtained in [5] for the perfect shell, and once again there were several critical loads in close proximity.

Work done in the plastic range was initiated by Tvergaard [7] who extended Koiter's [2] analysis of a cylindrical panel into the plastic range. Tvergaard found that for a high strain-hardening material the panel was only imperfection-sensitive if the panel curvature exceeded a certain value. Reddy [8] extended Syngellakis and Walker's [5] analysis of a simply supported cylindrical shell into the plastic range.

Experimental analyses were carried out by Walker and Davies [9] on fixed-ended steel cylinders in axial compression, and a simply supported stiffened cylinder made of araldite was tested by Syngellakis and Walker [5, 6].

The present analysis is essentially an extension of the work done by Syngellakis and Walker [6] into the plastic range. The analysis is concerned with the effects of geometric imperfections on the behavior of simply supported stiffened cylindrical shells in axial compression. Load-deformation behavior on the primary equilibrium path is investigated, and bifurcation into a mode that is antisymmetric with respect to the panel midgenerators, is sought. A selection of results is presented, and discussed with reference to earlier work.

2 Basic Results for the Primary Path

The shell considered comprises a circular cylinder with an even number of equally spaced longitudinal stiffeners, as shown in Fig. 1. The cylinder has length l, radius r, and wall thickness t_p. There are N stiffeners which have depth $2d$ and thickness t_s. Each panel has angular width $2\theta_0$ where $\theta_0 = \pi/N$.

Points on the midsurface of the ith panel are defined by the pair $(x, r\theta^{(i)})$ or (x_1, x_2) of cylindrical coordinates while points on the midsurface of the ith stiffener are defined by a pair (x,y) or (X_1, X_2) of cartesian coordinates. Distances normal to the panel midsurface are measured by the coordinate z, while the distances normal to the stiffener midsurface are measured by the coordinate Z. These coordinate systems are also shown in Fig. 1. The superscript (i) denoting the ith panel or stiffener is omitted when referring to any typical panel or stiffener. The centroids of the stiffeners are a distance $y = e$ from the midsurface of the shell.

Panel and stiffener displacement vectors are defined, respectively, by

$$\mathbf{u} = u_\alpha \mathbf{e}_\alpha + w\mathbf{e}_3, \quad \mathbf{U} = U_\alpha \mathbf{g}_\alpha + W\mathbf{g}_3 \tag{1}$$

where $\mathbf{e}_i$ and $\mathbf{g}_i$ are unit base vectors of the panels and stiffeners, respectively. Greek subscripts range from 1 to 2 and summation is implied over repeated indices here and elsewhere. Henceforth we write $(u_1, u_2) = (u,v)$ and $(U_1, U_2) = (U,V)$.

The initial stress-free imperfection in the panels is denoted by $\bar{w}$, and the corresponding imperfection in the stiffeners is denoted by $\bar{W}$. A fundamental requirement is that of continuity of displacements and slopes at the ith panel-stiffener junction, which can be expressed as

$$\mathbf{u}^{(i)}(x,\theta_0) = \mathbf{U}^{(i)}(x,e) = \mathbf{u}^{(i+1)}(x,-\theta_0),$$
$$(w+\bar{w})^{(i)}_{,\theta}(x,\theta_0) = -r(W+\bar{W})^{(i)}_{,y}(x,e)$$
$$= (w+\bar{w})^{(i+1)}_{,\theta}(x,-\theta_0). \tag{2}$$

Assuming that the stiffener cross sections remain straight and normal to the shell [5], the stiffener displacements can be obtained in terms of the panel displacements as follows:

$$U^{(i)}(x,y) = u^{(i)}(x,\theta_0) - (y-e)\,w^{(i)}_{,x}(x,\theta_0),$$
$$V^{(i)}(x,y) = \zeta\, w^{(i)}(x,\theta_0), \tag{3}$$
$$(W+\bar{W})^{(i)}(x,y) = v^{(i)}(x,\theta_0) - \frac{1}{r}(y-e)[(w+\bar{w})^{(i)}_{,\theta}(x,\theta_0)]$$

where $\zeta = 1, +(y-e)/r$.

The strain-displacement relations corresponding to Donnell-Mushtari-Vlasov shell theory [10] are used for a typical panel; these are

$$\epsilon_{\alpha\beta}(x_1,x_2) = \frac{1}{2}(u_{\alpha,\beta} + u_{\beta,\alpha}) - b_{\alpha\beta}w$$
$$+ \frac{1}{2}(w_{,\alpha}w_{,\beta} + w_{,\alpha}\bar{w}_{,\beta} + \bar{w}_{,\alpha}w_{,\beta}), \tag{4}$$
$$\kappa_{\alpha\beta}(x_1,x_2) = w_{,\alpha\beta}. \tag{5}$$

Here $\epsilon_{\alpha\beta}$ and $\kappa_{\alpha\beta}$ are the midsurface membrane and bending strain tensors and $b_{\alpha\beta}$ is the curvature tensor for the undeformed midsurface ($b_{22} = -1/r$, others are zero). The midsurface membrane and bending strains $E_{\alpha\beta}$ and $K_{\alpha\beta}$ for a typical stiffener, treated as a flat plate, are defined similarly. The strain tensors at any point through the thickness of a typical panel or stiffener are given by

$$\eta_{\alpha\beta}(x_1,x_2,z) = \epsilon_{\alpha\beta} - z\kappa_{\alpha\beta}, \quad H_{\alpha\beta}(X_1,X_2,Z) = E_{\alpha\beta} - ZK_{\alpha\beta}. \tag{6}$$

Small-strain J_2 deformation theory of plasticity is employed here since, for problems involving buckling of elastic-plastic thin shells, deformation theory is known to yield results that are generally in better agreement with experimental data than results obtained using flow theory. For the present problem the deviation from proportional loading is expected to be small, so it would seem reasonable to use deformation theory [11].

The following uniaxial stress-strain curve, first suggested in [12], is adopted here:

$$E\bar{\eta} = \bar{\sigma} \quad \text{for} \quad \bar{\sigma} \le \sigma_y,$$
$$E\bar{\eta} = \sigma_y[(\bar{\sigma}/\sigma_y)^n + n - 1]/n \quad \text{for} \quad \bar{\sigma} > \sigma_y, \tag{7}$$

where $\bar{\sigma}$, $\bar{\eta}$ are the effective stress and total effective strain, σ_y is the yield stress in simple tension, E is Young's modulus, and n is the strain-hardening parameter. This stress-strain curve

Downloaded 02 May 2010 to 171.66.16.246. Redistribution subject to ASME license or copyright; see http://www.asme.org/terms/Terms_Use.cfm

has a definite yield stress and the first derivative or tangent modulus is continuous at the yield stress. Assuming conditions of approximate plane stress in the panels and the stiffeners, the constitutive relations in the panels are

$$E_s\,\eta_{\alpha\beta} = (1+\nu_s)\,\sigma_{\alpha\beta} - \nu_s\,\sigma_{\gamma\gamma}\,\delta_{\alpha\beta} \tag{8}$$

with $2\nu_s = 1 + E_s(2\nu - 1)/E$, $E_s = \bar{\sigma}/\bar{\eta}$, while the constitutive relations in the stiffeners are identical to equations (8) with $\eta_{\alpha\beta}$ replaced by $H_{\alpha\beta}$. Here ν is Poisson's ratio and $\delta_{\alpha\beta}$ is the two-dimensional Kronecker delta.

Equation (8) can be inverted to obtain the stresses at any point within the panels; the same can be done for the stiffeners. Thus,

$$\boldsymbol{\sigma}^p = \mathbf{C}\,\boldsymbol{\eta}, \quad \boldsymbol{\sigma}^s = \mathbf{C}\,\mathbf{H} \tag{9}$$

where $\boldsymbol{\sigma}^p = (\sigma_{xx}, \sigma_{\theta\theta}, \sigma_{x\theta})^T$, $\boldsymbol{\sigma}^s = (\sigma_{xx}, \sigma_{yy}, \sigma_{xy})^T$

$\boldsymbol{\eta} = (\eta_{xx}, \eta_{\theta\theta}, 2\eta_{x\theta})$, $H = (H_{xx}, H_{\theta\theta}, 2H_{x\theta})$, and $\mathbf{C}$ is the usual constitutive matrix for plane stress with E and ν replaced by E_s and ν_s.

The initial imperfection chosen is one that corresponds approximately to the shape of the buckling mode of perfect stiffened cylinder [6, 8]; that is, the radial imperfection in the shell consists of a sinusoidal variation in the axial direction, the number of half-waves being left arbitrary, while the circumferential variation is a single half sine wave between two stiffeners, symmetrical about the lines $\theta^{(i)} = 0$. Thus,

$$\bar{w}^{(i)} = \mu^{(i)} \sin\alpha\xi\cos\beta\theta^{(i)}, \quad \mu^{(i+1)} = -\mu^{(i)} \tag{10}$$

where $\mu^{(i)}$ is the imperfection amplitude in the ith panel, $\xi = x/r$, $\alpha = m\pi r/l$ where m is the number of axial half-waves, and $\beta = N/2$. Furthermore, the corresponding imperfection in the ith stiffener can be obtained from the last of equations (3), i.e.,

$$\bar{W}^{(i)} = \frac{\beta}{r}\,(y-e)\,\mu^{(i)}\sin\alpha\xi. \tag{11}$$

The radial displacement $w^{(i)}$ must comprise a uniform expansion and a term of the same shape as the initial imperfection, which would allow for a "growth" of this imperfection. The symmetry of $w^{(i)}$ and $\bar{w}^{(i)}$ is supported by experimental evidence of Walker and Davis [9]. The displacement functions for the ith panel are thus

$$\begin{aligned} u^{(i)} &= u_{01}^{(i)}\,\xi + u_{02}^{(i)}\cos\alpha\xi\cos\beta\theta^{(i)}, \\ v^{(i)} &= v_{01}^{(i)}\sin\alpha\xi\sin\beta\theta^{(i)}, \\ w^{(i)} &= w_{01}^{(i)} + w_{02}^{(i)}\sin\alpha\xi\cos\beta\theta^{(i)}, \end{aligned} \tag{12}$$

with

$$\begin{aligned} &(u_{01}, u_{02}, v_{01}, w_{01}, w_{01})^{(i+1)} \\ &\quad = (u_{01}, -u_{02}, -v_{01}, w_{01}, -w_{02})^{(i)}. \end{aligned} \tag{13}$$

Using equations (3) the displacement functions $(U, V, W)^{(i)}$ for the ith stiffener are easily obtained.

From (4)–(6), (3), and (12), the vectors of strain may be written in terms of the displacement parameters as

$$\boldsymbol{\eta} = \mathbf{B}^P\mathbf{u}_0, \quad \mathbf{H} = \mathbf{B}^s\mathbf{u}_0 \tag{14}$$

for the ith panel and stiffener, where $\mathbf{u}_o^T = (u_{01}, u_{02}, v_{01}, w_{01}, w_{02})$, and $\mathbf{B}^P$ and $\mathbf{B}^s$ are 3×5 matrices whose elements are functions of the spatial coordinates, and of μ, v_{01}, and w_{02}.

Variations in the strains now amount to variations in the displacement parameters after substitution of (10) and (12) in (4) and (5). Thus

$$\delta\boldsymbol{\epsilon} = \mathbf{G}^P\delta\mathbf{u}_0, \quad \delta\boldsymbol{\kappa} = \mathbf{J}^P\delta\mathbf{u}_0, \quad \delta\mathbf{E} = \mathbf{G}^s\delta u_0, \quad \delta\mathbf{K} = \mathbf{J}^s\delta u_0, \tag{15}$$

where the elements of the matrices $\mathbf{G}^P$, $\mathbf{G}^s$, $\mathbf{J}^P$, and $\mathbf{J}^s$ are rather lengthy functions of the spatial coordinates and of μ, v_{01}, and w_{02}.

The principal virtual work, applied to the stiffened shell as a whole, becomes

$$\begin{aligned} \sum_{i=1}^{N}\Big[\delta\mathbf{u}_0^{(i)T}\Big\{&\int_{V^{p(i)}}(\mathbf{G}^{pT} - z\mathbf{J}^{pT})\,\mathbf{C}\,\mathbf{B}^p dV^{p(i)} \\ &+ \int_{V^{s(i)}}(\mathbf{G}^{sT} - Z\,\mathbf{J}^{sT})\,\mathbf{C}\,\mathbf{B}^s dV^{s(i)}\Big\}\mathbf{u}_o^{(i)} \\ &- \delta\mathbf{u}_o^{(i)T}\mathbf{F}^{(i)}\Big] = 0 \end{aligned} \tag{16}$$

where the last term is the external virtual work, with

$$\mathbf{F}^{(i)} = (-2\sigma l[t_p\theta_0 + t_s d/r], 0, 0, 0, 0)^T.$$

From the connections (13) and various symmetries peculiar to this problem, it can be shown [12] that integration over the areas $\mathbf{A}^{p(i)}$ and $\mathbf{A}^{s(i)}$ for the whole stiffened shell in (16) can be replaced by multiples of integrals over the interval $0 \le x \le 2l/m$, for a single panel and stiffener.

The necessary integrations over the areas were performed numerically using Gaussian quadrature, and integration through the thickness was carried out numerically, using a modification of Gaussian quadrature which incorporates sampling points on the surfaces of the panels and stiffeners.

The foregoing procedure then leads to a set of five nonlinear algebraic equations in $\mathbf{u}_0$ and σ for a given value of imperfection amplitude μ, when the coefficients of $\delta\mathbf{u}_0$ are set equal to zero. The solution of these equations, using $\mathbf{u}_{01}$ as the independent variable, was obtained by using a modified Newton-Raphson procedure with an acceleration scheme.

3 Conditions for Bifurcation

From (4) and (5) the incremental strain-displacement relations for the panels are

$$\begin{aligned} \dot{\epsilon}_{\alpha\beta} &= \frac{1}{2}(\dot{u}_{\alpha,\beta} + \dot{u}_{\beta,\alpha}) - b_{\alpha\beta}\dot{w} + \frac{1}{2}\dot{w}_{,\alpha}(w+\bar{w})_{,\beta} \\ &\quad + \frac{1}{2}\dot{w}_{,\beta}(w+\bar{w})_{,\alpha} \\ \dot{\kappa}_{\alpha\beta} &= \dot{w}_{,\alpha\beta}, \end{aligned} \tag{17}$$

with similar expressions for the stiffeners. The incremental constitutive relations are obtained from (9) and, after manipulation, reduce to

$$\dot{\boldsymbol{\eta}} = \mathbf{P}^{-1}\dot{\boldsymbol{\sigma}}^P, \quad \dot{\mathbf{H}} = \mathbf{P}^{-1}\dot{\boldsymbol{\sigma}}^s \tag{18}$$

where

$$\mathbf{P}^{-1} = \begin{bmatrix} \Phi f(\sigma_{xx},\sigma_{\theta\theta}) + 1/E_s & \text{SYMMETRIC} \\ -\Phi g(\sigma_{xx},\sigma_{\theta\theta}) - \nu_s/E_s & \Phi f(\sigma_{\theta\theta},\sigma_{xx}) + 1/E_s \\ 3\Phi\sigma_{x\theta}(2\sigma_{xx} - \sigma_{\theta\theta}) & 3\Phi\sigma_{x\theta}(2\sigma_{\theta\theta} - \sigma_{xx})\ \ 18\Phi\sigma_{x\theta}^2 + 2(1+\nu_s)/E_s \end{bmatrix} \tag{19}$$

Downloaded 02 May 2010 to 171.66.16.246. Redistribution subject to ASME license or copyright; see http://www.asme.org/terms/Terms_Use.cfm

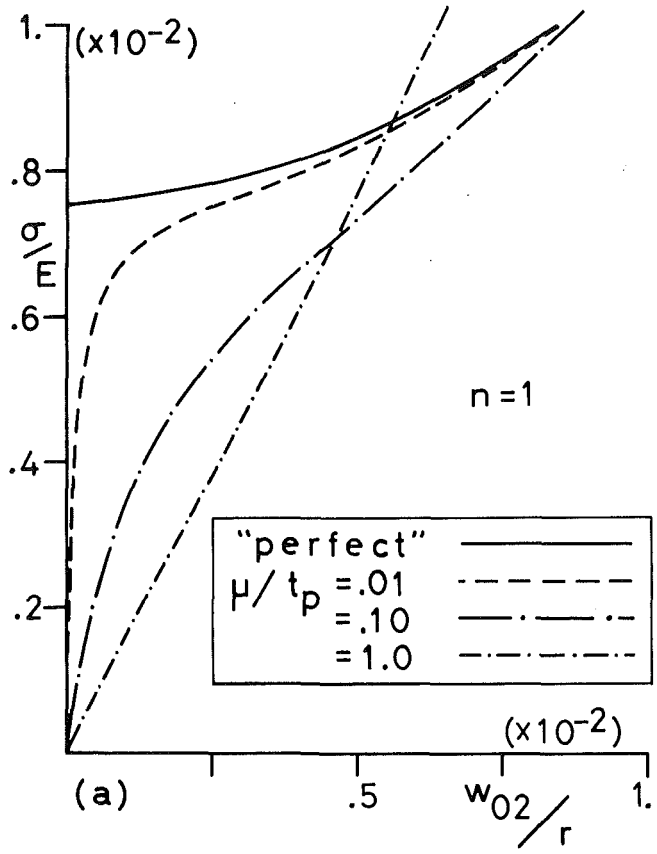

Fig. 2(a)

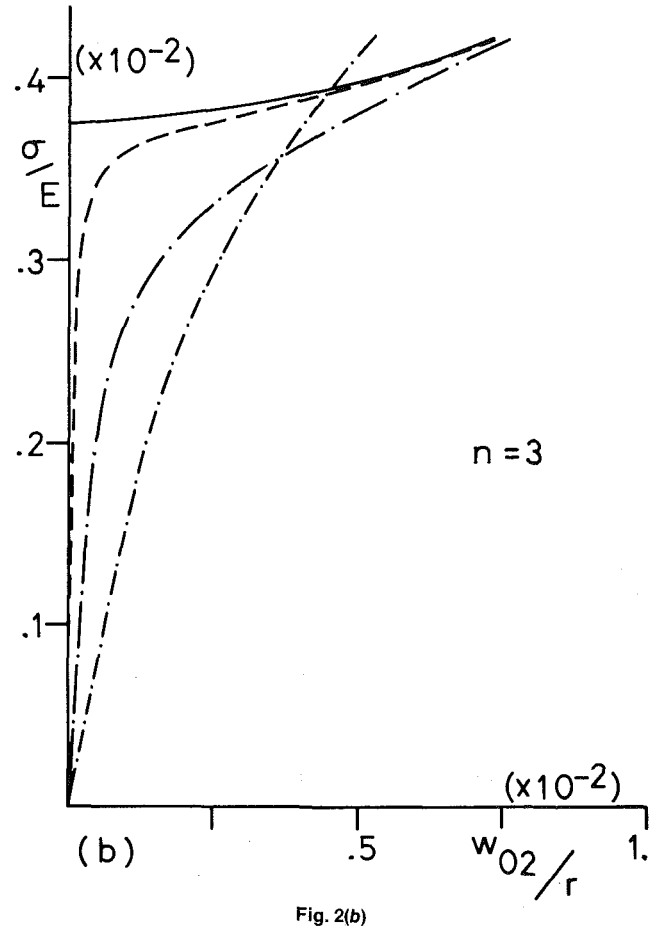

Fig. 2(b)

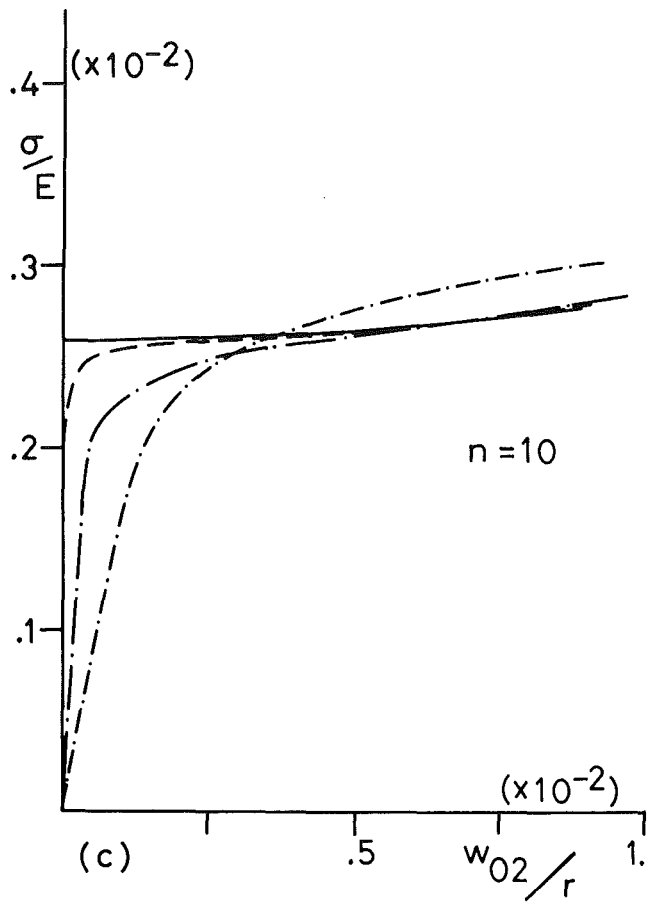

Fig. 2(c)

Fig. 2 Load versus w_{02}/r for a cylinder with $\sigma_Y = 0.002E$, $\nu = 0.3$, $m = 2$, $\alpha = 2$, $d/t_s = 5$, $r/t_p = 75$, $r/t_s = 80$, and 10 internal stiffeners

and $f(a,b) = 2a^2 - 2ab + \frac{1}{2}b^2$, $g(a,b) = a^2 - \frac{5}{2}ab + b^2$,

$$\Phi = (E_s - E_T)/(2E_sE_T\bar{\sigma}^2).$$

The variational statement of the eigenvalue problem for bifurcation is [13]

$$\sum_{i=1}^{N}\left[\int_{A^{p(i)}}(\delta\hat{\epsilon}^T\hat{\mathbf{n}} + \delta\hat{\kappa}^T\hat{\mathbf{m}} + \delta\hat{\psi}^T\mathbf{n}^0\hat{\psi})\,dA^{p(i)}\right.$$

$$\left. + \int_{A^{s(i)}}(\delta\hat{E}^T\hat{\mathbf{N}} + \delta\hat{\mathbf{K}}^T\hat{\mathbf{M}} + \delta\hat{\Psi}^T\mathbf{N}^0\hat{\Psi})\,dA^{s(i)}\right] = 0; \qquad (20)$$

here,

$$\mathbf{n}^0 = \begin{bmatrix} n_{xx} & n_{x\theta} \\ n_{x\theta} & n_{\theta\theta} \end{bmatrix} \quad \text{and} \quad \mathbf{N}^0 = \begin{bmatrix} N_{xx} & N_{xy} \\ N_{xy} & N_{yy} \end{bmatrix}$$

are the matrices of membrane stress resultants corresponding to the point on the primary path at which we are testing for bifurcation, and

$$\hat{\psi}^T = (\hat{w}_{,x}, \hat{w}_{,\theta}), \quad \hat{\Psi}^T = (\hat{W}_{,x}, \hat{W}_{,y}). \qquad (22)$$

Also, $\hat{(\ )}$ denotes the difference between incremental quantities on the primary and secondary paths; $\hat{\epsilon}$, $\hat{\kappa}$, $\hat{\mathbf{E}}$, and $\hat{\mathbf{K}}$ are eigenmodal strain vectors, and $\hat{\mathbf{n}}$, $\hat{\mathbf{m}}$, $\hat{\mathbf{N}}$, and $\hat{\mathbf{M}}$ are vectors of conjugate stress resultants.

The eigenmodal displacements for the ith panel are assumed to be of the form

Downloaded 02 May 2010 to 171.66.16.246. Redistribution subject to ASME license or copyright; see http://www.asme.org/terms/Terms_Use.cfm

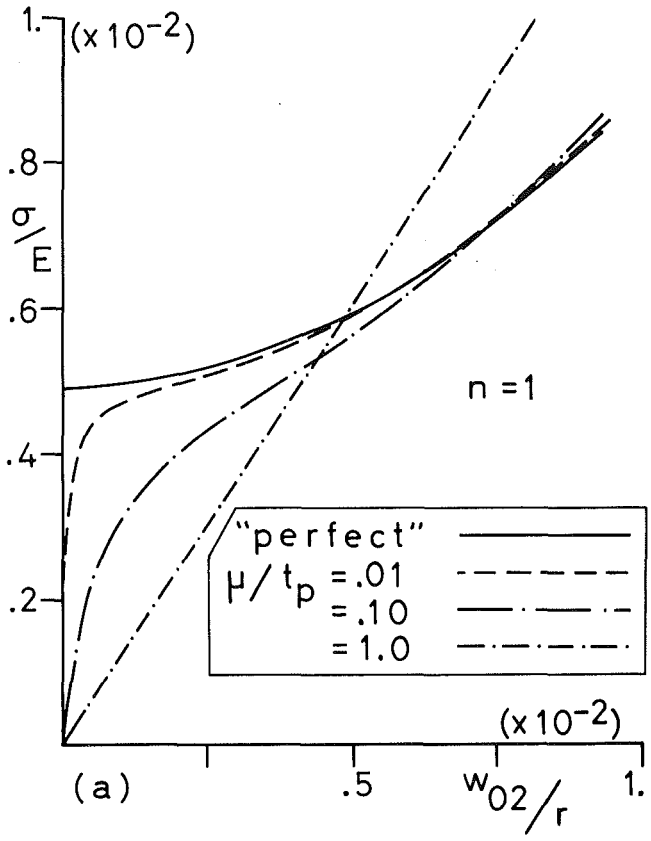

Fig. 3(a)

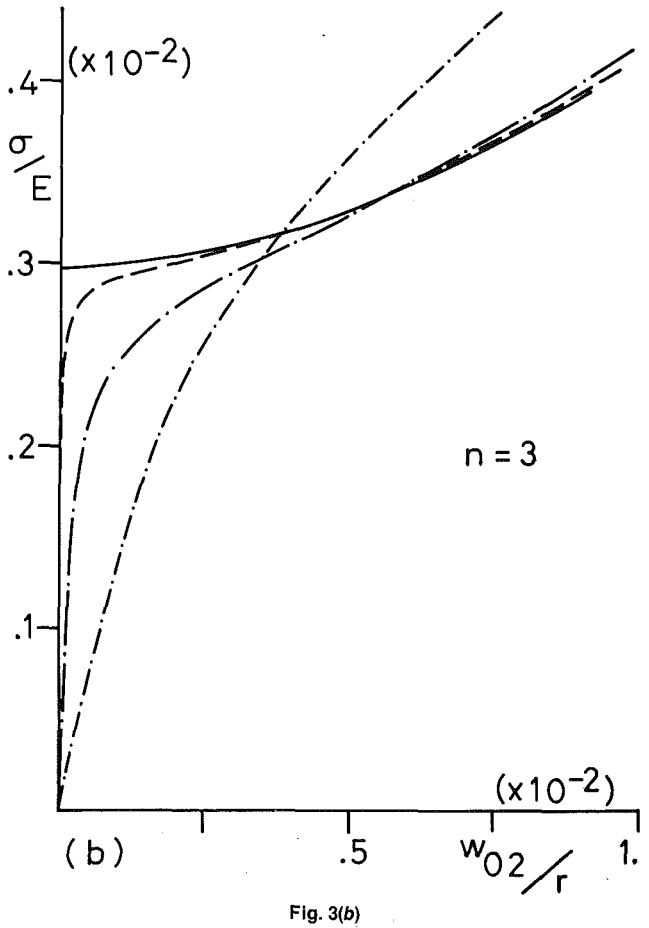

Fig. 3(b)

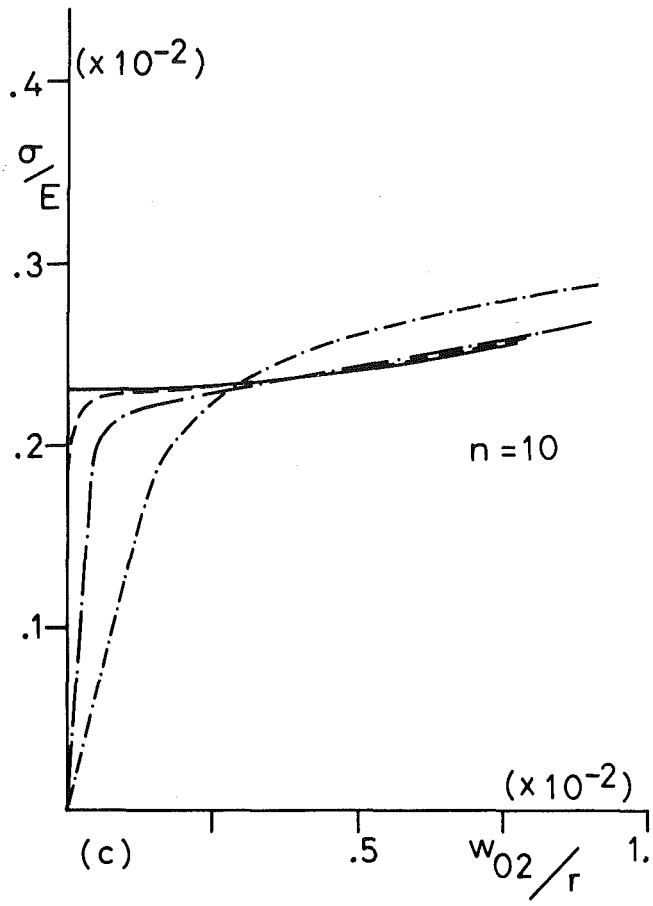

Fig. 3(c)

Fig. 3 Load versus w_{02}/r for a cylinder with $\sigma_y = 0.002E$, $\nu = 0.3$, $m = 2$, $\alpha = 2$, $d/t_s = 5$, $r/t_p = 150$, $r/t_s = 80$, and 10 internal stiffeners

$$\hat{u}^{(i)} = \hat{u}_1^{(i)} \cos\gamma\xi \sin\beta p\theta^{(i)}, \quad \hat{v}^{(i)} = \hat{v}_1^{(i)} \sin\gamma\xi \cos\beta p\theta^{(i)},$$
$$\hat{w}^{(i)} = \hat{w}_1^{(i)} \sin\gamma\xi \sin\beta p\theta^{(i)}, \tag{23}$$

with

$$(\hat{u}_1, \hat{v}_1, \hat{w}_1)^{(i+1)} = (\hat{u}_1, \hat{v}_1, \hat{w}_1)^{(i)}.$$

Here $\gamma = q\pi r/l$ with q, the number of half-waves in the axial direction, being an arbitrary integer. The number of half-waves between two stiffeners in the circumferential direction p is assumed to be an even integer because if p were odd, the stiffeners would not suppress the radial deflection waves along their lines of attachment, which is unlikely to occur in practice. This mode is antisymmetric with respect to the center of the ith panel $\theta^{(i)} = 0$. The corresponding eigenmodal displacements for the ith stiffener are obtained using the continuity conditions (3). Using (23), we may obtain expressions of the following form for the various eigenmodal strains:

$$(\hat{\epsilon}, \hat{\kappa}, \hat{\eta}, \hat{\mathbf{E}}, \hat{\mathbf{K}}, \hat{\mathbf{H}}) = (\mathbf{R}^p, \mathbf{S}^p, \mathbf{Q}^p, \mathbf{R}^s, \mathbf{S}^s, \mathbf{Q}^s)\,\hat{\mathbf{u}}_i, \tag{25}$$

where $\hat{\mathbf{u}}_1 = (\hat{u}_1, \hat{v}_1, \hat{w}_1)$ and $\mathbf{R}$, $\mathbf{Q}$, $\mathbf{S}$ are matrices whose elements are functions of the spatial coordinates and displacement parameters defined in Section 2.

From the conventional definition of the stress resultants together with (18) and (25), (20) becomes

$$\sum_{i=1}^{N} \left[\delta\hat{\mathbf{u}}_1^{(i)T} \int_{V^{p(i)}} \{ (\mathbf{R}^{pT} - z\,\mathbf{S}^{pT})\,\mathbf{P}\,\mathbf{Q}^p + \mathbf{E}^{pT}\,\mathbf{n}^0\,\mathbf{E}^p \}\,\hat{\mathbf{u}}_1^{(i)}\, dV^{p(i)} \right.$$

Downloaded 02 May 2010 to 171.66.16.246. Redistribution subject to ASME license or copyright; see http://www.asme.org/terms/Terms_Use.cfm

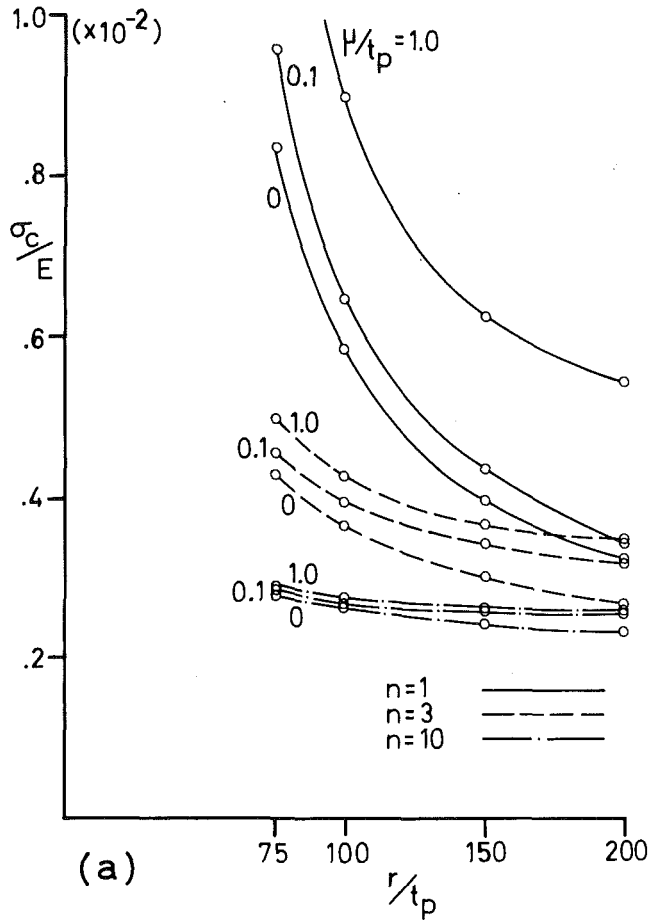

Fig. 4(a) $d/t_s = 5$

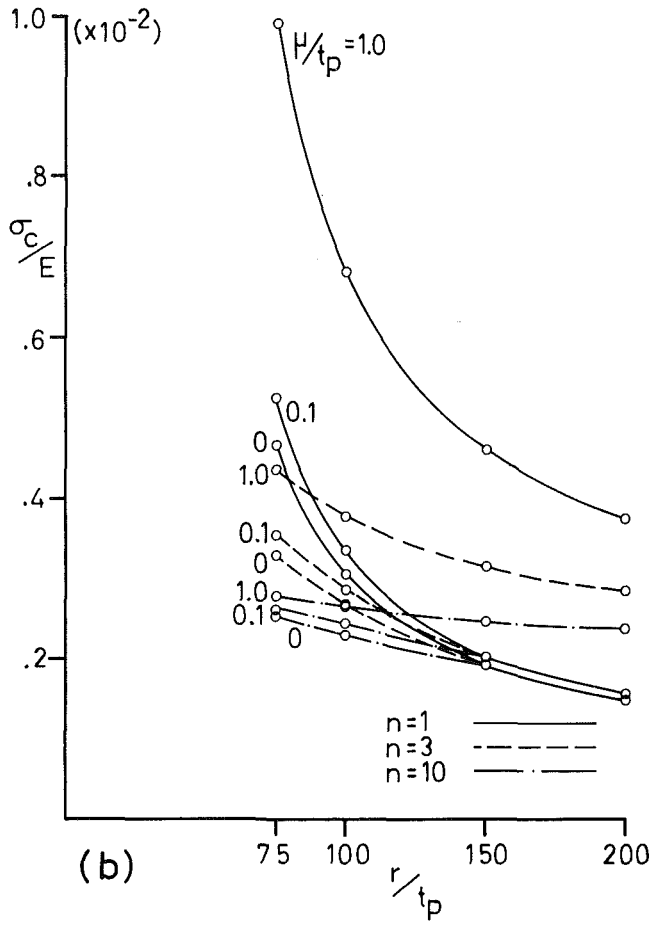

Fig. 4(b) $d/t_s = 10$

Fig. 4 *Critical stress versus radius/panel thickness for cylinders with* $\sigma_y = 0.002E$, $\nu = 0.3$, $m = 2$, $\alpha = 2$, *and* $r/t_s = 80$ *with 10 internal stiffeners*

$$+\delta\hat{\mathbf{u}}_1^{(i)T}\int_{V^{s(i)}}\{(\mathbf{R}^{sT}-Z\,\mathbf{S}^{sT})\,\mathbf{P}\,\mathbf{Q}^s+\mathbf{E}^{sT}\,\mathbf{N}^0\,\mathbf{E}^s\}\hat{\mathbf{u}}_1^{(i)}\,dV^{s(i)}\Big]=0, \tag{26}$$

where $\hat{\psi} = \mathbf{E}^p\,\hat{\mathbf{u}}_1$ and $\hat{\Psi} = \mathbf{E}^s\,\hat{\mathbf{u}}_1$, $\mathbf{E}^p$, and $\mathbf{E}^s$ being found from (22) and (23).

As in the numerical solution for the primary path, it is only necessary to perform the integration in (26) over selected "elements," due to the symmetries present in the problem. These elements, however, differ slightly from those used in Section 2. Once again, Gaussian quadrature is used to evaluate the surface integrals, and the modified Gaussian quadrature outlined in Section 2 is used for integration through the thickness. Equation (26) then reduces to

$$\mathbf{K}\,\hat{\mathbf{u}}_1 = \mathbf{0}, \tag{27}$$

and the critical load corresponds to the determinant of $\mathbf{K}$ being zero.

4 Numerical Results

In the corresponding elastic problem [6], all integrations were able to be carried out exactly, and the only numerical work involved was in the solution of the final set of equations. The approach of the present analysis is similar to that given in [6], except that the elastic-plastic material behavior necessitates the numerical evaluation of the integrals. We thus investigated the effectiveness of the present procedure by comparing our results, specialized to the elastic case, with those given in reference [6]. In all cases agreement was found to be excellent, with a maximum error of approximately 5 percent.

We now present a selection of results for internally stiffened cylinders. We consider a range of stiffened shells having $r/t_p = 75$ and 150, $r/t_s = 80$, and $d/t_s = 5$, with 10 stiffeners. Regarding material properties, we consider elastic materials ($n = 1$) and elastic-plastic materials having $\sigma_y = 0.002\,E$, $n = 3$ (high strain hardening) and $n = 10$ (low strain hardening). An axial half-wave number $m = 2$ is chosen, and we set $\alpha = m\pi r/l = 2$.

Figures 2 and 3 show curves of axial stress versus w_{02}/r for the various geometries and material properties considered, and imperfection amplitudes $\mu/t_p = 0.0005$ (designated "perfect"), 0.01, 0.10, and 1.0. The equilibrium paths are in all cases seen to be stable, and no limit points (load maxima) are found. Indeed, a number of other computations were carried out for various geometries and material parameters and in no cases were load maxima observed.

The intersections of the curves for the "perfect" shell and the vertical axes represent approximately the stress at which bifurcation occurs into the mode used for the imperfection. The corresponding "post-bifurcation" paths are stable, which one would expect in view of the fact that the shape of the imperfection corresponds approximately to the most stable bifurcation mode for the perfect shell found in the analysis of the initial postbuckling behavior by Syngellakis

Downloaded 02 May 2010 to 171.66.16.246. Redistribution subject to ASME license or copyright; see http://www.asme.org/terms/Terms_Use.cfm

and Walker [5]. Furthermore, the post-bifurcation curves for the "perfect" shells display behavior that is markedly more stable than that described by Tvergaard [7] for simply supported panels. This is significant when one considers that a flatness parameter ρ defined by Koiter [2] is greater than unity for the examples discussed here; Tvergaard [7] showed that for simply supported panels, the transition from stable to unstable postbuckling behavior took place at a value of ρ less than 0.5 for hardening parameters $n = 3$ and 10, so that his theory would almost certainly predict unstable postbuckling behavior for simply supported panels having the geometries and material properties that we are considering here.

One unexpected result is that for sufficiently large imperfections, the curve for the imperfect shell crosses that for the "perfect" shell, indicating that relatively large imperfections of the form considered, may actually have a beneficial effect. Overall these results are in accord with observations made in the elastic analyses in [1] and [3] to the effect that stiffeners can reduce or even eliminate the imperfection-sensitivity present in unstiffened cylinders.

Results for bifurcation into a mode that is antisymmetric with respect to panel midgenerators, are summarized in Fig. 4. In all cases, the effect of the initial imperfection appears to be beneficial in the sense that the larger the imperfection, the higher the stress is at which bifurcation into the antisymmetric mode occurs. Comparison of the results in Fig. 4(*a*) with those in Fig. 4(*b*) shows that the shells with deepeer stiffeners bifurcate at lower stresses than the corresponding shells with shallow stiffeners, presumably because of the relatively weak torsional stiffness of the deep stiffeners. Finally, the fact that the slopes of the elastic curves increase very rapidly with a decrease in radius-thickness ratio seems to indicate that there is a lower limit to r/t_p below which bifurcation is not possible for elastic shells. These observations also hold for a number of other geometries and material properties that were analyzed.

References

1 Hutchinson, J. W., and Amazigo, J. C., "Imperfection-Sensitivity of Eccentrically Stiffened Cylindrical Shells," *A.I.A.A. Journal*, Vol. 5, 1967, pp. 392–401.

2 Koiter, W. T., "Buckling and Post-Buckling Behavior of a Cylindrical Panel Under Axial Compression," *Rep. Trans. Nat. Aero, Res. Inst.*, Report S.476, Amsterdam, 1956.

3 Stephens, W. B., "Imperfection-Sensitivity of Axially Compressed Stringer Reinforced Cylindrical Panels Under Internal Pressure," *A.I.A.A. Journal*, Vol. 9, 1971, pp. 1713–1719.

4 Wang, J.T-S., and Lin, Y-J., "Stability of Discretely Stringer-Stiffened Cylindrical Shells, *A.I.A.A. Journal*, Vol. 11, 1973, 810–814.

5 Syngellakis, S., and Walker, A. C., "Elastic Buckling of Stiffened Cylindrical Shells," *Int. Symp. Integrity of Offshore Structures*, Glasgow, 1978.

6 Syngellakis, S., and Walker, A. C., "Elastic Local Buckling of Longitudinally Stiffened Cylinders," *Conf. Stability Problems of Eng. Structures and Components*, Cardiff, 1978.

7 Tvergaard, V., "Buckling of Elastic-Plastic Cylindrical Panel Under Axial Compression," *Int. Journal Solids Structures*, Vol. 13, 1977, pp. 957–970.

8 Reddy, B. D., "Buckling of Elastic-Plastic Discretely Stiffened Cylinders in Axial Compression," *Int. Journal Solids Structures*, Vol. 16, 1980, pp. 313–328.

9 Walker, A. C., and Davies, P., "The Collapse of Stiffened Cylinders," *Int. Conf. Steel Plated Structures*, Imperial College, London, 1976.

10 Sanders, J. L., "Nonlinear Theories for Thin Shells," *Quart. Appl. Math.*, Vol. 21, 1963, pp. 21–36.

11 Budiansky, B., "A Reassessment of Deformation Theories of Plasticity," ASME JOURNAL OF APPLIED MECHANICS, Vol. 26, 1959, pp. 259–264.

12 Duffett, G. A., "Plastic Buckling of Initially Imperfect Stiffened Cylinders in Axial Compression," M.Sc. (Eng.) Thesis, University of Cape Town, 1981.

13 Hutchinson, J. W., "Plastic Buckling," *Adv. Appl. Mech.*, Vol. 14, 1974, pp. 67–144.

Downloaded 02 May 2010 to 171.66.16.246. Redistribution subject to ASME license or copyright; see http://www.asme.org/terms/Terms_Use.cfm

On the Unsymmetric Eigenproblem for the Buckling of Shells Under Pressure Loading

H. A. Mang
Professor,
Institute of Structural Analysis
and Strength of Materials,
Technical University of Vienna,
Vienna, Austria

R. H. Gallagher
Dean,
College of Engineering,
The University of Arizona,
Tucson, Ariz. 85721
Fellow ASME

Consideration of the dependence of hydrostatic pressure on the displacements may result in significant changes of calculated buckling loads of thin arches and shells in comparison with loads calculated without consideration of this effect. The finite element method has made it possible to quantify these changes. On the basis of a shell theory of small displacements but moderately large rotations, this paper derives consistent incremental equilibrium equations for tracing, via the finite element method, the load-displacement path for thin shells subjected to nonuniform hydrostatic pressure and establishes the buckling condition from the incremental equilibrium equations. Within the framework of the finite element method, the character of hydrostatic pressure as one of a follower load is represented in the so-called pressure-stiffness matrix. For shells with loaded free edges, this matrix is unsymmetric. The principal objective of the present paper is to demonstrate that symmetrization of the pressure stiffness matrix resulting from linearization of the buckling condition yields buckling loads that are identical to the eigenvalues resulting from first-order perturbation analysis of the unsymmetric eigenproblem. A circular cylindrical shell with a free and a hinged end, subjected to hydrostatic pressure, is used as an example of the admissibility of symmetrizing the pressure stiffness matrix and for assessing its effect.

1 Introduction

In recent years, consideration of displacement-dependent loads has become a topic of intense interest to researchers in finite element analysis of thin shells. Loganathan, Chang, Abel, and Gallagher [1] reviewed analytical as well as numerical work on the effect of the dependence of hydrostatic pressure on the bifurcation point on the linearized prebuckling path. Their work was restricted to shells without loaded free edges. Cohen [2] and, in a broader context, Hibbitt [3], have shown that when there are no loaded free edges, a load potential exists, resulting within the framework of finite element analysis in a symmetric pressure stiffness matrix.

More recently, Mang [4] addressed the problem of shells with loaded free edges. He proposed an "a posteriori check" of the admissibility of symmetrizing the unsymmetric pressure stiffness matrix. This check is based on a comparison of two different approximations to the true eigenvalue. For both approximations symmetric "substitute buckling matrices" are employed. Within the context of tracing nonlinear load-displacement paths of thin shells, Frey and Cescotto [5] have used the same matrices. The advantage of this check is that no provisions for solving unsymmetric systems of algebraic equations have to be made in computer programs that are restricted to the handling of symmetric matrices. Depending on the structure of the available computer code, such provisions may involve major program changes.

Floegl and Mang [6] have applied the aforementioned concept to determination of buckling loads of thin arches and shells. Their study is restricted to the assumption of a linear prebuckling path. In his doctoral thesis, Chang [7] considered the displacement-dependence of hydrostatic pressure within the framework of buckling analysis of thin cylindrical and hyperboloidal shells.

The work described in this paper features (*a*) derivation of consistent incremental equilibrium equations, within the framework of a shell theory of small displacements but moderately large rotations, for tracing the nonlinear load-displacement path for thin shells subjected to nonuniform hydrostatic pressure; (*b*) derivation of the buckling condition from the incremental equilibrium equation; and (*c*) a mathematical proof concerning the admissibility of the aforementioned "a posteriori check" as a criterion for the significance of the asymmetry of the pressure stiffness matrix in the solution for eigenvalues of the linearized buckling condition.

The principal objective of the present paper, item (*c*) in the foregoing, is to provide the mathematical basis for the aforementioned "a posteriori check" for shells with loaded free edges. For this purpose, perturbation theory is employed. The "a posteriori check" is applied to the problem of a cylindrical shell with a free and a hinged edge subjected to hydrostatic pressure.

Contributed by the Applied Mechanics Division for publication in the JOURNAL OF APPLIED MECHANICS.
Discussion on this paper should be addressed to the Editorial Department, ASME, United Engineering Center, 345 East 47th Street, New York, N.Y. 10017, and will be accepted until two months after final publication of the paper itself in the JOURNAL OF APPLIED MECHANICS. Manuscript received by ASME Applied Mechanics Division, March, 1982.

Copyright © 1983 by ASME
Downloaded 02 May 2010 to 171.66.16.246. Redistribution subject to ASME license or copyright; see http://www.asme.org/terms/Terms_Use.cfm

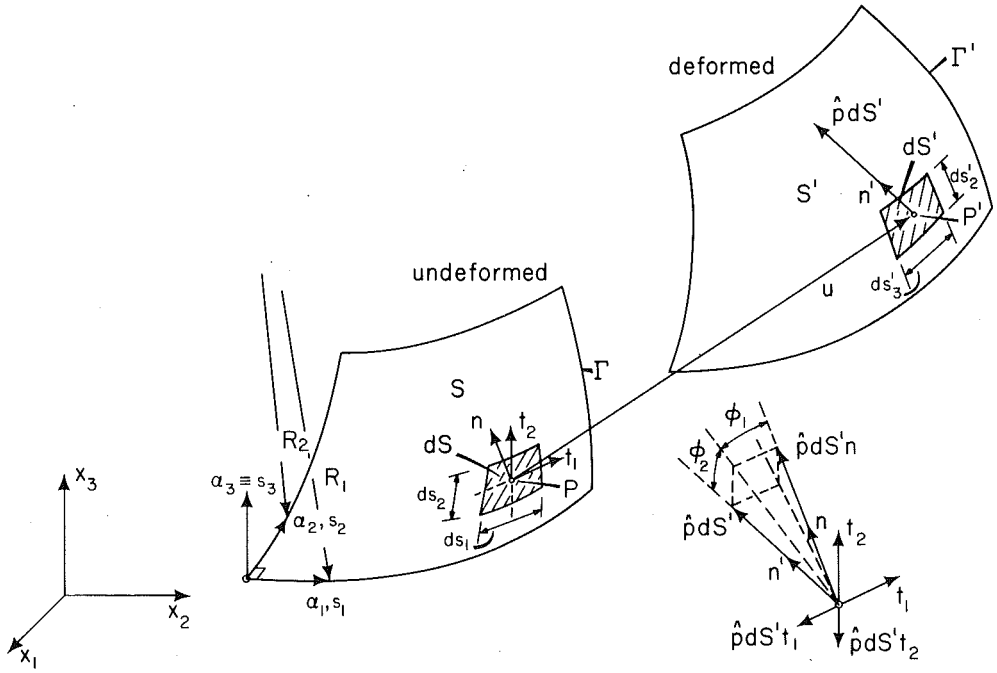

Fig. 1 Thin shell subjected to pressure load; components of pressure load in coordinate directions of undeformed shell

2 Theoretical Investigation

2.1 Derivation of Incremental Equilibrium Conditions. Figure 1 shows the middle surface S of the undeformed shell, the boundary of which is denoted as Γ; S is described by curvilinear, orthogonal surface coordinates α_i, $i = 1, 2, 3$, linked to a global Cartesian system of reference x_j, $j = 1, 2, 3$. Lengths measured along orthogonal parameter lines of the shell are denoted by s_i, $i = 1, 2, 3$. The side lengths of a differential element dS are given as $ds_i = \Lambda_i d\alpha_i$, $i = 1, 2$, where Λ_i are the Lamé parameters. The curvatures and the twist of the shell are given as $1/R_i$, $1 = 1, 2$, and $1/T$, respectively. The quantities $\mathbf{t}_1$ and $\mathbf{t}_2$ represent unit vectors parallel to the two orthogonal parameter lines passing through point P of S, $\mathbf{n}$ is the corresponding unit vector normal to dS.

Figure 1 also contains the middle surface S' of the deformed shell, the boundary of which is noted Γ'. The side lengths of the deformed differential elements $\underline{dS'}$ are denoted as ds_i', $i = 1,2$. The displacement vector $\mathbf{u} = \overline{PP'}$ can be expressed in terms of components u_1, u_2, $u_3 \equiv w$ parallel to α_1, α_2, and α_3.

Hydrostatic pressure remains normal to the shell as the shell deforms. Mathematically, this state of affairs can be expressed as:

$$\hat{\mathbf{p}}dS' = \hat{p}(\mathbf{u})dS'\mathbf{n}'. \tag{1}$$

In equation (1),

$$\hat{p}(\mathbf{u}) = (p + \nabla p \cdot \mathbf{u}) \tag{2}$$

is the absolute value of the pressure load; ∇p is the gradient of $p(\alpha_i)$, given as

$$\nabla p = \frac{\partial p}{\partial s_1}\mathbf{t}_1 + \frac{\partial p}{\partial s_2}\mathbf{t}_2 + \frac{\partial p}{\partial s_3}\mathbf{n}. \tag{3}$$

It follows that

$$\nabla p \cdot \mathbf{u} = \frac{\partial p}{\partial s_1}u_1 + \frac{\partial p}{\partial s_2}u_2 + \frac{\partial p}{\partial s_3}u_3. \tag{4}$$

In equation (1), $\mathbf{n}'$ is a unit vector normal to dS'.

Within the framework of a total Lagrangian formulation, the pressure load must be expressed in terms of components parallel to α_i, $i = 1, 2, 3$:

$$\hat{\mathbf{p}}dS' = \begin{Bmatrix} \hat{p}dS'\mathbf{n}' \cdot \mathbf{t}_1 \\ \hat{p}dS'\mathbf{n}' \cdot \mathbf{t}_2 \\ \hat{p}dS'\mathbf{n}' \cdot \mathbf{n} \end{Bmatrix}; \tag{5}$$

dS' is to be expressed in terms of dS:

$$dS' = (1 + \epsilon_{11} + \epsilon_{22})dS$$
$$= [1 + (e_{11} + e_{22}) + (\eta_{11} + \eta_{22})]dS. \tag{6}$$

In equation (6), e_{ii}, η_{ii}, $i = 1, 2$, are the linear and the nonlinear components, respectively, of the strain tensor. Consideration of geometric nonlinearity on the basis of a theory of "small displacements but moderately large rotations," as presented, for example, by Koiter [8], results in

$$\eta_{ii} = \frac{\phi_i^2}{2}, \quad i = 1, 2, \tag{7}$$

and in

$$\mathbf{n}' \cdot \mathbf{t}_1 = -\cos\phi_2 \sin\phi_1 = -\left(1 - \frac{\phi_2^2}{2} + \ldots\right)(\phi_1 - \ldots)$$

$$\mathbf{n}' \cdot \mathbf{t}_2 = -\cos\phi_1 \sin\phi_2 = -\left(1 - \frac{\phi_1^2}{2} + \ldots\right)(\phi_2 - \ldots)$$

$$\mathbf{n}' \cdot \mathbf{n} = \cos\phi_1 \cos\phi_2 = \left(1 - \frac{\phi_1^2}{2} + \ldots\right)\left(1 - \frac{\phi_2^2}{2} + \ldots\right) \tag{8}$$

where ϕ_1 and ϕ_2 are the rotations of the shell-normal as the shell deforms (see Fig. 1).

Substituting equation (4) into equation (2) and equations (7) into equation (6) and inserting the so-obtained results together with equations (8) into equation (5), and arranging terms according to their order in the displacements, yields

Downloaded 02 May 2010 to 171.66.16.246. Redistribution subject to ASME license or copyright; see http://www.asme.org/terms/Terms_Use.cfm

$$\hat{\mathbf{p}}dS' = \left\{\begin{matrix}0\\0\\p\end{matrix}\right\} + \left\{\begin{matrix}-p\phi_1\\-p\phi_2\\p(e_{11}+e_{22})+\left(\frac{\partial p}{\partial s_1}u_1+\frac{\partial p}{\partial s_2}u_2+\frac{\partial p}{\partial s_3}u_3\right)\end{matrix}\right\} + \tag{9}$$

$$+\left\{\begin{matrix}-p\phi_1(e_{11}+e_{22})-\left(\frac{\partial p}{\partial s_1}u_1+\frac{\partial p}{\partial s_2}u_2+\frac{\partial p}{\partial s_3}u_3\right)\phi_1\\-p\phi_2(e_{11}+e_{22})-\left(\frac{\partial p}{\partial s_1}u_1+\frac{\partial p}{\partial s_2}u_2+\frac{\partial p}{\partial s_3}u_3\right)\phi_2\\\left(\frac{\partial p}{\partial s_1}u_1+\frac{\partial p}{\partial s_2}u_2+\frac{\partial p}{\partial s_3}u_3\right)(e_{11}+e_{22})\end{matrix}\right\}$$

We have deleted terms of higher than quadratic order in the foregoing to be consistent with the representation of the internal forces.

Introducing local displacement vectors

$$\mathbf{u}^{(e)} = \psi^{(e)}\mathbf{q}^{(e)}, \quad e = 1, 2, \ldots r, \tag{10}$$

where the superscript refers to the considered finite element – one of a total of r elements – and where $\mathbf{q}^{(e)}$ is a vector of unknown nodal displacements associated with a matrix of selected shape functions, $\psi^{(e)}$, permits writing the virtual work of the external forces in the form of hydrostatic pressure as follows:

$$\delta A_a = \sum_{e=1}^{r}\int_{S'^{(e)}} \delta\mathbf{u}^T\hat{\mathbf{p}}dS'. \tag{11}$$

Note that here and in the following, element-oriented indices are omitted in the integrands of integrals extending over finite elements. The superscript "T" stands for "transpose."

Performing integrations and summation in equation (11) and arranging terms in the result according to their order in the nodal displacements, gives

$$\delta A_a = \delta\mathbf{q}^T(\mathbf{P} + \mathbf{K}_p^{(1)}(p)\mathbf{q} + \mathbf{K}_p^{(2)}(p, \mathbf{q})\mathbf{q}) \tag{12}$$

where $\mathbf{P}$ is the vector of work-equivalent node forces in the absence of follower-load effects whereas $\mathbf{K}_p{}^{(1)}(p)$ and $\mathbf{K}_p{}^{(2)}(p, \mathbf{q})$ are global pressure stiffness matrices of first and second order, respectively.

The virtual work of the internal forces is given as

$$\delta A_i = -\delta\mathbf{q}^T\mathbf{K}_S(\mathbf{q}^2)\mathbf{q} \tag{13}$$

where $\mathbf{K}_S(\mathbf{q}^2)$ is the secant stiffness matrix which is quadratic in the nodal displacements.

Substituting equations (12) and (13) into the virtual work equation

$$\delta A_i + \delta A_a = 0 \tag{14}$$

and denoting the sum of $\mathbf{K}_p{}^{(1)}(p)$ and $\mathbf{K}_p{}^{(1)}(p, \mathbf{q})$ as $\mathbf{K}_p(p, \mathbf{q})$ (global pressure stiffness matrix) results in

$$[\mathbf{K}_S(\mathbf{q}^2) - \mathbf{K}_p(p, \mathbf{q})]\{\mathbf{q}\} = \{\mathbf{P}\}, \tag{15}$$

representing the equilibrium equations for the discretized continuum.

To obtain the incremental equilibrium equations, equation (15) is first written in terms of $p + \Delta p$, $\mathbf{q} + \Delta\mathbf{q}$, and $\mathbf{P} + \Delta\mathbf{P}$. Expanding the so-obtained relationship in a Taylor series in $\Delta\mathbf{q}$, truncating this series after the linear terms in $\Delta\mathbf{q}$, and subtracting equation (15) as given in the foregoing yields

$$[\mathbf{K}_T(\mathbf{q}^2) - \mathbf{K}_{pT}(p+\Delta p, \mathbf{q})]\{\Delta\mathbf{q}\} = \{\Delta\mathbf{P} + \mathbf{K}_p(\Delta p, \mathbf{q})\mathbf{q}\}. \tag{16}$$

In equation (16), $\mathbf{K}_T(\mathbf{q}^2)$ is the tangent stiffness matrix, which is quadratic in the nodal displacements, and $\mathbf{K}_{pT}(p+\Delta p, \mathbf{q})$ is the tangent pressure stiffness matrix, which can be written as

$$\mathbf{K}_{pT}(p+\Delta p, \mathbf{q}) = \mathbf{K}_p^{(1)}(p+\Delta p) + \mathbf{K}_{pT}^{(2)}(p+\Delta p, \mathbf{q}) \tag{17}$$

with $\mathbf{K}_p{}^{(1)}(p+\Delta p)$ following from equation (12) and $\mathbf{K}_{pT}{}^{(2)}(p+\Delta p, \mathbf{q})$ representing the tangent pressure stiffness matrix of second order. $\mathbf{K}_p(\Delta p, \mathbf{q})$ on the right side of equation (16) can be written analogous to $\mathbf{K}_{pT}(p+\Delta p, \mathbf{q})$.

2.2 Buckling Condition. Replacing the symbol Δ in equation (16) by the variational symbol δ and setting $\delta p = 0$, resulting in $\delta P = 0$ and $\mathbf{K}_p(\delta p, \mathbf{q}) = \mathbf{0}$, gives

$$[\mathbf{K}_T(\mathbf{q}^2) - \mathbf{K}_{pT}(p, \mathbf{q})]\{\delta\mathbf{q}\} = \{\mathbf{0}\}. \tag{18}$$

Equation (18) is satisfied if the determinant of the coefficient matrix vanishes.

Consider now the linearized buckling problem, obtained by linearizing $\mathbf{K}_T(\mathbf{q}^2)$ and neglecting $\mathbf{K}_{pT}{}^{(2)}(p, \mathbf{q})$. The former matrix can be written as

$$\mathbf{K}_T(\mathbf{q}^2) = \mathbf{K} + \mathbf{K}_\sigma(\sigma(\mathbf{q}^2)) + \mathbf{K}_L(\mathbf{q}^2) \tag{19}$$

where $\mathbf{K}$ is the "small-displacement stiffness matrix," $K_\sigma(\sigma(\mathbf{q}^2))$ is the "initial-stress stiffness-matrix," and $K_L(\mathbf{q}^2)$ is the "initial-displacement stiffness-matrix." Linearization yields

$$\mathbf{K}_T^*(\mathbf{q}) = \mathbf{K} + \mathbf{K}_\sigma^*(\sigma(\mathbf{q})) + \mathbf{K}_L(\mathbf{q}) = \mathbf{K} + \chi[\mathbf{K}_\sigma^*(\sigma(\bar{\mathbf{q}}) + \mathbf{K}_L^*(\bar{\mathbf{q}})]. \tag{20}$$

In equation (20), $\bar{\mathbf{q}}$ is the vector of nodal displacements resulting from a linear analysis with $\bar{p}$ as the reference pressure; χ is the load intensity factor.

Replacing $\mathbf{K}_T(\mathbf{q}^2)$ in equation (18) by $\mathbf{K}_T^*(\mathbf{q})$ and $\mathbf{K}_{pT}(p, \mathbf{q})$ by $\chi\mathbf{K}_p{}^{(1)}(\bar{p})$, results in the linearized buckling condition:

$$[\mathbf{K} + \chi(\mathbf{K}_\sigma^*(\sigma(\bar{\mathbf{q}})) + \mathbf{K}_L^*(\bar{\mathbf{q}}) - \mathbf{K}_p^{(1)}(\bar{p})]\{\delta_\mathbf{q}\} = \{\mathbf{0}\}. \tag{21}$$

Linearization of equation (18) applies strictly only if there is no bending prior to buckling. In this case, $\mathbf{K}_L^*(\mathbf{q}) = 0$.

Cohen [2] has shown that in case of disregarding terms quadratic in the displacements in equation (9), which is consistent with linearization of equation (18), the virtual work of a nonuniform pressure load can be expressed as

$$\delta A_a = -\delta\Pi_a + \delta A_{a\Gamma} \tag{22}$$

where Π_a is a so-called "load potential." Within the framework of the finite element method, this load potential can be written as [2, 6]

$$\Pi_a = \sum_{e=1}^{r}\int_{S^{(e)}}\left[-p(1+e_{11}+e_{22})u_3 - \frac{1}{2}p\left(\frac{1}{R_1}+\frac{1}{R_2}\right)u_3^2 + \frac{1}{2}p\left(\frac{u_1^2}{R_1}+\frac{2u_1u_2}{T}+\frac{u_2^2}{R_2}\right) - \left(u_1\frac{\partial p}{\partial s_1}+u_2\frac{\partial p}{\partial s_2}+u_3\frac{\partial p}{\partial s_3}\right)u_3\right]dS. \tag{23}$$

$\delta A_{a\Gamma}$ is the virtual work of the pressure load acting on unsupported parts of the edge of the shell; $\delta A_{a\Gamma}$ is given as [2, 6]

$$\delta A_{a\Gamma} = -\sum_{j=1}^{s}\int_{\Gamma^{(j)}} pu_3(n_1\delta u_1 + n_2\delta u_2)d\Gamma \tag{24}$$

where n_1 and n_2 are the direction cosines of angles enclosed by

Downloaded 02 May 2010 to 171.66.16.246. Redistribution subject to ASME license or copyright; see http://www.asme.org/terms/Terms_Use.cfm

the outward normal to Γ and the parameter lines α_i, $i = 1, 2$. $\Gamma^{(j)}$ is one of a total of s element boundaries coinciding with the edge of the shell.

In matrix notation, equation (22) can be written as follows:

$$\delta A_a = \delta \mathbf{q}^T (\mathbf{P} + \mathbf{K}_p^{(1)}(p)\,\mathbf{q})$$

$$= \delta \mathbf{q}^T (\mathbf{P} + \mathbf{K}_{pS}(p)\,\mathbf{q} + \mathbf{K}_{p\Gamma}(p)\,\mathbf{q}). \quad (25)$$

Since $\mathbf{K}_{pS}(p)$ results from the load potential Π_a, this matrix is symmetric. Stemming from $\delta A_{a\Gamma}$, the matrix $\mathbf{K}_{p\Gamma}(p)$ is unsymmetric.

From equation (25) it follows that $\mathbf{K}_p{}^{(1)}(\bar{p})$ in equation (21) can be replaced by $\mathbf{K}_{pS}(\bar{p}) + \mathbf{K}_{p\Gamma}(\bar{p})$. Denoting

$$\mathbf{K}' = -\mathbf{K}_\sigma^*(\sigma(\bar{\mathbf{q}})) - \mathbf{K}_L^*(\bar{\mathbf{q}}) + \mathbf{K}_{pS}(\bar{p}) \quad (26)$$

which is a symmetric matrix, results in

$$[\mathbf{K} - \chi(\mathbf{K}' + \mathbf{K}_{p\Gamma})]\{\delta\mathbf{q}\} = \{\mathbf{0}\} \quad (27)$$

as the linearized buckling condition.

The unsymmetric matrix $\mathbf{K}_{p\Gamma}(p)$ is a sparsely populated, off-(main) diagonal matrix, resulting from line integrals, as compared to $\mathbf{K}'$, stemming from volume and surface integrals, respectively. It is important to assess its influence on the solution of the linearized buckling problem because available computer programs are generally restricted to the handling of symmetric matrices. This issue is considered next.

2.3 Criterion for Significance of Asymmetry of Pressure Stiffness Matrix in the Solution for Eigenvalues. If $\mathbf{K}_{p\Gamma}$ is a matrix representing a small change from $\mathbf{K}'$ in the sense of a first-order perturbation matrix, perturbation theory can be applied to give a mathematical estimate of the influence of $\mathbf{K}_{p\Gamma}$ on the solution of the substitute symmetric eigenproblem which is characterized by ommission of $\mathbf{K}_{p\Gamma}$ in equation (27). The actual eigenproblem will be termed "perturbed eigenproblem" whereas the substitute symmetric eigenproblem will be referred to as the "unperturbed eigenproblem." Thus, the unperturbed eigenproblem can be written as

$$[\mathbf{K} - \chi_{0i}\mathbf{K}']\{\delta\mathbf{q}_{0i}\} = \{\mathbf{0}\} \quad (28)$$

where χ_{0i} is the ith eigenvalue and $\delta\mathbf{q}_{0i}$ is the corresponding eigenvector. Assuming that all eigenvalues obtained from these equations are distinct and that each eigenvector is normalized with respect to $\mathbf{K}'$, yields

$$\delta\mathbf{q}_{0j}^T\mathbf{K}'\delta\mathbf{q}_{0i} = \delta_{ij}, \quad i,j = 1, 2\ .\ .\ n, \quad (29)$$

resulting in

$$\delta\mathbf{q}_{0j}^T\mathbf{K}\delta\mathbf{q}_{0i} = \chi_{0i}\delta_{ij}, \quad i,j = 1, 2\ .\ .\ n, \quad (30)$$

where δ_{ij} is the Kronecker symbol. In the following it will be tacitly understood that the range of indices i, j extends from 1 to n.

The perturbed eigenproblem is given as

$$[\mathbf{K} - \chi_i(\mathbf{K}' + \mathbf{K}_{p\Gamma})]\{\delta\mathbf{q}_i^{(R)}\} = \{\mathbf{0}\} \quad (31)$$

where χ_i is the ith eigenvalue and $\delta\mathbf{q}_i{}^{(R)}$ is the corresponding "right" eigenvector. The adjoint perturbed eigenproblem is defined as

$$[\mathbf{K} - \chi_j(\mathbf{K}' + \mathbf{K}_{p\Gamma}^T)]\{\delta\mathbf{q}_j^{(L)}\} = \{\mathbf{0}\} \quad (32)$$

where χ_j is the jth eigenvalue and $\delta\mathbf{q}_j{}^{(L)}$ is the corresponding "left" eigenvector.

Corresponding eigenvalues of the perturbed eigenproblem and the perturbed adjoint eigenproblem are identical. Corresponding right and left eigenvectors, on the other hand, are different.

Premultiplication of equation (31) by $\delta\mathbf{q}_j{}^{(L)^T}$ yields

$$\delta\mathbf{q}_j{}^{(L)^T}[\mathbf{K} - \chi_i(\mathbf{K}' + \mathbf{K}_{p\Gamma})]\delta\mathbf{q}_i^{(R)} = 0. \quad (33)$$

Premultiplication of equation (32) by $\delta\mathbf{q}_i{}^{(R)^T}$ gives

$$\delta\mathbf{q}_i{}^{(R)^T}[\mathbf{K} - \chi_j(\mathbf{K}' + \mathbf{K}_{p\Gamma}^T)]\delta\mathbf{q}_j^{(L)} = 0. \quad (34)$$

Transposing equation (34) and subtracting equation (33) from the result, gives

$$(\chi_i - \chi_j)\,\delta\mathbf{q}_j^{(L)^T}(\mathbf{K}' + \mathbf{K}_{p\Gamma})\,\delta\mathbf{q}_i^{(R)} = 0. \quad (35)$$

Thus, because of the assumption of distinct eigenvalues,

$$\delta\mathbf{q}_j^{(L)^T}(\mathbf{K}' + \mathbf{K}_{p\Gamma})\delta\mathbf{q}_i^{(R)} = 0. \quad (36)$$

Permutation of subscripts i and j in equations (33) and (34) results in

$$\delta\mathbf{q}_j^{(R)^T}(\mathbf{K}' + \mathbf{K}_{p\Gamma}^T)\,\delta\mathbf{q}_i^{(L)} = 0. \quad (37)$$

Normalization of "right" and "left" eigenvectors such that

$$\delta\mathbf{q}_i^{(L)^T}(\mathbf{K}' + \mathbf{K}_{p\Gamma})\,\delta\mathbf{q}_i^{(R)}$$

$$= \delta\mathbf{q}_i^{(R)^T}(\mathbf{K}' + \mathbf{K}_{p\Gamma}^T)\,\delta\mathbf{q}_i^{(L)} = 1 \quad (38)$$

results in the so-called "first biorthonormality relations" given as

$$\delta\mathbf{q}_j^{(L)^T}(\mathbf{K}' + \mathbf{K}_{p\Gamma})\,\delta\mathbf{q}_i^{(R)} = \delta\mathbf{q}_j^{(R)^T}(\mathbf{K}' + \mathbf{K}_{p\Gamma}^T)\,\delta\mathbf{q}_i^{(L)} = \delta_{ij}. \quad (39)$$

Substituting the first term in equation (39) into equation (33) and the second term in equation (39) into equation (34) after permutation of subscripts i and j in the latter, results in

$$\delta\mathbf{q}_j^{(L)^T}\mathbf{K}\delta\mathbf{q}_i^{(R)} = \delta\mathbf{q}_j^{(R)^T}\mathbf{K}\delta\mathbf{q}_i^{(L)} = \chi_i\delta_{ij}, \quad (40)$$

which is termed as "second biorthonormality relations."

If $\mathbf{K}_{p\Gamma}$ represents a small change from $\mathbf{K}'$ in the sense of a first-order perturbation matrix, the solutions of the perturbed and the adjoint perturbed eigenproblem can be written in the form

$$\left.\begin{aligned} \chi_i &= \chi_{0i} + \chi_{1i} \\ \delta\mathbf{q}_i^{(R)} &= \delta\mathbf{q}_{0i} + \delta\mathbf{q}_{1i}^{(R)} \\ \delta\mathbf{q}_i^{(L)} &= \delta\mathbf{q}_{0i} + \delta\mathbf{q}_{1i}^{(L)} \end{aligned}\right\} \quad (41)$$

where χ_{1i}, $\delta\mathbf{q}_{1i}{}^{(R)}$, and $\delta\mathbf{q}_{1i}{}^{(L)}$ represent first-order perturbations of the solution of the unperturbed symmetric eigenproblem.

Substituting the second and the third of equations (41) into the left expression of the first biorthonormality relations [see equation (39)] and omitting matrix products containing more than one field of perturbations, results in

$$\delta\mathbf{q}_{0j}^T\mathbf{K}'\delta\mathbf{q}_{0i} + \delta\mathbf{q}_{0j}^T(\mathbf{K}'\delta\mathbf{q}_{1i}^{(R)} + \mathbf{K}_{p\Gamma}\delta\mathbf{q}_{0i}) +$$

$$+ \delta\mathbf{q}_{1j}^{(L)T}\mathbf{K}'\delta\mathbf{q}_{0i} = \delta_{ij} \quad (42)$$

and, because

$$\delta\mathbf{q}_{0j}^T\mathbf{K}'\delta\mathbf{q}_{0i} = \delta_{ij} \quad (29)$$

it follows that

$$\delta\mathbf{q}_{0j}^T(\mathbf{K}'\delta\mathbf{q}_{1i}^{(R)} + \mathbf{K}_{p\Gamma}\delta\mathbf{q}_{0i}) + \delta\mathbf{q}_{1j}^{(L)T}\mathbf{K}'\delta\mathbf{q}_{0i} = 0. \quad (43)$$

Substituting equations (41) into the left expression of the

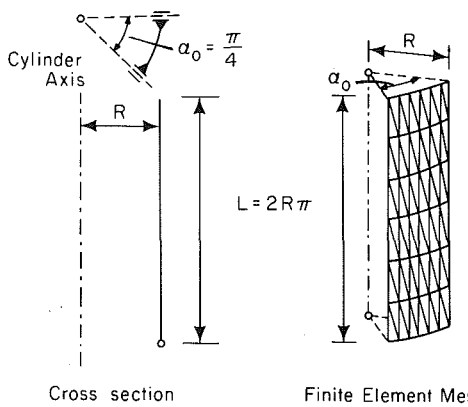

Fig. 2 Circular cylindrical shell with a free and a hinged end – finite element model for buckling analysis

Downloaded 02 May 2010 to 171.66.16.246. Redistribution subject to ASME license or copyright; see http://www.asme.org/terms/Terms_Use.cfm

second biorthonormality relations and omitting matrix products containing more than one field of perturbations, results in

$$\delta\mathbf{q}_{0j}^T\mathbf{K}\delta\mathbf{q}_{0i}+\delta\mathbf{q}_{0j}^T\mathbf{K}\delta\mathbf{q}_{1i}^{(R)}+\delta\mathbf{q}_{1j}^{(L)T}K\delta\mathbf{q}_{0i}=(\chi_{0i}+\chi_{1i})\,\delta_{ij} \tag{44}$$

and, because

$$\delta\mathbf{q}_{0j}^T\mathbf{K}\delta\mathbf{q}_{0i}=\chi_{0i}\delta_{ij}, \tag{30}$$

it follows that

$$\delta\mathbf{q}_{0j}^T\mathbf{K}\delta\mathbf{q}_{1i}^{(R)}+\delta\mathbf{q}_{1j}^{(L)T}\mathbf{K}\delta\mathbf{q}_{0i}=\chi_{1i}\delta_{ij}. \tag{45}$$

According to Meirovitch [9], the first-order perturbations $\delta\mathbf{q}_{1i}{}^{(R)}$ and $\delta\mathbf{q}_{1i}{}^{(L)}$ can be expressed as linear combinations of the n linearly independent eigenvectors $\delta\mathbf{q}_{0k}$, forming a basis in an n-dimensional vector space. Thus, $\delta\mathbf{q}_{1i}^{(R)}$ and $\delta\mathbf{q}_{1i}^{(L)}$ can be written as

$$\left.\begin{aligned}\delta\mathbf{q}_{1i}^{(R)} &= \sum_{k=1}^{n}\epsilon_{ik}\delta\mathbf{q}_{0k}\\ \delta\mathbf{q}_{1i}^{(L)} &= \sum_{k=1}^{n}\gamma_{ik}\delta\mathbf{q}_{0k}\end{aligned}\right\}\ i=1,2,\ldots n, \tag{46}$$

where ϵ_{ik} and γ_{ik} are small coefficients.

Substituting equations (46) into equation (43) results in

$$\delta\mathbf{q}_{0j}^T\left[\mathbf{K}'\left(\sum_{k=1}^{n}\epsilon_{ik}\delta\mathbf{q}_{0k}\right)+\mathbf{K}_{p\Gamma}\delta\mathbf{q}_{0i}\right]+\left(\sum_{k=1}^{n}\gamma_{jk}\delta\mathbf{q}_{0k}^T\right)\mathbf{K}'\delta\mathbf{q}_{0i}=0. \tag{47}$$

Making use of equation (29) gives

$$\epsilon_{ij}+\gamma_{ji}=-\delta\mathbf{q}_{0j}^T\mathbf{K}_{p\Gamma}\delta\mathbf{q}_{0i} \tag{48}$$

Substituting equations (46) into equation (45) results in

$$\delta\mathbf{q}_{0j}^T\mathbf{K}\left(\sum_{k=1}^{n}\epsilon_{ik}\delta\mathbf{q}_{0k}\right)+\left(\sum_{k=1}^{n}\gamma_{jk}\delta\mathbf{q}_{0k}^T\right)\mathbf{K}\delta\mathbf{q}_{0i}=\chi_{1i}\delta_{ij}. \tag{49}$$

Making use of equation (30) gives

$$\epsilon_{ij}\chi_{0j}+\gamma_{ji}\chi_{0i}=\chi_{1i}\delta_{ij}. \tag{50}$$

For $i\neq j$, equation (50) yields

$$\epsilon_{ij}\chi_{0j}+\gamma_{ji}\chi_{0i}=0. \tag{51}$$

Equations (48) and (51) result in

$$\left.\begin{aligned}\epsilon_{ij} &= -\delta\mathbf{q}_{0j}^T\mathbf{K}_{p\Gamma}\delta\mathbf{q}_{0i}\frac{\chi_{0i}}{\chi_{0i}-\chi_{0j}}\\ \gamma_{ji} &= \delta\mathbf{q}_{0j}^T\mathbf{K}_{p\Gamma}\delta\mathbf{q}_{0i}\frac{\chi_{0j}}{\chi_{0i}-\chi_{0j}}\end{aligned}\right\}\ i,j=1,2,\ldots n;\quad i\neq j. \tag{52}$$

For $i=j$, equation (50) yields

$$(\epsilon_{ii}+\gamma_{ii})\,\chi_{0i}=\chi_{1i}. \tag{53}$$

Equation (48) with $i=j$ and equation (53) result in

$$\chi_{1i}=-\delta\mathbf{q}_{0i}^T\mathbf{K}_{p\Gamma}\delta\mathbf{q}_{0i}\chi_{0i}. \tag{54}$$

Solving the unperturbed (symmetric) eigenproblem (equation (28)) and inserting the result, χ_{0i} and $\delta\mathbf{q}_{0i}$, into equation (54), permits checking a posteriori whether it has been admissible to apply first-order perturbation theory to obtain approximations to the eigenvalues of the actual (unsymmetric) eigenproblem (equation (31)). The respective condition is

$$|\chi_{1i}/\chi_{0i}|\ll 1 \tag{55}$$

In the following, it will be shown that this check is identical to the "a posteriori check" mentioned in the Introduction. The latter is based on a comparison of two approximations to the true eigenvalues. Both approximations are obtained from symmetric "substitute buckling matrices." One of them is χ_{0i}. The second one is resulting from symmetrization of the actual eigenproblem, that is from

$$\left\langle\mathbf{K}-\chi_i\left[\mathbf{K}'+\frac{1}{2}(\mathbf{K}_{p\Gamma}+\mathbf{K}_{p\Gamma}^T)\right]\right\rangle\{\delta\mathbf{q}_i\}=\{\mathbf{0}\}. \tag{56}$$

By analogy to equation (54), first-order perturbations χ_{1i} of the eigenvalues χ_{0i} resulting from solution of the unperturbed eigenproblem are obtained as

$$\chi_{1i}=-\delta\mathbf{q}_{0i}^T\left[\frac{1}{2}(\mathbf{K}_{p\Gamma}+\mathbf{K}_{p\Gamma}^T)\right]\delta\mathbf{q}_{0i}\chi_{0i}. \tag{57}$$

Noting that the right side of equation (54) contains a quadratic form in $\delta\mathbf{q}_{0i}$, $\mathbf{K}_{p\Gamma}$ in this equation can be symmetrized. Consequently, symmetrization of the actual eigenproblem (equation (56)) yields buckling loads that are identical (except for higher than first-order perturbations) to the eigenvalues resulting from first-order perturbation analysis of the unsymmetric eigenproblem (equation (41)). The difference of the two approximations to the true eigenvalue is $\chi_{0i}-(\chi_{0i}+\chi_{1i})$. This difference presents the basis for the "a posteriori check" according to equation (55).

3 Numerical Example

A circular cylindrical shell with a free and a hinged edge is analyzed. The length/radius ratio, L/R, is chosen as 2π. The radius/thickness ratio, R/h, is taken as 100. Young's modulus E and Poisson's ratio μ are chosen as 2.4×10^7 and 0.16, respectively. The shell is subjected to uniform radial pressure that remains normal to the deformed surface (hydrostatic pressure).

Since there is no a priori knowledge of the number of sine waves of the buckling mode shape in the circumferential direction, buckling analyses were performed for 2, 3, 4, and 5 waves. Because of symmetry of the mode shapes in the circumferential direction, it is sufficient to consider shell sectors permitting analysis of one half-wave of the mode shapes. Figure 2 refers to a mode shape with 4 sine waves. Consequently, the subtended angle α_0 for the shell sector shown in this figure is $\pi/4$. The analysis model of this sector consists of 72 curved triangular elements, whose formulation is described in reference [10].

The analytical solution for a circular cylindrical shell of identical dimensions but with both ends hinged was taken as a comparison solution. For the mesh shown in Fig. 2, the finite element solution for the critical pressure p_{CR} is only 0.45 percent larger than the comparison analytical solution [6], which is 35.549.

For the actual example problem, because of the free edge of the shell, a load potential does not exist. Thus, according to the "a posteriori check" mentioned in the Introduction and described at the end of Section 2.3, the eigenvalues of two symmetric "substitute buckling matrices" must be compared. The first one is the coefficient matrix in equation (27). The second one is the coefficient matrix in equation (57).

Table 1 shows that differences of corresponding eigenvalues for hydrostatic pressure is so small that condition (55) is satisfied. Thus, for the given problem the asymmetry of the pressure stiffness matrix is insignificant in the solution for eigenvalues. Computationally, it would have been more efficient if the mentioned "a posteriori check" had been

Downloaded 02 May 2010 to 171.66.16.246. Redistribution subject to ASME license or copyright; see http://www.asme.org/terms/Terms_Use.cfm

Table 1 Circular cylindrical shell with a free and a hinged end – comparison of buckling pressures due to uniform hydrostatic and constant direction pressure load

X = Pcr/35.549

LOADS	Number of Half Waves of Buckling Mode Shape in Circumferential Direction			
	4	6	8	10
Hydrostatic:				
[Eq. (27)]	0.9118	0.5552	0.8942	1.4043
[Eq. (57)]	0.9101	0.5542	0.8937	1.4041
Constant Dir.	0.9704	0.6237	0.9534	1.4627

performed on the basis of equation (54), requiring solution of only one symmetric eigenproblem. The reason for computing the first-order perturbation χ_{1i} as the difference of eigenvalues resulting from two symmetric eigenproblems was to avoid numerical inaccuracies resulting from inaccurate numerical determination of the eigenvectors $\delta\mathbf{q}_{0i}$. The latter are required for computation of χ_{1i} on the basis of equation (54).

It is clear from the results of Table 1 that the lowest buckling value occurs for a buckling mode with six half-waves in the circumferential direction. Note that the buckling load obtained by disregarding the dependence of the pressure load on the displacements is approximately 12 percent in excess of the value obtained by including this effect. Also, the latter is approximately 56 percent of that obtained for the cylindrical shell with both ends hinged.

4 Concluding Remarks

In this paper, consistent incremental equations for tracing the nonlinear load displacement were derived. The derivation was based on the assumption of a shell theory of small displacements but moderately large rotations. The term "consistent" refers to the pressure stiffness matrix resulting from a follower load of the form of nonuniform hydrostatic pressure. The derived pressure stiffness matrix is consistent with the tangent stiffness matrix resulting from the internal forces.

On the basis of the incremental equilibrium equations the buckling condition was derived and, subsequently, linearized. By means of perturbation theory it was demonstrated that symmetrization of the pressure stiffness matrix of first order, which is part of the linearized buckling matrix, yields buckling loads that are identical to the eigenvalues resulting from first-order perturbation analysis of the unsymmetric eigenproblem. This proof represents the mathematical basis for the suggested "a posteriori check" concerning the admissibility of symmetrizing the pressure stiffness matrix of first order.

On the basis of the presented theoretical concept it was demonstrated numerically, that for the chosen example problem the asymmetry of the pressure stiffness matrix is insignificant in the solution for eigenvalues.

5 Acknowledgments

The authors express their deep appreciation for the efforts of Dr. H. Floegl in the performance of the numerical computations and to Dr. Ye Tianqi for his assistance in the preparation of this manuscript. Helpful comments by Prof. F. Ziegler are gratefully acknowledged.

References

1 Loganathan, K., Chang, S. C., Gallagher, R. H., and Abel, J. F., "Finite Element Representation and Pressure Stiffness in Shell Stability Analysis," *Int. J. Num. Meth. Eng.*, Vol. 14, No. 9, 1979, pp. 1413–1420.

2 Cohen, G. A., "Conservativeness of a Normal Pressure Field Acting on a Shell," *AIAA J.*, Vol. 4, No. 10, 1966, p. 1886.

3 Hibbitt, H. D., "Some Follower Forces and Load Stiffness," *Int. J. Num. Meth. Eng.*, Vol. 14, No. 6, 1979, pp. 937–941.

4 Mang, H. A., "Symmetricability of Pressure Stiffness Matrices for Shells With Loaded Free Edges," *Int. J. Num. Meth. Eng.*, Vol. 15, No. 7, 1980, pp. 981–990.

5 Frey, F., and Cescotto, S., "Some New Aspects of Incremental Total Lagrangian Description in Nonlinear Analysis," *Int. Conf. Finite Elements in Nonlinear Mechanics*, Vol. 1, Geilo, Norway, 1977, pp. 005.1–005.20.

6 Floegl, H., and Mang, H., "Zum Einfluß der Verschiebungsabhängigkeit unglechförmigen hydrostatischen druckes auf das Ausbeulen dünner Schalen Allgemeiner Form," *Ing.-Arch.*, Vol. 50, 1981, pp. 15–30.

7 Chang, S. C., "An Integrated Finite Element Nonlinear Shell Analysis System With Interactive Computer Graphics," Report 81-4, 1981, Department of Structural Engineering, Cornell University, Ithaca, N. Y.

8 Koiter, W. T., "General Equations of Elastic Stability for Thin Shells," *Theory of Thin Shells*, University of Houston Press, 1967, pp. 187–230.

9 Meirovitch, L., *Computational Methods in Structural Dynamics*, Sijthoff and Noordhoff, 1980.

10 Thomas, G. R., and Gallagher, R. H., "A Triangular Thin Shell Finite Element: Linear Analysis," NASA Contractor Report 2482, 1976, Washington, D.C.

Downloaded 02 May 2010 to 171.66.16.246. Redistribution subject to ASME license or copyright; see http://www.asme.org/terms/Terms_Use.cfm

Analysis of Elastic Torsion in a Bar With Circular Holes by a Special Boundary Integral Method

D. A. Caulk
Engineering Mechanics Department,
General Motors Research Laboratories,
Warren, Mich. 48090
Assoc. Mem. ASME

Special boundary integral equations developed in an earlier paper are generalized here for torsion of an elastic bar with circular holes. In this approach, the solution on the boundary of each hole is represented by a series of circular harmonics, and the coefficients in these series are determined by a special system of boundary integral equations. For a cross section with only one hole, the entire system of equations is reduced without approximation to a single integral equation involving only the warping function on the outer boundary. For multiple holes, approximate equations are derived that retain only the first harmonic in the solution representation on each hole. The latter equations are solved analytically for a circular cross section weakened by a concentric ring of circular holes. Simple expressions are derived for torsional rigidity, warping, and maximum stress. The results for torsional rigidity are an improvement over previous ones obtained by another approximate method.

Introduction

In a recent paper, Barone and Caulk [1] proposed special boundary integral equations for solving Laplace's equation in two-dimensional regions with circular holes. In this approach, the boundary potential and its normal derivative are expressed in a series of circular harmonics on each hole. Special integral equations are introduced that individually "pick out" respective coefficients in these expansions and relate them to integrals over the outer boundary and the other holes in the region. The outer boundary is treated in the conventional way, and all integration on the holes is evaluated explicitly. Each special equation contains only one coefficient in the expansion for a given hole, and so the resulting system of integral equations is well conditioned, regardless of the number of terms in the expansion. These equations are particularly advantageous in problems where the boundary condition and the solution on the holes can be adequately characterized by the first one or two terms in the harmonic expansion. The explicit equations in [1] were limited to the case when a constant potential is specified on the boundary of each hole. In this paper, these equations are generalized to include the boundary conditions for the torsion problem.

The general advantages of boundary integral equations in torsion problems were first pointed out by Jaswon and Ponter [2], who expressed a preference for a warping function formulation because it simplifies application of the integral equations to multiply connected regions and yields an expression for torsional rigidity that depends only on boundary values of the solution.

For a cross section with circular holes, the expression for torsional rigidity depends only on the coefficient of the first harmonic of the warping function on each hole. Moreover, the boundary condition on any one hole is expressed by only the first harmonic in the expansion for the normal derivative of the warping function. Since the first-order harmonics play such a major role in the formulation, the special approach in [1] should be well suited to this problem.

In the past, torsion problems in multiply connected cross sections have been approached either by conformal mapping techniques or by special solution representations. Because conformal mapping is usually limited to doubly connected regions, most efforts have concentrated on special solution representations. Kondo [3] and Ling [4] both constructed special solution representations for a circular cross section weakened by a concentric ring of circular holes. Kondo formed a solution by integrating a series of singular stress functions distributed over the boundary. The coefficients in this series were determined by satisfying the boundary conditions pointwise. Ling proceeded in a similar manner using a representation based on a series of rotationally symmetric harmonic functions. Both authors used a stress function formulation but only Ling obtained results for torsional rigidity.

In this paper, the generalized boundary integral equations from [1] are used to formulate two different systems that have particular interest in the torsion problem. First, for a cross section with only one hole, the special integral equations are

Contributed by the Applied Mechanics Division for presentation at the 1983 ASME Applied Mechanics, Bioengineering, and Fluids Engineering Conference, Houston, Texas, June 20–22, 1983 of THE AMERICAN SOCIETY OF MECHANICAL ENGINEERS.

Discussion on this paper should be addressed to the Editorial Department, ASME, United Engineering Center, 345 East 47th Street, New York, N.Y. 10017, and will be accepted until two months after final publication of the paper itself in the JOURNAL OF APPLIED MECHANICS. Manuscript received by ASME Applied Mechanics Division, April, 1982; final revision, August, 1982. Paper No. 83-APM-15.

Copies will be available until February, 1984.

Copyright © 1983 by ASME
Downloaded 02 May 2010 to 171.66.16.246. Redistribution subject to ASME license or copyright; see http://www.asme.org/terms/Terms_Use.cfm

combined to form a single equation for the warping function on the outer boundary alone. The special kernel that appears in this equation carries the entire effect of the hole, without approximation. From the solution to this equation, the warping function on the hole or anywhere else in the cross section can be recovered by a simple quadrature over the outer boundary. Second, the general equations for regions with multiple holes are approximated by retaining only the first harmonic in the solution representation on the hole boundaries. These equations are solved analytically for a circular cross section weakened by a concentric ring of circular holes. Simple expressions are derived for the torsional rigidity, warping distribution, and maximum stress. These results compare extremely well with the exact solution in the case of a single eccentric hole, and for multiple holes the values for torsional rigidity show an improvement over those obtained by Ling [4].

The Torsion Problem

Consider a prismatic bar with cross section $\mathcal{R}$ containing N circular holes centered at points ξ^α ($\alpha = 1, 2,\ldots,N$). Let a_α denote the radius of hole α, ∂C^α its boundary, and $\partial\mathcal{R}$ the closed curve forming the outer boundary of the cross section. The warping function ϕ is single-valued and satisfies

$$\nabla^2\phi = 0 \text{ in } \mathcal{R}, \tag{1}$$

$$\frac{\partial\phi}{\partial n} = -\frac{1}{2}\frac{d}{ds}(r^2) \quad \text{on} \quad \partial\mathcal{R} + \sum_{\alpha=1}^{N}\partial C^\alpha,$$

where the arc length s is measured clockwise on $\partial\mathcal{R}$ and counterclockwise on the holes ∂C^α. Let ϕ and its outward normal derivative on ∂C^α be represented by

$$\phi = \phi_0^\alpha + \sum_{m=1}^{\infty}(\phi_{1m}^\alpha \sin m\theta^\alpha + \phi_{2m}^\alpha \cos m\theta^\alpha), \tag{2}$$

$$\frac{\partial\phi}{\partial n} = q_0^\alpha + \sum_{m=1}^{\infty}(q_{1m}^\alpha \sin m\theta^\alpha + q_{2m}^\alpha \cos m\theta^\alpha), \tag{3}$$

where ϕ_0^α, $\phi_{\lambda m}^\alpha$, q_0^α, $q_{\lambda m}^\alpha$ ($\alpha = 1,2,\ldots,N$; $\lambda = 1,2$; $m = 1,2,\ldots$) are constants and θ^α is the polar angle centered at ξ^α, measured relative to the x_1-axis. On ∂C^α, it is easy to show that

$$-\frac{1}{2}\frac{d}{ds}(r^2) = \xi_1^\alpha \sin\theta^\alpha - \xi_2^\alpha \cos\theta^\alpha, \tag{4}$$

and so the coefficients in (3) are specified by

$$q_0^\alpha = 0,\ q_{11}^\alpha = \xi_1^\alpha,\ q_{21}^\alpha = -\xi_2^\alpha,$$
$$q_{\lambda m}^\alpha = 0,\ (\lambda = 1,2;\ m = 2,3,\ldots). \tag{5}$$

The torsional rigidity G of the cross section can be expressed by

$$G/\mu = \int_{\mathcal{R}} r^2 da - \int_{\partial\mathcal{R}} \phi\frac{\partial\phi}{\partial n}ds - \sum_{\alpha=1}^{N}\int_{\partial C^\alpha}\phi\frac{\partial\phi}{\partial n}ds, \tag{6}$$

where μ is the elastic shear modulus. In this form, G depends only on the boundary values of the solution for ϕ. This suggests that boundary integral methods should be especially suited for computing torsional rigidity since they too involve only boundary quantities. Moreover, if (2)-(5) are used to evaluate the integrals on ∂C^α, equation (6) reduces to

$$G/\mu = \int_{\mathcal{R}} r^2 da - \int_{\partial\mathcal{R}} \phi\frac{\partial\phi}{\partial n}ds - \pi\sum_{\alpha=1}^{N} a_\alpha(\phi_{11}^\alpha \xi_1^\alpha - \phi_{21}^\alpha \xi_2^\alpha). \tag{7}$$

Hence, only the first harmonic in the series representation (2) enters the expression for G. Since the boundary conditions (4) also involve only the first harmonic, it seems particularly appropriate here to use boundary integral equations that directly exploit the representations (2) and (3). Such equations were recently proposed by Barone and Caulk [1] for the special case when $\phi = \phi_0 =$ constant on each hole. In the next section, these equations are generalized to include the boundary condition (4).

Basic Integral Equations

Consider the following harmonic functions:[1]

$$g(\mathbf{x},\mathbf{y}) = -\frac{1}{2\pi}\log|\mathbf{x}-\mathbf{y}|, \tag{8}$$

$$g_0^\beta(\mathbf{x}) = g(\mathbf{x},\xi^\beta) = -\frac{1}{2\pi}\log|\mathbf{x}-\xi^\beta|, \tag{9}$$

$$g_{1m}^\beta = \frac{a_\beta^m \sin m\theta^\beta}{2\pi|\mathbf{x}-\xi^\beta|^m}, \quad g_{2m}^\beta = \frac{a_\beta^m \cos m\theta^\beta}{2\pi|\mathbf{x}-\xi^\beta|^m}, \tag{10}$$
$$(\beta = 1,2,\ldots,N;\ m = 1,2,\ldots).$$

The special boundary integral equations are formed by using each of the functions in (8)-(10) together with ϕ in a statement of Green's second identity over the region $\mathcal{R}$. Integration on ∂C^α is done explicitly[2] using the representations (2) and (3). The resulting equations are

$$G(\mathbf{y}) + \int_{\partial\mathcal{R}}\left(\phi\frac{\partial g}{\partial n} - g\frac{\partial\phi}{\partial n}\right)ds + \sum_{\alpha=1}^{N}\left\{a_\alpha q_0^\alpha \log r_\alpha - \frac{1}{2}\sum_{m=1}^{\infty} b_\alpha^m\left[\left(\phi_{1m}^\alpha + \frac{a_\alpha}{m}q_{1m}^\alpha\right)\sin m\psi^\alpha + \left(\phi_{2m}^\alpha + \frac{a_\alpha}{m}q_{2m}^\alpha\right)\cos m\psi^\alpha\right]\right\} = 0, \tag{11}$$

$$\int_{\partial\mathcal{R}}\left(\phi\frac{\partial g_0^\beta}{\partial n} - g_0^\beta\frac{\partial\phi}{\partial n}\right)ds + \phi_0^\beta + a_\beta q_0^\beta \log a_\beta + \sum_{\substack{\alpha=1\\ \alpha\neq\beta}}^{N}\left\{a_\alpha q_0^\alpha \log r_{\alpha\beta} - \frac{1}{2}\sum_{m=1}^{\infty} b_{\alpha\beta}^m\left[\left(\phi_{1m}^\alpha + \frac{a_\alpha}{m}q_{1m}^\alpha\right)\sin m\psi^{\alpha\beta} + \left(\phi_{2m}^\alpha + \frac{a_\alpha}{m}q_{2m}^\alpha\right)\cos m\psi^{\alpha\beta}\right]\right\} = 0, \tag{12}$$

$$\int_{\partial\mathcal{R}}\left(\phi\frac{\partial g_{\lambda m}^\beta}{\partial n} - g_{\lambda m}^\beta\frac{\partial\phi}{\partial n}\right)ds + \frac{1}{2}(m\phi_{\lambda m}^\beta - a_\beta q_{\lambda m}^\beta) + \sum_{\substack{\alpha=1\\ \alpha\neq\beta}}^{N}\int_{\partial C^\alpha}\left(\phi\frac{\partial g_{\lambda m}^\beta}{\partial n} - g_{\lambda m}^\beta\frac{\partial\phi}{\partial n}\right)ds = 0, \tag{13}$$
$$(\lambda = 1,2;\ \beta = 1,2,\ldots,N;\ m = 1,2,\ldots)$$

where

$$b_\alpha = a_\alpha/r_\alpha,\ r_\alpha = |\mathbf{y}-\xi^\alpha|,\ \psi^\alpha = \theta^\alpha(\mathbf{y}), \tag{14}$$
$$b_{\alpha\beta} = a_\alpha/r_{\alpha\beta},\ r_{\alpha\beta} = |\xi^\alpha - \xi^\beta|,\ \psi^{\alpha\beta} = \theta^\alpha(\xi^\beta), \tag{15}$$

$$G(\mathbf{y}) = \begin{cases} -\phi(\mathbf{y});\ \mathbf{y}\in\{\mathcal{R}, \partial C^\alpha\}, \\ \frac{1}{2}\phi(\mathbf{y});\ \mathbf{y}\in\partial\mathcal{R}. \end{cases} \tag{16}$$

With the specification of appropriate boundary conditions, these equations determine the solution on the outer boundary

[1] Definitions here for $g_{\lambda m}^\beta$ differ by the constant multiplier $a_\beta^m/2\pi$ from those introduced in [1]. This is done for later convenience.

[2] Details are given in the Appendix.

Downloaded 02 May 2010 to 171.66.16.246. Redistribution subject to ASME license or copyright; see http://www.asme.org/terms/Terms_Use.cfm

as well as the unknown coefficients on the holes. Equation (11) is just the usual statement of Green's second identity for the fundamental solution (8). Note that the solution in the interior, also expressed by this equation, is given in terms of an integral on $\partial\mathcal{R}$ and a linear combination of the harmonic coefficients on the holes. In the remaining equations (12) and (13), the special functions (9) and (10) independently "pick out" a single coefficient from each series in (2) and (3) at a given hole β. Because of this local decoupling, the resulting integral equations are well conditioned, regardless of the number of harmonics in the solution representation on the hole boundary. This overcomes the limitation of standard methods that improve the accuracy of the solution by finer boundary discretization, at the ultimate expense of conditioning.

A Single Hole

For the special case of a single hole ($N = 1$), the integral equations (11)–(13) reduce to

$$G(\mathbf{y})+\int_{\partial\mathcal{R}}\left(\phi\frac{\partial g}{\partial n}-g\frac{\partial\phi}{\partial n}\right)ds+aq_0\log|\mathbf{y}-\xi| - \frac{1}{2}\sum_{m=1}^{\infty}b^m\left[\left(\phi_{1m}+\frac{a}{m}q_{1m}\right)\sin m\psi + \left(\phi_{2m}+\frac{a}{m}q_{2m}\right)\cos m\psi\right]=0, \tag{17}$$

$$\int_{\partial\mathcal{R}}\left(\phi\frac{\partial g_0}{\partial n}-g_0\frac{\partial\phi}{\partial n}\right)ds+\phi_0+(a\log a)q_0=0, \tag{18}$$

$$\int_{\partial\mathcal{R}}\left(\phi\frac{\partial g_{\lambda m}}{\partial n}-g_{\lambda m}\frac{\partial\phi}{\partial n}\right)ds+\frac{1}{2}(m\phi_{\lambda m}-aq_{\lambda m})=0, \tag{19}$$

where all Greek superscripts and subscripts have been dropped. Substituting ϕ_0 amd $\phi_{\lambda m}$ from (18) and (19) into (17) yields

$$G(\mathbf{y})+\int_{\partial\mathcal{R}}\left(\phi\frac{\partial g^*}{\partial n}-g^*\frac{\partial\phi}{\partial n}\right)ds+aq_0\log|\mathbf{y}-\xi| - \sum_{m=1}^{\infty}\frac{a}{m}b^m(q_{1m}\sin m\psi+q_{2m}\cos m\psi)=0, \tag{20}$$

where g^* is defined by the uniformly convergent series

$$g^*(\mathbf{x},\mathbf{y},\xi)=g(\mathbf{x},\mathbf{y})+\sum_{m=1}^{\infty}\frac{1}{m}b^m(g_{1m}\sin m\psi+g_{2m}\cos m\psi) = \frac{1}{2\pi}\left[-\log|\mathbf{x}-\mathbf{y}| + \sum_{m=1}^{\infty}\frac{a^{2m}/m}{|\mathbf{y}-\xi|^m|\mathbf{x}-\xi|^m}\cos m(\psi-\theta)\right] = g^*(\mathbf{y},\mathbf{x},\xi). \tag{21}$$

The solution on the hole boundary can be recovered from the solution to (20) by the single quadrature

$$\phi(\theta)=-aq_0\log a+\sum_{m=1}^{\infty}\frac{a}{m}(q_{1m}\sin m\theta+q_{2m}\cos m\theta) - \int_{\partial\mathcal{R}}\left(\phi\frac{\partial g_0^*}{\partial n}-g_0^*\frac{\partial\phi}{\partial n}\right)ds, \tag{22}$$

where g_0^* is defined by

$$g_0^*(\mathbf{x},\xi,\theta)=g_0(\mathbf{x},\xi)+\sum_{m=1}^{\infty}\frac{2}{m}(g_{1m}\sin m\theta+g_{2m}\cos m\theta) = \frac{1}{2\pi}\left\{-\log|\mathbf{x}-\xi|+\sum_{m=1}^{\infty}\frac{2a^m/m}{|\mathbf{x}-\xi|^m}\cos m[\theta(\mathbf{x})-\theta]\right\}. \tag{23}$$

In the torsion problem, q_0 and $q_{\lambda m}$ are specified by (5) so that (20) and (22) reduce to

$$G(\mathbf{y})+\int_{\partial\mathcal{R}}\left(\phi\frac{\partial g^*}{\partial n}-g^*\frac{\partial\phi}{\partial n}\right)ds - \frac{a^2}{|\mathbf{y}-\xi|}(\xi_1\sin\psi-\xi_2\cos\psi)=0, \tag{24}$$

$$\phi(\theta)=a(\xi_1\sin\theta-\xi_2\cos\theta)-\int_{\partial\mathcal{R}}\left(\phi\frac{\partial g_0^*}{\partial n}-g_0^*\frac{\partial\phi}{\partial n}\right)ds. \tag{25}$$

Hence, the several integral equations (11)–(13) can be reduced to the single equation (24) for the warping function on the outer boundary $\partial\mathcal{R}$. Because g^* has the same singular character as g, this equation can be solved by any one of the available numerical methods for boundary integral equations. Once the solution is found on $\partial\mathcal{R}$, single coefficients in the expansion for ϕ on the hole can be recovered by quadrature from (18) and (19) or the entire solution obtained directly from (25).

Equations corresponding to (20) and (22) can also be derived when $\partial\phi/\partial n$ is regarded as unknown on the hole boundary, but these will not be recorded here.

First-Order Equations

Suppose each series in (2) and (3) is approximated by only the first term. This would be the minimum number necessary for a nontrivial formulation of the torsion problem. In this case, we retain only those equations in (13) corresponding to $m=1$ and shorten the notation by letting $q_\lambda^\alpha = q_{\lambda 1}^\alpha$, $\phi_\lambda^\alpha = \phi_{\lambda 1}^\alpha$, and $g_\lambda^\alpha = g_{\lambda 1}^\alpha$. Then, with (A13) and (A15), equations (11)–(13) reduce to

$$G(\mathbf{y})+\int_{\partial\mathcal{R}}\left(\phi\frac{\partial g}{\partial n}-g\frac{\partial\phi}{\partial n}\right)ds+\sum_{\alpha=1}^{N}\left\{a_\alpha q_0^\alpha\log r_\alpha - \frac{1}{2}b_\alpha[(\phi_1^\alpha+a_\alpha q_1^\alpha)\sin\psi^\alpha+(\phi_2^\alpha+a_\alpha q_2^\alpha)\cos\psi^\alpha]\right\}=0, \tag{26}$$

$$\int_{\partial\mathcal{R}}\left(\phi\frac{\partial g_0^\beta}{\partial n}-g_0^\beta\frac{\partial\phi}{\partial n}\right)ds+\phi_0^\beta+a_\beta q_0^\beta\log a_\beta + \sum_{\substack{\alpha=1\\ \alpha\neq\beta}}^{N}\left\{a_\alpha q_0^\alpha\log r_{\alpha\beta}-\frac{1}{2}b_{\alpha\beta}[(\phi_1^\alpha+a_\alpha q_1^\alpha)\sin\psi^{\alpha\beta} + (\phi_2^\alpha+a_\alpha q_2^\alpha)\cos\psi^{\alpha\beta}]\right\}=0, \tag{27}$$

$$\int_{\partial\mathcal{R}}\left(\phi\frac{\partial g_1^\beta}{\partial n}-g_1^\beta\frac{\partial\phi}{\partial n}\right)ds+\frac{1}{2}(\phi_1^\beta-a_\beta q_1^\beta) + \sum_{\substack{\alpha=1\\ \alpha\neq\beta}}^{N}b_{\beta\alpha}\left\{a_\alpha q_0^\alpha\sin\psi^{\alpha\beta}+\frac{1}{2}b_{\alpha\beta}[(\phi_2^\alpha+a_\alpha q_2^\alpha)\sin 2\psi^{\alpha\beta} - (\phi_1^\alpha+a_\alpha q_1^\alpha)\cos 2\psi^{\alpha\beta}]\right\}=0, \tag{28}$$

Downloaded 02 May 2010 to 171.66.16.246. Redistribution subject to ASME license or copyright; see http://www.asme.org/terms/Terms_Use.cfm

$$\int_{\partial\mathcal{R}} \left(\phi \frac{\partial g_2^\beta}{\partial n} - g_2^\beta \frac{\partial \phi}{\partial n}\right) ds + \frac{1}{2}(\phi_2^\beta - a_\beta q_2^\beta) + \sum_{\substack{\alpha=1 \\ \alpha\neq\beta}}^{N} b_{\beta\alpha}\left\{a_\alpha q_0^\alpha \cos\psi^{\alpha\beta} + \frac{1}{2} b_{\alpha\beta}[(\phi_1^\alpha + a_\alpha q_1^\alpha)\sin 2\psi^{\alpha\beta} + (\phi_2^\alpha + a_\alpha q_2^\alpha)\cos 2\psi^{\alpha\beta}]\right\} = 0, \quad (29)$$

$$(\beta = 1,2,\ldots,N).$$

These are called the *first-order equations*, and their solution is the *first-order solution*.

With the boundary conditions (5), the first-order equations for the torsion problem are

$$G(\mathbf{y}) + \int_{\partial\mathcal{R}} \left(\phi \frac{\partial g}{\partial n} - g \frac{\partial \phi}{\partial n}\right) ds - \frac{1}{2} \sum_{\alpha=1}^{N} b_\alpha[(\phi_1^\alpha + a_\alpha \xi_1^\alpha)\sin\psi^\alpha + (\phi_2^\alpha - a_\alpha \xi_2^\alpha)\cos\psi^\alpha] = 0, \quad (30)$$

$$\int_{\partial\mathcal{R}} \left(\phi \frac{\partial g_0^\beta}{\partial n} - g_0^\beta \frac{\partial \phi}{\partial n}\right) ds + \phi_0^\beta - \frac{1}{2} \sum_{\substack{\alpha=1 \\ \alpha\neq\beta}}^{N} b_{\alpha\beta}[(\phi_1^\alpha + a_\alpha \xi_1^\alpha)\sin\psi^{\alpha\beta} + (\phi_2^\alpha - a_\alpha \xi_2^\alpha)\cos\psi^{\alpha\beta}] = 0, \quad (31)$$

$$\int_{\partial\mathcal{R}} \left(\phi \frac{\partial g_1^\beta}{\partial n} - g_1^\beta \frac{\partial \phi}{\partial n}\right) ds + \frac{1}{2}(\phi_1^\beta - a_\beta \xi_1^\beta) + \frac{1}{2} \sum_{\substack{\alpha=1 \\ \alpha\neq\beta}}^{N} b_{\beta\alpha} b_{\alpha\beta}[(\phi_2^\alpha - a_\alpha \xi_2^\alpha)\sin 2\psi^{\alpha\beta} - (\phi_1^\alpha + a_\alpha \xi_1^\alpha)\cos 2\psi^{\alpha\beta}] = 0, \quad (32)$$

$$\int_{\partial\mathcal{R}} \left(\phi \frac{\partial g_2^\beta}{\partial n} - g_2^\beta \frac{\partial \phi}{\partial n}\right) ds + \frac{1}{2}(\phi_2^\beta + a_\beta \xi_2^\beta) + \frac{1}{2} \sum_{\substack{\alpha=1 \\ \alpha\neq\beta}}^{N} b_{\beta\alpha} b_{\alpha\beta}[(\phi_1^\alpha + a_\alpha \xi_1^\alpha)\sin 2\psi^{\alpha\beta} + (\phi_2^\alpha - a_\alpha \xi_2^\alpha)\cos 2\psi^{\alpha\beta}] = 0, \quad (33)$$

$$(\beta = 1,2,\ldots,N).$$

Since ϕ_0^β appears only in the second of these equations, the other three may be solved separately for ϕ_λ^β and $\phi(\mathbf{y})$, $\mathbf{y} \in \partial\mathcal{R}$. A specific example is considered in the next section.

A Ring of Holes in a Circular Cross Section

In this section we consider a circular cross section weakened by N circular holes, evenly spaced in a concentric circular ring. The cross section has radius R, the holes all have radius a, and their centers are located on a circle of radius b. Let the coordinate axes be chosen such that

$$\xi_1^\alpha = b\cos\frac{2\pi\alpha}{N}, \quad \xi_2^\alpha = b\sin\frac{2\pi\alpha}{N}. \quad (34)$$

From symmetry, the unknowns ϕ_0^α and ϕ_λ^α can be expressed in terms of two independent constants in the form

$$\phi_0^\alpha = \phi_0, \quad \phi_1^\alpha = \phi_1\cos\frac{2\pi\alpha}{N}, \quad \phi_2^\alpha = -\phi_1\sin\frac{2\pi\alpha}{N},$$

$$(\alpha = 1,2,\ldots,N). \quad (35)$$

Now consider the first-order equations (30)–(33). Let (r,θ) be polar coordinates in the cross section, with the origin at the center. Then, on the outer boundary $\partial\mathcal{R}$,

$$ds = Rd\theta, \quad \frac{\partial g}{\partial n} = -\frac{1}{4\pi R}, \quad \frac{\partial \phi}{\partial n} = 0, \quad (36)$$

and from the geometry of the problem, it is easy to show that

$$\psi^{\alpha N} = \pi\left(\frac{\alpha}{N} - \frac{1}{2}\right),$$

$$b_\alpha = a\Big/\left[R^2 + b^2 - 2bR\cos\left(\theta - \frac{2\pi\alpha}{N}\right)\right]^{-1/2},$$

$$b_{\alpha N} = a\left(2b\sin\frac{\pi\alpha}{N}\right)^{-1}, \quad (37)$$

$$\sin\left(\psi^\alpha - \frac{2\pi\alpha}{N}\right) = \frac{R\sin\left(\theta - \frac{2\pi\alpha}{N}\right)}{\left[R^2 + b^2 - 2bR\cos\left(\theta - \frac{2\pi\alpha}{N}\right)\right]^{1/2}}.$$

Hence for $\beta = N$, equations (30)–(33) reduce to

$$\frac{1}{2}\phi(R,\theta) - \frac{1}{4\pi}\int_0^{2\pi} \phi(R,\theta)\,d\theta - \frac{1}{2}(\phi_1 + ab)\sum_{\alpha=1}^{N} \frac{aR\sin\left(\theta - \frac{2\pi\alpha}{N}\right)}{R^2 + b^2 - 2bR\cos\left(\theta - \frac{2\pi\alpha}{N}\right)} = 0, \quad (38)$$

$$R\int_0^{2\pi} \phi(R,\theta)\frac{\partial g_0^N}{\partial n}\,d\theta + \phi_0 + \frac{1}{4}\left(\frac{a}{b}\right)(\phi_1 + ab)\sum_{\alpha=1}^{N-1}\cot\frac{\pi\alpha}{N} = 0, \quad (39)$$

$$R\int_0^{2\pi} \phi(R,\theta)\frac{\partial g_1^N}{\partial n}\,d\theta + \frac{1}{2}(\phi_1 - ab) + \frac{1}{8}\left(\frac{a}{b}\right)^2(\phi_1 + ab)\sum_{\alpha=1}^{N-1}\csc^2\frac{\pi\alpha}{N} = 0, \quad (40)$$

$$R\int_0^{2\pi} \phi(R,\theta)\frac{\partial g_2^N}{\partial n}\,d\theta = 0. \quad (41)$$

Without loss in generality, we assume that the average value of ϕ on the outer boundary is zero, so that from (38)

$$\phi(R,\theta) = \frac{a}{R}(\phi_1 + ab)\sum_{\alpha=1}^{N} \frac{\sin\left(\theta - \frac{2\pi\alpha}{N}\right)}{1 + (b/R)^2 - 2(b/R)\cos\left(\theta - \frac{2\pi\alpha}{N}\right)} = N\frac{a}{b}(\phi_1 + ab)\sum_{m=1}^{\infty}\left(\frac{b}{R}\right)^{Nm}\sin Nm\theta. \quad (42)$$

With (A9), (A16), and (42), one can show that (40) is satisfied identically and the integral in (39) vanishes. Since by symmetry the finite sum in (39) vanishes, it follows that $\phi_0 = 0$. Finally, from (42) and (A14)

$$R\int_0^{2\pi} \phi(R,\theta)\frac{\partial g_1^N}{\partial n}\,d\theta = -\frac{1}{2}N^2\left(\frac{a}{b}\right)^2(\phi_1 + ab)\sum_{m=1}^{\infty} m\left(\frac{b}{R}\right)^{2Nm} = -\frac{1}{2}N^2\left(\frac{a}{b}\right)^2(\phi_1 + ab)\frac{(b/R)^{2N}}{[1 - (b/R)^{2N}]^2}, \quad (43)$$

$$\phi_1/ab = \frac{b^2 - \gamma_N a^2}{b^2 + \gamma_N a^2}, \quad (44)$$

where

$$\gamma_N = \frac{1}{4}\sum_{\alpha=1}^{N-1}\csc^2\frac{\pi\alpha}{N} - \frac{N^2(b/R)^{2N}}{[1 - (b/R)^{2N}]^2}. \quad (45)$$

Downloaded 02 May 2010 to 171.66.16.246. Redistribution subject to ASME license or copyright; see http://www.asme.org/terms/Terms_Use.cfm

Table 1 Torsional rigidity of a circular cylinder with a single eccentric hole ($a/R = 1/3$)

$\frac{b}{R-a}$	$2G/(\mu\pi R^4)$			
	First-order solution from (47) and (51)	Exact BIE formulation		Exact solution from [5]
		20 divisions	40 divisions	
0.20	0.97872	0.97873	0.97872	0.97872
0.40	0.95138	0.95140	0.95137	0.95137
0.60	0.90325	0.90328	0.90316	0.90312
0.80	0.82620	0.82574	0.82497	0.82473
0.90	0.76810	0.76583	0.76252	0.76168
0.92	0.75365	0.75057	0.74569	0.74454
0.94	0.73786	0.73367	0.72605	0.72446
0.96	0.72043	0.71473	0.70178	0.69968
0.98	0.70099	0.69321	0.66732	0.66555

Table 2 Torsional rigidity of a circular cylinder with a ring of N holes ($a/R = 1/4$, $b/R = 1/2$)

Number of holes	$2G/(\mu\pi R^4)$		
	First-order solution from (47) and (45)	Exact BIE formulation	Approximate first-order solution from (47) and (54)
2	0.8661	0.8657	0.8745
3	0.8224	0.8214	0.8276
4	0.7934	0.7893	0.7939

Table 3 Torsional rigidity in Ling's [4] examples

Case	$2G/(\mu\pi R^4)$		
	First-order solution from (47) and (45)	Exact BIE formulation	Ling's results
$N = 2, c/R = 0$ $a/R = 2/7, b/R = 3/7$	0.8739	0.8713	0.8809
$N = 2, c/R = 1/5$ $a/R = 1/5, b/R = 3/5$	0.8741	0.8732	0.8093
$N = 6, c/R = 1/5$ $a/R = 1/5, b/R = 3/5$	0.7261	0.7261	0.7305

Although the details will not be given here, it is possible to show from (30), (34)–(37), (42), (44), and (A6) that the first-order expression for ϕ at points inside $\mathfrak{R}$ can be expressed by

$$\phi(r,\theta) = \frac{a^2 b^2}{b^2 + \gamma_N a^2}\left\{ \sum_{m=1}^{\infty} N\left(\frac{rb}{R^2}\right)^{Nm} \sin Nm\theta + \left(\frac{r}{b}\right) \sum_{\alpha=1}^{N} \frac{\sin\left(\theta - \frac{2\pi\alpha}{N}\right)}{1 + (r/b)^2 - 2(r/b)\cos\left(\theta - \frac{2\pi\alpha}{N}\right)} \right\}. \quad (46)$$

This expression approaches (42) in the limit $r \to R$.

From (34)–(36) and (44), the expression (7) for the torsional rigidity becomes

$$G/\mu = \frac{1}{2}\pi R^4 \left\{ 1 - N\left[\left(\frac{a}{R}\right)^4 + \left(\frac{b}{R}\right)^4 \frac{4a^2}{b^2 + \gamma_N a^2} \right] \right\}. \quad (47)$$

The maximum shear stresses in this cross section occur on the lines of symmetry $\theta = 2\pi\alpha/N$ ($\alpha = 1,2,\ldots,N$), either on the outer boundary ($r = R$) or on the hole at $r = a + b$. On the outer boundary, the maximum shear stress calculated from (42) is

$$\tau_{\theta z}\left(R, \frac{2\pi\alpha}{N}\right) = \mu\sigma R\left\{ 1 + \left(\frac{a}{R}\right)^2 \frac{2b^2}{b^2 + \gamma_N a^2} \frac{N^2 (b/R)^N}{[1 - (b/R)^N]^2} \right\}, \quad (48)$$

where σ is the twist per unit length. To the first-order approximation on ∂C^α, we have

$$\frac{\partial\phi}{\partial\theta}\left(a+b, \frac{2\pi\alpha}{N}\right) = \left(\frac{a+b}{a}\right)\phi_1, \quad (49)$$

so that the maximum stress here is given by

$$\tau_{\theta z}\left(a+b, \frac{2\pi\alpha}{N}\right) = \mu\sigma R\left[\frac{b}{R}\left(\frac{2b^2}{b^2 + \gamma_N a^2}\right) + \frac{a}{R} \right]. \quad (50)$$

If b/R is large enough, the maximum shear stress in the cross section can occur on the hole rather than on the outer boundary.

An exact analytical solution to this problem is available [5] for the case of a single hole ($N = 1$). In this case, equation (45) reduces to

$$\gamma_1 = \frac{-(b/R)^2}{[1 - (b/R)^2]^2}, \quad (51)$$

and this can be used in (47) to compute the corresponding approximate value for G. For $a/R = 1/3$ and various degrees

Downloaded 02 May 2010 to 171.66.16.246. Redistribution subject to ASME license or copyright; see http://www.asme.org/terms/Terms_Use.cfm

of eccentricity, Table 1 compares the approximate rigidity obtained from (47) and (51) with the exact result from [5]. The agreement is extremely good, even when the hole is very close to the outer boundary. For comparison, we also show values obtained from numerical solutions to the exact integral equation (24). This equation was solved using a standard quadrature method [6] over divisions of the outer circle into 20 and 40 equal intervals. The value of ϕ_1 was recovered from (19) using the same quadrature and this result substituted in (47) to compute torsional rigidity. From (48), (50), and (51), the maximum stresses in this case are

$$\tau_{\theta z}\left(R, \frac{2\pi\alpha}{N}\right) = \mu\sigma\left[R + \frac{2ba^2}{(R-b)^2} + O\left(\frac{a^4}{R^4}\right)\right], \qquad (52)$$

$$\tau_{\theta z}\left(a+b, \frac{2\pi\alpha}{N}\right) = \mu\sigma\left[a+2b + \frac{2ba^2R^2}{(R^2-b^2)^2} + O\left(\frac{a^4}{R^4}\right)\right]. \qquad (53)$$

Up to terms of order $(a/R)^4$, these expressions are identical to the exact solution obtained by Macdonald [7].

For more than one hole ($N \geq 2$), no exact analytical solutions are available. When $b/R = 1/2$, equation (45) gives

$$\gamma_2 = -0.03444\ ,\ \gamma_3 = 0.5215\ ,\ \gamma_4 = 1.234. \qquad (54)$$

If we further assume that $a/R = 1/4$, the torsional rigidity for each case can be computed from (47). The results are shown in Table 2. Because of symmetry, the warping function can be determined completely by analyzing any one of N identical wedges of the cross section, each containing a single hole. Hence, we can determine a more accurate value for torsional rigidity by solving the exact integral equation (24) and using this solution in (19) and (47). These results are also listed in Table 2.

Figure 1 shows a comparison of the warping function inside the cross section, computed from the approximate result (46) and from a numerical solution of the exact equation (24). The approximate result (46) is reasonably good even for $N = 4$ when the holes are rather closely spaced. Note that the comparison is especially good in the region of maximum stress.

It is a simple matter to generalize the solution of this section to the case when the cross section also has a central hole, say of radius c. Because of symmetry, ϕ_0 and ϕ_λ vanish on the central hole (when $N \geq 2$) and all other results except torsional rigidity are unaffected. The torsional rigidity of this cross section is given by

$$G/\mu = \frac{1}{2}\pi R^4\left\{1 - \left(\frac{c}{R}\right)^4 - N\left[\left(\frac{a}{R}\right)^4 + \left(\frac{b}{R}\right)^4\left(\frac{4a^2}{b^2+\gamma_N a^2}\right)\right]\right\}. \qquad (55)$$

This generalization enables us to discuss the examples considered by Ling [4], who constructed a solution from a series of rotationally symmetric harmonic functions.

Ling considered three different examples, two of which contained central holes. These cases are given in Table 3, where we show Ling's values for torsional rigidity compared with those computed from (55) and from a numerical solution of the exact integral equation (24) on a symmetric wedge of the cross section containing a single hole. In the latter case, ϕ_1 was recovered from (19) as before and substituted in (47) to compute G. Based on the earlier results for a single hole (Table 1), it appears from Table 3 that the simple formula (55) is an improvement over Ling's results in every case.[3]

A Further Approximation

When the holes are sufficiently removed from the outer boundary of the cross section, it may be possible to further simplify the first-order equations (30)–(33) by assuming that the holes do not significantly affect the potential ϕ on $\partial\mathcal{R}$. Mathematically, this is equivalent to neglecting the summation in (30) because $b_\alpha << 1$. In this case, the boundary potential on $\partial\mathcal{R}$ is the same as for the simply connected cross section. The integrals in (32) and (33) can now be evaluated explicitly and the problem is reduced to a linear system of equations for the unknowns ϕ_λ^α. This decoupling between the holes and the outer boundary makes it possible to compare several hole configurations inside the same cross section, using the same solution for ϕ on $\partial\mathcal{R}$. For some simple cross sections, this boundary potential may be available from existing analytical solutions.

As an example, consider the problem of the previous section. Without the holes, the solution on the outer circle is $\phi = 0$, and so the integral in (32) vanishes. The solution for ϕ_1 is again given by (44), except that now

$$\gamma_N = \frac{1}{4}\sum_{\alpha=1}^{N-1}\csc^2\frac{\pi\alpha}{N}. \qquad (56)$$

Note that ϕ_1 is now independent of R. Values for torsional rigidity based on this approximation are given in the third column of Table 2. The accuracy of the results is remarkably good, considering that $b_\alpha = 1/2$.

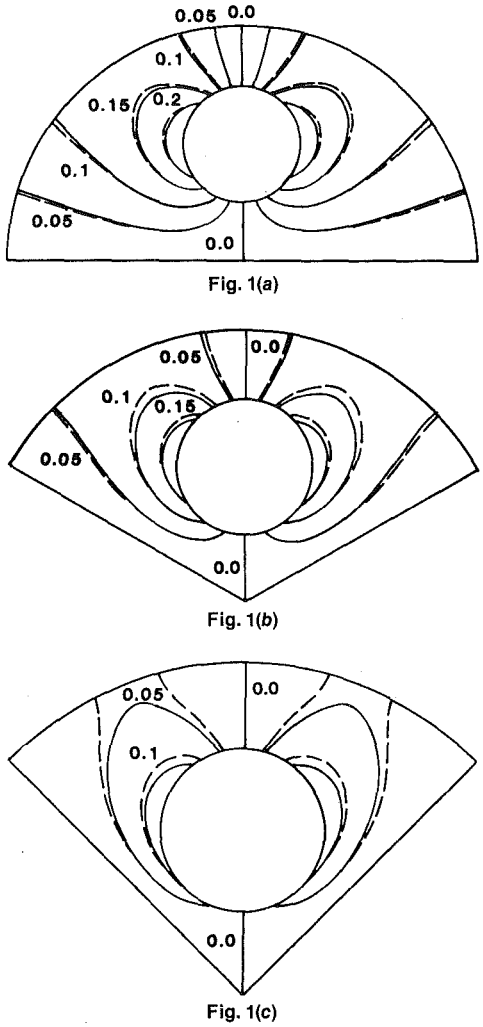

Fig. 1(a)

Fig. 1(b)

Fig. 1(c)

Fig. 1 Lines of constant axial displacement (ϕ/R) in symmetric cross sections with two, three, and four holes. Solid lines indicate results from the first-order solution (46) and dashed lines from the numerical solution of the exact boundary integral equation (24).

[3] Because there is no apparent reason for the unusually large difference in the second example, Ling's rather lengthy calculations are probably in error here.

Downloaded 02 May 2010 to 171.66.16.246. Redistribution subject to ASME license or copyright; see http://www.asme.org/terms/Terms_Use.cfm

References

1 Barone, M. R., and Caulk, D. A., "Special Boundary Integral Equations for Approximate Solution of Laplace's Equation in Two-Dimensional Regions With Circular Holes," *Q. J. Mech. Appl. Math.*, Vol. 34, 1981, pp. 265–268.

2 Jaswon, M. A., and Ponter, A. R., "An Integral Equation Solution of the Torsion Problem," *Proc. Royal Soc. London*, Series A, Vol. 273, 1963, pp. 237–246.

3 Kondo, M., "The Stress in a Twisted Circular Cylinder Having Circular Holes," *Phil. Mag.*, Vol. 22, 1936, pp. 1089–1109.

4 Ling, C. B., "Torsion of a Circular Tube With Longitudinal Circular Holes," *Quart. Appl. Math.*, Vol. 5, 1947, pp. 168–181.

5 Muskhelishvili, N. I., *Some Basic Problems of the Mathematical Theory of Elasticity*, Noordhoff, Netherlands, 1963.

6 Jaswon, M. A., and Symm, G. T., *Integral Equation Methods in Potential Theory and Elastostatics*, Academic Press, New York, 1977.

7 Macdonald, H. M., "On the Torsional Strength of a Hollow Shaft," *Proc. Camb. Phil. Soc.*, Vol. 8, 1893, pp. 62–68.

APPENDIX

This appendix supplies results of explicit integration used in the text. Specifically, we consider integrals of the form

$$\int_{\partial C^\alpha} \left(\phi \frac{\partial h}{\partial n} - h \frac{\partial \phi}{\partial n}\right) ds, \tag{A1}$$

where h stands for one of the kernels

$$g,\ g_0^\beta,\ g_{\lambda k}^\beta. \tag{A2}$$

For convenience, we introduce the notation

$$\mu_{\lambda m}^\alpha = \phi_{\lambda m}^\alpha + \frac{a_\alpha}{m} q_{\lambda m}^\alpha\ ,\ \nu_{\lambda m}^\alpha = \phi_{\lambda m}^\alpha - \frac{a_\alpha}{m} q_{\lambda m}^\alpha \tag{A3}$$

and omit most of the details since they parallel those of the more restricted integration considered in [1].

First, let $h = g$. Then

$$\int_{\partial C^\alpha} \left(\phi \frac{\partial g}{\partial n} - g \frac{\partial \phi}{\partial n}\right) ds = \begin{cases} a_\alpha q_0^\alpha \log r_\alpha - \dfrac{1}{2} \displaystyle\sum_{m=1}^{\infty} b_\alpha^m (\mu_{1m}^\alpha \sin m\psi^\alpha + \mu_{2m}^\alpha \cos m\psi^\alpha) \\ \qquad \text{when } b_\alpha < 1, \qquad (A4) \\ \dfrac{1}{2}\phi_0^\alpha + a_\alpha q_0^\alpha \log a_\alpha - \dfrac{1}{2} \displaystyle\sum_{m=1}^{\infty} \dfrac{a_\alpha}{m} (q_{1m}^\alpha \sin m\psi^\alpha + q_{2m}^\alpha \cos m\psi^\alpha) \\ \qquad \text{when } b_\alpha = 1, \qquad (A5) \\ \phi_0^\alpha + a_\alpha q_0^\alpha \log a_\alpha + \dfrac{1}{2} \displaystyle\sum_{m=1}^{\infty} b_\alpha^{-m} (\nu_{1m}^\alpha \sin m\psi^\alpha + \nu_{2m}^\alpha \cos m\psi^\alpha) \\ \qquad \text{when } b_\alpha > 1. \qquad (A6) \end{cases}$$

Next, let $h = g_0^\beta$. When $\beta = \alpha$, g_0^β and $\partial g_0^\beta / \partial n$ are both constant on ∂C^α and (A1) reduces to

$$\int_{\partial C^\alpha} \left(\phi \frac{\partial g_0^\alpha}{\partial n} - g_0^\alpha \frac{\partial \phi}{\partial n}\right) ds = \phi_0^\alpha + a_\alpha q_0^\alpha \log a_\alpha. \tag{A7}$$

When $\beta \neq \alpha$, we can set $\mathbf{y} = \xi^\beta$ in (A4)–(A6) to obtain

$$\int_{\partial C^\alpha} \left(\phi \frac{\partial g_0^\beta}{\partial n} - g_0^\beta \frac{\partial \phi}{\partial n}\right) ds = \begin{cases} a_\alpha q_0^\alpha \log r_{\alpha\beta} - \dfrac{1}{2} \displaystyle\sum_{m=1}^{\infty} b_{\alpha\beta}^m (\mu_{1m}^\alpha \sin m\psi^{\alpha\beta} + \mu_{2m}^\alpha \cos m\psi^{\alpha\beta}) \\ \qquad \text{when } b_{\alpha\beta} < 1, \qquad (A8) \\ \phi_0^\alpha + a_\alpha q_0^\alpha \log a_\alpha + \dfrac{1}{2} \displaystyle\sum_{m=1}^{\infty} b_{\alpha\beta}^{-m} (\nu_{1m}^\alpha \sin m\psi^{\alpha\beta} + \nu_{2m}^\alpha \cos m\psi^{\alpha\beta}) \\ \qquad \text{when } b_{\alpha\beta} > 1. \qquad (A9) \end{cases}$$

Lastly, let $h = g_{\lambda k}^\beta$. Now when $\mathbf{x} \in \partial C^\alpha$

Downloaded 02 May 2010 to 171.66.16.246. Redistribution subject to ASME license or copyright; see http://www.asme.org/terms/Terms_Use.cfm

$$\frac{\partial g_{1k}^{\beta}}{\partial n} = \frac{k}{2\pi} a_{\beta}^{k} r_{\beta}^{-(k+1)} \sin[(k+1)\theta^{\beta} - \theta^{\alpha}], \qquad (A10)$$

$$\frac{\partial g_{2k}^{\beta}}{\partial n} = \frac{k}{2\pi} a_{\beta}^{k} r_{\beta}^{-(k+1)} \cos[(k+1)\theta^{\beta} - \theta^{\alpha}], \qquad (A11)$$

so that for $\beta = \alpha$

$$\int_{\partial C^{\alpha}} \left(\phi \frac{\partial g_{\lambda k}^{\alpha}}{\partial n} - g_{\lambda k}^{\alpha} \frac{\partial \phi}{\partial n}\right) ds = \frac{1}{2} (k\phi_{\lambda k}^{\alpha} - a_{\alpha} q_{\lambda k}^{\alpha}). \qquad (A12)$$

When $\beta \neq \alpha$, we have for $\lambda = 1$

$$\int_{\partial C^{\alpha}} \left(\phi \frac{\partial g_{11}^{\beta}}{\partial n} - g_{11}^{\beta} \frac{\partial \phi}{\partial n}\right) ds = \begin{cases} b_{\beta\alpha}\left\{a_{\alpha} q_0^{\alpha} \sin \psi^{\alpha\beta} - \frac{1}{2} \sum_{m=1}^{\infty} m b_{\alpha\beta}^{m} [\mu_{1m}^{\alpha} \cos(m+1)\psi^{\alpha\beta} - \mu_{2m}^{\alpha} \sin(m+1)\psi^{\alpha\beta}]\right\} \\ \qquad \text{when } b_{\alpha\beta} < 1, \qquad (A13) \\ \frac{1}{2} b_{\beta\alpha} \sum_{m=1}^{\infty} m b_{\alpha\beta}^{-m} [\nu_{1m}^{\alpha} \cos(m-1)\psi^{\alpha\beta} - \nu_{2m}^{\alpha} \sin(m-1)\psi^{\alpha\beta}] \\ \qquad \text{when } b_{\alpha\beta} > 1, \qquad (A14) \end{cases}$$

and similarly for $\lambda = 2$

$$\int_{\partial C^{\alpha}} \left(\phi \frac{\partial g_{21}^{\beta}}{\partial n} - g_{21}^{\beta} \frac{\partial \phi}{\partial n}\right) ds = \begin{cases} b_{\beta\alpha}\left\{a_{\alpha} q_0^{\alpha} \cos \psi^{\alpha\beta} + \frac{1}{2} \sum_{m=1}^{\infty} m b_{\alpha\beta}^{m} [\mu_{1m}^{\alpha} \sin(m+1)\psi^{\alpha\beta} + \mu_{2m}^{\alpha} \cos(m+1)\psi^{\alpha\beta}]\right\} \\ \qquad \text{when } b_{\alpha\beta} < 1, \qquad (A15) \\ \frac{1}{2} b_{\beta\alpha} \sum_{m=1}^{\infty} m b_{\alpha\beta}^{-m} [\nu_{1m}^{\alpha} \sin(m-1)\psi^{\alpha\beta} + \nu_{2m}^{\alpha} \cos(m-1)\psi^{\alpha\beta}] \\ \qquad \text{when } b_{\alpha\beta} > 1. \qquad (A16) \end{cases}$$

Downloaded 02 May 2010 to 171.66.16.246. Redistribution subject to ASME license or copyright; see http://www.asme.org/terms/Terms_Use.cfm

An Analysis of Adhesive-Bonded Single-Lap Joints

Du Chen
Visiting Scholar.

Shun Cheng
Professor.
Mem. ASME

Department of Engineering Mechanics,
University of Wisconsin,
Madison, Wis. 53708

Because of the technical importance and difficulty of the analysis, the present problem has been treated, as seen in the literature, by a number of authors. In the current paper a unified method is presented that has advantages in several respects for the analysis of this difficult problem and may also be employed for solving other similar problems. The method is based on two-dimensional elasticity theory in conjunction with the variational principal of complementary energy. Minimizing the energy functional leads to two coupled, fourth-order ordinary differential equations with constant coefficients for the determination of the stresses. By means of the present approach, a closed-form solution, which is adaptable for any possible adhesive layer flexibility and capable of satisfying all the boundary stress conditions of the joint, is obtained. To illustrate the application of the present unified theory, three typical examples for flexible, medium, and inflexible adhesive layers are provided and comparisons are made among these examples and with other known solutions. Special attention is given to the stress distribution in the end zones where high stress intensities of the joints occur.

Introduction

As a consequence of the development, in recent years, of new adhesive materials, which can yield a strong bond between the adherends, chemists and engineers [1,2] have been searching for a better test specimen that could be adopted as a universal standard to generate basic data on the mechanical properties of adhesives. Their efforts have led to the selection of single-lap joints which possess several advantages over other test specimens [1,2]. In addition, such joints also happen to be one of the most commonly used structural elements in the manufacture of aerospace vehicles [1-5] and are also used extensively in the wood industry [1,6]. Because of these facts, a theoretical analysis of the stresses in lap joints, which could cover a broader range of practical applicability than those presently available, is required by both chemists and engineers when designing structures involving bonded joints.

Several theoretical analyses of this difficult problem have appeared in the literature since the early work by Goland and Reissner [7]. Their study concerns only two limiting cases, i.e., where the adhesive layer is so thin and stiff (i.e., the thickness and modulus of elasticity ratio of the adhesive is much less than that of the adherends) that its effect on the flexibility of the joint may be neglected and secondly, where the joint flexibility is mainly due to that of the adhesive layer. In the second case, the two adherends of the joint are considered as cylindrically bent plates and the adhesive layer in the joint is treated as a special kind of "connecting spring" acting between the two plates. With the aid of elementary beam-plate theory, two governing differential equations for the shearing and normal stresses acting on the bonding surfaces of the joint are obtained. Because of its intuitiveness and simplicity, this approach for joints with rather flexible adhesive layers (the second case) has been employed by other authors, with various modification, and/or extended to a variety of complicated situations such as nonidentical or nonisotropic adherends (Hart-Smith [8], Ojalvo and Eidinoff [9], Hahn [10], Dickson, et al. [11], Wah [12], Dong, et al. [13], Vinson and Renton [14], and Delale, et al. [15]). As for the first case [7], the existence of the adhesive layer is disregarded, the whole joint being considered as consisting of a continuous homogeneous material. The analysis for this case, however, is cumbersome and difficult to apply in practical situations as seen in [7]. According to this analysis, the maximum shearing stress occurs at both ends of the joint instead of actually vanishing there. This unavoidably yields adverse effects on the distribution and also intensity of stresses in the end zones in which it happens that high stress intensities of the joint occur [16]. Besides the two limiting cases, other cases that lie between these two cases and are not treated in [7] should also have a broad range of practical application, as demonstrated in [1]. Among the test specimens examined in [1], only the polyurethane-to-maple combination satisfies the Goland and Reissner criterion for joints with relatively flexible adhesives. The others fall between this criterion and that for joints with rigid adhesives.

The present work is intended to extend the previous analyses and present a unified theory applicable to all adhesive layer conditions, flexible, inflexible, and a medium

Contributed by the Applied Mechanics Division for presentation at the 1983 ASME Applied Mechanics, Bioengineering, and Fluids Engineering Conference, Houston, Texas, June 20-22, 1983 of THE AMERICAN SOCIETY OF MECHANICAL ENGINEERS.

Discussion on this paper should be addressed to the Editorial Department, ASME, United Engineering Center, 345 East 47th Street, New York, N.Y. 10017, and will be accepted until two months after final publication of the paper itself in the JOURNAL OF APPLIED MECHANICS. Manuscript received by ASME Applied Mechanics Division, February, 1982; final revision, August 1982. Paper No. 83-APM-14.

Copies will be available until July, 1984.

Copyright © 1983 by ASME
Downloaded 02 May 2010 to 171.66.16.246. Redistribution subject to ASME license or copyright; see http://www.asme.org/terms/Terms_Use.cfm

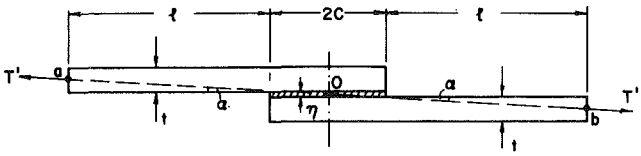

Fig. 1 Profile view of adhesive-bonded joint system

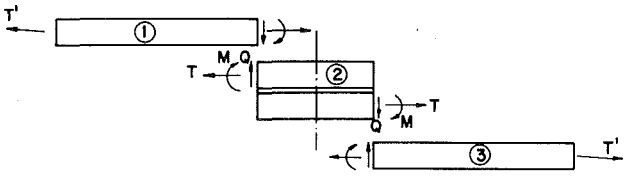

Fig. 2 Loads applied to the joint

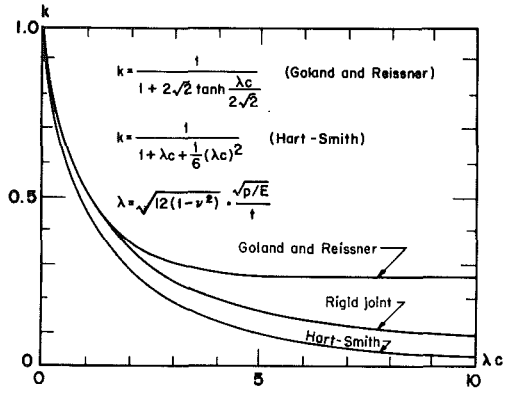

Fig. 3 Plot of moment factor k versus λc

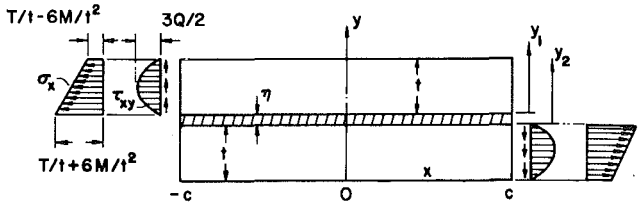

Fig. 4 Coordinate system and edge stresses

range of flexibility. In addition, by means of the present theory, all boundary stress conditions of the joint are strictly satisfied and the effect of the bonding material on the stress distribution is taken into account. The adhesive layer between the two adherends of the joint is treated in the same way that the adherends are treated, except that, in view of the thinness of the layer, simplifications regarding its stress distribution may be made. Then, through the use of two-dimensional elasticity theory in conjunction with the variational theorem of complementary energy, a solution in closed form is obtained which satisfies the stress-free boundary conditions. To illustrate the application of the present results and make comparisons with other known solutions, numerical examples are provided in which the influence of the bonding layer property on the stress distribution is examined and special attention is paid to the distribution and intensity of stresses in the end zones of the joint.

Formulation of the Problem

Consider two rectangular sheets of equal thickness t and length $(l + 2c)$. The two sheets are lap-jointed over the length $2c$ (Fig. 1). The bond between the two sheets is established by means of an adhesive layer whose thickness is η. The two unjointed ends of the sheets are simply supported and acted on by tensile forces of magnitude T' per unit of sheet width. The line of action of tensile forces $a0b$ is shown in Fig. 1, which makes a small angle α with the sheet plane. Let E and ν be the Young's modulus and Poisson's ratio of the sheets, E_c, ν_c the Young's modulus and Poisson's ratio of the adhesive layer, respectively. The main problem is the determination of the stress distribution in the joint region.

Because the sheet width is large compared with the sheet thickness, this problem may be treated as a problem in plane strain. We will further assume that the following order of magnitude relation is satisfied:

$$\eta << t << c << l \tag{1}$$

and that the tensile force T' is large enough, say

$$p = T'/t \sim E/1000 \tag{2}$$

(here p is the average tensile stress in the sheets). Actually these conditions are satisfied by most cases of practical importance.

Determination of the Joint Edge Loads

Figure 2 depicts the geometry and the sign convention for the analysis of joint edge loads. The system is divided into three parts as shown in Fig. 2. Considering the equilibrium of these parts separately and taking into account the deflection of the system, in [7] it was demonstrated that the edge tension acting on the joint is $T = T' \cos\alpha \cong T' = pt$ and the edge moment $M = k \cdot 1/2\ pt^2$ in which the moment reduction factor k depends only on the parameter λc. This relation and the definition of the parameter λ are shown in Fig. 3. Considering all overall equilibrium of part, 2 Fig. 2, we have the edge transverse force acting on the joint

$$Q = \frac{1}{2c}[(t+\eta)T - 2M] = \frac{1}{2c}[(1-k)t^2 + \eta t]p \tag{3}$$

Using this Q, it can be assumed that the joint is under the action of a set of well-balanced edge loads. In [8], Hart-Smith presents a different expression for k (Fig. 3). Since his k and the k given by Goland and Reissner [7] agree only for small values of λc (Fig. 3), a conclusion is drawn in [8] that the edge moment M given in [7] is valid only for short overlaps. However, a thorough study of Hart-Smith's rather complicated analysis shows that the effect of the deflected configuration of the joint on the static equilibrium of part 2, Fig. 2 has not actually been taken into account as was the case in [7]. Besides, Fig. 3 shows that for long overlaps results based on Hart-Smith's formula are rather close to those for rigid joints [17]. This is obviously an unfavorable feature since rigid joints can only be assumed in cases of short overlaps. Thus in the following treatment of the joint problem, Goland and Reissner's results for the joint edge loads will be used. We further assume that the normal stresses acting on the end faces of the two adherends has a linear distribution and shear stresses, a parabolic distribution that can be expected from classical beam-plate theory. The conversion form "edge loads" (T, M, Q) to "edge stresses" is given in Fig. 4.

Description of Stresses in the Joint

As shown in Fig. 4, axis x is placed at the bottom of the joint, with its origin located at the midspan. For convenience, coordinates $y_1 = y - (t+\eta)$ and $y_2 = y - t$ are also used occasionally. Let $(\sigma_{x1}, \sigma_{y1}, \tau_{xy1})$, $(\sigma_{x2}, \sigma_{y2}, \tau_{xy2})$, $(\sigma_{x3}, \sigma_{y3}, \tau_{xy3})$ be the stress components in the upper adherend, the lower adherend, and the adhesive layer, respectively. From two-dimensional elasticity theory, these stress components should satisfy the equations of equilibrium, conditions of continuity

Downloaded 02 May 2010 to 171.66.16.246. Redistribution subject to ASME license or copyright; see http://www.asme.org/terms/Terms_Use.cfm

of stress across the dividing lines ($y_1 = 0$ and $y_2 = 0$) of the three layers, and stress-free conditions on the top ($y_1 = t$) and bottom ($y_2 = -t$) surfaces of the joint.

$$\frac{\partial \sigma_{xi}}{\partial x} + \frac{\partial \tau_{xyi}}{\partial y} = 0, \quad \frac{\partial \tau_{xyi}}{\partial x} + \frac{\partial \sigma_{yi}}{\partial y} = 0 \quad (i = 1,2,3)$$

$$\begin{aligned} y_1 = t: &\quad \tau_{xy1} = 0, \ \sigma_{y1} = 0 \\ y_1 = 0: &\quad \tau_{xy1} = \tau_{xy3}, \ \sigma_{y1} = \sigma_{y3} \\ y_2 = 0: &\quad \tau_{xy2} = \tau_{xy3}, \ \sigma_{y2} = \sigma_{y3} \\ y_2 = -t: &\quad \tau_{xy2} = 0, \ \sigma_{y2} = 0 \\ x = c: &\quad \sigma_{x1} = 0, \ \tau_{xy1} = 0 \\ &\quad \sigma_{x3} = 0, \ \tau_{xy3} = 0 \end{aligned}$$

At the two ends of the joint, the stress conditions are:

$$x = c: \quad \sigma_{x1} = 0, \quad \tau_{xy1} = 0 \qquad (4.1,4.2)$$

$$\sigma_{x3} = 0, \quad \tau_{xy3} = 0 \qquad (4.3,4.4)$$

$$\sigma_{x2} = \left(\frac{T}{t} + \frac{6M}{t^2}\right) + \frac{12M}{t^2}\left(\frac{y_2}{t}\right) = \left[1 + 3k + 6k\left(\frac{y_2}{t}\right)\right]p \qquad (4.5)$$

$$\tau_{xy2} = \frac{6Q}{t}\left(\frac{y_2}{t}\right)\left(1 + \frac{y_2}{t}\right) = 3\left[(1-k)\frac{t}{c} + \frac{\eta}{c}\right]\left(\frac{y_2}{t}\right)\left(1 + \frac{y_2}{t}\right)p \qquad (4.6)$$

$$x = -c: \quad \sigma_{x1} = \left(\frac{T}{t} + \frac{6M}{t^2}\right) - \frac{12M}{t^2}\left(\frac{y_1}{t}\right) = \left[1 + 3k - 6k\left(\frac{y_1}{t}\right)\right]p \qquad (4.7)$$

$$\tau_{xy1} = -\frac{6Q}{t}\left(\frac{y_1}{t}\right)\left(1 - \frac{y_1}{t}\right) = -3\left[(1-k)\frac{t}{c} + \frac{\eta}{c}\right]\left(\frac{y_1}{t}\right)\left(1 - \frac{y_1}{t}\right)p \qquad (4.8)$$

$$\sigma_{x3} = 0, \quad \tau_{xy3} = 0 \qquad (4.9,4.10)$$

$$\sigma_{x2} = 0, \quad \tau_{xy2} = 0 \qquad (4.11,4.12)$$

In addition, these stress components should also satisfy compatability conditions. In this section, the possible stress distributions that satisfy all these stress conditions are investigated. The satisfaction of compatability conditions is treated in the next section. We start with two simplifications that form the basis of the theory to be developed:

(1) Based on the classical beam-plate theory, the longitudinal normal stresses in the upper and lower adherends of the joint (σ_{x1}, σ_{x2}) may be assumed to vary linearly with the transverse coordinate y.

(2) Since the adhesive layer is very thin compared with the two adherends, it is reasonable to assume that the shearing stress in the adhesive layer (τ_{xy3}) remains constant across the thickness of this layer.

Based on these two simplifications, a solution satisfying all of the stress conditions can be established as follows.

(*a*) For the upper adherend:

According to assumptions (1), stress σ_{x1} may be expressed as

$$\sigma_{x1} = \sigma_1(x) + \sigma_1^*(x)\frac{y_1}{t} \qquad (5)$$

where $\sigma_1(x)$ and $\sigma_1^*(x)$ are two unknown functions of x yet to be determined. Because of conditions (4.1), (4.7), we have two end conditions for each of the two unknown functions of x:

$$\begin{aligned} &\sigma_1|_{x=c} = 0, \quad \sigma_1^*|_{x=c} = 0 \\ &\sigma_1|_{x=-c} = (1+3k)p, \quad \sigma_1^*|_{x=-c} = -6kp \end{aligned} \qquad (6)$$

Then, making use of (6), from the equations of equilibrium and boundary conditions $\tau_{xy1} = 0$ and $\sigma_{y1} = 0$ on $y_1 = t$ it is readily deduced that in the upper adherend the other two stress components must be

$$\tau_{xy1} = \frac{d\sigma_1}{dx}(t - y_1) + \frac{d\sigma_1^*}{dx}\left(\frac{t}{2} - \frac{y_1^2}{2t}\right) \qquad (7)$$

$$\sigma_{y1} = \frac{d^2\sigma_1}{dx^2}\left(\frac{t^2}{2} + \frac{y_1^2}{2} - ty_1\right) + \frac{d^2\sigma_1^*}{dx^2}\left(\frac{t^2}{3} + \frac{y_1^3}{6t} - \frac{ty_1}{2}\right) \qquad (8)$$

Moreover, because of boundary conditions (4.2) and (4.8) there are still two more end conditions for σ_1 and σ_1^*:

$$\begin{aligned} &\frac{d\sigma_1}{dx}\bigg|_{x=c} = 0, \quad \frac{d\sigma_1^*}{dx}\bigg|_{x=c} = 0 \\ &\frac{d\sigma_1}{dx}\bigg|_{x=-c} = 3\left(1 - k + \frac{\eta}{t}\right)\frac{p}{c}, \quad \frac{d\sigma_1^*}{dx}\bigg|_{x=-c} = -6\left(1 - k + \frac{\eta}{t}\right)\frac{p}{c} \end{aligned} \qquad (9)$$

Thus, the distribution of stresses in the upper adherend is entirely determined by the two unknown functions σ_1 and σ_1^* which satisfy the end conditions (6) and (9).

(*b*) For the lower adherend:

In exactly the same way as for the upper adherend, the distribution of stresses in the lower adherend can be expressed as

$$\sigma_{x2} = \sigma_2(x) + \sigma_2^*(x)\frac{y_2}{t} \qquad (10)$$

$$\tau_{xy2} = \frac{d\sigma_2}{dx}(-t - y_2) + \frac{d\sigma_2^*}{dx}\left(\frac{t}{2} - \frac{y_2^2}{2t}\right) \qquad (11)$$

$$\sigma_{y2} = \frac{d^2\sigma_2}{dx^2}\left(\frac{t^2}{2} + \frac{y_2^2}{2} + ty_2\right) + \frac{d^2\sigma_2^*}{dx^2}\left(-\frac{t^2}{3} + \frac{y_2^3}{6t} - \frac{ty_2}{2}\right) \qquad (12)$$

where $\sigma_2(x)$ and $\sigma_2^*(x)$ are another two unknown functions of x, satisfying end conditions:

$$\begin{aligned} &\sigma_2|_{x=c} = (1+3k)p, \quad \sigma_2^*|_{x=c} = 6kp \\ &\sigma_2|_{x=-c} = 0, \quad \sigma_2^*|_{x=-c} = 0 \end{aligned} \qquad (13)$$

and

$$\begin{aligned} &\frac{d\sigma_2}{dx}\bigg|_{x=c} = -3\left(1 - k + \frac{\eta}{t}\right)\frac{p}{c}, \quad \frac{d\sigma_2^*}{dx}\bigg|_{x=c} = -6\left(1 - k + \frac{\eta}{t}\right)\frac{p}{c} \\ &\frac{d\sigma_2}{dx}\bigg|_{x=-c} = 0, \quad \frac{d\sigma_2^*}{dx}\bigg|_{x=-c} = 0 \end{aligned} \qquad (14)$$

Hence the distribution of stresses in the lower adherend is entirely determined by σ_2 and σ_2^*.

(*c*) For the adhesive layer:

In view of the preceding results (7), (11), and conditions of continuity of stress $\tau_{xy1} = \tau_{xy3}$ on $y_1 = 0$ and $\tau_{xy2} = \tau_{xy3}$ on $y_2 = 0$, the shearing stresses acting on the two bonding surfaces of this layer should be

Downloaded 02 May 2010 to 171.66.16.246. Redistribution subject to ASME license or copyright; see http://www.asme.org/terms/Terms_Use.cfm

$$\tau_{xy3}\,|_{y_1=0} = t\frac{d\sigma_1}{dx} + \frac{t}{2}\frac{d\sigma_2^*}{dx}, \quad \tau_{xy3}\,|_{y_2=0} = -t\frac{d\sigma_2}{dx} + \frac{t}{2}\frac{d\sigma_2^*}{dx}$$

But according to assumption (2), τ_{xy3} is independent of y, i.e.,

$$\tau_{xy3} = \tau(x).$$

Hence we must have

$$t\frac{d\sigma_1}{dx} + \frac{t}{2}\frac{d\sigma_1^*}{dx} = -t\frac{d\sigma_2}{dx} + \frac{t}{2}\frac{d\sigma_2^*}{dx} \tag{15}$$

and

$$\tau_{xy3} = \tau(x) = t\frac{d\sigma_1}{dx} + \frac{t}{2}\frac{d\sigma_1^*}{dx} \tag{16}$$

The boundary conditions (4.4) and (4.10) for τ_{xy3} are satisfied automatically because of (9). Integrating (15) and taking (6) and (13) into account yields

$$2\sigma_1 + \sigma_1^* + 2\sigma_2 - \sigma_2^* = 2p \tag{17}$$

This relation may be seen as a condition of "constraint" imposed on σ_1, σ_1^*, σ_2, σ_2^* for satisfying the condition (15). Substituting (16) into the equations of equilibrium, integrating, and making use of (4.3) and (4.9), we obtain

$$\sigma_{x3} = 0 \tag{18}$$

As for σ_{y3}, based on the results (8), (12), and conditions $\sigma_{y1} = \sigma_{y3}$ on $y_1 = 0$ and $\sigma_{y2} = \sigma_{y3}$ on $y_2 = 0$, this normal stresses acting on the two bonding surfaces of the adhesive layer should be

$$\sigma_{y3}\,|_{y_1=0} = \sigma(x) = \frac{t^2}{2}\frac{d^2\sigma_1}{dx^2} + \frac{t^2}{3}\frac{d^2\sigma_1^*}{dx^2} \tag{19.1}$$

and

$$\sigma_{y3}\,|_{y_2=0} = \sigma^*(x) = \frac{t^2}{2}\frac{d^2\sigma_2}{dx^2} - \frac{t^2}{3}\frac{d^2\sigma_2^*}{dx^2} \tag{19.2}$$

Here $\sigma(x)$ and $\sigma^*(x)$ are introduced for convenience. In addition, σ_{y3} and $\tau_{xy3} = \tau(x)$ should also satisfy the equations of equilibrium and thus the only solution for σ_{y3} which satisfies (19.1) and (19.2) is

$$\sigma_{y3} = \sigma + \frac{y_1}{\eta}(\sigma - \sigma^*) \tag{20)}$$

$$\frac{1}{\eta}(\sigma - \sigma^*) = -\frac{d\tau}{dx} \tag{21}$$

Applying (19.1), (19.2), and (16), equation (21) becomes

$$\left(\frac{t^2}{2\eta} + t\right)\frac{d^2\sigma_1}{dx^2} + \left(\frac{t^2}{3\eta} + \frac{t}{2}\right)\frac{d^2\sigma_1^*}{dx^2} - \frac{t^2}{2\eta}\frac{d^2\sigma_2}{dx^2} + \frac{t^2}{3\eta}\frac{d^2\sigma_2^*}{dx^2} = 0$$

Integrating the preceding equation twice with respect to x and taking end conditions (6), (9), (13), and (14) into account, it becomes

$$\left(\frac{1}{2}\frac{t}{\eta} + 1\right)\sigma_1 + \left(\frac{1}{3}\frac{t}{\eta} + \frac{1}{2}\right)\sigma_1^* - \frac{1}{2}\frac{t}{\eta}\sigma_2 + \frac{1}{3}\frac{t}{\eta}\sigma_2^* = \left[-\left(\frac{1-k}{2}\frac{t}{\eta} + \frac{1}{2}\right)\frac{x}{c} + \frac{1}{2}\right]p \tag{22}$$

This is another condition of constraint, besides (17), which σ_1, σ_1^*, σ_2, σ_2^* must satisfy. Finally, according to (20), (21), (19.1), and (16) we may rewrite σ_{y3} as

$$\sigma_{y3} = \sigma - y_1\frac{d\tau}{dx} = \left(\frac{t^2}{2}\frac{d^2\sigma_1}{dx^2} + \frac{t^2}{3}\frac{d^2\sigma_1^*}{dx^2}\right) - y_1\left(t\frac{d^2\sigma_1}{dx^2} + \frac{t}{2}\frac{d^2\sigma_1^*}{dx^2}\right) \tag{23}$$

It is seen that from the two conditions of constraint (17) and (22) any two unknown functions among the four, say σ_2 and σ_2^*, can be expressed in terms of the other two, σ_1 and σ_1^*. Solving for σ_2 and σ_2^* from (17) and (22) yields

$$\sigma_2 = A_1\sigma_1 + B_1\sigma_1^* + \left(c_{11} + c_{12}\frac{x}{c}\right)p$$

$$\sigma_2^* = A_2\sigma_1 + B_2\sigma_1^* + \left(c_{21} + c_{22}\frac{x}{c}\right)p \tag{24}$$

in which

$$A_1 = -7 - 6\frac{\eta}{t}, \quad B_1 = -4 - 3\frac{\eta}{t}$$

$$C_{11} = 4 + 3\frac{\eta}{t}, \quad C_{12} = -3\left(1 - k + \frac{\eta}{t}\right)$$

$$A_2 = -12 - 12\frac{\eta}{t}, \quad B_2 = -7 - 6\frac{\eta}{t}$$

$$C_{21} = 6 + 6\frac{\eta}{t}, \quad C_{22} = -6\left(1 - k + \frac{\eta}{t}\right)$$

Thus all the stress components in the joint can now be expressed in terms of the two independent functions $\sigma_1^*(x)$ and $\sigma_1^*(x)$.

Variational Method Based on the Principle of Complementary Energy

In the preceding analysis, only equations of equilibrium and boundary conditions involving stresses are satisfied. There are two unknown functions, σ_1 and σ_1^* yet to be determined. To obtain further equations for the determination of those two unknown functions, use has to be made of the compatability of stresses. In view of the simplifying assumptions made at the beginning of the stress analysis, this cannot be done in an exact manner. In what follows, it is done in a rational manner by means of variational theorem of complementary energy [18,19], which states that for all stresses satisfying the equilibrium conditions in the interior of an elastic body and on that part of its boundary surface where the surface forces are prescribed, the actual state of the stress, i.e., the stresses that satisfy the conditions of compatibility, is such that the variation of the complementary energy of the body vanishes. For the present problem, one of plane strain, the expression for the complementary energy to be minimized is

$$V = \frac{1}{2E'}\int_{-c}^{c}\int_{0}^{t}[\sigma_{x1}^2 + \sigma_{y1}^2 - 2\nu'\sigma_{x1}\sigma_{y1} + 2(1+\nu')\tau_{xy1}^2]dy_1dx + \frac{1}{2E_c'}\int_{-c}^{c}\int_{-\eta}^{0}[\sigma_{x3}^2 + \sigma_{y3}^2 - 2\nu_c'\sigma_{x3}\sigma_{y3} + 2(1+\nu_c')\tau_{xy3}^2]dy_1dx + \frac{1}{2E'}\int_{-c}^{c}\int_{-t}^{0}[\sigma_{x2}^2 + \sigma_{y2}^2 - 2\nu'\sigma_{x2}\sigma_{y2} + 2(1+\nu')\tau_{xy2}^2]dy_2dx \tag{25}$$

in which

$$E' = \frac{E}{1-\nu^2}, \quad \nu' = \frac{\nu}{1-\nu}, \quad E_c' = \frac{E_c}{1-\nu_c^2}, \quad \nu_c' = \frac{\nu_c}{1-\nu_c}$$

In Goland and Reissner's work [7], the first limiting case, i.e., where the adhesive layer is so thin that its effect on the flexibility of the joint may be neglected, is specified by the expression

$$\frac{\eta}{E_c} \le \frac{1}{10}\left(\frac{t}{E}\right) \tag{26}$$

Downloaded 02 May 2010 to 171.66.16.246. Redistribution subject to ASME license or copyright; see http://www.asme.org/terms/Terms_Use.cfm

By neglecting the second integral in (25), which respresents the complementary energy of the adhesive layer, this limiting case can be obtained as a special case of the general expression (25). The other limiting case in [7], i.e., where the joint flexibility is mainly due to that of the adhesive layer, is specified by the expression

$$\frac{\eta}{\mathrm{E}_c} \geq 10\left(\frac{t}{\mathrm{E}}\right) \tag{27}$$

This limiting case allows that the terms involving the transverse shear and transverse tension-compression stresses in the first and third integrals of the expression (25) be neglected as compared with the corresponding terms in the second integral. In the present paper, no simplifications for the energy expression (25) will be made, so a comprehensive theory that covers a wide range of η and t ratios of practical interest can be deduced.

After substituting expressions (5), (7), (8), (10)–(12), (16), (18), and (23) into (25), integrating with respect to y, and making use of (24) to eliminate σ_2 and σ_2^* in the integrand, we obtain

$$V = \frac{\mathrm{E}' t^2}{2} \int_{-1}^{1} W(\bar{\sigma}_1, \bar{\sigma}_1^*) d\xi \tag{28}$$

where

$$\bar{\sigma}_1 = \sigma_1/\mathrm{E}', \quad \bar{\sigma}_1^* = \sigma_1^*/\mathrm{E}', \quad \xi = x/c$$

$$\begin{aligned} W(\bar{\sigma}_1, \bar{\sigma}_1^*) &= e_1 \bar{\sigma}_1^2 + e_2 \bar{\sigma}_1 \bar{\sigma}_1^* + e_3 \bar{\sigma}_1^{*2} + e_4 \left(\frac{d\bar{\sigma}_1}{d\xi}\right)^2 \\ &+ e_5 \left(\frac{d\bar{\sigma}_1}{d\xi}\right)\left(\frac{d\bar{\sigma}_1^*}{d\xi}\right) + e_6 \left(\frac{d\bar{\sigma}_1^*}{d\xi}\right)^2 \\ &+ e_7 \left(\frac{d^2\bar{\sigma}_1}{d\xi^2}\right)^2 + e_8 \left(\frac{d^2\bar{\sigma}_1}{d\xi^2}\right)\left(\frac{d^2\bar{\sigma}_1^*}{d\xi^2}\right) \\ &+ e_9 \left(\frac{d^2\bar{\sigma}_1^*}{d\xi^2}\right)^2 + e_{10}\bar{\sigma}_1 \frac{d^2\bar{\sigma}_1}{d\xi^2} + e_{11}\bar{\sigma}_1 \frac{d^2\bar{\sigma}_1^*}{d\xi^2} \\ &+ e_{12}\bar{\sigma}_1^* \frac{d^2\bar{\sigma}_1}{d\xi^2} + e_{13}\bar{\sigma}_1^* \frac{d^2\sigma_1^*}{d\xi^2} + e_{14} \frac{d^2\bar{\sigma}_1}{d\xi^2} \\ &+ e_{15} \frac{d^2\bar{\sigma}_1^*}{d\xi^2} + e_{14}' \frac{d\bar{\sigma}_1}{d\xi} + e_{15}' \frac{d\bar{\sigma}_1^*}{d\xi} \\ &+ e_{16}\bar{\sigma}_1 + e_{17}\bar{\sigma}_1^* + e_{18} \end{aligned} \tag{29}$$

and

$$e_1 = \left(1 + A_1^2 - A_1A_2 + \frac{1}{3}A_2^2\right)\bar{c} \quad e_2 = \left(1 + 2A_1B_1 - A_1B_2 - A_2B_1 + \frac{2}{3}A_2B_2\right)\bar{c}$$

$$e_3 = \left(\frac{1}{3} + B_1^2 - B_1B_2 + \frac{1}{3}B_2^2\right)\bar{c}$$

$$e_4 = (1+\nu')\left(\frac{2}{3} + \frac{2}{3}A_1^2 - \frac{5}{6}A_1A_2 + \frac{4}{15}A_2^2\right)/\bar{c} + 2(1+\nu_c')\bar{\eta}\Big/(\bar{c}\,\bar{\mathrm{E}}_c')$$

$$e_5 = (1+\nu')\left(\frac{5}{6} + \frac{4}{3}A_1B_1 - \frac{5}{6}A_1B_2 - \frac{5}{6}A_2B_1 + \frac{8}{15}A_2B_2\right)\Big/\bar{c} + 2(1+\nu_c')\bar{\eta}\Big/(\bar{c}\,\bar{\mathrm{E}}_c')$$

$$e_6 = (1+\nu')\left(\frac{4}{15} + \frac{2}{3}B_1^2 - \frac{5}{6}B_1B_2 + \frac{4}{15}B_2^2\right)/\bar{c} + \frac{1}{2}(1+\nu_c')\bar{\eta}\Big/(\bar{c}\,\bar{\mathrm{E}}_c')$$

$$e_7 = \left(\frac{1}{20} + \frac{1}{20}A_1^2 - \frac{13}{180}A_1A_2 + \frac{11}{420}A_2^2\right)/\bar{c}^3 + \left(\frac{1}{4}\bar{\eta} + \frac{1}{2}\bar{\eta}^2 + \frac{1}{3}\bar{\eta}^3\right)\Big/(\bar{c}^3\bar{\mathrm{E}}_c')$$

$$e_8 = \left(\frac{13}{180} + \frac{1}{10}A_1B_1 - \frac{13}{180}A_1B_2 - \frac{13}{180}A_2B_1 + \frac{11}{210}A_2B_2\right)/\bar{c}^3 + \left(\frac{1}{3}\bar{\eta} + \frac{7}{12}\bar{\eta}^2 + \frac{1}{3}\bar{\eta}^3\right)\Big/(\bar{c}^3\bar{\mathrm{E}}_c')$$

$$e_9 = \left(\frac{11}{420} + \frac{1}{20}B_1^2 - \frac{13}{180}B_1B_2 + \frac{11}{420}B_2^2\right)/\bar{c}^3 + \left(\frac{1}{9}\bar{\eta} + \frac{1}{6}\bar{\eta}^2 + \frac{1}{12}\bar{\eta}^3\right)\Big/(\bar{c}^3\bar{\mathrm{E}}_c')$$

$$e_{10} = \nu'\left(-\frac{1}{3} - \frac{1}{3}A_1^2 + \frac{1}{3}A_1A_2 - \frac{1}{15}A_2^2\right)/\bar{c}$$

$$e_{11} = \nu'\left(-\frac{1}{4} - \frac{1}{3}A_1B_1 + \frac{1}{4}A_1B_2 + \frac{1}{12}A_2B_1 - \frac{1}{15}A_2B_2\right)/\bar{c}$$

$$e_{12} = \nu'\left(-\frac{1}{12} - \frac{1}{3}A_1B_1 + \frac{1}{4}A_2B_1 + \frac{1}{12}A_1B_2 - \frac{1}{15}A_2B_2\right)/\bar{c}$$

$$e_{13} = \nu'\left(-\frac{1}{15} - \frac{1}{3}B_1^2 + \frac{1}{3}B_1B_2 - \frac{1}{15}B_2^2\right)/\bar{c}$$

$$e_{16} = (e_{161} + e_{162}\xi)\bar{p}$$

$$e_{161} = \left[(2A_1 - A_2)c_{11} + \left(-A_1 + \frac{2}{3}A_2\right)c_{21}\right]\bar{c}$$

$$e_{162} = \left[(2A_1 - A_2)c_{12} + \left(-A_1 + \frac{2}{3}A_2\right)c_{22}\right]\bar{c}$$

$$e_{17} = (e_{171} + e_{172}\xi)\bar{p}$$

$$e_{171} = \left[(2B_1 - B_2)c_{11} + \left(-B_1 + \frac{2}{3}B_2\right)c_{21}\right]\bar{c}$$

$$e_{172} = \left[(2B_1 - B_2)c_{12} + \left(-B_1 + \frac{2}{3}B_2\right)c_{22}\right]\bar{c} \tag{30}$$

in which

$$\bar{c} = c/t, \quad \bar{\eta} = \eta/t, \quad \bar{\mathrm{E}}_c' = \mathrm{E}_c'/\mathrm{E}', \quad \bar{p} = p/\mathrm{E}'$$

(As for e_{14}, e_{15}, e_{14}', e_{15}', and e_{18}, they are of no use in the subsequent deductions as will be seen in the following.) Carrying out the variation $\delta V = 0$ under the end conditions (6) and (9) or their nondimensional forms

$$\begin{aligned} &\bar{\sigma}_1|_{\xi=1} = 0, \quad \bar{\sigma}_1^*|_{\xi=1} = 0 \\ &\bar{\sigma}_1|_{\xi=-1} = (1+3k)\bar{p}, \quad \bar{\sigma}_1^*|_{\xi=-1} = -6k\,\bar{p} \\ &\frac{d\bar{\sigma}_1}{d\xi}\Big|_{\xi=1} = 0, \quad \frac{d\bar{\sigma}_1^*}{d\xi}\Big|_{\xi=1} = 0 \\ &\frac{d\bar{\sigma}_1}{d\xi}\Big|_{\xi=-1} = 3(1-k+\bar{\eta})\bar{p}, \quad \frac{d\bar{\sigma}_1^*}{d\xi}\Big|_{\xi=-1} = -6(1-k+\bar{\eta})\bar{p} \end{aligned} \tag{31}$$

the variational equations for the $\bar{\sigma}_1$ and $\bar{\sigma}_1^*$ which render the complementary energy a minimum are obtained:

$$\left(2e_7\frac{d^4}{d\xi^4} + 2e_{19}\frac{d^2}{d\xi^2} + 2e_1\right)\bar{\sigma}_1 + \left(e_8\frac{d^4}{d\xi^4} + e_{20}\frac{d^2}{d\xi^2} + e_2\right)\bar{\sigma}_1^* = -(e_{161} + e_{162}\xi)\bar{p}$$

Downloaded 02 May 2010 to 171.66.16.246. Redistribution subject to ASME license or copyright; see http://www.asme.org/terms/Terms_Use.cfm

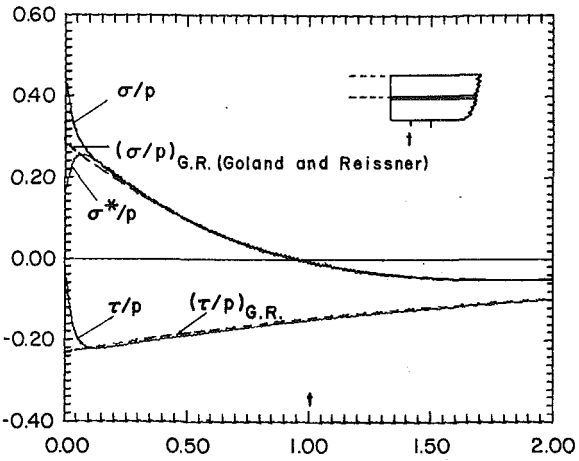

Fig. 5 Stress distribution along bonding surfaces for Example (1)

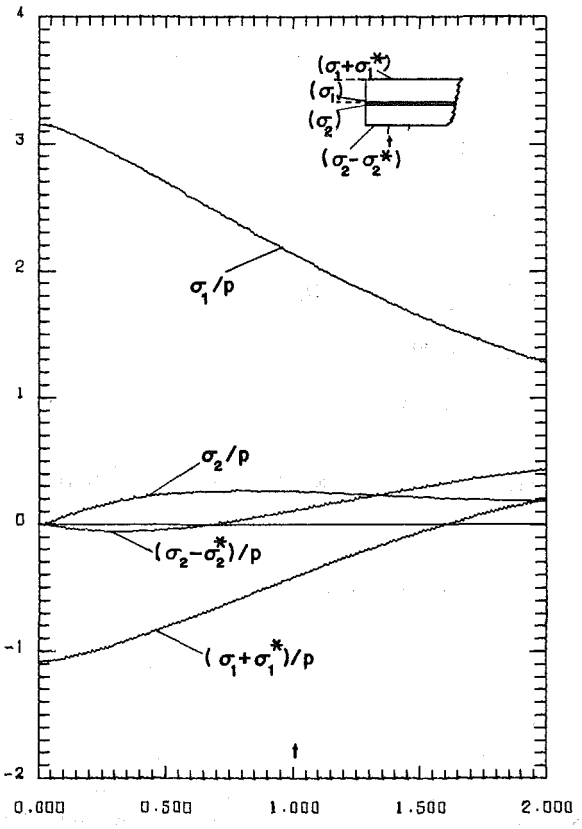

Fig. 6 Longitudinal normal stresses in adherends for Example (1)

$$\left(e_8\frac{d^4}{d\xi^4}+e_{20}\frac{d^2}{d\xi^2}+e_2\right)\bar{\sigma}_1+\left(2e_9\frac{d^4}{d\xi^4}+2e_{21}\frac{d^2}{d\xi^2}+2e_3\right)\bar{\sigma}_1^* = -(e_{171}+e_{172}\xi)\bar{p} \tag{32}$$

in which

$$e_{19}=e_{10}-e_4,\quad e_{20}=e_{11}+e_{12}-e_5,\quad e_{21}=e_{13}-e_6.$$

This is a set of two coupled ordinary differential equations with constant coefficients that can be integrated, together with end conditions (31), by known procedures [20]. By inspection, a particular solution for (32) is

$$\bar{\sigma}_{1p}=\frac{\bar{p}}{4e_1e_3-e_2^2}[(-2e_3e_{161}+e_2e_{171})+(-2e_3e_{162}+e_2e_{172})\xi]$$

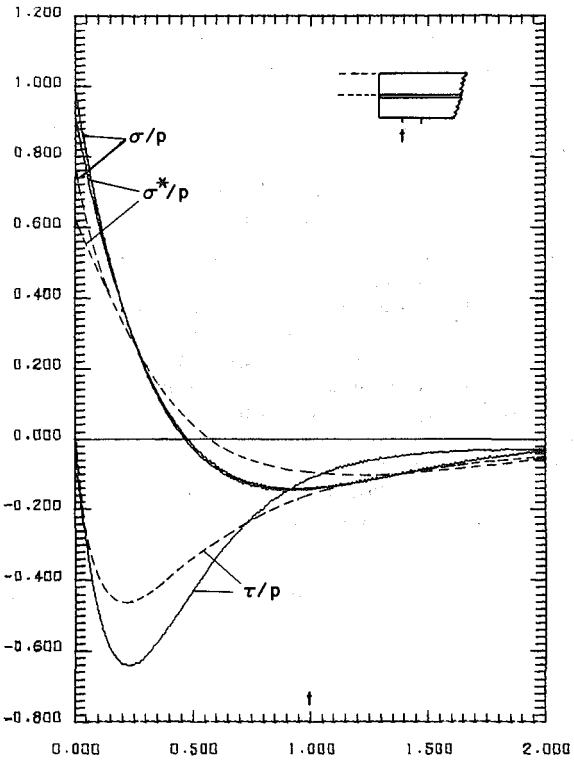

Fig. 7 Stress distribution along bonding surfaces for Examples (2) and (3)

$$\bar{\sigma}_{1p}^*=\frac{\bar{p}}{4e_1e_3-e_2^2}[(-2e_1e_{171}+e_2e_{161})+(-2e_1e_{172}+e_2e_{162})\xi]$$

From the characteristic equation of the homogeneous equations of (32), eight eigenvalues λ can be determined [20]. Calculation shows that in ordinary circumstances, the characteristic equation yields four real eigenvalues and four complex eigenvalues (unless the adhesive layer is extremely "stiff" compared with the two adherends, in which case the eight eigenvalues are all complex). The general solution of the homogeneous equation (32) has eight arbitrary constants to be determined from the eight end conditions (31). We note that the present method yields closed-form solutions.

Numerical Examples and Discussion

Example (1). The parameters are $c/t = 5.0$, $\eta/t = 0.04$, $E_c/E = 0.004$, $\nu = 0.25$, $\nu_c = 0.33$, and $p/E = 0.001$. Here we have

$$\frac{\eta}{E_c}=10\left(\frac{t}{E}\right)$$

So this is an example of a joint with a relatively flexible adhesive layer. The shearing and normal stresses acting on the bonding surfaces (i.e., τ, σ, σ^*) calculated for the end zones of the joint are shown in Fig. 5. For comparison, the results obtained by Goland and Reissner's method are also given in Fig. 5 (dotted lines). It is seen that differences occur only at a very narrow region near the edge of the joint. For shearing stress, the result obtained by the Goland and Reissner method reaches its maximum at the edge of the joint instead of actually vanishing there and this maximum value is slightly greater than that obtained by the present method, for which the maximum value occurs at a distance about $0.2t$ from the edge. For normal stress, the present method reveals that the

Downloaded 02 May 2010 to 171.66.16.246. Redistribution subject to ASME license or copyright; see http://www.asme.org/terms/Terms_Use.cfm

normal stresses σ and σ^* which act on the upper and lower bonding surfaces, respectively, may have quite different values in a very narrow region near the edge of joint, and the unique value derived through the Goland and Reissner method is approximately halfway between them. Figure 6 shows the distribution of longitudinal normal stresses in the two adherends of the joint. It shows that the maximum stress intensity occurs at the edge of the loaded adherend and is determined by the edge loads. Because of the existence of the edge moment, this maximum stress intensity is much greater than the average tensile stress p in the sheets.

Example (2). $\eta/t = 0.01$, $E_c/E = 0.1$, other parameters are the same as in Example (1). Here we have

$$\frac{\eta}{E_c} = \frac{1}{10}\left(\frac{t}{E}\right)$$

So this is an example of a relatively inflexible adhesive layer. The distribution of shearing and normal stresses acting on the bonding surfaces of the joint as calculated from the analysis presented herein (only for the end zones of the joint) is shown in Fig. 7 (solid lines). Compared with Example (1), the intensity of these stresses is considerably increased. This means that an inflexible adhesive layer is unfavorable for the strength of the joint. In this example the normal stresses σ and σ^* acting on the upper and lower bonding surfaces, respectively, are found to be much closer. This can be explained by the fact that the adhesive layer in this example is much thinner than that in Example (1). As for the distribution of longitudinal normal stresses in the adherends, we find no significant differences from what is shown in Fig. 6. except that the longitudinal normal stresses in the loaded adherend in this case decay more rapidly. Hence the longitudinal normal stresses in the adherends are not so sensitive to the adhesive property as those stresses acting on the bonding surfaces.

Example (3). $\eta/t = 0.02$, $E_c/E = 0.02$, other parameters are the same as in Examples (1) and (2). Here we have

$$\frac{\eta}{E_c} = \frac{t}{E}$$

This is one of the examples (high-modulus epoxy steel adherends [1]) with an adhesive layer that can not be considered as either "flexible" or "inflexible." It is an example that Goland and Reissner's work does not cover. This example can be treated the same way as are Examples (1) and (2). Numerical results are also given in Fig. 7 (dotted lines). As compared to results of Examples (1) and (2), these figures show that the stress intensity on the bonding surfaces of the joint is twice the corresponding stress intensity found in Example (1) and is about two-thirds of what is found in Example (2). Thus, it has been demonstrated above that, for those cases that can neither be considered as flexible nor inflexible, the stress intensity on the bonding surfaces of the joint can have quite different values from those of limiting cases. Hence the present analysis, which is applicable to all adhesive layer flexibility, should be employed.

References

1 River, B. H., and Gillespie, R. H., "Measurement of Shear Modulus and Shear Strength of Adhesives," Research Report, Forest Products Laboratory, U.S. Department of Argiculture, prepared for Department of Housing and Urban Development, Mar. 1978.

2 Patrick, R. L., ed., *Treatise on Ahesion an Adhesives*, Vol. 4, Marcel Dekker, New York, 1976.

3 Guess, T. R., Allred, R. E., and Gerstle, F. P., "Adhesive Shear Strengths: Evaluation of the Lap Shear Configuration," Sandia Laboratories, Albuquerque, N. M. Document No. SAND 75-0483, 1975.

4 Frazier, T. B., and Lajoie, A. D., "Durability of Adhesive Bonded Joints," Bell Helicopter Division of Textron. Prepared for Air Force Materials Laboratory, Dayton, Ohio. Available from the U.S. Dept. of Commerce, National Tech. Information Service, Document AD-A007-873, 1974.

5 Zabora, R. F., Clinton, S. W., and Bell, J. E., "Adhesive Property Phenomenons and Test Techniques," AFFDL-TR-71-68, The Boeing Co., Seattle, Wash., 1971.

6 Goodman, J. R., "Layered Wood Systems With Interlayer Slip," *Wood Science*, Vol. 1, No. 3, 1969, pp. 148–158.

7 Goland, M., and Reissner, E., "The Stresses in Cemented Joints," ASME JOURNAL OF APPLIED MECHANICS, Vol. 11, 1944, pp. A17–A22.

8 Hart-Smith, L. J., "Adhesive-Bonded Single-Lap Joints," NASA CR-112236, Jan. 1973.

9 Ojalvo, I. U., and Eidinoff, H. L., "Bond Thickness Effects Upon Stresses in Single-Lap Adhesive Joints," *AIAA Journal*, Vol. 16, No. 3, Mar. 1978, pp. 204–211.

10 Hahn, K., "Stress Distribution in Adherends of Bonded Lap Joints," Douglas Aircraft Co., Research Report SM-40010, 1961.

11 Dickson, J. N., Hsu, T. M., and McKinney, J. M., "Development of an Understanding of the Fatigue Phenomena of Bonded and Bolted Joints in Advanced Filamentary Composite Materials," Vol. 1, AFFDL-TR-72-64, June, 1972.

12 Wah, T., "Stress Distribution in a Bonded Anisotropic Lap Joint," ASME *Journal of Engineering Materials and Technology*, Vol. 95, 1973, pp. 174–181.

13 Dong, S. B., Matthiesen, R. B., Pister, K. S., and Taylor, R. L., "Analysis of Structural Laminates," ARL 76, Wright-Patterson Air Force Base, 1961.

14 Renton, W. J., and Vinson, J. R., "The Analysis and Design of Anisotropic Bonded Joints," Univ. of Delaware, MAETR 171, Aug. 1974.

15 Delale, F., Erdogan, F., and Aydimogln, M. N., "Stresses in Adhesively Bonded Joints: A Closed-Form Solution," *J. of Composite Materials*, Vol. 15, May, 1981, pp. 249–271.

16 Chen, D., Cheng, S., and Gerhardt, T. D., "Thermal Stress in Laminated Beams," *Journal of Thermal Stresses*, Jan. 1982, pp. 67–84.

17 Kelsey, S., and Benson, N. K., Institute für Statik und Dynamik, Technische Hochschule Stuttgart, ISO Report No. 10, 1966.

18 Washizu, K., *Variational Methods in Elasticity and Plasticity*, Pergaman Press, New York, 1968.

19 Wang, C. T., *Applied Elasticity*, McGraw-Hill, New York, 1953.

20 Hildebrand, F. B., *Advanced Calculus for Applications*, Prentice-Hall, Englewood Cliffs, N.J. 1976.

Downloaded 02 May 2010 to 171.66.16.246. Redistribution subject to ASME license or copyright; see http://www.asme.org/terms/Terms_Use.cfm

Y. Takeuti
Professor.
Mem. ASME

R. Ishida
Research Associate.

Y. Tanigawa
Lecturer.

Department of Mechanical Engineering,
University of Osaka Prefecture,
Mozu, Sakai, 591, Japan

On an Axisymmetric Coupled Thermal Stress Problem in a Finite Circular Cylinder

This paper presents a general treatment of the transient thermal stresses of a finite circular cylinder with consideration of the thermomechanical coupling effect using a new technique. The method used is quite useful for the solution of a wide range of transient thermal stress problems in two or three dimensions. From numerical results, we can find that there is a clear effect on the thermal stress distribution when the coupling term is taken into account.

Introduction

It is well known that uncoupling of the temperature and stress problems is permissible whenever simultaneous inertia effects are small and the value of the coupling parameter is small. In our previous paper [1], we found the effect that is the most powerful for finding the thermal stress distribution in a sudden change of temperature. From our results, it is more important to consider the coupling term than to consider the inertia term for common metals in pure thermal stress problems. Therefore, it may be stated that it is sufficient to consider only the effect of the coupling term. Moreover, in our recent studies [2, 3], a new solving method was obtained for two or three-dimensional coupled problems using an additional harmonic function. However, the method used in obtaining coupled thermal stress solution is inconvenient for finite cylinders. In the present study, an another new method is proposed for the wide range of coupled thermal stress problems by means of the usual thermoelastic displacement potential amd Love's displacement function directly.

Analysis

The temperature change T governed by the corrected heat conduction equation with coupling term for the axisymmetric problems is

$$\kappa \Delta T = T_{,t} + (T^* \beta / C_v \gamma) e_{,t} \tag{1}$$

where κ is the thermal diffusivity, C_v is the specific heat at constant volume, e is the volumetric strain, T^* is the reference temperature, γ is the density, and

$$\Delta = \partial^2/\partial r^2 + r^{-1}\partial/\partial r + \partial^2/\partial z^2, \quad \beta = \alpha E/(1-2\nu)$$

where ν is Poisson's ratio, E is Young's modulus, and α is the linear thermal-expansion coefficient. As shown in Fig. 1, a finite, solid circular cylinder with radius a and length $2L$ is partially heated in the axial direction by surface heat generation and then the corrected heat conduction equation can be written in nondimensional form:

$$\Delta_1 \bar{T} = \bar{T}_{,\tau} + \delta(1-\nu)/(1+\nu)\bar{e}_{,\tau} \tag{2}$$

where $\tau = \kappa t/a^2$, $\bar{T} = \lambda T/Qa$, $\Delta_1 = \partial^2/\partial\rho^2 + \rho^{-1}\partial/\partial\rho + \partial^2/\partial\zeta^2$, $\rho = r/a$, $\zeta = z/a$, $\bar{e} = \bar{u}_{,\rho} + \bar{u}/\rho + \bar{w}_{,\zeta}$, $(\bar{u},\bar{w}) = \lambda(u,w)/\alpha Qa$, and

$$\delta = (1+\nu)/(1-\nu) T^* \alpha\beta / C_v \gamma$$

where λ is the thermal conductivity, Q is the heat generation per unit time per unit area.

The governing equations for the thermoelastic displacement potential Φ and Love's displacement function $\bar{L}$ are given by

$$\Delta_1 \Phi = m\bar{T} \tag{3}$$

$$\Delta_1 \Delta_1 \bar{L} = 0 \tag{4}$$

where $m = (1+\nu)/(1-\nu)$.

The stress components and the volumetric strain become

$$\bar{\sigma}_{rr} = m^{-1}[\Phi_{,\rho\rho} - \Delta_1\Phi + (\nu\Delta_1\bar{L} - \bar{L}_{,\rho\rho})_{,\zeta}],$$

$$\bar{\sigma}_{\theta\theta} = m^{-1}[\rho^{-1}\Phi_{,\rho} - \Delta_1\Phi + (\nu\Delta_1\bar{L} - \rho^{-1}\bar{L}_{,\rho})_{,\zeta}],$$

$$\bar{\sigma}_{zz} = m^{-1}[\Phi_{,\zeta\zeta} - \Delta_1\Phi + \{(2-\nu)\Delta_1\bar{L} - \bar{L}_{,\zeta\zeta}\}_{,\zeta}],$$

$$\bar{\sigma}_{rz} = m^{-1}[\Phi_{,\rho\zeta} + \{(1-\nu)\Delta_1\bar{L} - \bar{L}_{,\zeta\zeta}\}_{,\rho}]. \tag{5}$$

$$\bar{e} = \Delta_1\Phi + (1-2\nu)\Delta_1\bar{L}_{,\zeta} \tag{6}$$

where $\bar{\sigma}_{ij} = (1-\nu)\lambda\sigma_{ij}/\alpha QEa$.

From equations (2), (3), and (6), we obtain

$$\Delta_1\bar{T} = (1+\delta)\bar{T}_{,\tau} + m^{-1}(1-2\nu)\delta\Delta_1\bar{L}_{,\zeta\tau} \tag{7}$$

Now we introduce a function $\bar{T}'$ defined as

$$\bar{T}' = \bar{T} + m^{-1}\{(1-2\nu)/(1+\delta)\}\delta\Delta_1\bar{L}_{,\zeta} \tag{8}$$

Contributed by the Applied Mechanics Division for publication in the JOURNAL OF APPLIED MECHANICS.

Discussion on this paper should be addressed to the Editorial Department, ASME, United Engineering Center, 345 East 47th Street, New York, N.Y. 10017 and will be accepted until two months after final publication of the paper itself in the JOURNAL OF APPLIED MECHANICS. Manuscript received by ASME Applied Mechanics Division, April, 1982; final revision, July, 1982.

Copyright © 1983 by ASME
Downloaded 02 May 2010 to 171.66.16.246. Redistribution subject to ASME license or copyright; see http://www.asme.org/terms/Terms_Use.cfm

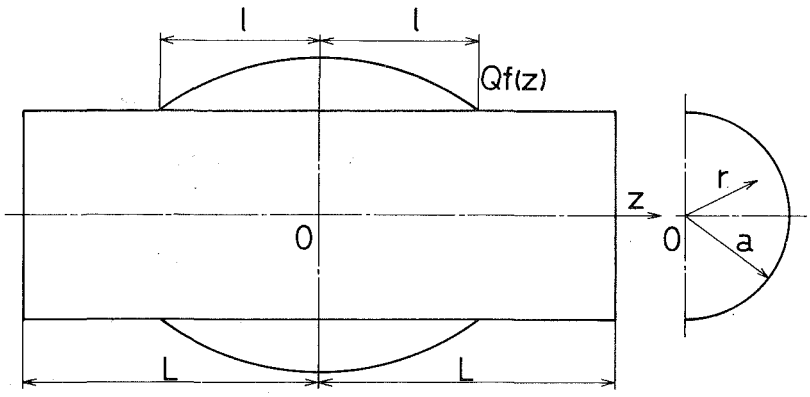

Fig. 1 Circular cylinder with an arbitrarily axisymmetric heat supply

Substituting equation (8) into (7) and considering the relation of equation (4), we obtain[1]

$$\Delta_1 \bar{T}' = (1+\delta)\bar{T}'_{,\tau} \tag{9}$$

The initial condition and boundary conditions are

$$\text{at} \quad \tau=0, \quad \bar{T}=0 \quad \text{and} \quad \bar{L}=0, \tag{10}$$

$$\text{for} \quad \rho=1, \quad \bar{T}_{,\rho}+H_1\bar{T}=f(\zeta) \quad \text{and} \quad \bar{\sigma}_{rr}=\bar{\sigma}_{rz}=0, \tag{11}$$

$$\text{for} \quad \zeta=\pm\zeta_1, \quad \bar{T}_{,\zeta}+H_2\bar{T}=0 \quad \text{and} \quad \bar{\sigma}_{zz}=\bar{\sigma}_{rz}=0 \tag{12}$$

where $\zeta_1 = L/a$, $H_i = \gamma_i a/\lambda, (i=1,2)$.

γ_i is the heat transfer coefficient and $f(\zeta)$ is an arbitrary function of ζ. For convenience, we assume that $f(\zeta)$ is symmetric function with respect to $\zeta=0$.

We introduce the following expression for $\bar{T}$ and $\bar{\sigma}_{ij}$:

$$\bar{T} = \bar{T}_0 + \bar{T}_1 \tag{13}$$

$$\bar{\sigma}_{ij} = \bar{\sigma}^0_{ij} + \bar{\sigma}^1_{ij} \tag{14}$$

in which $\bar{T}_0$ and $\bar{\sigma}^0_{ij}$ are the temperature and stress components for the steady state, while $\bar{T}_1$ and $\bar{\sigma}^1_{ij}$ are additional terms for the transient state.

Let us now consider the steady state solution. Since the right-hand side of equation (2) disappears for the steady state, it follows that

$$\Delta_1 \bar{T}_0 = 0 \tag{15}$$

On account of the symmetry of $f(\zeta)$, the solution for equation (15) can be written as

$$\bar{T}_0 = \sum_{j=1}^{\infty} A_j \cos\omega_j\zeta I_0(\omega_j\rho)/\{H_1 I_0(\omega_j)+\omega_j I_1(\omega_j)\} \tag{16}$$

where

$$A_j = I_c/\{\zeta_1 + H_2/(\omega_j^2+H_2^2)\}, \quad I_c = 2\int_0^{\zeta_1} f(\zeta)\cos\omega_j\zeta d\zeta \tag{17}$$

where $I_n(x)$ is the modified Bessel function of nth order and ω_j are the jth positive roots of

$$H_2\cos\omega\zeta_1 - \omega\sin\omega\zeta_1 = 0 \tag{18}$$

Considering equation (16), a suitable particular solution of equation (3) has the form

$$\Phi_0 = m\sum_{j=1}^{\infty} A_j\cos\omega_j\zeta/2\omega_j^2 \times \omega_j\rho I_1(\omega_j\rho)/\{H_1 I_0(\omega_j)+\omega_j I_1(\omega_j)\} \tag{19}$$

[1] The equation of this type has been introduced by Boley [4] under a different method without consideration of stress-free boundary conditions in a doubly connected domain.

For our present problem, a general solution for the function $\bar{L}_0$ is given by

$$\begin{aligned}\bar{L} = m\Big[&\sum_{j=1}^{\infty} A_j \sin\omega_j\zeta/\omega_j^3 \times \{E_{j0}\omega_j\rho I_1(\omega_j\rho)+F_{j0}I_0(\omega_j\rho)\}+\\ &+\sum_{s=1}^{\infty}\sin k_s\zeta/k_s^3\times\{E_{s0}k_s\rho I_1(k_s\rho)+F_{s0}I_0(k_s\rho)\}\\ &+\sum_{l=1}^{\infty} J_0(\beta_l\rho)/\beta_l^3\times\\ &\times(E_{l0}\beta_l\zeta\cosh\beta_l\zeta+F_{l0}\sinh\beta_l\zeta)+C_0'\rho^2\zeta/2+D_0'\zeta^3/2\Big]\end{aligned} \tag{20}$$

where $k_s = \pi s/\zeta_1$ $(s=1, 2, \ldots\ldots)$, $J_n(x)$ is the Bessel function of nth order, and β_l are the lth positive roots of

$$J_1(\beta)=0 \tag{21}$$

Substituting equations (19) and (20) into equation (5), we obtain the steady-state stress components $\bar{\sigma}^0_{ij}$. It follows then that

$$\begin{aligned}\bar{\sigma}^0_{\theta\theta} = &-(1-2\nu)C_0'+2\nu D_0'-\sum_{j=1}^{\infty}A_j\cos\omega_j\zeta\{(1-2\nu)E_{j0}I_0(\omega_j\rho)+\\ &+F_{j0}I_1(\omega_j\rho)/\omega_j\rho\}-\sum_{s=1}^{\infty}\cos k_s\zeta\{(1-2\nu)E_{s0}I_0(k_s\rho)+\\ &+F_{s0}I_1(k_s\rho)/k_s\rho\}+\sum_{l=1}^{\infty}[\{E_{l0}(\beta_l\zeta\sinh\beta_l\zeta+\cosh\beta_l\zeta)+\\ &+F_{l0}\cosh\beta_l\zeta\}J_1(\beta_l\rho)/\beta_l\rho+2\nu E_{l0}J_0(\beta_l\rho)\cosh\beta_l\zeta]-\\ &-\frac{1}{2}\sum_{j=1}^{\infty}A_j\cos\omega_j\zeta I_0(\omega_j\rho)/\{H_1I_0(\omega_j)+\omega_jI_1(\omega_j)\}\end{aligned} \tag{22}$$

$$\begin{aligned}\bar{\sigma}^0_{zz} = &\,2(2-\nu)C_0'+2(1-\nu)D_0'\\ &-\sum_{j=1}^{\infty}A_j\cos\omega_j\zeta\,[E_{j0}\{2(2-\nu)I_0(\omega_j\rho)+\\ &+\omega_j\rho I_1(\omega_j\rho)\}+F_{j0}I_0(\omega_j\rho)]\\ &+\sum_{s=1}^{\infty}\cos k_s\zeta\,[E_{s0}\{2(2-\nu)I_0(k_s\rho)+\\ &+k_s\rho I_1(k_s\rho)\}+F_{s0}I_0(k_s\rho)]+\sum_{l=1}^{\infty}[E_{l0}\{(1-2\nu)\cosh\beta_l\zeta-\end{aligned}$$

Downloaded 02 May 2010 to 171.66.16.246. Redistribution subject to ASME license or copyright; see http://www.asme.org/terms/Terms_Use.cfm

$$-\beta_l\zeta\sinh\beta_l\zeta\}-F_{l0}\cosh\beta_l\zeta\,]J_0(\beta_l\rho)-$$

$$-\frac{1}{2}\sum_{j=1}^{\infty}A_j\cos\omega_j\zeta\{2I_0(\omega_j\rho)$$

$$+\omega_j\rho I_1(\omega_j\rho)\}/\{H_1I_0(\omega_j)+\omega_jI_1(\omega_j)\} \tag{23}$$

For the sake of brevity, the other expressions for thermal stresses are omitted here. The unknown constants in the preceding expression can be determined from equations (11) and (12).

The steady state solution $\bar{T}_0'$ for equation (9) can be derived as the following from considering equation (16).

$$\bar{T}_0'=\sum_{j=1}^{\infty}A_j\cos\omega_j\zeta P_jI_0(\omega_j\rho)/\{H_1I_0(\omega_j)+\omega_jI_1(\omega_j)\} \tag{24}$$

where P_j is an arbitrary constant.

Consequently, from equation (8), we have

$$\bar{T}_0=\sum_{j=1}^{\infty}A_j\cos\omega_j\zeta P_jI_0(\omega_j\rho)/\{H_1I_0(\omega_j)+\omega_jI_1(\omega_j)\}-$$

$$-2\delta\delta_1\Big\{\sum_{j=1}^{\infty}A_j\cos\omega_j\zeta E_{j0}I_0(\omega_j\rho)+\sum_{s=1}^{\infty}E_{s0}\cos k_s\zeta I_0(k_s\rho)+$$

$$+\sum_{l=1}^{\infty}E_{l0}J_0(\beta_l\rho)\cosh\beta_l\zeta+C_0\Big\} \tag{24}'$$

where $\delta_1=(1-2\nu)/(1+\delta)$, $C_0=C_0'+D_0'$.

The next step is to find the transient solution. Applying the method of separation of variables, we have

$$\bar{T}_1'=\sum_{j=1}^{\infty}\cos\omega_j\zeta\sum_{m=1}^{\infty}C_{jm}J_0(\alpha_m\rho)\exp\{-(\alpha_m^2+\omega_j^2)\tau/(1+\delta)\} \tag{25}$$

where α_m are the mth positive roots of

$$H_1J_0(\alpha)-\alpha J_1(\alpha)=0 \tag{26}$$

The preceding transcendental equation for the eigenvalue α is derived from the following boundary condition for the temperature component $\bar{T}_1'$.

$$\text{for}\quad \rho=1,\quad \bar{T}_{1,\rho}'+H_1\bar{T}_1'=0 \tag{27}$$

The unknown constants C_{jim} are to be determined from the initial condition. In the same way, we can find $\bar{L}_1$ for the transient state from equation (4), and L_1 has the similar form to equation (20). Consequently, from equation (8), we have

$$\bar{T}_1=\sum_{j=1}^{\infty}\cos\omega_j\zeta\sum_{m=1}^{\infty}C_{jm}J_0(\alpha_m\rho)\exp\{-(\alpha_m^2+\omega_j^2)\tau/(1+\delta)\}$$

$$-2\delta\delta_1\Big\{\sum_{j=1}^{\infty}A_j\cos\omega_j\zeta E_{j1}I_0(\omega_j\rho)+\sum_{s=1}^{\infty}E_{s1}\cos k_s\zeta I_0(k_s\rho)+$$

$$+\sum_{l=1}^{\infty}E_{l1}J_0(\beta_l\rho)\cosh\beta_l\zeta+C_1\Big\},\quad C_1=C_1'+D_1' \tag{28}$$

Substituting equations (24)′ and (28) into equation (10), we have

$$\sum_{j=1}^{\infty}\cos\omega_j\zeta\Big[A_jP_jI_0(\omega_j\rho)/\{H_1I_0(\omega_j)+$$

$$+\omega_jI_1(\omega_j)\}+\sum_{m=1}^{\infty}C_{jm}J_0(\alpha_m\rho)\Big]-$$

$$-2\delta\delta_1\Big\{\sum_{j=1}^{\infty}A_j\cos\omega_j\zeta\,(E_{j0}+E_{j1})I_0(\omega_j\rho)+$$

$$+\sum_{s=1}^{\infty}\cos k_s\zeta\,(E_{s0}+E_{s1})I_0(k_s\rho)+$$

$$+\sum_{l=1}^{\infty}J_0(\beta_l\rho)(E_{l0}+E_{l1})\cosh\beta_l\zeta+C_0+C_1\Big\}=0 \tag{29}$$

Moreover, the following relations can be derived from equation (29)

$$A_jP_jI_0(\omega_j\rho)/\{H_1I_0(\omega_j)+\omega_jI_1(\omega_j)\}+\sum_{m=1}^{\infty}C_{jm}J_0(\alpha_m\rho)=0 \tag{30}$$

and

$$E_{j0}+E_{j1}=0,\quad E_{s0}+E_{s1}=0,\quad E_{l1}+E_{l0}=0,\ C_1+C_0=0. \tag{31}$$

Equation (31) is equivalent to the initial condition for $\bar{L}$. Therefore we obtain the following relation:

$$\sum_{j=1}^{\infty}\cos\omega_j\zeta\sum_{m=1}^{\infty}C_{jm}J_0(\alpha_m\rho)=$$

$$-\sum_{j=1}^{\infty}A_j\cos\omega_j\zeta I_0(\omega_j\rho)/\{H_1I_0(\omega_j)+\omega_jI_1(\omega_j)\}-$$

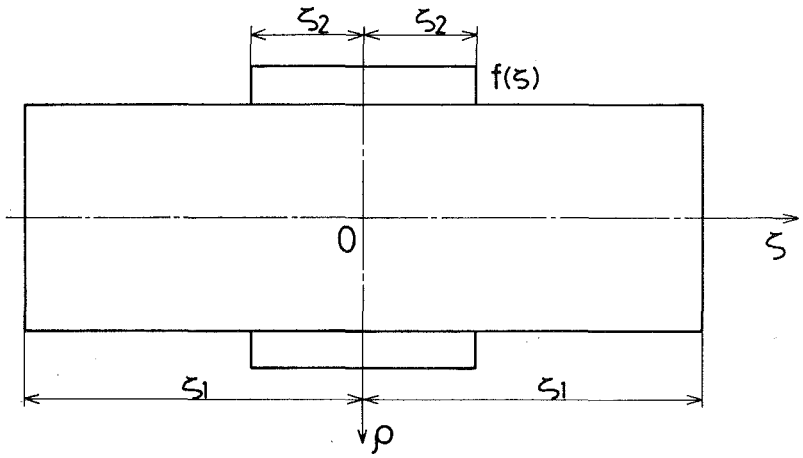

Fig. 2 Circular cylinder with the step functional form of heat supply

Downloaded 02 May 2010 to 171.66.16.246. Redistribution subject to ASME license or copyright; see http://www.asme.org/terms/Terms_Use.cfm

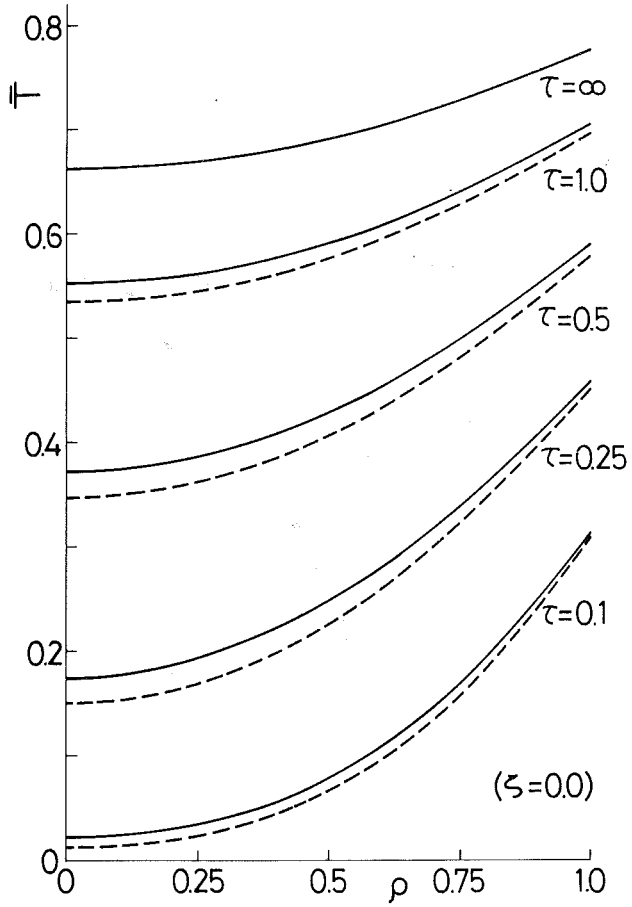

Fig. 3 Temperature distribution on the middle cross section of the cylinder ($\zeta = 0$)

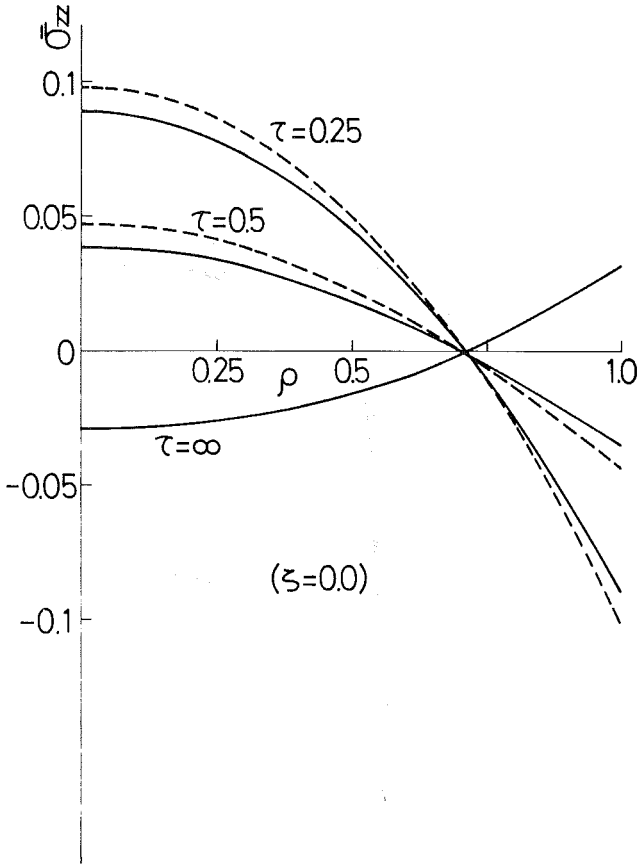

Fig. 4 Axial stress distribution on the middle cross section of the cylinder ($\zeta = 0$)

$$-2\delta\delta_1\Big\{\sum_{j=1}^{\infty}A_j\cos\omega_j\zeta E_{j0}I_0(\omega_j\rho)+\sum_{s=1}^{\infty}\cos k_s\zeta E_{s0}I_0(k_s\rho)+$$

$$+\sum_{l=1}^{\infty}E_{l0}J_0(\beta_l\rho)\cosh\beta_l\zeta+C_0\Big\} \tag{32}$$

By applying the method of series expansion over the whole region, using the kernels, which are $\cos\omega_j\zeta$ and $J_0(\alpha_m\rho)$, we can find the unknown constants C_{jm} on each j and m. Now, we rewrite

$$C_{jm}=A_jC_mP_{jm}/J_0(\alpha_m),\quad C_m=2\alpha_m^2/(\alpha_m^2+H_1^2) \tag{33}$$

then we have

$$P_{jm}=-[1+2\delta\delta_1E_{j0}\{H_1I_0(\omega_j)$$

$$+\omega_jI_1(\omega_j)\}]/(\alpha_m^2+\omega_j^2)-4\delta\delta_1\cos\omega_j\zeta_1/I_c\times$$

$$\times\Big[H_2\sum_{s=1}^{\infty}(-1)^s\{H_1I_0(k_s)+k_sI_1(k_s)\}$$

$$/\{(\omega_j^2-k_s^2)(\alpha_m^2+k_s^2)\}\times E_{s0}+$$

$$+H_1\sum_{l=1}^{\infty}(\beta_l\sinh\beta_l\zeta_1+H_2\cosh\beta_l\zeta_1)J_0(\beta_l)E_{l0}$$

$$/\{(\omega_j^2+\beta_l^2)(\alpha_m^2-\beta_l^2)\}+$$

$$+H_1H_2C_0/(\omega_j^2\alpha_m^2)\Big] \tag{34}$$

Substituting equation (33) and (34) into equation (28), we obtain the following expression for $\bar{T}_1$.

$$\bar{T}_1=\sum_{j=1}^{\infty}A_j\cos\omega_j\zeta\sum_{m=1}^{\infty}C_mJ_0(\alpha_m\rho)\Theta(\tau)/J_0(\alpha_m)$$

$$-2\delta\delta_1\Big\{\sum_{j=1}^{\infty}A_j\cos\omega_j\zeta E_{j1}I_0(\omega_j\rho)+\sum_{s=1}^{\infty}E_{s1}\cos k_s\zeta I_0(k_s\rho)+$$

$$+\sum_{l=1}^{\infty}E_{l1}J_0(\beta_l\rho)\cosh\beta_l\zeta+C_1\Big\} \tag{35}$$

where

$$\Theta(\tau)=P_{jm}\exp\{-(\alpha_m^2+\omega_j^2)\tau/(1+\delta)\} \tag{36}$$

Considering equation (35), the corresponding particular solution for Φ_1 has the form

$$\Phi_1=-m\sum_{j=1}^{\infty}A_j\cos\omega_j\zeta\sum_{m=1}^{\infty}C_mJ_0(\alpha_m\rho)\Theta(\tau)$$

$$/\{J_0(\alpha_m)(\alpha_m^2+\omega_j^2)\}-$$

$$-m\delta\delta_1\Big\{\sum_{j=1}^{\infty}A_j\cos\omega_j\zeta/\omega_j^2\times E_{j1}\omega_j\rho I_1(\omega_j\rho)$$

$$+\sum_{s=1}^{\infty}\cos k_s\zeta/k_s^2\times E_{s1}k_s\rho I_1(k_s\rho)+$$

$$+\sum_{l=1}^{\infty}E_{l1}(\cosh\beta_l\zeta+\beta_l\zeta\sinh\beta_l\zeta)J_0(\beta_l\rho)/\beta_l^2$$

$$+C_1'\rho^2/2+D_1'\zeta^2\Big\} \tag{37}$$

Downloaded 02 May 2010 to 171.66.16.246. Redistribution subject to ASME license or copyright; see http://www.asme.org/terms/Terms_Use.cfm

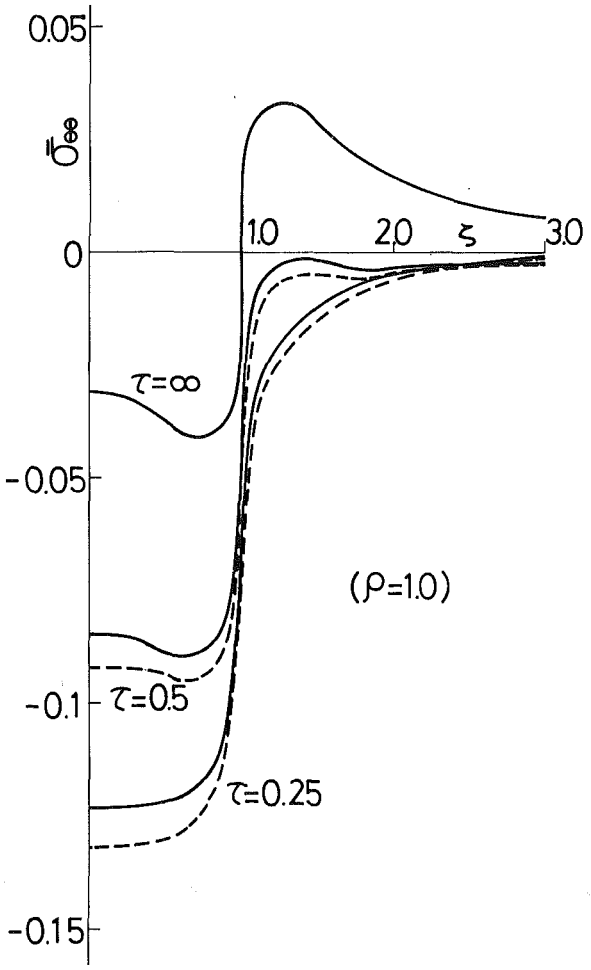

Fig. 5 Hoop stress distribution on the lateral surface of the cylinder (ρ = 1)

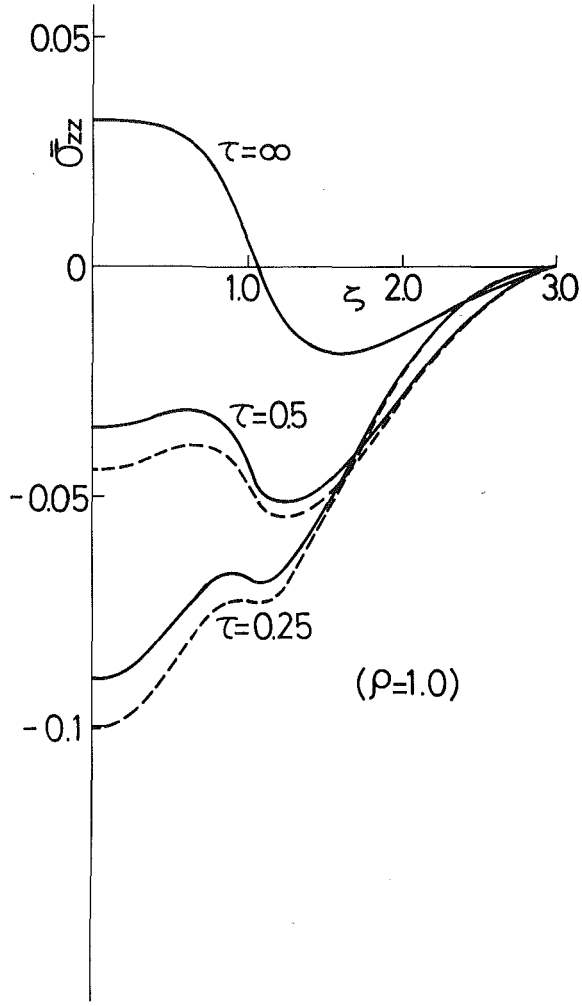

Fig. 6 Axial stress distribution on the lateral surface of the cylinder (ρ = 1)

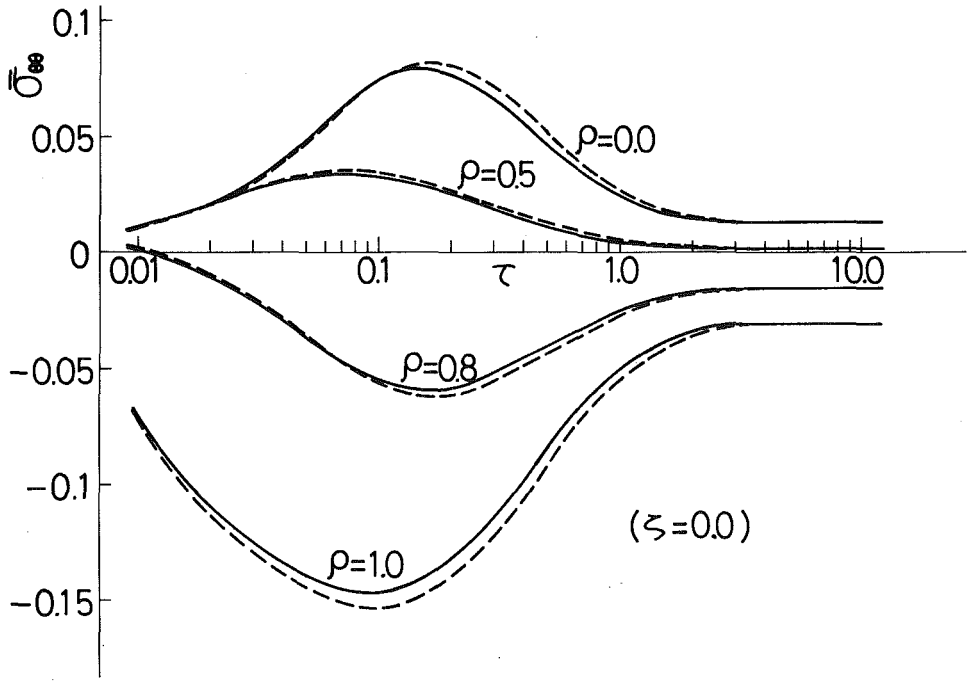

Fig. 7 Hoop stress variation with time on the middle cross section of the cylinder (ζ = 0)

Downloaded 02 May 2010 to 171.66.16.246. Redistribution subject to ASME license or copyright; see http://www.asme.org/terms/Terms_Use.cfm

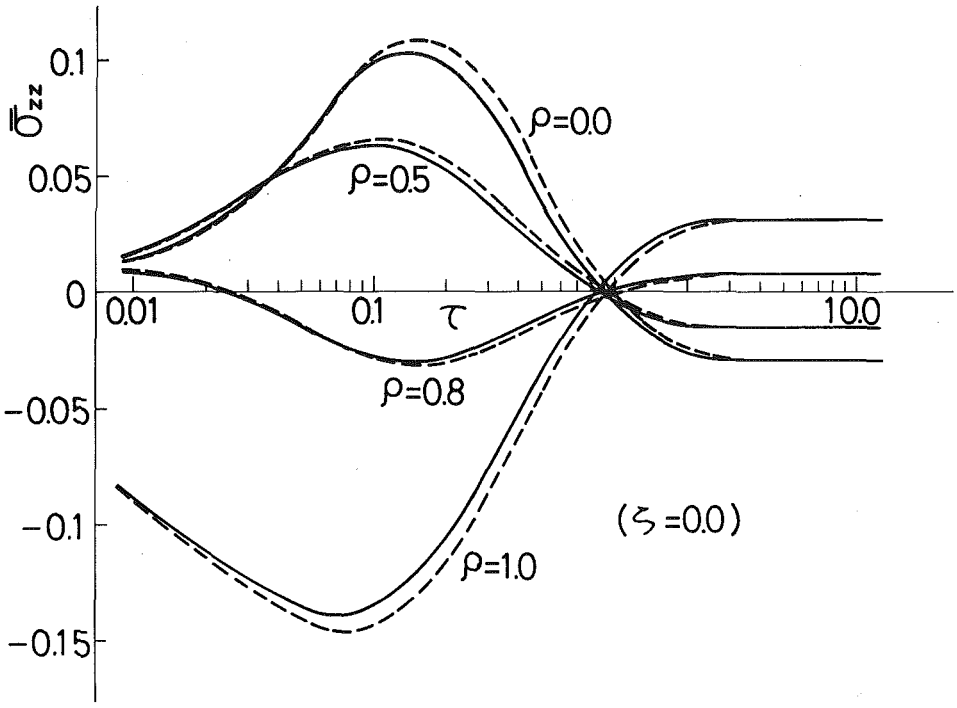

Fig. 8 Axial stress variation with time on the middle cross section of the cylinder ($\zeta = 0$)

Thus, by equation (5), we can obtain the required solutions of $\tilde{\sigma}_{ij}^{1}$ for the transient state. For example,

$$\tilde{\sigma}_{\theta\theta}^{1} = -\delta_1 C_1' + 2(\delta\delta_1 + \nu)D_1' - \sum_{j=1}^{\infty} A_j \cos\omega_j\zeta\{E_{j1}\delta_1 I_0(\omega_j\rho) + F_{j1} I_1(\omega_j\rho)/\omega_j\rho\} - \sum_{s=1}^{\infty} \cos k_s\zeta\{E_{s1}\delta_1 I_0(k_s\rho) + F_{s1} I_1(k_s\rho)/k_s\rho\} + \sum_{l=1}^{\infty} [\{E_{l1}(\delta\delta_1+1)(\beta_l\zeta\sinh\beta_l\zeta + \cosh\beta_l\zeta) + F_{l1}\cosh\beta_l\zeta\} J_1(\beta_l\rho)/\beta_l\rho + 2(\delta\delta_1+\nu)E_{l1}J_0(\beta_l\rho)\cosh\beta_l\zeta] - \sum_{j=1}^{\infty} A_j\cos\omega_j\zeta \sum_{m=1}^{\infty} \frac{C_m\Theta(\tau)}{(\alpha_m^2+\omega_j^2)J_0(\alpha_m)}\{(\alpha_m^2+\omega_j^2)J_0(\alpha_m\rho) - \alpha_m J_1(\alpha_m\rho)/\rho\} \quad (38)$$

$$\tilde{\sigma}_{zz}^{1} = 2(\delta\delta_1 + 2 - \nu)C_1' + 2(1-\nu)D_1' + \sum_{j=1}^{\infty} A_j\cos\omega_j\zeta\,[E_{j1}\{2(\delta\delta_1+2-\nu)I_0(\omega_j\rho) + (\delta\delta_1+1)\omega_j\rho I_1(\omega_j\rho)\} + F_{j1}I_0(\omega_j\rho)] + \sum_{s=1}^{\infty}\cos k_s\zeta\,[E_{s1}\{2(\delta\delta_1+2-\nu)I_0(k_s\rho) + (\delta\delta_1+1)k_s\rho I_1(k_s\rho)\} + F_{s1}I_0(k_s\rho)] + \sum_{l=1}^{\infty}[E_{l1}\{\delta_1\cosh\beta_l\zeta - (\delta\delta_1+1)\beta_l\zeta\sinh\beta_l\zeta\} - F_{l1}\cosh\beta_l\zeta J_0(\beta_l\rho)] - \sum_{j=1}^{\infty} A_j\cos\omega_j\zeta\sum_{m=1}^{\infty}\frac{\alpha_m^2 C_m\Theta(\tau)}{(\alpha_m^2+\omega_j^2)J_0(\alpha_m)}J_0(\alpha_m\rho) \quad (39)$$

For the sake of brevity, the other expressions for thermal stresses are omitted here. The unknown constant in the preceding expressions can be determined from equations (11) and (12). Hence, using equations (13) and (14), we find that the final expressions for $\bar{T}$ and $\tilde{\sigma}_{ij}$ are completely determined.

Numerical Calculation

As an illustrative purpose of the foregoing solutions, the cylinder has the following geometric and material properties, as shown in Fig. 2, when $\nu = 0.3$ and $\delta = 0.08$:

$$f(\zeta) = \begin{cases} 1(-\zeta_2 < \zeta < \zeta_2, & \text{where} \quad \zeta_2 = l/a) \\ 0(\text{for other } \zeta) \end{cases}$$

$$2\zeta_1 = 6, \quad 2\zeta_2 = 2, \quad H_1 = 1.0, \quad H_2 = 0.1.$$

Figures 3[2] and 4 show the temperature and axial stress distributions along the radial direction on the middle cross section of the cylinder ($\zeta = 0.0$) at various dimensionless times τ. Figures 5 and 6 show the hoop stress and axial stress distributions along the axial direction on the lateral surface of the cylinder ($\rho = 1.0$) at various dimensionless times. Figures 7 and 8 show the time variation of the hoop stress and axial stress on the middle cross section.

From these figures showing the hoop stress and axial stress distributions, we may also observe that the influence of the coupling term on the stress distribution is considerable and causes the distinct difference between the coupled result and the uncoupled one. From Figs. 7 and 8, it can be seen that the maximum stress of $\tilde{\sigma}_{\theta\theta}$ and $\tilde{\sigma}_{zz}$ on the surface of the middle cross section is decreased in the first short period ($\tau < 0.01$) of heating when the coupling effect is taken into account; however, in the next time interval ($\tau > 0.01$), these maximum stresses are increased by the effect of the coupling term, and

[2] In these figures the coupled solutions are plotted as dotted lines and also the corresponding numerical results for the uncoupled solutions are shown by the solid lines for comparison.

Downloaded 02 May 2010 to 171.66.16.246. Redistribution subject to ASME license or copyright; see http://www.asme.org/terms/Terms_Use.cfm

the difference between the coupled and uncoupled results becomes considerably more than in the case of the short time period.

In the numerical calculation of the infinite series, we found the combination of subscripts j, m, etc., considering the satisfactory convergency. For example, we adopt $j = 25$ and $m = 40$ in the double infinite series.

Conclusions

It is obvious that our exact analytical solution is valid for the whole time interval. The numerical results obtained are applicable to thermal shock problems in industry because the value of the coupling parameter δ adopted is a realistic value of ordinal metals. It appears from the figures that coupled solutions exhibit definite differences between the coupled results and uncoupled ones in the stress distributions and clear lags in temperature distributions.

References

1 Takeuti, Y., and Furukawa, T., "Some Considerations on Thermal Shock Problems in a Plate," ASME JOURNAL OF APPLIED MECHANICS, Vol. 48, 1981, pp. 113–118

2 Takeute, Y., and Tanigawa, Y., "On a New Method for Axisymmetric Coupled Thermoelastic Problems," *Journal of Thermal Stresses*, Vol. 4, 1981, pp. 461–478

3 Tanigawa, Y., and Takeuti, Y., "Coupled Thermoelastic Problem in Three-Dimensions," *Zeit. Angew. Math. Mech.*, Bd. 62, 1982, pp. 221–228.

4 Boley, B. A., "Applied Thermoelasticity," *Proceedings of the 13th Midwestern Mechanics Conference*, Vol. 7, pp. 3–16.

Downloaded 02 May 2010 to 171.66.16.246. Redistribution subject to ASME license or copyright; see http://www.asme.org/terms/Terms_Use.cfm

J. R. Hutchinson
Professor of Civil Engineering,
University of California,
Davis, Calif. 95616
Mem. ASME

S. D. Zillmer
Technical Staff,
Rockwell International,
North American Aircraft Operations,
201 North Douglas,
El Segundo, Calif. 90245

Vibration of a Free Rectangular Parallelepiped

A series solution of the general equations of linear elasticity is used to determine accurate natural frequencies for the vibrations of a rectangular parallelepiped with traction-free surfaces. The series solution is found to converge to accurate frequencies with the use of very few terms. Resulting frequences are tabulated for comparison with previous experimental results and are shown graphically for comparison with elementary rod, beam, and plate solutions. The comparisons with elementary solutions show good agreement, and comparisons with the experiment results shows excellent agreement.

Introduction

A series solution for the determination of the natural frequencies of vibration of a solid, isotropic, linearly elastic, rectangular parallelepiped is developed, and natural frequencies are evaluated over a representative range of the parameters. The series solution is found to converge rapidly as more terms are chosen. This series method has been applied to the vibrations of various circular cylindrical body problems, references [1-5], with much success.

The problem of the vibrating rectangular parallelepiped was first investigated in terms of the general elasticity equations by Mindlin and Fox [6] in 1960. They considered the vibration of an infinitely long bar of rectangular cross section with traction-free faces. Their solution, of course, does not permit traction-free ends, but could provide insights into the more general problem in the same way that the Pochhammmer-Chree solution provides insight into the finite-length, circular, cylindrical bar problem as in reference [2].

Many approximate solutions are well known for special cases of the vibration of a free rectangular parallelepiped. If one dimension is very large compared to the other two the parallelepiped will act as a long beam. Its vibrations will thus be flexural, torsional, or axial beam vibrations. The solutions for this elementary behavior can be found in many vibrations texts (e.g., [7]). For a shorter beam, the effects of shear and rotary inertia become important for transverse beam vibrations, and the theory proposed by Timoshenko [8] could be introduced. For the axial and torsional vibrations of shorter beams, the inclusion of radial inertia terms for axial motion and axial inertia terms for torsion which were introduced by Love [9] can become important. If one dimension is small compared to the other two then the free rectangular parallelepiped becomes a free rectangular plate, many solutions of which are tabulated in the monograph by Leissa [10]. For thick plates, the Mindlin Plate Theory [11] which is the two-dimensional analog of the Timoshenko Beam Theory could be applied. In this paper comparisons are only made with the elementary theories except for the axial motion case.

There is experimental data available for the rectangular parallelepiped which has dimensions in the range not covered by the elementary theories. The 1960 paper by Spinner et al. [12] and the 1970 paper by Spence and Seldin [13] give highly accurate results which provide an excellent check on the analytical results. Comparison of the analytical results with these experimental studies shows excellent correlation.

The solution method was first introduced by Mathieu [14] in 1890 at which time the rapid convergence to the correct solution was clearly established. The method of solution as applied to this problem involves combining exact solutions of the governing equations in three double series, which term-by-term satisfy the shear stress boundary conditions. The boundary conditions on normal stress are satisfed by orthogonalization on the boundaries. This leads to an eigenvalue matrix that is searched for zero's in order to determine the natural frequencies.

Method of Solution

The four types of solution forms that are derived from application of the Helmholtz Displacement Potential are tabulated in Table 1. Sinusoidal motion is assumed so that each term is considered as multiplied by sin ωt. In the table, the terms s and c in braces refer to the sine and cosine, respectively, with the argument αx for the first set in braces in the first column, βy for the second set in column 1, δz for the third set in Column 1, $\bar{\alpha} x$ for the first set in Columns 2, 3, and 4, $\bar{\beta} y$ for the second set of Columns 2, 3, and 4, and $\bar{\delta} z$ for the third set in Columns 2, 3, and 4. The relations between the wave numbers are:

$$\alpha^2 + \beta^2 + \delta^2 = \omega^2 / {c_1}^2 \tag{1}$$

$$\bar{\alpha}^2 + \bar{\beta}^2 + \bar{\delta}^2 = \omega^2 / {c_2}^2 \tag{2}$$

Contributed by the Applied Mechanics Division for publication in the JOURNAL OF APPLIED MECHANICS.

Discussion on this paper should be addressed to the Editorial Department, ASME, United Engineering Center, 345 East 47th Street, New York, N.Y. 10017, and will be accepted until two months after final publication of the paper itself in the JOURNAL OF APPLIED MECHANICS. Manuscript received by ASME Applied Mechanics Division, January, 1982; final revision, August, 1982.

Copyright © 1983 by ASME
Downloaded 02 May 2010 to 171.66.16.246. Redistribution subject to ASME license or copyright; see http://www.asme.org/terms/Terms_Use.cfm

Table 1 Solution forms in cartesian coordinates

	(1)	(2)	(3)	(4)
u	$\alpha \begin{Bmatrix}-s\\c\end{Bmatrix}\begin{Bmatrix}s\\c\end{Bmatrix}\begin{Bmatrix}c\\s\end{Bmatrix}$	$\bar{\beta}\begin{Bmatrix}s\\c\end{Bmatrix}\begin{Bmatrix}-s\\c\end{Bmatrix}\begin{Bmatrix}c\\s\end{Bmatrix}$	$-\bar{\delta}\begin{Bmatrix}s\\c\end{Bmatrix}\begin{Bmatrix}s\\c\end{Bmatrix}\begin{Bmatrix}c\\-s\end{Bmatrix}$	0
v	$\beta\begin{Bmatrix}c\\s\end{Bmatrix}\begin{Bmatrix}c\\-s\end{Bmatrix}\begin{Bmatrix}c\\s\end{Bmatrix}$	$-\bar{\alpha}\begin{Bmatrix}c\\-s\end{Bmatrix}\begin{Bmatrix}c\\s\end{Bmatrix}\begin{Bmatrix}c\\s\end{Bmatrix}$	0	$\bar{\delta}\begin{Bmatrix}c\\s\end{Bmatrix}\begin{Bmatrix}c\\s\end{Bmatrix}\begin{Bmatrix}c\\-s\end{Bmatrix}$
w	$\delta\begin{Bmatrix}c\\s\end{Bmatrix}\begin{Bmatrix}s\\c\end{Bmatrix}\begin{Bmatrix}-s\\c\end{Bmatrix}$	0	$\bar{\alpha}\begin{Bmatrix}c\\-s\end{Bmatrix}\begin{Bmatrix}s\\c\end{Bmatrix}\begin{Bmatrix}s\\c\end{Bmatrix}$	$-\bar{\beta}\begin{Bmatrix}c\\s\end{Bmatrix}\begin{Bmatrix}-s\\c\end{Bmatrix}\begin{Bmatrix}s\\c\end{Bmatrix}$
σ_x	$-(K+2\mu\alpha^2)\begin{Bmatrix}c\\s\end{Bmatrix}\begin{Bmatrix}s\\c\end{Bmatrix}\begin{Bmatrix}c\\s\end{Bmatrix}$	$2\mu\bar{\alpha}\bar{\beta}\begin{Bmatrix}c\\-s\end{Bmatrix}\begin{Bmatrix}-s\\c\end{Bmatrix}\begin{Bmatrix}c\\s\end{Bmatrix}$	$-2\mu\bar{\alpha}\bar{\delta}\begin{Bmatrix}c\\-s\end{Bmatrix}\begin{Bmatrix}s\\c\end{Bmatrix}\begin{Bmatrix}c\\-s\end{Bmatrix}$	0
σ_y	$-(K+2\mu\beta^2)\begin{Bmatrix}c\\s\end{Bmatrix}\begin{Bmatrix}s\\c\end{Bmatrix}\begin{Bmatrix}c\\s\end{Bmatrix}$	$-2\mu\bar{\alpha}\bar{\beta}\begin{Bmatrix}c\\-s\end{Bmatrix}\begin{Bmatrix}-s\\c\end{Bmatrix}\begin{Bmatrix}c\\s\end{Bmatrix}$	0	$2\mu\bar{\beta}\bar{\delta}\begin{Bmatrix}c\\s\end{Bmatrix}\begin{Bmatrix}-s\\c\end{Bmatrix}\begin{Bmatrix}c\\-s\end{Bmatrix}$
σ_z	$-(K+2\mu\delta^2)\begin{Bmatrix}c\\s\end{Bmatrix}\begin{Bmatrix}s\\c\end{Bmatrix}\begin{Bmatrix}c\\s\end{Bmatrix}$	0	$2\mu\bar{\alpha}\bar{\delta}\begin{Bmatrix}c\\-s\end{Bmatrix}\begin{Bmatrix}s\\c\end{Bmatrix}\begin{Bmatrix}c\\-s\end{Bmatrix}$	$-2\mu\bar{\beta}\bar{\delta}\begin{Bmatrix}c\\s\end{Bmatrix}\begin{Bmatrix}-s\\c\end{Bmatrix}\begin{Bmatrix}c\\-s\end{Bmatrix}$
τ_{xy}	$2\mu\alpha\beta\begin{Bmatrix}-s\\c\end{Bmatrix}\begin{Bmatrix}c\\-s\end{Bmatrix}\begin{Bmatrix}c\\s\end{Bmatrix}$	$\mu(\bar{\alpha}^2-\beta^2)\begin{Bmatrix}s\\c\end{Bmatrix}\begin{Bmatrix}c\\s\end{Bmatrix}\begin{Bmatrix}c\\s\end{Bmatrix}$	$-\mu\bar{\beta}\bar{\delta}\begin{Bmatrix}s\\c\end{Bmatrix}\begin{Bmatrix}c\\-s\end{Bmatrix}\begin{Bmatrix}c\\-s\end{Bmatrix}$	$\mu\bar{\alpha}\bar{\delta}\begin{Bmatrix}-s\\c\end{Bmatrix}\begin{Bmatrix}c\\s\end{Bmatrix}\begin{Bmatrix}c\\-s\end{Bmatrix}$
τ_{yz}	$2\mu\beta\delta\begin{Bmatrix}c\\s\end{Bmatrix}\begin{Bmatrix}c\\-s\end{Bmatrix}\begin{Bmatrix}-s\\c\end{Bmatrix}$	$-\mu\bar{\alpha}\bar{\delta}\begin{Bmatrix}c\\-s\end{Bmatrix}\begin{Bmatrix}c\\s\end{Bmatrix}\begin{Bmatrix}-s\\c\end{Bmatrix}$	$\mu\bar{\alpha}\bar{\beta}\begin{Bmatrix}c\\-s\end{Bmatrix}\begin{Bmatrix}c\\-s\end{Bmatrix}\begin{Bmatrix}s\\c\end{Bmatrix}$	$\mu(\bar{\beta}^2-\delta^2)\begin{Bmatrix}c\\s\end{Bmatrix}\begin{Bmatrix}c\\s\end{Bmatrix}\begin{Bmatrix}s\\c\end{Bmatrix}$
τ_{zx}	$2\mu\alpha\delta\begin{Bmatrix}-s\\c\end{Bmatrix}\begin{Bmatrix}s\\c\end{Bmatrix}\begin{Bmatrix}-s\\c\end{Bmatrix}$	$\mu\bar{\beta}\bar{\delta}\begin{Bmatrix}s\\c\end{Bmatrix}\begin{Bmatrix}-s\\c\end{Bmatrix}\begin{Bmatrix}-s\\c\end{Bmatrix}$	$\mu(\delta^2-\alpha^2)\begin{Bmatrix}s\\c\end{Bmatrix}\begin{Bmatrix}s\\c\end{Bmatrix}\begin{Bmatrix}s\\c\end{Bmatrix}$	$\mu\bar{\alpha}\bar{\beta}\begin{Bmatrix}-s\\c\end{Bmatrix}\begin{Bmatrix}-s\\c\end{Bmatrix}\begin{Bmatrix}s\\c\end{Bmatrix}$

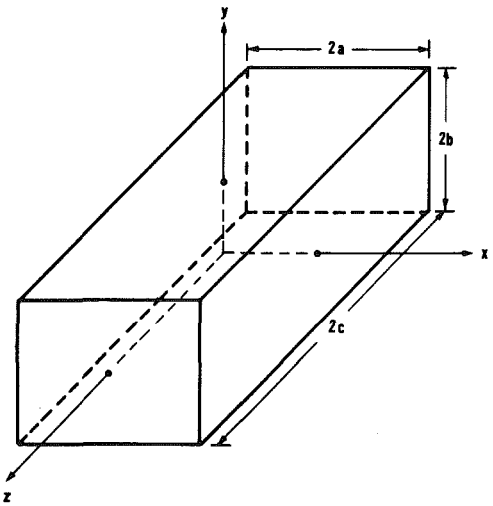

Fig. 1 Coordinates and dimensions for the rectangular parallelepiped

where ω is the natural frequency and c_1 and c_2 are the dilitational and shear wave velocities, respectively. The constant K appearing in Table 1 is $\omega^2\lambda/c_1{}^2$. The constants λ and μ are the Lame's constants.

The physical dimensions and coordinate system used for this problem is shown in Fig. 1. By centering the coordinate system as shown in Fig. 1 it is necesary to consider only one octant. The boundray conditions can thus be expressed as:

$$\tau_{xy}\,(a, y, z) = 0 \tag{3}$$

$$\tau_{xy}\,(x, b, z) = 0 \tag{4}$$

$$\tau_{yz}\,(x, b, z) = 0 \tag{5}$$

$$\tau_{yz}\,(x, y, c) = 0 \tag{6}$$

$$\tau_{zx}\,(a, y, z) = 0 \tag{7}$$

$$\tau_{zx}\,(x, y, c) = 0 \tag{8}$$

$$\sigma_x\,(a, y, z) = 0 \tag{9}$$

$$\sigma_y\,(x, b, z) = 0 \tag{10}$$

$$\sigma_z\,(x, y, c) = 0 \tag{11}$$

The solution is formed by taking linear combinations of the four types of solution forms in Table 1. It can be seen that there are eight possible combinations of the two terms in each of the three sets of braces; however, since one may exchange x for y for z there are only four separate cases that need to be considered to cover all of the possible motions. Because of the complexity of equation development and the similarities between the four cases, equation development in this paper will be restricted to only one of the four cases. Details for the other three cases can be found in reference [15]. The case considered is formed by using the top term in each of the three sets of braces. Linear combinations of four solution types are chosen in three series. The expression for the shear stress τ_{xy} is shown in the following:

$$\tau_{xy} = \mu \sum_{m=1}^{NX} \sum_{n=1}^{NY} A_{mn}\, f_{mn}\,(z) \sin \alpha_m x \cos \beta_n y$$

$$+ \mu \sum_{m=1}^{NY} \sum_{n=1}^{NZ} B_{mn}\, g_{mn}\,(x) \cos \beta_m y \cos \delta_n z$$

$$+ \mu \sum_{m=1}^{NZ} \sum_{n=1}^{NX} C_{mn}\, h_{mn}\,(y) \cos \delta_m z \sin \alpha_n z \tag{12}$$

where

$$f_{mn} = -A_1\, 2\alpha\beta \cos \delta z + [A_2(\bar{\alpha}^2 - \bar{\beta}^2) - A_3\, \delta\bar{\beta} - A_4\, \bar{\alpha}\bar{\delta}] \cos \bar{\delta} z \tag{13}$$

$$g_{mn} = -B_1\, 2\alpha\beta \sin \alpha x + [B_2(\bar{\alpha}^2 - \bar{\beta}^2) - B_3\, \bar{\delta}\bar{\beta} - B_4\, \bar{\alpha}\bar{\delta}] \sin \alpha x \tag{14}$$

$$h_{mn} = -C_1 2\alpha\beta \cos \beta y + [C_2(\bar{\alpha}^2 - \bar{\beta}^2) - C_3\, \bar{\delta}\bar{\beta} - C_4\, \bar{\alpha}\bar{\delta}] \cos \bar{\beta} y \tag{15}$$

Similar linear combinations are taken for the displacements and other stress components. In these series wave numbers and the singly subscripted coefficients A, B, and C are chosen to identically satisfy the shear-stress boundary conditions (equations (3)–(8)). The wave numbers are chosen as follows:

For the A series:

$$\alpha_m = \bar{\alpha}_m = (m-1)\,\frac{\pi}{a}\,; \quad m = 1, 2, 3 \ldots NX \tag{16}$$

Downloaded 02 May 2010 to 171.66.16.246. Redistribution subject to ASME license or copyright; see http://www.asme.org/terms/Terms_Use.cfm

Table 2 Convergence to experimental fundamental beam frequencies

	DIMENSIONS							
CASE	1	2	3	4	5	6	7	8
2a	3.1433	3.1433	3.1433	3.1433	2.5405	2.5405	1.9055	1.9055
2b	2.5404	2.5404	1.9055	1.9055	3.1433	3.1433	3.1433	3.1433
2c	7.882	7.010	7.546	7.249	7.882	7.010	7.546	7.249

		FREQUENCIES							
	CASE	1	2	3	4	5	6	7	8
TERMS	1,1,2	19,362	22,777	18,354	19,442	20,933	24,577	22,206	23,462
	2,2,4	17,539	20,989	16,035	17,057	19,591	23,313	20,909	22,167
	3,3,6	17,191	20,674	15,449	16,500	19,363	23,101	20,691	21,980
	4,4,8	17,076	20,568	15,250	16,308	19,286	23,030	20,617	21,908
	5,5,10	17,023	20,520	15,160	16,221	19,252	22,996	20,583	21,875
	6,6,10	16,995	20,495	15,112	16,175	19,232	22,979	20,565	21,856
	EXP	16,941	20,432	14,983	16,052	19,203	22,934	20,495	21,789

Experimental values labeled "EXP" are from Spinner et al. [12].
Listed dimensions are in centimeters, frequencies are in Hertz.
The transverse direction is the "y" direction ($2b$ dimension).
The numbers listed in the "TERMS" column are the number of terms in the series NX, NY, and NZ, respectively.

$$\beta_n = \bar{\beta}_n = (2n-1)\pi/2b; \quad n=1, 2, 3 \ldots NY \tag{17}$$

For the B series:

$$\beta_m = \bar{\beta}_m = (2m-1)\pi/2b; \quad m=1, 2, 3 \ldots NY \tag{18}$$

$$\delta_n = \bar{\delta}_n = (n-1)\pi/c; \quad n=1, 2, 3 \ldots NZ \tag{19}$$

For the C series:

$$\delta_m = \bar{\delta}_m = (m-1)\pi/c; \quad m=1, 2, 3 \ldots NZ \tag{20}$$

$$\alpha_n = \bar{\alpha}_n = (n-1)\pi/c; \quad n=1, 2, 3 \ldots NX \tag{21}$$

where NX, NY, and NZ are the number of terms in the x, y, and z directions, respectively.

There is an arbitrariness in the choice of the singly subscripted coefficients A, B, and C. A good choice is as follows:

$$A_1 = (\alpha_m^2 + \beta_n^2 - \bar{\delta}_{mn}^2)/\delta_{mn} \sin \delta_{mn} c \tag{22}$$

$$A_2 = 0 \tag{23}$$

$$A_3 = 2\,\alpha_m / \sin \bar{\delta}_{mn}\, c \tag{24}$$

$$A_4 = 2\,\beta_n / \sin \bar{\delta}_{mn}\, c \tag{25}$$

$$B_1 = (\beta_m^2 + \delta_n^2 - \bar{\alpha}_{mn}^2)/\alpha_{mn} \sin \alpha_{mn}\, a \tag{26}$$

$$B_2 = -2\,\beta_m / \sin \bar{\alpha}_{mn}\, a \tag{27}$$

$$B_3 = -2\,\delta_n / \sin \bar{\alpha}_{mn}\, a \tag{28}$$

$$B_4 = 0 \tag{29}$$

$$C_1 = (\delta_m^2 + \alpha_n^2 - \beta_{mn}^2)/\beta_{mn} \cos \beta_{mn}\, b \tag{30}$$

$$C_2 = 2\,\alpha_n / \cos \bar{\beta}_{mn}\, b \tag{31}$$

$$C_3 = 0 \tag{32}$$

$$C_4 = -2\,\delta_m / \cos \bar{\beta}_{mn}\, b \tag{33}$$

With this choice of coefficients and wave numbers it can be seen that the boundary conditions (equations (3), (4)) on τ_{xy} are identically satisfied. The choice also identically satisfies the other boundary conditions on τ_{yz} and τ_{zx}.

The boundary conditions on the normal stress are satisfied by orthogonalization on the boundary as follows:

$$\int_0^c \int_0^b \sigma_x\,(a, y, z) \sin \beta_j\, y \cos \delta_i z\, dydz = 0 \tag{34}$$

where

$$\beta_j = (2j-1)\pi/2b \quad j=1, 2, 3 \ldots NY \tag{35}$$

$$\delta_i = (i-1)\pi/c \quad i=1, 2, 3 \ldots NZ \tag{36}$$

$$\int_0^c \int_0^a \sigma_y\,(x, b, z) \cos \alpha_i x \cos \delta_j z\, dxdz = 0 \tag{37}$$

where

$$\alpha_i = (i-1)\pi/a \quad i=1, 2, 3 \ldots NX \tag{38}$$

$$\delta_j = (j-1)\pi/c \quad j=1, 2, 3 \ldots NZ \tag{39}$$

$$\int_0^b \int_0^a \sigma_z\,(x, y, c) \sin \beta_i y \cos \alpha_i x\, dxdy = 0 \tag{40}$$

where

$$\beta_i = (2i-1)\pi/2b \quad i=1, 2, 3 \ldots NY \tag{41}$$

$$\alpha_j = (j-1)\pi/a \quad j=1, 2, 3 \ldots NX \tag{42}$$

Evaluating the integral in equation (40) gives:

$$\begin{aligned} A_{ji}\left(\frac{ab}{4}\right)\Bigg\{ & \frac{(\alpha_j^2+\beta_i^2-\bar{\delta}_{ij}^2)}{\delta_{ij} \tan \delta_{ij} c}\left(-\frac{\omega^2}{c_1^2}\,\frac{\lambda}{\mu} - 2\delta_{ij}^2\right) \\ & + 4\bar{\delta}_{ij}\,(\alpha_j^2+\beta_i^2)/\tan \bar{\delta}_{ij} c\Bigg\} \\ & + \frac{b}{2}\sum_n^{NZ} B_{in}\Bigg\{\frac{(\beta_i^2+\delta_n^2-\bar{\alpha}_{in}^2)}{\alpha_{in}^2-\alpha_j^2}\left(-\frac{\omega^2}{c_1^2}\,\frac{\lambda}{\mu} - 2\delta_n^2\right) \\ & - \frac{4\delta_n^2\bar{\alpha}_{in}^2}{\bar{\alpha}_{in}^2-\alpha_j^2}\Bigg\}(-1)^j(-1)^n \\ & + \left(\frac{a}{2}\right)^* \sum_m^{NZ} C_{mj}\Bigg\{-\frac{(\delta_m^2+\alpha_j^2-\bar{\beta}_{mj}^2)}{\beta_{mj}^2-\beta_i^2}\left(-\frac{\omega^2}{c_1^2}\,\frac{\lambda}{\mu} - 2\delta_m^2\right) \\ & + \frac{4\delta_m^2\bar{\beta}_{mj}^2}{\bar{\beta}_{mj}^2-\beta_i^2}\Bigg\} \\ & (-1)^i(-1)^m = 0 \end{aligned} \tag{43}$$

Downloaded 02 May 2010 to 171.66.16.246. Redistribution subject to ASME license or copyright; see http://www.asme.org/terms/Terms_Use.cfm

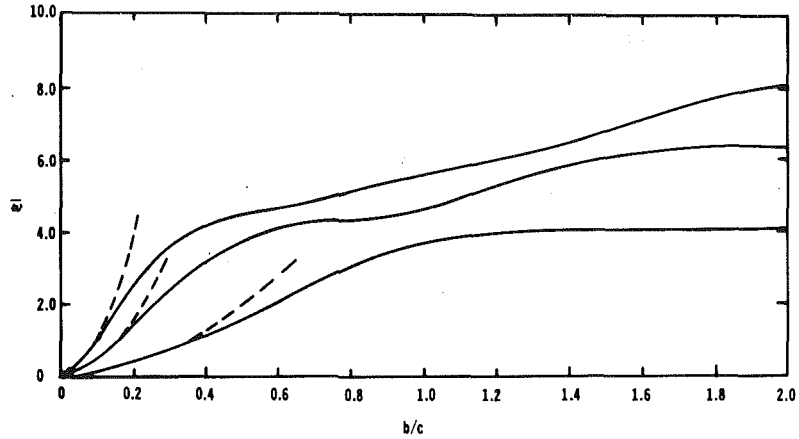

Fig. 2 The first three frequencies of the even beam modes. Transverse displacement is in the *y* direction and is an even function of the length coordinate *z*. $a = b = 0.5$, Poisson's ratio = 0.3, and the length $2c$ varies. (——): the series solution, (····): elementary beam theory.

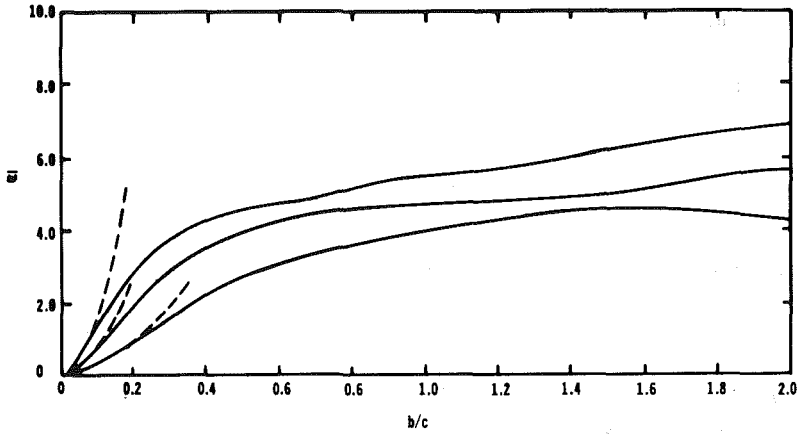

Fig. 3 The first three frequencies of the odd beam modes. Transverse displacement is in the *y* direction and is an odd function of the length coordinate *z*. $a = b = 0.5$, Poisson's ratio = 0.3, and the length $2c$ varies. (——): the series solution; (····): elementary beam theory.

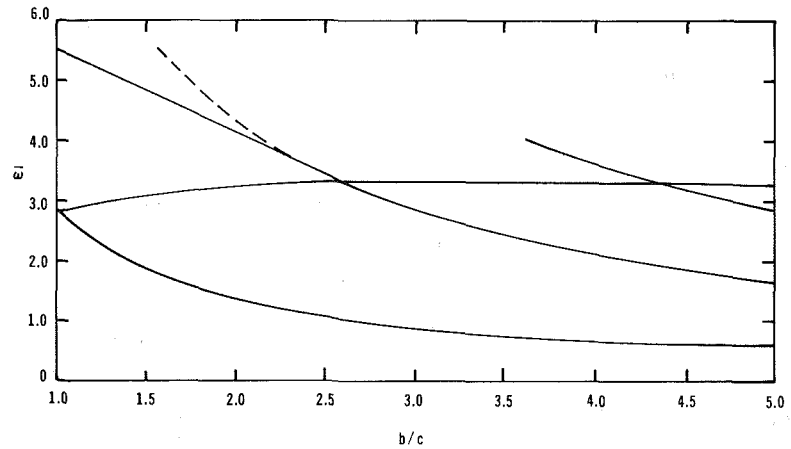

Fig. 4 The first three frequencies of the odd longitudinal modes. Longitudinal displacement is in the *y* direction and is an odd function of the *y* coordinate. $a = c = 0.5$, Poisson's ratio = 0.3, and the longitudinal dimension $2b$ varies. (——): the series solution; (····): one-dimensional bar theory; (—·—·—): one-dimensional bar theory with cross-sectional inertia correction.

where

$$\left(\frac{ab}{4}\right)^{*} = \begin{cases} ab/2 & \text{for } j=1 \\ ab/4 & \text{for } j\neq 1 \end{cases}$$

$$\left(\frac{a}{2}\right)^{*} = \begin{cases} a & \text{for } j=1 \\ a/2 & \text{for } j\neq 1 \end{cases}$$

Evaluating the integral in equation (34) gives:

Downloaded 02 May 2010 to 171.66.16.246. Redistribution subject to ASME license or copyright; see http://www.asme.org/terms/Terms_Use.cfm

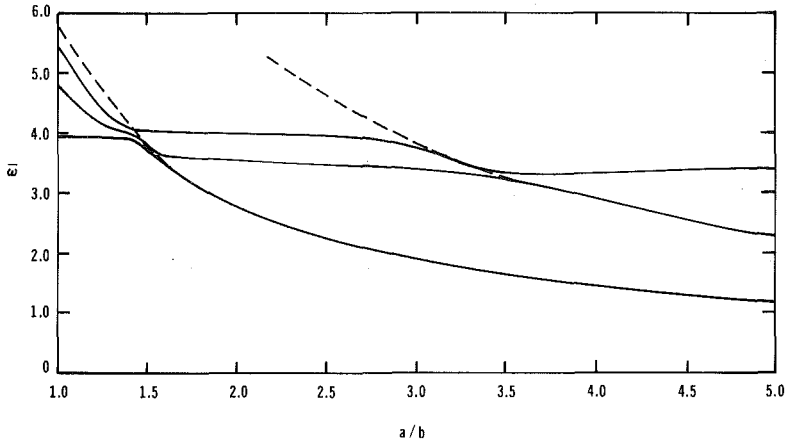

Fig. 5 The first three frequencies of the even longitudinal modes. Longitudinal displacement is in the y direction and is an even function of the y coordinate. a = c = 0.5, Poisson's ratio = 0.3, and the longitudinal dimension 2b varies. (——): the series solution; (— — —): one-dimensional bar theory; (—·—·—·): one-dimensional bar theory with cross-sectional inertia correction.

$$\frac{b}{2}\sum_{m}^{NX} A_{mj}\left[\frac{(\alpha_m^2+\beta_j^2-\bar{\delta}_{mj}^2)}{\delta_{mj}^2-\delta_i^2}\left(-\frac{\omega^2}{c_1^2}\ \frac{\lambda}{\mu}-2\alpha_m^2\right)-\frac{4\alpha_m^2\bar{\delta}_{mj}^2}{\bar{\delta}_{mj}^2-\delta_i^2}\right](-1)^i(-1)^m$$

$$+\left(\frac{bc}{4}\right)^{*} B_{ji}\left\{\frac{(\beta_j^2+\delta_j^2-\bar{\alpha}_{ij}^2)}{\alpha_{ij}\tan\alpha_{ij}a}\left(-\frac{\omega^2}{c_1^2}\ \frac{\lambda}{\mu}-2\alpha_{ij}^2\right)+4\bar{\alpha}_{ij}\ (\beta_j^2+\delta_j^2)/\tan\bar{\alpha}_{ij}a\right\}$$

$$+\left(\frac{c}{2}\right)^{*}\sum_{n}^{NX} C_{in}\left\{-\frac{(\delta_i^2+\alpha_n^2-\bar{\beta}_{in}^2)}{\beta_{in}^2-\beta_j^2}\left(-\frac{\omega^2}{c_1^2}\ \frac{\lambda}{\mu}-2\alpha_n^2\right)+\frac{4\alpha_n^2\bar{\beta}_{in}^2}{\bar{\beta}_{in}^2-\beta_j^2}\right\}(-1)^i(-1)^n=0 \tag{44}$$

where

$$\left(\frac{bc}{4}\right)^{*}=\begin{cases} bc/2 & \text{for } i=1\\ bc/4 & \text{for } i\neq 1\end{cases}$$

$$\left(\frac{c}{2}\right)^{*}=\begin{cases} c & \text{for } i=1\\ c/2 & \text{for } i\neq 1\end{cases}$$

Evaluating the integral in equation (37) gives:

$$\left(\frac{a}{2}\right)^{*}\sum_{n}^{NY} A_{in}\left\{\frac{(\alpha_i^2+\beta_n^2-\bar{\delta}_{in}^2)}{\delta_{in}^2-\delta_j^2}\left(-\frac{\omega^2}{c_1^2}\ \frac{\lambda}{\mu}-2\beta_n^2\right)-\frac{4\beta_n^2\bar{\delta}_{in}^2}{\delta_{in}^2-\delta_j^2}\right\}(-1)^j(-1)^n$$

$$+\left(\frac{c}{2}\right)^{*}\sum_{m}^{NY} B_{mj}\left\{\frac{(\beta_m^2+\delta_j^2-\bar{\alpha}_{mj}^2)}{\alpha_{mj}^2-\alpha_i^2}\left(-\frac{\omega^2}{c_1^2}\ \frac{\lambda}{\mu}-2\beta_m^2\right)-\frac{4\beta_m^2\bar{\alpha}_{mj}^2}{\bar{\alpha}_{mj}^2-\alpha_i^2}\right\}(-1)^i(-1)^m$$

$$+\left(\frac{ac}{4}\right)^{*} C_{ji}\left\{\frac{(\delta_j^2+\alpha_i^2-\bar{\beta}_{ij}^2)}{\beta_{ij}}\tan\beta_{ij}b\left(-\frac{\omega^2}{c_1^2}\ \frac{\lambda}{\mu}-2\beta_{ij}^2\right)+4\bar{\beta}_{ij}(\alpha_i^2+\delta_j^2)\tan\bar{\beta}_{ij}b\right\}=0 \tag{45}$$

where

$$\left(\frac{a}{2}\right)^{*}=\begin{cases} a & \text{for } i=1\\ a/2 & \text{for } i\neq 1\end{cases}$$

$$\left(\frac{c}{2}\right)^{*}=\begin{cases} c & \text{for } j=1\\ c/2 & \text{for } j\neq 1\end{cases}$$

$$\left(\frac{ac}{4}\right)^{*}\begin{cases} ac & \text{for } i=1 \text{ and } j=1\\ ac/2 & \text{for } i=1 \text{ or } j=1\\ ac/4 & \text{for } i\neq 1 \text{ and } j\neq 1\end{cases}$$

Equations (43), (44), and (45) can be put into matrix form. The form in the case when $NX = NY = NZ = 2$ is,

$$\begin{bmatrix} X & O & O & O & X & X & O & O & X & O & X & O\\ O & X & O & O & O & O & X & X & X & O & X & O\\ O & O & X & O & X & X & O & O & O & X & O & X\\ O & O & O & X & O & O & X & X & O & X & O & X\\ X & O & X & O & X & O & O & O & X & X & O & O\\ X & O & X & O & O & X & O & O & O & O & X & X\\ O & X & O & X & O & O & X & O & X & X & O & O\\ O & X & O & X & O & O & O & X & O & O & X & X\\ X & X & O & O & X & O & X & O & X & O & O & O\\ O & O & X & X & O & X & O & X & O & X & O & O\\ X & X & O & O & O & X & O & X & O & O & X & O\\ O & O & X & X & O & X & O & X & O & O & O & X \end{bmatrix}\begin{bmatrix} A_{11}\\ A_{12}\\ A_{21}\\ A_{22}\\ B_{11}\\ B_{12}\\ B_{21}\\ B_{22}\\ C_{11}\\ C_{12}\\ C_{21}\\ C_{22}\end{bmatrix}=\begin{bmatrix} 0\end{bmatrix} \tag{46}$$

Downloaded 02 May 2010 to 171.66.16.246. Redistribution subject to ASME license or copyright; see http://www.asme.org/terms/Terms_Use.cfm

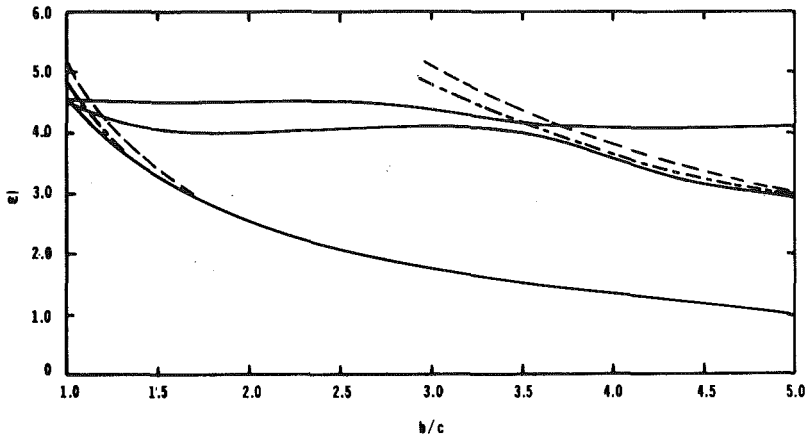

Fig. 6 The first three frequencies of the odd torsional modes. Angular displacement is about the *y* axis and is an odd function of the *y* coordinate. $a = c = 0.5$, Poisson's ratio = 0.3, and the length $2b$ varies. (——): the series solution; (— — — —): one-dimensional bar theory. The first frequency for the series, one-dimensional, and one-dimensional with cross-sectional inertia correction are coincident for the graphical accuracy. The second frequency for the one-dimensional and one-dimensional with cross-sectional inertia correction are coincident for the graphical accuracy.

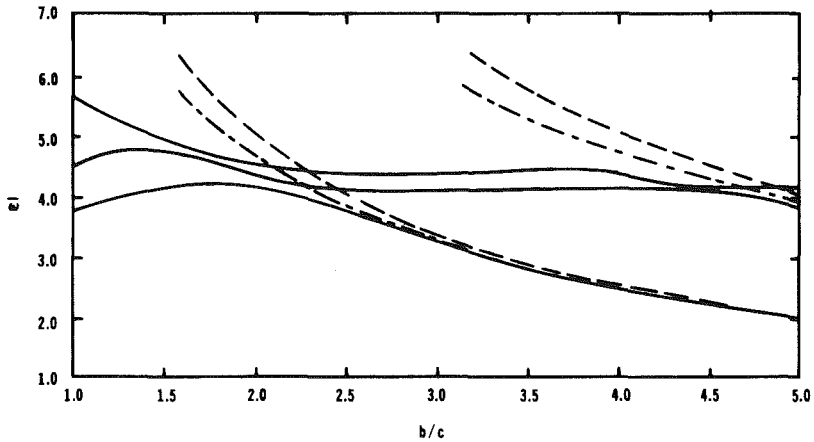

Fig. 7 The first three frequencies of the even torsional modes. Angular displacement is about the *x* axis and is an even function of the *x* coordinate. $b = c = 0.5$, Poisson's ratio = 0.3, and the length $2a$ varies. (——): the series solution; (— — — —): one-dimensional bar theory. The one-dimensional bar theory and one-dimensional bar theory with cross-sectional inertia correction are coincident for the graphical accuracy.

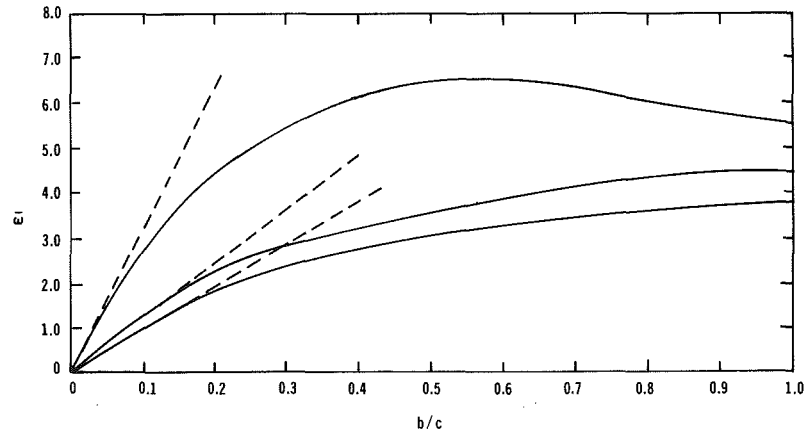

Fig. 8 The first three frequencies of the symmetric-symmetric plate modes. Transverse displacement is in the *y* direction and is an even function of both the coordinates in the plane of the plate, *x* and *z*. $a = c = 0.5$, Poisson's ratio = 0.3, and the thickness $2b$ varies. (——): the series solution; (— — — —): thin plate theory.

Downloaded 02 May 2010 to 171.66.16.246. Redistribution subject to ASME license or copyright; see http://www.asme.org/terms/Terms_Use.cfm

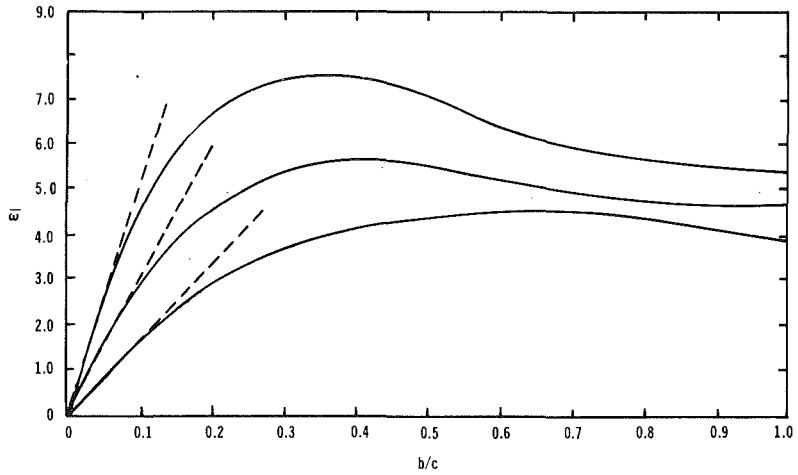

Fig. 9 The first three frequencies of the symmetric-antisymmetric plate modes. Transverse displacement is in the *y* direction and is an even function of the *x* coordinate in the plane of the plate and an odd function of the *z* coordinate in the plane of the plate. $a = c = 0.5$, Poisson's ratio = 0.3, and the thickness $2b$ varies. (——): the series solution; (— — — —): thin plate theory.

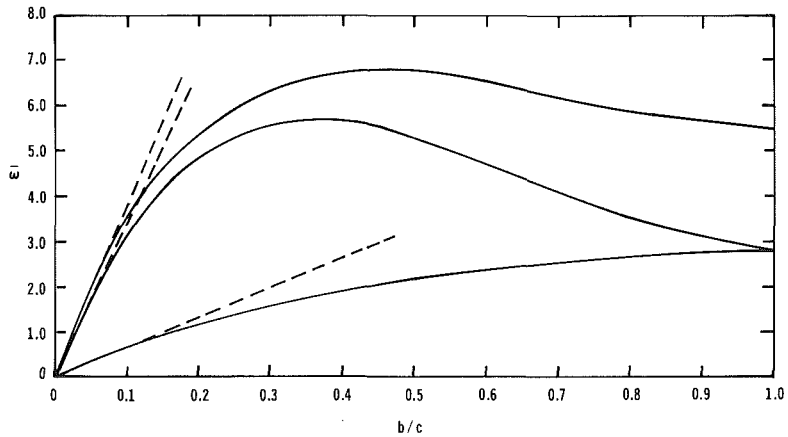

Fig. 10 The first three frequencies of the antisymmetric-antisymmetric plate modes. Transverse displacement is in the *y* direction and is an odd function of both coordinates in the plane of the plate, *x* and *z*. $a = c = 0.5$, Poisson's ratio = 0.3, and the thickness $2b$ varies. (——): the series solution; (— — — —): thin plate theory.

where X's indicate the positions of the nonzero coefficients. For arbitrary numbers of terms in each series the row and column dimensions, ND, for the matrix are,

$$ND = NX \cdot NY + NY \cdot NZ + NX \cdot NZ \tag{47}$$

The coefficients of the matrix in equation (46) are functions of the dimensions, properties, and natural frequency. For chosen dimensions and properties the natural frequencies are those that will make the determinant of the coefficients in equation (46) approach zero.

Results

The equations for all four cases, which include all possible modes of vibration for the rectangular parallelepiped, have been programmed for determination of the natural frequencies on a minicomputer (LSI 11). As in the case of cylinders it was found that for a cube, the convergence was excellent, but as one or two of the dimensions become large compared to the other(s) the rate of convergence diminishes. Increasing the number of terms in the long dimension tends to compensate for the lessening of covergence but does lead to a larger matrix for equivalent accuracy.

Table 2 shows the convergence to the experimental beam frequencies found by Spinner et al. [12]. As can be seen, the frequencies converge from above in a regular fashion to the experimental values as more terms are chosen in the series. Similar comparisons were made to the experimental results of Spence and Seldin [13] and show the same close correlation.

Figures 2–10 are the results of the parameter study. In all of these figures only the lowest three natural frequencies are plotted. The ordinate in all cases is a frequency parameter $\bar{\omega}$ which is defined as

$$\bar{\omega} = \omega / c_2 \tag{48}$$

This frequency could have been made dimensionless by multiplying by one of the characteristic lengths; however, since the appropriate choice of characteristic length would depend on the comparison to be made, the form in equation (48) was considered more practical. The frequency parameter is a function of the lengths, a, b, and c, and Poisson's ratio. For Figs. 2–10 Poisson's ratio was chosen as 0.3.

The convergence for the points plotted in Figs. 2–10 was established by choosing consecutively larger numbers of terms until the answers on consecutive runs were within the accuracy required for plotting purposes. For example if one looks at the answers in Table 2, it is evident that for plotting purposes

Downloaded 02 May 2010 to 171.66.16.246. Redistribution subject to ASME license or copyright; see http://www.asme.org/terms/Terms_Use.cfm

the number of terms could be 4, 4, 8 (*NX*, *NY*, *NZ*, respectively), and even 3, 3, 6 would be adequate. In cases where one of the dimensions approached zero the curves were extrapolated to zero. For instance, in Fig. 2, frequency values were estabished at b/c equal to 0.1, 0.2, 0.3, etc. and the curves were extended to zero at b/c equal to zero.

Figures 2 and 3 show frequencies that correspond to transverse vibrations of a square cross-section beam where the thickness to length ratio is b/c. For these figures the number of terms varied from 2, 2, 20 at b/c equal to 0.1 to 6, 6, 4 at b/c equal to 2.0. Elementary beam solutions are the parabolas shown by the dashed lines, which are asymptotic to the series solutions for small thickness to length ratio b/c.

Figures 4 and 5 show the frequencies that correspond to the longitudinal modes of a rod of square cross section. In these figures b/c represents the length to thickness ratio. For these figures the number of terms varied from 5, 5, 5 at b/c equal to 1.0 to 4, 8, 4 at b/c equal to 5.0. Also shown are the elementary rod solution and the elementary rod solution with a radial inertia correction. The series solutions can be seen to be asymptotic to the elementary solutions as the length to thickness ratio b/c becomes large.

Figures 6 and 7 show the frequencies that correspond to the torsional modes of a rod of square cross section. For these figures, b/c also represents the length to thickness ratio. For Fig. 6 the number of terms varied from 5, 5, 6 at b/c equal to 1.0 to 4, 8, 4 at b/c equal to 5.0. For Fig. 6, the number of terms varied from 5, 5, 5 at at b/c equal to 1.0 to 8, 4, 4 at b/c equal to 5.0. The elementary solution for torsion is shown by dashed lines. The elementatry torsion solution with the axial inertia correction was also calculated, but it did not differ significantly from the elementary solution. Again asymptotic behavior is seen between the series solution and the elementary solution for increasing length ot thickness ratio b/c.

Figures 8–10 show the frequencies that correspond to this square plate behavior. The ratio b/c in these figures is the thickness parameter or thickness to length of side ratio. For Fig. 8 the number of terms varied from 9, 2, 9 at b/c equal to 0.15 to 5, 5, 5 at b/c equal to 1.0. For Figs. 9 and 10 the number of terms was, 5, 5, 5 for the entire range. The elementary plate solutions from reference [10] are shown as dashed lines. The behavior of the series solution is again asymptotic to the elmentary theory as the thickness parameter b/c approaches zero.

Conclusions

It has been demonstrated that this form of series solution leads to the determination of accurate natural frequencies even with the severe limitations placed by the use of a minicomputer on the size and complexity of the numerical manipulations. Solutions have been found for a class of previously unsolved problems in which the rectangular parallelpiped is approximately cubic in shape. The solutions were also shown to be asymptotic to elementary beam and plate solutions as the dimensions approached those appropriate to the elementary theories. The method could thus be used for a basis of comparison for evaluating the accuracy and range of applicability of various higher order approximate theories, such as the Timoshenko beam theory and the Mindlin plate thoery. It could also be used as a basis of comparison for approximate solution methods including finite element and boundary element methods.

References

1 Hutchinson, J. R., "Axisymmetric Vibrations of s Solid Elastic Cylinder Encased in A Rigid Container," *Journal of the Acoustical Society of America*, Vol. 42, 1967, pp. 398–402.

2 Hutchinson, J. R., "Axisymmetric Vibrations of a Free Finite Length Rod," *Journal of the Acoustical Society of America*, Vol. 51, 1972, pp. 233–240.

3 Hutchinson, J. R., "Axisymmetric Flexural Vibrations of a Thick Free Circular Plate," ASME JOURNAL OF APPLIED MECHANICS, Vol. 46, 1979, pp. 139–244.

4 Hutchinson, J. R., "Vibrations of Solid Cylinders," ASME JOURNAL OF APPLIED MECHANICS, Vol. 47, 1980, pp. 901–907.

5 Hutchinson, J. R., "Transverse Vibrations of Beams, Exact Versus Approximate Solutions," ASME JOURNAL OF APPLIED MECHANICS, Vol. 47, 1981, pp. 923–928 .

6 Mindlin, R. D., and Fox, E. A., "Vibrations and Waves in Elastic Bars of Rectangular Cross Section," ASME JOURNAL OF APPLIED MECHANICS, March 1960, pp. 152–158.

7 Meirovitch, L., *Analytical Methods in Vibrations*, Macmillan, New York, 1967.

8 Timoshenko, S. P., "On the Correction for Shear of the Differential Equation for Transverse Vibrations of Prismatic Bars," *Philosophical Magazine*, Vol. 41, 1921, pp. 744–746.

9 Love, A. E. H., *A Treatise on the Mathematical Theory of Elasticity*, Dover, New York, 1944, pp. 428–429.

10 Leissa, A. W., *Vibration of Plates*, NASA SP-160, 1969.

11 Mindlin, R. D., "Influence of Rotary Inertia and Shear on Flexural Motions of Isotropic, Elastic Plates," ASME JOURNAL OF APPLIED MECHANICS, Vol. 18, 1951, pp. 31–38.

12 Spinner, S., Reichard, T. W., and Tefft, W. E., "A Comparison of Experimental and Theoretrical Relations Between Young's Modulus and the Flexural and Longitudinal Resonance Frequencies of Uniform Bars," *Journal of Research*, NBS, Vol. 64A, 1960, pp. 147–155.

13 Spence, G. B., and Seldin, E. J., "Sonic Resonances of a Bar and Compound Torsion Oscillator," *Journal of Applied Physics*, Vol. 41, 1970, pp. 3383–3389.

14 Mathieu, E., *Theorie de l' Elasticite Des Corps Solides*, Gauthier-Villars, Paris, 1890, pp. 140–181.

15 Zillmer, S. D., "Vibrations of a Free Rectangular Parallelepiped," Thesis of Master of Science in Engineering, University of California, Davis, Calif., 1981.

Downloaded 02 May 2010 to 171.66.16.246. Redistribution subject to ASME license or copyright; see http://www.asme.org/terms/Terms_Use.cfm

R. S. Atkatsh
Senior Research Engineer,
Weidlinger Associates,
New York, N.Y. 10001

M. P. Bieniek
Professor,
Department of Civil Engineering,
Columbia University,
New York, N.Y. 10027
Mem. ASME

I. S. Sandler
Partner,
Weidlinger Associates,
New York, N.Y. 10001
Mem. ASME

Theory of Viscoplastic Shells for Dynamic Response

A viscoplastic shell model is formulated that utilizes the shell membrane strains and curvatures as the kinematic variables and the shell stress resultants (membrane forces and moments) as the dynamic variables. The viscoplastic shell model combines the concepts of Perzyna's viscoplastic constitutive equations with Bieniek's shell stress resultant formulation. The model is incorporated into the Elastoplastic Shell Analysis code (EPSA) for the analysis of shells in an acoustic medium subjected to dynamic loadings that produce moderately large elastoviscoplastic deformations in the shell. An example is presented to demonstrate the effect of material rate dependence on structural response.

Introduction

Impact loadings from explosive sources generally deform structural components at high strain rates. These strain rates are manifested via elastoviscoplastic structural response in many materials. This paper discusses the development of an efficient, practical, and theoretically sound method of analyzing the viscoplastic dynamic response of shell structures.

A generalization of the viscoplastic constitutive model as defined by Perzyna [1] has been employed in the formation of a system of equations defining a viscoplastic shell model in the general manner proposed by Bieniek and Funaro [2] for elastoplastic shells. This resulting shell model is then incorporated into the nonlinear finite difference/finite element code EPSA [3, 4]. The shell model utilizes the shell membrane strains and curvatures as the kinematic variables and the shell stress resultants (membrane forces and moments) as the dynamic variables. When compared to the alternative through-the-thickness integration method of calculating stress resultants, this approach offers considerable advantages in terms of both computer storage and speed. Additionally, the model can be fit to experimental data representing various loading combinations (biaxial bending and stretching) at various loading rates on plate and shell specimens.

The qualitative and quantitative aspects of the viscoplastic shell model are presented through an examination of a number of multidimensional loading combinations at various loading rates for a particular material type. The incorporation of the model into the EPSA code is outlined, and a study is presented of the effects of viscoplastic material response on the dynamic behavior of a cylindrical shell in an acoustic medium subjected to impulsive loading.

Contributed by the Applied Mechanics Division for publication in the JOURNAL OF APPLIED MECHANICS.

Discussion on this paper should be addressed to the Editorial Department, ASME, United Engineering Center, 345 East 47th Street, New York, N.Y. 10017, and will be accepted until two months after final publication of the paper itself in the JOURNAL OF APPLIED MECHANICS. Manuscript received by ASME Applied Mechanics Division, February, 1982; final revision, August, 1982.

Material Constitutive Equations

The incorporation of the viscoplastic shell model into the EPSA code for usage in solving three-dimensional, shell-type structural problems required the selection of a general form for the viscoplastic constitutive relations. The representation chosen was based on Perzyna's model [1]. The governing arguments for this selection were:

1 The functional form of the constitutive relations is of sufficient generality so that a broad range of material behavior under impact loading could be represented.

2 Experimental verification by Hayashi and Tanimoto [5] of a Perzyna type formulation for describing the response of annealed aluminum to impulsive torque and tension loadings.

3 Retention by the constitutive model of certain basic elements of the classical theory of plasticity that have proved to be a practical and accurate tool of analysis for elastoplastic structures. In particular, uniqueness arguments of the type made by Drucker [6] are applicable.

4 The model incorporates multidimensional stress-strain states including loading and unloading paths.

5 A shell model formulation could be established incorporating the material constitutive equations.

6 A stable solution scheme for the viscoplastic shell equations could be established.

7 The model is effective in capturing complex material behavior while still being cost-effective from a computational point of view.

The particular case of constitutive relations chosen is that of elastic visco-perfectly plastic material behavior for which the static yield function in stress space is the von Mises yield condition

Copyright © 1983 by ASME
Downloaded 02 May 2010 to 171.66.16.246. Redistribution subject to ASME license or copyright; see http://www.asme.org/terms/Terms_Use.cfm

$$F(s_{ij}) = \frac{1}{2}\frac{s_{ij}s_{ij}}{K^2} - 1 \tag{1}$$

where s_{ij} are the deviatoric stresses, $K = \sigma_0/\sqrt{3}$, and σ_0 is the uniaxial static yield stress.

Perzyna postulated a set of constitutive equations to represent viscoplastic strain hardening behavior for arbitrary loading histories [1]. Included in this specification is the direction of the viscoplastic strain rate and the magnitude of allowable stress beyond the static yield surface.

These relations are mathematically stated as

$$\dot{\epsilon}_{ij}^{p} = \gamma[F]K\Phi[F(s_{ij})]\frac{\partial F}{\partial s_{ij}} = \bar{\lambda}\frac{\partial F}{\partial s_{ij}} \tag{2}$$

where $\gamma[F]$ and $\Phi[F]$ are material functions that can be chosen to represent the results of experimental tests on the dynamic behavior of a particular material. Current available experimental methods consist of one-dimensional stress-strain tests performed using a hydropneumatic machine or a Hopkinson bar technique [7].

Figure 1 shows a one-dimensional yield stress versus strain rate curve. Manjoine [8] states that this "S" shaped curve is typical of metals tested within a given range of strain rates. The particulars of the curve vary for each material type.

An approximation or fit to this characteristic yield stress versus strain rate curves is made by the following expression

$$\dot{\epsilon}_{11}^{p} = a_1 (F)^{1/n_1} + a_2 (F)^{n_2} (F_L - F)^{-n_3} \tag{3}$$

where

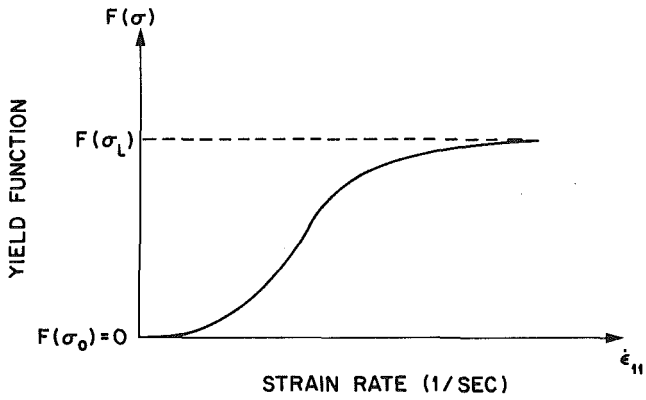

Fig. 1 Yield function versus strain rate; typical behavior for mild steel

$$F_L = \left(\frac{\sigma_L}{\sigma_0}\right)^2 - 1 \tag{4}$$

and σ_L is a limiting one-dimensional yield stress achieved from dynamic tests at the highest of strain rates of interest.

Note that equation (3) can be reduced to either a convex or concave power law (with or without an upper limiting stress) representation of the yield stress versus strain rate behavior.

This one-dimensional experimental data can be represented in Perzyna's formulation by assuming $\Phi[F] = F$ and using a suitable functional form for $\gamma[F]$. Then specializing equation (2) to one-dimensional behavior in terms of the static yield function $F(s_{ij})$

$$\dot{\epsilon}_{11}^{p} = \frac{2}{\sqrt{3}}\gamma F\sqrt{F+1} \tag{5}$$

Equations (3) and (5) state that the material response function $\gamma[F]$ is

$$\gamma[F] = \frac{\sqrt{3}}{2}\left[\frac{a_1}{(F)^{1-1/n_1}\sqrt{F+1}} + \frac{a_2 (F)^{n_2-1}}{(F_L - F)^{n_3}\sqrt{F+1}}\right] \tag{6}$$

The general character of equation (6) is that γ approaches infinity at the asymptotes $F = 0$ and $F = F_L$. This behavior can also be represented by the expression

$$\gamma[F] = \bar{a}_1 F^{-\bar{n}_1} (F_L - F)^{-\bar{n}_2} \tag{7}$$

Appropriate values of the material constants $\bar{a}_1$, $\bar{n}_1$, and $\bar{n}_2$ are determined by curves fitting to one-dimensional stress-strain rate experimental data.

As an illustrative example, the uniaxial behavior of a mild steel [9] within the strain rate range of $(10)^0$ to $(10)^3$ 1/sec is investigated. The curve fit and parameter values using equation (7) are shown in Fig. 2 for the mild steel material.

Shell Constitutive Equations

Shell structures resist external loading by developing internal biaxial forces and moments. Two alternative computational approaches for obtaining these internal resultants are presented.

***(a)* Through-the-Thickness Integration.** The shell stress resultants are obtained by numerically integrating the shell stresses through the thickness of the shell element. For this technique, the time increments of strain at any point of the shell are expressed in terms of the strain and curvature increments of the middle surface.

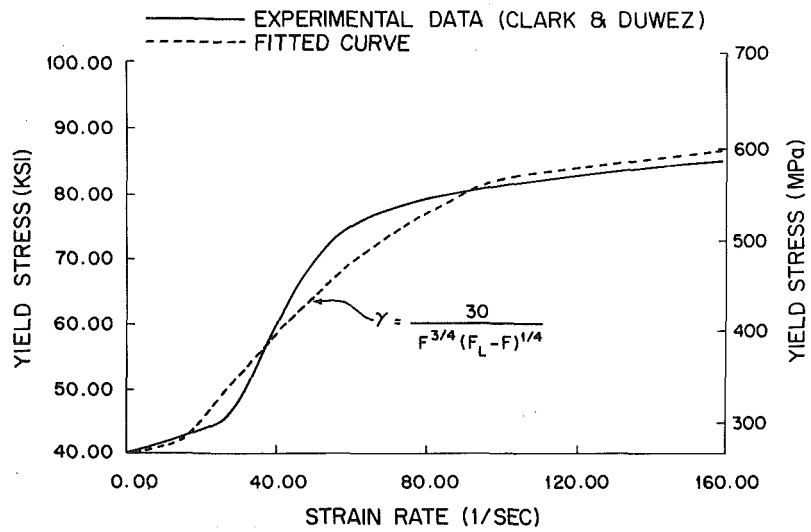

Fig. 2 One-dimensional yield stress versus strain rate; mild steel

Downloaded 02 May 2010 to 171.66.16.246. Redistribution subject to ASME license or copyright; see http://www.asme.org/terms/Terms_Use.cfm

The stress increments $\Delta_N \sigma_{ij}$ are computed from the material constitutive equations

$$\Delta_N \sigma_{ij} = \sigma_{ij}^N - \sigma_{ij}^{N-1} = C_{ijkl} \Delta_N (\epsilon_{kl} - \epsilon_{kl}^p) \tag{8}$$

where σ_{ij}^N is the stress tensor after "N" time increments and C_{ijkl} is the elastic moduli matrix. The total strain increment is separated into elastic and inelastic components. Equation (8) may be interpreted as

$$\sigma_{ij}^N = \bar{\sigma}_{ij} - C_{ijkl} \Delta_N \epsilon_{kl}^p \tag{9}$$

where $\bar{\sigma}_{ij}$ is the stress tensor based on a trial assumption of total elastic behavior occurring within the Nth time step.

Writing the viscoplastic relations (equation (2)) in time incremental fashion

$$\Delta_N \epsilon_{ij}^p = \Delta t \gamma \, KF(\delta_{ij}^N) \frac{\partial F}{\partial \delta_{ij}^N} = \lambda \frac{\partial F}{\partial \delta_{ij}^N} \tag{10}$$

λ is a non-negative variable which must be determined as follows:

$$\lambda = \gamma \Delta t K F(\tilde{\delta}_{ij} - C_{ijkl} \Delta_N \epsilon_{kl}^p) \tag{11}$$

Noting $\partial F / \partial \delta_{ij}^N = \delta_{ij}^N / K^2$ and $C_{ijkl} \delta_{kl} = 2G \, \delta_{ij}$, equation (11) becomes:

$$\lambda = \gamma \Delta t K F\left(\tilde{\delta}_{ij} - \frac{2G\lambda}{K^2} \delta_{ij}^N\right) \tag{12}$$

Equating arguments of function $F(\delta_{ij})$ yields,

$$\delta_{ij}^N = \tilde{\delta}_{ij} / (1 + 2G\lambda / K^2) \tag{13}$$

and

$$\lambda = \gamma \Delta t K \left[\frac{\frac{1}{2} \tilde{\delta}_{ij} \tilde{\delta}_{ij}}{(1 + 2G\lambda/K^2)^2 K^2} - 1 \right] \tag{14}$$

Rearranging equation (14) gives:

$$\left(\frac{4G^2}{K^2}\right)\lambda^3 + \left(\frac{4G}{K^2} + \frac{4G^2 \gamma \Delta t}{K^3}\right)\lambda^2 + \left(1 + \frac{4G\gamma\Delta t}{K}\right)\lambda - \gamma \Delta t K (F(\tilde{\delta}_{ij})) = 0 \tag{15}$$

The real root is extracted from equation (15) with a cubic equation solver.

The shell stress resultants are obtained from the integrals

$$N_{ij} = \int_{-h/2}^{h/2} \sigma_{ij} dZ \quad M_{ij} = \int_{-h/2}^{h/2} \sigma_{ij} Z \, dZ \tag{16}$$

using equation (9).

(*b*) Viscoplastic Shell Model—Direct Formulation. The direct shell model formulation relates the dynamic variables S_k (membrane forces and bending moments) to the kinematic variables e_k (strains and curvatures of the shell's middle surface)

$$S_k = \{N_{11}, \; N_{22}, \; N_{12}, \; M_{11}, \; M_{22}, \; M_{12}\}$$
$$e_k = \{\epsilon_{11}, \; \epsilon_{22}, \; \epsilon_{12}, \; \kappa_{11}, \; \kappa_{22}, \; \kappa_{12}\} \tag{17}$$

The quasi-static shell formulation is derived from that proposed by Bieniek and Funaro [2] for elastoplastic shell analysis. Higher order approximations have been made in the specification of the variable yield surface, the limit surface, and the hardening law, resulting in a more accurate representation of the quasi-static elastoplastic shell behavior.

The quasi-static yield surface in stress resultant space is

$$F(S_k) = I_N + I_N^2 - I_N^3 + I_M^* + 0.8 |I_{NM}| \tag{18}$$

which describes the current yield surface as the loading path moves from an initial yield surface $F_0(S_k)$ toward the limit surface $F_L(S_k)$.

$$F_0(S_k) = I_N + I_M + 2|I_{NM}| \tag{19}$$

$$F_L(S_k) = 2 \, I_N - I_N^2 + \frac{4}{9} I_M \tag{20}$$

where I_N, I_M, and I_M^* are stress resultant invariants defined as

$$I_N \equiv \frac{1}{N_0^2} (N_{11}^2 + N_{22}^2 - N_{11}N_{22} + 3 \, N_{12}^2) \tag{21}$$

$$I_M \equiv \frac{1}{M_0^2} (M_{11}^2 + M_{22}^2 - M_{11}M_{22} + 3 \, M_{12}^2) \tag{22}$$

$$I_{NM} \equiv \frac{1}{N_0 M_0} \left(N_{11}M_{11} + N_{22}M_{22} - \frac{1}{2} N_{11} \, M_{22} - \frac{1}{2} N_{22} M_{11} + 3 \, N_{12} \, M_{12}\right) \tag{23}$$

$$I_M^* = \frac{1}{M_0^2} \left[(M_{11} - M_{11}^*)^2 + (M_{22} - M_{22}^*)^2 - (M_{11} - M_{11}^*)(M_{22} - M_{22}^*) + 3(M_{12} - M_{12}^*)^2\right] \tag{24}$$

and

$$N_0 = \sigma_0 h, \quad M_0 = \sigma_0 h^2 / 6 \tag{25}$$

where σ_0 is the static yield strength.

The quantities M_{ij}^*, which will be referred to as "hardening parameters" are defined by

$$\text{If} \quad F = 1 \quad \text{and} \quad \frac{\partial F}{\partial S_k} \dot{S}_k > 0; \quad \dot{M}_{ij}^* = \beta_{ij} (1 - F_L) \frac{M_0}{\kappa_0} \dot{\kappa}_{ij}^p \tag{26}$$

$$\text{If} \quad F < 1 \quad \text{or} \quad \frac{\partial F}{\partial S_k} \dot{S}_k \leq 0: \quad \dot{M}_{ij}^* = 0$$

The elastic law

$$S_k = E_{kl} (e_l - e_l^p) \tag{27}$$

is used where E_{kl} is the elastic shell stiffness matrix.

In order to generalize the model to include strain rate effects along the lines of equation (2), the plastic strain rate tensor is assumed to depend on the stress resultant intensity through the associated flow rule

$$\dot{e}_k^p = \gamma_R K \Phi[F(S_k)] \frac{\partial F(S_k)}{\partial S_k} = \bar{\lambda} \frac{\partial F(S_k)}{\partial S_k} \tag{28}$$

Solving for λ, one obtains

$$\lambda = \gamma_R \Delta t K \, F\left(\tilde{S}_k - E_{kl} \lambda \frac{\partial F}{\partial S_l}\right) \tag{29}$$

Because equation (29) cannot be solved in closed form for λ, it is solved iteratively using a modified regula falsi method.

γ_R is a physical function that should be chosen to represent the results of multiaxial tests on plate and shell specimens of a particular material. These experiments should consist of biaxial bending and stretching tests conducted at various loading rates of concern. The present lack of such experimental data precludes the possibility of choosing this function to fit measured results. Therefore, at this time, γ_R will be chosen such that the produced stress resultants obtained via the proposed viscoplastic shell model satisfactorily represent those obtained using the through-the-thickness approach for various loading paths.

For the mild steel material [9], previously discussed, the proposed form of the function γ_R is

$$\gamma_R = \frac{\bar{A}_1 [I_N, I_M^*]}{(F_R)^{\bar{n}_1} \left(1 - \left(\frac{\sigma_0}{\sigma_L}\right)^2 F_R\right)^{\bar{n}_2}} \tag{30}$$

Downloaded 02 May 2010 to 171.66.16.246. Redistribution subject to ASME license or copyright; see http://www.asme.org/terms/Terms_Use.cfm

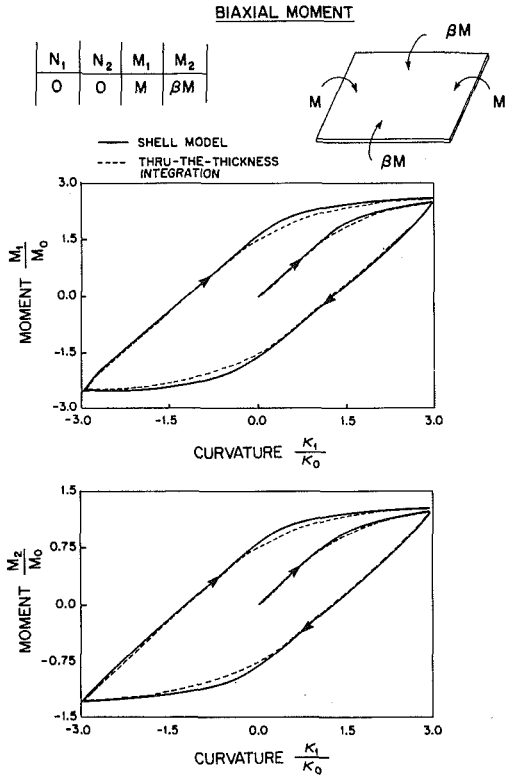

Fig. 3 Viscoplastic shell behavior; moment versus curvature; $\dot{\kappa}_1 h$ = 120 1/sec

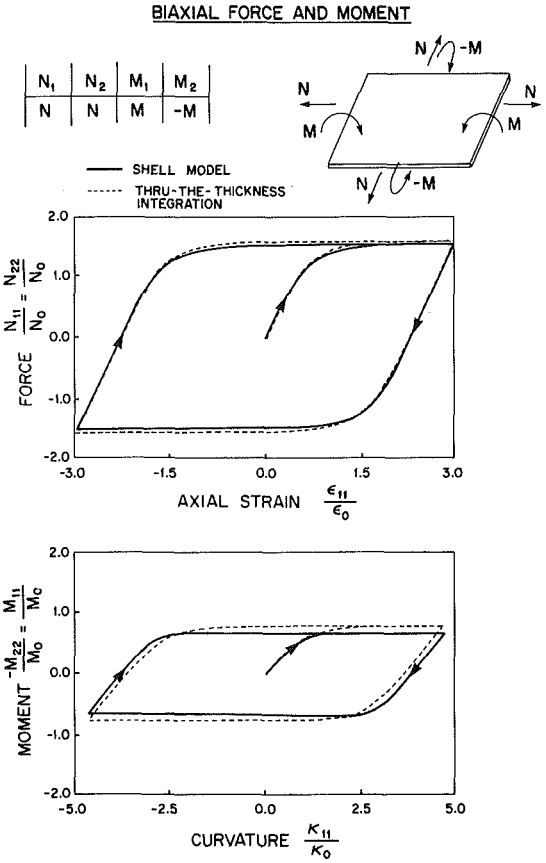

Fig. 4 Viscoplastic shell behavior; loading rate = 120 1/sec

where

$$\bar{A}_1[I_N, I_M^*] = A_1\left(\frac{I_N + A_2 A_3 I_M^*}{I_N + A_3 I_M^*}\right) \tag{31}$$

and

$$F_R = C_1(I_N + I_N^2 - I_N^3) + C_2(I_M^*) + C_3 |I_{NM}| \tag{32}$$

This formulation represents a model with eight parameters ($\bar{n}_1, \bar{n}_2, A_1, A_2, A_3, C_1, C_2, C_3$), whose values are chosen such that the viscoplastic shell model results correspond to the calculated through-the-thickness viscoplastic shell behavior for various loading rates and paths.

Comparison of Through-the-Thickness and Shell Model Results for the Behavior of Mild Steel

Multidimensional structural response involves the determination of biaxial shell forces and moments for various combinations of induced axial and bending strains. With this in mind, a series of loading cases is introduced, with each case reflecting a particular stress state feature.

The multidimensional loading paths chosen include:

(*i*) One-dimensional force;
(*ii*) One-dimensional moment;
(*iii*) Biaxial moments;
(*iv*) Biaxial stress resultant states dominated by a particular force and/or moment component;
(*v*) Equal magnitude biaxial forces and biaxial moments with differing directional (sign) combinations.

Continuing the illustrative example of mild steel behavior, the viscoplastic shell model parameters of equations (30), (31), and (32) were determined such that the shell model results matched the through-the-thickness results for the loading paths listed in the foregoing for loading rates $(10)^0$ to $(10)^3$ 1/sec.

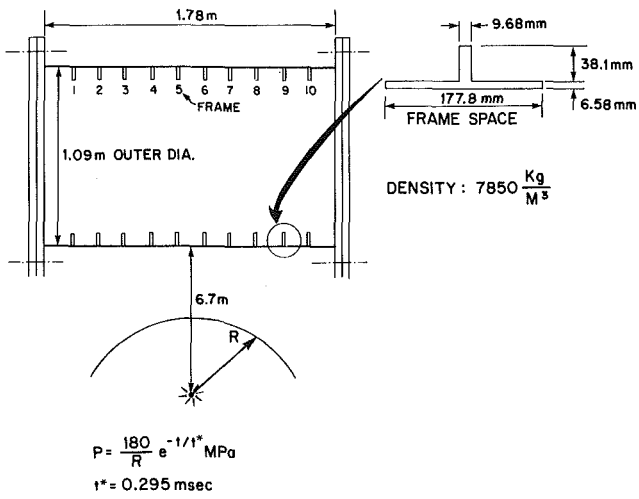

Fig. 5 Stiffened cylindrical shell immersed in an acoustic medium

For the mild steel considered, the determined material constants are

$$\bar{n}_1 = 3/4 \quad \bar{n}_2 = 1/4$$
$$A_1 = 20.0 \quad A_2 = 1.0 \quad A_3 = 1.0$$
$$C_1 = 1.0 \quad C_2 = 0.4 \quad C_3 = 0.8$$

The loading cases represent a variety of biaxial stress resultant states dominated by a particular force and/or moment. Various radial loading paths of stretching ($\Delta\epsilon$) and bending ($\Delta\kappa$) strain increments were prescribed to produce the biaxial stress resultant states $N_1 = N$, $N_2 = \alpha N$, $M_1 = M$, and $M_2 = \beta M$. These loading cases were investigated for loading rates varying from $(10)^0$ to $(10)^3$ 1/sec. For the sake

Downloaded 02 May 2010 to 171.66.16.246. Redistribution subject to ASME license or copyright; see http://www.asme.org/terms/Terms_Use.cfm

of brevity, the loading rate of 120 1/sec is chosen to illustrate the shell model's applicability. Each of the featured cases consists of a cyclic loading curve. The viscoplastic shell model captures the essential features and characteristics of the through-the-thickness integration calculations, as shown in Figs. 3 and 4.

Therefore, for the various loading combinations that can occur in shell structures, it is shown that the model provides a good definition of the viscoplastic shell behavior as determined by the through-the-thickness integration procedure. the selection of suitable but different model parameters should provide the same favorable approximations for other structural metals.

Viscoplastic Shell Analysis Using EPSA

The EPSA code with the inclusion of a viscoplastic shell model was used to investigate the elastoviscoplastic, large deflection, transient response of shell structures. A brief description of the EPSA code is as follows (for details, see references [3, 4]).

The nonlinear shell equations are of the Donnell-Vlasov type for thin shells. The geometric nonlinearities are accounted for in the strain-displacement relations. The structural equations of motion are derived from the principle of virtual work and discretized using a finite element/finite difference technique [10]. The fluid-structure interaction is accounted for by means of the Doubly Asymptotic Approximation expressed in terms of orthogonal fluid expansion functions [11].

The stiffeners are modeled as beam elements. Their axial strain and curvature are determined from the strain compatability conditions at the stiffener-shell interface. The constitutive equations of the stiffeners are obtained by reducing the present shell equations to the case of a single axial force and a single bending moment.

The viscoplastic shell theory is incorporated into the EPSA code rather than the alternative through-the-thickness technique. This is because the shell theory employs less memory parameters per element than the through-the-thickness approach. Also, the solution procedure for the shell model requires approximately 50 percent less computer time than through-the-thickness.

EPSA analyses were performed to determine the response of a stiffened cylindrical shell, constructed of mild steel, immersed in an acoustic medium subjected to pressure loading, Fig. 5. The pressure loading radiates spherically from the source point as shown in Fig. 5.

The EPSA model of the one-quarter shell and stiffeners consists of a 1440 element mesh. Figure 6 illustrates the results of two EPSA analyses, one using an elastoplastic shell model (quasi-static yield strength), the other using a viscoplastic shell model. Figure 6 shows that inclusion of strain rate effects in the analysis reduces the calculated deflection patterns across the length of the shell at the circumferential zero degree line. Preliminary comparison with the available experimental data shows that the analysis based on the elastoviscoplastic shell model results in a much closer approximation of the actual shell behavior.[1]

Conclusions

A method of analysis of the dynamic response of elastoviscoplastic stiffened shell structures has been presented. The shell (and stiffener) constitutive equations have been developed in terms of the shell strain components (strains and curvatures of the middle surface) and the shell stress resultants (membrane forces and bending and torsional moments). The resulting theory has been tested by comparison to the conventional calculations employing through-the-thickness integration of the stress components. The comparison shows good accuracy and exhibits the efficiency of this continuum aproach. Presently, work is being conducted on the extensions of this theory to include materials with arbitrary strain hardening properties under quasi-static loads.

The elastoviscoplastic constitutive equations have been incorporated into a previously developed shell computer code (EPSA), which possesses the capability of dealing with moderately large shell deflections and with the effect of interaction with an acousting medium. An example of a submerged stiffened shell subjected to explosive shock loading is given. It demonstrates the effect of the strain-rate dependence of the material behavior on the response of a structure that is typical for the intended scope of application of this method.

References

1 Perzyna, P., "Fundamental Problems in Viscoplasticity," *Advances in Applied Mechanics*, Vol. 9, 1966, Academic Press, New York, pp. 243-377.

[1] A detailed discussion of the experimental data and the results of this analysis must be presented in a separate report.

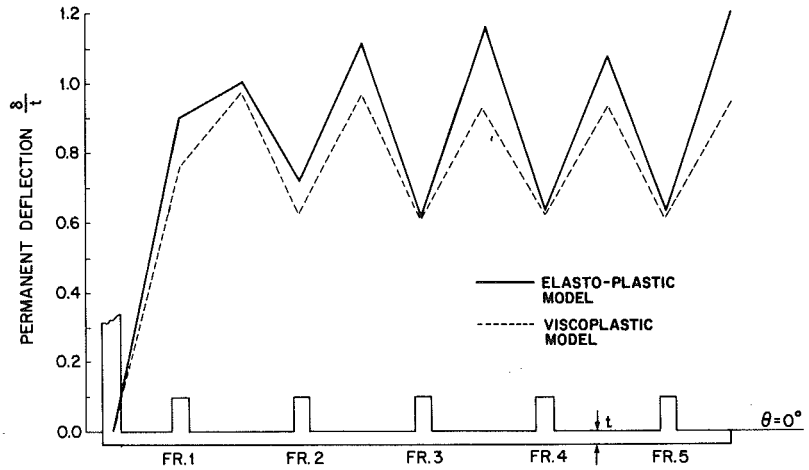

Fig. 6 Permanent deflection of stiffened cylindrical shell subjected to dynamic loading

Downloaded 02 May 2010 to 171.66.16.246. Redistribution subject to ASME license or copyright; see http://www.asme.org/terms/Terms_Use.cfm

2 Bieniek, M. P., and Funaro, J. R., "Elasto-Plastic Behavior of Plates and Shells," Report No. DNA 3945T, Weidlinger Associates, New York, Mar. 1976.

3 Atkatsh, R., Bieniek, M. P., and Baron, M. L., "Dynamic Elasto-Plastic Response of Shells in an Acoustic Medium-EPSA Code," accepted for Publication in the *International Journal for Numerical Methods in Engineering*, Mar. 1982.

4 Atkatsh, R., and Daddazio, R. P., "Dynamic Elasto-Plastic Response of Shells in an Acoustic Medium—Users Manual for the EPSA Code," Technical Report No. 27, Weidlinger Associates, New York, Mar. 1980.

5 Hayashi, T., and Tanimoto, N., "Behavior of Materials Under Dynamic Combined Stresses of Torsion and Tension," IUTAM Symposium, *High Velocity of Solids*, Springer-Verlag, New York, 1978.

6 Drucker, D., "On Uniqueness in the Theory of Plasticity," *Q. Appl. Math.*, Vol. 14, 1956, pp. 35-42.

7 Lindholm, U. S., "Review of Dynamic Testing Techniques and Material Behavior," Conference on Mechanical Properties of Materials at High Rates of Strain, Institute of Physics, London, 1974.

8 Manjoine, M. J., "Effect of Rate of Strain on the Flow Stress of Gas Turbine Alloys at 1200 and 1500 F," *Proc. Amer. Soc. Testing Materials*, Vol. 50, 1950, pp. 931-947.

9 Clark, D. S., and Duwez, P. E., "The Influence of Strain Rate on Some Tensile Properties of Steel," *Proc. Amer. Soc. Testing Materials*, Vol. 50, 1950, pp. 560-575.

10 Atkatsh, R. S., Bieniek, M. P., and Baron, M. L., "A Finite Difference Variational Method for Bending of Plates," *Computers and Structures*, Vol. 11, 1980, pp. 573-577.

11 Bleich, H. H., DiMaggio, F. L., Baron, M. L., and Ranlet, D., "Transient Response of Submerged Shells of Finite Length to Full Envelopment Type Shock Waves, Part I: Acoustic Approximations for Uncoupling Fluid-Structure Interaction Problem," Technical Report No. 13, Weidlinger Associates, New York, July 1974.

Downloaded 02 May 2010 to 171.66.16.246. Redistribution subject to ASME license or copyright; see http://www.asme.org/terms/Terms_Use.cfm

A Linear Theory for Pretwisted Elastic Beams

S. Krenk
Risø National Laboratory,
Roskilde, Denmark

A linear theory for pretwisted elastic beams subjected to general loads is developed from the potential energy functional. The longitudinal strain distribution is that of a similar beam without pretwist supplemented by terms from the warping function and its longitudinal derivative. The paper contains a general system of differential equations and gives explicit solutions for homogenous extension, torsion, and bending. The theory accounts explicitly for the shear center, the elastic center, and the axis of pretwist. The resulting torsion-extension coupling is in agreement with a recent asymptotic result from three-dimensional elasticity apart from the limitation imposed by neglecting deformations of the cross sections in their own plane.

1 Introduction

Beams of a shape generated by rotating an approximately constant cross section along the axis of the beam find wide application in rotors, and their static and dynamic behavior is therefore of considerable interest. A full three-dimensional analysis is complicated on account of the helical shape of the boundary generators, and it is therefore desirable to have a beam theory that accounts specifically for the pretwist of the beam. In such a theory one would expect a coupling between torsion and extension—the beam untwists in extension—and also some influence on the flexibility in extension, torsion, and bending is to be expected. The torsion-extension coupling is an odd function of the rate of pretwist, and the leading term may serve to identify the governing mechanism of the coupling.

It turns out that an explicit formula for the leading term of the torsion-extension coupling of a pretwisted isotropic beam can be derived from the full three-dimensional equations of elasticity, Krenk [1]. This result is obtained by equating external and internal work and therefore takes the form of an integral over the cross section. The form of the integral is interesting in the following respects. The coupling is the sum of two terms, one due to longitudinal strains created by the mismatch of the warped sections due to pretwist, and another created by local rotations in the cross sections if the elastic center is not on the axis of pretwist. While the second term clearly reflects the influence of the deformations of the cross sections in their own plane, an effect usually ignored in technical beam theories, the first term shows the coupling mechanism to be a mismatch of the warped sections. Furthermore in the leading term this mismatch is represented by the longitudinal derivative of the St. Venant warping function of a similar cross section in a beam without pretwist.

This discussion leads to the following conclusions concerning the foundation of technical theories for pretwisted beams. In order to contain the correct leading term of the torsion-extension coupling, a beam theory must include warping and make use of its longitudinal derivative to define strain. On the other hand, quadratic terms in the rate of pretwist, necessary to evalate changes in flexibility, appear to require the solution of additional boundary value problems for the cross section. If this possibility is excluded—e.g., for reasons of economy or complexity—the effect of pretwist appears through the longitudinal derivative of the St. Venant warping function.

In this paper a linear theory for pretwisted elastic beams under general loads is developed by assuming that the cross sections are only deformed in the longitudinal direction of the beam, and that this deformation is described by the warping function from homogeneous torsion of a similar beam without pretwist. Similar assumptions lie behind the works of Rosen [2] and Hodges [3] treating the special cases of homogeneous torsion and extension, respectively. The basic assumptions as well as the resulting equations are different from those associated with an assumption of "helical fibers," Houbolt and Brooks [4], Krenk and Gunneskov [5]. Thus the present approach consistently accounts for circular and nearly circular cross sections.

The differential equations of the theory are derived from the potential energy and thus follow solely from the assumed displacement field. By this process stress boundary conditions are not satisfied locally on the curved surface. In homogeneous loading this error is quadratic in the rate of pretwist, but, for example, in nonhomogeneous torsion an error is present even in the absence of pretwist. The elastic properties of the material only appear as the two factors E and G, where the present use of G implies transverse isotropy with respect to the axis of pretwist. A more general form of the elastic energy density would allow helical axies of

Contributed by the Applied Mechanics Division for presentation at the 1983 Applied Mechanics, Bioengineering, and Fluids Engineering Conference, Houston, Texas, June 20–22, 1983 of THE AMERICAN SOCIETY OF MECHANICAL ENGINEERS.

Discussion on this paper should be addressed to the Editorial Department, ASME, United Engineering Center, 345 East 47th Street, New York, N.Y. 10017, and will be accepted until two months after final publication of the paper itself in the JOURNAL OF APPLIED MECHANICS. Manuscript received by ASME Applied Mechanics Division, January, 1982; final revision, June 1982. Paper No. 83-APM-9.

Copies will be available until February, 1984.

Copyright © 1983 by ASME
Downloaded 02 May 2010 to 171.66.16.246. Redistribution subject to ASME license or copyright; see http://www.asme.org/terms/Terms_Use.cfm

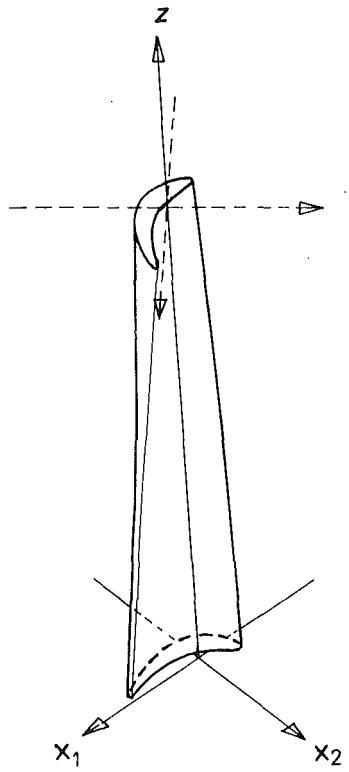

Fig. 1 Coordinate system

anisotropy, but this is independent of the coordinates used in the calculations.

After the sectional constants, the generalized loads, and the equilibrium equations have been derived, explicit solutions are found for homogeneous extension, torsion, and bending. All coupling terms depend on the longitudinal derivative of the warping function and therefore vanish for circular cross sections. An additional coupling due to material anisotropy could be introduced through the elastic energy density. The theory accounts specifically for the position of the shear center and the elastic center with respect to the axis of pretwist. Finally the relation between the present theory, that of "helical fibers," and asymptotic results from three-dimensional elasticity is discussed.

2 Some Concepts from Cylindrical Beams

The beam is described in a $\{x_\alpha, z\}$ coordinate system, $\alpha = 1,2$, with the z-axis as the axis of the beam, Fig. 1. Each cross section is assumed to remain undeformed, and the displacement vector u_α can therefore be written in terms of generalized displacements $\xi_\alpha(z)$ and $\phi(z)$.

$$u_\alpha = \xi_\alpha - e_{\alpha\beta}x_\beta\phi = (\xi_\alpha - e_{\alpha\beta}a_\beta\phi) - e_{\alpha\beta}(x_\beta - a_\beta)\phi \qquad (2.1)$$

$e_{\alpha\beta}$ is the permutation symbol, and summation over repeated indices is implied. While the first form of (2.1) is in terms of the displacement ξ_α of the point $x_\alpha = 0$, the second form is written in terms of the displacement $(\xi_\alpha - e_{\alpha\beta}a_\beta\phi)$ of a pole a_β of the cross section. In order to separate bending and torsion the pole a_β should be chosen to be the shear center as defined in equations (2.10) and (2.11). The displacement component w is assumed to be of the form

$$w = \zeta - x_\alpha(\xi'_\alpha - e_{\alpha\beta}a_\beta\phi') - \omega\theta \qquad (2.2)$$

where $\zeta(z)$ and $\theta(z)$ are generalized displacements, and a prime denotes differentiation with respect to z. $\omega(x_\alpha)$ is the warping function of the section associated with homogeneous torsion.

The strains following from (2.1) and (2.2) in the case of a cylindrical beam are

$$\epsilon_{\alpha\beta} = \frac{1}{2}(u_{\alpha,\beta} + u_{\beta,\alpha}) = 0 \qquad (2.3)$$

$$\epsilon = w' = \zeta' - x_\alpha(\xi'_\alpha - e_{\alpha\beta}a_\beta\phi')' - \omega\theta' \qquad (2.4)$$

$$\gamma_\alpha = u'_\alpha + w_{,\alpha} = -\mathrm{m}_{,\alpha}\theta - e_{\alpha\beta}(x_\beta - a_\beta)\phi' \qquad (2.5)$$

according to the small strain definition. In the case of homogeneous torsion $\theta = \phi' = \text{const.}$, and the normalized shear strain $\tilde{\gamma}_\alpha$ is defined from (2.5).

$$\tilde{\gamma}_\alpha = -\omega_{,\alpha} - e_{\alpha\beta}(x_\beta - a_\beta) \qquad (2.6)$$

The general shear strain (2.5) can then be expressed as

$$\gamma_\alpha = \tilde{\gamma}_\alpha\theta - e_{\alpha\beta}(x_\beta - a_\beta)(\phi' - \theta) \qquad (2.7)$$

The normalized shear strain $\tilde{\gamma}_\alpha$ is related to the normalized shear stress $\tilde{\tau}_\alpha$, that can be be derived from a stress function Φ.

$$\tilde{\tau}_\alpha = G\,\tilde{\gamma}_\alpha = e_{\alpha\beta}\,\Phi_{,\beta} \qquad (2.8)$$

As is well known, the differential equation for Φ follows from application of the operator $e_{\alpha\gamma}\partial_\gamma$ to (2.6).

$$(G^{-1}\Phi_{,\alpha})_{,\alpha} = -2 \qquad (2.9)$$

The boundary conditions are $\Phi = \Phi_j = \text{const.}$ on each boundary contour. For convenience $\Phi \equiv 0$ on the outer contour.

The warping function $\omega(x_\alpha)$ follows from integration of (2.6), and the integration constant as well as the location of the pole a_β can be determined by specifying that $\omega(x_\alpha)$ shall be orthogonal to the normal stress distributions from stretching and bending, i.e.,

$$\int_A \omega E dA = 0 \qquad (2.10)$$

$$\int_A x_\alpha \omega E dA = 0 \qquad (2.11)$$

3 Pretwisted Beams

In the case of pretwisted beams each section is rotated through the angle βz, Fig. 1. The displacements are assumed in the form (2.1) and (2.2), and the strains in the $\{x_\alpha, z\}$ system are used. This leaves (2.3) and (2.5) unchanged, while the normal strain ϵ now includes an extra term, because the warping function ω rotates with the section.

$$\epsilon = \zeta' - x_\alpha(\xi'_\alpha - e_{\alpha\beta}a_\beta\phi')' - \omega\theta' - \omega'\theta \qquad (3.1)$$

The function ω' follows from the rotation of ω.

$$\omega' = -\beta x_\alpha e_{\alpha\beta}\omega_{,\beta} \qquad (3.2)$$

When $\omega_{,\beta}$ is eliminated by use of (2.6),

$$\omega' = -\beta[x_\alpha(x_\alpha - a_\alpha) - x_\alpha e_{\alpha\beta}\tilde{\gamma}_\beta] \qquad (3.3)$$

In [4] Houbolt and Brooks introduced the effect of pretwist on the longitudinal strain without consideration of warping through the term $\beta x_\alpha x_\alpha \phi'$. The term (3.3) differs both in the explicit dependence on the pole (shear center) and in the dependence on the torsional shear strain distribution. As pointed out by Rosen [2] the latter term makes the present approach consistent in the case of a circular cylinder.

The equilibrium equations for the beam are derived from the potential energy, and it is observed that the strain energy does not depend on ξ''_α explicitly but on η'_α, where

$$\eta_\alpha = \xi'_\alpha - e_{\alpha\beta}a_\beta\phi' \qquad (3.4)$$

With this notation the strain energy takes the form

$$U_i = \frac{1}{2}\int_L\int_A (E\epsilon^2 - G\gamma_\alpha\gamma_\alpha)\,dA\,dz$$

$$= \frac{1}{2}\int_L\int_A \{E(\zeta' - x_\alpha\eta'_\alpha - \omega\theta' - \omega'\theta)^2 + G|\tilde{\gamma}_\alpha\theta - e_{\alpha\beta}(x_\beta - a_\beta)(\phi' - \theta)|^2\}\,dA\,dz \qquad (3.5)$$

Downloaded 02 May 2010 to 171.66.16.246. Redistribution subject to ASME license or copyright; see http://www.asme.org/terms/Terms_Use.cfm

Table 1 Sectional constants

$$F=\int_A EdA \qquad S_\alpha=\int_A x_\alpha EdA$$

$$I_{\alpha\beta}=\int_A x_\alpha x_\beta EdA \qquad I_{\omega\omega}=\int_A \omega^2 EdA$$

$$I_r{}^2=\int_A r^2 EdA \qquad I_r{}^2{}_\alpha=\int_A r^2 x_\alpha EdA$$

$$I_r{}^4=\int_A r^4 EdA \qquad I_r{}^4=\int_A R^2 GdA$$

$$S_{\omega'}=\int_A \omega' EdA=-\beta(I_r{}^2-a_\alpha S_\alpha)$$

$$I_{\omega'\alpha}=\int_A \omega' x_\alpha EdA=-\beta(I_r{}^2{}_\alpha-a_\beta I_{\alpha\beta})$$

$$I_{\omega'\omega}=\int_A \omega'\omega EdA=-\beta\int_A r^2\omega EdA=-\beta I_r{}^2{}_\omega$$

$$I_{\omega'\omega'}=\int_A \omega'\omega' EdA=\beta^2(I_r{}^4+a_\alpha I_{\alpha\beta}a_\beta-2I_r{}^2{}_\alpha a_\alpha)$$

$$K=\int_A \tilde{\gamma}_\alpha\tilde{\gamma}_\alpha GdA=2\int_{A_0}\Phi dA$$

The integrations over A are independent of the generalized displacements, and can therefore be carried out for any given cross section. In particular, simplification of two of the integrals weighted with G are possible. Introduce the sectional constant K as the moment of $\tilde{\tau}_\alpha$ with respect to the pole a_β.

$$\begin{aligned}K&=-\int_A G\tilde{\gamma}_\alpha e_{\alpha\beta}(x_\beta-a_\beta)dA\\&=-\int_A \Phi_{,\beta}(x_\beta-a_\beta)dA\\&=-\sum_j \Phi_j\oint C_j(x_\beta-a_\beta)n_\beta^j ds+2\int_A \Phi dA\\&=2\sum_j \Phi_j A_j^{(i)}+2\int_A \Phi dA\end{aligned}\tag{3.6}$$

Here the stress function Φ from (2.8) has been introduced, and the integral reformulated by use of Gauss' theorem. C_j are the inner contours, and $A_j^{(i)}$ the areas enclosed by the contours C_j. Thus by (3.6) K is twice the volume contained by Φ within the outer contour C_o—i.e., the ordinary torsional modulus. Another necessary integral is

$$\begin{aligned}\int_A G\tilde{\gamma}_\alpha\tilde{\gamma}_\alpha dA&=-\int_A \tilde{\tau}_\alpha(\omega_{,\alpha}+e_{\alpha\beta}(x_\beta-a_\beta))dA\\&=-\int_A \omega_{,\alpha}e_{\alpha\beta}\Phi_{,\beta}dA+K\\&=\sum_j \Phi_j\oint C_j d\omega+K=K\end{aligned}\tag{3.7}$$

where the last equality follows from the uniqueness of the warping function ω.

It is convenient to introduce the notation

$$R^2=(x_\alpha-a_\alpha)(x_\alpha-a_\alpha)\tag{3.8}$$

$$r^2=x_\alpha x_\alpha-x_\alpha e_{\alpha\beta}\tilde{\gamma}_\beta\tag{3.9}$$

The strain energy (3.5) can then be written in the form

Table 2 Generalized loads

$$p_\alpha=\int_A q_\alpha dA \qquad p=\int_A qdA$$

$$m_\alpha=-\int_A x_\alpha qdA \qquad m=\int_A x_\alpha e_{\alpha\beta}q_\beta dA$$

$$b=-\int_A \omega qdA$$

$$\begin{aligned}U_i=\frac{1}{2}\int_L\{&F(\zeta')^2+I_{\alpha\beta}\eta_\alpha'\eta_\beta'+I_{\omega\omega}(\theta')^2+I_{\omega'\omega'}\theta^2\\&-2S_\alpha\zeta'\eta_\alpha'-2S_{\omega'}\zeta'\theta+2I_{\omega'\alpha}\eta_\alpha'\theta+2I_{\omega'\omega}\theta\theta'\\&+(I_R{}^2-K)(\phi'-\theta)^2+K(\phi')^2\}dz\end{aligned}\tag{3.10}$$

where the sectional constants are given in Table 1. It should be noted that Kollbrunner and Hajdin [6] in their treatment of cylindrical beams of thin-walled closed section impose a local assumption on the direction of the shear stress, and the following integration then leads to a different definition of the sectional constant $I_R{}^2$.

At this point it may be of interest to interject an alternative form of the sectional constant $S_{\omega'}$ for a beam with constant E and G. By use of (3.3), (3.6), and (3.8)

$$S_{\omega'}=-\beta\left[\frac{E}{G}(I_R{}^2-K)+a_\alpha(S_\alpha-a_\alpha F)\right]\tag{3.11}$$

When the shear center a_α is also the elastic center, e.g., in the case of a doubly symmetric cross section, the last term vanishes, and $S_{\omega'}=-\beta(I_R{}^2-K)E/G$. This is the form in which the coupling between extension and torsion appears in the result of Hodges [3].

The external work is

$$U_e=\int_L(p_\alpha\xi_\alpha+p\zeta+m_\alpha\eta_\alpha+m\phi+b\theta)dz\tag{3.12}$$

where the generalized loads are defined in Table 2 in terms of volume forces $\{q_\alpha,q\}$.

The equilibrium equations and the boundary conditions follow from variations of the potential energy $U=U_i-U_e$ with respect to the generalized displacements. After integration by parts the first variation takes the form

$$\begin{aligned}\delta U=\int_L\{&-(N'+p)\delta\zeta-(Q_\alpha'+p_\alpha)\delta\xi_\alpha\\&-(B'+M_w-M_{\omega'}+b)\delta\theta\\&-((M_S+M_w+a_\alpha e_{\alpha\beta}Q_\beta)'+m)\delta\phi\}dz\\&+[N\delta\zeta+Q_\alpha\delta\xi_\alpha+M_\alpha\delta\eta_\alpha+B\delta\theta+(M_S\\&+M_w+a_\alpha e_{\alpha\beta}Q_\beta)\delta\phi]\end{aligned}\tag{3.13}$$

where the generalized forces are defined in Table 3.

The equilibrium equations follow from the integrand,

$$N'+p=0\tag{3.14}$$

$$Q_\alpha'+p_\alpha=0\tag{3.15}$$

$$B'M_w-M_{\omega'}+b=0\tag{3.16}$$

$$(M_S+M_w+a_\alpha e_{\alpha\beta}Q_\beta)'+m=0\tag{3.17}$$

The boundary conditions are chosen from the products in the brackets. It is noted that $\delta\xi_\alpha'$ and $\delta\phi'$ only occur in the combination $\eta_{\alpha'}$ leaving three scalar and two vector boundary conditions.

4 Homogeneous Loading

When a beam with constant cross section apart from a uniform pretwist is subjected to constant N, M, or M_α, the

Downloaded 02 May 2010 to 171.66.16.246. Redistribution subject to ASME license or copyright; see http://www.asme.org/terms/Terms_Use.cfm

Table 3 Generalized forces

$$N = F\zeta' = S_\alpha \eta'_\alpha - S_{\omega'}\theta = \int_A \epsilon E dA$$

$$M_\alpha = -S_\alpha \zeta' + I_{\alpha\beta}\eta'_\beta + I_{\omega'\alpha}\theta = -\int_A x_\alpha \epsilon E dA$$

$$M_{\omega'} = -S_{\omega'}\zeta' + I_{\omega'\alpha}\eta'_\alpha + I_{\omega'\omega}\theta' + I_{\omega'\omega'}\theta = -\int_A \omega' \epsilon E dA$$

$$B = I_{\omega\omega}\theta' + I_{\omega'\omega}\theta = -\int_A \omega \epsilon E dA$$

$$M_w = (I_R^2 - K)(\phi' - \theta) \qquad M_S = K\phi'$$

$$Q_\alpha = -(M'_\alpha + m_\alpha) \qquad M = M_S + M_w + a_\alpha e_{\alpha\beta} Q_\beta$$

stress distribution according to the present theory can be found explicitly. It is convenient to treat the scalar loads N from M separately from the vectorial load M_α.

In the case of constant tension and torsion θ and ϕ' are constants, related through

$$M = M_S + M_w = I_R^2 \phi' - (I_R^2 - K)\theta \tag{4.1}$$

The equilibrium equation (3.16) with $B' = 0$ then gives

$$M_{\omega'} = M_w = \left(1 - \frac{K}{I_R^2}\right)(M - K\theta) \tag{4.2}$$

The factor in (4.2) occurs repeatedly and will be denoted by κ, i.e.,

$$\kappa = \left(1 - \frac{K}{I_R^2}\right) \tag{4.3}$$

where $0 < \kappa < 1$. For thin-walled open sections $\kappa \simeq 1$. The case of pure tension gives an interpretation of κ. In that case it follows from (4.1) that $\phi' = \kappa\theta$, and thus the warping intensity θ can not in general be identified with the rate of twist ϕ'. It now follows from the definitions of N, M, and M_ω, in Table 3 that

$$F\zeta' - S_\alpha \eta'_\alpha - S_{\omega'}\theta = N \tag{4.4}$$

$$-S_\alpha \zeta' + I_{\alpha\beta}\eta'_\beta + I_{\omega'\alpha}\theta = 0 \tag{4.5}$$

$$-S_{\omega'}\zeta' + I_{\omega'\alpha}\eta'_\alpha + (I_{\omega'\omega'} + \kappa K)\theta = \kappa M \tag{4.6}$$

In order to obtain the solution in a convenient form the sectional constants S_α, $I_{\alpha\beta}$, and $I_{\omega'\alpha}$ are referred to the elastic center c_α by the transformations

$$S_\alpha = F c_\alpha \tag{4.7}$$

$$I_{\alpha\beta} = I^c_{\alpha\beta} + F c_\alpha c_\beta \tag{4.8}$$

$$I_{\omega'\alpha} = I^c_{\omega'\alpha} + S_{\omega'} c_\alpha \tag{4.9}$$

This transformation does not change the definition of ω and ω'. From a combination of (4.4) and (4.5)

$$I^c_{\alpha\beta}\eta'_\beta = c_\alpha N - I^c_{\omega'\alpha}\theta \tag{4.10}$$

The solution is expressed in terms of the inverse of $I^c_{\alpha\beta}$, here called $J^c_{\alpha\beta}$.

$$\eta'_\alpha = J^c_{\alpha\beta}(c_\beta N - I^c_{\omega'\beta}\theta) \tag{4.11}$$

When η'_α is eliminated from (4.4) and (4.6), the resulting equations in ζ' and θ are readily solved. The determinant is

$$D = F(\kappa K + I_{\omega'\omega'} - I^c_{\omega'\alpha}J^c_{\alpha\beta}I^c_{\omega'\beta}) - S^2_{\omega'} \tag{4.12}$$

and the solution in terms of ζ' and ϕ' is

$$\zeta' = \frac{\kappa F}{D}\left\{\frac{S_{\omega'}}{F} - I^c_{\omega'\alpha}J^c_{\alpha\beta}c_\beta\right\}M + \left\{\frac{1}{F} + c_\alpha J^c_{\alpha\beta}c_\beta + \frac{1}{D}\left[I^c_{\omega'\alpha}J^c_{\alpha\beta}I^c_{\omega'\beta} + F\left(\frac{S_{\omega'}}{F} - I^c_{\omega'\alpha}J^c_{\alpha\beta}c_\beta\right)^2\right]\right\}N \tag{4.13}$$

$$\phi' = \frac{\kappa F}{D}\left\{\frac{S_{\omega'}}{F} - I^c_{\omega'\alpha}J^c_{\alpha\beta}c_\beta\right\}N + \left\{1 - \frac{\kappa F}{D}\left[I_{\omega'\omega} - I^c_{\omega'\alpha}J^c_{\alpha\beta}I^c_{\omega'\beta} - \frac{S^2_{\omega'}}{F}\right]\right\}\frac{M}{K} \tag{4.14}$$

Generally the extensional rigidity is decreased by pretwist. The normal force N acts through the z-axis and the term $c_\alpha J^c_{\alpha\beta}c_\beta$ is due to eccentric loading of the cross section. Conversely the torsional rigidity is increased by pretwist.

It is noted that the factor to M in (4.13) is equal to the factor to N in (4.14). This is a consequence of the reciprocal theorem, because on the z-axis $\omega' = 0$, and ζ' is therefore the longitudinal strain on the z-axis.

In the case of constant bending, equation (4.1) takes the form

$$\phi' = \kappa\theta \tag{4.15}$$

whereby

$$M_w = -M_S = -\kappa K\theta \tag{4.16}$$

In order to obtain equations similar to (4.4)-(4.6) it is assumed that θ is a trigonometric function of argument βz, whereby $\theta'' = -\beta^2\theta$. This assumption is verified in the following equations. A similar assumption was used by Goodier and Griffin [7]. The definition of N and M_α from Table 3 are now combined with (3.16), whereby

$$F\zeta' - S_\alpha \eta'_\alpha - S_{\omega'}\theta = 0 \tag{4.17}$$

$$-S_\alpha \zeta' + I_{\alpha\beta}\eta'_\beta + I_{\omega'\alpha}\theta = M_\alpha \tag{4.18}$$

$$-S_{\omega'}\zeta' + I_{\omega'\alpha}\eta'_\alpha + (I_{\omega'\omega'} + \beta^2 I d_{\omega\omega} + \kappa K)\theta = 0 \tag{4.19}$$

By use of the transformation (4.7)-(4.9) equation (4.17) is reduced to

$$\zeta' - c_\alpha \eta'_\alpha = \frac{S_{\omega'}}{F}\theta \tag{4.20}$$

while (4.19) gives

$$\theta = \frac{-I^c_{\omega'\alpha}\eta'_\alpha}{\kappa K + I_{\omega'\omega'} + \beta^2 I_{\omega\omega} - S^2_{\omega'}/F} \tag{4.21}$$

Elimination of θ and ζ' from (4.18) then gives

$$\left(I^c_{\alpha\beta} = \frac{I^c_{\omega'\alpha}I^c_{\omega'\beta}}{\kappa K + I_{\omega'\omega'} + \beta^2 I_{\omega\omega} - S^2_{\omega'}/F}\right)\eta'_\beta = M_\alpha \tag{4.22}$$

When the inverse of the matrix in (4.22) is called $J^*_{\alpha\beta}$, the solution is

$$\eta'_\alpha = J^*_{\alpha\beta}M_\beta \tag{4.23}$$

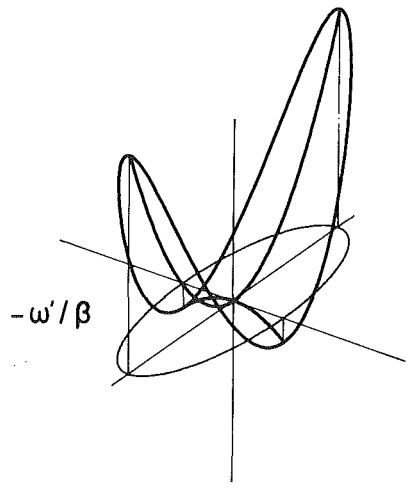

Fig. 2 Longitudinal strain in present theory for ellipse, $a/b = 3.0$

Downloaded 02 May 2010 to 171.66.16.246. Redistribution subject to ASME license or copyright; see http://www.asme.org/terms/Terms_Use.cfm

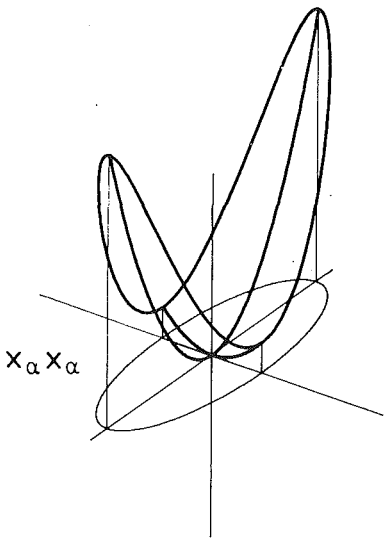

Fig. 3 Longitudinal strain in helical fiber theory for ellipse, $a/b = 3.0$

In this equation η'_α, $J^*_{\alpha\beta}$, and M_β can be transformed to local coordinate axes rotating with the cross section. In the local coordinates the matrix is constant and the moments trigonometric functions of argument βz, and the local components of η'_α are therefore trigonometric functions of argument βz. By transforming (4.21) to local coordinates, the assumption that θ is a trigonometric function of argument βz is confirmed, and the solution is given by (4.15), (4.21), and (4.23).

For cross sections with vanishing $I^c_{\omega' \alpha'}$ e.g., doubly symmetric sections, homogeneous bending does not give rise to any linear terms in β. This is confirmed by the asymptotic result for elliptic cross sections by Goodier and Griffin [7] and the result for a narrow rectangular cross section by Maunder and Reissner [8].

5 Discussion

The present theory has been established by modifying the usual theory for cylindrical beams so as to obtain the best reproduction of the exact asymptotic torsion-extension coupling term of order $0(\beta)$. Through use of the potential energy functional this also leads to higher order terms in β. While the formula for the asymptotic torsion-extension coupling is valid for isotropic beams of arbitrary cross section and therefore is essential in validating the theory, the only available asymptotic results for the bending case appear to be concerned with slender doubly symmetric cross sections.

The asymptotic results for bending of pretwisted beams with narrow rectangular or elliptical cross section both give a correction to the flexibility of order $0(\beta^2)$ with Poisson's ratio ν as a factor [7, 8]. In the present theory pretwist will not change the bending flexibility of beams with doubly symmetric cross section. This is an expected consequence of the omission of transverse deformations of the cross sections and does not represent a contradiction but merely indicates a limitation in accuracy.

A much more detailed comparison can be made regarding the homogeneous torsion-extension problem. The leading term of the stretch ζ' induced by a torsion moment M follows from (4.13) in the form

$$\zeta' \sim \left\{ \frac{S_{\omega'}}{F} - I^c_{\omega' \alpha} J^c_{\alpha\beta} c_\beta \right\} \frac{M}{K} \tag{5.1}$$

In the notation of the present paper the exact asymptotic result from [1] is

$$\zeta' \sim \left\{ \frac{S_{\omega'}}{F} - I^c_{\omega' \alpha} J^c_{\alpha\beta} c_\beta \right\} \frac{M}{K}$$

$$- \beta \frac{\nu}{1+\nu} \frac{M}{K} \int_A E\, x_\alpha (\omega_{,\alpha} - e_{\alpha\lambda} a_\lambda)(x_\beta e_{\beta\gamma} J^c_{\gamma\delta} c_\delta)\, dA \tag{5.2}$$

It is important to note two independent ways in which the last term in (5.2) can vanish: the elastic center on the axis of pretwist, or vanishing Poisson ratio.

The torsion-extension coupling can also be compared with the similar term in theories based on an assumption of helical fibers [4, 5]. Consider the case of an elliptical cross section with semiaxes a and b, and the axis of pretwist offset c from the center along the axis $2b$. The warping function is [9]

$$\omega = \frac{a^2 - b^2}{a^2 + b^2} x_1 (x_2 - c) \tag{5.3}$$

Let the loading be homogeneous torsion. Upon elimination of the torsion moment the coupling relation of the present theory becomes

$$\zeta' \sim -\frac{\beta}{4} \frac{a^2 - b^2}{a^2 + b^2} (a^2 - b^2 + 4c^2) \phi' \tag{5.4}$$

This result is asymptotically exact for $\nu = 0$, although a considerable beam length may be required to create the assumed homogeneous loading condition. The presence of the factor $(a^2 - b^2)$ eliminates coupling for circular cross sections.

In theories based on the assumption of helical fibers the torsion-extension coupling is represented by the polar moment around the axis of pretwist, and (5.4) is replaced with

$$\zeta' \sim -\beta \frac{I_{\alpha\alpha}}{F} \phi' = -\frac{\beta}{4} (a^2 + b^2) \left(1 + \frac{(2c)^2}{a^2 + b^2} \right) \phi' \tag{5.5}$$

It is seen that this expression is different from (5.4) both with respect to the influence of the shape and the offset from the axis of pretwist. In (5.5) there is no distinction between offset along the minor or major axes, and the coupling does not reduce to zero, when a approaches b. For $c = 0$ the difference arises solely from replacing $-\omega'/\beta$ with $x_\alpha x_\alpha$. These functions are shown in Figs. 2 and 3, from which it is seen that the difference decreases with increasing slenderness, although the distributions along the minor axis remain basically different.

Also the longitudinal stress distribution is of interest, and for homogeneous torsion of pretwisted beams with elliptic cross section and $c_\alpha = 0$ the asymptotic result can be extracted from [10]. The present theory gives

$$\sigma/E = \left[-\frac{1}{4} (a^2 - b^2) + (x_1^2 - x_2^2) \right] \frac{a^2 - b^2}{a^2 + b^2} \beta \phi' \tag{5.6}$$

while the asymptotic result is

$$\sigma/E = \left(1 + \frac{\nu}{1+\nu} \frac{8a^2 b^2}{3a^4 + 3b^4 + 2a^2 b^2} \right) \times$$

$$\times \left[-\frac{1}{4} (a^2 - b^2) + (x_1^2 - x_2^2) \right] \frac{a^2 - b^2}{a^2 + b^2} \beta \phi' \tag{5.7}$$

It is seen that the two distributions only differ by a constant factor that depends on ν and the ratio a/b. For $a/b = 3$ the relative error in (5.6) is $0.27\nu/(1+\nu)$, and it decreases with increasing slenderness.

Downloaded 02 May 2010 to 171.66.16.246. Redistribution subject to ASME license or copyright; see http://www.asme.org/terms/Terms_Use.cfm

References

1 Krenk, S., "The Torsion-Extension Coupling in Pretwisted Elastic Beams," *International Journal of Solids and Structures* (to appear).

2 Rosen, A., "The Effect of Initial Twist on the Torsional Rigidity of Beams—Another Point of View," ASME JOURNAL OF APPLIED MECHANICS, Vol. 47, 1980, pp. 389–392.

3 Hodges, D. H., "Torsion of Pretwisted Beams Due to Axial Loading," ASME JOURNAL OF APPLIED MECHANICS, Vol. 47, 1980, pp. 393–397.

4 Houbolt, J. C., and Brooks, G. W., "Differential Equations of Motion for Combined Flapwise Bending, Chordwise Bending, and Torsion of Twisted Nonuniform Rotor Blades," NACA Report 1346, 1958.

5 Krenk, S., and Gunneskov, O., "Statics of Thin-Walled Pretwisted Beams," *International Journal of Numerical Methods in Engineering*, Vol. 17, 1981, pp. 1407–1426.

6 Kollbrunner, C. F., and Hajdin, *Dünnwandige Stäbe 1*, Springer-Verlag, Berlin, 1972.

7 Goodier, J. N., and Griffin, D. S., "Elastic Bending of Pretwisted Bars," *International Journal of Solids and Structures*, Vol. 5, 1969, pp. 1231–1245.

8 Maunder, L., and Reissner, E., "Pure Bending of Pretwisted Rectangular Plates," *Journal of the Mechanics and Physics of Solids*, Vol. 5, 1957, pp. 261–266.

9 Timoshenko, S., and Goodier, J. N., *Theory of Elasticity*, McGraw-Hill, New York, 1951.

10 Okubo, H., "The Torsion and Stretching of Spiral Rods," *Quarterly of Applied Mathematics*, Vol. 9, 1951, pp. 263–272.

Downloaded 02 May 2010 to 171.66.16.246. Redistribution subject to ASME license or copyright; see http://www.asme.org/terms/Terms_Use.cfm

S. J. Tsao
Graduate Student.

V. V. Varadan
Associate Professor.

V. K. Varadan
Associate Professor.
Mem. ASME

Wave Propagation Group,
Department of Engineering Mechanics,
The Ohio State University,
Columbus, Ohio 43210

T-Matrix Approach to Scattering of Elastic (*SH*-) Waves by an Inclined Surface Void

This study is concerned with the T-matrix method to solve the scattering of SH-waves by an inclined surface-breaking void in a homogeneous elastic half space. Additional complications arising from the inclination of the surface cavity have been overcome by using suitable basis functions for the surface displacements in the T-matrix method and the method of images. Numerical results are presented for elliptical cavities for two different angles of inclination, two aspect ratios for various angles of incidence, observation, and frequency. The T-matrix results are compared with the results obtained from a hybrid finite-element wave-expansion method.

1 Introduction

The scattering of acoustic, electromagnetic, and elastic waves by surface-breaking cracks in an elastic half space is of current interest. The complexity of the problem is increased when the cracks are inclined to the free surface. The present study is devoted to analyzing the scattering features of *SH*-waves by inclined surface-breaking "cracks" in an elastic half space. The crack is modeled as an elliptical cavity of large aspect ratio. The results presented herein are of relevance to many structural engineering applications (e.g., welded joints) and also to other environmental and oceanographic fields.

As far as the present status of the problem under investigation is concerned, we would like to emphasize that more theoretical and experimental work on inclined surface-breaking cracks is needed. Although experimental studies involving electromagnetic waves in a magnetizable medium-*E-MAT* experiment and theoretical studies of scattering by a vertical "mathematical" surface-breaking crack [1] have been initiated, to the author's knowledge, inclined surface-breaking cracks have not been previously studied at wavelengths comparable to crack length.

Keeping these remarks in view, we shall present a numerical approach to study the *SH*-wave scattering by oblique cracks. At the present time vertical edge cracks have been studied by integral equation methods [1] and the inclined edge crack has been analyzed at very low frequencies by the method of matched asymptotic expansions [2]. Recently experimental results have become available for *SH*-wave scattering using *E-MAT*'s to generate *SH*-wave motion [3]. In this paper we wish to present a numerical approach to study *SH*-wave scattering by an inclined elliptical cavity of varying aspect ratio. A combination of image theory and the *T*-matrix method will be applied to yield results of good accuracy. These results will be compared to results obtained by a finite-element wave-function expansion method.

The *T*-matrix method for scattering of acoustic and electromagnetic waves was first developed by Waterman [4, 5] and later extended to elastic wave scattering by Varadan and Pao [6]. Subsequently, this method has been widely used in two and three-dimensional scattering problems involving all the three wave fields (for a detailed bibliography, and the present status of the method, see reference [17]). It may be remarked here that in the two-dimensional scattering of elastic waves, the *P*-wave (longitudinal) and *SV*-wave (in-plane transverse) are always coupled at the boundary; and thus make the analysis complicated even for a simple geometry. However, the *SH*-wave (antiplane transverse) scattering problem is completely uncoupled and involves only the solution of a scalar wave equation. We have previously

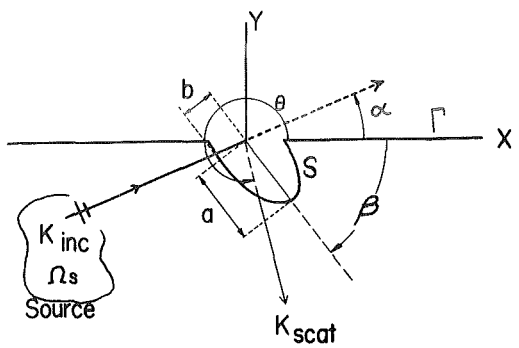

Fig. 1 Elliptical crack shape considered in computations

Contributed by the Applied Mechanics Division for presentation at the 1983 ASME Applied Mechanics, Bioengineering, and Fluids Engineering Conference, Houston, Texas, June 20–22, 1983 of THE AMERICAN SOCIETY OF MECHANICAL ENGINEERS.

Discussion on this paper should be addressed to the Editorial Department, ASME, United Engineering Center, 345 East 47th Street, New York, N.Y. 10017, and will be accepted until two months after final publication of the paper itself in the JOURNAL OF APPLIED MECHANICS. Manuscript received by ASME Applied Mechanics Division, March, 1982; final revision, July, 1982. Paper No. 83-APM-13.

Copies will be available until July, 1984.

Copyright © 1983 by ASME
Downloaded 02 May 2010 to 171.66.16.246. Redistribution subject to ASME license or copyright; see http://www.asme.org/terms/Terms_Use.cfm

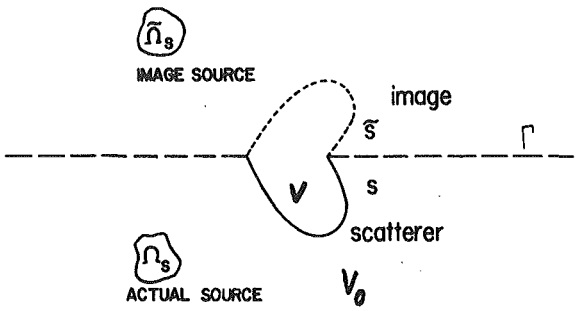

Fig. 2 Equivalent scattering geometry by using method of images corresponding to Fig. 1

studied the scattering of *SH*-waves by cylindrical and lens shaped (singular-tip cracks) cross section [8]; and discussed the effect of the shape on the frequency dependence of the scattered field.

For the problem (See Fig. 1) under consideration, we observe that the total field should satisfy the boundary condition on the surface of the crack as well as on the free surface (Neumann boundary condition). However, this additional requirement on the boundary condition makes the ready application of the *T*-matrix method rather difficult. The problem is thus reformulated in terms of an equivalent problem using image theory derived from the half space Green's function (See Fig. 2). Such a method has earlier been applied to solve the problem of *SH*-wave scattering from a vertical surface-breaking crack [9]. Since the crack is oblique in this case and the equivalent scatterer shown in Fig. 2 has a concavity near the free surface, incoming wave functions (Hankel functions of the second kind) have been used to expand the surface field. This leads to better numerical results.

Numerical results of backscattering, bistatic scattering cross sections, as functions of frequency have been presented for an elliptical surface-breaking crack in Aluminum inclined at 45 deg, 60 deg with major to minor axis ratio equal to 2.0 and 4.0. Various incident angles (α) are considered (see Fig. 2). The results have also been compared with vertical surface-breaking cracks. The results obtained with the *T*-matrix method have been compared with those of a Unimoment (finite element) method and the suitability of the two methods for the problem at hand are discussed. The frequency spectra can be interpreted by considering the interference between the speculary reflected waves and creeping waves.

2 *T*-Matrix Formulation and the Method of Images

Time harmonic, plane, horizontally polarized shear waves (*SH*-waves) propagating in the $x-y$ plane and polarized in the z-direction propagate in an elastic half space characterized by the Lame constants λ and μ and density ρ. An edge crack, infinitely long in the z-direction and of elliptical cross section scatters the incident waves (see Fig. 1). Since the incident wave displacement $\mathbf{u}^i = \hat{z}\phi^i(x,y)$ and the crack is infinitely long in the z-coordinate, the scattered displacement field $\mathbf{u}^s = \hat{z}\phi^s(x,y)$. This is called the antiplane strain problem of elastodynamics. Thus, the total field $\mathbf{u}$ in the medium is given by

$$\mathbf{u} = \mathbf{u}^i + \mathbf{u}^s \tag{1}$$

where $\mathbf{u}$, $\mathbf{u}^i$, and $\mathbf{u}^s$ satisfy Navier's equation which now simplifies to the scalar Helmholtz equations,

$$(\nabla^2 + k^2)\phi = 0 \tag{2}$$

where $k = \omega/c_s$, $c_s = \sqrt{\mu/\rho}$.

The Green's function $g(\mathbf{r},\mathbf{r}')$ for the scalar wave equation is well known. In two dimensions

$$g(\mathbf{r}-\mathbf{r}') = i\pi H_0^{(1)}(k|\mathbf{r}-\mathbf{r}'|) \tag{3}$$

where $H_0^{(1)}$ is the cylindrical Hankel function of the first kind. The preceding form of the Green's function known as the principal Green's function g_0 satisfies radiation conditions at infinity, but does not satisfy proper boundary conditions on Γ, the surface of the half space. Since the surface Γ is traction-free, we must require

$$\hat{y}\cdot\nabla g(\mathbf{r},\mathbf{r}')|_{y=0} = 0$$

where $\hat{y}$ is the normal to the free surface. In general, this can be considered as the principal Green's function g_0 plus some combination of wave function satisfying the homogeneous Helmholtz equation and radiation condition. The half-space Green's function g will be

$$g = g_0 + \tilde{g}_0 = i\pi[H_0^{(1)}(kR) + H_0^{(1)}(k\tilde{R})] \tag{4}$$

where

$$R = |\mathbf{r}-\mathbf{r}'| = ((x-x')^2 + (y-y')^2)^{1/2}$$
$$\tilde{R} = ((x-x')^2 + (y+y')^2)^{1/2} \tag{5}$$

The tilde on g indicates the reflection of any point about the axis, including source, scatterer, and medium (see Fig. 2). For a homogeneous isotropic medium, the Green's function depends only on $|\mathbf{r}-\mathbf{r}'|$. Using the Green's function as given by equation (4) and recalling that in the present problem, the surface under consideration is the surface S of the inclined cavity as well as the free surface, i.e., $SU\Gamma$: the integral representation can be written as

$$\int_{SU\Gamma} [\phi_+(\mathbf{r}')\hat{n}\cdot\nabla g(\mathbf{r},\mathbf{r}') - g(\mathbf{r},\mathbf{r}')\hat{n}\cdot\nabla\phi_+(\mathbf{r}')]dS$$
$$= \begin{cases} 4\pi\phi^s(\mathbf{r}); & \mathbf{r}\epsilon V \\ -4\pi\phi^i(\mathbf{r}); & \mathbf{r}\epsilon V_0 \end{cases} \tag{6}$$

This is the well-known Helmholtz integral formula where ϕ_+ is the total surface field on the surfaces S and Γ and $\hat{n}\cdot\nabla\phi_+$ is its normal gradient. Since Neumann boundary conditions must be satisfied on S as well as Γ, the integral on Γ disappears and the integration S may be written in the following form

$$\frac{1}{4\pi}\int_{SU\tilde{S}} \phi_+(\mathbf{r}')\hat{n}\cdot\nabla g_0(k|\mathbf{r}-\mathbf{r}'|)\,dS$$
$$= \begin{cases} \phi^s(\mathbf{r}); & \mathbf{r}\text{ outside } SU\tilde{S} \\ -\phi^i(\mathbf{r}) + \tilde{\phi}^i(r)); & r\text{ inside } SU\tilde{S} \end{cases} \tag{7}$$

where $\tilde{S}$ is the image of S, and $\tilde{\phi}^i$ is an image source. We have simplified the treatment of the half-space problem by using image theory to a problem involving a body symmetric about the x-axis in an infinite elastic medium.

The procedure was easy since the half-space Green's function is known analytically. A similar procedure can also be used for the case of Dirichlet boundary conditions.

A *T*-matrix for the inclined cavity can be derived from equation (7), as in reference [6]. Solutions of the scalar Helmholtz equation in cylindrical polar coordinates can be represented as

$$\begin{Bmatrix} Re \\ Ou \end{Bmatrix} \phi_{n\sigma}(k\mathbf{r}) = \sqrt{\epsilon_n} \begin{Bmatrix} J_n(kr) \\ H_n^{(1)}(kr) \end{Bmatrix}$$
$$\cos n\theta; \quad \sigma = 1; \quad n\,\epsilon[0,\infty]$$
$$\sin n\theta; \quad \sigma = 2; \quad n\,\epsilon[1,\infty] \tag{8}$$

Downloaded 02 May 2010 to 171.66.16.246. Redistribution subject to ASME license or copyright; see http://www.asme.org/terms/Terms_Use.cfm

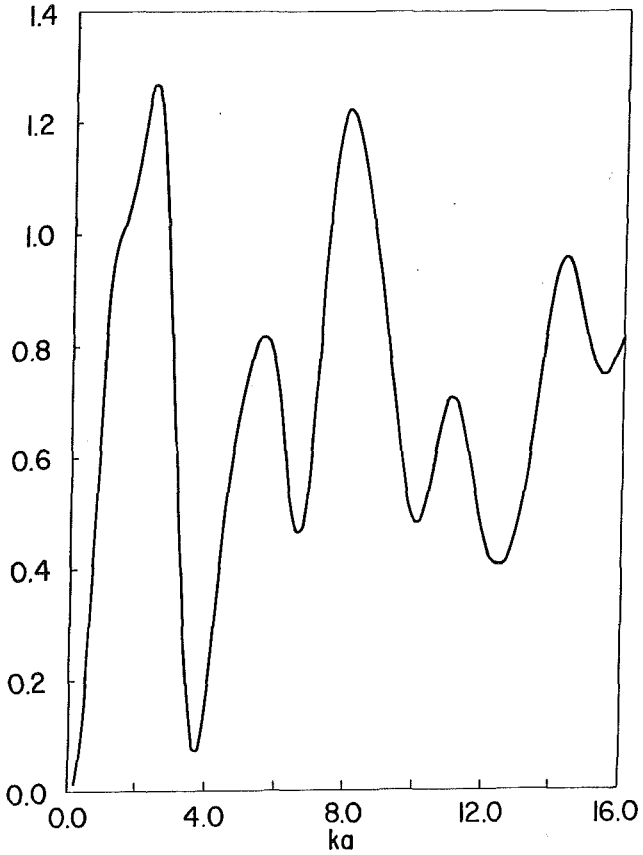

Fig. 3 Backscattering cross section for wave incident at α = 60 deg, β = 60 deg, and a/b = 2.0

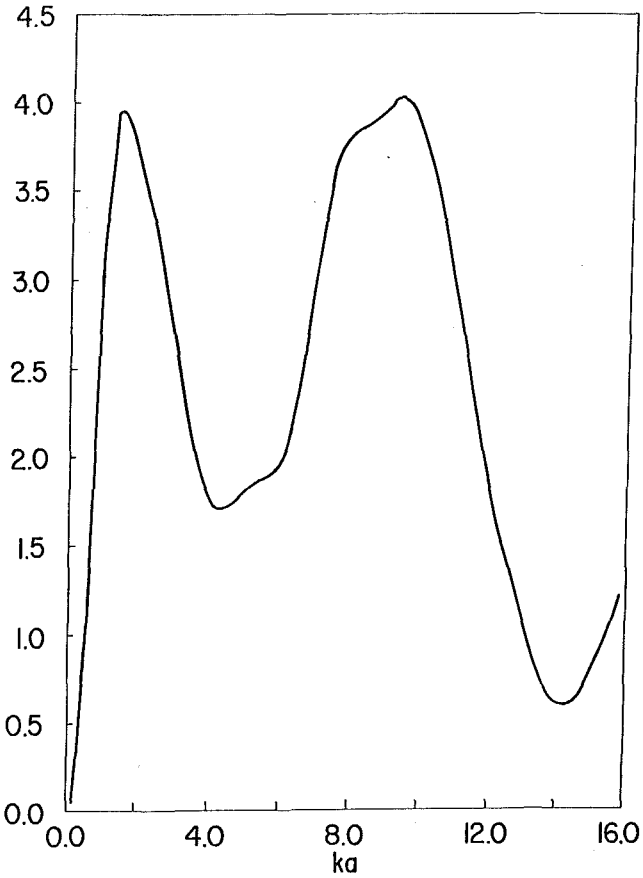

Fig. 4 Backscattering cross section for wave incident at α = 150 deg, β = 60 deg, and a/b = 2.0

where $\sqrt{\epsilon_n}$ is the Neumann factor. When $n=0$, $\sqrt{\epsilon_n} = 1$, otherwise $\sqrt{\epsilon_n} = \sqrt{2}$. We now use this orthogonal basis to expand the incident field, its image, the principal Green's function, as well as the surface field using Bessel functions and the Hankel functions of the first and second kind as appropriate. Thus

$$\phi^i + \tilde{\phi}^i = e^{ikr\cos\alpha} + e^{ikr\cos\tilde{\alpha}} = \sum_{\sigma}\sum_{n} A_{n\sigma} Re\phi_{n\sigma} \tag{9}$$

where

$$A_{n\sigma} = 2(i)^n \sqrt{\epsilon_n} \cos n\alpha \, \delta_{\sigma 1}. \tag{10}$$

and α is the incident angle and $\tilde{\alpha} = \pi - \alpha$.

Similarly, ϕ^s can be represented as

$$\phi^s = \sum_{\sigma}\sum_{n} f_{n\sigma} \, Ou \, \phi_{n\sigma} \tag{11}$$

where ϕ^s satisfies radiation conditions at distances far from $SU\tilde{S}$. The Green's function may be expanded in the form

$$g_0(k|\mathbf{r}-\mathbf{r}'|) = i\pi H_0^{(1)}(k|\mathbf{r}-\mathbf{r}'|)$$

$$= i\pi \sum_{\nu}\sum_{m} Ou \, \phi_{m\nu}(kr>) Re\phi_{m\nu}(kr<) \tag{12}$$

where $r>$ and $r<$ denote the greater and lesser of r and r', respectively. Now assume that the surface field ϕ_+ can be expanded in the form

$$\phi_+ = \sum_{\nu}\sum_{m} \alpha_{m\nu} \, Ou \, \phi^*_{m\nu}(kr') \tag{13}$$

where $\phi^*_{m\nu}$ is simply the complex conjugate of $\phi_{m\nu}$ and thus contains a Hankel function of the second kind. This choice is preferred because the inclined edge crack has a concavity on its boundary. For this case, use of the regular wave functions leads to poorly converging results. Using equations (10)–(13) in equation (7) we get

$$A_{n\sigma} = -\frac{i}{4} Q_{n\sigma,m\nu} \, \alpha_{m\nu} \tag{14}$$

$$f_{n\sigma} = \frac{i}{4} \bar{Q}_{n\sigma,m\nu} \, \alpha_{m\nu} \tag{15}$$

where

$$Q_{n\sigma,m\nu}(\phi,\phi^*) = \int_{SU\tilde{S}} \hat{n} \cdot \nabla Ou\phi_{n\sigma} Ou \, \phi^*_{m\nu} \, dS \tag{16}$$

$$\bar{Q}_{n\sigma,m\nu}(Re\phi,\phi^*) = \int_{SU\tilde{S}} \hat{n} \cdot \nabla (Re\phi_{n\sigma}) Ou \, \phi^*_{m\nu} \, dS \tag{17}$$

Eliminating the surface field coefficient α from equations (14) and (15) we obtain in vector-matrix notation

$$f = Ta \tag{18}$$

where

$$T = -\bar{Q}(Re\phi, Ou\,\phi^*) Q^{-1}(Ou\,\phi, Ou\,\phi^*) \tag{19}$$

is the T-matrix of an inclined cavity. It is important to note that the T-matrix is independent of the directions of incidence and observation as well as the form of the incident wave. It only depends on the geometry of the scatterer, boundary condition on S, and the frequency ω of the incident wave.

Downloaded 02 May 2010 to 171.66.16.246. Redistribution subject to ASME license or copyright; see http://www.asme.org/terms/Terms_Use.cfm

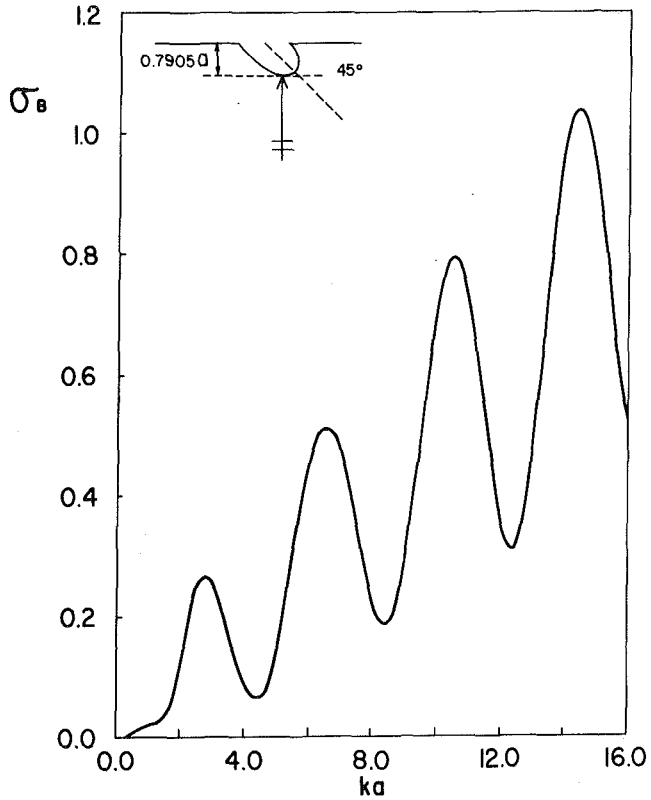

Fig. 5 Backscattering cross section for wave incident at $\alpha = 90$ deg, $\beta = 45$ deg, and $a/b = 2.0$

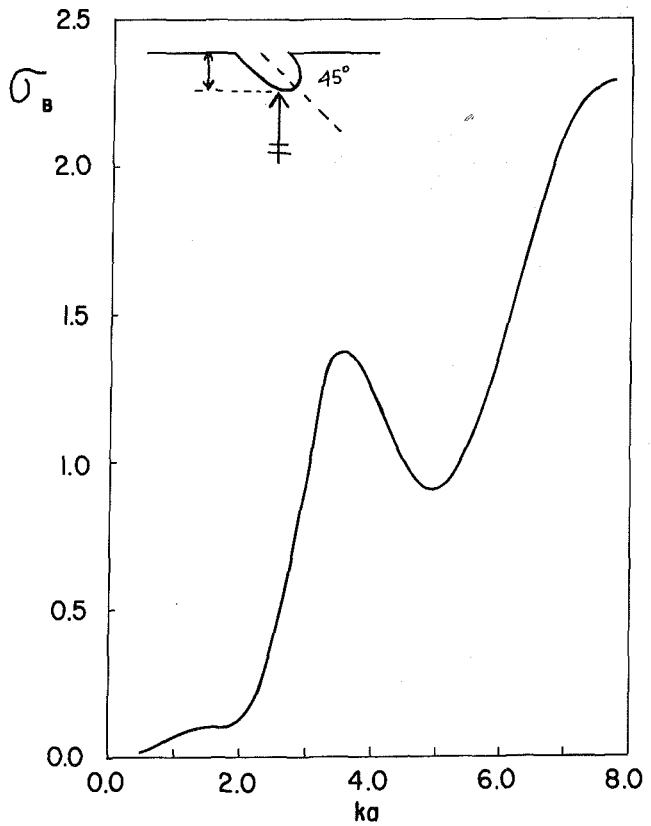

Fig. 6 Backscattering cross section for wave incident at $\alpha = 90$ deg, $\beta = 45$ deg, and $a/b = 4.0$

One of the measurable quantities that is of practical interest is the rate of energy flux $\sigma(\alpha,\theta)$, the scattering cross section,

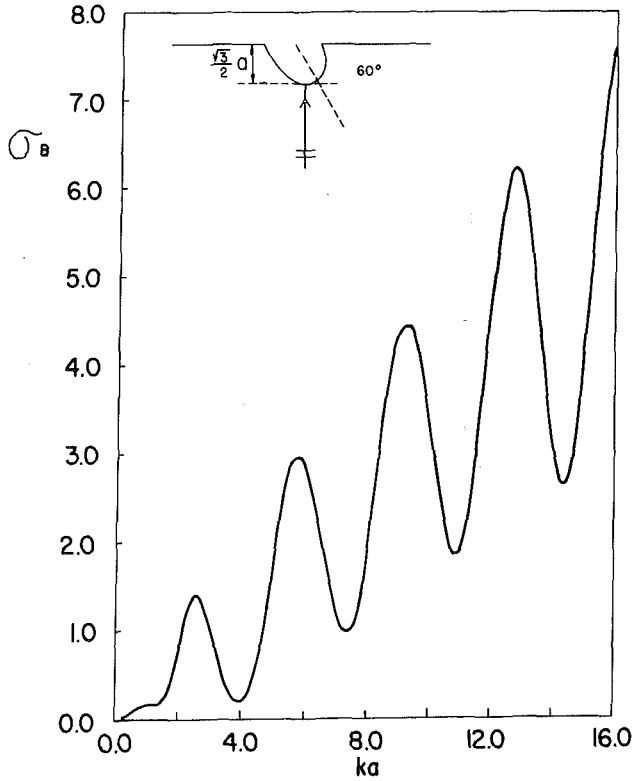

Fig. 7 Backscattering cross section for wave incident at $\alpha = 90$ deg, $\beta = 60$ deg, and $a/b = 2.0$

at distances far from the scatterer. The asymptotic form of the scattered field is

$$\phi^s(r) \to f(\alpha,\theta)\, e^{ikr} \sqrt{2/(i\pi kr)} \tag{20}$$

as $r \to \infty$, where the far-field scattering amplitude is defined by

$$f(\alpha,\theta) = \sum_n (-1)^n \sqrt{\epsilon_n}\, (f_{n1} \cos n\theta + f_{n2} \sin n\theta). \tag{21}$$

The bistatic scattering cross section $\sigma(\alpha,\theta)$ may be written as

$$\sigma(\alpha,\theta) = \frac{1}{ka} |f(\alpha,\theta)|^2 \tag{22}$$

The backscattering cross section is obtained by setting $\theta = \alpha + \pi$.

3 Numerical Procedure and Discussion of Results

The general procedure for formulating the T-matrix was briefly presented in Section 2. For computational purposes, the Q-matrix was evaluated using the Gauss-Legendre quadrature formula. Considerable simplification of the Q-matrix elements was facilitated by the symmetry afforded by the image theory. In this case, the Q-matrix as given in equations (16) and (17) has a block diagonal form, i.e., $\sigma = \nu$.

The symmetry and reciprocity properties of the T-matrix and unitarity of the S-matrix ($S = 1\text{-}2T$) have been used to check the accuracy of the computed results. Symmetry and unit characteristics checked to within 5 percent up to $ka = 16.0$ for an elliptical cavity with aspect ratio $a/b = 2.0$, but for higher values of the aspect ratio like $a/b = 4.0$, the error is of the order of 15 percent at $ka = 7.51$. At higher frequencies and higher aspect ratios, the Q-matrix becomes highly ill conditioned leading to numerical inaccuracy.

Downloaded 02 May 2010 to 171.66.16.246. Redistribution subject to ASME license or copyright; see http://www.asme.org/terms/Terms_Use.cfm

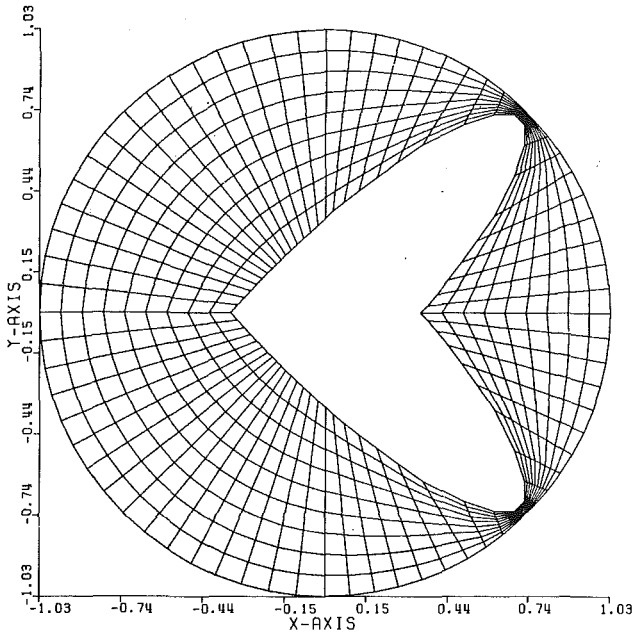

Fig. 8 Finite element mesh for inclined elliptical cavity in a half space and its mirror reflection

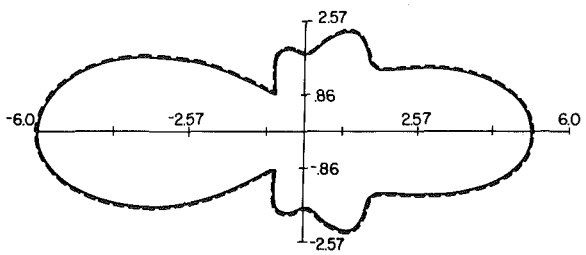

Fig. 9 Comparison of the polar plots obtained using the finite element and *T*-matrix methods for a wave incident at α = 165 deg for *a*/*b* = 2.0 and *ka* = 5.0

As mentioned in the Introduction, the numerical computation involving *T*-matrix elements will lead to unsatisfactory results if we use regular basis functions for the expansion of the surface field. This has been overcome by assuming an expansion in terms of Hankel functions of the second kind.

The plots for backscattering and bistatic scattering cross sections for various incident and observation angles have been presented as functions of wave frequency. Two angles of inclination (β = 45 deg, 60 deg) have been considered. In all the figures, a/b denotes the ratio of the length to the half width of the elliptical crack, α is the incident angle measured from the positive x-axis, and θ is the observation angle (see Fig. 1).

Figures 3–11 display the backscattering and bistatic scattering cross sections versus ka for various α,θ,β, and a/b. It can be seen from these figures that for far field scattering, the backscattering of the incident waves coming from the concave part (for example Fig. 4) is much larger than that coming from the convex part (Fig. 3); and the sharper the crack tip, the smaller is the scattered far field.

In Figs. 5–7, the wave is incident normal to the free surface, and in this case, we observed that the scattering cross section displays regularly spaced maxima and minima. This can be interpreted as the interference between the waves that are reflected from the free surface Γ and the waves that undergo specular reflection from a point on the crack face C. The point is one for which the normal to S coincides with the normal to Γ namely $\hat{n} = -\hat{y}$. The path difference between the two waves is equal to $2l$ where l is the vertical distance of the point of specular reflection from the free surface. We can then show that the spacing Δka between the minima is given by

$$\Delta ka = 2\pi a/2l$$

If the crack is vertical, "l" is independent of the width of the crack. In this case we obtain

$$\Delta ka = \pi$$

In Fig. 5, for $a/b = 2.0$, $2l = 1.581a$ and in this case

$$\Delta ka = 2\pi/1.581 = 3.974$$

In Fig. 6, $a/b = 4.0$, the crack is quite narrow and the point of specular reflection is very nearly at the tip of the crack. For an angle of inclination $\beta = 45$ deg, we obtain

$$\Delta ka = 2\pi/\sqrt{2} = 4.442$$

and in Fig. 7 for $\beta = 60$ deg, $a/b = 2.0$, we obtain

$$\Delta ka = 2\pi/\sqrt{3} = 3.6276.$$

Thus, all the values of Δka are matched with those obtained from each plot.

Analysis of a similar problem has been done using the unimoment method. The unimoment method, which is a hybrid finite-element wave-function expansion method, was first developed by K. K. Mei for electromagnetic wave problems [10]. It is concerned with an expansion in cylindrical wave functions of the scattered field outside a circle enclosing the cross section of the crack. The finite element approximation, is invoked in the region between the circle and the surface of the crack (see Fig. 8). The unknown coefficients associated with both solutions are determined by demanding continuity of the field and its partial derivative on the artificial boundary. This method has been adapted to the problem of *SH*-wave scattering by cavities in elastic solids [11]. Hence, it would be worthwhile to make a comparison between the accuracy and other features of both these methods as applied to the present problem.

In Fig. 9, the polar plots for $ka = 5.0$, $\beta = 45$ deg, and aspect ratio $a/b = 2.0$ are presented, using both these methods. For this particular problem the unimoment methods required five times more computer time than the *T*-matrix method. Thus, we conclude that both in terms of accuracy and economy, the *T*-matrix method seems to be better suited in solving scattering problems involving simple shapes such as the ones considered in this paper.

Acknowledgment

This research was supported by the National Science Foundation Industry and University Grant through the Welding Research Center of the Ohio State University. The authors would like to thank Professors K. F. Graff and L. Adler for many helpful discussions. The authors are grateful to Mr. J. H. Su for the use of his finite-element computer program. The use of the Instructional and Research Computer Center is gratefully acknowledged.

References

1 Mendelsohn, D. A., Achenbach, J. D., and Keer, L. M., "Scattering of

Downloaded 02 May 2010 to 171.66.16.246. Redistribution subject to ASME license or copyright; see http://www.asme.org/terms/Terms_Use.cfm

Elastic Waves by a Surface-Breaking Crack," *Wave Motion*, Vol. 2, 1980, pp. 277-279.

2 Datta, S. K., "Diffraction of *SH*-Waves by an Edge Crack," ASME JOURNAL OF APPLIED MECHANICS, Vol. 46, 1979, pp. 101-106.

3 Datta, S. K., "Diffraction of Medium and Long Wavelength *SH*-Waves by Edge Cracks," *J. Appl. Phys.*, to appear.

4 Waterman, P. C., "New Formulation of Acoustic Scattering," *J. Acoust. Soc. Am.*, Vol. 45, 1969, pp. 1417-1429.

5 Waterman, P. C., "Matrix Formulation of Electromagnetic Scattering," *Proc. IEEE*, Vol. 53, 1965, pp. 805-812.

6 Varadan, V. V., and Pao, Y. H., "Scattering Matrix for Elastic Waves, I. Theory," *J. Acoust. Soc. Am.*, Vol. 60, 1976, pp. 556-566.

7 Varadan, V. K., and Varadan, V. V., Eds., *Acoustic, Electromagnetic and Elastic Wave Scattering—Focus on T-Matrix Approach*, Pergamon Press, New York, 1980.

8 Varadan, V. V., Tsao, S. J., Wall, D. J. N., and Varadan, V. K., "Elastic Wave Scattering From Surface Breaking Cylindrical Cracks: *SH* Waves," *J. Acoust. Soc. Am.*, Vol. 71, 1982, pp. 1384-1390.

9 Chang, S. K., and Mei, K. K., "Application of the Unimoment Method to Electromagnetic Scattering of Dielectric Cylinders," *IEEE Trans. on Antennas and Propagation AP-24*, 1976, pp. 35-42.

10 Su, J. H., Varadan, V. V., and Varadan, V. K., "Unimoment Method of Elastic Wave Scattering," *DARPA/AF Review of Progress in Quantitative NDE*, Vol. 1, Thompson, D. O., and Chimenti, D. E., eds., Plenum, New York, 1982.

Downloaded 02 May 2010 to 171.66.16.246. Redistribution subject to ASME license or copyright; see http://www.asme.org/terms/Terms_Use.cfm

N. Triantafyllidis
Department of Aerospace Engineering,
University of Michigan,
Ann Arbor, Mich. 48109

R. Abeyaratne
College of Engineering,
Michigan State University,
East Lansing, Mich. 48824
Assoc. Mem. ASME

Instabilities of a Finitely Deformed Fiber-Reinforced Elastic Material

The instabilities of a finitely deformed Blatz-Ko material reinforced with fibers in a single direction (an anisotropic, nonlinearly elastic material) are examined. The loading is one of plane strain uniaxial stress with the load axis being inclined with respect to the fiber direction. In general one finds a critical applied stress (or stretch) at which surface instabilities of the body occur. This is then followed by a shear band-type instability. For a certain range of fiber orientations these instabilites appear a maximum stress level has been reached. It has also been found that when the fiber direction approaches the loading axis, the material is stabilized in tension but destabilized in compression.

1 Introduction

The mechanical properties of a ductile solid play an important role in determining its failure mechanism at high strain levels. Failure modes of particular interest are those due to a loss of stability, which can either be of a local or a global character. A local (or material) instability refers to one that occurs at a point in the body once a certain critical state of stress or strain has been reached at that point, irrespective of the conditions at the boundary. Such an instability is often associated with a shear band-type failure mode and occurs when the governing displacement equations of equilibrium lose ellipticity. On the other hand, a global (or geometric) instability is associated with a buckling type of failure that is critically dependent on the details of the boundary conditions.

A common way of strengthening certain materials, mainly elastomers, is by reinforcing them with fibers along a given direction. The present study examines the aforementioned stability properties of a fiber reinforced composite, modeled as a homogeneous, anisotropic material.

Here, attention is focused on the plane strain deformation of a hyperelastic material reinforced with a single family of fibers. More specifically, we examine the isotropic constitutive model proposed by Blatz and Ko [1] generalized in order to account for reinforcement. The choice of a Blatz-Ko material for the matrix was made because it exhibits shear band-type local instabilities at sufficiently large strain levels (Knowles and Sternberg [2]). On the other hand, in the presence of suitable reinforcement we find that *no* such local instabilities exist in the material when subjected to a state of plane strain uniaxial tension in the direction of the fibers. However, if the tensile stress is directed normal to the reinforcement, the material exhibits the same instabilities as does a Blatz-Ko material. It is apparent, therefore, that the direction of reinforcement significantly influences the stability properties of the composite.

In order to investigate the effect of the anisotropy on global stability, we study the bifurcation buckling of a plane strain, uniaxially stressed half space bounded by a traction-free surface. The buckling mode here is of the form of a surface wave exponentially decaying amplitude. For both types of instabilities we examine the dependence of the bifurcation stress (or stretch) on the fiber orientation. The effect of the relative proportion of fibers as well as the stiffness of the fibers are also considered.

The onset of surface instabilities in finitely strained orthotropic solids has been studied by Biot [3], Hill and Hutchinson [4], and others. Recently, the bifurcation of a transversely isotropic elastic material has been considered by Kurashige [5] and Arcisz [6]. These studies restrict attention to the particular (orthotropic) cases in which the applied stress is normal to and parallel to the fibers, respectively. On the other hand, material instabilities of the shear band type have been examined by Rice [7], Knowles and Sternberg [8], and others. Douglas and Jaunzemis [9] have formulated the conditions for a loss of ellipticity of a general, transversely isotropic, elastic material and analyzed the particular examples of hydrostatic pressure and simple shear. However, an investigation that studies the effect of an arbitrary direction of reinforcement on either geometric or material instabilities does not appear to have been carried out.

2 Preliminaries

Consider a body occupying the region R_0 in an undeformed configuration and let $\mathbf{X}$ denote the position vector of a typical particle. A deformation of the body is described by

$$x_i = \hat{x}_i(\mathbf{X}) \qquad (2.1)^1$$

which transforms R_0 into a region R and where $\mathbf{x}$ denotes the

Contributed by the Applied Mechanics Division for publication in the JOURNAL OF APPLIED MECHANICS.

Discussion on this paper should be addressed to the Editorial Department, ASME, United Engineering Center, 345 East 47th Street, New York, N. Y. 10017, and will be accepted until two months after final publication of the paper itself in the JOURNAL OF APPLIED MECHANICS. Manuscript received by ASME Applied Mechanics Division, May, 1982; final revision, September, 1982.

[1] All vector and tensor components are taken with respect to a fixed rectangular Cartesian frame. We use standard indicial notation with Greek and Latin subscripts having the respective ranges (1, 2) and (1, 2, 3).

Copyright © 1983 by ASME
Downloaded 02 May 2010 to 171.66.16.246. Redistribution subject to ASME license or copyright; see http://www.asme.org/terms/Terms_Use.cfm

which transforms R_0 into a region R and where $\mathbf{x}$ denotes the position vector of a material point in the deformed configuration. The components of the deformation gradient tensor $\mathbf{F}$ and the left and right Cauchy-Green tensors $\mathbf{B}$ and $\mathbf{C}$ are given by

$$F_{ij} = \partial \hat{x}_i / \partial X_j, \; B_{ij} = F_{ik} F_{jk}, \; C_{ij} = F_{ki} F_{kj}, \tag{2.2}$$

and in view of the invertibility of (2.1) the Jacobian of the deformation is positive, $J = \det \mathbf{F} > 0$.

If $\boldsymbol{\sigma}$ is the Cauchy (or true) stress tensor field accompanying the deformation at hand, the equilibrium equations, in the absence of body forces, are

$$\partial \sigma_{ij} / \partial x_j = 0, \quad \sigma_{ij} = \sigma_{ji}. \tag{2.3}$$

Suppose now that the body under consideration is homogeneous and elastic and that it possesses an elastic potential W representing the strain energy per unit undeformed volume. The components of true stress are given by

$$\sigma_{ij} = \frac{2}{J} f_{ik} F_{jl} \, \partial W / \partial C_{kl}. \tag{2.4}$$

The principal scalar invariants of the Cauchy-Green tensors $\mathbf{B}$ and $\mathbf{C}$ are

$$I_1 = C_{ii}, \quad I_2 = \frac{1}{2} (C_{ii} \, C_{jj} - C_{ij} \, C_{ij}), \quad I_3 = J^2 = \det \mathbf{C}. \tag{2.5}$$

If the material under consideration is *transversely isotropic*, with the preferential "fiber" direction in the undeformed configuration given by the (constant) unit vector A, then the elastic potential W depends on the three isotropic invariants I_1, I_2, I_3 as well as on two additional invariants I_4 and I_5 where

$$I_4 = C_{ij} \, A_i \, A_j, \quad I_5 = C_{ij} \, C_{ik} \, A_j \, A_k \tag{2.6}$$

(see Spencer [10]). It is apparent from (2.2) and (2.6) that $\sqrt{I_4}$ represents the extensional ratio $|\mathbf{FA}| / |\mathbf{A}|$ of a fiber. Consequently the deformation (2.1) carries the direction of reinforcement $\mathbf{A}$ into the direction defined locally by the unit vector $\mathbf{a}$

$$a_i = F_{ij} \, A_j / \sqrt{I_4}. \tag{2.7}$$

Under these conditions we have $W = W(\mathbf{C}, \mathbf{A}) = W(I_1, I_2, I_3, I_4, I_5)$ with the corresponding constitutive law given by (2.4)-(2.7) as

$$\sigma_{ij} = \frac{2}{J} \left\{ I_3 \frac{\partial W}{\partial I_3} \delta_{ij} + \left(\frac{\partial W}{\partial I_1} + I_1 \frac{\partial W}{\partial I_2} \right) B_{ij} - \frac{\partial W}{\partial I_2} B_{ik} \, B_{kj} + I_4 \frac{\partial W}{\partial I_4} a_i \, a_j + I_4 \frac{\partial W}{\partial I_5} (B_{jk} \, a_i \, a_k + B_{ik} \, a_j \, a_k) \right\}. \tag{2.8}$$

A special form of the elastic potential for a compressible, isotropic material was adopted by Blatz and Ko [1] on the basis of experimental data obtained by them in tests of a foam rubber. We consider here a Blatz-Ko material modified in the simplest possible manner to allow for fibers embedded in the direction $\mathbf{A}$ and take

$$W = \frac{\mu}{2} \{ I_2 I_3^{-1} + 2 I_3^{1/2} - 5 + f(I_4) \}, \quad f(I_4) = \alpha (I_4 - 1)^m. \tag{2.9}$$

The Baltz-Ko material corresponds to the choice $\alpha = 0$. Here, the infinitesimal shear modulus μ and the anisotropy parameter α are both positive (>0) and the hardening exponent m is taken to be an even, positive integar. Equations (2.8) and (2.9) yield the corresponding constitutive law

$$\sigma_{ij} = \mu \{ \delta_{ij} - \frac{1}{J} \, B_{ij}^{-1} + \frac{I_4}{J} f' \, (I_4) a_i \, a_j \}. \tag{2.10}$$[2]

[2] The Cayley-Hamilton theorem has also been used in deriving the particular form in (2.10). Kurashige [5] has previously considered such a constitutive law.

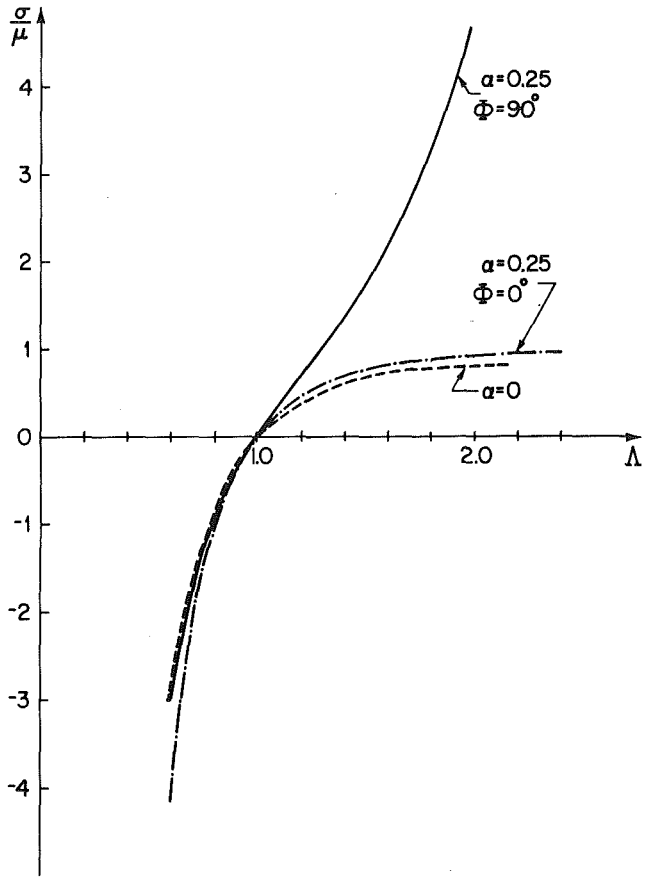

Fig. 1 Response curves in plane strain uniaxial stress. Stress versus stretch.

In order to motivate our particular choice of material, we examine a state of plane strain uniaxial stress parallel to the x_1-axis, $\sigma_{11} = \sigma$, $\sigma_{22} = 0$, $\lambda_3 = 1$. When the fibers are parallel to the direction of loading, $A_1 = 1$, $A_2 = A_3 = 0$, it can readily be shown from (2.6) and (2.10) that the applied stress σ and the transverse stretch λ_2 are related to the principal stretch $\lambda_1 = \Lambda$ by

$$\sigma / \mu = 1 - \Lambda^{-8/3} + \Lambda^{4/3} f' \, (\Lambda^2), \quad \lambda_2 = \Lambda^{-1/3}. \tag{2.11}$$

In view of the specific form of f given in (2.9) it follows that in tension $\sigma \to + \infty$ as $\Lambda \to + \infty$ and likewise in compression $\sigma \to - \infty$ as $\Lambda \to 0+$. On the other hand, if the fibers are normal to the direction of loading, $A_1 = A_3 = 0$, $A_2 = 1$, one finds that

$$\sigma / \mu = 1 - \Lambda^{-3} \lambda_2^{-1}, \quad \Lambda = \lambda_2^{-3} - \lambda_2 \, f' \, (\lambda_2^2). \tag{2.12}$$

In this case, one has $\sigma \to \mu$ as $\Lambda \to \infty$ in tension whereas in compression $\sigma \to - \infty$ as $\Lambda \to 0+$.

Figure 1 displays graphs of the stress-stretch relation σ versus Λ for the material under consideration here with $\alpha = 0.25$, $m = 2$, as well as for the isotropic Blatz-Ko material. It is clear that in tension, the fibers have a "strengthening effect" when aligned with the direction of stressing whereas they have relatively no effect when aligned in a direction normal to it. At any intermediate orientation of the fibers one expects the response to lie somewhere between these two cases.

Moreover, it may be observed in (2.12) and (2.11) that at severe extensions, $\Lambda \to + \infty$, the anisotropy term f becomes insignificant in (2.12) but that it dominates in (2.11). Thus the material behavior approaches that of a Baltz-Ko material in the former case and is quite different (much "stiffer") in the latter. As a consequence, we will find that the material loses ellipticity when the fibers are normal to the axis of loading but

Downloaded 02 May 2010 to 171.66.16.246. Redistribution subject to ASME license or copyright; see http://www.asme.org/terms/Terms_Use.cfm

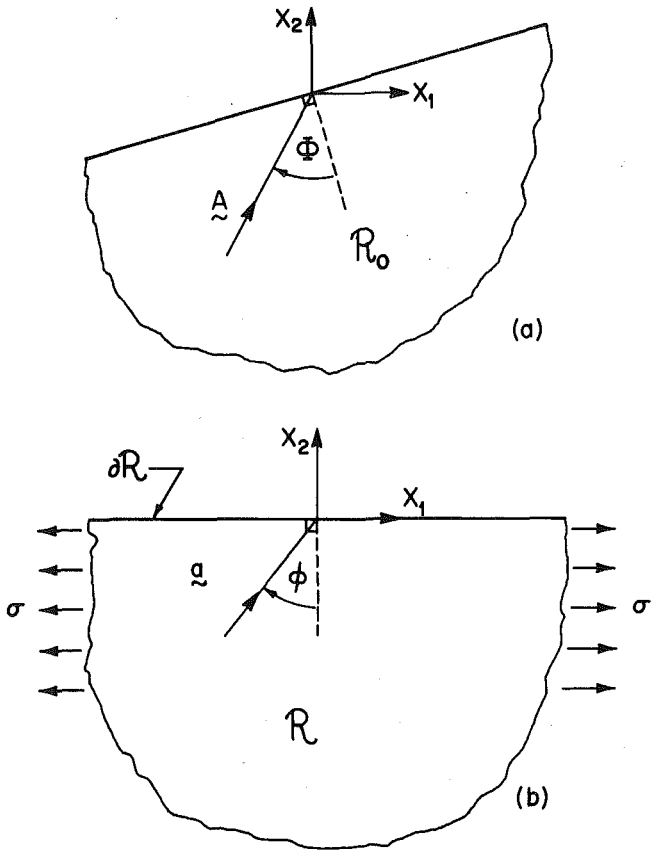

Fig. 2 Cross section of the body; (*a*) undeformed and (*b*) deformed

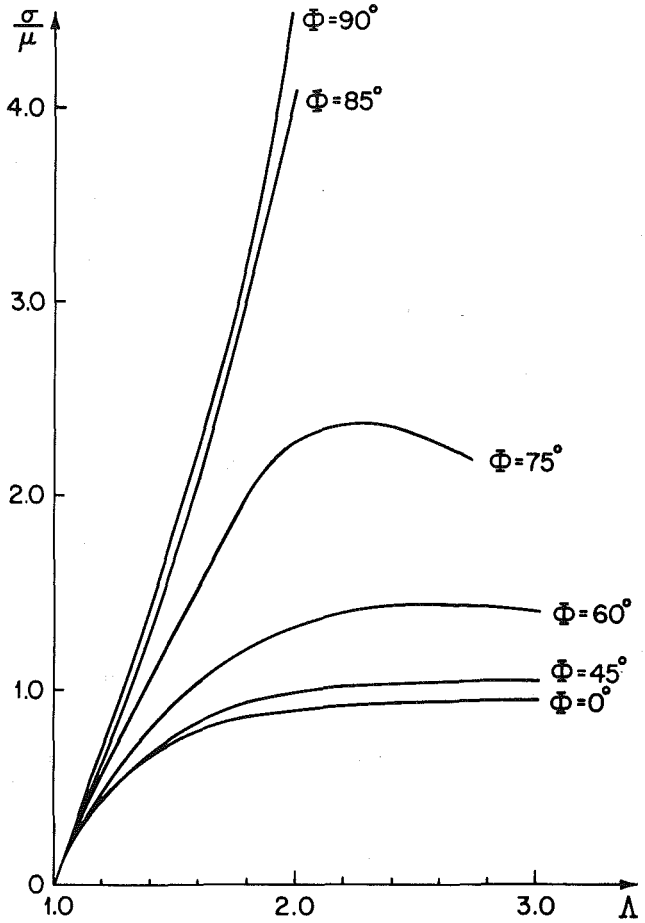

Fig. 3 Response curves in plane strain uniaxial tension. Stress versus stretch for different undeformed fiber angles Φ.

that it always remains elliptic when the fibers are parallel to it. The stability of a state of plane strain uniaxial tension may thus be expected to be highly dependent on the fiber orientation.

It is convenient to scale the stresses with respect to the infinitesimal shear modulus μ and thus we will henceforth formally set $\mu = 1$.

3 Plane Strain Uniaxial Stress

Suppose that the region occupied by the undeformed body is a half space[3] (Fig. 2(*a*)), and consider a homogeneous plane strain deformation in the plane of the fibers that leaves the boundary free of traction. We choose a rectangular Cartesian coordinate frame such that the fibers lie parallel to the $(x_1, x_2)-$plane and with the deformed half-space boundary coinciding with the $(x_1, x_3)-$plane (Fig. 2(*b*)). Then the components $F_{3\alpha}$, $F_{\alpha 3}$ of the deformation gradient tensor vanish while $F_{33} = 1$. In the case of a transversely isotropic material, this assures that the shear components $\sigma_{3\alpha}$ of the true stress tensor also vanish. Consequently the coordinate directions chosen here are principal for σ and

$$\sigma_{11} = \sigma, \sigma_{22} = 0, \quad \sigma_{ij} = 0 \ (i \neq j). \tag{3.1}$$

Since the components A_3, a_3 of the fiber directions vanish, it follows from (2.10) that $\sigma_{33} = 1 - 1/J$.

The fiber directions **A**, **a** are defined by the angles Φ, ϕ made by the fibers with a normal to the undeformed and deformed boundary, respectively (Fig. 2).

Here we view the applied stress σ and the fiber angle in the undeformed configuration Φ as being prescribed and seek to determine the deformed fiber angle ϕ and the left Cauchy-Green tensor **B**. Solving (2.10) for $\mathbf{B}^{-1}$ gives

$$B_{ij}^{-1} = J\left\{\delta_{ij} - \sigma_{ij} + \frac{I_4}{J} f'(I_4) a_i a_j\right\}. \tag{3.2}$$

Elementary manipulation[4] of equations (2.1), (2.2), (2.7) and (3.2) yields the following scalar equations:

$$\begin{aligned} J &= [I_4^{-1} - I_4 f'(I_4)]/(1 - \sigma \sin^2 \phi), \\ I_4 &= (1 - \sigma \cos^2 \phi) J^3/(1 + J^4 \sigma^2 \sin^2 \phi \cos^2 \phi), \\ a J^8 &+ b J^4 + c = 0, \end{aligned} \tag{3.3}$$

where

$$\begin{aligned} a &= \sigma^2(1-\sigma)^2 \sin^2 \phi \cos^4 \phi \cos^2 \Phi, \quad c = \sin^2 \phi \cos^2 \Phi, \\ b &= \{[(1-\sigma)^2 + \sigma^2 \sin^4 \phi] \cos^2 \Phi \\ &\quad - (1 - \sigma \cos^2 \phi)^2\} \cos^2 \Phi. \end{aligned} \tag{3.4}$$

The three algebraic equations in (3.3) are to be solved for J, I_4 and ϕ. Thereafter the Cauchy-Green deformation tensor **B** may be computed from (3.2) and in particular, the stretch ratio in the direction of the traction-free surface, Λ,

$$\Lambda \equiv (B_{11}^{-1})^{1/2} = J \cos\Phi / \sqrt{I_4} \cos\phi. \tag{3.5}$$

may be determined.

For given values of the applied stress σ and the undeformed fiber angle Φ equations (3.3) were solved numerically for the Jacobian $J(>0)$, fiber stretch ratio $\sqrt{I_4}$, and deformed fiber

[3] The results in this and the next section continue to hold true for a strip of finite dimensions.

[4] The principal steps involved consist of (*i*) computing the determinant of each side of (3.2), (*ii*) utilizing $|\mathbf{A}| = 1$ in conjunction with (2.7), and (*iii*) computing B_{11}^{-1} from (2.7) as well as from the maping of the boundary.

Downloaded 02 May 2010 to 171.66.16.246. Redistribution subject to ASME license or copyright; see http://www.asme.org/terms/Terms_Use.cfm

angle ϕ ($0 \leq \phi \leq \pi/2$). Figure 3 displays the resulting stress-stretch response, a graph of σ versus Λ, for different values of the fiber angle Φ in the case of tension ($\sigma > 0$). Keeping in mind that the undeformed fiber angle Φ is measured from a normal to the boundary, one observes that the material becomes "stiffer" as the fiber is aligned more closely with the direction of stressing, i.e., increasing Φ. It should be noted that (except in the case $\Phi = 0$ deg, 90 deg) the stress reaches a maximum, say σ_m, at some value of stretch Λ_m as is clearly seen in the curves corresponding to $\Phi = 60$ deg, 75 deg. The value of σ_m is observed to increase with the fiber angle whereas the corresponding value of stretch Λ_m decreases.

4 Material Instabilities – Loss of Ellipticity

In this section we examine the change of the local stability properties of the composite material due to the presence of the reinforcment. After setting down the general conditions for such an instability, we examine its implications in the particular case of plane strain uniaxial stress.

The local instability criterion to be examined here is that for the onset of shear bands. Failures of this type are often observed in highly strained ductile solids. The mathematical condition corresponding to the initiation of a shear band at a given point in a body is the loss of ellipticity of the displacement equations of equilibrium at the point in question (Rice [6], Knowles and Sternberg [8]).

If $\mathbf{u}(\mathbf{x})$ denotes a further incremental displacement field from a homogeneous equilibrium state of a finitely deformed hyperelastic body, the corresponding incremental equilibrium equations linearized about this configuration are (Douglas and Jaunzamis [9])

$$L_{ijkl}\, u_{k,lj} = 0 \quad \text{on} \quad R. \tag{4.1}$$

Here a comma followed by a subscript denotes partial differentiation with respect to the corresponding x-coordinate. The incremental moduli L_{ijkl} are given by

$$L_{ijkl} = \frac{4}{J} F_{ip}\, F_{jq}\, F_{kr}\, F_{ls} \frac{\partial^2 W}{\partial C_{rs} \partial C_{pq}} + \sigma_{lj}\, \delta_{ik} \tag{4.2}$$

where $\boldsymbol{\sigma}$, $\mathbf{F}$, and J denote the Cauchy stress tensor, deformation gradient $\mathbf{F}$, and Jacobian associated with the homogeneous equilibrium state. In the case of the reinforced Blatz-Ko material (2.9) these moduli may be explicitly calculated, leading to

$$\begin{aligned} L_{ijkl} = \frac{2}{J} 3\{ & B_{ij}\, B_{kl} - \frac{1}{2}(B_{ik}\, B_{jl} + B_{il}\, B_{jk}) \\ & - I_1 B_{ij}\, \delta_{kl} + B_{kl}\, \delta_{ij}) \\ & + (B_{in}\, B_{nj} \delta_{kl} + B_{kn}\, B_{nl}\, \delta_{ij}) \\ & + (I_2 + \frac{1}{2} J^3)\delta_{ij}\, \delta_{kl} + \frac{1}{2}(I_2 - J^3)(\delta_{ik}\delta_{jl} + \delta_{il}\delta_{jk}) \\ & + I_4^2 J^2 f''(I_4) a_i a_j a_k a_l \} + \sigma_{lj}\delta_{ki}. \end{aligned} \tag{4.3}$$

The incremental equilibrium equations (4.1) are elliptic if and only if

$$\det (L_{ijkl}\, m_j\, m_l) \neq 0 \tag{4.4}$$

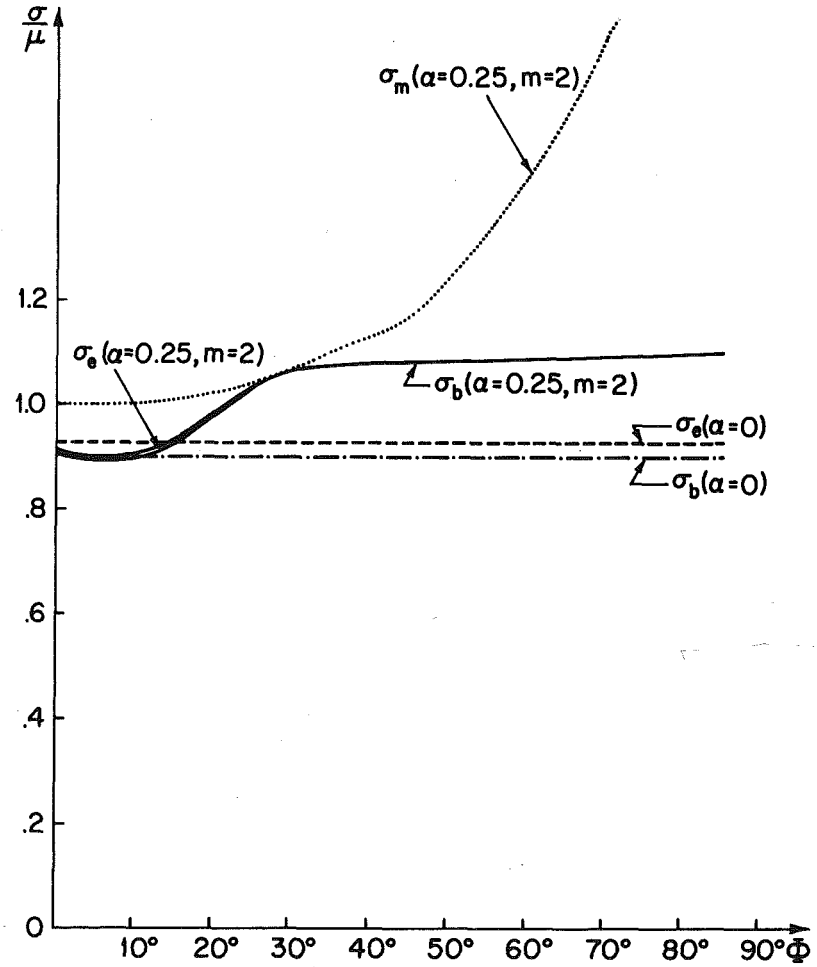

Fig. 4 Variation of the critical stresses σ_b, σ_e with fiber orientation (tension). Lises $\alpha = 0$ corresponds to unreinforced material.

Downloaded 02 May 2010 to 171.66.16.246. Redistribution subject to ASME license or copyright; see http://www.asme.org/terms/Terms_Use.cfm

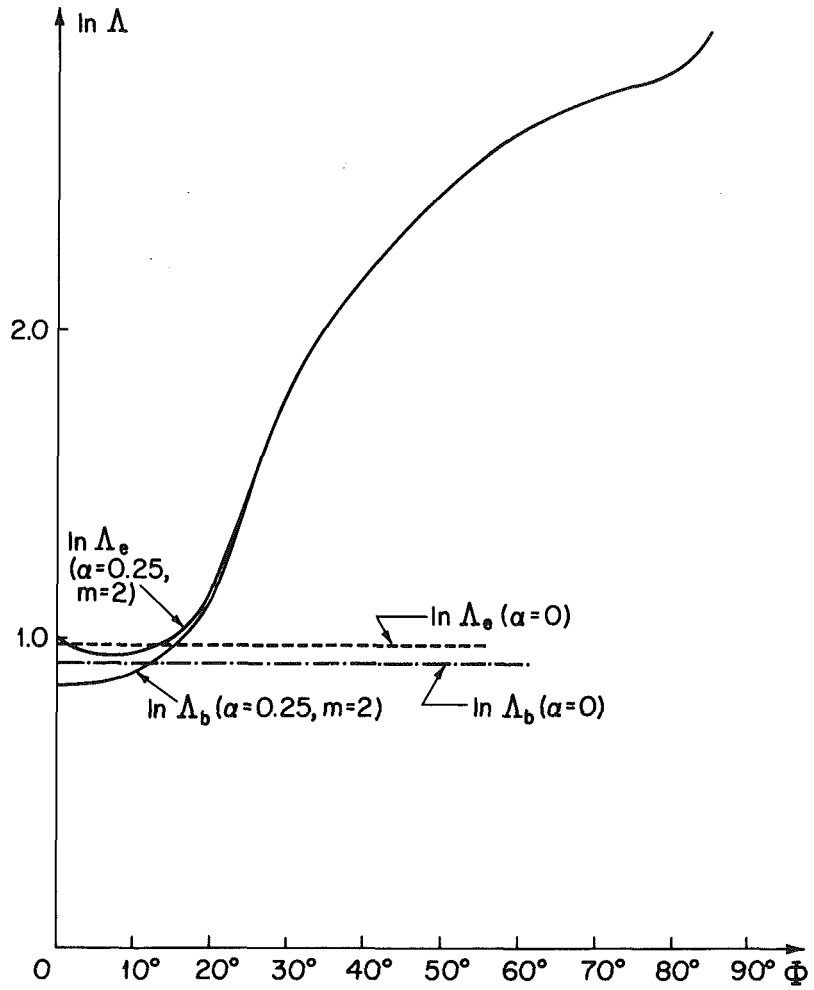

Fig. 5 Variation of the critical stretches with fiber orientaiton (tension)

for every unit vector **m**. When specialized to plane strain (4.4) yields

$$P(Z) = \det [L_{\alpha 2 \beta 2} Z^2 + (L_{\alpha 1 \beta 2} + L_{\alpha 2 \beta 1}) Z + L_{\alpha 1 \beta 1}] \neq 0 \quad (4.5)$$

for all real numbers Z ($Z = m_2/m_1$). A loss of ellipticity of the material is therefore equivalent to the presence of at least one real zero of the characteristic polynomial $P(Z)$.

In the particular case of a state of plane strain uniaxial stress the polynomial $P(Z)$ can be written explicitly by substituting the field quantities determined in Section 3 into (4.3) and (4.5). The question of a loss of ellipticity may then be addressed by studying the zeros of $P(Z)$. This was carried out numerically. For various fiber orientations Φ, we determined the stress σ (or stretch Λ) at which ellipticity fails; the results are discussed in Section 6.

In the special case when the fibers are oriented parallel to the traction-free boundary, $\Phi = \pi/2$, one finds from (2.11), (3.2), and (3.3) that

$$\begin{aligned} L_{1111} &= 3\lambda_1^{-8/3} + \lambda_1^{4/3} f'(\lambda_1^2) + 2\lambda_1^{10/3} f''(\lambda_1^2), \\ L_{2121} &= 1 + \lambda_1^{4/3} f'(\lambda_1^2), \\ L_{1212} &= L_{1221} = L_{2112} = \lambda_1^{-8/3}, \\ L_{1122} &= L_{2211} = 1, \quad L_{2222} = 3. \end{aligned} \quad (4.6)$$

where $f(\lambda_1^2) = \alpha(\lambda_1^2 - 1)^m$ and with the remaining inplane moduli being zero. It is not difficult to show that in this case the polynomial $P(Z)$ in (4.5) is now a biquadratic, and that for sufficiently large values of α, its coefficients are all positive when $\lambda_1 > 1$ (or equivalently $\sigma > 0$). Thus with suitable reinforcement, loss of ellipticity can always be prevented for tensile loading parallel to the fibers. On the other hand, one can readily show that the characteristic polynomial always has a real root, and so ellipticity is lost, in the presence of a sufficiently large compressive stress σ. This is also true, both in tension and compression, when the fibers are oriented normal to the loading direction ($\Phi = 0$).

5 Geometric Instabilities – Surface Bifurcation

Material instabilities in the form of shear localization occur at rather high strain levels. In general, and depending on the specific geometry and boundary conditions, a buckling-type global instability often precedes the onset of the more severe local instabilities mentioned in the preceding section. A simple problem that can be used to investigate the effect of reinforcement on the geometric stability of the Blatz-Ko material is the buckling of a half space under conditions of plane strain uniaxial stress. As will be subsequently see, the bifurcation mode is a surface-type mode whose amplitude decays exponentially with the distance from the free surface.

A bifurcation eigenmode $\mathbf{u}(\mathbf{x})$ is required to satisfy the incremental equilibrium equations (4.1), the traction boundary condition on the free surface (Douglas and Jaunzemis [9])

$$L_{\alpha\beta\gamma\delta} u_{\gamma,\delta} n_\beta = 0 \quad \text{on} \quad \partial R, \quad (5.1)$$

and decay condition at infinity,

$$u_\alpha \to 0, \; u_{\alpha,\beta} \to 0 \quad \text{as} \quad |\mathbf{x}| \to \infty, \quad x_2 < 0. \quad (5.2)$$

Downloaded 02 May 2010 to 171.66.16.246. Redistribution subject to ASME license or copyright; see http://www.asme.org/terms/Terms_Use.cfm

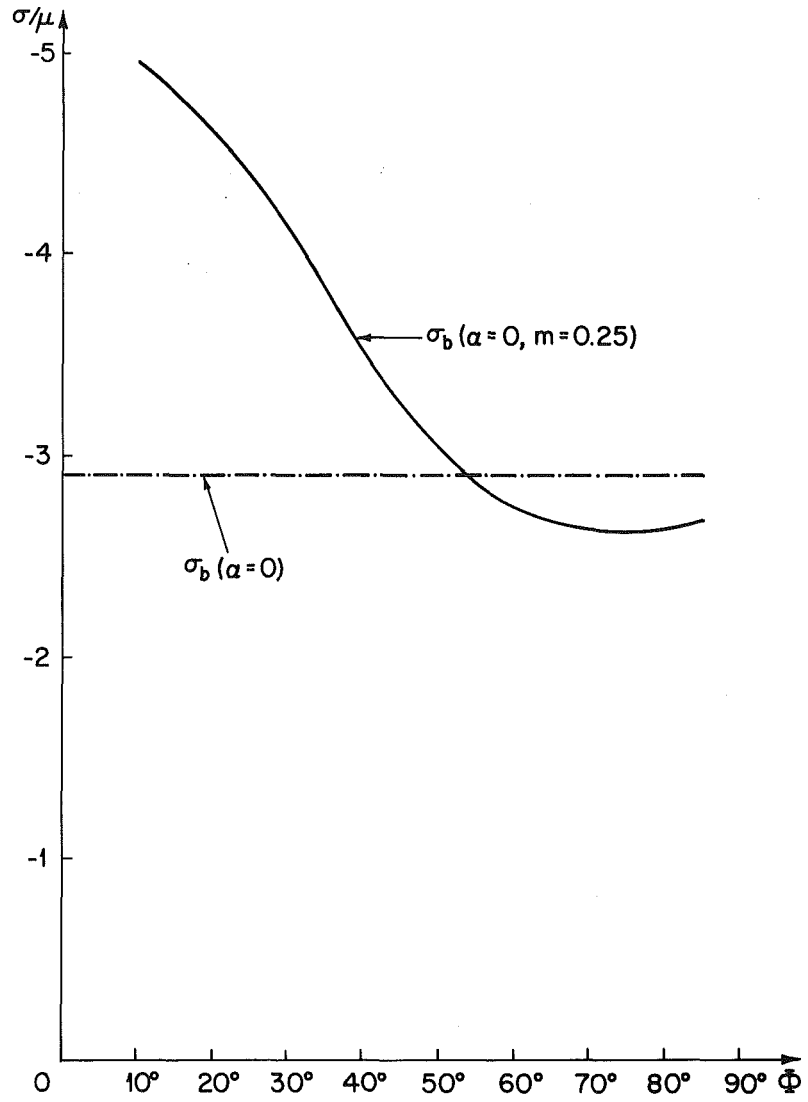

Fig. 6 Variation of the critical buckling stress σ_b with the fiber orientation (compression)

Assuming that the buckling eigenmode $\mathbf{u}(\mathbf{x})$ is twice continuously differentiable and bounded on the half space R, one can always ensure the existence of a Fourier transform $\tilde{\mathbf{u}}(\omega, x_2) = \mathfrak{F}\{\mathbf{u}(x_1, x_2) | x_1 \to \omega\}$ in the sense of distributions (Schwartz [12]). Although $\mathbf{u}$ is required to be a function in the classical sense, $\tilde{\mathbf{u}}$ in general will not be so. Consequently, the subsequent equations (5.3)–(5.8) of this section are to be interpreted in the distribution sense.

On taking the Fourier transform of the equilibrium equations (4.1) with respect to x_1 we obtain the following ordinary differential equation with respect to x_2 for $\tilde{\mathbf{u}}$

$$L_{\alpha 2\beta 2}\tilde{u}_{\beta,22} - i\omega(L_{\alpha 1\beta 2} + L_{\alpha 2\beta 1})\tilde{u}_{\beta,2} - \omega^2 L_{\alpha 1\beta 1}\tilde{u}_\beta = 0, \tag{5.3}$$

whose solution conforming to the decay condition (5.2) is

$$\tilde{u}_\alpha(\omega, x_2) = \begin{cases} \xi_1(\omega)A_\alpha^{(1)} \exp(-i\omega x_2 Z^{(1)}) + \xi_2(\omega)A_\alpha^{(2)} \exp(-i\omega x_2 Z^{(2)}) & \text{for } \omega > 0, \\ 0 & \text{for } \omega = 0, \\ \xi_1(\omega)\bar{A}_\alpha^{(1)} \exp(-i\omega x_2 \bar{Z}^{(1)}) + \xi_2(\omega)\bar{A}_\alpha^{(2)} \exp(-i\omega x_2 Z^{(2)}) & \text{for } \omega < 0. \end{cases} \tag{5.4}$$

Here $Z^{(1)}$ and $Z^{(2)}$ are the roots of the characteristic polynomial (4.5) which have positive imaginary part and a bar denotes complex conjugation. The complex (constant) unit vectors $\mathbf{A}^{(1)}$ and $\mathbf{A}^{(2)}$ satisfy

$$\{L_{\alpha 2\beta 2}(Z^{(\gamma)})^2 + (L_{\alpha 1\beta 2} + L_{\alpha 2\beta 1})Z^{(\gamma)} + L_{\alpha 1\beta 1}\} A_\beta^{(\gamma)} = 0 \quad \text{(no sum on } \gamma) \tag{5.5}$$

and ξ_1, ξ_2 are arbitrary generalized functions of ω. It should be noted that the existence of four complex roots of $P(Z)$ is ensured by the fact that we are focusing attention on the buckling modes that occur before the material loses ellipticity (and thus $P(Z)$ has no real roots).

Taking the Fourier transform of the traction-free boundary condition (5.1) gives

$$L_{\alpha 2\beta 2}\tilde{u}_{\beta,2} - i\omega L_{\alpha 2\beta 1}\tilde{u}_\beta = 0 \quad \text{for} \quad x_2 = 0, \tag{5.6}$$

since $n_1 = 0$, $n_2 = 1$. On using (5.4) in (5.6) one finds that the coefficients ξ_1, ξ_2 must necessarily satisfy

$$S_{\alpha\beta}\xi_\beta = 0 \quad \text{for} \quad \omega > 0, \quad \bar{S}_{\alpha\beta}\xi_\beta = 0 \quad \text{for} \quad \omega < 0, \tag{5.7}$$

with

$$S_{\alpha\beta} = L_{\alpha 2\gamma 2}Z^{(\beta)}A_\gamma^{(\beta)} + L_{\alpha 2\gamma 1}A_\gamma^{(\beta)} \quad \text{(no sum on } \beta). \tag{5.8}$$

Since according to (5.4) ξ_α cannot have pointwise support at

Downloaded 02 May 2010 to 171.66.16.246. Redistribution subject to ASME license or copyright; see http://www.asme.org/terms/Terms_Use.cfm

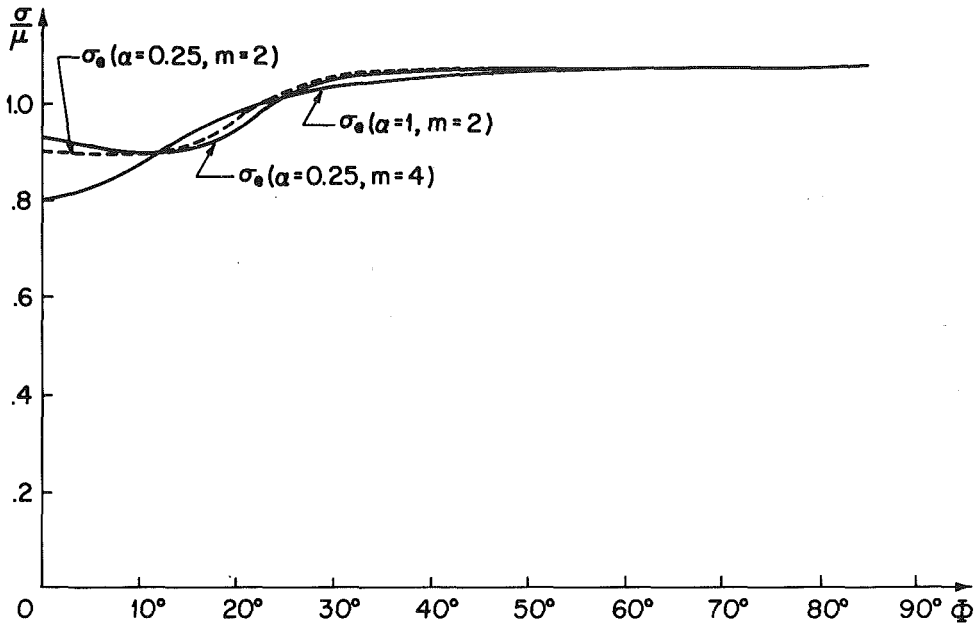

Fig. 7 Variation of the critical stress σ_e with the fiber orientation for different materials

$\omega=0$, if a nontrivial solution (ξ_1,ξ_2) to (5.7) is to exist, it is necessary and sufficient that

$$\det S=0, \tag{5.9}$$

which then ensures the existence of a nontrivial buckling eigenmode.

The *buckling condition* (5.9) was examined numerically for various fiber orientations Φ and the smallest value of the applied stress σ (or stretch Λ) for which (5.9) holds was determined. The results are described in Section 6.

One can easily deduce from (5.3) that $\mathbf{u}(x_1, x_2)$ decays exponentially with the depth x_2 from the free surface. The analysis does not, however, determine the x_1-dependence of the eigenmode. This is, of course, to be expected in view of the absence of any characteristic length in the problem.

Finally we note that bifurcation problems of this type have been previously considered by Biot [3], Hutchinson and Tvergaad [11], and others for orthotropic materials. These studies preassume the form of the bifurcation eigenmode and thus, at least in principle, lead to conditions that are necessary for buckling in the prescribed eigenmode only.

6 Results and Discussion

The numerical results reported here for the onset of a surface bifurcation and the loss of ellipticity of the reinforced Blatz-Ko material were based on a straightforward numerical implementation of the analysis presented in Sections 4 and 5. Of main interest in these calculations has been the dependence of the bifurcation and loss of ellipticity stresses σ_b, σ_e, (and the corresponding surface stretch ratios Λ_b, Λ_e), on the fiber angle Φ. The influence of the "density of reinforcement" which was assumed to be represented by the parameter α in the constitutive model (2.9) as well as that of the "fiber stiffness" characterized by the exponent m in the aforementioned equation was also examined.

For purposes of references we note that the unreinforced (isotropic) Blatz-Ko material loses ellipticity at $\sigma_e/\mu \simeq -13.17$, ($\Lambda_e \simeq 0.37$) in compression, [2]. Similarly a surface-type bifurcation first occurs at $\sigma_b/\mu \simeq 0.915$ ($\Lambda_b \simeq 2.52$) in tension and at $\sigma_b/\mu \simeq -2.9$ ($\Lambda_b \simeq 0.6$) in compression, [5].

In Fig. 4 we have plotted σ_b and σ_e versus Φ for plane strain tension ($\sigma > 0$) in the case of a material with $\alpha = 0.25$ and $m = 2$. Note that the value of σ_e is very close to that of σ_b (with $\sigma_e \geq \sigma_b$ for Φ less than $\simeq 27$ deg and $\sigma_b \geq \sigma_e$ for Φ greater than $\simeq 27$ deg. For fiber angles Φ exceeding $\simeq 27$ deg it is almost impossible to distinguish between the stress levels corresponding to bifurcation and loss of elliptiticy. For sufficiently small values of Φ the fibers in fact *weaken* the material with respect to its stability, with the instabilities occuring at stress levels that are less than the corresponding values for the isotropic case. Thereafter, the critical stresses σ_b, σ_e increase continuously with Φ. The relatively slow increase in σ_b and σe with respect to increasing Φ may be explained in part by the fact that the stress-stretch curves for this material are rather flat at sufficiently large stretches (Fig. 3). As will be seen in Fig. 5, the *stretches* at which these instabilities occur in fact increase sharply with Φ. The maximum stress σ_m, as described at the end of Section 3, is also shown in this figure. For angle Φ less than $\simeq 27$ deg, bifurcation and loss of ellipticity occur before the maximum stress σ_m is reached while when Φ exceeds this value these phenomena occur after σ_m has been attained, i.e., at stretch ratios exceeding Λ_m.

In Fig. 5 we have plotted the logarithmic surface strains at instability, $\epsilon_b = ln\ \Lambda_b$ and $\epsilon_e = ln\ \Lambda_e$, under the preceding conditions. One observes again that for sufficiently small fiber angles Φ the fibers weaken the material against instability. As before, the distinction between σ_b and σ_e for Φ exceeding $\simeq 27$ deg is virtually impossible. Also not that the critical strains increase sharply with relatively small changes in the undeformed fiber angle Φ, and the predicted critical surface strain levels rapidly reach values that appear to be unrealistically high.

Figure 6 depicts the dependence of the bifurcation stress σ_b on the fiber angle Φ for the same material as before but in the case of compression ($\sigma < 0$).The stress at a loss of ellipticity in this case was considerably higher than σ_b and is thus not shown in this figure. (For example at $\Phi = 45$ deg it is found that $\sigma_e/\mu \simeq -19.5$.) We note two main differences between the tensile and compressive cases. In compression σ_b is highly dependent on the fiber angle Φ, presumably as a result of the steepness of the stress-stretch curves (Fig. 1). Secondly, bifurcation occurs at a stress level that is considerably smaller than σ_e. In contrast to the tensile case, here σ_b decrease with Φ. We also note that the reinforced material is weaker than

Downloaded 02 May 2010 to 171.66.16.246. Redistribution subject to ASME license or copyright; see http://www.asme.org/terms/Terms_Use.cfm

the unreinforced one for the fiber angles close to 90 deg (see also Arcisz [6]).

To investigate the effect of the material properties on stability, we have changed both the "fiber density" parameter α and the "fiber stiffness' parameter m and recalculated σ_b and σ_e in the case of tension. The variation of σ_e is shown in Fig. 7, with σ_b having values very close to σ_e as in the case discussed previously. It is of interest to note that the increase in m does not seem to significantly alter the stability properties of the material, for small angles Φ.

In conclusion, the results presented here for the particular Blatz-Ko material indicate that reinforcement in the direction of stressing provides the "greatest stability" in the case of tensile loading but "weakens" the material in the case of compression. The opposite is true when the fibers are normal to the load.

Acknowledgments

The results reported in this paper were obtained in the course of an investigation supported in part by the National Science Foundation through Grant CME 81-06581.

References

1 Blatz, P. J., and Ko, W. L., "Application of Finite Elastic Theory to the Deformation of Rubbery Materials," *Transaction of the Society of Rheology*, Vol. 6, 1962, pp. 223–251.

2 Knowles, J. W., and Sternberg, E., "On the Ellipticity of the Equations of Nonlinear Elastostatics for a Special Material," *Journal of Elasticity*, Vol. 5, 1975, pp. 341–361.

3 Biot, M. A., *Mechanics of Incremental Deformations*, Wiley, New York, 1965.

4 Hill, R., and Hutchinson, J. W., "Bifurcation Phenomena in the Plane Tension Test," *Journal of the Mechanics and Physics of Solids*, Vol. 23, 1975, pp. 239–264.

5 Kurashige, M., "Instability of a Transversely Isotropic Elastic Slab Subjected to Axial Loads," ASME JOURNAL OF APPLIED MECHANICS, Vol. 48, 1981, pp. 351–356.

6 Arcisz, M., "Bifurcation Conditions for Ideal Fiber-Reinforced Materials," *International Journal of Solids and Structures*, Vol. 16, 1980, pp. 1109–1121.

7 Rice, J. R., "The Localization of Plastic Deformation," *Proceedings of the 14th IUTAM Congress*, Koiter, W. T., ed., Delft, Netherlands, Aug. 1976, pp. 207–220.

8 Knowles, J. K., and Sternberg, E., "On the Failure of Ellipticity of the Equations for Finite Elastostatic Plane Strain," *Archive for Rational Mechanics and Analysis*, Vol. 63, 1977, pp. 321–326.

9 Douglas, W. J., and Jaunzemis, W., "Stability of Prestrained Laminated Media," *Proceedings of the 5th Symposium on Naval Structural Mechanics*, Wendt, F. W., et al., eds., 1967, pp. 679–700.

10 Spencer, A. J. M., *Deformations of Fiber-Reinforced Materials*, Oxford University Press , 1972.

11 Hutchinson, J. W., and Tvergaard, V., "Surface Instabilities on Statically Strained Plastic Solids," *International Journal of Mechanical Sciences*, Vol. 22, 1980, pp. 339–354.

12 Schwartz, L., *Theorie des Distributions*, Herrmann, 1950.

Downloaded 02 May 2010 to 171.66.16.246. Redistribution subject to ASME license or copyright; see http://www.asme.org/terms/Terms_Use.cfm

T. J. Delph
Department of Mechanical Engineering and Mechanics,
Lehigh University,
Bethlehem, Pa. 18015

G. Herrmann
Professor and Chairman,
Division of Applied Mechanics,
Stanford University,
Stanford, Calif. 94305
Fellow, ASME

An Effective Dispersion Theory for Layered Composites

A new approximate theory for wave propagation in a periodically layered elastic body is proposed. In its present state, the theory is valid for either propagation normal to the layering or for propagation under antiplane strain conditions. The theory is based on microstructural theories of elasticity, and makes use of a collocation technique in conjunction with the exact solution for wave propagation in an unbounded elastic body. The results are considered to hold promise for formulating accurate approximate solutions to certain types of boundary-initial value problems for composite bodies.

Introduction

The increasing use of layered composites in light weight, high-strength structures has led to a corresponding increase in efforts to analyze the dynamic behavior of these materials. In most of these analyses, the composite is modeled as a periodically layered body, with the constituent layers composed of homogeneous, linearly elastic material. The layers may be assumed to be isotropic or to have some specified anisotropy. Initial/boundary value problems may then be formulated for such a body within the framework of the classical theory of elasticity, but the heterogeneous nature of the body makes exact solutions very difficult to obtain. For this reason, an approximate theory is usually required for practical applications.

If the wavelengths of interest are considerably greater than the characteristic layer thicknesses, then the effective modulus theory may be used. Here the body is modeled as a homogeneous, but anisotropic, solid, with the material constants derived in some fashion from the properties of the constituent layers. The effective modulus theory becomes invalid, however, when the wavelengths are on the order of the layer thicknesses. At these shorter wavelengths, the successive reflection and refraction of waves from layer interfaces tend to break down the structure of progressive waves. This leads to a marked dispersive effect not predicted by the effective modulus theory.

To account for this dispersive effect, an approximate theory that in some fashion takes into account the heterogeneous nature of the body is required. A number of such theories, which could be collectively called microstructural theories, have appeared in the literature in recent years. Perhaps the earliest example is the effective stiffness theory of Sun, Achenbach, and Herrmann [1, 2] which was later extended by Drumheller and Bedford [3, 4]. Other representative work in this area includes that of Hegemier and co-workers [5-7], the mixture theory of Bedford and Stern [8], and the recent work of McNiven and Mengi [9]. A somewhat different approach is taken by Kohn, Krumhansl, and Lee [10], and Nemat-Nasser and co-workers [11, 12], who emphasize variational techniques. More complete bibliographies may be found in references [13] and [14].

In this paper we set forth a new microstructural theory for wave propagation in a periodically layered solid. In its present formulation, this theory is valid for one-dimensional wave propagation normal to the layering and for two-dimensional propagation under conditions of antiplane strain. The new theory, to be known as the *effective dispersion theory*, is conceptually simple, yet seems to be at least as accurate, and in some cases significantly more accurate, than other existing theories.

The effective dispersion theory is based in part on earlier theories of linear elasticity with microstructure set forth by Mindlin [15] and Kunin [16]. In the general theories of these

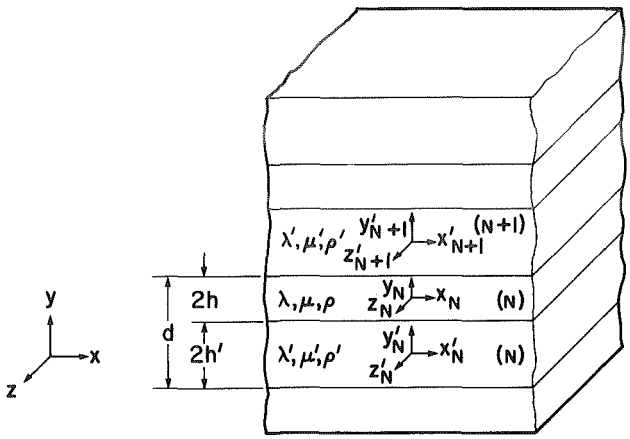

Fig. 1 Geometry of layered elastic solid

Contributed by the Applied Mechanics Division for publication in the JOURNAL OF APPLIED MECHANICS.

Discussion on this paper should be addressed to the Editorial Department, ASME, United Engineering Center, 345 East 47th Street, New York, N.Y. 10017, and will be accepted until two months after final publication of the paper itself in the JOURNAL OF APPLIED MECHANICS. Manuscript received by ASME Applied Mechanics Division, January, 1981; final revision, August, 1982.

Copyright © 1983 by ASME
Downloaded 02 May 2010 to 171.66.16.246. Redistribution subject to ASME license or copyright; see http://www.asme.org/terms/Terms_Use.cfm

authors, no definite procedure is given for determining the coefficients in the differential equations of motion. In the present work these are determined by matching as closely as possible the predictions of the approximate theory to the known solutions for one-dimensional and antiplane strain wave propagation in an unbounded, periodically layered body [17, 18]. It is from this matching procedure that the effective dispersion theory takes its name.

Governing Equations and Boundary Conditions

The layered body, B, is assumed to be composed of periodically alternating layers of homogeneous, isotropic, linearly elastic material (Fig. 1). The layers have thicknesses $2h$; $2h'$, densities ρ; ρ' and elastic constants λ,μ; λ',μ'. Any two adjacent layers comprise a *unit cell*, and this unit cell is repeated periodically along the y-axis. The body is taken to be of unbounded extent along the z-axis, but bounded in planes parallel to the x-y plane by the curve $C(x,y)$, which we assume to be continuously differentiable in x and y.

As noted in the Introduction we will consider only the case of wave propagation in antiplane strain (SH-wave propagation). However, in the special case of wave propagation normal to the layering, the resulting theory is also applicable to longitudinal wave propagation if the characteristic shear wave speed for each layer is replaced by the characteristic longitudinal wave speed. For antiplane strain motion, the displacement component parallel to the z-axis is taken to be the only nonzero displacement component and is assumed to be a function only of time and the x and y coordinates. We now assume that the displacements in the Nth unit cell are given by

$$\begin{aligned} w(x,y,t) &= w_0(x,y,t)\Big|_{y_N=0} + y_N(x,y,t)\Big|_{y_N=0} \\ w'(x,y,t) &= w_0(x,y,t)\Big|_{y'_N=0} \end{aligned} \tag{1}$$

Here w and w' are the displacements in the layers with unprimed and primed constants, respectively. y_N and y'_N are local coordinates having their origin at the midplane of the layers with unprimed and primed constants, respectively. The validity of equation (1) depends partly on the assumption that the layers with unprimed constants are sufficiently stiff compared to the layers with primed constants so that all the deformation is essentially confined to the softer layers. For the typical composite used in structural applications, the moduli of the stiffer layers are on the order of 50 to 100 times greater than those in the softer layers. Thus for such materials this assumption can be expected to agree well with reality at the lower frequencies and wave numbers for which the effective dispersion theory is valid.

In the ensuing analysis we will follow the procedure utilized by Achenbach, Sun, and Herrmann [2] in dealing with a similar problem. First we postulate specific forms for the strain and kinetic energy density functions. The reason behind the choice of a particular functional form here will be mentioned subsequently. We take

$$\begin{aligned} W = {} & A_{ijkl}e_{ij}e_{kl}/2 + B_{ijkl}e_{ij}\gamma_{kl}/2 + C_{ijkl}\gamma_{ij}\gamma_{kl}/2 \\ & + D_{ijklmn}\kappa_{ijk}\kappa_{lmn}/2 + E_{ijklmn}\kappa_{ijk}\theta_{lmn}/2 \\ & + F_{ijklmn}\theta_{ijk}\theta_{lmn}/2. \end{aligned} \tag{2}$$

Here $A_{ijkl},\ldots,F_{ijklmn}$ are constants to be determined and e_{ij}, γ_{ij}, κ_{ijk}, and θ_{lmn} are various microstructural strain measures introduced by Mindlin [15]. In our case, only certain of these are taken to be nonzero. These are, following the notation of [2]

$$\begin{aligned} e_{32} &= e_{23} = \partial_y w_0/2 \\ e_{13} &= e_{31} = \partial_x w_0/2 \\ \gamma_{23} &= \partial_y w_0 - \psi \\ \theta_{223} &= \partial_{yy} w_0 - \partial_y \psi \\ \kappa_{223} &= \partial_y \psi \\ \kappa_{123} &= \kappa_{321} = \partial_x \psi/2 \end{aligned} \tag{3}$$

where

$$\partial_y(\ ) = \frac{\partial}{\partial y}(\ ).$$

All other microstructural strain measures not defined explicitly in (3) are assumed to vanish. Furthermore, we assume for the sake of simplicity that

$$\begin{aligned} & A_{2323} = A_{2332} = A_{3223} = A_{3232} \\ & A_{1313} = A_{3131} = A_{1331} = A_{3131} \\ & A_{1323} = A_{2313} = A_{1332} = A_{3213} = A_{3123} = A_{2331} \\ & \qquad = A_{3132} = A_{3231} = 0 \\ & B_{2323} = B_{3232} \\ & B_{1323} = B_{3123} = 0 \\ & D_{223123} = D_{123223} = D_{223321} = D_{321223} = 0 \\ & D_{123123} = D_{321321} = D_{123321} = D_{321123} \\ & E_{123223} = E_{321223} = 0 \end{aligned} \tag{4}$$

The kinetic energy density is

$$T = b_1 \dot{w}_0^2/2 + b_2 \dot{\psi}^2/2 \tag{5}$$

where the superposed dot indicates partial differentiation with respect to time. The assumed forms for the strain and kinetic energy densities are now substituted into Hamilton's principle, which we write as

$$\delta \int_B \int_{t_0}^{t_1} (T - W)\, dt\, dV + \int_{t_0}^{t_1} W_e\, dt = 0 \tag{6}$$

As usual, the variations δw_0 and $\delta\psi$ are assumed to vanish at $t = t_0$, t_1. W_e is the work done by external tractions on the bounding surface of the body. Again, following [2], we assume this to be given by

$$\delta W_e = \int_s [P(x,y)\,\delta w_0 + M(x,y)\,\delta\psi + Q(x,y)\,D\delta w_0]\,dS \tag{7}$$

Here D is the normal derivative operator on the bounding curve $C(x,y)$ given by $D = n_x\partial/\partial_x + n_y\partial/\partial_y$ and n_x and n_y are, respectively, the x and y components of the unit normal vector to $C(x,y)$. Body forces are assumed to vanish.

The derivation of the governing equations and the associated boundary conditions now follows that presented in [2], which we will not repeat in detail. Briefly, we make use of equations (2)–(4) to define the following generalized stress quantities

$$\begin{aligned} \tau_{23} &\equiv \partial W/\partial e_{23} = (A_{2323} + B_{2323}/2)\partial_y w_0 - B_{2323}\psi/2 \\ \tau_{13} &\equiv \partial W/\partial e_{13} = A_{1313}\partial_x w_0 \\ \sigma_{23} &\equiv \partial W/\partial \gamma_{23} = (B_{2323}/2 + C_{2323})\partial_y w_0 - C_{2323}\psi \\ \mu_{123} &\equiv \partial W/\partial \kappa_{123} = D_{123123}\partial_x \psi \\ \mu_{223} &\equiv \partial W/\partial \kappa_{223} = (D_{223223} - \\ & \qquad E_{223223}/2)\partial_y \psi + E_{223223}\partial_{yy} w_0/2 \\ \chi_{223} &\equiv \partial W/\partial \theta_{223} = (E_{223223}/2 - F_{223223})\partial_y \psi + F_{223223}\partial_{yy} w_0 \end{aligned} \tag{8}$$

Equations (7) and (8), after several applications of the divergence theorem, then yield the equations of motion

$$\begin{aligned} & -b_1 \ddot{w}_0 + \partial_y \tau_{23} + \partial_x \tau_{13} - \partial_{yy}\chi_{223} + \partial_y \sigma_{23} = 0 \\ & -b_2 \ddot{\psi} + \partial_y \mu_{223} + \partial_x \mu_{123} - \partial_y \chi_{223} + \sigma_{23} = 0 \end{aligned} \tag{9}$$

Downloaded 02 May 2010 to 171.66.16.246. Redistribution subject to ASME license or copyright; see http://www.asme.org/terms/Terms_Use.cfm

with the associated natural boundary conditions on the surface bounded by $C(x,y)$

$$\{-n_x\tau_{13}-n_y(\tau_{23}+\sigma_{23}-\partial_y\chi_{223})$$
$$-[(1-n_x^2)\partial_x n_x-n_x n_y(\partial_y n_x+\partial_x n_y)$$
$$+(1-n_y^2)\partial_y n_y]n_y^2\chi_{223}+n_y[-n_x n_y\partial_x\chi_{223}+(1-n_y^2)\partial_y\chi_{223}]$$
$$+[-n_x n_y\partial_x n_y+(1-n_y^2)\partial_y n_y]\chi_{223}+P(x,y)]\}\delta w_0=0 \quad (10)$$
$$[-n_x\mu_{123}-n_y(\mu_{223}-\chi_{223})+M(x,y)]\delta\psi=0$$
$$[-n_y^2\chi_{223}+Q(x,y)]D\delta u_0=0$$

Note that the last of equations (10) implies that $Q(x,y)$ must vanish on surfaces where $n_y=0$ if $D\delta u_0\neq 0$. This is somewhat analogous to a restriction present in the effective stiffness theory [2].

Determination of Coefficients

We now have to determine the various constants in the expressions for the strain and kinetic energy densities given by equations (2) and (5). To this end, we rewrite equations (9) as

$$-b_1\ddot{w}_0+a_1\partial_{yy}w_0+a_2\partial_{yyyy}w_0-a_3\partial_y\psi-a_4\partial_{yyy}\psi+a_7\partial_{xx}w_0=0$$
$$-b_2\ddot{\psi}+a_3\partial_y w_0+a_4\partial_{yyy}w_0-a_5\psi-a_6\partial_{yy}\psi+a_8\partial_{xx}\psi=0 \quad (11)$$

where, with the aid of equation (4), we have defined

$$a_1=A_{2323}+B_{2323}+C_{2323} \qquad a_5=C_{2323}$$
$$a_2=-F_{223223} \qquad a_6=E_{223223}-F_{223223}-D_{223223}$$
$$a_3=B_{2323}/2+C_{2323} \qquad a_7=A_{1313} \quad (12)$$
$$a_4=E_{223223}/2-F_{223223} \qquad a_8=D_{123123}$$

Before proceeding further, we will pause to note that the form of the displacement equations of motion (11) for the special case of wave propagation normal to the layering ($\partial/\partial x=0$) is identical in form to equations of motion for an elastic body with microstructure proposed by Kunin [16] on the basis of an analysis of a generalized continuum model. These equations are claimed by Kunin to represent the most general second-order approximation to the one-dimensional equations of motion of an elastic body with microstructure, and were, in fact, the primary motivation behind the particular choice of strain and kinetic energy density functions made in equations (2), (4), and (5).

To determine the unknown coefficients in the equations of motion (11), we take the approach of matching the behavior of the approximate solution as closely as possible to the exact solution for wave propagation in an unbounded layered body, paying particular attention to matching the dispersion spectrum. It is known [19], that the general solution to an initial/boundary value problem may be expressed in terms of a Fourier integral involving the dispersion spectrum for the system under consideration. Hence matching the dispersion spectrum of the approximate system as closely as possible to that of the exact system ought to be expected to minimize the error incurred in solutions of the approximate equations to initial/boundary value problems, at least at the lower frequencies and wave numbers for which the approximate model is valid. It might be noted that Mindlin plate theory, which makes use of a "correction coefficient" to match the lowest cut-off frequency to the exact value, has been employed very successfully for similar purposes.

In order to examine the case of harmonic wave propagation in an unbounded body, we assume solutions of the form

$$w_0=Ae^{i(k_x x+k_y y-\omega t)}; \quad \psi=Be^{i(k_x x+k_y y-\omega t)} \quad (13)$$

Substitution of (13) into (11) yields a set of two linear, homogeneous equations in A and B; the requirement that the determinant of the matrix of coefficients vanishes gives the dispersion equation in the form

$$\alpha\omega^4+(\beta k_y^4+\gamma k_y^2+\delta+\phi k_x^2)\omega^2+\xi k_y^2+\sigma k_x^2+\theta k_y^4+\rho k_x^2k_y^2$$
$$+\tau k_x^4+k_y^6+\epsilon k_x^2k_y^4=0 \quad (14)$$

where

$$\alpha=b_1b_2/T; \quad \beta=a_2b_2/T; \quad \gamma=(a_6b_1-a_1b_2)/T$$
$$\delta=-a_5b_1/T; \quad \xi=(a_1a_5-a_3^2)/T;$$
$$\theta=(2a_3a_4-a_1a_6-a_2a_5)/T$$
$$\phi=-(a_7b_2+a_8b_1)/T; \quad (15)$$
$$\sigma=a_5a_7/T; \quad \rho=(a_1a_8-a_6a_7)/T$$
$$\tau=a_7a_8/T; \quad \epsilon=-a_2a_8/T; \quad T=a_2a_6-a_4^2$$

Primary attention will be given to the spectral behavior for propagation normal to the layering, since this is known [18], to be the most complicated part of the spectrum. Specifically, the exact spectrum for propagation normal to the layering displays a marked banded structure. It is divided into regions known as Brillouin zones within which the spectrum is real-valued, continuous, and single-valued. The spectrum is discontinuous and double-valued at the ends of the Brillouin zones, the points of discontinuity between the real branches being connected by complex branches known as stopping bands. Further details are given in reference [17].

In order to simplify the resulting analysis, we will initially take the variation of all terms in equation (11) with x to vanish and set $k_x=0$ in equation (14). We first wish to match the approximate spectrum for propagation normal to the layering resulting from equation (14) to the exact result for an unbounded body as given by reference [17]. To this end we make use of a simple collocation technique where the approximate spectrum will be required to match the exact frequency and slope at zero wave number, and at the wave number defining the end of the first Brillouin zone $k_y=k_B$ where the frequency is double-valued with $\omega=\omega_B$ and $\omega=\omega_D$. More specifically, we will require that

$$\left.\frac{d\omega}{dk_y}\right|_{\substack{\omega=0\\k_y=0}}=c_g; \quad \omega\Big|_{k_y=k_B}=\omega_B; \quad \omega\Big|_{k_y=k_B}=\omega_D$$
$$\left.\frac{d\omega}{dk_y}\right|_{\substack{\omega=\omega_B\\k_y=k_B}}=0; \quad \left.\frac{d\omega}{dk_y}\right|_{\substack{\omega=\omega_D\\k_y=k_B}}=0. \quad (16)$$

where c_g is the slope of the exact spectrum at $\omega=k=0$. Here $k_B=(\pi/2)(h+h')^{-1}$ and the quantities c_g, ω_B, and ω_B may be obtained from the exact dispersion relation for an unbounded layered body.

Upon introducing (16) into (14), we obtain five linear equations for the six parameters α, β, γ, δ, ξ, and θ. The five equations serve to determine five of the parameters in terms of c_g, ω_B, ω_D, and k_B, and the remaining parameter, which we will take to be θ. We obtain

$$\alpha=-\frac{k_B^4}{\omega_B^2\omega_D^2}(\theta+2k_B{}^2)$$
$$\beta=\frac{1}{k_B{}^2}\left[\left(\frac{2}{c_g{}^2}+Rk_B^2\right)\theta+\frac{3k_B^2}{c_g{}^2}+2Rk_B{}^4\right]$$
$$\delta=\frac{k_B{}^2}{c_g{}^2}(2\theta+3k_B{}^2)$$
$$\xi=-k_B{}^2(2\theta+3k_B{}^2)$$
$$\gamma=-2\left[\left(\frac{2}{c_g{}^2}+Rk_B{}^2\right)\theta+\frac{3k_B{}^2}{c_g{}^2}+2Rk_B{}^4\right] \quad (17)$$

where

$$R=-\frac{(\omega_B{}^2+\omega_D{}^2)}{\omega_B^2\omega_D^2}.$$

Downloaded 02 May 2010 to 171.66.16.246. Redistribution subject to ASME license or copyright; see http://www.asme.org/terms/Terms_Use.cfm

The matching procedure to this point has left the value of θ undetermined. In order to specify a value of θ, we first impose the fundamental requirement that the approximate dispersion spectrum yield real-valued frequencies for all values of wave number. This requirement insures the stability of the displacement fields given by equation (13) in that exponential growth of the displacements with time is not allowed. A straightforward argument based on equations (14) and (17) indicates that this will be the case if and only if the following three inequalities are satisfied:

$$2 < c \leq 6 \tag{18}$$

$$(2-c) R k_B{}^2 c_g{}^2 + (3-2c) \leq 0 \tag{19}$$

$$h(k_y) \equiv \beta^2 k_y{}^8 + (2\beta\gamma - 4\alpha) k_y{}^6 + (\gamma^2 + 2\beta\delta - 4\alpha\theta) k_y{}^4 + (2\gamma\delta - 4\alpha\xi) k_y{}^2 + \delta^2 \geq 0 \tag{20}$$

where $c = -\theta / k_B{}^2$ and we note that $R k_B{}^2 c_g{}^2 < 0$. Inspection reveals that it is always possible to pick a value of c so as to satisfy jointly the inequalities (18) and (19).

The function $h(k_y)$ as defined by the inequality (20) is a fourth-order polynomial in $k_y{}^2$ whose coefficients depend on the parameter θ through equations (17). Since $h(0) = \delta^2 \geq 0$, it is apparent that the inequality (20) will be satisfied for all values of k_y if and only if $h(k_y)$ has no real roots, or at most double real roots. Due to the complexity of $h(k_y)$, numerical analysis is required to determine whether or not there exist values of θ such that $h(k_y)$ has no real roots, or double real roots, and such that inequalities (18) and (19) are satisfied. If this is the case, then for these values of θ, the dispersion equation (14) will yield only real frequencies and thus guarantee stable displacements.

To complete the determination of the parameter θ, we now consider the question of inverting the first six of equations (15) to determine the coefficients of the equations of motion in terms of the six parameters α, β, γ, δ, ξ, and θ. Since the equations of motion are homogeneous, one of the coefficients may be fixed arbitrarily. We will take this coefficient to be a_6 and normalize the remaining seven coefficients with respect to a_6. The inversion procedure then yields

$$\begin{aligned}
\frac{a_1}{a_6} &= -\left(\frac{a_2}{a_6}\right)\left(\frac{\delta}{\beta}\,\frac{a_6}{a_5} + \frac{\gamma}{\beta}\right) \\
\frac{a_3}{a_6} &= \pm\left(\frac{a_2}{a_6}\right)^{1/2}\left[\left(\frac{\alpha\xi}{\beta\delta} - \frac{\gamma}{\beta}\right)\frac{a_5}{a_6} - \frac{\delta}{\beta}\right]^{1/2} \\
\frac{a_4}{a_6} &= \pm\left(\frac{a_2}{a_6}\right)^{1/2}\left(1 + \frac{\alpha}{\beta\delta}\,\frac{a_5}{a_6}\right)^{1/2} \\
\frac{b_1}{a_6} &= \frac{a_2}{a_6}\,\frac{\alpha}{\beta} \\
\frac{b_2}{a_6} &= -\frac{\alpha}{\delta}\,\frac{a_5}{a_6}
\end{aligned} \tag{21}$$

where the ratio a_5/a_6 is a root of

$$\left(\frac{\alpha\theta}{\beta\delta} - 1\right)\left(\frac{a_5}{a_6}\right)^2 + \frac{\gamma}{\beta}\left(\frac{a_5}{a_6}\right) + \frac{\delta}{\beta} \pm 2\left(\frac{a_5}{a_6}\right)\left(1 + \frac{\alpha}{\beta\delta}\,\frac{a_5}{a_6}\right)^{1/2} \times \left[\left(\frac{\alpha\xi}{\beta\delta} - \frac{\gamma}{\beta}\right)\frac{a_5}{a_6} - \frac{\delta}{\beta}\right]^{1/2} = 0. \tag{22}$$

The positive sign in the last term in equation (22) is to be taken when a_3 and a_4 are of the same sign, and the negative sign when they are of the opposite sign. The ratio a_2/a_6 is left as yet undetermined.

Since θ is not completely determined by the requirement that the frequencies in the approximate spectrum be real, we now seek to obtain a value of θ which, besides yielding real frequencies, also gives real roots for a_5/a_6 in equation (22). Squaring equation (22), we obtain the following fourth-order polynomial in a_5/a_6

$$\left[\left(\frac{\alpha\theta}{\beta\delta} - 1\right)^2 - 4\frac{\alpha}{\beta\delta}\left(\frac{\alpha\xi}{\beta\delta} - \frac{\gamma}{\beta}\right)\right]\left(\frac{a_5}{a_6}\right)^4 + \left[2\frac{\gamma}{\beta}\left(\frac{\alpha\theta}{\beta\delta} - 1\right) - 4\left(\frac{\alpha\xi}{\beta\delta} - \frac{\gamma}{\beta}\right) + 4\frac{\alpha}{\beta^2}\right] \times \left(\frac{a_5}{a_6}\right)^3 + \left[\frac{\gamma^2}{\beta^2} + 2\frac{\delta}{\beta}\left(\frac{\alpha\theta}{\beta\delta} - 1\right) + 4\frac{\delta}{\beta}\right]\left(\frac{a_5}{a_6}\right)^2 + 2\frac{\gamma\delta}{\beta^2}\left(\frac{a_5}{a_6}\right) + \frac{\delta^2}{\beta^2} = 0 \tag{23}$$

where the coefficients are functions of the parameter θ. Due to its complexity, the roots of equation (23) must be determined numerically. When this is done, a rather surprising fact emerges, namely, that equation (23) and $h(k_y)$ as defined by the inequality (20) both exhibit a double real root for the same value of θ. Furthermore, for values of θ greater than this value, equation (23) and $h(k_y)$ both have distinct real roots, while for values less than this value, they have no real roots. This behavior was checked numerically using several different sets of values of ω_B, ω_D, c_g, and k_B and the criterion for double roots of a fourth-order polynomial derived from the theory of eliminants [20]. In every case the same value of θ produced a double real root for both $h(k_y)$ and equation (23). It is thus concluded that this behavior is not coincidental.

We now see that θ may be determined uniquely as the value that yields double real roots for $h(k_y)$ and equation (23), thus simultaneously satisfying the inequality (20) and the condition that a_5/a_6 be real. Furthermore the quantity a_5/a_6 will be determined uniquely as well. The ambiguity in the signs of a_3 and a_4 may be resolved by numerically determining whether the positive or negative sign must be taken in the last term of equation (22) in order that the double real root a_5/a_6 satisfy (22). Of course, the remaining two roots of $h(k_y)$ must be complex to insure real frequencies. Numerical analysis is required to test the satisfaction of this requirement.

Once θ is determined, the approximate dispersion spectrum is completely specified. We now take up the question of finding the ratio (a_2/a_6) which, with the values of θ and (a_5/a_6) obtained from the procedure just described and equations (17), will determine all of the coefficients on the equations of motion. This is accomplished in a straightforward manner [21] by simply requiring continuity of the displacement components u and u' from equation (1) at the layer interfaces when $k_y = k_B$ and $\omega = \omega_B$. This requirement gives

$$\frac{a_2}{a_6} = \left\{\frac{k_B\left[\left(\frac{\alpha\xi}{\beta\delta} - \frac{\gamma}{\beta}\right)\frac{a_5}{a_6} - \frac{\delta}{\beta}\right]^{1/2} \pm k_B{}^3\left(1 + \frac{\alpha}{\beta\delta}\,\frac{a_5}{a_6}\right)^{1/2}}{k_B{}^2\left(\frac{\delta}{\beta}\,\frac{a_6}{a_5} + \frac{\gamma}{\beta}\right) + k_B{}^4 + \omega_B{}^2\,\frac{\alpha}{\beta}}\right\}^2 \tag{24}$$

The positive sign is taken in the second term of the numerator of (24) if a_3 and a_4 are taken to be of opposite sign, while the negative sign is taken if a_3 and a_4 are of the same sign.

This completes the specification of the one-dimensional theory. We now return to a consideration of two-dimensional wave propagation in antiplane strain for which $k_x \neq 0$. We

Downloaded 02 May 2010 to 171.66.16.246. Redistribution subject to ASME license or copyright; see http://www.asme.org/terms/Terms_Use.cfm

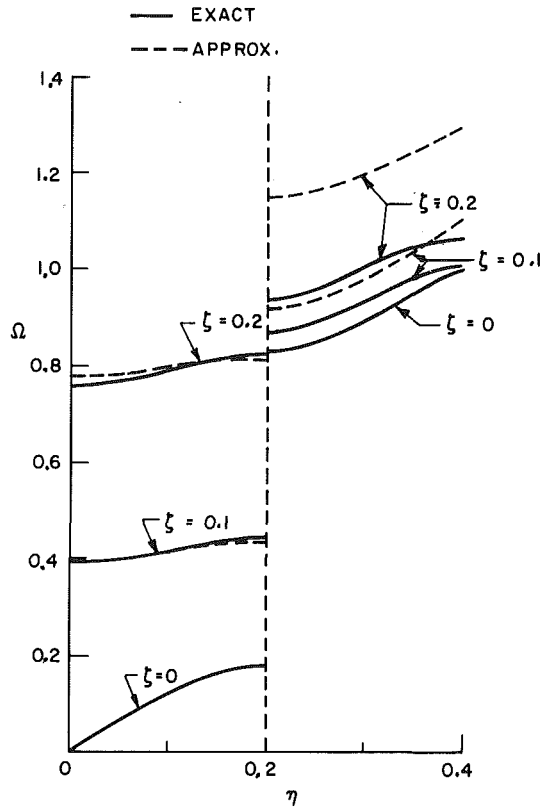

Fig. 2 Curves of constant ζ

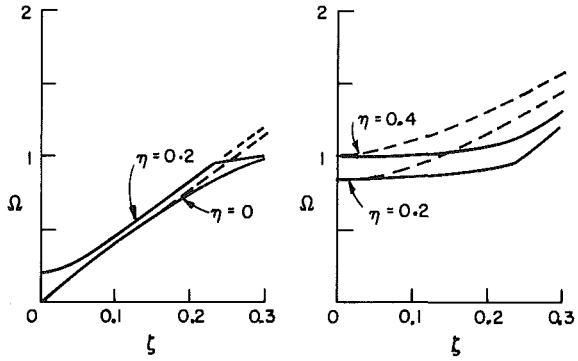

Fig. 3 Curves of constant η at Brillouin zone ends

retain the expressions for the coefficients previously developed in the one-dimensional case, which leaves only the constants a_7 and a_8 in equation (11) to be determined. We again adopt the procedure of matching dispersion spectra, now utilizing the results of Delph, Herrmann, and Kaul [18] who give the exact dispersion relation for *SH*-wave propagation in an unbounded body. We require that

$$\left.\frac{\partial\omega}{\partial k_x}\right|_{\omega=k_x=k_y=0} = s_g; \quad \left.\frac{\partial\omega}{\partial k_y}\right|_{k_y=k_B} = 0 \tag{25}$$

where s_g is the exact value for the unbounded body obtained from reference [18]. The second of equations (24) is similar to the requirements imposed by the fourth and fifth of equations (16); however now we require that these relations be maintained when $k_x \neq 0$. Equations (25), in conjunction with equations (15) and (17), yield

$$a_7/a_6 = s_g{}^2 b_1/a_6;$$
$$a_8/a_6 = s_g{}^2(b_1/a_6)/[(a_1/a_6) - 2k_B{}^2(a_2/a_6)] \tag{26}$$

To within a factor of a_6, all the constants appearing in the equations of motion (11) are now completely determined. Utilizing equations (15), (17), and (26) in equation (14), we may, after a considerable amount of algebra, write the dispersion equation as

$$\omega^2 = s_g{}^2 k_x{}^2 + f(k_y) \tag{27}$$

where $f(k_y)$ is the double-valued function

$$f(k_y) = [-(\beta k_y{}^4 + \gamma k_y{}^2 + \delta) \pm \sqrt{D}]/2\alpha \tag{28}$$

where

$$D = (\beta k_y{}^4 + \gamma k_y{}^2 + \delta)^2 - 4\alpha(\xi k_y{}^2 + \theta k_y{}^4 + k_y{}^6) \tag{29}$$

Necessary and sufficient conditions have been given in the one-dimensional analysis so that $f(k_y) \geq 0$ for all real values of k_y. This requirement was necessary to insure real frequencies and, indeed, supplied the rationale for a part of the matching procedure. It can be seen from equation (27) that, for $f(k_y) \geq 0$, the frequency ω will always be real-valued in the present case. For constant values of k_y, the spectral lines given by equation (26) describe hyperbolae in the $\omega - k_x$ plane. In the special case $k_y = 0$, the lowest branch degenerates to the straight line $\omega = s_g k_x$.

Numerical Results and Discussion

We now wish to compare the results of the approximate theory to the exact results for wave propagation in an unbounded layered body. For this purpose, material and geometric parameters taken from reference [18] were used to evaluate the approximate dispersion equation (27). These were $h'/h = 4$, $\mu/\mu' = 0.02$, and $\mu\rho'/\mu'\rho = 0.06$. Also following [18], we introduce the nondimensional frequency $\Omega = 2h\omega/\pi c_T$ and nondimensional wave numbers $\zeta = 2hk_x/\pi$ and $\eta = 2hk_y/\pi$, where $c_T = \sqrt{\mu/\rho}$. For these constants it is found that the conditions set forth in the preceding section for ω to be real-valued for all values of k_y are satisfied.

Figure 2 shows both the exact and approximate spectral lines of constant ζ over the first two Brillouin zones as plotted on the extended zone scheme. Here we have considered only waves with positive group velocity, which corresponds to the acoustic branch in the first Brillouin zone and the optical branch in the second Brillouin zone. It can be seen that, for the case of propagation normal to the layering ($\zeta = 0$), the exact and approximate results agree extremely well over both Brillouin zones. The agreement continues to be quite good in the first Brillouin zone through $\zeta = 0.20$, but worsens for values of ζ increasing away from zero in the second Brillouin zone. These tendencies are also apparent in Fig. 3, which shows the spectral lines of constant η bounding the first two Brillouin zones.

Figures 4(*a*), (*b*), and (*c*) show the real and imaginary part of η on the imaginary branch connecting the first two Brillouin zones. Note that the exact value of $Re(\eta)$ is constant on those branches. The agreement for $\zeta = 0$ is quite good, but becomes worse with increasing ζ, though still adequate through $\zeta = 0.10$.

The exact and approximate displacement mode shapes at the right-hand end of the first Brillouin zone are sketched in Fig. 5 for propagation normal to the layering ($\zeta = 0$). The exact mode shapes are taken from [18]. Here l and l' are local coordinates having their origins at the midplanes of the layers with unprimed and primed constants, respectively, and being normalized by the layer thickness. The agreement between exact and approximate mode shapes in Fig. 5 can be seen to be excellent. The assumption that all of the deformation occurs in the softer layers can be seen to be very nearly satisfied. Figure 6 shows the exact and approximate mode shapes at two points in the interior of the first Brillouin zone. Here the agreement is not as good as at the zone end. This is not sur-

Downloaded 02 May 2010 to 171.66.16.246. Redistribution subject to ASME license or copyright; see http://www.asme.org/terms/Terms_Use.cfm

prising in view of the fact that the exact displacements are in general quasi-periodic as discussed in [18], while the approximate displacements given by equations (1) and (13) are strictly periodic. Also continuity of displacement at the layer interfaces in the effective dispersion theory is only approximate, as may be noted from the figure.

As noted in the Introduction, there exist in the literature a number of approximate theories for wave propagation in a layered composite of the type considered in this work. Most of these theories are intended for use in initial/boundary value problems, as is the present work. However comparisons between them are usually based on the results for an unbounded body because of the relative ease with which such comparisons may be made and also because of the paucity of exact solutions to initial/boundary value problems for layered bodies. We follow this approach here as well. The principal strength of the effective dispersion theory is that it is able to reproduce with fair to excellent accuracy the exact dispersion spectrum over the first two Brillouin zones, the agreement being especially good for the case of wave propagation normal to the layering. In addition, it contains the complex branch, or stopping band, between the first two Brillouin zones, which may be of some importance in applications.

By way of comparison, a significant number of existing theories seem to be limited in validity to the first Brillouin zone and lack the complex branch or stopping band between the first two Brillouin zones. Examples are the earlier effective stiffness theory [1, 2], the mixture theory of Stern and Bedford [8], and the more recent work of McNiven and Mengi [9]. A second-order extension of the effective stiffness theory due to Bedford and Drumheller [3, 4, 14] does considerably better in this regard and contains the stopping band. However, it appears from an inspection of published results (Fig. 18 of reference [14] versus the present Fig. 2) that the effective dispersion theory offers better accuracy over this portion of the spectrum. The theory of Hegemier and coworkers [5–7] takes a somewhat different approach from those cited previously and can, in fact, exactly reproduce the dispersion spectrum if all the terms in an infinite series are retained. However the complexities of the theory limit it to the use of one or two terms in practice. Although the results contained in these papers have been displayed in a somewhat inconvenient form for comparison, it appears that the stopping band is modeled, but that the effective dispersion

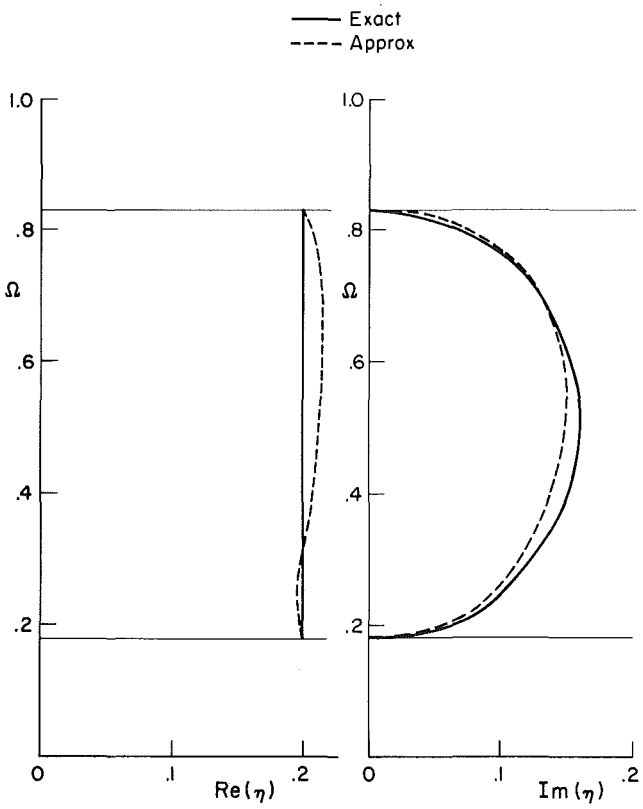

Fig. 4(a) $\zeta = 0$

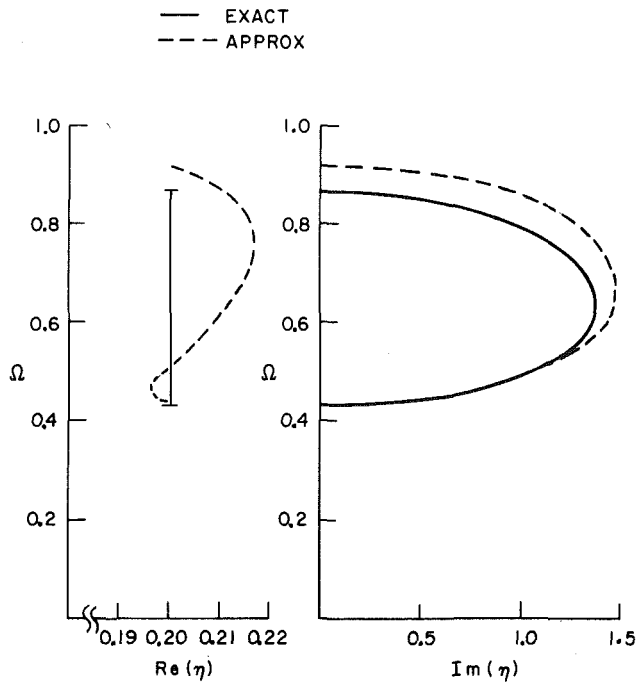

Fig. 4(b) $\zeta = 0.10$

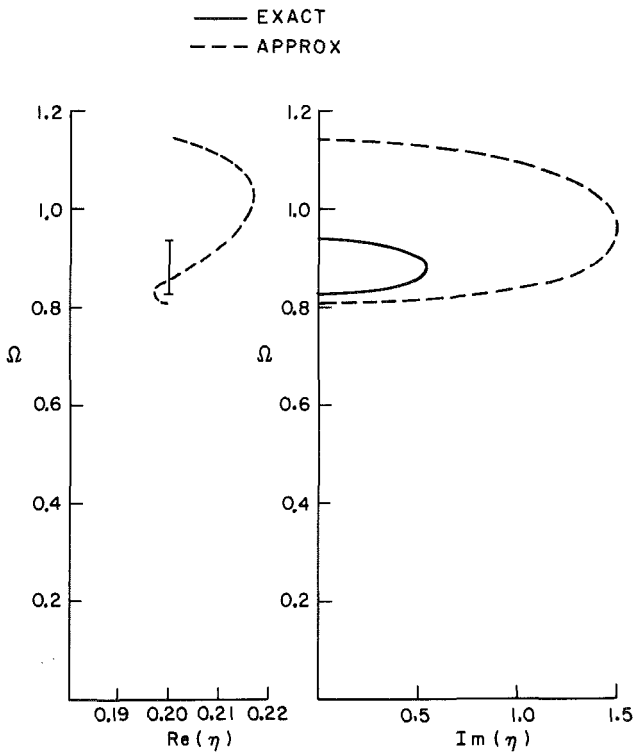

Fig. 4(c) $\zeta = 0.20$

Fig. 4 Complex branch between first two Brillouin zones

Downloaded 02 May 2010 to 171.66.16.246. Redistribution subject to ASME license or copyright; see http://www.asme.org/terms/Terms_Use.cfm

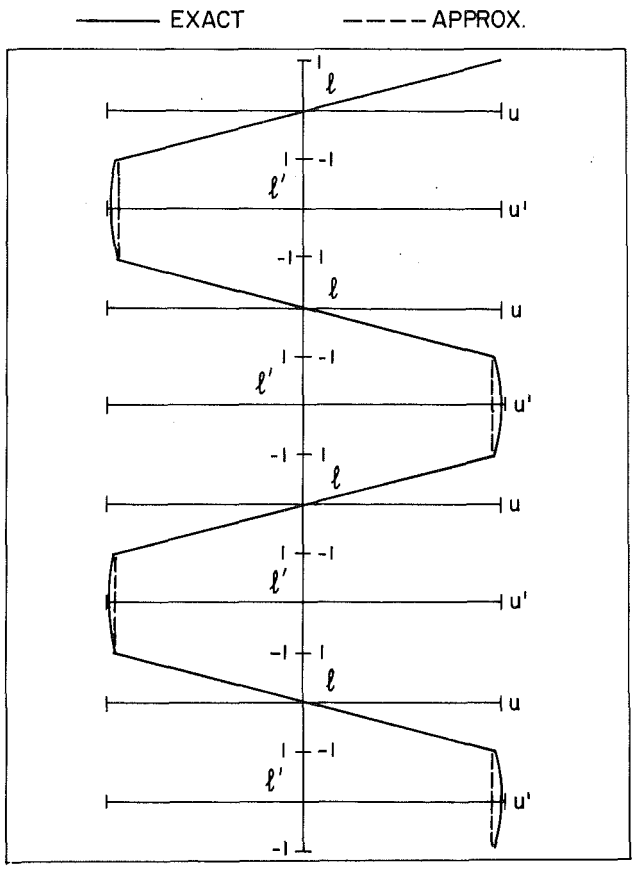

Fig. 5 Exact and approximate mode shapes of right-hand end of first Brillouin zone ($\zeta = 0$)

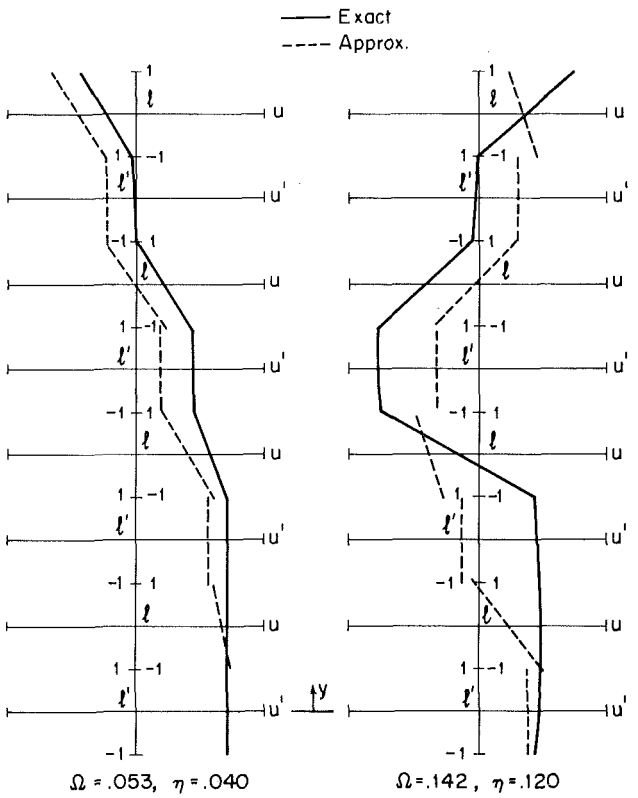

Fig. 6 Exact and approximate mode shapes at two points in the interior of first Brillouin zone ($\zeta = 0$)

theory offers better accuracy over the second Brillouin zone. A similar comment applies to the work of Minagawa and Nemat-Nasser [12].

The effective dispersion theory as presently formulated does, however, have several drawbacks. One is that there seems to be no guarantee that a value of the parameter θ can be found so that the inequalities (18–20) are simultaneously satisfied. It appears that these inequalities must be individually tested for each set of material and geometric parameters under consideration, and that no definite statement can be made as to the range of applicability of the effective dispersion theory. On the other hand, the numerical example presented in this paper was chosen to represent a typical composite material, and here it was shown that it was possible to satisfy all the relevant inequalities. It therefore seems likely that the effective dispersion theory will be applicable to the analysis of a number of classes of composite materials of practical interest.

Another difficulty, which seems to be shared to some extent with other microstructural theories, has to do with the proper treatment of the boundary conditions given by equations (10). At the present time we are unable to give a prescription for calculating the boundary forces P, Q, and M for a specified set of nonvanishing traction boundary conditions. The most obvious method for dealing with such a problem would be to take P as the applied traction and Q and M to vanish. This method, however, seems to us to be overly simplistic and not really in keeping with the microstructural approach. Another difficulty in dealing with nonvanishing boundary tractions is the fact that the coefficient a_6 in the equations of motion has not been specified uniquely. This causes no difficulty in dealing with traction-free or displacement boundary conditions, but introduces a degree of arbitrariness when treating nonvanishing boundary tractions. The resolution of these problems must await further study.

We close by briefly discussing the difficulties involved in extending the validity of the present theory to plane strain conditions, which is of considerably greater technological interest. The difficulties here are primarily due to the coupling of longitudinal and shear waves in plane strain. This fact, coupled with the heterogeneous nature of the body under consideration, leads to a situation that is in general quite complicated. The case of plane-strain wave propagation in an unbounded layered body has recently been analyzed by Delph, Herrmann, and Kaul [22, 23]. Here it is shown that the exact dispersion spectrum is double-valued and of a quite complex nature, with an intricate relationship between real and complex portions of the spectrum. At the moment it is not clear as to how a successful modeling of this complex problem ought to proceed.

Acknowledgments

The authors gratefully acknowledge many helpful discussions with Professor Raj K. Kaul of the State University of New York at Buffalo.

This research was supported in part by the Office of Naval Research Contract N00014-76-C-0054 to Stanford University.

References

1 Sun, C.-T., Achenbach, J. D., and Herrmann, G., "Continuum Theory for a Laminated Medium," ASME Journal of Applied Mechanics, Vol. 35, 1968, pp. 467–475.

2 Achenbach, J. D., Sun, C.-T., and Herrmann, G., "On the Vibrations of a Laminated Body," ASME Journal of Applied Mechanics, Vol. 35, 1968, pp. 689–696.

3 Drumheller, D. S., and Bedford, A., "Wave Propagation in Elastic

Downloaded 02 May 2010 to 171.66.16.246. Redistribution subject to ASME license or copyright; see http://www.asme.org/terms/Terms_Use.cfm

Laminates Using a Second Order Microstructure Theory," *Int. J. Solids and Structures*, Vol. 10, 1974, pp. 61–76.

4 Bedford, A., and Drumheller, D. S., "On a Generalized Effective Stiffness Theory," ASME JOURNAL OF APPLIED MECHANICS, Vol. 41, 1974, pp. 305–307.

5 Hegemier, G. A., and Nayfeh, A. H., "A Continuum Theory for Wave Propagation in Laminated Composites. Case I: Propagation Normal to the Laminates," ASME JOURNAL OF APPLIED MECHANICS, Vol. 40, 1973, pp. 503–510.

6 Hegemier, G. A., and Bache, T. C., "A Continuum Theory for Wave Propagation in Laminated Composites. Case II: Propagation Parallel to the Laminates," *J. Elasticity*, Vol. 3, 1973, pp. 125–140.

7 Hegemier, G. A., and Bache, T. C., "A General Continuum Theory with Microstructure for Wave Propagation in Elastic Laminated Composites," ASME JOURNAL OF APPLIED MECHANICS, Vol. 41, 1974, pp. 101–105.

8 Stern, M., and Bedford, A., "Wave Propagation in Elastic Laminates Using a Multicontinuum Theory," *Acta Mech.*, Vol. 15, 1972, pp. 21–38.

9 McNiven, H. D., and Mengi, Y., "A Mixture Theory for Elastic Laminated Composites," *Int. J. Solids Structures*, Vol. 15, 1979, pp. 281–302.

10 Kohn, W., Krumhansl, J. A., and Lee, E. H., "Variational Methods for Dispersion Relations and Elastic Properties of Composite Materials," ASME JOURNAL OF APPLIED MECHANICS, Vol. 39, 1972, pp. 327–336.

11 Nemat-Nasser, S., and Fu, F. C. L., "Harmonic Waves in Layered Composites: Bounds on Frequencies," ASME JOURNAL OF APPLIED MECHANICS, Vol. 41, 1974, pp. 288–290.

12 Minagawa, S., and Nemat-Nasser, S., "On Harmonic Waves in Layered Composites," ASME JOURNAL OF APPLIED MECHANICS, Vol. 44, 1977, pp. 689–695.

13 Herrmann, G., Kaul, R. K., and Delph, T. J., "On the Continuum Modeling of the Dynamic Behavior of Layered Composites," *Archives of Mechanics*, Vol. 28, Warszawa, 1976, pp. 405–421.

14 Bedford, A., Drumheller, D. S., and Sutherland, H. J., "On Modeling the Dynamics of Composite Materials," in: *Mechanics Today*, Vol. 3, Nemat-Nasser, S., ed., 1976, pp. 1–54.

15 Mindlin, R. D., "Microstructure in Linear Elasticity," *Arch. Rat. Mech. Anal.*, Vol. 16, 1964, pp. 51–78.

16 Kunin, I. A., "Theory of Elasticity With Spatial Dispersion: One-Dimensional Complex Structure," *PMM*, Vol. 30, 1966, pp. 866–874.

17 Lee, E. H., and Yang, W. H., "On Waves in Composite Materials With Periodic Structure," *SIAM Journal of Applied Mathematics*, Vol. 25, 1973, pp. 492–499.

18 Delph, T. J., Herrmann, G., and Kaul, R. K., "Harmonic Wave Propagation in a Periodically Layered, Infinite Elastic Body: Antiplane Strain," ASME JOURNAL OF APPLIED MECHANICS, Vol. 45, 1978, pp. 343–349.

19 Whitham, G. B., *Linear and Nonlinear Waves*, Wiley-Interscience, New York, 1974.

20 Littlewood, D. E., *A University Algebra*, Dover Publications, New York, 1970.

21 Delph, T. J., Ph.D. thesis, Department of Applied Mechanics, Stanford University, Stanford, Calif., 1976.

22 Delph, T. J., Herrmann, G., and Kaul, R. K., "Harmonic Wave Propagation in a Periodically Layered, Infinite Elastic Body: Plane Strain, Analytical Results," ASME JOURNAL OF APPLIED MECHANICS, Vol. 46, 1979, pp. 113–119.

23 Delph, T. J., Herrmann, G., and Kaul, R. K., "Harmonic Wave Propagation in a Periodically Layered, Infinite Elastic Body: Plane Strain, Numerical Results," ASME JOURNAL OF APPLIED MECHANICS, Vol. 47, 1980, pp. 531–537.

Downloaded 02 May 2010 to 171.66.16.246. Redistribution subject to ASME license or copyright; see http://www.asme.org/terms/Terms_Use.cfm

G. S. Beaupre[1]
Research Assistant.

G. Herrmann
Chairman.
Fellow ASME

Division of Applied Mechanics,
Stanford University,
Stanford, Calif. 94305

Steady-State Point-Source Excitation of a Laminated Composite

Steady-state periodic excitation at a point of an extended, periodically laminated, elastic composite is considered in antiplane strain. The curves of constant phase are determined in the geometric optics approximation. The associated distribution of group velocity is also calculated.

Introduction

The propagation of horizontally polarized, harmonic shear waves through a periodically layered elastic body of unbounded extent is examined here in the geometric optics approximation. The geometric optics approach is valid when the relevant wavelength is small in comparison with some characteristic dimension of the problem. Under this approximation any quantity that describes the wave field can be expressed in the form of an amplitude, which varies slowly in space and time, multiplied by a phase factor of the form $e^{-i\Omega S}$, where Ω is the frequency and S is the phase. The surfaces S = constant, which are surfaces of constant phase, will be examined for the steady-state case of a constant frequency point source.

Infinite Medium

The propagation of horizontally polarized, harmonic shear waves through a periodically layered body of infinite extent has been analyzed in some detail in [1] and is summarized here as far as is needed in the following.

The system to be considered consists of an infinite sequence of two alternating layers, each of which is homogeneous, isotropic, and perfectly bonded to the adjoining layers. A unit cell is defined as the union of any two adjacent layers. The two lamellae of a typical unit cell have elastic constants λ, μ; λ', μ', thicknesses $2h$; $2h'$, and densities ρ; ρ', see Fig. 1.

By utilizing the equations of elasticity and imposing continuity conditions, which specify that the displacements and stresses are continuous at each layer interface, we can write the equation of motion for the laminated body. For the infinite medium this equation takes on the form of a partial differential equation with coefficients that are periodic in the direction perpendicular to the layering with period $d = 2h + 2h'$. Application of the one-dimensional theory of Floquet for differential equations with periodic coefficients leads to the result that the details of the motion of the entire laminated body can be obtained by considering only one unit cell. Therefore the boundary conditions for one unit cell using Floquet's theory represent a set of four homogeneous equations which are sufficient to describe the entire laminated body.

For a nontrivial solution the determinant of the matrix of coefficients of these four homogeneous equations must vanish, yielding the dispersion equation $H'(\Omega, \eta, \zeta) = 0$ or in expanded form

$$4\gamma\alpha\alpha' \cos \pi\eta(1+\epsilon) + (\gamma\alpha - \alpha')^2 \cos \pi(\alpha - \epsilon\alpha') - (\gamma\alpha + \alpha')^2 \cos \pi(\alpha + \epsilon\alpha') = 0 \quad (1)$$

Here $\alpha = \sqrt{\Omega^2 - \zeta^2}$, $\alpha' = \sqrt{\sigma^2\Omega^2 - \zeta^2}$, where Ω, ζ, and η are, respectively, the nondimensional frequency and wave numbers defined by

$$\Omega = \frac{2h\omega}{\pi\sqrt{\mu/\rho}}; \quad \zeta = \frac{2h}{\pi} k_z; \quad \eta = \frac{2h}{\pi} k_y \quad (2)$$

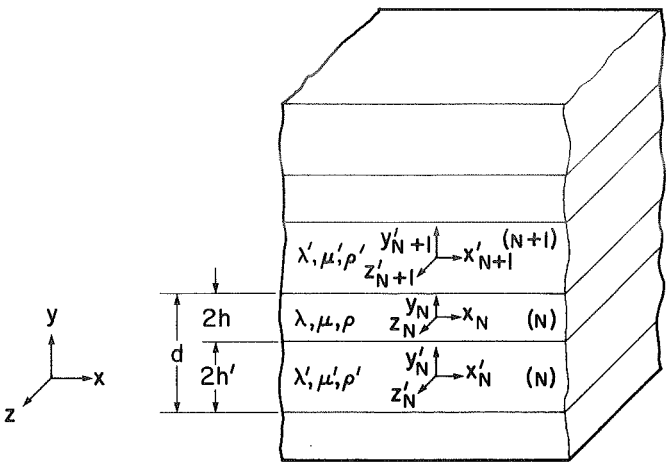

Fig. 1 Geometry of layered elastic solid

[1] Present address: Harvard Medical School, Department of Orthopaedic Surgery, Cambridge, Mass. 02138.

Contributed by the Applied Mechanics Division for publication in the JOURNAL OF APPLIED MECHANICS.

Discussion on this paper should be addressed to the Editorial Department, ASME, United Engineering Center, 345 East 47th Street, New York, N.Y. 10017, and will be accepted until two months after final publication of the paper itself in the JOURNAL OF APPLIED MECHANICS. Manuscript received by ASME Applied Mechanics Division, October, 1980; final revision, July, 1982.

Copyright © 1983 by ASME
Downloaded 02 May 2010 to 171.66.16.246. Redistribution subject to ASME license or copyright; see http://www.asme.org/terms/Terms_Use.cfm

where ω, k_z, and k_y are, respectively, the circular frequency in radians per unit of time, the wave number in the direction parallel to the layering, and the wave number in the direction perpendicular to the layering. In addition, the geometric and material parameters are defined in the following manner: γ is the ratio of shear moduli (μ/μ'), ϵ is the ratio of layer thicknesses ($2h'/2h$), and σ is the ratio of shear wave speeds $\sigma=\sqrt{\mu\rho'/\mu'\rho}$.

Since the dispersion equation relates a nondimensional frequency to two nondimensional wave numbers, the roots of this equation define a surface in three-dimensional frequency wave-number space. A qualitative sketch of this surface is shown in Fig. 2. It is seen that the surface is discontinuous at $\eta = n/(1+\epsilon)$, $n = 1, 2, 3, \ldots$. These planes of discontinuity divide the surface into bands known as Brillouin zones. At the end of each Brillouin zone the dispersion equation admits complex as well as real roots. These portions of the dispersion spectrum for which the wave numbers are complex are called stopping bands and correspond to regions of the spectrum where harmonic waves are not propagated but attenuated exponentially. Curves of constant frequency on the surface over the first two Brillouin zones are shown in Fig. 3. These curves play an important part in the construction of the surfaces of constant phase.

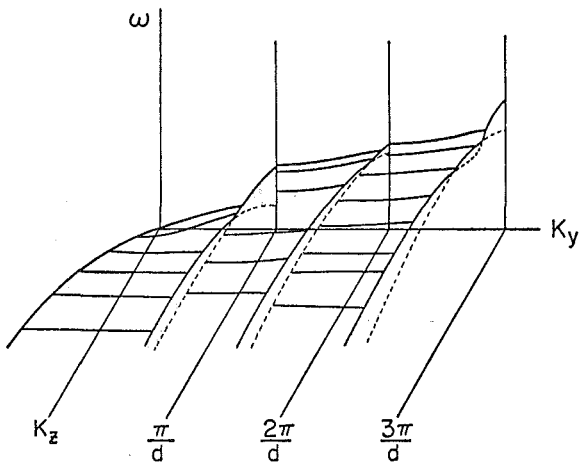

Fig. 2 Dispersion surface for SH waves in a layered elastic solid

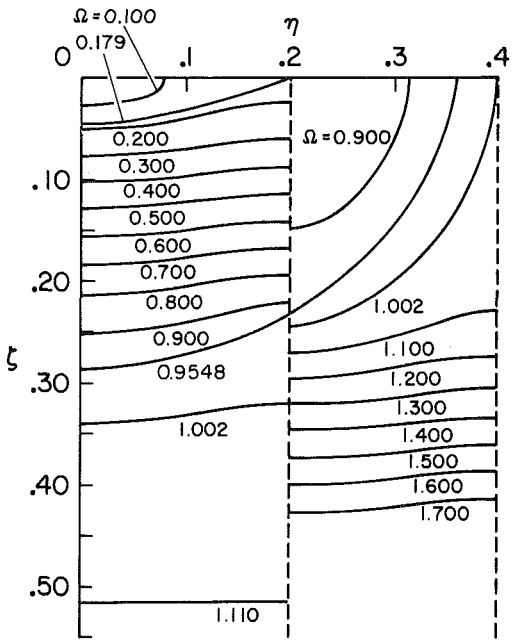

Fig. 3 Curves of constant Ω on the antiplane strain dispersion surface

Geometric Optics

Following the notation and methodology outlined in [2], we write the phase S in the form $S = t-\sigma(x)$. The wave fronts defined by $S(x, t) = 0$ can be found by examining the surfaces $\sigma(x)$ = constant, for fixed time. These "snapshots" give the successive positions of the wave front in physical space. To find the shape of these wave fronts in physical space we begin by rewriting the dispersion equation for the steady-state case of a single frequency, say $\Omega = \Omega_0$. Doing this, the dispersion relation takes the form

$$H(p_1, p_2)=0; \quad p_i=\sigma_{x_i} \tag{3}$$

where the p_i are defined by η/Ω_0 and ζ/Ω_0, respectively. The dispersion relation in this form is called the eikonal equation or equation of geometrical optics. The standard method of solving (3) is by means of the characteristic or ray equations, which proceed as follows [2]:

Consider an equation in n independent variables ($x_1, x_2, \ldots x_n$) and a function $\sigma(x_1, x_2, \ldots x_n)$ which satisfies a differential equation $H(\mathbf{p}, \sigma, \mathbf{x})$ where $\mathbf{p}$ and $\mathbf{x}$ are vectors of dimension n and

$$p_i \equiv \frac{\partial\sigma}{\partial x_i}=\sigma_{x_i} \quad i=1, 2, 3, \ldots n \tag{4}$$

We wish to find whether there are any curves in x-space for which the differential equation $H(\mathbf{p}, \sigma, \mathbf{x})$ reduces to a set of first-order ordinary differential equations. We begin by noting that any curve in x-space may be written in the parametric form $\mathbf{x} = \mathbf{x}(\lambda)$. The total derivative of σ along one of these curves is given by

$$\frac{d\sigma}{d\lambda}=\frac{\partial\sigma}{\partial x_i}\frac{dx_i}{d\lambda}=p_i\frac{dx_i}{d\lambda} \tag{5}$$

where the summation convention is employed. In addition, consider the total derivative of p_i along the same curve

$$\frac{dp_i}{d\lambda}=\frac{d}{d\lambda}\frac{\partial\sigma}{\partial x_i}=\frac{\partial^2\sigma}{\partial x_i\partial x_j}\frac{dx_j}{d\lambda} \tag{6}$$

Finally let us take the x_i derivative of $H(\mathbf{p}, \sigma, \mathbf{x}) = 0$ which gives

$$\frac{\partial^2\sigma}{\partial x_i\partial x_j}\frac{\partial H}{\partial p_j}+\frac{\partial H}{\partial\sigma}\frac{\partial\sigma}{\partial x_i}+\frac{\partial H}{\partial x_i}=0 \tag{7}$$

By choosing the following as our definition for the special curves in x-space

$$\frac{dx_i}{d\lambda}=\frac{\partial H}{\partial p_i} \tag{8}$$

we may combine (6) and (7) to give

$$\frac{dp_i}{d\lambda}=-p_i\frac{\partial H}{\partial\sigma}-\frac{\partial H}{\partial x_i} \tag{9}$$

The use of (7) in (4) then yields

$$\frac{d\sigma}{d\lambda}=p_i\frac{\partial H}{\partial p_i} \tag{10}$$

The set of equations (8)–(10) now represent a complete set of $(2n+1)$ ordinary differential equations for determining a characteristic curve $x_i(\lambda)$ and the values of σ and p_i along it.

Specializing these results to our case gives

$$\frac{dx_i}{d\lambda}=(\nabla_p H)_i; \quad \frac{dp_i}{d\lambda}=0; \quad \frac{d\sigma}{d\lambda}=(\mathbf{p}\cdot\nabla_p H) \tag{11}$$

Downloaded 02 May 2010 to 171.66.16.246. Redistribution subject to ASME license or copyright; see http://www.asme.org/terms/Terms_Use.cfm

where λ is a parameter along the characteristic curve (ray). The second of equations (11) indicates that p_i are constant along rays, hence the ray direction $\nabla_p H$ is constant and therefore the rays are straight lines. Since the p_i are constant we can integrate (11) directly. For the case of a point source of constant frequency located at the origin, we can readily obtain,

$$x_i = l_i s; \quad \sigma = \mathbf{p}\cdot\mathbf{l}s \tag{12}$$

where $\mathbf{l}$ is a unit vector defined by

$$\mathbf{l} = \frac{\nabla_p H}{\| \nabla_p H \|} \tag{13}$$

and s is the distance from the source measured along a ray. From these equations we find that the wave front $S = 0$ is located at

$$s = \frac{t}{\mathbf{p}\cdot\mathbf{l}} \tag{14}$$

and the coordinates of a point on the wave front are

$$x_i = \frac{t}{\mathbf{p}\cdot\mathbf{l}} l_i \tag{15}$$

By varying p_i over all values satisfying $H(p_1, p_2) = 0$ for $\Omega = \Omega_0$ we can find the entire wave front. It should be noted that these wave fronts can be found by examining curves of constant frequency in wave-number space (Fig. 3). If for example we choose a particular value for Ω, say 0.9 (see Fig. 4), then $\mathbf{l}$ is merely the unit normal to the curve for any choice of p_i satisfying $H(p_1, p_2) = 0$ for $\Omega = 0.9$. By varying p_i along the curve we can trace out the entire wave front (Fig. 5).

Because the eikonal equation is unchanged by switching from p_i to $-p_i$ the wave fronts will be symmetric in the x_1, x_2 axis. A complete wave front for $\Omega = 1.0$ is shown in Fig. 6.

With the aid of a compass and two triangles a very simple geometric construction of these wave fronts is possible. We begin by drawing a coordinate system with the same orientation as the coordinate system in Fig. 3. From Fig. 3 choose a value for Ω and select a point along the curve Ω = constant. Now draw the normal to the curve at this point. With the aid of the triangles draw a line passing through the origin of our new coordinate system that is parallel to this normal. Now working with Fig. 3 project the wave-number vector onto the unit normal vector. The length of this vector is proportional to $\mathbf{p}\cdot\mathbf{l}$ (since $\mathbf{l}$ is a unit vector). All that remains is to take the inverse of this length. This is accomplished by drawing a reference hyperbola and using the compass to measure the inverse. This length is then measured from the origin of our new coordinate system along the parallel to $\mathbf{l}$. This is the first point of the wave front. The process is repeated for different points on the same curve Ω = constant until a sufficient number of points exists in order to pass a smooth curve through them.

The wavefront of course gives no information concerning energy distribution. It may be of interest, though, to examine the magnitude and direction of velocity of energy propagation. To accomplish this, a numerical finite-difference calculation was carried out to show the group velocity vector at points on the zero phase curves. Here the group velocity is defined as:

$$\mathbf{c}_g = -\left(\frac{\partial H'}{\partial \eta}\mathbf{e}_\eta + \frac{\partial H'}{\partial \zeta}\mathbf{e}_\zeta\right) \Big/ \frac{\partial H'}{\partial \Omega}$$

where H' is the dispersion relation written as a function of Ω, ζ, η which were previously defined and $\mathbf{e}_\eta$, $\mathbf{e}_\zeta$ which are unit vectors in the direction perpendicular and parallel to the layering, respectively. Figures 7(*a*–*d*) are wave fronts for different frequencies but also include group velocity information. The magnitude of the group velocity vector normalized by the phase velocity $\sqrt{\mu/\rho}$ is drawn radially

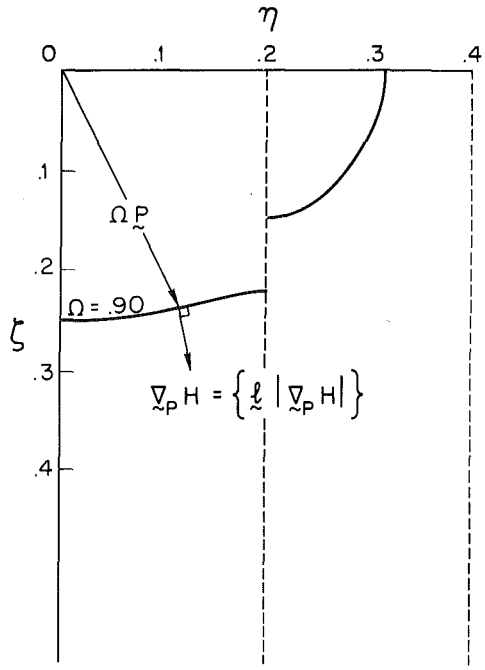

Fig. 4 Curve of $\Omega = 0.9$ showing vectors p and l

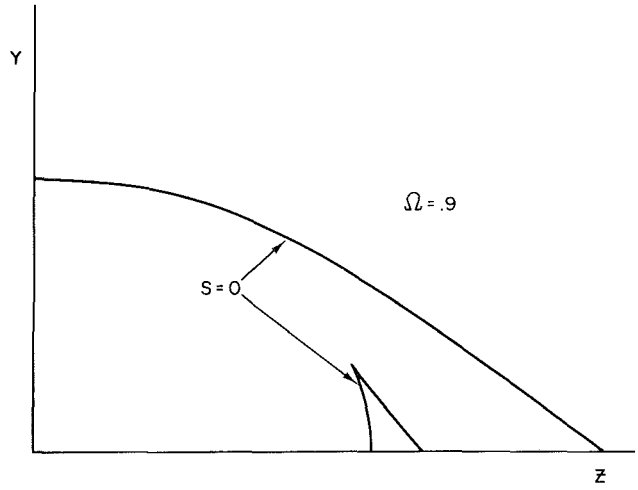

Fig. 5 Curve of constant phase for $\Omega = 0.9$

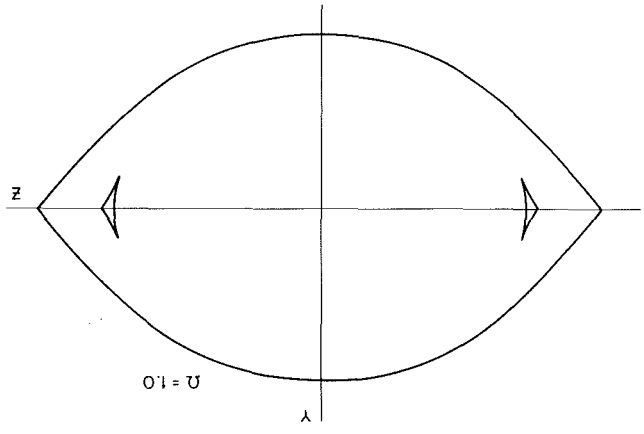

Fig. 6 Complete wave front for $\Omega = 1.0$

Downloaded 02 May 2010 to 171.66.16.246. Redistribution subject to ASME license or copyright; see http://www.asme.org/terms/Terms_Use.cfm

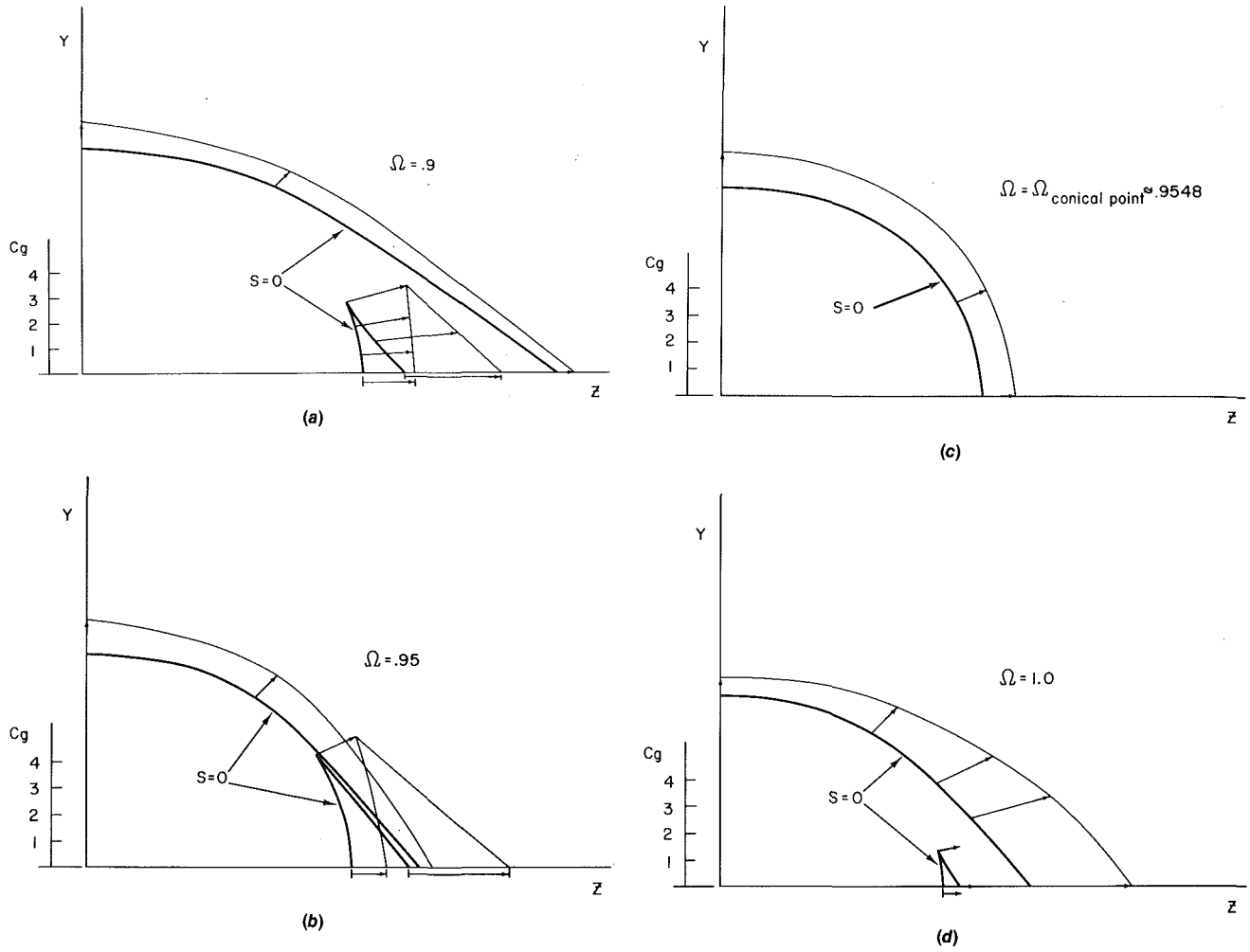

Fig. 7 Distribution of group velocity on curves of constant plane

outward from each zero phase curve where the vectors begin, not at the origin but at the appropriate point on each phase curve. It should be noted that the zero phase curve passing through the conical point (Fig. 7(*c*)) has a pointwise discontinuity in the value of the group velocity at the conical point [3].

Conclusion

Through the utilization of the geometric optics approximation, surfaces of constant phase were examined for the case of a point source imbedded in a periodically layered elastic body. Knowledge of the shape of these surfaces is the first step toward understanding how more complicated signals propagate. For instance, we already know from examining these zero phase surfaces that an observer stationed somewhere within the medium would detect one, two, or three distinct signals depending on one's orientation with respect to the source. An observer stationed along the z axis would detect three unique signals whereas an observer stationed along the y axis would detect only one. A similar phenomenon occurs in the case described in [2] for waves in a MHD plasma.

It should be mentioned that these results apply to an equivalent homogeneous medium that is anisotropic and not to the actual piecewise constant medium.

Acknowledgment

The authors are most grateful to Professor J. B. Keller for many valuable discussions and suggestions. This research was supported in part by ONR Contract N00014-76-C-0054.

References

1 Delph, T. J., Herrmann, G., and Kaul, R. K., "Harmonic Wave Propagation in a Periodically Layered, Infinite Elastic Body: Antiplane Strain," ASME JOURNAL OF APPLIED MECHANICS, Vol. 45, 1978, pp. 343–349.

2 Whitman, G. B., *Linear and Nonlinear Waves*, Wiley, New York, 1974, pp. 65–67 and 235–262.

3 Delph, T. J., Herrmann, G., and Kaul, R. K., "On Coalescence of Frequencies and Conical Points in the Dispersion Spectra of Elastic Bodies," *Int. J. Solids Structures*, Vol. 13, 1977, pp. 423–436.

Downloaded 02 May 2010 to 171.66.16.246. Redistribution subject to ASME license or copyright; see http://www.asme.org/terms/Terms_Use.cfm

The Interface Crack Between Dissimilar Anisotropic Composite Materials

S. S. Wang
Associate Professor.
Assoc. Mem. ASME

I. Choi[1]
Research Associate.
Department of Theoretical and Applied Mechanics,
University of Illinois,
Urbana, Ill. 61801

The fundamental nature of an interface crack between dissimilar, strongly anisotropic composite materials under general loading is studied. Based on Lekhnitskii's stress potentials and anisotropic elasticity theory, the formulation leads to a pair of coupled governing partial differential equations. The case of an interlaminar crack with fully opened surfaces is considered first. The problem is reduced to a Hilbert problem which can be solved in a closed form. Oscillatory stress singularities are observed in the asymptotic solution. To correct this unsatisfactory feature, a partially closed crack model is introduced. Formulation of the problem results in a singular integral equation which is solved numerically. The refined model exhibits an inverse square-root stress singularity for commonly used advanced fiber-reinforced composites such as a graphite-epoxy system. Extremely small contact regions are found for the partially closed interlaminar crack in a tensile field and, therefore, a simplified model is proposed for this situation. Physically meaningful fracture mechanics parameters such as stress intensity factors and energy release rates are defined. Numerical examples for a crack between θ and $-\theta$ graphite-epoxy composites are examined and detailed results are given.

1 Introduction

In view of the rapidly increasing use of high-modulus, high-strength, fiber-reinforced composite materials in advanced engineering structures such as high-performance aircraft, damage tolerance and reliability of the composite materials and structures have been of significant concern. Interface cracking, sometimes also called delamination or interlaminar cracking, is considered one of the most commonly encountered types of damage in the failure of composites. The interface crack problem in fiber composite materials is concerned with debonding or separation between two strongly anisotropic laminae or plies, resulting from thermomechanical loading and/or fabrication/process-induced defects such as incomplete wetting between layers.

Although significant progress has been made in solving some elasticity problems of interface cracks between dissimilar isotropic materials [1-14], the problem of an interlaminar crack or delamination between two dissimilar, strongly anisotropic composite materials remains inadequately treated. Because of the complexities involved, the majority of work reported in the literature has dealt with various aspects of the problem from approximate and experimental point of views, for example, references [15-22]. The difficulties associated with the current problem involve not only the inherently singular crack-tip stress field but also the significant coupling between in-plane and interlaminar deformations in the composites, i.e., the simultaneous existence of mode *I*, *II*, and *III* fracture, due to materials' inherent anisotropy. The very limited elasticity solutions for the composite interface crack problem available in the literature [23-25] possess a controversial oscillatory stress singularity – a situation similar to that in dissimilar isotropic solids – which leads to the well-known physical absurdity of crack surface interpenetration.

Unsatisfactory features of the oscillatory stress singularity for an interface crack between dissimilar isotropic solids were discussed by many researchers. Several models, including crack tip closure and relative slip conditions between crack surfaces have been proposed, e.g., by Comninou [12, 13] and Achenbach, et al. [14], to correct these undesirable features. However, similar advancements of interlaminar crack theory in dissimilar anisotropic materials have not yet been made, to the authors' knowledge. In view of the practical importance of the problem, a rigorously theoretical development is presented in this paper to address the fundamental behavior of an interface crack between dissimilar, strongly anisotropic composites and to establish models that correct the controversial, oscillatory crack-tip characteristics.

In the next section, formulation of the problem by using theory of anisotropic elasticity is presented. A general

[1] Presently, Technical Specialist, Xerox Corporation, Rochester, N.Y. 14644.

Contributed by the Applied Mechanics Division for presentation at the 1983 ASME Applied Mechanics, Bioengineering, and Fluids Engineering Conference, Houston, Texas, June 20-22, 1983 of THE AMERICAN SOCIETY OF MECHANICAL ENGINEERS.

Discussion on this paper should be addressed to the Editorial Department, ASME, United Engineering Center, 345 East 47th Street, New York, N.Y. 10017, and will be accepted until two months after final publication of the paper itself in the JOURNAL OF APPLIED MECHANICS. Manuscript received by ASME Applied Mechanics Division, October, 1981; find revision, June, 1982. Paper No. 83-APM-6.

Copies will be available until February, 1984.

Copyright © 1983 by ASME
Downloaded 02 May 2010 to 171.66.16.246. Redistribution subject to ASME license or copyright; see http://www.asme.org/terms/Terms_Use.cfm

solution based on Lekhnitskii's complex-variable stress potentials [26] is obtained. The case of a fully opened interlaminar crack between dissimilar anisotropic composites is considered first in Section 3 by using Clements' procedure [24] but with a stress formulation. The problem is reduced to a Hilbert problem which can be solved in a closed form. The closed-form solution possesses an oscillatory stress singularity; thus, a partially closed crack model is introduced in Section 4 to correct the physically inadmissible aspects. Mathematical formulation of the partially closed crack leads to a singular integral equation which is solved numerically by using the method developed by Erdogan, et al. [27]. The partially closed crack model is shown to exhibit an inverse square-root stress singularity. For an interlaminar crack between dissimilar anisotropic composites in a tensile field, crack-surface contact regions are shown to be extremely small, based on the partially closed crack solution; therefore, a simplified model to account for this situation is proposed. The model discards the oscillatory near-field character and approximates the crack-tip stress field with an inverse square-root singularity. Because solution structures of the partially closed crack model and the approximate model for very small crack-surface closure are similar to that of an interface crack in dissimilar isotropic materials [12] and the well-known homogeneous crack problems, physically meaningful fracture mechanics parameters such as stress intensity factors and energy release rates can be introduced consistently. Numerical examples for an interlaminar crack between $[\theta/-\theta]$ graphite-epoxy composites are presented. Results obtained by the three different approaches are given and compared in the paper.

2 Basic Formulation

Consider a composite composed of dissimilar, anisotropic elastic solids. The constitutive equations of each individual solid with rectilinear anisotropy of a general form are denoted by generalized Hooke's law in contracted notation as

$$\epsilon_i = S_{ij}\sigma_j \quad (i,j=1,2,3,4,5,6), \tag{1}$$

where the repeated subscript indicates summation, and S_{ij} is the compliance tensor. The engineering strains, ϵ_i, in equation (1) are defined in a Cartesian coordinate system by

$$\epsilon_1=\epsilon_x=\frac{\partial u}{\partial x},\quad \epsilon_2=\epsilon_y=\frac{\partial v}{\partial y},\quad \epsilon_3=\epsilon_z=\frac{\partial w}{\partial z},$$

$$\epsilon_4=2\epsilon_{yz}=\frac{\partial w}{\partial y}+\frac{\partial v}{\partial z},\quad \epsilon_5=2\epsilon_{xz}=\frac{\partial w}{\partial x}+\frac{\partial u}{\partial z},$$

$$\epsilon_6=2\epsilon_{xy}=\frac{\partial u}{\partial y}+\frac{\partial v}{\partial x}, \tag{2}$$

where u, v, and w are the components of displacement. The stresses, σ_i, are defined in an analogous manner.

The composite considered here is subjected to tractions acting on a surface parallel to the generator, i.e., the z-axis, and not varying along the z-axis. Consequently, the composite is under generalized plane deformation [26], in which all components of stress and displacement are independent of z. In an anisotropic body under such a condition, ϵ_z vanishes identically. Thus, from equations (1) and (2), it follows that

$$\frac{\partial u}{\partial x}=\tilde{S}_{1j}\sigma_j,\quad \frac{\partial v}{\partial y}=\tilde{S}_{2j}\sigma_j,\quad \frac{\partial w}{\partial y}=\tilde{S}_{4j}\sigma_j,$$

$$\frac{\partial w}{\partial x}=\tilde{S}_{5j}\sigma_j,\quad \frac{\partial u}{\partial y}+\frac{\partial v}{\partial x}=\tilde{S}_{6j}\sigma_j, \tag{3}$$

and

$$\sigma_z=-S_{3j}\sigma_j/S_{33}, \tag{4}$$

where

$$\tilde{S}_{ij}=S_{ij}-S_{i3}S_{j3}/S_{33}\quad (i,j\neq 3).$$

Under these assumptions, the equations of equilibrium without body forces read

$$\frac{\partial\sigma_x}{\partial x}+\frac{\partial\tau_{xy}}{\partial y}=0,\quad \frac{\partial\tau_{xy}}{\partial x}+\frac{\partial\sigma_y}{\partial y}=0,\quad \frac{\partial\tau_{xz}}{\partial x}+\frac{\partial\tau_{yz}}{\partial y}=0. \tag{6}$$

The well-known Lekhnitskii stress functions F and Ψ satisfying the foregoing equilibrium equations are defined [26] as

$$\sigma_x=\frac{\partial^2 F}{\partial y^2},\quad \sigma_y=\frac{\partial^2 F}{\partial x^2},\quad \tau_{xy}=-\frac{\partial^2 F}{\partial x\,\partial y}, \tag{7a,b,c}$$

$$\tau_{xz}=\frac{\partial\Psi}{\partial y},\quad \tau_{yz}=-\frac{\partial\Psi}{\partial x}. \tag{7e,f}$$

Substituting equations (7*a–f*) into (3) and eliminating u, v, and w, one obtains the following system of governing partial differential equations:

$$\begin{cases} L_3F+L_2\Psi=0, & (8a)\\ L_4F+L_3\Psi=0, & (8b)\end{cases}$$

where

$$L_2=\tilde{S}_{44}\frac{\partial^2}{\partial x^2}-2\tilde{S}_{45}\frac{\partial^2}{\partial x\,\partial y}+\tilde{S}_{55}\frac{\partial^2}{\partial y^2}, \tag{9a}$$

$$L_3=-\tilde{S}_{24}\frac{\partial^3}{\partial x^3}+(\tilde{S}_{25}+\tilde{S}_{46})\frac{\partial^3}{\partial x^2\,\partial y}-(\tilde{S}_{14}+\tilde{S}_{56})\frac{\partial^3}{\partial x\,\partial y^2}+\tilde{S}_{15}\frac{\partial^3}{\partial y^3}, \tag{9b}$$

$$L_4=\tilde{S}_{22}\frac{\partial^4}{\partial x^4}-2\tilde{S}_{26}\frac{\partial^4}{\partial x^3\,\partial y}+(2\tilde{S}_{12}+\tilde{S}_{66})\frac{\partial^4}{\partial x^2\,\partial y^2}-2\tilde{S}_{16}\frac{\partial^4}{\partial x\,\partial y^3}+\tilde{S}_{11}\frac{\partial^4}{\partial y^4}. \tag{9c}$$

Lekhnitskii [26] has shown that the general solution for equations (8*a*) and (8*b*) can be expressed as

$$F=\sum_{k=1}^{3}\{F_k(x+\mu_k y)+\overline{F_k(x+\mu_k y)}\}, \tag{10a}$$

$$\Psi=\sum_{k=1}^{3}\{\eta_k F_k'(x+\mu_k y)+\overline{\eta_k F_k'(x+\mu_k y)}\}, \tag{10b}$$

where the prime denotes differentiation of the associated function with respect to its argument, and the overbar denotes the conjugates of complex variables. In equations (10*a*) and (10*b*) the coefficients μ_k are roots of the following algebraic characteristic equation:

$$f_4(\mu)f_2(\mu)-f_3^2(\mu)=0, \tag{11a}$$

and

$$\eta_k=-f_3(\mu_k)/f_2(\mu_k)=-f_4(\mu_k)/f_3(\mu_k), \tag{11b}$$

where

$$f_2(\mu_k)=\tilde{S}_{55}\mu_k^2-2\tilde{S}_{45}\mu_k+\tilde{S}_{44}, \tag{12a}$$

$$f_3(\mu_k)=\tilde{S}_{15}\mu_k^3-(\tilde{S}_{14}+\tilde{S}_{56})\mu_k^2+(\tilde{S}_{25}+\tilde{S}_{46})\mu_k-\tilde{S}_{24} \tag{12b}$$

$$f_4(\mu_k)=\tilde{S}_{11}\mu_k^4-2\tilde{S}_{16}\mu_k^3+(2\tilde{S}_{12}+\tilde{S}_{66})\mu_k^2-2\tilde{S}_{26}\mu_k+\tilde{S}_{22}. \tag{12c}$$

With the aid of equations (10*a*) and (10*b*), the components of stress and displacement can be shown to have the forms

$$\sigma_x=\sum_{k=1}^{3}\{\mu_k^2F_k''(Z_k)+\overline{\mu_k^2F_k''(Z_k)}\}, \tag{13a}$$

Downloaded 02 May 2010 to 171.66.16.246. Redistribution subject to ASME license or copyright; see http://www.asme.org/terms/Terms_Use.cfm

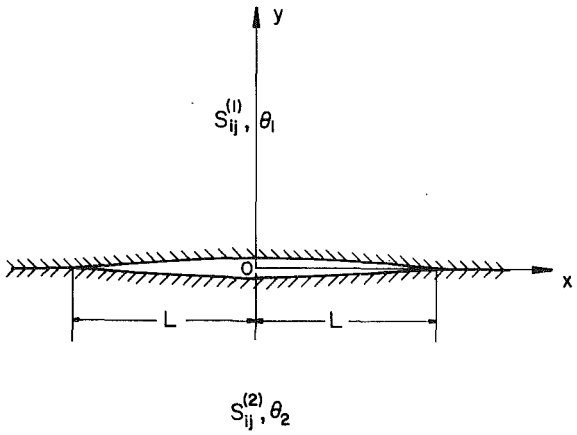

Fig. 1 A fully opened interface crack between θ_1 and θ_2 composites

$$\sigma_y = \sum_{k=1}^{3} \{F_k''(Z_k) + \overline{F_k''(Z_k)}\}, \tag{13b}$$

$$\tau_{yz} = -\sum_{k=1}^{3} \{\eta_k F_k''(Z_k) + \overline{\eta_k F_k''(Z_k)}\}, \tag{13c}$$

$$\tau_{xz} = \sum_{k=1}^{3} \{\mu_k \eta_k F_k''(Z_k) + \overline{\mu_k \eta_k F_k''(Z_k)}\}, \tag{13d}$$

$$\tau_{xy} = -\sum_{k=1}^{3} \{\mu_k F_k''(Z_k) + \overline{\mu_k F_k''(Z_k)}\}, \tag{13e}$$

and

$$u = \sum_{k=1}^{3} \{p_k F_k'(Z_k) + \overline{p_k F_k'(Z_k)}\}, \tag{14a}$$

$$v = \sum_{k=1}^{3} \{q_k F_k'(Z_k) + \overline{q_k F_k'(Z_k)}\}, \tag{14b}$$

$$w = \sum_{k=1}^{3} \{t_k F_k'(Z_k) + \overline{t_k F_k'(Z_k)}\}, \tag{14c}$$

where

$$Z_k = x + \mu_k y, \tag{15a}$$

$$p_k = \tilde{S}_{11}\mu_k^2 + \tilde{S}_{12} - \tilde{S}_{14}\eta_k + \tilde{S}_{15}\eta_k\mu_k - \tilde{S}_{16}\mu_k, \tag{15b}$$

$$q_k = \tilde{S}_{12}\mu_k + \tilde{S}_{22}/\mu_k - \tilde{S}_{24}\eta_k/\mu_k + \tilde{S}_{25}\eta_k - \tilde{S}_{26}, \tag{15c}$$

$$t_k = \tilde{S}_{14}\mu_k + \tilde{S}_{24}/\mu_k - \tilde{S}_{44}\eta_k/\mu_k + \tilde{S}_{45}\eta_k - \tilde{S}_{46}. \tag{15d}$$

Having established the basic formulation and general solutions for the stress and displacement in an anisotropic composite, one can now proceed with the study of an interlaminar crack between dissimilar anisotropic composites.

3 Fully Opened Interface Crack Between Dissimilar Anisotropic Composites

Consider a crack of length $2L$ lying along the interface of two anisotropic elastic solids as shown in Fig. 1. Denote the nominal stresses at infinity as σ_y^∞, τ_{yz}^∞, and τ_{xy}^∞. Then, boundary conditions along the interface $y = 0$ are

$$\sigma_y^{(\alpha)} = -\sigma_y^\infty, \quad \tau_{yz}^{(\alpha)} = -\tau_{yz}^\infty,$$

$$\tau_{xy}^{(\alpha)} = -\tau_{xy}^\infty, \qquad \text{for } |x| < L, \ (\alpha = 1,2), \tag{16}$$

and interface continuity conditions require that

$$\sigma_y^{(1)} = \sigma_y^{(2)}, \quad \tau_{yz}^{(1)} = \tau_{yz}^{(2)}, \quad \tau_{xy}^{(1)} = \tau_{xy}^{(2)},$$

$$u^{(1)} = u^{(2)}, \quad v^{(1)} = v^{(2)}, \quad w^{(1)} = w^{(2)}, \tag{17}$$

for $|x| > L$, where the superscripts 1 and 2 denote the upper and lower materials, respectively. To solve this boundary-value problem, the method developed by Clements [24] is used. From equations (13) and (14) with $F_k''(Z_k) = \phi_k(Z_k)$, the functions Ω_i may be defined as

$$\Omega_1(z) = \sum_{k=1}^{3} \{p_k^{(1)}\phi_k^{(1)}(z) - \overline{p_k^{(2)}}\ \overline{\phi_k^{(2)}}(z)\}, \tag{18a}$$

$$\Omega_2(z) = \sum_{k=1}^{3} \{q_k^{(1)}\phi_k^{(1)}(z) - \overline{q_k^{(2)}}\ \overline{\phi_k^{(2)}}(z)\} \tag{18b}$$

$$\Omega_3(z) = \sum_{k=1}^{3} \{t_k^{(1)}\phi_k^{(1)}(z) - \overline{t_k^{(2)}}\ \overline{\phi_k^{(2)}}(z)\}, \tag{18c}$$

$$\Omega_4(z) = \sum_{k=1}^{3} \{\phi_k^{(1)}(z) - \overline{\phi_k^{(2)}}(z)\}, \tag{18d}$$

$$\Omega_5(z) = -\sum_{k=1}^{3} \{\eta_k^{(1)}\phi_k^{(1)}(z) - \overline{\eta_k^{(2)}}\ \overline{\phi_k^{(2)}}(z)\}, \tag{18e}$$

$$\Omega_6(z) = -\sum_{k=1}^{3} \{\mu_k^{(1)}\phi_k^{(1)}(z) - \overline{\mu_k^{(2)}}\ \overline{\phi_k^{(2)}}(z)\}, \tag{18f}$$

for $Im(z) = Im(x + iy) = y > 0$, where $\overline{\phi_k(z)} = \overline{\phi_k(\bar{z})}$. For $y < 0$, the superscripts, 1 and 2, are exchanged. From equations (16) and (17), it follows that $\Omega_i = 0$ $(i = 4,5,6)$ and Ω_j $(j = 1,2,3)$ are analytic functions with cuts on $|x| < L$. Solving equations (18*a–f*) for $\phi_k^{(1)}(z)$ and $\overline{\phi_k^{(2)}}(z)$, one obtains

$$\phi_i^{(1)}(z) = b_{ij}\Omega_j(z), \quad \overline{\phi_i^{(2)}}(z) = b_{(i+3)j}\Omega_j(z) \quad (i,j = 1,2,3), \tag{19}$$

for $y > 0$; and similarly,

$$\overline{\phi_i^{(1)}}(z) = -\bar{b}_{ij}\Omega_j(z), \quad \phi_i^{(2)}(z) = -\bar{b}_{(i+3)j}\Omega_j(z), \tag{20}$$

for $y < 0$, where b_{ij} are known constants. Substituting equations (19) and (20) into equation (16) and noting that

$$\lim_{y\to 0^+}\phi_k^{(1)}(Z_k) = \lim_{y\to 0^+}\phi_k^{(1)}(z) = \phi_k^{(1)+}(x), \tag{21a}$$

$$\lim_{y\to 0^+}\overline{\phi_k^{(1)}(Z_k)} = \lim_{y\to 0^+}\overline{\phi_k^{(1)}(z)} = \overline{\phi_k^{(1)-}}(x), \tag{21b}$$

one has

$$d_{ij}\Omega_j^+(x) - \bar{d}_{ij}\Omega_j^-(x) = h_i(x) \quad (i,j = 1,2,3), \tag{22}$$

for $|x| < L$, where d_{ij} are known functions of μ_k, η_k, and b_{ij}, and $h_i(x)$ are known functions related to the nominal stresses. Multiplying equation (22) by constants N_i, it follows that

$$N_i d_{ij}\Omega_j^+(x) - N_i \bar{d}_{ij}\Omega_j^-(x) = N_i h_i(x) \quad \text{for } |x| < L. \tag{23}$$

The N_i are chosen such that

$$N_i d_{ij} = C_j, \qquad N_i \bar{d}_{ij} = \lambda C_j. \tag{24}$$

Eliminating C_j from equation (24), one has

$$(\bar{d}_{ij} - \lambda d_{ij})N_i = 0. \tag{25}$$

These equations have a nontrivial solution if

$$|\bar{d}_{ij} - \lambda d_{ij}| = 0. \tag{26}$$

Let λ_γ $(\gamma = 1,2,3)$ denote the roots of equation (26) and the corresponding values of N_i and C_i be expressed by $N_{\gamma i}$ and $C_{\gamma i}$. Equation (23) may be rewritten as

$$\{C_{\gamma k}\Omega_k^+(x)\} - \lambda_\gamma\{C_{\gamma k}\Omega_k^-(x)\} = N_i h_i(x) \quad \text{for } |x| < L. \tag{27}$$

Downloaded 02 May 2010 to 171.66.16.246. Redistribution subject to ASME license or copyright; see http://www.asme.org/terms/Terms_Use.cfm

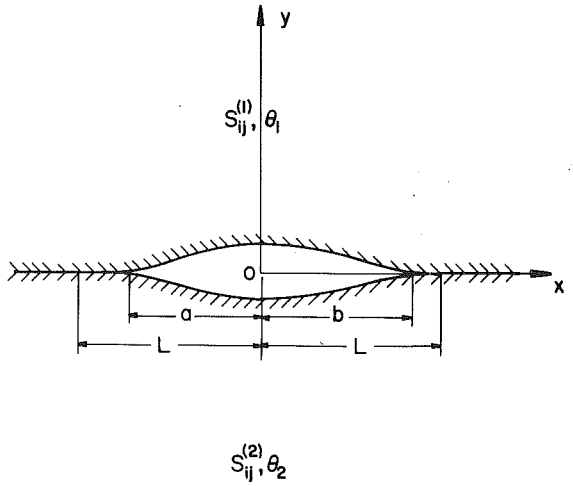

Fig. 2 Coordinates and geometry of a partially closed interface crack between θ_1 and θ_2 composites

The solution for equation (27) has been given by Muskhelishvili [28] as

$$C_{\gamma k}\Omega_k(z) = \frac{X_\gamma(z)}{2\pi i}\int_{-L}^{L} \frac{N_{\gamma i}\, h_i(t)}{X_\gamma^+(t)\,(t-z)}\,dt, \tag{28}$$

where

$$\begin{cases} X_\gamma(z) = (z-L)^{\delta_\gamma - 1}(z+L)^{-\delta_\gamma}, & (29a) \\ \delta_\gamma = \dfrac{1}{2\pi i} ln\ \lambda_\gamma. & (29b) \end{cases}$$

In equations (29*a*) and (29*b*), the branches of $X_\gamma(z)$ are chosen such that $zX_\gamma(z) \to 1$ as $|z| \to \infty$, and the argument of λ_γ is selected to lie between 0 and 2π. If the h_i are constants, equation (28) can be reduced to

$$\Omega_k(z) = \sum_\gamma C_{k\gamma}^{-1}\frac{N_{\gamma i}\, h_i}{1-\lambda_\gamma}\{1+[L(1-2\delta_\gamma)-z]X_\gamma(z)\}, \tag{30}$$

provided that the matrix $[C_{\gamma k}]$ is nonsingular. The δ_γ in equations (29*a*) and (29*b*) are complex in general; thus, the stresses and relative displacements oscillate violently when x approaches the crack tip. The oscillatory singularity leads to interpenetration of two faces of the crack and overlapping of the materials. Moreover, the stress intensity factors do not have the same physical meaning as those in homogeneous cases. Nevertheless, the energy release rates can be defined by using Irwin's virtual crack extension concept [25, 29] as

$$\begin{aligned} G &= G_1 + G_2 + G_3 \\ &= \lim_{\delta\alpha\to 0}\frac{1}{2\delta\alpha}\int_\alpha^{\alpha+\delta\alpha}\{\sigma_y(x,0;\alpha)[v^{(1)}(x,0;\alpha+\delta\alpha) \\ &\quad - v^{(2)}(x,0;\alpha+\delta\alpha)] + \tau_{xy}(x,0;\alpha)[u^{(1)}(x,0;\alpha+\delta\alpha) \\ &\quad - u^{(2)}(x,0;\alpha+\delta\alpha)] + \tau_{yz}(x,0;\alpha)[w^{(1)}(x,0;\alpha+\delta\alpha) \\ &\quad - w^{(2)}(x,0;\alpha+\delta\alpha)]\}dx, \end{aligned} \tag{31}$$

where α and $\alpha+\delta\alpha$ denote the initial and incremental positions of the crack tip. The three terms in equation (31) are noted to be strongly coupled, and integration of each individual one cannot be carried out in an explicit form.

4 Partially Closed Interface Crack Between Dissimilar Anisotropic Materials

The solution presented in the preceding section possesses an oscillating crack-tip field, which leads to an undesirable crack-surface overlapping. The same situation also occurs in the case of an interface crack between dissimilar isotropic media. In this section the formulation given in Sections 2 and 3 is extended to examine an interface crack with partially closed crack surfaces between dissimilar, strongly anisotropic composites. As will be seen later, the physical absurdity of crack-surface interpenetration and the violent oscillation of the crack-tip stress field are removed in this model. A better description of the fundamental nature of the interface crack behavior in dissimilar anisotropic composite materials is achieved.

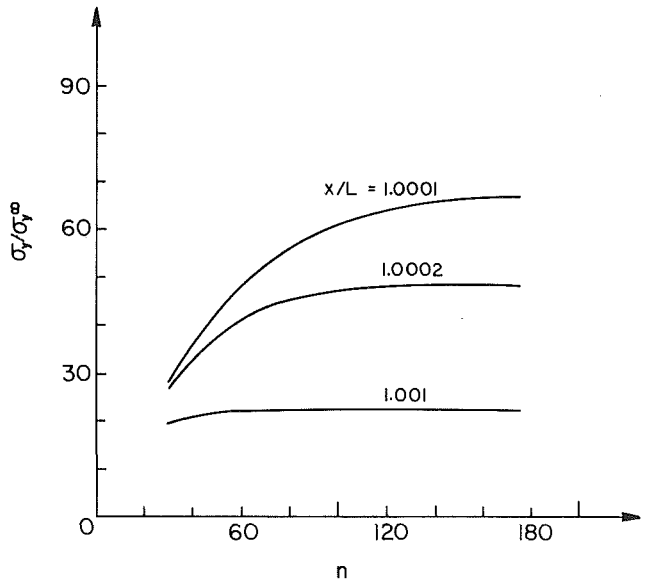

Fig. 3 Convergence of crack-tip normal stress σ_y along the plane of the interface crack, $y = 0$ (partially closed crack model)

Consider a crack located along the interface between two dissimilar anisotropic media. Let the crack surfaces be partially closed with frictionless contact in the intervals $(-L, a)$ and (b, L) and opened in the interval (a,b) as shown in Fig. 2. For simplicity and without loss of generality, we assume that the composite is subjected to nominal stresses σ_y^∞, τ_{xy}^∞, τ_{yz}^∞ at infinity and that the roots μ_k of the characteristic equation, equation (11*a*), are purely imaginary. [This is generally true for commonly used high-modulus, fiber-reinforced composites such as the graphite-epoxy composite]. Under these conditions, it can be shown that along $y = 0$ the following relationships hold:

$$d_{11}(\Omega_1^+ - \Omega_1^-) + d_{12}(\Omega_2^+ + \Omega_2^-) + d_{13}(\Omega_3^+ - \Omega_3^-) = -\sigma_y^\infty \quad \text{for } a<x<b, \tag{32a}$$

$$d_{21}(\Omega_1^+ + \Omega_1^-) + d_{22}(\Omega_2^+ - \Omega_2^-) + d_{23}(\Omega_3^+ + \Omega_3^-) = -\tau_{xy}^\infty \quad \text{for } |x|<L, \tag{32b}$$

$$d_{31}(\Omega_1^+ + \Omega_1^-) + d_{32}(\Omega_2^+ - \Omega_2^-) + d_{33}(\Omega_3^+ + \Omega_3^-) = -\tau_{yz}^\infty \quad \text{for } |x|<L, \tag{32c}$$

where Ω_1, and Ω_3 are analytic functions with cuts on $|x| < L$, and Ω_2 is an analytic function with a cut on $a < x < b$. Solving equations (32*b*) and (32*c*), one has

$$\Omega_1(z) = \frac{e_{11}}{2\pi\sqrt{z^2-L^2}}\int_a^b \frac{\sqrt{L^2-t^2}}{t-z} l_2(t)\,dt + e_{12}\left(1-\frac{z}{\sqrt{z^2-L^2}}\right), \tag{33a}$$

$$\Omega_3(z) = \frac{e_{21}}{2\pi\sqrt{z^2-L^2}}\int_a^b \frac{\sqrt{L^2-t^2}}{t-z} l_2(t)\,dt + e_{22}\left(1-\frac{z}{\sqrt{z^2-L^2}}\right), \tag{33b}$$

Downloaded 02 May 2010 to 171.66.16.246. Redistribution subject to ASME license or copyright; see http://www.asme.org/terms/Terms_Use.cfm

where $l_2(t) = \Omega_2^+(t) - \Omega_2^-(t)$, and

$$e_{11} = \frac{d_{32}\ d_{23} - d_{22}\ d_{33}}{d_{21}\ d_{33} - d_{31}\ d_{23}},\quad e_{12} = \frac{d_{23}\ \tau_{yz}^{\infty} - d_{33}\ \tau_{xy}^{\infty}}{2(d_{21}\ d_{33} - d_{31}\ d_{23})},$$

$$e_{21} = \frac{d_{31}\ d_{22} - d_{21}\ d_{32}}{d_{21}\ d_{33} - d_{31}\ d_{23}},\quad e_{22} = \frac{d_{31}\ \tau_{xy}^{\infty} - d_{21}\ \tau_{yz}^{\infty}}{2(d_{21}\ d_{33} - d_{31}\ d_{23})}, \tag{34}$$

Substituting equations (33*a*) and (33*b*) into (32*a*), one has

$$\frac{\beta}{\pi}\int_{-1}^{1}\frac{\hat{l}_2(s)}{s-s_0}\,ds + \frac{1}{\pi}\int_{-1}^{1}\frac{\Lambda(s_0,s)}{s-s_0}\hat{l}_2(s)\,ds = f(s_0), \tag{35}$$

where $\hat{l}_2(s) = l_2(t)$, and

$$\Lambda(s_0,s) = -i(d_{11}\ e_{11} + d_{13}\ e_{21})\left\{\sqrt{\frac{L^2-t^2}{L^2-t_0^2}} - 1\right\}, \tag{36a}$$

$$f(s_0) = -\sigma_y^{\infty} - \frac{i\ t_0}{\sqrt{L^2-t_0^2}}\{d_{11}\ e_{12} + d_{13}\ e_{22}\}, \tag{36b}$$

$$\beta = -i(d_{12} + d_{11}\ e_{11} + d_{13}\ e_{21}), \tag{36c}$$

$$t = \frac{b+a}{2} + \frac{b-a}{2}s,\quad t_0 = \frac{b+a}{2} + \frac{b-a}{2}s_0. \tag{36d}$$

In addition to equation (35), the single valuedness of displacement requires

$$\int_{-1}^{1}\hat{l}_2(s)\ ds = 0. \tag{37}$$

It may be noted that Ω_1 and Ω_3 satisfy the condition similar to equation (37), since they are of the order of $1/z^2$ as $|z| \to \infty$. Finally, the separation condition and the condition of unilateral constraint require that

$$v^{(1)}(x,0) - v^{(2)}(x,0) \geq 0 \quad \text{for } a \leq x \leq b, \tag{38a}$$

$$\sigma_y(x,0) \leq 0 \quad \text{for } -L < x \leq a,\ b \leq x < L. \tag{38b}$$

In order to solve the singular integral equation, equation (35), the numerical method developed by Erdogan and Gupta [27] is used. Let

$$\hat{l}_2(s) = \frac{\omega(s)}{\sqrt{1-s^2}}, \tag{39}$$

where $\omega(s)$ is a bounded, continuous function in the closed interval $|s| \leq 1$. Then, for $-L < t_0 < a$ and $b < t_0 < L$ on the crack surface $y = 0$, one has

$$\sigma_y = \sigma_y^{\infty} + \frac{it_0}{\sqrt{L^2-t_0^2}}\{d_{11}\ e_{12} + d_{13}\ e_{22}\}$$

$$+ \frac{\beta}{\pi}\int_{-1}^{1}\frac{\omega(s)\ ds}{(s-s_0)\sqrt{1-s^2}} + \frac{1}{\pi}\int_{-1}^{1}\frac{\Lambda(s_0,s)\ \omega(s)}{(s-s_0)\sqrt{1-s^2}}ds. \tag{40}$$

Since the contact is smooth, there should be no singularity at $s_0 = \pm 1$, and

$$\sigma_y = 0. \tag{41}$$

Thus, equation (41) provides two conditions for determining the unknowns, a and b. The discretized form of equation (35) may be written as [27]

$$\sum_{k=1}^{n}\frac{\omega(s_k)}{n(s_k - s_{0r})}\{\beta + \Lambda(s_{0r},\ s_k)\} = f(s_{0r}), \tag{42}$$

where

$$s_k = \cos\left[\frac{(2k-1)\pi}{2n}\right] \quad (k = 1,2,\ldots,n), \tag{43a}$$

$$s_{0r} = \cos\left(\frac{r\pi}{n}\right) \quad (r = 1,2,\ldots,n-1). \tag{43b}$$

Since $s_k \neq \pm 1$ in equation (43*a*), equation (41) may be replaced by equation (42) with $s_{0r} = \pm 1$. Furthermore, equation (37) requires

$$\sum_{k=1}^{n}\omega(s_k) = 0. \tag{44}$$

In actual computation of the nonlinear contact problem, values of a and b are assumed first. The system of n linear equations, equations (42) and (44), are solved for the n unknowns $\omega(s_k)$. Once $\omega(s_k)$ are determined, σ_y at $s_0 = \pm 1$ can be calculated. New refined values for a and b are chosen again. This process is repeated until σ_y at $s_0 = \pm 1$ vanishes. The resulting solution is checked against the constraint conditions, equations (38*a*) and (38*b*).

From equations (33*a*), (33*b*), and (39), one can see that the stresses in the vicinity of a partially closed crack tip have an inverse square-root singularity. We remark that the correctness of the inverse square-root singularity at a closed crack tip is independently checked by using an eigenfunction expansion method (see Appendix 1). Defining the stress intensity factors by

$$K_1 = \lim_{x \to \pm L^-}\sqrt{2|x \mp L|}\,\sigma_y,\quad K_2 = \lim_{x \to \pm L^+}\sqrt{2|x \mp L|}\,\tau_{xy}, \tag{45a,b}$$

$$K_3 = \lim_{x \to \pm L^+}\sqrt{2|x \mp L|}\,\tau_{yz}, \tag{45c}$$

where $L^{\pm} = L \pm 0$, one has

$$K_1/\sqrt{L} = -i(d_{11}\ e_{11} + d_{13}\ e_{21})M \pm i(d_{11}\ e_{12} + d_{13}\ e_{22}), \tag{46a}$$

$$K_2/\sqrt{L} = \mp d_{22}M + \tau_{xy}^{\infty}, \tag{46b}$$

$$K_3/\sqrt{L} = \mp d_{32}M + \tau_{yz}^{\infty}, \tag{46c}$$

with

$$M = \int_{-1}^{1}\frac{\omega(s)}{(s-s_0)\sqrt{1-s^2}}\sqrt{1 - \left(\frac{b+a}{2L} + \frac{b-a}{2L}s\right)^2}\,ds, \tag{47a}$$

$$s_0 = \frac{\pm 2L - b - a}{b-a}. \tag{47b}$$

The upper sign is for the right crack tip, and the lower sign is for the left tip. The energy release rate can be evaluated by considering the relative displacements, u, v, and w, as

$$v^{(1)} - v^{(2)} = 0,\quad u^{(1)} - u^{(2)} = A_2\sqrt{2|\delta\alpha + \alpha - x|},$$

$$w^{(1)} - w^{(2)} = A_3\sqrt{2|\delta\alpha + \alpha - x|}, \tag{48}$$

as $x \to \alpha$, where

$$A_2 = \pm i\ e_{11}M - i\ e_{12},\quad A_3 = \pm i\ e_{21}M - i\ e_{22}. \tag{49}$$

Therefore, the total energy release rate can be determined from equation (31) as

$$G = G_2 + G_3 = \frac{\pi}{4}(A_2\ K_2 + A_3\ K_3). \tag{50}$$

It is noted that, for an interface crack between dissimilar isotropic solids in a tensile field, Comninou [12, 13] has shown that the contact zone is about 10^{-4} to 10^{-7} times the length of the crack. However, for an interface crack under shear loading, one of the contact zones is about half the size of the crack and the other is less than 10^{-7} times the crack length. It has also been pointed out [12] that a restriction on the range of Dundur's bimaterial constant may exist in determining the size of the contact zone numerically. Thus, it is possible that there is no computationally feasible solution for some cases with certain combinations of elastic constants. Actually, for the present high-modulus graphite-epoxy composites under shear loading, it is impossible to satisfy one of the conditions, equation (38*a*) or (38*b*), numerically.

Downloaded 02 May 2010 to 171.66.16.246. Redistribution subject to ASME license or copyright; see http://www.asme.org/terms/Terms_Use.cfm

5 Approximate Model for Interface Crack With Very Small Contact Area

As pointed out first by England [3] and Malyshev, et al. [4] and later by Comninou [12], the region of oscillatory solutions is extremely small in general compared to the size of an interface crack in dissimilar isotropic media under certain loading conditions. Similar phenomena exist in the present problem of an interlaminar crack between two anisotropic materials subjected to uniform tensile loading σ_y^∞. The region of oscillatory analytical solutions obtained from Section 3 is found to be of the order of 10^{-6} to 10^{-8} times the crack length. It has been argued, for example, by Erdogan [7], that the very localized abnormity may not be significant in practical terms of linear elastic fracture mechanics and the singular stresses outside the small oscillatory stress region are considered to play an important role in the fracture of composite materials. Nonetheless, the crack surface overlapping is physically inadmissible. The purpose of the study in this section is to propose a simplified model for this situation, which can be free from this difficulty, by disregarding the small oscillatory field. The model will be shown to provide a convenient means for obtaining useful information on the interlaminar crack behavior in composites.

A major feature of the present model is that the stress field at the crack tip may be approximated by an inverse square-root singularity. Thus, the commonly referred stress intensity factors can be defined consistently by extrapolation. More explicitly, for an interlaminar crack with very small crack closure under given loading, we let $a \to -L$ and $b \to L$ in the solution for a partially closed crack case discussed in the preceding section. Mathematically, this is equivalent to finding an approximate solution of equation (22) for a fully opened crack by following the same procedure [from equations (32)–(44)] as that for a partially closed crack. Note that in so doing, the step from equation (32) to (33) is an approximation for determining Ω_k in equation (28) or (30), because, in this case, $\Omega_2(z)$ as well as $\Omega_1(z)$ and $\Omega_3(z)$ are also analytic functions with a cut on $|x| < L$ along $y = 0$. Note also that this mathematical approximation has the effect of smoothing the oscillatory singularity to an inverse square-root singularity. The opening mode stress intensity factor K_1 is therefore, defined by

$$K_1 = \lim_{x \to \pm L^+} \sqrt{2|x \mp L|}\,\sigma_y, \tag{51}$$

instead of equation (45*a*). It can be shown that K_1 takes the form as

$$K_1 = \pm i\, d_{12}\, \omega(\pm 1). \tag{52}$$

Similarly, with $A_1 = \mp\omega(\pm 1)$ the relative displacement can be determined as

$$v^{(1)} - v^{(2)} = A_1\sqrt{2|\delta\alpha + \alpha - x|}. \tag{53}$$

In equations (52) and (53), the $\omega(\pm 1)$ may be conveniently evaluated by using the formulas developed by Krenk [31], i.e.,

$$\omega(1) = \frac{1}{n}\sum_{k=1}^{n} Q_k\, \omega(s_k), \tag{54a}$$

$$\omega(-1) = \frac{1}{n}\sum_{k=1}^{n} Q_k\, \omega(s_{n+1-k}), \tag{54b}$$

where

$$Q_k = \sin\left[\frac{(2n-1)(2k-1)\pi}{4n}\right] / \sin\left[\frac{(2k-1)\pi}{4n}\right]. \tag{55}$$

The total strain energy release rate then has the form

$$G = \frac{\pi}{4}(A_1K_1 + A_2K_2 + A_3K_3). \tag{56}$$

It is noted that if the contact area becomes global at one end and is very localized at the other end of the interlaminar crack under certain loading, a combination of the partially closed crack model (discussed in Section 4) for the closed crack tip and the approximate crack model (described in this section) for the other crack tip can be used conveniently. Details of the more general case and treatment are given in an associated paper [30].

Table 1 Dominant values of δ_n for asymptotic stress and displacement fields of a fully opened interlaminar crack

$\pm\theta^a$	δ_1	$\delta_{2,3}$
15 deg	0.5	$0.5 \pm i\,0.00642315$
30 deg	0.5	$0.5 \pm i\,0.02399757$
45 deg	0.5	$0.5 \pm i\,0.03434233$
60 deg	0.5	$0.5 \pm i\,0.02942129$
75 deg	0.5	$0.5 \pm i\,0.01579694$

[a] θ is defined as the angle measured counterclockwise from the positive z-axis to the fiber direction in the x-z plane

6 Numerical Examples and Discussion

To illustrate the basic theories and solutions for the different crack models derived in Sections 3, 4, and 5 and the fundamental nature of the interlaminar crack problem in bonded anisotropic composites, the numerical example of a crack lying along the interface of two anisotropic composites subjected to a uniform nominal tensile loading σ_y^∞ is con-

Table 2 Interlaminar normal and shear stresses along the plane of the crack[a]

x/L	σ_y/σ_y^∞			$\tau_{yz}/\sigma_y^\infty$		
	Fully opened crack		Partially closed crack model	Fully opened crack		Partially closed crack model
	Analytical model[b]	Approximate model[c]		Analytical model[b]	Approximate model[c]	
1.0001	68.29	65.35	65.31	21.83	22.57	22.57
1.0002	48.59	48.23	48.23	14.11	14.39	14.39
1.0005	30.97	31.00	31.00	7.813	7.874	7.874
1.0010	22.02	22.03	22.03	4.928	4.947	4.947
1.0050	9.966	9.967	9.967	1.584	1.586	1.586
1.0100	7.094	7.094	7.094	0.9344	0.9349	0.9349
1.0500	3.280	3.280	3.280	0.2346	0.2346	0.2346
1.1000	2.403	2.403	2.403	0.1165	0.1165	0.1165
1.5000	1.343	1.343	1.343	0.01467	0.01467	0.01467
2.0000	1.155	1.155	1.155	0.00451	0.00451	0.00451

[a] $\tau_{xy}^\infty = \tau_{yz}^\infty = 0$; $\theta = \pm 45$ deg
[b] Model given in Section 3
[c] Model given in Section 5
$n = 130$ (equations (42) and (44)); $a/L = 1 - 4.8 \times 10^{-8}$

Downloaded 02 May 2010 to 171.66.16.246. Redistribution subject to ASME license or copyright; see http://www.asme.org/terms/Terms_Use.cfm

Table 3 Stress intensity factors and energy release rates[a] for an interface crack between +45 deg and −45 deg graphite-epoxy composites

	Approximate model[b]	Partially closed crack model
$K_1/(\sigma_y^\infty\sqrt{L})$	0.9556	−0.03897
$K_2/(\sigma_y^\infty\sqrt{L})$	0.0	0.0
$K_3/(\sigma_y^\infty\sqrt{L})$	0.4164	0.4163
$G_1E/[(\sigma_y^\infty)^2L]$	1.272	0.0
$G_2E/[(\sigma_y^\infty)^2L]$	0.0	0.0
$G_3E/[(\sigma_y^\infty)^2L]$	0.1833	0.1832
$G\ E/[(\sigma_y^\infty)^2L]$	1.455	0.1832

[a] $E = 10^6$ psi (a scaling factor)
[b] Fully opened crack with square-root singularity (Section 5)

sidered. Let the upper space be occupied by a composite with θ^2 fiber orientation, and the lower one by a $-\theta$ composite. Assume that the anisotropic composite has the following material elastic constants typical of a high-modulus graphite-epoxy composite:

$$E_L = 20\times10^6 \text{ (psi)},\ E_T = E_z = 2.1\times10^6 \text{ (psi)},$$
$$G_{LT} = G_{Lz} = G_{Tz} = 0.85\times10^6 \text{ (psi)}, \quad (57)$$
$$\nu_{LT} = \nu_{Tz} = \nu_{Lz} = 0.21,$$

where the subscripts L, T, and z refer to the longitudinal, transverse, and through-thickness directions, respectively.

For this problem, the model and analysis of a fully opened interlaminar crack described in Section 3 are used first. Values of δ_n characterizing the interlaminar crack-tip stress and displacement fields are determined. For different degrees of anisotropy in the two composites, i.e., various θ's, for example, the first three dominant δ_n are shown in Table 1. Note that the order of the interlaminar crack-tip stress singularity, i.e., $(\delta_n - 1)$, is found to be identical to that obtained by using an independent method of approach (i.e., the eigenfunction expansion technique [32]). The imaginary parts of δ_2 and δ_3 are *very small* in general, decrease as the θ changes to either direction, and vanish when $\theta = 0$ deg and 90 deg. This situation is anticipated, since in these limiting cases the two materials become identical with a single phase; thus, oscillatory characteristics of the field solution should not appear. The asymptotic stress field and fracture mechanics parameters such as stress intensity factors and energy release rates are evaluated for the fully opened crack case and will be discussed later.

Since solutions based on the consideration of a fully opened crack give controversial oscillatory asymptotic fields, the problem is further examined by introducing the partially closed crack model described in Section 4. As discussed previously, the formulation leads to the singular integral equation, equation (35), which can be solved numerically. The numerical method whose accuracy and stability have been well established by Erdogan, et al. [27] requires one to solve the system of n linear equations, i.e., equations (42) and (44). Convergence of the results in the numerical work is related to the degree of discretization of equation (35), i.e., the proper number of terms, n, used in equation (42). The effect of n on the solution convergence is illustrated in Fig. 3. The transverse normal stress σ_y near the tip of the partially closed crack is shown to converge rapidly as the n increases. For convenience, $n = 130$ is used for all numerical computations in this study to ensure the accuracy and convergence of the results.

[2] θ is defined as the angle measured counterclockwise from the positive z-axis to the fiber direction in the x-z plane.

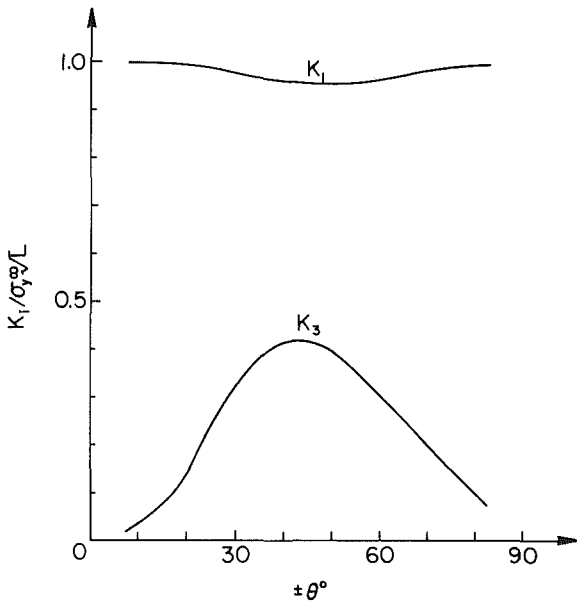

Fig. 4 Stress intensity factors for an interface crack (approximate model) between graphite-epoxy composites with θ and $-\theta$ fiber orientations

Comparisons of the three different approaches (or models) for the interface crack between 45 deg and −45 deg graphite-epoxy composites under uniform tensile loading σ_y^∞ are given in Tables 2 and 3. The interlaminar normal and shear stresses, σ_y and τ_{yz}, along $y = 0$ near the crack tip are tabulated in Table 2. Under this loading condition, differences among the stress solutions obtained from the three distinct approaches are negligible except for $x/L \leq 10^{-4}$. We note that even though the results obtained by using different models coincide with each other in the range of tabulation, the characteristics at the crack tip are very different. That is, in the partially closed interlaminar crack model, the normal stress is finite as $x \to L^+$, whereas in the fully opened crack model the σ_y becomes unbounded with violent oscillation. Of course the oscillatory character disappears as the approximate model discussed in Section 5 is used. This nature of the problem is anticipated since the contact length of the crack surface is found to be extremely small as shown in the Table based on the current theory for a partially closed crack.

The interlaminar crack behavior may be also described by the fracture mechanics parameters, K_i and G_i. The interface stress intensity factors and energy release rates for the problem are given in Table 3 for illustration by using the present partially closed crack analysis. Solutions obtained from the approximate model are shown also for comparison, since the contact zone of the crack surface is small enough.

Downloaded 02 May 2010 to 171.66.16.246. Redistribution subject to ASME license or copyright; see http://www.asme.org/terms/Terms_Use.cfm

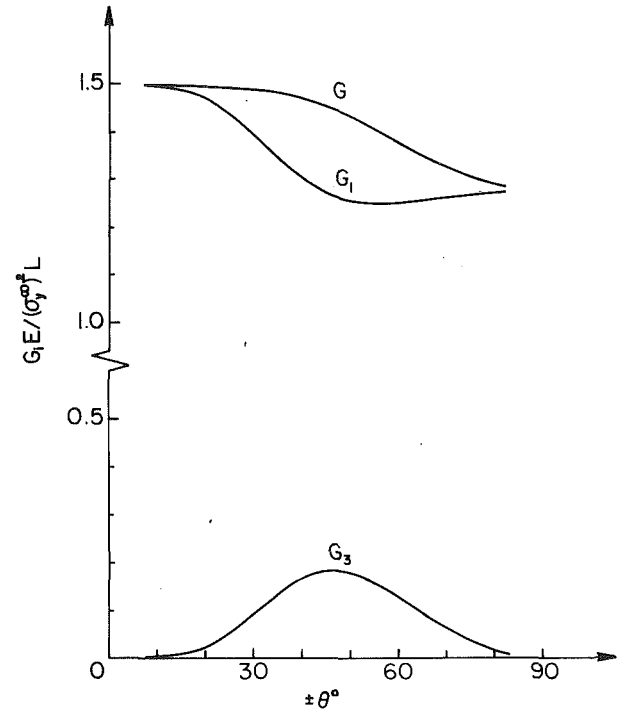

Fig. 5 Energy release rates for an interface crack (approximate model, $E = 10^6$ psi) in $[\theta/-\theta]$ graphite-epoxy composites

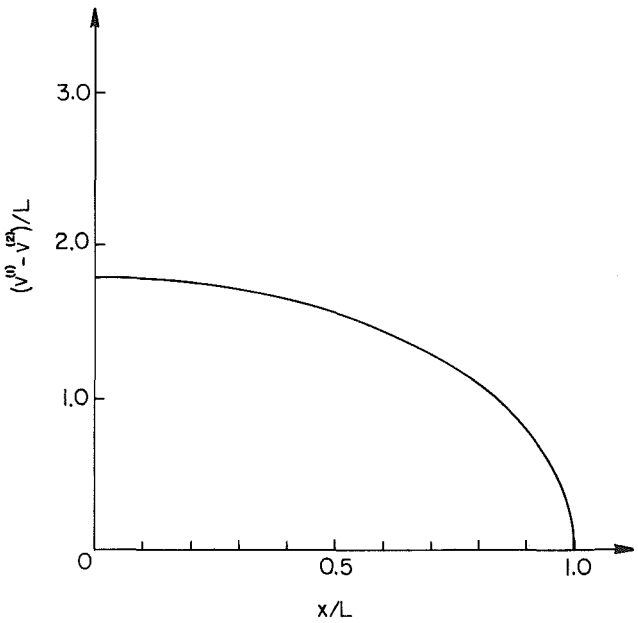

Fig. 6 Interface crack opening gap in $[\theta/-\theta]$ graphite-epoxy composites subjected to a nominal tensile load, $\sigma_y^\infty = 10^6$ psi (approximate model)

The results shown in the Table provide insight in the difference (e.g., the values of K_1 and G_1) of the crack-tip behavior obtained by the two approaches. In the limiting case of a crack in a homogeneous material, $K_1/(\sigma_y^\infty\sqrt{L})$ is known to be 1; thus, the results for the partially closed crack case have a discontinuity, which is physically undesirable.

We further remark that the total energy release rate for the problem, $G = G_1 + G_2 + G_3$, has been calculated conveniently from the analytic solution using the fully opened crack model of Section 3 and has a $GE/[(\sigma_y^\infty)^2L]$ value of 1.4000. This is very close to the value obtained from the approximate model of Section 5.

The interlaminar crack-tip stress intensity factors and energy release rates in the $[\theta/-\theta]$ composites with different degrees of anisotropy as introduced by changing fiber orientation are studied also. Since the crack surface closure is extremely small as shown in Table 2, the approximate crack model described in Section 5 is used and solutions are reported in Figs. 4 and 5. The results show that the maximum K_3 and G_3 occur in the case of $\pm\theta = \pm 45$ deg and that, as the θ approaches 0 deg and 90 deg, K_3 and G_3 tend to vanish. Finally, the interface crack opening gap under a nominal tensile loading of $\sigma_y^\infty = 10^6$ (psi) is plotted in Fig. 6. From the figure, it is seen that the deformed crack surface may be approximated by $1.79\sqrt{1-(x/L)^2}$. Thus, in this case, the shape of crack opening appears to be similar to that in a homogeneous crack problem.

7 Conclusions

Based on the developments in the previous sections, the following conclusions may be reached:

1 Using Lekhnitskii's stress potentials and Clements' approach but with a stress formulation, one can examine the problem of an interfacial crack between dissimilar anisotropic materials in some detail. However, solutions obtained by this approach contain controversial oscillatory singularities, which are physically inadmissible.

2 The model of a partially closed interface crack with frictionless crack surface contact between dissimilar anisotropic materials is therefore proposed to correct the controversial features. Formulation for this model leads to a singular integral equation. Numerical results for K_1, K_2, K_3 and G_1, G_2, G_3 have been obtained by solving the singular integral equation. In this model, the order of the stress singularity near the crack tip is found numerically to be an inverse square-root singularity.

3 A simplified model is developed for the case of an interlaminar crack with a very small area of crack-surface contact (determined by the partially closed crack solution). This model approximates crack-tip stresses with an inverse square-root singularity. It can be conveniently incorporated into computational fracture mechanics methods such as hybrid-stress F.E.M. for complex fracture problems of composites.

4 With the inverse square-root stress singularity for the approximate crack model and for the partially closed crack model, physically meaningful fracture mechanics parameters such as stress intensity factors and energy release rates for each individual mode of an interlaminar crack between dissimilar anisotropic composites can be defined consistently with those for a homogeneous crack and for an interface crack with partially closed tips between dissimilar isotropic media [12].

5 Comparisons of interlaminar stresses obtained from the three approaches are made; differences in stress solutions are negligible except in the very small neighborhood of the crack tip, which may be of little significance in practical terms of linear elastic fracture mechanics. Due to the difference in the singular nature between a partially closed crack model and an approximate crack model, fracture mechanics parameters such as the mode *I* stress intensity factor and energy release rate obtained from the different approaches for an interlaminar crack are found to be different, whereas the quantities associated with the mode *II* and *III* fracture seem to be consistent.

6 Since the singular stresses outside the small oscillatory crack-tip region are considered to play an important role in the interlaminar fracture of composite materials, the proposed approximate model for an interface crack with very

Downloaded 02 May 2010 to 171.66.16.246. Redistribution subject to ASME license or copyright; see http://www.asme.org/terms/Terms_Use.cfm

small closure may provide a convenient means to determine physically meaningful fracture mechanics parameters for evaluating interlaminar failure behavior of composite materials, when used in conjunction with other models discussed in the paper.

8 Acknowledgments

The research work described in this paper was supported in part by the Office of Naval Research (ONR), Arlington, Va., under Grant N000 14-79-C-0579. The authors are grateful to Drs. N. Perrone and Y. Rajapakse of ONR for their constant support. The authors are also indebted to Professor M. Comninou of the University of Michigan for reading the manuscript and suggestions and to Professor H. T. Corten of the University of Illinois for the encouragement during the course of this study.

9 References

1 Williams, M. L., "The Stresses Around a Fault or Crack in Dissimilar Media," *Bulletin of the Seismology Society of America*, Vol. 49, 1959, pp. 199-204.

2 Zak, A. R., and Williams, M. L., "Crack Point Stresses Singularities at a Bi-Material Interface," ASME JOURNAL OF APPLIED MECHANICS, Vol. 30, 1963, pp. 142-143.

3 England, A. H., "A Crack Between Dissimilar Media," ASME JOURNAL OF APPLIED MECHANICS, Vol. 32, 1965, pp. 400-402.

4 Malyshev, B. M., and Salganik, R. L., "The Strength of Adhesive Joints Using Theory of Fracture," *International Journal of Fracture Mechanics*, Vol. 1, 1965, pp. 114-128.

5 Sih, G. C., and Rice, J. R., "The Bending of Plates of Dissimilar Materials With Cracks," ASME JOURNAL OF APPLIED MECHANICS, Vol. 31, 1964, pp. 477-482.

6 Rice, J. R., "Plane Problems of Cracks in Dissimilar Media," ASME JOURNAL OF APPLIED MECHANICS, Vol. 32, 1965, pp. 418-423.

7 Erdogan, F., "Stress Distributions in Bonded Dissimilar Materials With Cracks," ASME JOURNAL OF APPLIED MECHANICS, Vol. 32, 1965, pp. 403-410.

8 Erdogan, F., and Gupta, G., "The Stress Analysis of Multilayered Composites With a Flaw," *International Journal of Solids and Structures*, Vol. 7, 1971, pp. 39-61.

9 Erdogan, F., and Gupta, G., "Layered Composite With an Interfacial Flaw," *International Journal of Solids and Structures*, Vol. 7, 1971, pp. 1089-1107.

10 Atkinson, C., "On Stress Singularities and Interfaces in Linear Elastic Fracture Mechanics," *International Journal of Fracture*, Vol. 13, 1977, pp. 807-820.

11 Goree, J. G., and Venezia, W. A., "Bonded Elastic Half Planes With an Interface Crack and a Perpendicular Intersecting Crack that Extends Into the Adjacent Materials—I and II," *International Journal of Engineering Science*, Vol. 15, 1977, pp. 1-17 and pp. 19-27.

12 Comninou, M., "The Interface Crack," ASME JOURNAL OF APPLIED MECHANICS, Vol. 44, 1977, pp. 631-636.

13 Comninou, M., "The Interface Crack in a Shear Field," ASME JOURNAL OF APPLIED MECHANICS, Vol. 45, 1978, pp. 287-290.

14 Achenbach, J. D., Keer, L. M., and Chen, S. H., "Loss of Adhesion at the Tip of an Interface Crack," *Journal of Elasticity*, Vol. 9, 1979, pp. 397-424.

15 Rybicki, E. F., Schmeser, D. W., and Fox, J., "An Energy Release Rate Approach for Stable Crack Growth in the Free-Edge Delamination," *Journal of Composite Materials*, Vol. 11, 1977, pp. 470-487.

16 Wang, A. S. D., and Crossman, F. W., "Initiation and Growth of Transverse Cracks and Edge Delamination in Composite Laminates, Part 1: An Energy Method," Technical Report, Department of Mechanical Engineering and Mechanics, Drexel University, Philadelphia, Pa., 1979.

17 Crossman, F. W., Warren, W. J., Wang, A. S. D., and Law, G. E., Jr., "Initiation and Growth of Transverse Cracks and Edge Delamination in Composite Laminates, Part 2: Experimental Correlation," Technical Report, Department of Mechanical Engineering and Mechanics, Drexel University, Philadelphia, Pa., 1979.

18 Bascom, W. D., Bitner, J. L., Moulton, R. J., and Siebert, A. R., "The Interlaminar Fracture of Organic Matrix Woven Reinforcement Composites," *Composite Journal*, Vol. 40, 1980, pp. 9-18.

19 Wang, S. S., "An Analysis of Delamination in Angle-Ply Fiber-Reinforced Composites," ASME JOURNAL OF APPLIED MECHANICS, Vol. 47, 1980, pp. 64-70.

20 Wang, S. S., and Wang, H. T., "Interlaminar Crack Growth in Fiber Reinforced Composite During Fatigue," ASME *Journal of Engineering Materials and Technology*, Vol. 101, 1979, pp. 34-41.

21 Wilkins, D. J., Eisenmann, J. R., Camin, R. A., Margolis, W. S., and Benson, R. A., "Characterizing Delamination Growth in Graphite-Epoxy," *Damage in Composite Materials: Basic Mechanisms, Accumulation, Tolerance and Characterization, ASTM STP 775*, American Society for Testing and Materials, 1982, pp. 168-183.

22 O'Brien, T. K., "Characterization of Delamination Onset and Growth in a Composite Laminate," NASA Technical Memorandum 81940, NASA-Langley Research Center, Hampton, Va., 1981.

23 Gotoh, M., "Some Problems of Bonded Anisotropic Plates With Cracks Along the Bond," *International Journal of Fracture Mechanics*, Vol. 3, No. 5, 1967, pp. 253-265.

24 Clements, D. L., "A Crack Between Dissimilar Anisotropic Media," *International Journal of Engineering Science*, Vol. 9, 1971, pp. 257-265.

25 Willis, J. R., "Fracture Mechanics of Interfacial Cracks," *Journal of Mechanics and Physics of Solids*, Vol. 19, 1971, pp. 353-368.

26 Lekhnitskii, S. G., *Theory of Elasticity of an Anisotropic Body*, Holden-Day, San Francisco, 1963.

27 Erdogan, F., and Gupta, G. D., "On the Numerical Solution of Singular Integral Equations," *Quarterly of Applied Mathematics*, Vol. 30, 1972, pp. 525-534.

28 Muskhelishvili, N. I., *Singular Integral Equations*, P. Noordhoff, Groningen, 1953.

29 Irwin, G. R., "Analysis of Stresses and Strains Near the End of a Crack Traversing a Plate," ASME JOURNAL OF APPLIED MECHANICS, Vol. 24, Vol. 69, 1957, pp. 361-364.

30 Wang, S. S., and Choi, I., "The Interface Crack Behavior in Dissimilar Anisotropic Composites Under Mixed Mode Loading," ASME JOURNAL OF APPLIED MECHANICS, Vol. 50, 1983, pp. 179-183.

31 Krenk, S., "On the Use of the Interpolation Polynomial for Solutions of Singular Integral Equations," *Quarterly of Applied Mathematics*, Vol. 32, 1975, pp. 479-484.

32 Wang, S. S., "Edge Delamination in Angle-Ply Composite Laminates," NASA Contract Report, NASA CR-165439, NASA Lewis Research Center, Cleveland, Ohio, Feb. 1981.

APPENDIX 1

Stress Singularity for a Closed Interface Crack

Following the procedure given in [26], one may write equations (10*a*) and (10*b*) in slightly different forms as

$$F=\sum_{k=1}^{6} F_k(Z_k), \quad \Psi=\sum_{k=1}^{6} \eta_k F_k'(Z_k). \tag{A.1}$$

By choosing $F_k(Z_k)$ as follows

$$F_k(Z_k)=C_k Z_k^{\delta+2}/[(\delta+1)(\delta+2)], \tag{A.2}$$

then, from equations (13), (14), and (*A*.2), the stress and displacement may be expressed as

$$\sigma_x = \sum_{k=1}^{6} C_k \mu_k^2 Z_k^{\delta}, \quad \tau_{xz}=\sum_{k=1}^{6} C_k \eta_k \mu_k Z_k^{\delta},$$

$$\sigma_y = \sum_{k=1}^{6} C_k Z_k^{\delta}, \quad \tau_{yz}=-\sum_{k=1}^{6} C_k \eta_k Z_k^{\delta},$$

$$\tau_{xy}=-\sum_{k=1}^{6} C_k \mu_k Z_k^{\delta}, \tag{A.3}$$

$$u = \sum_{k=1}^{6} C_k p_k Z_k^{\delta+1}/(\delta+1), \quad v=\sum_{k=1}^{6} C_k q_k Z_k^{\delta+1}/(\delta+1),$$

$$w=\sum_{k=1}^{6} C_k t_k Z_k^{\delta+1}/(\delta+1). \tag{A.4}$$

Along the interlaminar crack surfaces (in frictionless contact), i.e., $\phi=\pi$ and $-\pi$, one has

$$\tau_{yz}^{(1)}(r,\pi)=\tau_{xy}^{(1)}(r,\pi)=\tau_{yz}^{(2)}(r,-\pi)=\tau_{xy}^{(2)}(r,-\pi)=0,$$
$$\sigma_y^{(1)}(r,\pi)=\sigma_y^{(2)}(r,-\pi), \quad v^{(1)}(r,\pi)=v^{(2)}(r,-\pi). \tag{A.5}$$

Along the ply interface, i.e., $\phi=0$, continuity conditions for σ_i and u_i require

$$\{\sigma_y^{(1)},\tau_{yz}^{(1)},\tau_{xy}^{(1)},u^{(1)},v^{(1)},w^{(1)}\} = \{\sigma_y^{(2)},\tau_{yz}^{(2)},\tau_{xy}^{(2)},u^{(2)},v^{(2)},w^{(2)}\}. \tag{A.6}$$

Substituting equations (*A*.3) and (*A*.4) into equations (*A*.5) and (*A*.6), one obtains the following linear equations:

Downloaded 02 May 2010 to 171.66.16.246. Redistribution subject to ASME license or copyright; see http://www.asme.org/terms/Terms_Use.cfm

$$\sum_{k=1}^{3} \{\alpha\eta_k^{(1)} C_k^{(1)} + \eta_{k+3}^{(1)} C_{k+3}^{(1)}/\alpha\} = 0, \tag{A.7a}$$

$$\sum_{k=1}^{3} \{\alpha\mu_k^{(1)} C_k^{(1)} + \mu_{k+3}^{(1)} C_{k+3}^{(1)}/\alpha\} = 0, \tag{A.7b}$$

$$\sum_{k=1}^{3} \{\eta_k^{(2)} C_k^{(2)}/\alpha + \alpha\eta_{k+3}^{(2)} C_{k+3}^{(2)}\} = 0, \tag{A.7c}$$

$$\sum_{k=1}^{3} \{\mu_k^{(2)} C_k^{(2)}/\alpha + \alpha\mu_{k+3}^{(2)} C_{k+3}^{(2)}\} = 0, \tag{A.7d}$$

$$\sum_{k=1}^{3} \{\alpha C_k^{(1)} + C_{k+3}^{(1)}/\alpha - C_k^{(2)}/\alpha - \alpha C_{k+3}^{(2)}\} = 0, \tag{A.7e}$$

$$\sum_{k=1}^{3} \{\alpha q_k^{(1)} C_k^{(1)} + q_{k+3}^{(1)} C_{k+3}^{(1)}/\alpha - q_k^{(2)} C_k^{(2)}/\alpha - \alpha q_{k+3}^{(2)} C_{k+3}^{(2)}\} = 0, \tag{A.7f}$$

$$\sum_{k=1}^{6} \{C_k^{(1)} - C_k^{(2)}\} = 0, \tag{A.7g}$$

$$\sum_{k=1}^{6} \{\eta_k^{(1)} C_k^{(1)} - \eta_k^{(2)} C_k^{(2)}\} = 0, \tag{A.7h}$$

$$\sum_{k=1}^{6} \{\mu_k^{(1)} C_k^{(1)} - \mu_k^{(2)} C_k^{(2)}\} = 0, \tag{A.7i}$$

$$\sum_{k=1}^{6} \{p_k^{(1)} C_k^{(1)} - p_k^{(2)} C_k^{(2)}\} = 0, \tag{A.7j}$$

$$\sum_{k=1}^{6} \{q_k^{(1)} C_k^{(1)} - q_k^{(2)} C_k^{(2)}\} = 0, \tag{A.7k}$$

$$\sum_{k=1}^{6} \{t_k^{(1)} C_k^{(1)} - t_k^{(2)} C_k^{(2)}\} = 0, \tag{A.7l}$$

where $\alpha = e^{i\pi\delta}$. The system of 12 homogeneous linear equations (A.7a)-(A.7l) in $C_k^{(\alpha)}$ has a nontrivial solution only if the coefficient matrix vanishes; thus one must have

$$P(\alpha) = 0, \tag{A.8}$$

where P is a polynomial of twelfth order in α. Solving equation (A.8) by a proper numerical method provides one with the eigenvalues δ_n. The δ_n such that

$$-1 < Re(\delta_n) < 0 \tag{A.9}$$

characterize the order of stress singularity of the crack tip. It is found that $\delta = -0.5$ always occurs in the numerical solution of equation (A.8) for commonly used high-modulus composites such as the graphite-epoxy with material properties given by equation (57).

Downloaded 02 May 2010 to 171.66.16.246. Redistribution subject to ASME license or copyright; see http://www.asme.org/terms/Terms_Use.cfm

S. S. Wang
Associate Professor.
Assoc. Mem. ASME

I. Choi[1]
Research Associate.

Department of Theoretical and Applied Mechanics,
University of Illinois,
Urbana, Ill. 61801

The Interface Crack Behavior in Dissimilar Anisotropic Composites Under Mixed-Mode Loading

A study of an interlaminar crack between dissimilar, anisotropic composites under mixed-mode loading is presented. Based on the theoretical development in [1], the problem is modeled by using a partially closed interface crack model for the closed tip and an approximate model for the other tip. Solutions are obtained for the interlaminar crack between dissimilar composites with various degrees of anisotropy under general mixed-mode loading conditions. Crack closure, contact stresses, crack-tip stress intensity factors, and energy release rates are determined for each case.

1 Introduction

The interface crack problem in dissimilar, anisotropic composite materials has been recently studied in reference [1]. It has been shown that in a nominal tensile field the interlaminar crack possesses a very small, oscillatory crack-tip field and that, in practical terms of fracture mechanics, an approximate model may be used for this case. The model, in which the stress at an interlaminar crack tip is approximated by an inverse square-root singularity, has been shown [1] to provide a convenient approach and excellent solutions for the problem. In the case of an interlaminar crack subjected to loading other than pure tension, the partially closed crack model proposed in [1] may be needed. In fact, in a practical composite fracture problem, an interlaminar crack is generally subjected to complex, mixed-mode loading due to the inherent anisotropy and nonhomogeneity of the material system. Thus, the behavior of an interface crack between dissimilar anisotropic composites under a general loading condition is of significant interest and practical importance in the failure of composite materials.

A similar problem of an interface crack in dissimilar isotropic materials was first considered by Comninou, et al. [2]. In their model, the contact length of the crack surface is found to be extremely small for one tip, but is of the same order of the crack length for the other tip. Comninou [3] also showed that in a pure shear field, the crack-surface contact length depends on a bimaterial parameter related to elastic constants of the dissimilar solids. As the value of the bimaterial parameter decreases, the size of the shorter contact zone decreases until it becomes impossible to specify accurately the area of crack closure in numerical calculations. The situation is found to be even worse in the commonly used composite material system [1], since the value of the corresponding parameter is so small that generally it is impossible to determine the solution numerically. In this paper, the fundamental nature of an interface crack between dissimilar, anisotropic composite materials subjected to general mixed-mode loading is studied. Based on the information obtained in [1-3], the crack is modeled as being partially closed at one tip and fully opened at the other tip. The approximate model with an inverse square-root singularity proposed in [1] is used for the open end of the crack.

In the next section, some of the basic equations given in [1] are reviewed for later use in this paper. Expressions of fracture mechanics parameters for an interlaminar crack such as stress intensity factors and energy release rates are given for both tips of the crack to describe the interface crack behavior. Numerical examples are presented for an interlaminar crack between θ^2 and $-\theta$ composites of a high-modulus, graphite-epoxy material system subjected to general mixed-mode loading. The contact zone size of crack surfaces and other related physical quantities describing the interlaminar crack field are shown to be related to material anisotropy and the applied normal to shear stress ratio in Section 3. Several important conclusions derived from the results are given in Section 4.

2 Formulation

Consider a crack of length $2L$ lying at the interface of two dissimilar, anisotropic elastic solids (Fig. 1) subjected to the nominal stresses, σ_y^∞, τ_{yz}^∞, and τ_{xy}^∞. Assume that the crack is opened up in the interval $(-L,b)$ and that the crack surfaces are in frictionless contact in the interval (b,L) under the

[1] Presently, Technical Specialist, Xerox Corporation, Rochester, N.Y. 14644.

Contributed by the Applied Mechanics Division for presentation at the 1983 ASME Applied Mechanics, Bioengineering, and Fluids Engineering Conference, Houston, Texas, June 20-22, 1983 of THE AMERICAN SOCIETY OF MECHANICAL ENGINEERS.

Discussion on this paper should be addressed to the Editorial Department, ASME, United Engineering Center, 345 East 47th Street, New York, N.Y. 10017, and will be accepted until two months after final publication of the paper itself in the JOURNAL OF APPLIED MECHANICS. Manuscript recevied by ASME Applied Mechanics Division, October, 1981; final revision, June, 1982. Paper No. 83-APM-7.

Copies will be available until February, 1984.

[2] θ is defined as the angle measured counterclockwise from the positive z-axis to the fiber direction in the x-z plane (Fig. 1).

Copyright © 1983 by ASME
Downloaded 02 May 2010 to 171.66.16.246. Redistribution subject to ASME license or copyright; see http://www.asme.org/terms/Terms_Use.cfm

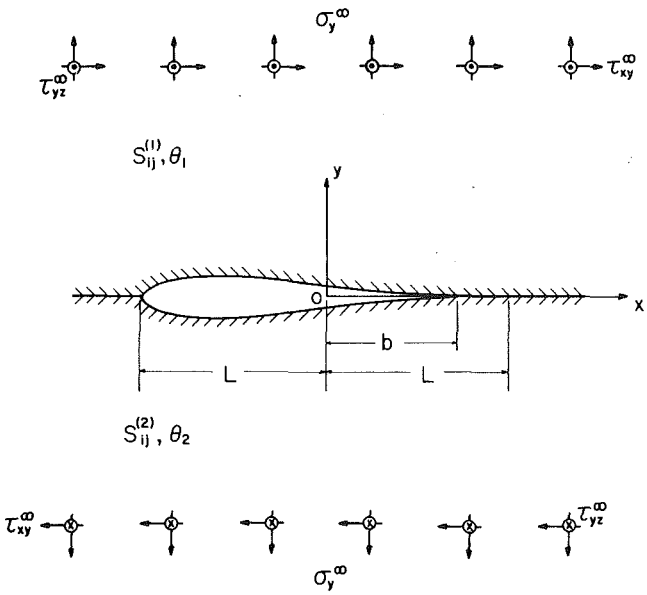

Fig. 1 Coordinates and geometry of an interface crack with a closed tip between θ_1 and θ_2 composites under mixed-mode loading, σ_y^∞, τ_{xy}^∞, and τ_{yz}^∞

loading. From the previous paper [1], the following relationships on $y = 0$ must hold for this case:

$$d_{11}(\Omega_1^+ - \Omega_1^-) + d_{12}(\Omega_2^+ + \Omega_2^-) + d_{13}(\Omega_3^+ - \Omega_3^-) = -\sigma_y^\infty \quad \text{for} \quad -L < x < b, \tag{1a}$$

$$d_{21}(\Omega_1^+ + \Omega_1^-) + d_{22}(\Omega_2^+ - \Omega_2^-) + d_{23}(\Omega_3^+ + \Omega_3^-) = -\tau_{xy}^\infty \quad \text{for} \quad |x| < L, \tag{1b}$$

$$d_{31}(\Omega_1^+ + \Omega_1^-) + d_{32}(\Omega_2^+ - \Omega_2^-) + d_{33}(\Omega_3^+ + \Omega_3^-) = -\tau_{yz}^\infty \quad \text{for} \quad |x| < L, \tag{1c}$$

where the d_{ij} are known quantities related to material constants. The Ω_1 and Ω_3 are analytic functions with cuts on $|x| < L$, and Ω_2 is an analytic function with a cut on $-L < x < b$. In establishing equations (1*a–c*) for commonly used advanced composite systems, the characteristic roots μ_k are found to be purely imaginary in general, as discussed in [1]. Solving equations (1*b*) and (1*c*), one has

$$\Omega_1(z) = \frac{e_{11}}{2\pi\sqrt{z^2-L^2}} \int_{-L}^{b} \frac{\sqrt{L^2-t^2}}{t-z}\, l_2(t)\,dt + e_{12}\left(1 - \frac{z}{\sqrt{z^2-L^2}}\right), \tag{2a}$$

$$\Omega_3(z) = \frac{e_{21}}{2\pi\sqrt{z^2-L^2}} \int_{-L}^{b} \frac{\sqrt{L^2-t^2}}{t-z}\, l_2(t)\,dt + e_{22}\left(1 - \frac{z}{\sqrt{z^2-L^2}}\right), \tag{2b}$$

where $z = x + iy$, $l_2(t) = \Omega_2^+(t) - \Omega_2^-(t)$, and

$$e_{11} = \frac{d_{32}d_{23} - d_{22}d_{33}}{d_{21}d_{33} - d_{31}d_{23}}, \quad e_{12} = \frac{d_{23}\tau_{yz}^\infty - d_{33}\tau_{xy}^\infty}{2(d_{21}d_{33} - d_{31}d_{23})}, \tag{2c}$$

$$e_{21} = \frac{d_{31}d_{22} - d_{21}d_{32}}{d_{21}d_{33} - d_{31}d_{23}}, \quad e_{22} = \frac{d_{31}\tau_{xy}^\infty - d_{21}\tau_{yz}^\infty}{2(d_{21}d_{33} - d_{31}d_{23})}. \tag{2d}$$

As discussed in the associated paper [1], the mathematical approximation leading to equations (2*a–d*) from (1) has the effect of smoothing the oscillatory stress singularity to an inverse square-root singularity for the left crack tip at $x = -L$. Substituting equations (2*a–d*) into equation (1*a*), we obtain a singular integral equation of the following form:

$$\frac{\beta}{\pi}\int_{-1}^{1} \frac{\hat{l}_2(s)}{s-s_0}\,ds + \frac{1}{\pi}\int_{-1}^{1} \frac{\Lambda(s_0,s)}{s-s_0}\,\hat{l}_2(s)\,ds = f(s_0), \tag{3a}$$

where $\hat{l}_2(s) = l_2(t)$, and

$$\Lambda(s_0,s) = -i(d_{11}e_{11} + d_{13}e_{21})\left\{\sqrt{\frac{L^2-t^2}{L^2-t_0^2}} - 1\right\}, \tag{3b}$$

$$f(s_0) = -\sigma_y^\infty - \frac{it_0}{\sqrt{L^2-t_0^2}}\{d_{11}e_{12} + d_{13}e_{22}\}, \tag{3c}$$

$$\beta = -i(d_{12} + d_{11}e_{11} + d_{13}e_{21}), \tag{3d}$$

$$t = \frac{b-L}{2} + \frac{b+L}{2}s, \quad t_0 = \frac{b-L}{2} + \frac{b+L}{2}s_0. \tag{3e}$$

The single valuedness of displacement requires [1]

$$\int_{-1}^{1} \hat{l}_2(s)\,ds = 0. \tag{4}$$

The separation condition for the opened portion of crack surfaces and the unilateral constraint for the crack-surface contact problem are

$$v^{(1)}(x,0) - v^{(2)}(x,0) \geq 0 \quad \text{for} \quad -L \leq x \leq b, \tag{5a}$$

$$\sigma_y(x,0) \leq 0 \quad \text{for} \quad b \leq x \leq L. \tag{5b}$$

The singular integral equation (3*a*) with the constraint condition, equation (4), can be solved by using the numerical method developed by Erdogan, et al. [4]. Let

$$\hat{l}_2(s) = \frac{\omega(s)}{\sqrt{1-s^2}}, \tag{6}$$

where $\omega(s)$ is a bounded continuous function in the interval $|s| \leq 1$. Then, for $b < t_0 < L$ along $y = 0$, one has

$$\sigma_y = \sigma_y^\infty + \frac{it_0}{\sqrt{L^2-t_0^2}}\{d_{11}e_{12} + d_{13}e_{22}\} + \frac{\beta}{\pi}\int_{-1}^{1} \frac{\omega(s)\,ds}{(s-s_0)\sqrt{1-s^2}} + \frac{1}{\pi}\int_{-1}^{1} \frac{\Lambda(s_0,s)\,\omega(s)}{(s-s_0)\sqrt{1-s^2}}\,ds. \tag{7}$$

Since the stress is finite at $s_0 = 1$ due to smooth contact, it is required that

$$\sigma_y = 0, \tag{8}$$

which provides a condition for determining the unknown constant b. Following the same procedure given in [1], the discretized form of equation (3*a*) can be written as

$$\sum_{k=1}^{n} \frac{\omega(s_k)}{n(s_k - s_{0r})}\{\beta + \Lambda(s_{0r},s_k)\} = f(s_{0r}), \tag{9}$$

where

$$s_k = \cos\left[\frac{(2k-1)\pi}{2n}\right] \qquad (k = 1,2,\ldots,n), \tag{10a}$$

$$s_{0r} = \cos\left(\frac{r\pi}{n}\right) \qquad (r = 1,2,\ldots,n-1). \tag{10b}$$

Because $s_k \neq 1$ in equation (10*a*), one can replace equation (8) by using equation (9) with $s_{0r} = 1$ and has

$$\sum_{k=1}^{n} \omega(s_k) = 0. \tag{11}$$

Downloaded 02 May 2010 to 171.66.16.246. Redistribution subject to ASME license or copyright; see http://www.asme.org/terms/Terms_Use.cfm

Since the crack tips at $x = L$ and at $x = -L$ have different deformation configurations (i.e., opened at $x = -L$ and closed at $x = +L$), the interface stress intensity factors $K_1(-L)$ and $K_1(+L)$ must be evaluated in accordance with the relationships for each individual model proposed in [1] (i.e., the approximate model at $x = -L$ and the partially closed model at $x = +L$ in the present case). The stress intensity factor K_2 and K_3 are defined as before [1]. Thus, one has the following expressions for K_i $(i = 1, 2, 3)$:

$$K_1(-L) = \lim_{x \to -L^+} \sqrt{2|x+L|}\,\sigma_y,$$

$$K_1(+L) = \lim_{x \to L^-} \sqrt{2|x-L|}\,\sigma_y, \tag{12a}$$

$$K_2(\pm L) = \lim_{x \to \pm L^+} \sqrt{2|x \mp L|}\,\tau_{xy},$$

$$K_3(\pm L) = \lim_{x \to \pm L^+} \sqrt{2|x \mp L|}\,\tau_{yz}, \tag{12b}$$

where $L^{\pm} = L \pm 0$. From equations (12*a*) and (12*b*), one can show that

$$K_1(-L)/\sqrt{L} = -i\,d_{12}\,\omega(-1), \tag{13a}$$

$$K_1(+L)/\sqrt{L} = -i(d_{11}e_{11} + d_{13}e_{21})M + i(d_{11}e_{12} + d_{13}e_{22}), \tag{13b}$$

$$K_2(\pm L)/\sqrt{L} = \mp d_{22}M + \tau_{xy}^{\infty}, \quad K_3(\pm L)/\sqrt{L} = \mp d_{32}M + \tau_{yz}^{\infty} \tag{13c}$$

where

$$M = \int_{-1}^{1} \frac{\omega(s)}{(s-s_0)\sqrt{1-s^2}} \sqrt{1-\left(\frac{b-L}{2L} + \frac{b+L}{2L}s\right)^2}\,ds. \tag{13d}$$

As $x \to \alpha$, the relative displacements near the crack tip can be shown to be

$$v^{(1)} - v^{(2)} = A_1\sqrt{2|\delta\alpha + \alpha - x|}, \quad u^{(1)} - u^{(2)} = A_2\sqrt{2|\delta\alpha + \alpha - x|},$$
$$w^{(1)} - w^{(2)} = A_3\sqrt{2|\delta\alpha + \alpha - x|}, \tag{14}$$

where α denotes the position of the crack tip, and

$$A_1(-L) = \omega(-1), \quad A_1(+L) = 0,$$

$$A_2(\pm L) = \pm ie_{11}M - ie_{12}, \quad A_3(\pm L) = \pm ie_{21}M - ie_{22}. \tag{15}$$

Using Irwin's virtual crack extension concept with the aid of equations (13) and (14), one obtains the total energy release rate G for each crack tip as

$$G = \frac{\pi}{4}\sum_i A_i K_i, \tag{16}$$

where $i = 1, 2, 3$ for the left tip at $x = -L$, and $i = 2, 3$ for $x = +L$. As is shown in [1], the solution has an oscillatory character near the fully opened interlaminar crack tip; thus, $\omega(-1)$ does not exist in the mathematically exact solution. Nevertheless, in the approximate model, it is possible to find the $\omega(-1)$ by extrapolation [1]. To this end, the formula developed by Krenk [5] is used here to carry out the numerical computation,

$$\omega(-1) = \frac{1}{n}\sum_{k=1}^{n} \omega(s_{n+1-k}) \sin\left[\frac{(2n-1)(2k-1)\pi}{4n}\right] \Big/ \sin\left[\frac{(2k-1)\pi}{4n}\right]. \tag{17}$$

3 Numerical Examples

Consider a high-modulus, graphite-epoxy fiber-reinforced composite with the following elastic constants:

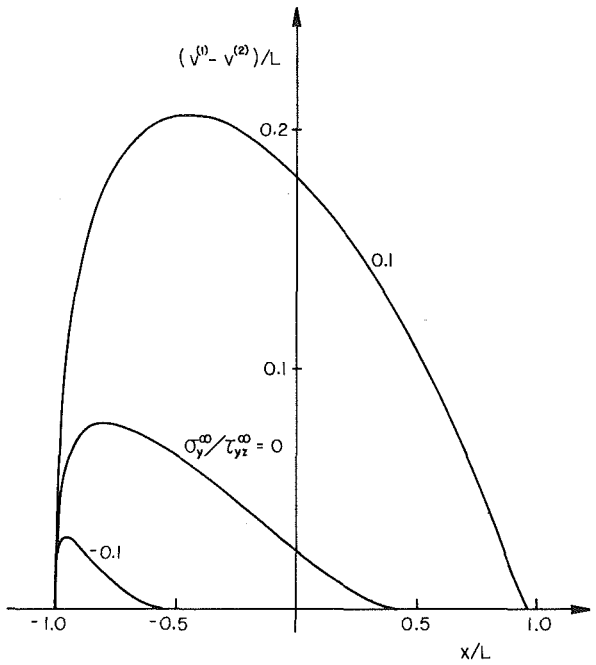

Fig. 2 Crack opening gaps under various mixed-mode loading ($\theta_1 = -\theta_2 = 45$ deg)

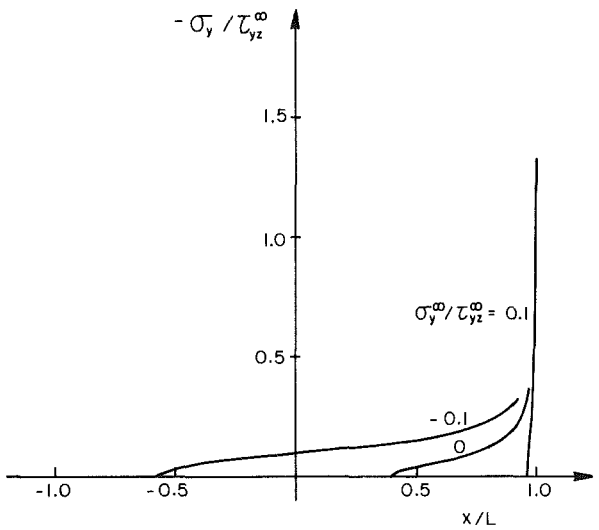

Fig. 3 Contact stress distributions along the closed crack surface under several mixed-mode loading conditions ($\theta_1 = -\theta_2 = 45$ deg)

$$E_{11} = E_{22} = 2.1 \times 10^6 \text{ (psi)}, \quad E_{33} = 20 \times 10^6 \text{ (psi)},$$
$$G_{12} = G_{31} = G_{32} = 0.85 \times 10^6 \text{ (psi)}, \tag{18}$$
$$\nu_{12} = \nu_{31} = \nu_{32} = 0.21,$$

where the subscripts, 1, 2, and 3 refer to transverse, thickness, and fiber directions, respectively. Let the upper space be occupied by the $\theta_1 = 45$ deg composite and the lower one by the $\theta_2 = -45$ deg composite. For this composite system, it can be shown numerically that

$$d_{11} = d_{22} = d_{23} = d_{31} = 0. \tag{19}$$

From equations (1) and (19), Ω_1 is seen to be uncoupled with Ω_2 and Ω_3. Thus, for simplicity and without loss of generality, the τ_{xy}^{∞} is set to be zero in the numerical examples studied in this paper.

In the actual computation, the value of b is assumed first. Then, the system of n linear equations (9) and (11) for $\omega(s_k)$

Downloaded 02 May 2010 to 171.66.16.246. Redistribution subject to ASME license or copyright; see http://www.asme.org/terms/Terms_Use.cfm

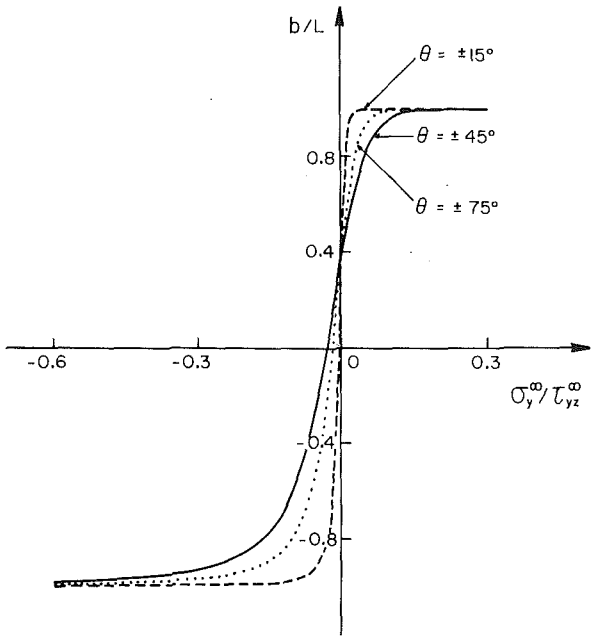

Fig. 4 Variation of crack-surface contact zone versus mixed-mode loading ratio for various θ_1/θ_2 composite $\theta_1 = -\theta_2 = \theta$)

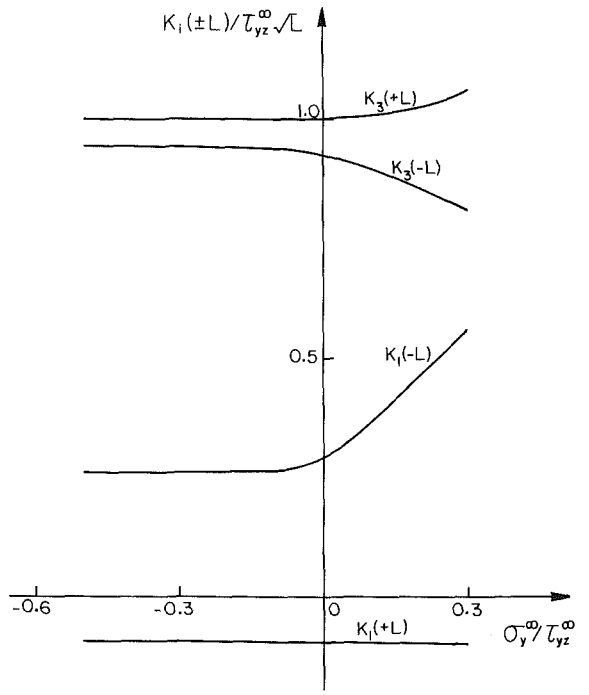

Fig. 5 Stress intensity factor solutions for the interlaminar crack between $[\theta_1/\theta_2]$ composites under various mixed-mode loading ($\theta_1 = -\theta_2 = 45$ deg)

are solved. With each $\omega(s_k)$ being determined, the condition equation (8) is checked by using equation (9), and a refined value of b is introduced. The iteration is carried out until equation (8) is satisfied, and the final solution is checked against the constraint conditions, equations (5*a*) and (5*b*).

The interlaminar crack behavior in a mixed-mode loading field of σ_y^∞ and τ_{yz}^∞ with $\tau_{yz}^\infty = 10^6$ (psi) is illustrated first by the relative displacement of crack surfaces, $[v^{(1)} - v^{(2)}]/L$, shown in Fig. 2. The crack opening gaps are observed to be very sensitive to the change of σ_y^∞. As the σ_y^∞ decreases, the contact length of crack surfaces increases rapidly. It is noted that, in the limiting case of $\tau_{yz}^\infty = 0$ and $\sigma_y^\infty < 0$, the solution for a fully closed crack does not exist. This is true also for the

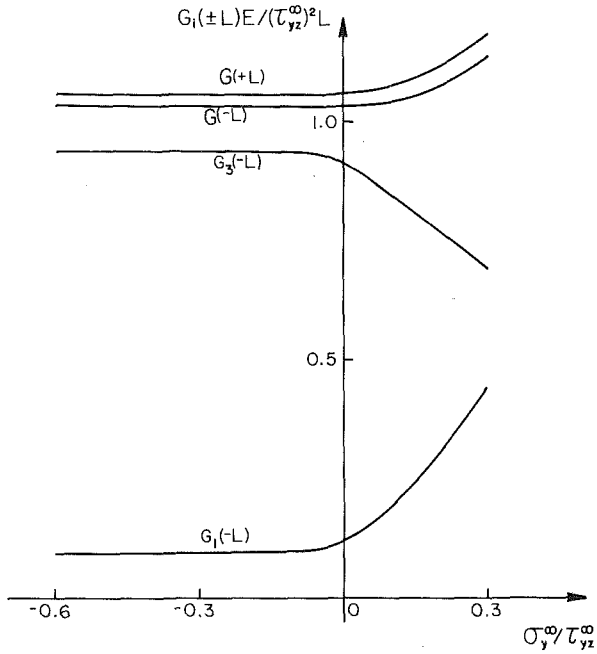

Fig. 6 Energy release rates for the interlaminar crack between $[\theta_1/\theta_2]$ composites under various mixed-mode loading ($E = 10^6$ psi, $\theta_1 = -\theta_2 = 45$ deg)

isotropic interface crack case, as pointed out by Comninou [2]. The corresponding contact stress, σ_y, along the closed portion of the crack surface is shown in Fig. 3 for the same loading ratios. The contact stress σ_y becomes unbounded as $x/L \to 1$ and is identically zero along the opened portion of the crack.

The influence of material anisotropy, as characterized by changing fiber orientation θ, on the interlaminar crack behavior is shown in Fig. 4. Variations of contact zone size for the cases of different θ's are shown in Fig. 4. It is observed that the crack-surface contact length in the [45 deg/ − 45 deg] composite is the smallest one under a negative loading ratio of $\sigma_y^\infty/\tau_{yz}^\infty$ among several θ's studied, while it is the largest under a positive $\sigma_y^\infty/\tau_{yz}^\infty$. As the $\sigma_y^\infty/\tau_{yz}^\infty$ increases, the contact length decreases, and a closure of about 10^{-4} times the crack length at $\sigma_y^\infty/\tau_{yz}^\infty \geq 0.3$ is found for the [45 deg/45 deg] graphite-epoxy composite case.

The stress intensity factors are determined (Fig. 5) for an interlaminar crack in a composite system with ±45 deg fiber orientations under various combinations of σ_y^∞ and τ_{yz}^∞. The effect of change in compressive nominal stress, σ_y^∞, on the stress intensity factors is found to be relatively small. For the left tip, which is assumed to be fully opened, the approximate model [1] with inverse square-root stress singularity is used. The $K_1(-L)$ is thereby computed from the left of $-L$ and, thus, must be positive (i.e., in tension). There seems to be a change in the dominant mode from mode *III* to mode *I* at this tip, as the ratio of applied normal stress σ_y^∞ to shear stress τ_{yz}^∞ increases. For the right crack tip, which is found to be partially closed, the $K_1(+L)$ is computed from the left of L and must be negative (i.e., in compression). It is clear that, at this end of the crack, mode *III* is always dominant and K_1 is insensitive to the mixed-mode loading ratio. The crack-tip energy release rates are shown in Fig. 6 for the same problem. It is interesting to note that the right crack tip may be more critical than the left one in terms of the total energy release rate, G, even thought severe closure occurs near $x = L$. Again, a transition of the dominant mode from mode *III* to mode *I* at $x = -L$ is shown in the figure due to the change in energy release rates, $G_1(-L)$ and $G_3(-L)$. It is further noted that G_1 vanishes identically for the right tip because of the crack closure.

Downloaded 02 May 2010 to 171.66.16.246. Redistribution subject to ASME license or copyright; see http://www.asme.org/terms/Terms_Use.cfm

4 Conclusions

A study of the interface crack behavior in dissimilar, anisotropic composite materials under general mixed-mode loading conditions is presented. Based on the theoretical development and numerical results obtained in the previous sections, the following conclusions may be reached:

1 An interface crack between dissimilar, anisotropic composites under mixed-mode loading may be treated conveniently to have an open tip by using the approximate model and a closed end with a finite length of crack closure by using the partially closed model. The closure length of the crack surface depends on, among other parameters, the ratio of appplied normal stress to shear stress in a given composite system.

2 When the antiplane shear stress τ_{yz}^{∞} is dominant, the contact length of the crack surface becomes significant and has a dimension comparable to the total crack length in general.

3 Variation of the crack-surface contact zone is sensitive to the ratio of normal stress to shear stress applied. Altering the degree of anisotropy of the two anisotropic composites by changing fiber orientation leads to a significant change in contact area at the closed crack tip in the composite under mixed-mode loading.

4 The contact stress rises rapidly as the closed tip of the interlaminar crack is approached. The stress gradient increases with the ratio of applied normal stress to antishear stress, $\sigma_y^{\infty}/\tau_{yz}^{\infty}$.

5 Stress intensity factors and energy release rates associated with both tips of the interlaminar crack are found to be less sensitive to the change of compressive nominal stress (i.e., $\sigma_y^{\infty} < 0$), but vary significantly as the nominal stress σ_y^{∞} increases in tension.

5 Acknowledgments

The research work described in this paper was supported in part by the Office of Naval Research (ONR), Arlington, Va., under Grant N00014-79-C-0579. The authors are grateful to Drs. N. Perrone and Y. Rajapakse of ONR for their constant support. The authors are also indebted to Professor M. Comninou of the University of Michigan for reading the manuscript and suggestions and to Professor H. T. Corten of the University of Illinois for his encouragement during the course of this study.

References

1 Wang, S. S., and Choi, I., "The Interface Crack Between Dissimilar Anisotropic Composite Materials," ASME JOURNAL OF APPLIED MECHANICS, 1982, Vol. 50, 1982, pp. 169–178.

2 Comninou, M., and Schmueser, D., "The Interface Crack in a Combined Tension-Compression and Shear Field," ASME JOURNAL OF APPLIED MECHANICS, Vol. 46, 1979, pp. 345–348.

3 Comninou, M., "The Interface Crack in a Shear Field," ASME JOURNAL OF APPLIED MECHANICS, Vol. 45, 1978, pp. 287–290.

4 Erdogan, F., and Gupta, G. D., "On the Numerical Solution of Singular Integral Equations," *Quarterly of Applied Mathematics*, Vol. 30, 1972, pp. 525–534.

5 Krenk, S., "On the Use of the Interpolation Polynomial for Solutions of Singular Integral Equations," *Quarterly of Applied Mathematics*, Vol. 32, 1975, pp. 479–484.

Downloaded 02 May 2010 to 171.66.16.246. Redistribution subject to ASME license or copyright; see http://www.asme.org/terms/Terms_Use.cfm

W. J. Bottega
Research Assistant.

A. Maewal
Assistant Professor.
Assoc. Mem. ASME

Yale University,
Section of Applied Mechanics,
2157 Yale Station,
New Haven, Conn. 06520

Delamination Buckling and Growth in Laminates[1]

The phenomenon of delamination buckling and growth in a compressively loaded, two-layer circular plate is analyzed. Geometrical nonlinearity is included in the model in order to determine the effect of postbuckling stiffness on the delamination growth process, and the influence of imperfections in the form of transverse loads is also examined.

Introduction

In this paper we present solutions to a model problem in order to elucidate the effect of geometrical nonlinearity in delamination buckling and growth in layered structures. Such problems arise in the analysis of laminated plates and shells that are subjected to compressive loads parallel to the layers after partial debonding between the laminae has occurred as a consequence, for example, of low-velocity normal impact. The debonded area may buckle under compressive loads and subsequently spread, thus causing a possible decrease in the compressive load-carrying capacity of the structure. As a result, modeling of this phenomenon is of some technical significance.

Our analysis is motivated by some recent experimental [1, 2] and theoretical [3–5] investigations on delamination buckling and growth. Our work differs from the other investigations in a number of ways, and, as will be evident in what follows, the approach we have used leads to a somewhat more explicit quantitative description of the delamination buckling and growth process, at least within the context of the simple problems we have chosen to analyze.

In particular, we consider a two-layer, clamped circular plate with a concentric penny-shaped delamination. The plate is assumed to be subjected to a uniform compressive load parallel to the layers at its boundary. Because of its circumferential symmetry, the problem can be treated as one-dimensional, with the result that the essential features of the phenomenon can be described without the need for solution of formidable two-dimensional, moving, intermediate-boundary problems. Our method of solution is based on asymptotic analysis of the postbuckling behavior of the delaminated layers as a function of the (variable) delamination size which is then obtained by an energy balance criterion. For the sake of completeness we also present results for the effect of imperfections that have been assumed to be in the form of small transverse loads which tend to pull apart the layers. Our results in this regard are not very surprising in that the imperfections do not have any noticeable effect on the delamination process.

Two-Layer Circular Plate With Initial Penny-Shaped Delamination

We consider a clamped, two-layer, symmetrically laminated circular plate with a concentric penny-shaped delaminated area of radius $\bar{a}_0$, as shown in Fig. 1. When the plate is subjected to a uniform compressive stress resultant of magnitude $2\bar{N}$ at the edge, the layers may buckle in the region of delamination, which may subsequently spread. Our object in what follows is to present an analytical and quantitative description of this phenomenon under the assumption that the radius of the initial delaminated area is large enough for the delamination buckling and growth to precede overall buckling of the plate. The restriction just mentioned essentially delineates what may be referred to as the class of pure delamination buckling and growth problems.

Our basic physical assumption, as that of Chai et. al [5], is that delamination growth is governed by a Griffith type criterion according to which the creation of new debonded area requires energy release of $\bar{\gamma}$ per unit area, with $\bar{\gamma}$ being a characteristic quantity associated with the bond. We further assume that the macroscopic aspects of the delamination process – such as the load deflection curve – which are of main interest to us here, can be adequately modeled by the classical, von Karman's geometrically nonlinear plate theory. Consequently, if the delamination growth is assumed to be monotonic, the equilibrium states of the plate can be obtained by seeking deflection fields and delamination radius, a, which extremize the functional

$$\Pi(u,w;a) = I_B + I_M{}^{(1)} + I_M{}^{(2)} + 2P\,u(1) + \gamma(a^2 - a_0{}^2), \tag{1}$$

subject to the kinematic conditions $w(a) = w'(a) = 0$, where

$$I_B = \int_0^a \left[w''^2 + 2\nu\, w'' \frac{w'}{r} + \left(\frac{w'}{r}\right)^2 \right] r dr, \tag{2}$$

---

[1] Sponsored by the National Science Foundation.

Contributed by the Applied Mechanics Division for presentation at the 1983 ASME Applied Mechanics, Bioengineering, and Fluids Engineering Conference, Houston, Texas, June 20–22, 1983 of THE AMERICAN SOCIETY OF MECHANICAL ENGINEERS.

Discussion on this paper should be addressed to the Editorial Department, ASME, United Engineering Center, 345 East 47th Street, New York, N.Y. 10017, and will be accepted until two months after final publication of the paper itself in the JOURNAL OF APPLIED MECHANICS. Manuscript received by ASME Applied Mechanics Division, October, 1981; final revision, May, 1982. Paper No. 83-APM-3.

Copies will be available until February, 1984.

Copyright © 1983 by ASME
Downloaded 02 May 2010 to 171.66.16.246. Redistribution subject to ASME license or copyright; see http://www.asme.org/terms/Terms_Use.cfm

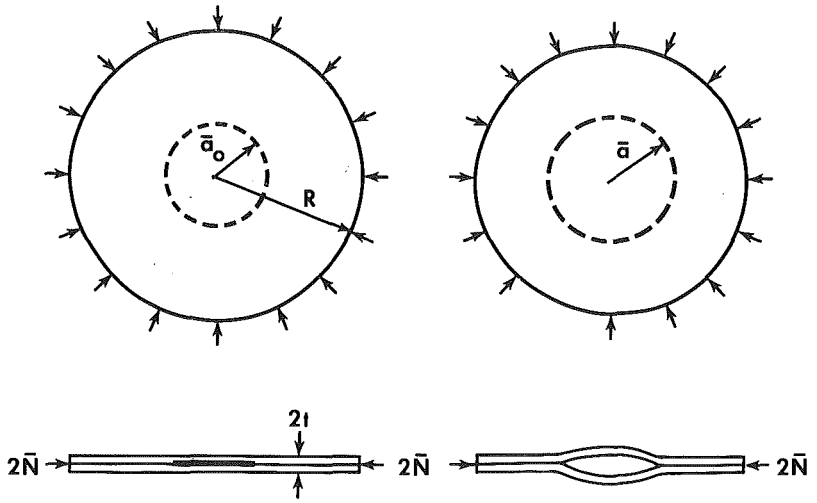

Fig. 1 Circular plate with penny-shaped delamination

$$I_M^{(1)} = C\int_o^a \left[\left(u' + \frac{1}{2}w'^2\right)^2 + 2\nu\left(u' + \frac{1}{2}w'^2\right)\frac{u}{r} + \left(\frac{u}{r}\right)^2\right] rdr, \tag{3}$$

$$I_M^{(2)} = C\int_a^1 \left[u'^2 + 2\nu u'\frac{u}{r} + \left(\frac{u}{r}\right)^2\right] rdr. \tag{4}$$

The functionals in (2)–(4) represent the strain energy due to bending and stretching of the upper layer only, since we can restrict our attention to it because of symmetry. In these equations u and w denote, respectively, the radial and transverse deflections of the layer midsurface, both nondimensionalized by the plate radius R, as are the delamination radius a and the radial coordinate. Furthermore, the quantities $\gamma = \tilde{\gamma} R^2/D$ and $P = \tilde{N}R^2/D$ in (1) are nondimensional surface energy and the applied compressive stress resultant, respectively, with D being the bending stiffness of the layer. The quantity $C = 12R^2/t^2$ in (3) and (4) is a radius to thickness ratio parameter, and ν denotes the Poisson's ratio of the material of the plate which has been assumed to be isotropic for the sake of simplicity.

The problem just formulated is a "moving intermediate boundary problem" in calculus of variations. Without giving the details of the rather straightforward calculation of the first variation of the functional Π, we note that due to the variable delamination tip radius a, the variation $\delta f(a)$ of any function is given by [6]:

$$\delta f(a) = \delta f^*(a) - f'(a)\,\delta a$$

where $\delta f^*(a)$ is determined by the kinematic conditions on f. With this stipulation, the condition for vanishing of the first variation of Π with respect to the deflections leads to (*i*) the usual coupled differential equations for stretching and bending in the interval $(0,a)$, and (*ii*) the linear membrane equation in $(a,1)$, together with (*iii*) the continuity conditions at the delamination tip, and (*iv*) the boundary conditions. In addition, however, the requirement that the first variation of Π with respect to the radius of the delamination area should vanish leads to the transversality condition

$$\gamma = \frac{1}{2}w''^2(a). \tag{5}$$

According to (5) the delamination growth is governed by the release of the bending strain energy at the delamination tip – a result similar to the one derived in [7] by means of a slightly different approach. A little consideration shows that the delamination does not grow for

$$\gamma > \frac{1}{2}w''^2(a_o)$$

and once the condition (5) is satisfied for $a = a_o$, the debonded area grows with the plate occupying a series of equilibrium states such that the transversality condition is always satisfied.

A consequence of the growth condition is that unless the layers in the delaminated area buckle, the delamination cannot spread. This follows from the fact that the prebuckling deformation of the layer is one of pure radial compression, unaffected by the presence of the delamination, and is given by

$$u_o(r) = -\frac{Pr}{C(1+\nu)}, \quad w_o(r) = 0. \tag{6}$$

Consequently, for a description of the delamination growth process, we now analyze the buckling and postbuckling behavior of the delaminated area. As the first step we define the functions

$$u(r) = u_o(r) + u^*(r), \quad w = w^*(r), \tag{7}$$

and calculate the transition functional

$$\Pi^*(u^*,w^*,a) = \Pi(u_o + u^*, w^*, a) - \Pi(u_o, 0, a). \tag{8}$$

On using (1)–(4), (6), and (7) and requiring the first variation of Π^* to vanish we obtain

(*i*) the differential equations:

$$(L^{(1)} + PB^{(1)})w + N_2^{(1)}(u,w) + N_3^{(1)}(w) = 0, \quad 0 \le r \le a \tag{9}$$

$$L^{(2)}u + N_2^{(2)}(w) = 0, \quad 0 \le r \le a \tag{10}$$

$$L^{(2)}U = 0, \quad a \le r \le 1 \tag{11}$$

where

$$L^{(1)}w = w'''' + \frac{2w'''}{r} - \frac{w''}{r^2} + \frac{w'}{r^3}, \tag{12a}$$

$$B^{(1)}w = w'' + \frac{w'}{r} \tag{12b}$$

$$N_2^{(1)}(u,w) = -C\left[(u'w')' + \frac{u'w'}{r} + \frac{\nu}{r}(uw')'\right], \tag{12c}$$

$$N_3^{(1)}(w) = \frac{3}{2}w'^2w'' + \frac{1}{2}w'^3, \tag{12d}$$

$$L^{(2)}u = u'' + \frac{u'}{r} - \frac{u}{r^2}, \tag{12e}$$

Downloaded 02 May 2010 to 171.66.16.246. Redistribution subject to ASME license or copyright; see http://www.asme.org/terms/Terms_Use.cfm

$$N_2^{(2)}(w) = (1-\nu)\frac{w'^2}{r} + w'w'', \tag{12f}$$

(*ii*) the continuity and boundary conditions:

$$u(0) = 0, \quad w'(0) = \left[w'' - \frac{w'}{r}\right]_{r=0} = 0 \tag{13a}$$

$$w(a) = w'(a) = 0, \tag{13b}$$

$$u(a) = U(a), \quad u'(a) + \nu\frac{u(a)}{a} = U'(a) + \nu\frac{U(a)}{a}, \tag{13c}$$

$$U'(1) + \nu U(1) = 0, \tag{13d}$$

and

(*iii*) the transversality condition:

$$\gamma = \frac{1}{2}w''^2(a)$$

which has been discussed earlier. In the equations listed in the foregoing, and in what follows we have set

$$u^* = \begin{cases} u, & 0 \le r \le a \\ U, & a \le r \le 1 \end{cases}$$

and have similarly replaced w^* by w for the sake of convenience of notation.

Equations (9)–(13) basically define the nonlinear buckling problem for a clamped circular plate of radius a. The problem differs from the usual case treated, for example, in [8], due to the presence of the annular elastic region in the interval $a \le r \le 1$. Once the solution to equations (9)–(13) is known as a function of the delamination tip radius a, the latter can be calculated from the transversality condition.

Asymptotic Analysis. The set (9)–(13) is most conveniently solved by an asymptotic method. Thus we assume expansions of the form

$$\begin{aligned} u &= \epsilon u_1 + \epsilon^2 u_2 + \ldots \\ w &= \epsilon w_1 + \epsilon^2 w_2 + \ldots \\ U &= \epsilon U_1 + \epsilon^2 U_2 + \ldots \\ P &= P_c + \epsilon P_1 + \epsilon^2 P_2 + \ldots \end{aligned} \tag{14}$$

together with appropriate normalization condition on (u_1, w_1, U_1) and conditions on $(u_i, w_i, U_i, i \ge 2)$ in order to define ϵ, the amplitude of the buckling mode. The substitution of the ansatz (14) into (9)–(13) leads to a sequence of linear problems of which the following set is sufficient for inferring the essential nonlinear behavior:

$$-(L^{(1)} + P_c B^{(1)})w_i = P_{i-1}B^{(1)}w_1 + f_i, \quad i = 1,2,3; \quad 0 \le r \le a, \tag{15a}$$

$$L^{(2)}u_i = -g_i, \quad i = 1,2; \quad 0 \le r \le a, \tag{15b}$$

$$L^{(2)}U_i = 0, \quad i = 1,2; \quad a \le r \le 1, \tag{15c}$$

where $P_0 = 0$ and

$$g_1 = 0, \quad g_2 = N_2^{(2)}(w_1), \quad f_2 = N_2^{(1)}(u_1, w_1), \tag{16a}$$

$$f_3 = N_2^{(1)}(u_1, w_2) + N_2^{(1)}(u_2, w_1) + N_3(w_1) + P_1 B^{(1)} w_2. \tag{16b}$$

The boundary and continuity conditions for various functions in (15) are the same as (13) with (u, w, U) replaced by (u_i, w_i, U_i) for all i.

The solution of the first-order problem is not affected by the presence of the annular region, and is given by [8]

$$w_1(r) = \{J_0(ka) - J_0(kr)\}/\{J_0(ka) - 1\}, \quad k = \sqrt{P_c}, \tag{17a}$$

$$u_1(r) = U_1(r) = 0, \tag{17b}$$

where we have used the normalization $w_0(0) = 1$, and where J_i represents the Bessel function of the first kind of order i. The buckling load P_c is determined from the characteristic equation

$$J_1(ka)/[J_0(ka) - 1] = 0 \tag{18}$$

which is independent of the Poisson's ratio, and yields the lowest eigenvalue

$$ka = 3.832, \quad P_c = 14.68/a^2 \equiv P_c^*/a^2. \tag{19}$$

This result suggests the scaling

$$N = P/P_c^*, \quad N_i = P_i/P_c^*, \tag{20a}$$

for subsequent analysis, so that

$$N_c = 1/a^2. \tag{20b}$$

We now present the results for the second-order problem. Since the homogeneous operator on the left-hand side of (15*a*) is singular, for the solution of this equation to exist for $i \ge 2$, the right-hand side should be orthogonal to the nontrivial solution (17*a*) of the homogeneous problem. This solvability condition leads to

$$N_1 \equiv P_1/P_c^* = 0, \tag{21}$$

which, on substitution into (15*a*) for $i = 2$ yields, with $w_2(0) = 0$,

$$w_2(r) = 0. \tag{22}$$

The solution of the second-order in-plane problem (15*b*,*c*), however, does not vanish, and is given by

$$u_2(r) = b_I r + f(r), \tag{23a}$$

$$U_2(r) = b_0[\alpha r + (1/r)], \tag{23b}$$

where

$$f(r) = \frac{k}{4}\frac{[(1+\nu)J_0(kr)J_1(kr) - \nu kr\{J_0^2(kr) + J_1^2(kr)\}]}{[J_0(ka) - 1]^2}, \tag{24a}$$

$$\alpha = (1-\nu)/(1+\nu), \tag{24b}$$

and

$$b_0 = [af(a) - a^2 f'(a)]/2, \tag{24c}$$

$$b_I = b[(1/a^2) + \alpha] - f(a)/a. \tag{24d}$$

The solution of the third-order problem is not necessary for including the essential nonlinear effects, but the solvability condition for (15*a*) for $i = 3$ yields

$$N_2(a) = -\frac{\int_0^a [N_3(w_1) + N_2^{(1)}(u_2, w_1)]w_1 r dr}{\int_0^a w_1 B^{(1)} w_1 r dr}. \tag{25}$$

The analysis of the buckling and postbuckling behavior of the delaminated part of the layer is now complete. The main results are that to second order in ϵ,

$$\begin{aligned} u(r;\epsilon,a) &= \epsilon^2 u_2(r;a) \\ w(r;\epsilon,a) &= \epsilon w_1(r;a) \\ U(r;\epsilon,a) &= \epsilon^2 U_2(r;a) \\ N(\epsilon,a) &= (1/a^2) + \epsilon^2 N_2(a) \end{aligned} \tag{26}$$

where w_1, u_2, and U_2 are given by (17*a*), (23), and (24), and N_2 can be obtained from (25). With (6) and (26) and the expression for compressive deflection at the edge

$$u_R = -[u_0(1) + \epsilon^2 U_2(1)], \tag{27}$$

the load deflection (N, u_R) curve of the plate along the

Downloaded 02 May 2010 to 171.66.16.246. Redistribution subject to ASME license or copyright; see http://www.asme.org/terms/Terms_Use.cfm

postbuckling path can be calculated by using $\epsilon \geq 0$ as a parameter, with $\epsilon = 0$ at the onset of buckling.

To use the delamination growth criterion (5), we obtain, with (17) and (26), the result

$$\gamma = \frac{1}{2}\epsilon^2 k^4 [J_0''(ka)/\{J_0(ka) - 1\}]^2 \tag{28a}$$

where ka is given by (19). Using this numerical value and those of the Bessel function and its derivatives in (28*a*) we have

$$\epsilon^2 = 23.83 a^4 \gamma \equiv q_0 a^4 \gamma. \tag{28b}$$

Since ϵ vanishes at the bifurcation point and increases monotonically along the postbuckling path, equation (28*b*) indicates that for

$$\epsilon^2 < q_0 a^4 \gamma \tag{29}$$

the equilibrium states of the plate are characterized by $a = a_0$ and (26) and (27), with ϵ as a (positive) parameter. However, there is also a delamination growth path, described by (26), (27), and (28*b*), with "a" as a parameter, along which the radius of the debonded area grows quasi-statically. The intersection of the postbuckling path (for a given a_0) with the delamination growth path defines the load at which the growth of the debonded area begins, and once this load is attained the delamination tip radius increases quasi-statically such that the delamination growth path is followed.

Discussion of Numerical Results. For a description of the numerical results based on the analysis just presented, it is convenient to introduce a modified thickness to radius ratio parameter

$$\eta_0^2 = P_c^*/[C(1+\nu)] = P_c^*(t/R)^2/[12(1+\nu)] \tag{30}$$

which is the inverse of the slope of the load-deflection (N, u_R) curve along the prebuckling path (recall (6), (19), and (20)). We also introduce a modified surface energy parameter

$$\gamma^* = \gamma R^2/(P_c^* t^2), \tag{31}$$

which is given by $\gamma^* = 12\bar{\gamma}(1-\nu^2)R^4/(Et^5 P_c^*)$ in terms of dimensional quantities.[2]

Numerical results have been obtained for $\nu = 0.3$ and $\eta_0 = 0.02$ ($R/t = 50$) and various values of the surface energy parameter γ^*. In Fig. 2 the postbuckling paths corresponding to $a_0 = 0.4$ and $a_0 = 0.8$ have been displayed together with the delamination growth path for $\gamma^* = 10$.

Consider first the case of the smaller initial delamination tip radius ($a_0 = 0.4$). Whether the plate is subjected to a force-controlled or a deformation-controlled loading program, the prebuckling path is followed until the delamination buckles at $N = 6.25$. The postbuckling path is then followed until it intersects the delamination growth path at $N \sim 7$ when the radius of the delaminated area begins to grow. The character of the ensuing growth is, however, dependent on the type of loading. In the case of force-controlled loading the delamination grows catastrophically until the layers are completely debonded. However, if the loading is deformation controlled, the delamination first grows in an unstable manner, with the applied load dropping to a value of $N = 4.2$. Any subsequent increase in the edge compressive displacement causes a stable monotonic increase in the size of the delamination.

In contrast to the behavior described for $a_0 = 0.4$, it can be seen from Fig. 2 that growth in a plate with initial delamination radius $a_0 = 0.8$ will be stable whether the loading is force controlled or deformation controlled. The reason for this vastly different behavior is the existence of critical delamination radii corresponding to the minimum in the N-a curve (a_N) and the minimum in the u_R-a curve (a_u) along the delamination growth path (see Fig. 4). For the case shown in Fig. 2, $a_u = 0.58$ and $a_N = 0.74$. If the initial delamination radius is greater than a_N, the growth occurs in a stable manner in a force-controlled test, whereas similar transition in

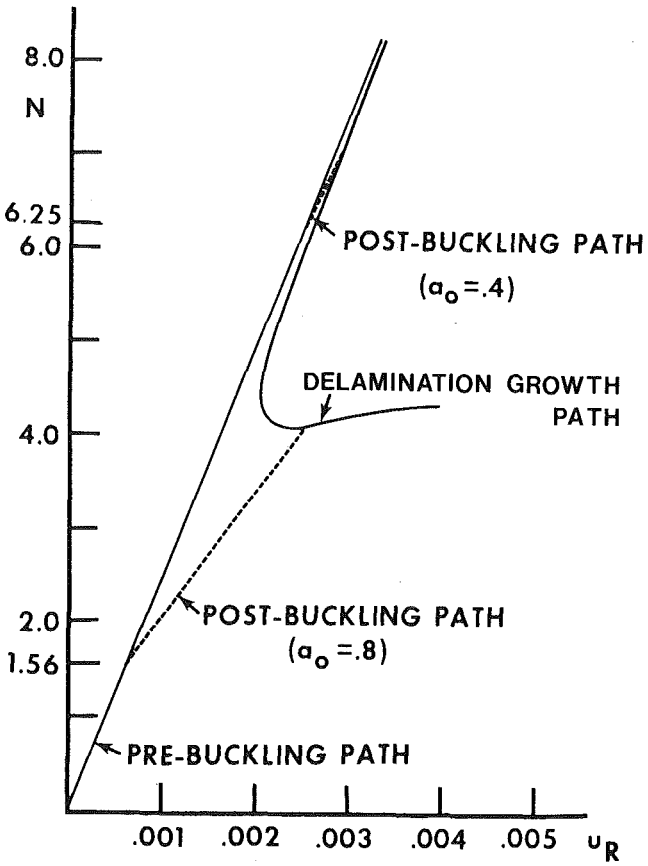

Fig. 2 Load versus edge displacement for circular plate with penny-shaped delamination ($\gamma^* = 10$ and $\eta_0 = 0.02$)

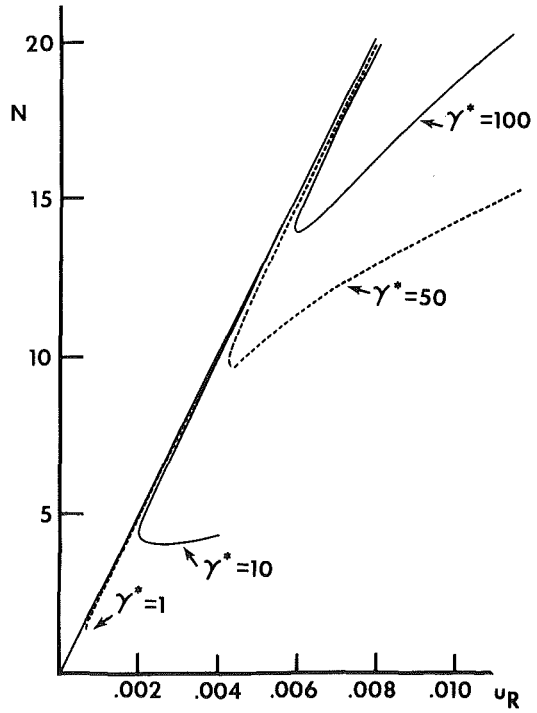

Fig. 3 Comparison of delamination growth paths of circular plate ($\eta_0 = 0.02$)

[2] For $\nu = 0.3$ and $\eta_0 = 0.02$, $\gamma^* = 0(100)$ for PMMA layers bonded with Solithane [9], and $\gamma^* = 0(10)$ for graphite layers bonded with Epoxy [2, 5].

Downloaded 02 May 2010 to 171.66.16.246. Redistribution subject to ASME license or copyright; see http://www.asme.org/terms/Terms_Use.cfm

qualitative behavior for a deformation-controlled test occurs at delamination radius a_u.

The delamination path shown in Fig. 2 ends when $a=1$, i.e., at complete debonding of the plate. Let N^* be the corresponding load and $a_o{}^*$ be the initial delamination radius such that the associated postbuckling path intersects the dropping part of the delamination growth path at $N=N^*$. It is evident that $a_o{}^*$ defines a "threshold" radius in that whenever the initial delamination radius is below $a_o{}^*$, the growth of the debonded area will always be catastrophic in a force-controlled test.

Another situation that leads to catastropic growth, independent of the initial delamination size, arises when $a_u>1$ in deformation-controlled loading and when $a_N>1$ in force-controlled loading. This occurs for relatively low values of γ^*, as shown in Fig. 3, so that it can be concluded that unless the bonding energy is sufficiently large, once delamination growth commences it leads to catastrophic failure.

The stabilizing of the delamination growth path for higher values of bond energy is due to the presence of the second term in $(26)_4$. As a result, if the postbuckling stiffness of the layer is not taken into account, the stabilization of the delamination growth process cannot be predicted. Moreover, in situations where the postbuckling stiffness of the layer vanishes or is negative, delamination growth will always be catastrophic in a force-controlled test. An example of such a case is a rectangular plate with a similar delaminated area through its width, which has been analyzed in [5] wherein results have been given in terms of energy release rates only. We have analyzed this problem as well, in the spirit of the preceding formulation for the circular plate, but the results have not been presented here for the sake of brevity.

From the foregoing discussion, it would appear that postbuckling stiffness of the layer affects the qualitative features of the delamination phenomenon to a certain extent. Consequently, on the basis of results from the theory of elastic stability it appears to be worthwhile to examine the effect of imperfections as well. We do so in the next section.

Effect of Imperfections on Delamination Growth

We consider the simplest type of imperfection in the form of a concentrated load at the center of the circular plate, directed away from the delamination, thus tending to pull apart the layers. This type of imperfection is expected to simulate, at least qualitatively, the effect of more realistic geometrical imperfections. To incorporate the transverse load in the analysis we need to make only slight modifications in the method of solution, and we summarize the results here.

We begin the analysis by including the effect of imperfection in the transition functional (8) and defining

$$\bar{\Pi}=\Pi^*-2\mu w(0) \tag{32}$$

where, with $\bar{\mu}$ being the applied load,

$$\mu=\bar{\mu}R/2\pi D. \tag{33}$$

Extremization of $\bar{\Pi}$ leads to the same set of equations as (9)-(13) except that $(13a)_3$ is replaced by

$$\left[w''-\frac{w'}{r}\right]_{r=0}=\mu. \tag{34}$$

The solution of the nonlinear problem is sought as an asymptotic series in two parameters ϵ and μ/ϵ. The solutions up to $0(\epsilon^2, 1)$ for u, w, and U turn out to be the same as (26*a-c*), but (26*d*) is modified to

$$N(\epsilon,a,\mu)=(1/a^2)+\epsilon^2 N_2(a)+\frac{\mu}{\epsilon}\hat{N}_1 \tag{35}$$

where $\hat{N}_1$ is obtained from the solvability condition for the $0(\mu/\epsilon\ \epsilon)$ problem obtained from (9), (13*b*), and (33). In particular for $\nu=0.3$, we obtain

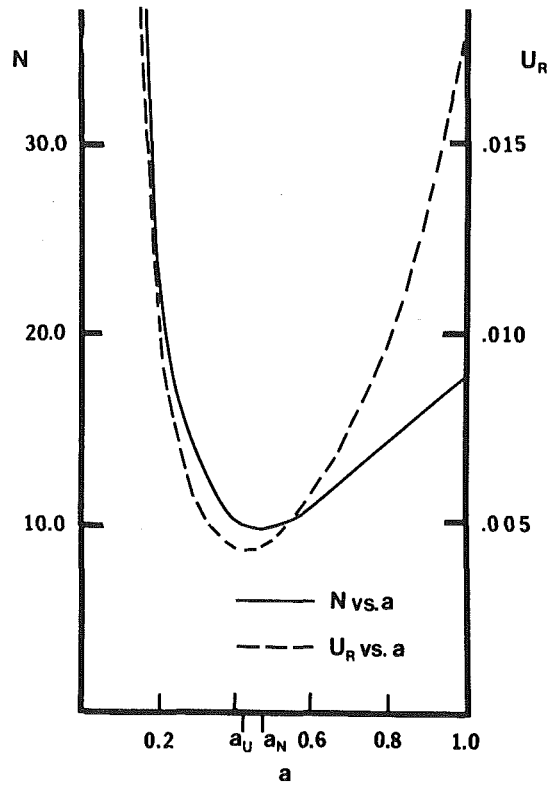

Fig. 4 Load versus delamination radius and edge displacement versus delamination radius ($\gamma^*=50$ and $\eta_o=0.02$)

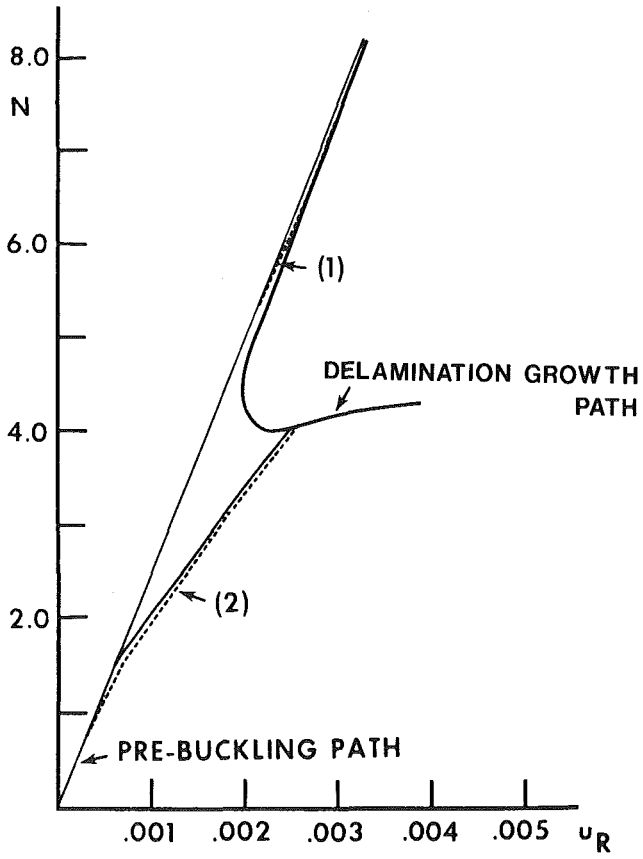

Fig. 5 Load versus edge displacement for circular plate with load imperfection ($\gamma^*=10$, $\eta_o=0.02$, and $\delta=0.1$); (1) $a_o=0,4$; (2) $a_o=0.8$

$$\hat{N}_1=-2.9/\eta_o{}^2 \tag{36}$$

where η_o is defined by (30). Thus the load deflection curve for

Downloaded 02 May 2010 to 171.66.16.246. Redistribution subject to ASME license or copyright; see http://www.asme.org/terms/Terms_Use.cfm

the delaminated plate can be generated in the manner already described. The equilibrium path of the imperfect structure is obtained from (27), (35), and (36) with $a=a_0$ and ϵ as a parameter satisfying (29). Once the delamination growth condition (28*b*) is satisfied with $a=a_0$, the equilibrium path is calculated from (27), (28*b*), (35), and (36) with *"a"* as a parameter.

The numerical results have been obtained for $\eta_0=0.02$ ($R/t=50$) and $\gamma^*=10$, and are shown in Fig. 5. The magnitude of the imperfection $\tilde{\mu}$ has been chosen such that if this load is applied to a completely debonded layer, the deflection under the load is given by $\tilde{\delta}\equiv(\tilde{w}(0)/t)=0.1$. It is evident from the figure that the imperfection has only a minor effect.

References

1 Rhodes, M. D., Williams, J. G., and Starnes, J. H., Jr., "Effect of Low-Velocity Impact Damage on the Compressive Strength of Graphite-Epoxy Hat-Stiffened Panels," NASA Tech. Note D-8411, Apr. 1977.

2 Knauss, W. G., Babcock, C. D., Chai, H., "Visualization of Impact Damage of Composite Plates by Means of the Moire Technique," NASA CR-159261, Apr. 1980.

3 Kachanov, L. M., "Separation Failure of Composite Materials," *Mekh. Polim.*, No. 5, 1976, pp. 918–922.

4 Kachanov, L. M., "Layering in Glass-Fiber Pipes Subjected to External Pressure," *Mekh. Polim.*, No. 6, 1975, pp. 1106–1108.

5 Chai, H., Babcock, C. D., and Knauss, W. G., "One-Dimensional Modelling of Failure in Laminated Plates by Delamination Buckling," *Int. J. Solids Structures*, Vol. 17, 1981, pp. 1069–1083.

6 Gelfand, I. M., and Fomin, S. V., *Calculus of Variations*, Prentice-Hall, Englewood Cliffs, N.J., 1963.

7 Burridge, R., and Keller, J. B., "Peeling, Slipping and Cracking—Some One-Dimensional Free-Boundary Problems in Mechanics," *SIAM Review*, Vol. 20, 1978, pp. 31–61.

8 Thompson, J. M. T., and Hunt, G. W., *A General Theory of Elastic Stability*, Wiley-Interscience, New York, 1973.

9 Anderson, G. P., Bennett, S. J., and DeVries, K. L., *Analysis and Testing of Adhesive Bonds*, Academic Press, New York, 1977.

Downloaded 02 May 2010 to 171.66.16.246. Redistribution subject to ASME license or copyright; see http://www.asme.org/terms/Terms_Use.cfm

Experimental Determination of Stresses in Damaged Composites Using an Electric Analogue

S. B. Batdorf
School of Engineering and Applied Science,
University of California,
Los Angeles, Calif. 90024
Hon. Mem. ASME

Inadequate knowledge of the local stress distributions in damaged composites has been a major obstacle to progress in the understanding of damage accumulation and ultimate failure of such materials. Theoretical treatments of three-dimensional uniaxially reinforced composites are difficult, and direct experimental observations of stresses around interior flaws are not feasible. An experimental determination of stress distributions can be made using an electric analogue. A scaled model of the composite including the damage is made with the fibers replaced by conducting rods and the matrix replaced by an electrolyte. The resistivity ratio of rods to electrolyte is taken equal to the elastic modulus ratio of matrix to fiber. A tensile force applied in the fiber direction is modeled by applying a potential gradient in the rod direction. The displacement distribution in the composite is then modeled by the potential distribution in the analogue to an accuracy somewhat better than that given by shear lag theory. Thus stress distributions can be found by measuring potentials in the analogue with the aid of an electric probe.

Introduction

A few decades ago it began to be recognized that certain fibers such as glass, boron, carbon, or graphite, and more recently kevlar could be prepared with several times the specific strength and stiffness obtainable in conventional structural materials. As a result a very substantial development effort was undertaken to capitalize on these properties. In spite of the extensive use now being made of fibrous composites, there is a widespread feeling that current applications still fall far short of the ultimate potential of such materials. The slow progress in practical application of composites is no doubt due in part to the fact that the theoretical foundations relating to the strength and stiffness of these materials have been very inadequate up to the present time. The stiffness of undamaged composites is pretty well understood even in the case of complicated laminated structures. But one of the great virtues of the long-fiber composite is the fact that the tensile failure load greatly exceeds the load at which the first fiber fails. The stiffness of greatest concern in critical parts must therefore be stiffness of the damaged composite. Consequently, as a practical matter the determination of both the stiffness and the ultimate load on a composite require an understanding of the mechanics of damage accumulation. The most serious obstacle to progress in this area is probably inadequate knowledge concerning the stress distribution in a damaged composite. This becomes evident from the following brief review of progress in this field.

The theory underlying progressive damage and ultimate failure of a collection of independent fibers, or a bundle, was worked out several decades ago by Daniels and Coleman [1, 2]. They showed that the strength of a bundle is substantially less than the average strength of the fibers of which it is composed. When a bundle of strong fibers is bound together by a relatively weak matrix to form a unidirectionally reinforced composite, the strength can be substantially improved. When a given fiber breaks, the load it no longer carries is transmitted to neighboring fibers as a result of shearing forces in the matrix, and some distance from the break it is transferred back into the original fiber, thus localizing the damage. Rosen [3] analyzed such a composite by conceptually dividing the composite into many slices, or minibundles, connected end-to-end. The length of each minibundle was taken to be the ineffective length of a broken fiber, or the shear transfer length. The load given up by a broken fiber was assumed to be equally distributed to all remaining fibers in a minibundle, and the theory of Daniels and Coleman was used to find its ultimate strength. Zweben [4] revised the theory to take into account the fact that the load given up by a broken fiber is mainly taken up by the immediate neighbors. In this model of damage accumulation the fiber adjacent to a break is more apt to fail than a distant fiber and this gives rise to the possibility of crack growth and eventual instability of the type first studied by Griffith in the case of homogeneous materials [5]. An effort by Zweben and Rosen [6] to carry the analysis to the point of instability for composites was unsuccessful due to analytical complexities, and the authors proposed first occurrence of a double break (the theory for which they succeeded in working out) as a conservative estimate of composite strength.

Using an entirely different approach, Harlow and Phoenix [7, 8] obtained a virtually exact solution for the strength of a two-dimensional composite (a tape one fiber thick) on the

Contributed by the Applied Mechanics Division for publication in the JOURNAL OF APPLIED MECHANICS.

Discussion on this paper should be addressed to the Editorial Department, ASME, United Engineering Center, 345 East 47th Street, New York, N.Y. 10017, and will be accepted until two months after final publication of the paper itself in the JOURNAL OF APPLIED MECHANICS. Manuscript received by ASME Applied Mechanics Division, May, 1982; final revision, June, 1982.

Copyright © 1983 by ASME
Downloaded 02 May 2010 to 171.66.16.246. Redistribution subject to ASME license or copyright; see http://www.asme.org/terms/Terms_Use.cfm

basis of a highly idealized local load-sharing rule. They assumed that the load given up by a series of broken fibers of any order was completely taken up by the two immediately adjacent neighbors, i.e., each of the two fibers adjacent to a break of any multiplicity takes 50 percent of the load. Hedgepeth [9] found that the proper figure is 33 percent for a single break and progressively less for higher order breaks. R. L. Smith [10] generalized the Harlow and Phoenix result and gave an approximate solution for the two-dimensional problem for arbitrary stress concentration factors in the fibers adjacent to the crack. Batdorf [11] gave an approximate solution for a three-dimensional fibrous composite for arbitrary stress concentration factors.

As a result of the difficulties associated with the analytical study of three-dimensional composites, a number of authors have studied damage accumulation and ultimate failure using a Monte Carlo approach [10, 12, 13]. The studies that make use of specific local load-sharing rules have usually made arbitrary assumptions in regard to stress concentration factors which generally tend to give too large a share of the total load to the immediately adjacent neighbors.

Calculations of the stiffness of damaged composites are similarly handicapped by lack of knowledge of stress distribution. Gottesman, Hashin, and Brull have shown how to obtain estimates for upper and lower bounds on composite stiffness using a variational approach [14]. The upper bound employs the principle of minimum potential energy and makes use of an admissible displacement field. The lower bound is based on a consideration of minimum complementary energy, and employs an admissible stress field. The discrepancy between upper and lower bounds is approximately a factor 2 for $\alpha = 0.2$ where α is a measure of crack density per unit area.

The reason that available treatments of strength and stiffness of damaged composites are generally either rather crude approximations or are left in parametric form employing unknown parameters is the serious lack of knowledge concerning the stress distributions in damaged composites. The most widely employed source of information in this field is a paper by Hedgepeth and Van Dyke [15] in which local stress concentration factors are found for three-dimensional uniaxially reinforced composites using shear lag theory. Unfortunately numerical results were only furnished for a very limited number of crack sizes (1, 2, 4, 9, 12, 16, etc. broken fibers) and for each crack size only one neighboring fiber was considered. Moreover, only the stress concentration factor was found, not the entire stress distribution. All the missing information could in principle be obtained using Hedgepeth and Van Dyke's equations but unfortunately they contain an undefined parameter Gh described only as the effective matrix shear stiffness. G is the matrix shear modulus but h is some unknown function of the fiber diameter, interfiber spacing, and composite geometry (square, hexagonal, or some other type of array).

Recently Goree and Gross have applied a modified shear lag analysis to find detailed stress distributions for the three-dimensional case [16]. In their approach the matrix was conceptually divided into cells of square cross section with a fiber at the center of each cell. One consequence of their model for material behavior is that the force transmitted by a fiber to one of its nearest neighbors is independent of the ratio of fiber diameter to fiber spacing. The authors recognized the approximate nature of this feature of their model, and in a later paper [17] they employed an effective shear stiffness derived from experimental data on boron aluminum. However, the general dependence of h on fiber volume fraction and geometry for three-dimensional composites remains unknown at the present time.

An alternative approach for finding detailed stress distributions in damaged composites is to resort to experiment, but this also entails certain difficulties. It is obviously impractical to mount strain gauges on individual fibers. Optical techniques such as photoelasticity, Moire patterns, and stress coat are largely limited to the study of surface phenomena.

Fortunately an experimental approach based on the use of an electric analogue can be employed. The analogue is related but somewhat superior to the shear lag approximation for composite behavior. Like shear lag, it assumes that all displacements are parallel to the fibers. Unlike shear lag, in the analogue the matrix carries its proper share of the direct stress.

Higgins' extensive review of electrical analogues to mechanics problems [18] lists one paper giving an electric analogue technique for solving shear lag problems [19], and at least one paper has been published since on the subject [20]. However, the approach in those papers is quite different from that proposed here. In references [19] and [20] the differential equations of shear lag are replaced by difference equations, and a network of resistors is constructed to solve the resulting set of simultaneous linear algebraic equations. The continuous system is thus discretized, and the values of the various resistances have to be calculated in some way. The network becomes very complicated for a three-dimensional composite.

The present approach uses a scaled model of the composite (including all damage) with conducting rods replacing the fibers and an electrolyte replacing the matrix. It will be shown that by proper scaling and choice of the resistivity ratio of rods to electrolyte the differential equations and boundary conditions for the potential in the electrical system are the same as those for the displacements in the mechanical system. Thus by measuring potential distributions in the electrical system with a probe, the strains and therefore the stresses can be found for the composite.

Equations Governing Composite Behavior

It will be assumed, as in shear lag theory, that all displacements are parallel to the reinforcing fibers. If the fibers are aligned parallel to the z-axis (see Fig. 1), then

$$u = v = 0 \tag{1}$$

where u and v are the transverse displacements. The other main assumption of shear lag theory, that the matrix carries only shear, is not made here.

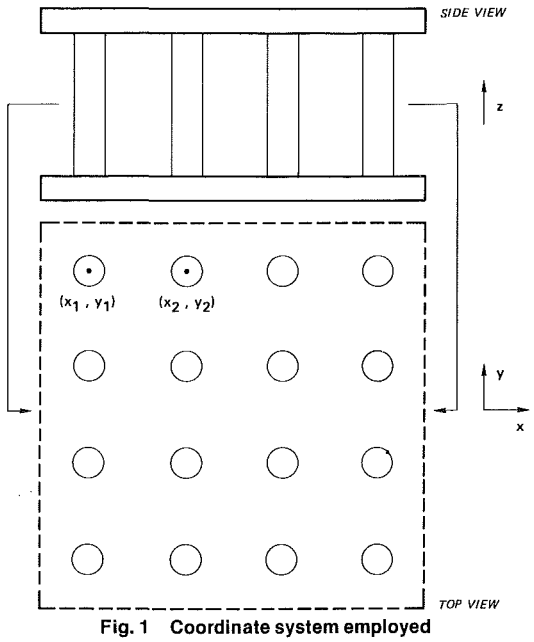

Fig. 1 Coordinate system employed

Downloaded 02 May 2010 to 171.66.16.246. Redistribution subject to ASME license or copyright; see http://www.asme.org/terms/Terms_Use.cfm

The displacements in the kth fiber will be denoted by $w(x_k,y_k,z)$, where (x_k,y_k) are the coordinates of the center line of the fiber. Applying Hooke's law to the fiber

$$\sigma_z(x_k,y_k,z) = E_f \frac{dw(x_k,y_k z)}{dz} \tag{2}$$

For the matrix material, Hooke's law implies that

$$\tau_{zx} = G_m \gamma_{zx} = G_m \frac{\partial w}{\partial x} \tag{3a}$$

$$\tau_{zy} = G_m \gamma_{zy} = G_m \frac{\partial w}{\partial y} \tag{3b}$$

$$\sigma_z = E'_m \epsilon_y = E' \frac{\partial w}{\partial z} \tag{3c}$$

Here G_m is the shear modulus of the matrix material, and E'_m is the tensile stiffness of the material when lateral expansion and contraction are forbidden. It is related to Young's modulus E_m by the relation

$$E'_m = \frac{E(1-\nu)}{1-\nu-2\nu^2} \tag{4}$$

where ν is Poisson's ratio.

Equilibrium in the kth fiber requires that

$$A_f \frac{d\sigma_z(x_k,y_k,z)}{dz} = \oint (\tau_{zy}dx + \tau_{zx}dy) \tag{5}$$

where the integral is taken around the circumference of the fiber. Using Hooke's law, the equation becomes

$$A_f E_f \frac{d^2 w_f(x_k,y_k z)}{dz^2} = G_m \oint \left(\frac{\partial w_m}{\partial y} dx + \frac{\partial w_m}{\partial x} dy \right) \tag{6}$$

or

$$\frac{d^2 w_f}{dz^2} = \frac{G_m}{E_f A_f} \oint \left(\frac{\partial w_m}{\partial y} dx + \frac{\partial w_m}{\partial x} dy \right) \tag{7}$$

The boundary conditions are determined by the applied loading. If the rest length of the composite is L and it is extended to length $L + \Delta L$, then

$$w_f(x_k,y_k,\pm L/2) = \pm \Delta L/2 \tag{8}$$

If the fiber is unbroken the differential equation (7) and the boundary conditions (8) define its strain and therefore also its stress distribution. If it is broken at location z_{ko} the stress and strain at z_{ko} are zero. Thus each fiber segment obeys (7) and one of the boundary conditions (8). The other boundary condition becomes

$$\frac{dw_f}{dz}(x_k,y_k,z_{ko}) = 0 \tag{9}$$

Equilibrium of the matrix in the z-direction requires that

$$\frac{\partial \tau_{zx}}{\partial x} + \frac{\partial \tau_{zy}}{\partial y} + \frac{\partial \sigma_z}{\partial z} = 0 \tag{10}$$

Applying Hooke's law this becomes

$$G_m \left(\frac{\partial^2 w_m}{\partial x^2} + \frac{\partial^2 w_m}{\partial y^2} \right) + E'_m \frac{\partial^2 w_m}{\partial z^2} = 0$$

or

$$\frac{\partial^2 w_m}{\partial x^2} + \frac{\partial^2 w_m}{\partial y^2} + \alpha^2 \frac{\partial^2 w_m}{\partial z^2} = 0 \tag{11}$$

where

$$\alpha^2 = E'_m / G_m \tag{12}$$

The end boundary conditions are the same as for the fibers

$$w_m(x,y,\pm L/2) = \pm \Delta L/2 \tag{13}$$

The side boundary conditions are a statement of continuity of w,

$$w_m = w_f \quad \text{at all interfaces.} \tag{14}$$

Electric Analogue

For simplicity, let us initially consider an electric analogue in which fibers and matrix are replaced by a geometrically similar array of conducting rods immersed in a weakly conducting electrolyte. Fundamentally, the analogy exploits the similarity between Hooke's law and Ohm's law.

According to Ohm's law, in the kth rod the current density j is given by

$$A_r j_z(x_k,y_k,z) = \frac{d\phi(x_k,y_k,z)}{dz}(1/\rho_r) \tag{15}$$

where ϕ is the electrical potential and ρ_r and A_r are the resistivity and area of the rod, respectively. In the electrolyte, Ohm's law states that

$$\mathbf{j} = \nabla\phi(1/\rho_e) \tag{16}$$

where ρ_e is the resistivity of the electrolyte.

Conservation of charge implies that in the rod

$$A_r \frac{dj_z}{dz} = \oint (j_{ey}dx + j_{ex}dy) \tag{17}$$

Here the integral is to be taken around the periphery of the rod, and j_{ex} and j_{ey} are the x and y components of the current density in the electrolyte. Applying Ohm's law, the equation can be written

$$(A_r/\rho_r) \frac{d^2\phi_r}{dz^2} = \frac{1}{\rho_e} \oint \left(\frac{\partial \phi_e}{\partial y} dx + \frac{\partial \phi_e}{\partial x} dy \right) \tag{18}$$

or

$$\frac{d^2\phi_r}{dz^2} = \frac{\rho_r}{A_r \rho_e} \oint \left(\frac{\partial \phi_e}{\partial y} dx + \frac{\partial \phi_e}{\partial x} dy \right) \tag{19}$$

The boundary conditions for the kth rod are

$$\phi(x_k,y_k,\pm L/2) = \pm \phi_0/2 \tag{20}$$

where ϕ_0 is the potential difference between the rod ends. If the rod is broken at location z_{ko} equation (19) applies to each segment. In this case one boundary condition of type (20) applies while the other is obtained by noting that at the break the current is zero, as a result of which (using (15))

$$\frac{d\phi_r}{dz}(x_k,y_k,z_{ko}) = 0 \tag{21}$$

The differential equation for the electrolyte is obtained by noting the fact that for steady currents

$$\nabla \cdot \mathbf{j}_e = 0 \tag{22}$$

Applying Ohm's law (16) we obtain

$$\nabla^2 \phi_e = 0 \tag{23}$$

The end boundary conditions are

$$\phi_e(x,y,\pm L/2) = \pm \phi_0/2 \tag{24}$$

while the side boundary conditions are

$$\phi_e = \phi_r \tag{25}$$

at every interface.

In comparing the differential equations and boundary conditions for rods and electrolyte with those for fibers and matrix, we see that the only flaw in the analogy is in the matrix and electrolyte differential equations, (11) and (23), respectively. This discrepancy can be eliminated by using a scale factor for the z dimension differing from that common to the x and y dimensions. Let us introduce the coordinate

$$s \equiv \alpha z \tag{26}$$

Then (23) becomes

$$\frac{\partial^2 \phi_e}{\partial x^2} + \frac{\partial^2 \phi_e}{\partial y^2} + \alpha^2 \frac{\partial^2 \phi_e}{\partial s^2} = 0 \tag{27}$$

With the transformation (26), (19) becomes

$$\frac{d^2\phi}{ds^2} = \frac{\rho_r}{\alpha^2 A_r \rho_e} \oint \left(\frac{\partial \phi_e}{\partial y} dx + \frac{\partial \phi_e}{\partial x} dy \right) \tag{28}$$

Downloaded 02 May 2010 to 171.66.16.246. Redistribution subject to ASME license or copyright; see http://www.asme.org/terms/Terms_Use.cfm

The end boundary conditions become

$$\phi(x,y,\pm\alpha L/2)=\phi_0/2 \tag{29}$$

while the side boundary conditions retain their previous form:

$$\phi_e=\phi_r \tag{30}$$

at all rod-electrolyte interfaces. Thus the electrical system is a faithful analogue of the mechanical system provided that the resistivity ratios are chosen appropriately.

To see how the choice is to be made we note that if the ratio of rod diameter to fiber diameter is K, the point (x,y,z) in the composite corresponds to point $(Kx,Ky,\alpha Kz)$ in the electric analogue. What is needed is a choice that will make

$$\frac{\phi(Kx,Ky,\alpha Kz)}{\phi_0}=\frac{w(x,y,z)}{\Delta L} \tag{31}$$

for all values of x, y, and z. A little reflection will convince the reader that with this choice

$$(1/\Delta L)\oint\left(\frac{\partial w}{\partial y}\,dx+\frac{\partial w}{\partial x}\,dy\right)=(1/\phi_0)\oint\left(\frac{\partial \phi}{\partial y}\,dx+\frac{\partial \phi}{\partial x}\,dy\right) \tag{32}$$

From (31) it follows that

$$\frac{1}{\phi_0}\frac{d^2\phi}{ds^2}=\frac{1}{K^2\Delta L}\frac{d^2w}{dz^2} \tag{33}$$

From (7), (28), and (33)

$$\frac{G_m}{E_fA_f\Delta L}\oint\left(\frac{\partial w}{\partial y}\,dx+\frac{\partial w}{\partial x}\,dy\right)$$

$$=\frac{\rho_r}{K^2\alpha^2A_r\rho_e\phi_0}\oint\left(\frac{\partial \phi}{\partial y}\,dx+\frac{\partial \phi}{\partial x}\,dy\right) \tag{34}$$

Using (12), (32), (33), and the fact that

$$A_r/A_f=K^2 \tag{35}$$

we obtain for the desired resistivity ratio

$$\rho_r/\rho_e=E_m'/E_f \tag{36}$$

With this resistivity ratio, the analogue relation (31) holds for any arbitrary array of fibers aligned parallel to the z-axis, with any arbitrary distribution of fiber fractures. The strain and therefore the stress distribution in both fiber and matrix can thus be found by constructing a geometrically similar array of conducting rods with scale factor K in the x and y directions and αK in the z-direction, immersing it in an electrolyte of appropriate resistivity, applying a potential to the ends, and measuring the potential distribution with a probe.

Discussion

Up to this point only simple tension has been considered. Pure bending can be simulated by changing the end boundary conditions. For example, bending in the x-z plane can be simulated by applying a linearly varying potential to the rod ends:

$$\phi(x,y,\pm L/2)=\pm\phi_1 x/a \tag{37}$$

where a is the half-width of the composite. Combined tension and bending is simulated by

$$\phi(x,y,\pm L/2)=\pm\phi_0\pm\phi_1 x/a \tag{38}$$

Shear can be simulated by taking

$$\phi(\pm 0.5a,y,z)=\pm\phi_2 \tag{39}$$

Debonding without friction between fiber and matrix can be simulated by applying insulating tape over the appropriate portion of a conducting rod. Debonding with friction can be simulated by using tape with the appropriate resistivity. Cracks in the matrix can be simulated by placing insulating sheet in the appropriate places in the electrolyte.

A number of techniques can be employed for finding the stiffness of a damaged composite. Gottesman, Hashin, and Brull [14] bound the stiffness by finding the energy and the complementary energy in tension or in shear, and also use the self-consistent theory to obtain an approximate answer. Alternatively a shear lag approach or numerical techniques such as finite element calculations can be employed. All of these are somewhat laborious. Using the electrical analogue approach the stiffness determination is much simpler. It was pointed out in the preceding section that elastic modulus and resistivity are inversely related. As a consequence of this, the ratio of the stiffness of a damaged composite to that of the undamaged composite is simply the ratio of the overall resistance of the undamaged to that of the damaged electrical analogue.

Acknowledgments

The author is indebted to R. A. Westmann for calling attention to the possibility of improving the analogue by the use of different scaling factors in the longitudinal and transverse directions, and to T. J. Higgins for his generous aid in reviewing the literature to see whether the electrical analogue proposed here had been discovered earlier. Support by the Office of Naval Research (Grant N00014-76-C-0445) is gratefully acknowledged.

References

1 Daniels, H.E., "The Statistical Theory of the Strength of Bundles of Threads," *Proc. Roy. Soc. London*, Series *A*, Vol. 183, 1945, pp. 405–435.

2 Coleman, B.D., "On the Strength of Classical Fibers and Fiber Bundles," *J. Mech. Phys. Solids*, Vol. 7, No. 1, 1959, pp. 66–70.

3 Rosen, B.W., "Tensile Failure of Fibrous Composites," *AIAA J.*, Vol. 2, No. 12, 1964, pp. 1985–1991.

4 Zweben, C., "Tensile Failure of Fiber Composites," *AIAA J.*, Vol. 6, No. 12, 1968, pp. 2231–2235.

5 Griffith, A.A., "The Theory of Rupture," Proc. *1st Int. Conf. Appl. Mech.*, Delft, 1920, pp. 55–63.

6 Zweben, C., and Rosen, B.W., "A Statistical Theory of Composite Strength With Application to Composite Materials," *J. Mech. Phys. Solids*, Vol. 18, pp. 189–206.

7 Harlow, D.G., and Phoenix, S.L., "Probability Distributions for the Strength of Composite Materials I: Two-Level Bounds," *Int. J. Fract.* Vol. 17, 1981, pp. 347–372.

8 Harlow, D.G., and Phoenix, S.L., "Probability Distributions for the Strength of Composite Materials II: A Convergent Sequence of Tight Bounds," *Int. J. Fract.*, Vol. 17, 1981, pp. 601–630.

9 Hedgepeth, J.M., "Stress Concentrations in Filamentary Structures," NASA TN D882, Langley Research Center, 1961.

10 Smith, R.L., 1980, "A Probability Model for Fibrous Composites With Local Load-Sharing," *Proc. R. Soc. London*, Series *A*, Vol. 372, 1980, pp. 539–553.

11 Batdorf, S.B., "Tensile Strength of Unidirectionally Reinforced Composites - I," *J. of Reinf. Pl. and Comp.*, Vol. 1, Apr. 1982, pp. 153–164.

12 Ho, Kong P., "A Monte Carlo Study of the Strength of Unidirectional Fiber-Reinforced Composites," *J. Comp. Mat.*, Vol. 13, Oct. 1978, pp. 311–328.

13 Manders, P.W., Bader, M.G., and Chou, T.W., "Monte Carlo Simulation of the Strength of Composite Fiber Bundles," to be published.

14 Gottesman, T., Hashin, Z., and Brull, M.A., "Effective Elastic Moduli of Cracked Fiber Composites," *Third International Conference on Composite Materials*, Paris, France, Aug. 1980.

15 Hedgepeth, J., and Van Dyke, P., "Local Stress Concentrations in Imperfect Filamentary Composite Materials," *J. of Composite Materials*, Vol. 1, 1967, pp. 294–309.

16 Goree, J.G., and Gross, R.S., "Stresses in a Three-Dimensional Unidirectional Composite Containing Broken Fibers," *Eng. Fr. Mech.*, Vol. 13, 1980, pp. 395–405.

17 Goree, J.G., and Gross, R.S., "Analysis of a Unidirectional Composite Containing Broken Fibers and Matrix Damage," *Eng Fr. Mech.*, Vol. 13, 1980, pp. 563–578.

18 Higgins, T.J., "Electroanalogic Methods," *Applied Mechanics Reviews*, Jan. and Feb. 1956; Feb. and Aug. 1957.

19 Newton, R.E., "Electrical Analogy for Shear Lag Problems," *Proc. Soc. for Exp. Stress Anal.*, Vol. 2, No. 2, 1944, pp. 71–80.

20 Kolosov, L.V., and Bel'mas, I.V., "Use of Electrical Models for Investigating Composites," Translated from *Mekhanika Kompositnykli Materialov*, No. 1, Jan.-Feb. 1981, pp. 129–133.

Downloaded 02 May 2010 to 171.66.16.246. Redistribution subject to ASME license or copyright; see http://www.asme.org/terms/Terms_Use.cfm

Quantitative Determination of Stress and Strain Distributions During High Axial Compression of Aluminium With the Aid of Small Ruby Particles

S. Hoekstra

M. A. Munnig Schmidt-van der Burg

H. Galenkamp

H. van Wijngaarden

Philips Research Laboratories,
5600 JA Eindhoven,
The Netherlands

Line shift measurements of the sharp R_1 ruby fluorescence line with respect to a neon reference line are used for the determination of quantitative stress distributions during high axial compression of cylindrical samples of aluminium between two transparent sapphire anvils. At the sample-anvil interface small ruby particles are embedded in the aluminium surface as optomechanical sensors for local stress and strain measurements. The experimental results are used to verify computer calculations based on the finite element method. The measurement technique was recently described by Brouha et al. [5, 6]. In this paper some modifications and new results will be presented and the use of pure sapphire anvils with a stress-sensitive top layer of ruby obtained by implantation of Cr^{3+} ions will be discussed.

Introduction

The wavelength of the sharp R_1 ruby ($\alpha-Al_2O_3$: Cr^{3+}) fluorescence line has become a widely used standard for pressure measurements in gasketed diamond-anvil cells [1–4]. In these high pressure cells many liquids and samples have been studied in a fluid environment providing hydrostatic conditions. The pressure dependence of the R_1 line (with a wavelength of 694.2 nm at normal pressure and room temperature) in 0.5 percent Cr-doped ruby was calibrated by Piermarini et al. [3], and the results of these measurements indicated an essentially linear hydrostatic pressure dependence of 0.365 nm/GPa. The shift in wavelength of the fluorescence R_1 line can be measured by a relatively simple optical system as described by Barnett et al. [2].

In our experiments, wavelength shifts of the R_1 line are used for the quantitative determination of stress distributions during high axial compression of aluminium samples between two transparent sapphire (Al_2O_3) anvils, as described by Brouha et al. [5, 6]. For that purpose, small ruby particles of about 70 μm are embedded in the aluminium surface, and act as optomechanical sensors at the sample-anvil interface. By using a large number of these particles the stress distribution can be determined. At the same time the material flow pattern at the sample-anvil interface can be derived from the change in position of the same ruby particles as they move along with the surrounding material.

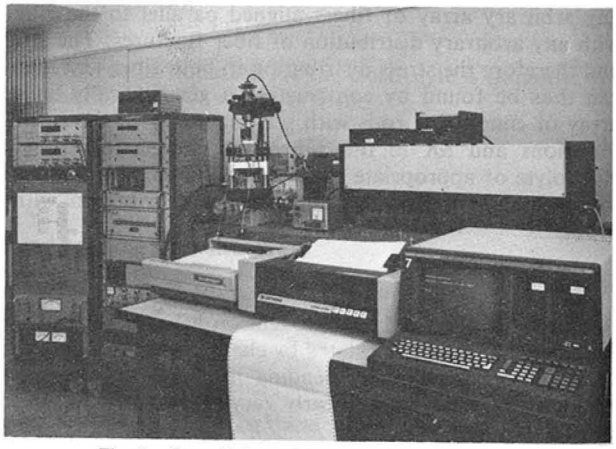

Fig. 1 Overall view of the experimental setup

It is clear that the stress sensor must be dimensionally small in relation to the total sample in order not to disturb the surface too much during the deformation process. However, ruby particles can be completely avoided by making use of sapphire anvils implanted with Cr. In that case, the material displacements are usually obtained from the deformation of grid patterns [7]. The displacements of the ruby particles measured at the sample-anvil interface, which fully characterize the frictional behavior, and the true stress-strain curve of the aluminium employed, are the input data for the

Contributed by the Applied Mechanics Division for publication in the JOURNAL OF APPLIED MECHANICS.

Discussion on this paper should be addressed to the Editorial Department, ASME, United Engineering Center, 345 East 47th Street, New York, N.Y. 10017, and will be accepted until two months after final publication of the paper itself in the JOURNAL OF APPLIED MECHANICS. Manuscript received by ASME Applied Mechanics Division, January 1982; final revision, June, 1982.

Copyright © 1983 by ASME

Downloaded 02 May 2010 to 171.66.16.246. Redistribution subject to ASME license or copyright; see http://www.asme.org/terms/Terms_Use.cfm

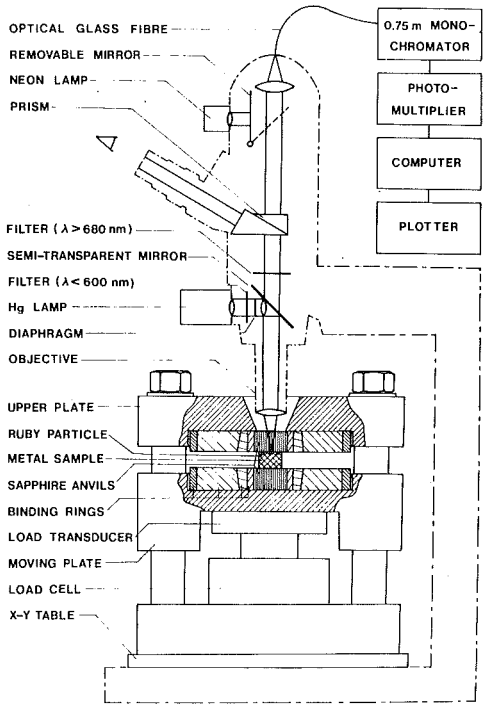

Fig. 2 Schematic drawing of the measuring system

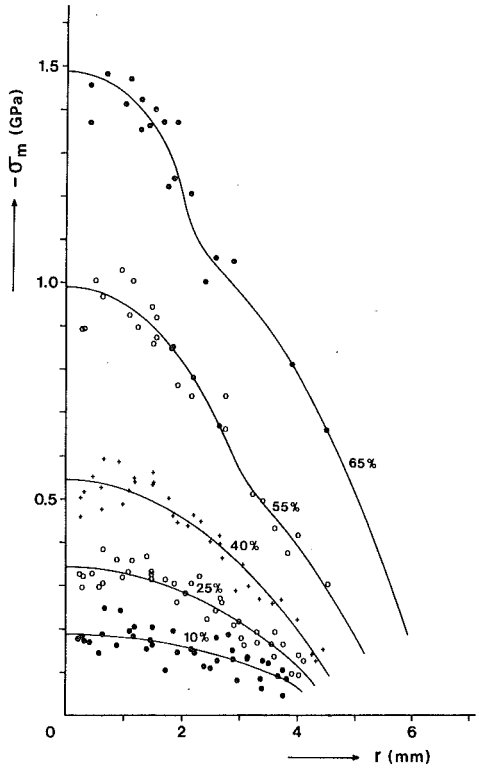

Fig. 3 Plot of the hydrostatic component σ_m of the stress tensor versus the radial position r of each ruby particle at successive height reductions of a polycrystalline cylindrical sample with an initial height of 2.0 mm

finite element calculation of the local stress distributions and are compared with the experimental results.

Experimental Procedure

The experiments are carried out with polycrystalline and monocrystalline samples of aluminium with a purity of 99.5 percent and 99.9999 percent, respectively. These samples have a cylindrical shape with a diameter of 8 mm and a height of 2 mm or 1.3 mm. The polycrystalline samples have axisymmetrical properties and a grain size of about 200 μm. In the case of the single crystals the compression axis is parallel to the $<001>$ cube direction. The cylinder planes are finished to optical flatness and parallelism and no lubricant is applied.

Figure 1 shows an overall view of the experimental setup and a schematic arrangement is shown in Fig. 2. The system consists of a pressure unit containing two sapphire anvils, an optical microscope attached to a monochromator, a photomultiplier, and computer facilities. The transparent sapphire anvils with a diameter of 25 mm and a height of 20 mm permit the surface of the sample to be observed during the plastic deformation process. Since the ultimate tensile strength of sapphire (0.19 GPa) is much lower than the compressive strength (2.1 GPa), it is necessary to prestress the sapphire anvils with the aid of binding rings, as shown in Fig. 2. One of the main parts of the pressure unit is an accurate load transducer enabling the applied load on the sample to be directly compared with the values derived from the measured stress distribution.

About 40 ruby particles are embedded in one surface of the aluminium sample along two mutually rectangular diameters, to act at the same time as stress sensors and position markers. The plastic deformation process consists of applying a number of successive load steps until the height of the sample is reduced by about 70 percent. After each load step, the displacement of each ruby particle and the shift in wavelength of the R_1 fluorescence line are measured to determine the material flow pattern and the stress distribution of the hydrostatic component at the sample-anvil interface. The entire pressure unit can be displaced by means of the $x-y$ table of the microscope with an accuracy of 2 μm. The objective of the microscope is a Leitz UM 32 objective with a long working distance and a numerical aperture of 0.30. As shown in Fig. 2, the objective protrudes into the conical hole in the upper plate of the pressure unit.

The ruby fluorescence R lines are excited by high-intensity mercury light, which passes through a filter transparent to wavelengths smaller than 600 nm. By combining this with a second filter transparent to wavelengths higher than 680 nm, it is possible to eliminate the intense mercury light and to observe the fluorescent rubies in the microscope. After positioning a ruby particle in the reticle of the eyepiece, the prism is removed and the ruby light is focused by a lens on an optical glass fiber attached to the slit-shaped entrance of a 0.75 m monochromator (with slit widths adjusted to 100 μm). The light intensity at the exit of the monochromator is measured by a photomultiplier and recorded on a plotter.

The R_1 line occurs at 694.2 nm with a spectral line half-width of 0.65 nm at normal pressure and room temperature, while the shift due to hydrostatic pressure in a fluid environment amounts to 0.365 nm/GPa [3]. A neon lamp is used as an internal wavelength standard because the neon spectrum contains several strong lines near the wavelength of the R_1 ruby line. One of these lines occurs at 692.95 nm and this line is used as a reference line in our experiments. The neon light enters the optical glass fiber by means of a separate mirror which is removed immediately after the neon line is measured in order to be able to record the neon and ruby spectrum in the same run. This allows the measurement of the R_1 line shift with an accuracy of about 0.02 nm, corresponding to 0.05 GPa, if no line broadening occurs due to shear stresses.

The decrease in height of the aluminium sample at successive load steps is derived from the change in distance between the two anvils and is measured with an accuracy of about 5 μm. The diaphragm indicated in Fig. 2 with a small aperture of 150 μm is necessary in order to be able to isolate a

Downloaded 02 May 2010 to 171.66.16.246. Redistribution subject to ASME license or copyright; see http://www.asme.org/terms/Terms_Use.cfm

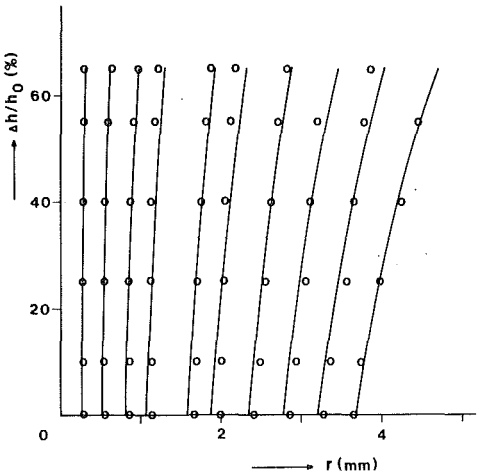

Fig. 4 Plot of the radial position r of each ruby particle along one-half diameter, indicated by the open circles, versus successive height reductions $\Delta h/h_0$ of a polycrystalline cylindrical sample with an initial height of 2.0 mm. The solid lines are calculated curves fitted to the measured displacements and these curves are used as input data for the finite-element computer program.

specific circular area on the sample with a diameter of 30 μm, as will be discussed later.

Experimental and Numerical Results

Figure 3 is a representative example of measurements on polycrystalline cylindrical samples of aluminium, while similar results were obtained on monocrystalline samples, as will be described in the following section. The hydrostatic component σ_m of the stress tensor of each ruby particle, derived from the shift in wavelength of the R_1 fluorescence line, is plotted versus its radial position r after height reductions of 10, 25, 40, 55, and 65 percent. In Fig. 4 the radial position of each ruby particle along one half diameter is indicated by open circles and is plotted versus the height reduction $\Delta h/h_0$ as a result of the successive load steps. Due to their irregular shape only a small area of some ruby particles remains visible during the deformation process and these particles are, therefore, no longer measurable after a certain height reduction because the light intensity becomes too small as compared with the noise. It is also possible that some ruby particles may completely disappear into the aluminium during the deformation process, and for these reasons a number of measuring points is absent in the plots of Figs. 3 and 4 at higher deformations.

Figure 3 shows that after a height reduction of about 40 percent a peak is formed in the central region of the sample. This peak is induced by a local sticking of the aluminium touching the anvils, because lubricants cannot be used in our experiments due to the fact that they cause displacements of the entire sample during the deformation process. In all cases the sticking appears at higher deformations within a ring-shaped band with a width of about 2 mm, and is located halfway the radius of the deformed sample.

The calculations are based on the finite element method using the MARC general purpose finite element computer program [8]. This program contains special options for large strain plasticity analyses, while effects of elastic deformation and a combined kinematic-isotropic strain hardening model are taken into account (Nagtegaal and De Jong [9]). The true stress-strain curve of the aluminium actually measured in a standard tensile test, as shown in Fig. 5, and calculated curves fitted to the radial displacements of the ruby particles measured with respect to the corresponding height reduction are used as input data. These calculated curves are of the type

$$\Delta h = \alpha(1 - r_0^2/r^2)h_0 \qquad (1)$$

as shown by the solid lines in Fig. 4. In this formula, Δh is the

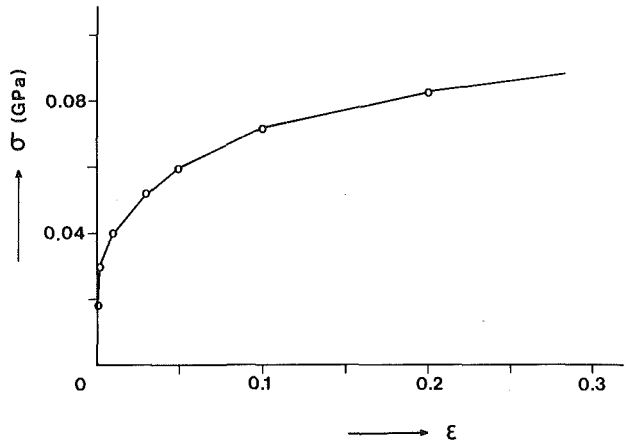

Fig. 5 True stress-strain curve of polycrystalline aluminium from a standard tensile test

decrease in height of the sample, h_0 is the initial height of the sample, r_0 is the initial radial position of a ruby particle, r is the current radial position of a ruby particle, and α is a geometrical factor (in the case of incompressibility without friction, $\alpha = 1$). A good fit can be obtained by regarding α as a function of r_0, because in that case the local stick-slip behavior at higher deformations can be simulated. In the results presented here the following relation was used

$$\alpha = \alpha_1 - \alpha_2(r_0)^2 \qquad (2)$$

where $\alpha_1 = 2$ and $\alpha_2 = 0.028$ mm^{-2}. The stress distribution calculated for the hydrostatic component is shown in Fig. 6 by dashed lines and a fair correspondence is noticed with the measured results indicated by solid lines, which are the same as shown in Fig. 3. Apart from this stress distribution, it is also possible to calculate the stress distributions of the normal component and the shear component, but these results will be discussed in the following section. The calculations had to be limited up to height reductions of 48 percent because at larger deformations the elements of the mesh became too distorted. In all cases a combined kinematic-isotropic strain hardening model was used [9].

Discussion

In Fig. 3 the hydrostatic component σ_m of the stress tensor is plotted versus the radial position r of each ruby particle because of the axisymmetrical character of the deformation process in the case of polycrystalline samples. As can be seen, the scatter around the drawn curves is larger than the accuracy of measurement of the R_1 line shift corresponding to 0.05 GPa. One of the explanations might be the polycrystalline character of the material with an average grain size of 200 μm, because each grain with its specific orientation will behave in a different way with respect to the deformation process. However, the same scatter was observed in the case of monocrystalline samples with a cube orientation, which is symmetrical and stable until height reductions of about 70 percent are achieved [10]. These measurements also revealed that the expected transition from a circular to a square cross section of the monocrystalline samples, due to the position of the four <110> slip directions, did not occur. It was further observed that the stress distributions of the hydrostatic component measured in two different crystallographic directions at several height reductions did not show any difference. In fact, all results were similar to the stress distributions for polycrystalline material as shown in Fig. 3. It is assumed that the friction conditions at the sample-anvil interface are responsible for these experimental results. As is known, lubricants reduce friction and control or improve the uniformity of flow in the material. They also reduce wear and keep the sample from sticking to the anvils, but in our case no

Downloaded 02 May 2010 to 171.66.16.246. Redistribution subject to ASME license or copyright; see http://www.asme.org/terms/Terms_Use.cfm

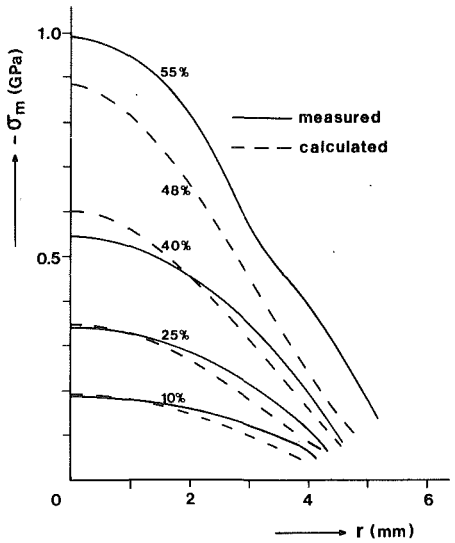

Fig. 6 Measured and calculated stress distributions of the hydrostatic component σ_m at successive height reductions of a polycrystalline cylindrical sample. The measured curves are the same as shown in Fig. 3.

lubricants could be applied and it is believed that the overall friction constrains the deformation process too much. This leads to a local stick-slip behavior as observed in all our experiments and the creation of new material at the surface.

Another reason for the scatter observed in the measured stress distributions might be the irregular shape and size of the ruby particles and the dependence of the R_1 line shift on the orientation of the c-axis in each ruby particle with respect to the compression axis [11], but this could not be proved in a satisfactory manner.

The fit in Fig. 4 between the prescribed radial displacements (solid lines) and the measured displacements (open circles) of the ruby particles is mainly influenced by the factor α in equation (1). It appears that a good fit can be obtained by using equation (2). Besides, this choice of α results in a good correspondence between the measured and calculated stress distributions of the hydrostatic component σ_m, as presented in Fig. 6. It has to be noticed, however, that the shape of the calculated stress distributions of σ_m is fairly sensitive to changes in the factor α, as shown by Nagtegaal and De Jong [9]. These authors, for example, used a constant value for α, namely $\alpha = 1.15$ (in their notation $\beta = 1/\alpha = 0.87$) and they did not find any increase in the calculated stress distributions near the center of the specimen due to local sticking at higher deformations. This is in conflict with the experimental results. By using equation (2), however, such an increase does appear in the calculated stress distributions, as shown in Fig. 6, because in that case the local stick-slip behavior is better described than when constant values are used for the factor α.

Data based on the true stress-strain curve from a standard tensile test of the aluminium used in this investigation are only available up to a deformation of about 30 percent. This means that the measured curve shown in Fig. 5 has to be extrapolated for data with respect to large deformations. It appears, however, that small changes in such an extrapolation particularly influence the height of the calculated stress distributions and not their shape. These influences are large because σ_m is much larger than the Von Mises stress. Nevertheless, both input data for the finite element computer program, i.e., the true stress-strain curve and the prescribed displacement curves, result in a good correspondence between the measured and calculated stress distributions of the hydrostatic component σ_m (Fig. 6), but it would be desirable to know the input data more precisely, for example the true stress-strain curve at large deformations.

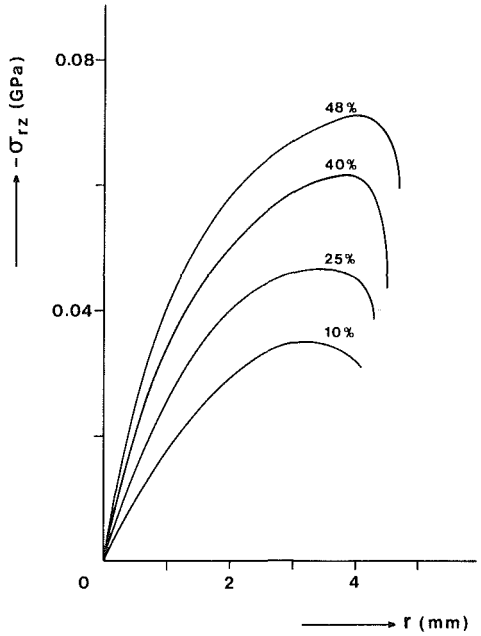

Fig. 7 Calculated stress distribution of the shear component σ_{rz} at successive height reductions of a polycrystalline cylindrical sample

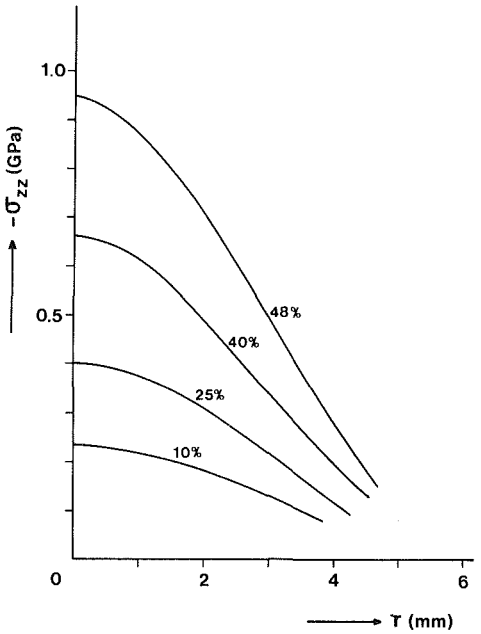

Fig. 8 Calculated stress distribution of the normal component σ_{zz} at successive height reductions of a polycrystalline cylindrical sample

In our experiments it is assumed that the shift measured for the R_1 ruby fluorescence line only depends on the hydrostatic component σ_m of the stress tensor defined by

$$\sigma_m = \frac{1}{3}(\sigma_{rr} + \sigma_{\theta\theta} + \sigma_{zz}) \tag{3}$$

Figure 7 shows that the stress distributions calculated for the shear component σ_{rz} at the sample-anvil interface are fairly small with respect to the stress distributions of the hydrostatic component σ_m (Fig. 6). This explains why local sticking of the aluminium to the anvils may occur as observed in all our experiments. If friction is zero between the sample and the anvil ($\alpha \approx 1$ and $\sigma_{rz} = 0$) then $\sigma_{rr} = \sigma_{\theta\theta} = 0$, σ_{zz} equals the Von Mises stress, and $\sigma_m = 1/3\ \sigma_{zz}$ (see equation (3)). Because $\alpha \neq 1$ (and therefore $\sigma_{rz} \neq 0$), friction is introduced in the calculations, from which it appears that

$$\sigma_{rr} \approx \sigma_{\theta\theta} \approx \sigma_{zz} \tag{4}$$

Downloaded 02 May 2010 to 171.66.16.246. Redistribution subject to ASME license or copyright; see http://www.asme.org/terms/Terms_Use.cfm

Table 1 Representation of the results derived from a polycrystalline cylindrical sample based on Fig. 3

Height Reduction (%)	Measured Load (kN)	Load Transducer (kN)	Deviation (kN)
10	6.7	6.3	+0.4
25	12.6	11.3	+1.3
40	21.2	21.5	-0.3
55	43.0	46.4	-3.4
65	84.1	83.3	+0.8

which means that, according to equation (3)

$$\sigma_m \approx \sigma_{zz} \tag{5}$$

The validity of this equation is also apparent from the comparison between the calculated stress distributions of the normal component σ_{zz}, shown in Fig. 8, and the hydrostatic component σ_m, shown in Fig. 6. As can be seen, the stress distributions are almost equal to each other and on the basis of these numerical results it may be concluded that equation (5) can be applied in our situation. This conclusion is further supported by the experimental results, as shown in Table 1. The values indicated for the measured load L_M are derived from the following integral (where R is the radius of the sample)

$$L_M = 2\pi \int_{r=0}^{r=R} \sigma_m(r) r dr \tag{6}$$

and are compared with the values of the total applied load on the sample L_T obtained by means of the load transducer. These values must be equal to

$$L_T = 2\pi \int_{r=0}^{r=R} \sigma_{zz}(r) r dr \tag{7}$$

where σ_{zz} is the normal component of the stress distribution at the sample-anvil interface. The fact that Table 1 shows a fair correspondence between the values of L_M and L_T indicates that in our experiments $\sigma_m \approx \sigma_{zz}$ and that the aforementioned assumption is justified, which is also apparent from the good agreement between the measured and calculated stress distributions of the hydrostatic component σ_m as shown in Fig. 6.

The photomultiplier used in the measuring system described by Brouha et al. [5, 6] had a dark current of 10 nA. In our experiments it has been replaced by a new one with cooling facilities that reduce the dark current to 0.02 nA. After this modification it was found that with a localized spot of 130 μm on the aluminium sample without any ruby particles, the sapphire anvil showed an R_1 line with a light intensity of 5 nA due to about 1 ppm Cr impurities. Because the sapphire anvils are prestressed with the aid of binding rings, they cause a shift in wavelength of the R_1 ruby fluorescence line corresponding with a stress component of 0.3 GPa (without any applied load). On the basis of this prestress it is clear that under these circumstances the combination of sapphire anvils containing Cr impurities (where the mercury light passes through) and ruby particles produces a greater fluorescence shift and hence a higher stress than expected because the R_1 line of the anvil is superposed on the R_1 line of a ruby particle. Moreover, considerable line broadening is observed because the stresses vary in a direction normal to the anvil. To minimize the influence of the sapphire anvil acting as a ruby particle, it is necessary to reduce the aperture of the diaphragm indicated in Fig. 2 to 150 μm, which means that on the aluminium sample a circular area with a diameter of 30 μm can be isolated instead of 130 μm. In this situation the contribution of the anvil to the total light intensity is decreased from 5 nA to approximately 0.4 nA, which is an acceptable level because peaks with light intensities of less than 6 nA are neglected. The isolated area of 30 μm is, indeed, smaller than the average ruby size of 70 μm but during the deformation process the ruby particles become more and more deeply embedded in the aluminium surface and sometimes disappear completely. For that reason smaller ruby particles can hardly be used.

It is clear that the problem of sapphire anvils containing Cr impurities can be solved more easily by using anvils with a zero Cr content, but on the other hand pure sapphire anvils with a stress-sensitive top layer of ruby obtained by implantation of Cr^{3+} ions, as suggested by Tangena [12], provide the possibility of measuring stress components without making use of separate ruby particles. In that case the material displacements can be obtained from the deformation of grid patterns [7]. Experiments with the aid of implanted sapphire anvils, however, showed that the measured values based on the shift in wavelength of the R_1 line were more than 50 percent lower than the total applied loads on the sample, but the scatter band of the measuring points was much less than in the case of separate ruby particles. The main reason for the poor correspondence between the measured values and the values based on the load transducer is the definitely nonhydrostatic character of the very complex stress configuration in the sapphire anvil, caused by elastic deformation (bending) of the anvils themselves during the deformation process. Moreover, the stresses measured at the surface of the implanted anvil will not be equal to the stresses in the aluminium sample. This means that the introduction of an implanted sapphire anvil raises serious mathematical and experimental complications. However, by calibrating such an implanted anvil it may be possible to make use of this new measuring technique and to omit the separate ruby particles.

Acknowledgments

Grateful thanks are due to Dr. M. Brouha and Dr. J. E. De Jong for many helpful discussions in the course of the investigation.

References

1 Piermarini, G. J., Block, S., and Barnett, J. D., "Hydrostatic Limits in Liquids and Solids to 100 kbar," *Journal of Applied Physics*, Vol. 44, 1973, pp. 5377-5382.

2 Barnett, J. D., Block, S., and Piermarini, G. J., "An Optical Fluorescence System for Quantitative Pressure Measurement in the Diamond-Anvil Cell," *The Review of Scientific Instruments*, Vol. 44, 1973, pp 1-9.

3 Piermarini, G. J., Block, S., Barnett, J. D., and Forman, R. A., "Calibration of the Pressure Dependence of the R_1 Ruby Fluorescence Line to 195 kbar," *Journal of Applied Physics*, Vol. 46, 1975, pp. 2774-2780.

4 Piermarini, G. J., and Block, S., "Ultrahigh Pressure Diamond-Anvil Cell and Several Semiconductor Phase Transition Pressures in Relation to the Fixed Point Pressure Scale," *The Review of Scientific Instruments*, Vol. 46, 1975, pp. 973-979.

5 Brouha, M., De Jong, J. E., and Van Der Weide, K. J. A., "Experimental Verification of Finite Element Analysis on Axisymmetric Deformation Processes," *Proceedings of the Seventh North American Metalworking Research Conference*, Ann Arbor, Mich., 1979, pp. 57-64.

6 Brouha, M., De Jong, J. E., and Galenkamp, H., "Experimental and Numerical Determination of Stress and Flow Patterns in Large Axial Compression of Aluminum Cylinders," *Proceedings of the Seventh International AIRAPT High Pressure Conference*, Le Creusot, France, 1980, pp. 318-320.

7 Danckert, J., and Wanheim, T., "The Use of a Square Grid as an Alternative to a Circular Grid in the Determination of Strains," *Journal of Mechanical Working Technology*, Vol. 3, 1979, pp. 5-15.

8 MARC General Purpose Finite Element Programme, Version J1, MARC Analysis Research Corporation, Palo Alto, Calif., 1979.

9 Nagtegaal, J. C., and De Jong, J. E., "Some Computational Aspects of Elastic-Plastic Large Strain Analysis," *International Journal for Numerical Methods in Engineering*, Vol. 17, 1981, pp. 15-41.

10 Hoekstra, S., "Development and Transition of Rolling Textures in Face-Centered Cubic Single Crystals of Aluminium, Copper and Silver," Bachelor Thesis, Twente University of Technology, Enschede, The Netherlands, 1973.

11 Besson, J. M., and Pinceaux, J. P., "Uniform Stress Conditions in the Diamond-Anvil Cell at 200 Kilobars," *The Review of Scientific Instruments*, Vol. 50, 1979, pp. 541-543.

12 Tangena, A. G., Private Communication, 1980.

Downloaded 02 May 2010 to 171.66.16.246. Redistribution subject to ASME license or copyright; see http://www.asme.org/terms/Terms_Use.cfm

Dynamics of Asymmetric Nonconservative Systems

D. J. Inman
Assistant Professor,
Department of Mechanical and Aerospace Engineering,
State University of New York at Buffalo,
Buffalo, N.Y. 14260
Assoc. Mem. ASME

This work examines a linear, asymmetric lumped parameter system. Results on the qualitative behavior of a certain subclass of such systems are presented. In particular, necessary and sufficient conditions for the existence of a linear transformation that transforms an asymmetric system into an equivalent symmetric system are derived. Results on the stability and instability of such systems are presented and stated in terms of the original asymmetric system's coefficient matrices. This work is compared with that of other authors and numerical examples illustrating the utility and correctness of the results are presented.

Introduction

Recently several authors [1-4] have considered the vibrations of asymmetric dynamical systems which may be successfully modeled by a vector differential equation of the form

$$A\ddot{x}(t)+B\dot{x}(t)+Cx(t)=f(t) \tag{1}$$

where A, B, and C are general real $n \times n$ matrices (lacking any particular symmetry or definiteness) and where $x(t)$ and $f(t)$ are n-dimensional column vectors of generalized coordinates and forces, respectively. Problems of this type arise in vehicle dynamics as well as in the study of circulatory systems and, as pointed out by Fawzy and Bishop [4], have not been properly catered to.

The objective of this work is to point out that many of the problems in the form of (1) can be transformed into an equivalent symmetric problem. Such transformations have been successfully used for the case $B=0$ by Huseyin and Leipholz [5] who introduced the terminology pseudoconservative systems to describe asymmetric systems that can be transformed into an equivalent symmetric system. This work is an extension of the concepts of pseudoconservative systems used in [5] to systems with velocity-dependent and gyroscopic forces.

Specifically, a necessary and sufficient condition for (1) to be transformable into a symmetric system by an eigenvalue preserving transformation is presented. In addition, the stability of (1) is discussed in relation to the *KTC* stability theorem [6]. The examples proposed by Fawzy and Bishop [4] and Washed and Bishop [3] are considered and used to verify the presented results.

Contributed by the Applied Mechanics Division for presentation at the 1983 ASME Applied Mechanics, Bioengineering, and Fluids Engineering Conference, Houston, Texas, June 20-22, 1983, of THE AMERICAN SOCIETY OF MECHANICAL ENGINEERS.

Discussion on this paper should be addressed to the Editorial Department, ASME, United Engineering Center, 345 East 47th Street, New York, N.Y. 10017, and will be accepted until two months after final publication of the paper itself in the JOURNAL OF APPLIED MECHANICS. Manuscript received by ASME Applied Mechanics Division, March, 1982. Paper No. 83-APM-4.

Copies will be available until February, 1984.

Background

It has been shown by Tausskey and Zassenhaus [7] that every real square matrix can be represented as the product of two real symmetric matrices. This allows asymmetric matrices to be further classified by the following definition.

Definition. A matrix A is said to be symmetrizable if and only if it can be expressed as the product of two symmetric matrices one of which is positive-definite.

Tausskey [8] goes on to show that a matrix A is symmetrizable if and only if any of the following hold

(*i*) A is similar to a symmetric matrix;
(*ii*) A has real eigenvalues and a full set of eigenvectors;
(*iii*) $A^T=S^{-1}AS$ where S is symmetric and positive-definite; and
(*iv*) A becomes symmetric when multiplied by a suitable positive-definite matrix.

Here, A^T denotes the transpose of the matrix A, and A^{-1} denotes the inverse of the matrix A.

The class of dynamical systems considered here are those described by equation (1) with the following restrictions:

(*a*) A is nonsingular, and
(*b*) $A^{-1}B$ and $A^{-1}C$ are symmetrizable.

The eigenvalue problem associated with (1) is

$$(\lambda^2 A+\lambda B+C)q=0 \tag{2}$$

where λ is a complex number and q is a constant column vector. Since A is nonsingular it is convenient to write (3) as

$$(\lambda^2 I+\lambda A^{-1}B+A^{-1}C)q=0 \tag{3}$$

which necessarily has the same eigenvalues as (2). Here, I denotes the $n \times n$ identity matrix. The results of this work are formulated in terms of equation (3).

Results

The problem now becomes one of finding conditions on the matrices $A^{-1}B$ and $A^{-1}C$ that will insure the existence of a transformation that simultaneously symmetrizes them. Since each of these matrices is symmetrizable, they may be expressed in terms of the following factorization:

Copyright © 1983 by ASME
Downloaded 02 May 2010 to 171.66.16.246. Redistribution subject to ASME license or copyright; see http://www.asme.org/terms/Terms_Use.cfm

$$A^{-1}B = S_1 S_2$$
$$A^{-1}C = T_1 T_2$$

where S_2 and T_2 are symmetric and S_1 and T_1 are symmetric and positive-definite (denoted $T_1 > 0$, $S_1 > 0$).

The first result is motivated by the concept of proportional damping.

Theorem I. If $B = \alpha A + \beta C$ where α and β are real constants, then equation (3) can be transformed into a symmetric system by an eigenvalue preserving transformation.

The validity of the result may be established as follows. If $B = \alpha A + \beta C$, then $A^{-1}B = \alpha I + \beta A^{-1}C$ and equation (3) becomes

$$[\lambda^2 I + \lambda(\alpha I + \beta A^{-1}C) + A^{-1}C\,]q = 0$$

Since $A^{-1}C = T_1 T_2$ where T_1 is positive-definite, the preceding equation may be written as

$$[\lambda^2 T_1^{-1/2} T_1^{1/2} + \lambda(\alpha T_1^{-1/2} T_1^{1/2} + \beta T_1^{1/2} T_2 T_1^{1/2}) + T_1^{1/2} T_2 T_1^{1/2}]r = 0 \tag{4}$$

by using the substitution $q = T_1^{1/2} r$ and premultiplying by $T_1^{-1/2}$. Here, $T_1^{1/2}$ denotes the positive-definite square root of the positive-definite matrix T_1 and $T_1^{-1/2}$ denotes its inverse. Thus,

$$[\lambda^2 I + \lambda(\alpha I + \beta T_1^{1/2} T_2 T_1^{1/2}) + T_1^{1/2} T_2 T_1^{1/2}]r = 0 \tag{5}$$

is symmetric since $T_1^{1/2} T_2 T_1^{1/2} = (T_1^{1/2} T_2 T_1^{1/2})^T$. The nonsingularity of T_1 insures that the characteristic equation remains unchanged and the eigenvalues associated with (5) and (3) are the same.

A stronger result may be stated by considering the symmetric factors of each of the coefficient matrices of (3).

Theorem II. The eigenvalue problem of equation (3) is similar to a symmetric eigenvalue problem if and only if there exists at least one factorization of $A^{-1}B$ and $A^{-1}C$ such that $T_1 = S_1$.

First, assume that $T_1 = S_1$. Then equation (3) becomes

$$(\lambda^2 I + \lambda T_1 S_2 + T_1 T_2)q = 0.$$

Premultiplying by $T_1^{-1/2}$ and using the substitution $q = T_1^{1/2} r$ yields

$$(\lambda^2 I + \lambda T_1^{1/2} S_2 T_1^{1/2} + T_1^{1/2} T_2 T_1^{1/2})r = 0, \tag{6}$$

where each coefficient is symmetric.

Next assume that equation (3) can be transformed into a symmetric system, i.e., that there exists a nonsingular transformation P such that

$$(\lambda^2 I + \lambda P^{-1}(A^{-1}B)P + P^{-1}A^{-1}CP)r = 0$$

is symmetric and where $q = Pr$. This matrix is symmetric if and only if each of the coefficients of λ is symmetric, i.e.,

$$P^{-1}A^{-1}B\,P = P^T (A^{-1}B)^T (P^{-1})^T$$

and

$$P^{-1}A^{-1}C\,P = P^T (A^{-1}C)^T (P^{-1})^T.$$

This last equality may be written as

$$A^{-1}C = (PP^T)(A^{-1}C)^T (P^{-1})^T P^{-1}$$

where the matrix PP^T is necessarily positive-definite and

$$\begin{aligned}[(A^{-1}C)^T (P^{-1})^T P^{-1}]^T &= (P^{-1})^T (P^{-1}A^{-1}C) \\ &= (P^T)^{-1} P^T (A^{-1}C)^T (P^{-1})^T P^{-1} \\ &= (A^{-1}C)^T (P^{-1})^T P^{-1}\end{aligned}$$

is symmetric. The same development follows for $A^{-1}B$ so that

$$A^{-1}B = (PP^T)(A^{-1}B)^T (P^{-1})^T P^{-1}.$$

The factors of each matrix then become

$$S_2 = (A^{-1}B)^T (P^{-1})^T P^{-1}, \quad T_2 = (A^{-1}C)^T (P^{-1})^T P^{-1}$$

and

$$T_1 = S_1 = PP^T.$$

Thus $A^{-1}C$ and $A^{-1}B$ have at least one factorization of the form $A^{-1}B = S_1 S_2$, $A^{-1}C = S_1 T_2$.

This result provides a necessary and sufficient condition for the existence of a linear transformation that transforms (3) into an equivalent symmetric system. When this condition is satisfied by a given system, the dynamics of the system can be described in terms of the well-developed theory for damped symmetric systems. The next results discuss the question of stability of asymmetric systems that satisfy conditions (*a*) and (*b*) in the foregoing, and $S_1 = T_1$. In the following results $f(t)$ is taken to be identically zero.

Theorem III. If $S_1 = T_1$ and if the eigenvalues of $A^{-1}B$ and $A^{-1}C$ are positive real numbers, then the equilibrium of equation (1) is asymptotically stable.

It is first noted that if $A^{-1}B$ and $A^{-1}C$ have positive eigenvalues, then S_2 and T_2 are positive-definite [9]. For $T_1 = S_1$ equation (6) becomes

$$(\lambda^2 I + S_1 S_2 \lambda + S_1 T_2)r = 0.$$

Premultiplying this expression by the nonsingular matrix S_1^{-1} does not change the associated characteristic equation and yields

$$(\lambda^2 S_1^{-1} + \lambda S_2 + T_2)r = 0$$

Each coefficient matrix here is symmetric and positive-definite, a well-known condition for asymptotic stability (see for instance [10]).

The next obvious extension is to examine the stability when S_2 is positive-semidefinite. This is the case if $A^{-1}B$ is allowed to have zero as well as positive eigenvalues. This question has been answered by Moran [11] and by Walker and Schmitendorf [12] for symmetric systems. The same results are true for asymmetric systems under the hypothesis of Theorem II as the next two results show.

Theorem IV. If $S_1 = T_1$, if the eigenvalues of $A^{-1}C$ are positive real numbers and if the eigenvalues of $A^{-1}B$ are nonnegative then the equilibrium of equation (1) is asymptotically stable if and only if the $n^2 \times n$ matrix

$$R = \begin{bmatrix} A^{-1}B \\ A^{-1}B(A^{-1}C) \\ A^{-1}B(A^{-1}C)^2 \\ \vdots \\ A^{-1}B(A^{-1}C)^{n-1} \end{bmatrix}$$

has rank n.

The proof of this result follows directly from the proof given in [12] for symmetric systems, with some minor adjustments to keep track of the asymmetries.

First, assume the rank of R is n, and examine the equilibrium of (1). Rather than using (6), it is more convenient in this case to write (1) as

$$I\ddot{x} + S_1 S_2 \dot{x} + S_1 T_2 x = 0$$

and to premultiply by S_1^{-1}. This yields

$$S_1^{-1}\ddot{x} + S_2 \dot{x} + T_2 x = 0 \tag{7}$$

Downloaded 02 May 2010 to 171.66.16.246. Redistribution subject to ASME license or copyright; see http://www.asme.org/terms/Terms_Use.cfm

where S_1^{-1} and T_2 are symmetric positive-definite and S_2 is symmetric positive-semidefinite. Next, define the Liapunov function $V(x,\dot{x})$ by

$$V(x,\dot{x}) = \dot{x}^T S_1^{-1}\dot{x} + x^T T_2 x > 0$$

where

$$\dot{V}(x,\dot{x}) = -2\dot{x}^T S_2 \dot{x} \leq 0$$

since S_2 is positive-semidefinite. According to La Salle's invariance principle [12,15] the equilibrium of this system is asymptotically stable if it can be shown that the only solution satisfying $\dot{V}=0$ is the equilibrium solution $x=\dot{x}=0$. This follows exactly as in the proof given in [12]. Let $x=\dot{x}=0$ denote a motion such that $\dot{V}(x,x)=0$, that is, $\dot{x}^T S_2 \dot{x}=0$. Since S_2 is symmetric this requires $S_2\dot{x}=0$, and $S_2\ddot{x}=0$. Premultiplying these expressions by S_1 yields

$$S_1 S_2 \dot{x} = 0 \tag{8}$$

$$S_1 S_2 \ddot{x} = 0 \tag{9}$$

Since $S_2\dot{x}=0$, equation (7) becomes

$$S_1^{-1}\ddot{x} + T_2 x = 0$$

or upon premulitiplying by $S_1 S_2 S_1$:

$$S_1 S_2 \ddot{x} + S_1 S_2 (S_1 T_2) x = 0.$$

Then (9) yields that $S_1 S_2 (S_1 T_2)\dot{x} = 0$ (10)

This process is repeated, yielding the following equations

$$A^{-1}B(A^{-1}C)^k \dot{x} = 0, \quad k = 0,1,2, \ldots \tag{11}$$

Since R has rank n, and $\dot{x}$ is an n vector, equations (11) imply that $\dot{x}(t)$ is identically zero. Thus $\ddot{x}$ is also zero and from equation (7), $T_2 x = 0$. Since T_2 is nonsingular, $x(t)$ must also be identically zero. Thus, the only solution satisfying $\dot{V}(x,\dot{x}) = 0$ is $x = \dot{x} = 0$ and La Salle's invariance principle requires the equilibrium of (1) to be asymptotically stable.

Next, assume that the equilibrium of equation (1) is asymptotically stable. The proof that the rank of R is n follows directly from the argument given in [12]. The proof given there does not use the symmetry of the coefficient matrices but rather that the eigenvalue problem $(\lambda A - C)y = 0$ has positive real eigenvalues and a complete set of eigenvectors. This is the case here since, $A^{-1}C$ is symmetrizable and by property (*ii*) has a complete set of eigenvectors. Also, $A^{-1}C$ has positive eigenvalues by hypothesis.

Another interpretation of the stability result for systems with semidefinite damping is given by Moran [11] for symmetric systems. This result states that the equilibrium is asymptotically stable if and only if none of the modal vectors of the undamped problem (i.e., equation (1) with $S_2 = 0$) lie in the null space of the damping matrix. That this result holds true for the system of Theorem IV follows directly from the nonsingularity of S_1. It is easy to verify the following equivalent result.

Corollary V. If $S_1 = T_1$, if the eigenvalues of $A^{-1}C$ are all positive real numbers and if the eigenvalues of $A^{-1}B$ are non-negative then the equilibrium of equation (1) is asymptotically stable if and only if none of the eigenvectors of $A^{-1}C$ lie in the null space of $A^{-1}B$.

A result on the instability of symmetrizable systems ($T_1 = S_1$) can also be easily obtained as the next statement indicates.

Theorem VI. If $S_1 = T_1$ and if $A^{-1}C$ has all negative real eigenvalues, then the equilibrium of equation (1) is unstable.

This result follows from examining the eigenvalue problem (6) in terms of quadratic forms. Let $\bar{r}^T$ denote the complex conjugate transpose of r. Premultiplying (6) by $\bar{r}^T$ yields the scalar equation

$$\lambda^2 + \bar{r}^T T_1^{1/2} S_2 T_1^{1/2} r + \bar{r}^T T_1^{1/2} T_2 T_1^{1/2} r = 0$$

where $\bar{r}^T r = 1$. Solving this for λ yields

$$2\lambda_{n_{1,2}} = -\bar{r}^T T_1^{1/2} S_2 T_1^{1/2} r \pm [(\bar{r}^T T_1^{1/2} S_2 T_1^{1/2} r)^2 - 4\bar{r}^T T_1^{1/2} T_2 T_1^{1/2} r]^{1/2} \tag{8}$$

If the eigenvalues of $A^{-1}C$ are all negative then T_2 is negative definite [9] and

$$-4\bar{r}^T T_1^{1/2} T_2 T_1^{1/2} r = -4\bar{q}^T T_2 q > 0$$

for all eigenvectors r. Hence, the discriminant is always greater in magnitude than $\bar{r}^T T_1^{1/2} S_2 T_1^{1/2} r$, so that one of the pair $\lambda_{n_{1,2}}$ is a positive real number.

The following results pertain to those systems that have symmetrizable coefficients but do not satisfy the condition of Theorem II ($T_1 \neq S_1$). Then one cannot transform (3) into a symmetric system. As pointed out in [10], however, the problem may be transformed into that of a damped gyroscopic system with symmetric stiffness and its stability may then be discussed in terms of the *KTC* theorem [6].

Theorem VII. If the symmetric matrix $(A^{-1}B)T_1 + T_1(A^{-1}B)^T$ is positive-definite and if $A^{-1}C$ does not have a zero eigenvalue, then the equilibrium of equation (1) is stable if and only if all of the eigenvalues of $A^{-1}C$ are positive numbers.

This result follows from calculating the symmetric part of the velocity-dependent term and applying the *KTC* theorem. If $S_1 \neq T_1$, then equation (3) becomes

$$(\lambda^2 I + \lambda T_1^{-1/2} A^{-1} B T_1^{1/2} + T_1^{1/2} T_2 T_1^{1/2}) r = 0$$

where $r = T_1^{-1/2} q$. The symmetric part of the coefficient of λ is

$$\frac{1}{2}(T_1^{-1/2} A^{-1} B T_1^{1/2} + T_1^{1/2}(A^{-1}B)^T T_1^{-1/2}) = \frac{1}{2} T_1^{-1/2}(A^{-1}BT_1 + T_1(A^{-1}B)^T) T_1^{-1/2}.$$

This last expression is positive-definite if and only if the symmetric matrix $A^{-1}BT_1 + T_1(A^{-1}B)^T$ is positive-definite, as assumed. Thus, according to the *KTC* theorem, the stability of (1) under these assumptions is determined completely by the eigenvalues of T_2, i.e., the eigenvalues of $A^{-1}C$. If $A^{-1}C$ has all positive eigenvalues then, as stated earlier, T_2 is positive-definite and (3) is stable. If $A^{-1}C = T_1 T_2$ has a negative eigenvalue, then T_2 is not positive-definite and (3) becomes unstable.

Examples

Several examples of asymmetric systems have appeared in the literature as illustrations of theories developed for systems lacking any symmetry. These examples are used here to provide an illustration of the foregoing theory and to serve as a comparison.

The first example is one considered by Washed and Bishop [3]:

$$I\ddot{x} + \begin{bmatrix} 2 & 4 \\ 1 & 2 \end{bmatrix} x + \begin{bmatrix} 10 & 8 \\ 0 & 1 \end{bmatrix} x = \begin{bmatrix} 1 \\ 0 \end{bmatrix} e^{2it} \tag{9}$$

The solution to (9) is presented in [3] as an example of a theory developed for general asymmetric systems. It so happens, however, that application of Theorem II in the foregoing shows that this system is equivalent to a related symmetric problem. Thus, the solution of (9) can be found by any number of well-known techniques developed for symmetric systems. In addition, Theorem III offers a solution to the stability problem posed in [3] for this class of symmetrizable systems.

Downloaded 02 May 2010 to 171.66.16.246. Redistribution subject to ASME license or copyright; see http://www.asme.org/terms/Terms_Use.cfm

To see that the example in (9) satisfies the conditions of Theorem II some minor matrix manipulations are required. Note, that

$$A^{-1}B=\begin{bmatrix}2 & 4\\ 1 & 2\end{bmatrix}=\begin{bmatrix}1.2461 & -.2769\\ -.2769 & .3115\end{bmatrix}\begin{bmatrix}2.8889 & 5.7778\\ 5.7778 & 11.5556\end{bmatrix}$$

$$A^{-1}C=\begin{bmatrix}10 & 8\\ 0 & 1\end{bmatrix}=\begin{bmatrix}1.2961 & -.2769\\ -.2769 & .3115\end{bmatrix}\begin{bmatrix}10 & 8.8889\\ 8.8889 & 11.1111\end{bmatrix}$$

so that $T_1 = S_1$, and by application of Theorem II the eigenvalue problem associated with equation (9) is similar to a symmetric eigenvalue problem.

According to the previous theorems the stability of equation (9) may be indicated by calculating the eigenvalues of $A^{-1}B$ and $A^{-1}C$. The eigenvalues of $A^{-1}B$ in this example are $\lambda_{1,2}=0,4$, and those of $A^{-1}C$ are $\lambda_{1,2}=1,\ 10$. Hence, $A^{-1}C$ has positive real eigenvalues and $A^{-1}B$ has non-negative real eigenvalues. Thus the results of Theorem V apply. To see if the equilibrium is asymptotically stable requires knowledge of the rank of

$$\begin{bmatrix}2 & 4\\ 1 & 1\\ 20 & 20\\ 10 & 10\end{bmatrix}\sim\begin{bmatrix}0 & 0\\ 1 & 2\\ 0 & 0\\ 1 & 1\end{bmatrix}\sim\begin{bmatrix}0 & 0\\ 1 & 0\\ 0 & 0\\ 0 & 1\end{bmatrix}$$

which is obviously $2 = n$. Thus, the result states that the equilibrium of this example is asymptotically stable. This is in agreement with the eigenvalue calculation for (9) which is given in [3] to be

$$\lambda_{1,2}=-1\pm 2i$$
$$\lambda_{3,4}=-1\pm i$$

where $i=\sqrt{-1}$.

As a second example, consider the asymmetric problem given by:

$$\begin{bmatrix}1 & 1\\ 0 & 1\end{bmatrix}\ddot{x}+\begin{bmatrix}9 & 20\\ 3 & 8\end{bmatrix}\dot{x}+\begin{bmatrix}-5 & -6\\ -4 & 0\end{bmatrix}x=0 \qquad (10)$$

Premultiplying this by A^{-1} yields

$$I\ddot{x}+\begin{bmatrix}6 & 12\\ 3 & 8\end{bmatrix}\dot{x}+\begin{bmatrix}-1 & -6\\ -4 & 0\end{bmatrix}x=0 \qquad (11)$$

The eigenvalues of $A^{-1}B$ are $\lambda_{1,2} = 7\pm(1/2)\sqrt{148}$ and those of $A^{-1}C$ are $\lambda_{1,2} = -1/2\pm(1/2)\sqrt{97}$. Thus, both coefficient matrices have real distinct eigenvalues and by (*ii*) are symmetrizable. However, a simple computation (see Appendix) shows that there does not exist a factorization of $A^{-1}B$ and $A^{-1}C$ such that $T_1 = S_1$. Thus, Theorems I–VI cannot be applied. However, the fact that $A^{-1}C$ has one negative eigenvalue suggests that this system may be unstable. Since $A^{-1}C$ does not have a zero eigenvalue suggests that Theorem VII may be applicable.

According to Theorem VII if $A^{-1}BT_1 + T_1(A^{-1}B)^T$ is positive-definite, then the equilibrium of equation (11) is unstable. To calculate T_2 note that $(A^{-1}C) = T_1T_2$, $T_1>0$, thus $T_2 = T_1^{-1}(A^{-1}C)$. Let T_1^{-1} be a general symmetric matrix denoted

$$T_1^{-1}=\begin{bmatrix}a & b\\ b & c\end{bmatrix}$$

where it is desired to calculate a, b, and c so that T_1 is positive-definite. Thus

$$T_2=\begin{bmatrix}a & b\\ b & c\end{bmatrix}\begin{bmatrix}-1 & -6\\ -4 & 0\end{bmatrix}=\begin{bmatrix}-a-4b & -6a\\ -b-4c & -6b\end{bmatrix}$$

Requiring T_2 to be symmetric and T_1 to be positive-definite yields the following relationships for a, b, and c

$$ac>b^2$$
$$6a=4(b+c).$$

One convenient solution is $a=2$, $b=0$, and $c=3$. Then, T_2 becomes

$$T_1\begin{bmatrix}\frac{1}{2} & 0\\ 0 & \frac{1}{3}\end{bmatrix}.$$

Thus $(A^{-1}B)T_1 + T_1(A^{-1}B)^T$ becomes

$$(A^{-1}B)T_1+T_1(A^{-1}B)^T=\begin{bmatrix}6 & \frac{11}{2}\\ \frac{11}{2} & \frac{16}{3}\end{bmatrix}$$

which is positive-definite. Thus, the hypothesis of Theorem VII is satisfied and the equilibrium of equation (11) is unstable. This analysis agrees with a calculation of the eigenvalues associated with (11) which are $\lambda_1 = 0.3742$, $\lambda_2 = -13.5133$, and $\lambda_{3,4} = 0.4035 \pm 0.2136\ i$, indicating an unstable equilibrium.

Discussion

It has been demonstrated that a certain class of asymmetric, damped linear dynamic systems can be shown to have behavior similar to an associated symmetric system. Namely, many of the results available for symmetric systems can be applied to asymmetric systems provided the coefficient matrices have real distinct eigenvalues. The examples used to illustrate these results are taken from literature [1–4] which develops a theory of general asymmetric systems without such restrictions. While these examples happen to satisfy the hypothesis of the theorems presented here, it should be pointed out that the theory developed in [1–4] is for a more general class of systems and that there is no reason to believe that all practical systems will satisfy conditions (*a*) and (*b*) in the foregoing.

It also should be noted that an earlier work by Walker [14] states more general stability theorems for the equilibrium of equation (1). His results are derived from a Liapunov method which makes no assumptions on the coefficients of (1) except that A is symmetric and positive-definite. In particular Walker shows that the equilibrium of equation (1) is asymptotically stable if there exists a symmetric positive-definite matrix G such that $GA^{-1}B$ is positive-definite and $GA^{-1}C$ is symmetric and positive-definite. This result immediately proves Theorem III in the foregoing with $G = S_1^{-1}$, since S_2 and T_2 are positive-definite by hypothesis.

There are many results available in stability theory for equation (1). The intent of this work is not to give a complete stability analysis of the equilibrium of (1) but rather to show conditions under which (1) may be treated with the theory available for symmetric second-order systems.

Acknowledgments

The author wishes to thank Prof. K. Huseyin for stimulating this work and Prof. J. A. Walker for his valuable comments. This work was conducted under NSF grant number MEA8112826.

References

1 Bishop, R. E. D., and Price, W. G., "An Investigation Into the Linear Theory of Ship Response to Waves," *Journal of Sound and Vibration*, Vol. 62, No. 3, 1979, pp. 353-363.

2 Fawzy, I., "Orthogonality of Generally Normalized Eigenvector and Eigenrows," *AIAA Journal*, Vol. 15, No. 2, 1977, pp. 276-278.

Downloaded 02 May 2010 to 171.66.16.246. Redistribution subject to ASME license or copyright; see http://www.asme.org/terms/Terms_Use.cfm

3 Washed, I. F. A., and Bishop, R. E. D., "On the Equations Governing the Free and Forced Vibrations of a General Non-Conservative System," *Journal of Mechanical Engineering Science*, Vol. 18, No. 1, 1976, pp. 6–10.

4 Fawzy, I., and Bishop, R. E. D., "On the Dynamics of Linear Non-Conservative Systems," *Proceedings of the Royal Society*, London, Series A, Vol. 352, 1976, pp. 25–40.

5 Huseyin, K., and Leipholz, H. H. E., "Divergence Instability of Multiple-Parameter Circulatory Systems," *Quarterly of Applied Math.*, Vol. 31, No. 2, 1973, pp. 185–197.

6 Zajac, E. E., "The Kelvin-Tait-Chetaev Theorem and Extensions," *Journal of Aeronautical Sciences*, Vol. 11, 1964, pp. 46–49.

7 Tausskey, O., and Zassenhaus, H., "On the Similarity Transformation Between a Matrix and its Transpose," *Pacific Journal of Mathematics*, Vol. 9, 1959, pp. 893–896.

8 Tausskey, O., "Positive Definite Matrices and Their Role in the Study of the Characteristic Roots of General Matrices," *Advances in Mathematics*, Vol. 2, 1968, pp. 175–186.

9 Tausskey, O., "Problem," *American Mathematical Monthly*, Vol. 66, 1959, p. 427.

10 Huseyin, K., *Vibrations and Stability of Multiple Parameter Systems*, Noordhoff, 1978.

11 Moran, T. J., "A Simple Alternative to the Routh-Hurwitz Criteria for Symmetric Systems," ASME JOURNAL OF APPLIED MECHANICS, Vol. 37, 1970, pp. 1168–1170.

12 Walker, J. A., and Schmitendorf, W. E., "A Simple Test for Asymptotic Stability in Partially Dissipative Symmetric Systems," ASME JOURNAL OF APPLIED MECHANICS, Vol. 40, 1973, pp. 1120–1121.

13 La Salle, J. P., "Stability Theory for Ordinary Differential Equations," *Journal of Differential Equations*, Vol. 4, 1968, pp. 57–65.

14 Walker, J. A., "On the Stability of Linear Discrete Dynamic Systems," ASME JOURNAL OF APPLIED MECHANICS, Vol. 37, 1970, pp. 271–275.

APPENDIX

The question of how to calculate the factors of a symmetrizable matrix is discussed in [10]. Here it is shown that the matrices $A^{-1}B = S_1S_2$ and $A^{-1}C = T_1T_2$ of the second example do not have any factorizations such that $T_1 = S_1$. Hence $A^{-1}B$ and $A^{-1}C$ cannot be simultaneously symmetrized by the same transformation. It is desired to find a symmetric positive-definite matrix P (from *iv*) such that $PA^{-1}B$ and $PA^{-1}C$ are both symmetric. To that end let

$$P=\begin{bmatrix} a & b \\ b & c \end{bmatrix},$$

then

$$PA^{-1}B=\begin{bmatrix} 6a+3b & 12a+8b \\ 6b+3c & 12b+8c \end{bmatrix}$$

and

$$PA^{-1}C=\begin{bmatrix} -a-4b & -6a \\ -b-4c & -6b \end{bmatrix}$$

Symmetry of both matrices then requires that

$$\begin{aligned} 6b+3c&=12a+8b \\ b+4c&=6a \end{aligned} \qquad (A1)$$

Positive-definiteness of P requires

$$\begin{aligned} a&>0 \\ ac&>b^2 \end{aligned} \qquad (A2)$$

It will be shown that the problem posed by (*A*1) and (*A*2) does not have a solution. Equation (*A*1) may be written in matrix form as

$$\begin{bmatrix} 14 & -3 \\ 1 & 4 \end{bmatrix}\begin{bmatrix} b \\ c \end{bmatrix}=6a\begin{bmatrix} 2 \\ 1 \end{bmatrix}$$

which has the unique solution

$$\begin{bmatrix} b \\ c \end{bmatrix}=a\begin{bmatrix} -2.73 \\ 2.18 \end{bmatrix}$$

for all values of a. Thus, $b = -2.73a$ and $c = 2.18a$ so that $b^2 = 7.45a^2$ and $ac = 2.18a^2$. Then

$$ac=2.18a^2<7.45a^2=b^2$$

and condition (*A*2) cannot be satisfied.

Downloaded 02 May 2010 to 171.66.16.246. Redistribution subject to ASME license or copyright; see http://www.asme.org/terms/Terms_Use.cfm

B. H. Tongue
Assistant in Research and Graduate Student.
Student Mem. ASME

E. H. Dowell
Professor.
Mem. ASME

Department of Mechanical and Aerospace Engineering,
Princeton University,
Princeton, N.J. 08544

Component Mode Analysis of Nonlinear, Nonconservative Systems

In this paper a method for attacking coupled linear-nonlinear problems is developed. This method allows one to express the equations of motion with a number of equations proportional to the number of nonlinear constraints on the system rather than to the number of linear modes of the system. Both steady state and transient solutions are investigated for a system possessing cubic nonlinearities.

Introduction

Certain structures can be viewed as being made up of components that behave linearly with a number of nonlinear mechanisms attached to them. An example would be an airplane with a linear fuselage and wing that contacts the ground through a nonlinear landing gear. Problems of this sort can be analyzed by examining the linear and nonlinear portions separately and then joining them through an appropriate constraint function. As will be shown, this simplifies the process of obtaining the full equations of motion for the structure and also expresses these equations in a very compact form. These equations of motion are analyzed for the case of steady state and transient oscillations. Several authors have studied the dynamics of interconnected systems in terms of their component parts [1-8]. The procedure to be used here is an extension of the method developed by Dowell [1].

Problem Formulation

Figure 1 is a mathematical model which could represent a fuselage and wing on a landing gear. The beam is assumed to be linear and its displacement is $w(x,t)$. Forces can be applied to the beam at discrete points. At x_k, the kth spring-mass-damper (SMD) is attached to the beam, and its displacement is given by z_k. The equations of motion can now be found by treating the beam and SMD independently and then constraining them to have a common point of attachment by the use of Lagrange multipliers.

The kinematic energy is expressed as:

$$T=\frac{1}{2}\sum_{i=1}^{I} M_i \dot{a}_i^2+\frac{1}{2}\sum_{j=1}^{J} \tilde{M}_j \dot{z}_j^2 \tag{1}$$

where M_i is the generalized mass of the beam associated with the ith eigenmode, a_i is the associated generalized coordinate, $\tilde{M}_j$ is the mass of the landing gear, and z_j is the landing gear displacement.

The potential energy is defined as:

$$V=\frac{1}{2}\sum_{i=1}^{I} M_i a_i^2 \omega_i^2+\frac{1}{2}\sum_{j=1}^{J} \tilde{M}_j \omega_{z_j}{}^2 z_j^2+\sum_{j=1}^{J} \epsilon_j \frac{z_j^4}{4} \tag{2}$$

where ω_i, ω_{z_j} are the natural frequencies of the beam and landing gear, respectively, and ϵ_j is a nonlinear spring constant associated with the landing gear.

One can introduce damping in the landing gear through a dissipation function:

$$D=\sum_{j=1}^{J}\left[\xi_{z_j}\omega_{z_j}\dot{z}_j^2\tilde{M}_j+\sigma_j\frac{\dot{z}_j^4}{4}\right] \tag{3}$$

where ξ_{z_j} is a linear damping coefficient and σ_j is a nonlinear damping coefficient.

The displacement of the beam can be expressed as a sum of its eigenmodes and generalized coordinates associated with the eigenmodes:

$$w(x,t)=\sum_{i=1}^{I} a_i(t)\phi_i(x) \tag{4}$$

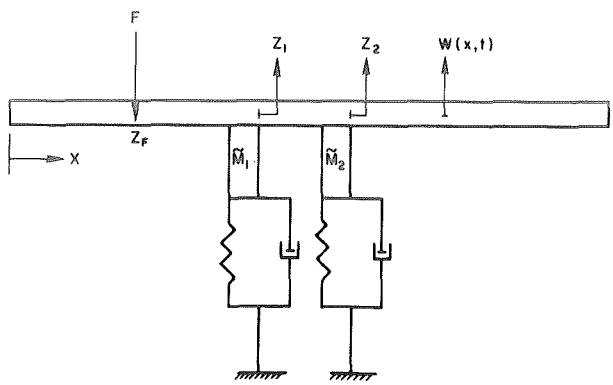

Fig. 1 Mathematical model of a body having both linear and nonlinear components

[1] This work was supported by NSF Grant CME-7916933.

Contributed by the Applied Mechanics Division for presentation at the 1983 ASME Applied Mechanics, Bioengineering, and Fluids Engineering Conference, Houston, Texas, June 20-22, 1983 of THE AMERICAN SOCIETY OF MECHANICAL ENGINEERS.

Discussion on this paper should be addressed to the Editorial Department, ASME, United Engineering Center, 345 East 47th Street, New York, N.Y. 10017, and will be accepted until two months after final publication of the paper itself in the JOURNAL OF APPLIED MECHANICS. Manuscript received by ASME Applied Mechanics Division, April 1982. Paper No. 83-APM-1.

Copies will be available until February, 1984.

Copyright © 1983 by ASME
Downloaded 02 May 2010 to 171.66.16.246. Redistribution subject to ASME license or copyright; see http://www.asme.org/terms/Terms_Use.cfm

The (constraint) conditions that equate the landing gear and fuselage (beam) displacements are:

$$z_j = \sum_{i=1}^{I} a_i(t)\,\phi_i(x_j) \tag{5}$$

The generalized nonconservative work can be expressed as:

$$\delta W_{NC} = \sum_{b=1}^{B}\sum_{i=1}^{I} F_b \phi_i(x_b)\,\delta a_i \tag{6}$$

where F_b is a force on the beam applied at point $x = x_b$.

The standard method of solution would be to use equation (5) to eliminate z_j and $\dot{z}_j$ from equations (1)–(3). The Lagrangian, $L = T - V$, could then be formed and Lagrange's equations:

$$\frac{d}{dt}\left(\frac{\partial L}{\partial \dot{a}_i}\right) - \frac{\partial L}{\partial a_i} + \frac{\partial D}{\partial \dot{a}_i} = Q_i \quad \text{where} \quad Q_i = \sum_{b=1}^{B} F_b \phi_i(x_b)$$

used to determine the equations of motion in terms of the a_i's. However one must note that even for a simple nonlinearity such as the cubic nonlinearity examined here, equations (2) and (3) involve taking a summation of I modes, raising the sum to the fourth power and then differentiating term by term. Obviously for more involved nonlinearities the calculations become even more elaborate. An alternate method is therefore applied. Equations (1)–(3) are left as they are but new functions:

$$f_j = \sum_{i=1}^{I} a_i(t)\,\phi_i(x_j) - z_j = 0 \quad j = 1,2,3,\ldots$$

are formed. These represent the constraint that the SMD's and the beam remain in contact. The Lagrangian is altered as follows,

$$L = T - V + \sum_{j=1}^{J} \beta_j f_j$$

where β_j are Lagrange multipliers.

Lagrange's equations can now be invoked with respect to a_i, z_j, and β_j, yielding three sets of equations:

$$M_i[\ddot{a}_i + \omega_i^2 a_i] - \sum_{j=1}^{J} \beta_j \phi_i(x_j) = \sum_{b=1}^{B} F_b \phi_i(x_b) \tag{7}$$

$$\tilde{M}_j[\ddot{z}_j + \omega_{z_j}^2 z_j + 2\xi_{z_j}\omega_{z_j}\dot{z}_j] + \epsilon_j z_j^3 + \sigma_j \dot{z}_j^3 + \beta_j = 0 \tag{8}$$

$$\sum_{i=1}^{I} a_i \phi_i(x_j) - z_j = 0 \tag{9}$$

Steady State Motion

To examine steady state behavior, the method of harmonic balance is employed. This involves expressing the variables in harmonic form:

$$\begin{aligned} F_b &= F_b^c \cos(\omega t) + F_b^s \sin(\omega t) \\ z_j &= z_j^c \cos(\omega t) + z_j^s \sin(\omega t) \\ a_i &= a_i^c \cos(\omega t) + a_i^s \sin(\omega t) \\ \beta_j &= \beta_j^c \cos(\omega t) + \beta_j^s \sin(\omega t) \end{aligned} \tag{10}$$

Equations (7)–(10) are then substituted into:

$$\int_0^{2\pi/\omega} [\;] \begin{matrix} \cos(\omega t) \\ \sin(\omega t) \end{matrix} dt = 0$$

This separates the first harmonic response. The resulting equations for the cosine terms are:

$$\sum_{i=1}^{I} a_i^c \phi_i(x_j) - z_j^c = 0 \tag{11}$$

$$M_i(\omega_i^2 - \omega^2)a_i^c - \sum_{j=1}^{J} \beta_j^c \phi_i(x_j) = \phi_i(x_b) F_b^c \tag{12}$$

$$\tilde{M}_j\{-\omega^2 z_j^c + \omega_{z_j}{}^2 z_j^c + 2\xi_{z_j}\omega_{z_j} z_j^s \omega\} + \frac{3}{4}\epsilon_j[(z_j^c)^3 + z_j^c (z_j^s)^2] + \frac{3}{4}\omega^3 \sigma_j[(z_j^s)^3 + z_j^s (z_j^c)^2] + \beta_j^c = 0 \tag{13}$$

and a similar set is obtained for the sine terms. Equation (13) can be solved for β_j^c, the result substituted in equation (12), and equation (12) (in terms of a_i^c) substituted into equation (11) to yield:

$$\sum_{i=1}^{I} \phi_i(x_k) \left[\frac{\sum_{b=1}^{B} \phi_i(x_b) F_b^c + \sum_{j=1}^{J} \phi_i(x_j) \left[\begin{matrix} -\frac{3}{4}\epsilon_j[(z_j^c)^3 + z_j^c (z_j^s)^2] \\ -\frac{3}{4}\omega^3 \sigma_j[(z_j^s)^3 + (z_j^c)^2 z_j^s] \\ -\tilde{M}_j\{z_j^c(\omega_{z_j}^2 - \omega^2) + 2\xi_{z_j}\omega_{z_j}\omega z_j{}^s\} \end{matrix} \right]}{M_i[\omega_i^2 - \omega^2]} \right] - z_k^c = 0 \quad k = 1,2,\ldots \tag{14}$$

A similar expression is obtained for the sine terms.

Note that all the nonlinear terms are explicit and separate from the linear portion. By setting ϵ_j and σ_j to zero, one can reduce the results to the linear case. If the standard solution method had been used the result would have been $2I$ equations, where I is the number of linear modes. Using the present component mode method has reduced the number of equations to $2J$ where J is the number of nonlinear constraints. If the mechanism under examination is comprised of many linear modes but only a few nonlinear constraints, then one can see that a great reduction in the number of equations takes place. Furthermore, the formulation lends itself to numerical calculation. After initially setting ϵ_j and σ_j to zero, one can solve the linear problem and then slowly increase the nonlinear coefficients to avoid the convergence problems sometimes associated with obtaining solutions to nonlinear problems.

Transient Motion

In order to study the transient motion of the system, one must formulate a new solution to equations (7)–(9). Two approaches will be illustrated, the primitive mode method and the reduced mode method.

To develop the primitive mode method, one expands a_i, z_j, and β_j in a truncated Taylor series in time:

Downloaded 02 May 2010 to 171.66.16.246. Redistribution subject to ASME license or copyright; see http://www.asme.org/terms/Terms_Use.cfm

$$a_i(t+\Delta t) = a_i(t) + \dot{a}_i(t)\,\Delta t + \ddot{a}_i(t)\left(\frac{\Delta t}{2}\right)^2$$

$$z_j(t+\Delta t) = z_j(t) + \dot{z}_j(t)\,\Delta t + \ddot{z}_j(t)\left(\frac{\Delta t}{2}\right)^2 \tag{15}$$

$$\beta_j(t+\Delta t) = \beta_j(t) + \dot{\beta}_j(t)\,\Delta t + \ddot{\beta}_j(t)\left(\frac{\Delta t}{2}\right)^2$$

Assume that $a_i(0)$, $\dot{a}_i(0)$, $z_j(0)$, and $\dot{z}_j(0)$ are known. Inserting equation (8) into equation (7) and using (9) to express $\ddot{z}_j$ in terms of $\ddot{a}_i$ yields:

$$M_i\ddot{a}_i(t) + \sum_{j=1}^{J}\phi_i(x_j)\tilde{M}_j\sum_{k=1}^{I}\ddot{a}_k\phi_k(x_j) = \sum_{b=1}^{B}F_b\phi_i(x_b) - a_i\omega_i{}^2M_i - \sum_j\phi_i(x_j)[\epsilon_j z_j{}^3 + \tilde{M}_j\omega_{z_j}{}^2 z_j + 2\tilde{M}_j\xi_{z_j}\omega_{z_j}\dot{z}_j + \sigma_j\dot{z}_j{}^3] \tag{16}$$

These equations can be expressed in matrix form as

$$\left[\sum_{j=1}^{J}\Phi_j\Phi_j^T\tilde{M}_j + [M]\right]\begin{Bmatrix}\ddot{a}_1\\ \cdot\\ \cdot\\ \cdot\\ \ddot{a}_I\end{Bmatrix} = \begin{bmatrix}\Phi_1^F & \Phi_2^F & \cdots & \Phi_B^F\end{bmatrix}\begin{Bmatrix}F_1\\ \cdot\\ \cdot\\ \cdot\\ F_B\end{Bmatrix} - [\Omega^2]\,[M]\begin{Bmatrix}a_1\\ \cdot\\ \cdot\\ \cdot\\ a_I\end{Bmatrix} - [\Phi_1\ \ \Phi_2\ \cdots\ \Phi_j]\begin{Bmatrix}\tilde{M}_1 z_1\omega_{z_1} + \epsilon_1 z_1^3 + \sigma_1\dot{z}_1^3 + 2\tilde{M}_1\xi_{z_1}\omega_{z_1}\dot{z}_1\\ \cdot\\ \cdot\\ \cdot\\ \tilde{M}_J z_J\omega_{z_J}{}^2 + \epsilon_J z_J^3 + \phi_J\dot{z}_J^3 + 2\tilde{M}_J\xi_{z_J}\omega_{z_J}\dot{z}_J\end{Bmatrix}$$

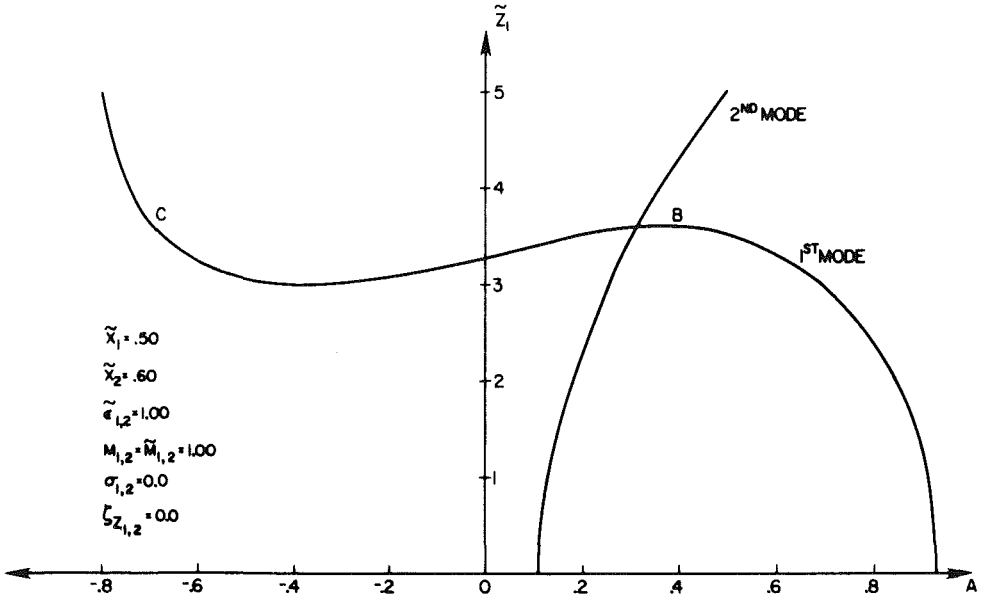

Fig. 2 Amplitude of SMD with stiffening springs at $\tilde{x}_1 = 0.5$ ($\tilde{z}_1$) versus ratio of SMD at $\tilde{x}_2$ versus amplitude of SMD at $\tilde{x}_1 = 0.5$ (A) for first two modes of system

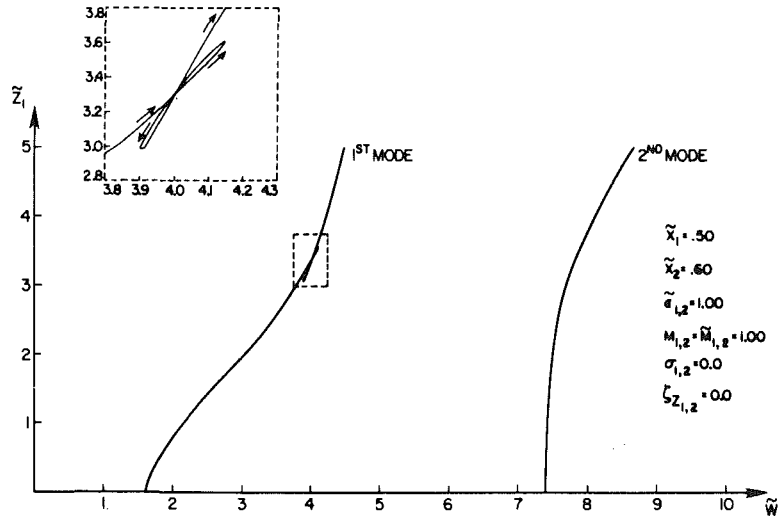

Fig. 3 Amplitude of SMD with stiffening springs at $\tilde{x}_1 = 0.5$ ($\tilde{z}_1$) versus nondimensionalized frequency of vibration ($\tilde{\omega}$) for first two modes of system

Downloaded 02 May 2010 to 171.66.16.246. Redistribution subject to ASME license or copyright; see http://www.asme.org/terms/Terms_Use.cfm

where

$$\Phi_k = \begin{bmatrix} \phi_1(x_k) \\ \cdot \\ \cdot \\ \phi_I(x_k) \end{bmatrix}; \quad \Phi_j^F = \begin{bmatrix} \phi_1(x_j) \\ \cdot \\ \cdot \\ \phi_B(x_j) \end{bmatrix};$$

$$[M] = \begin{bmatrix} M_1 & & \\ & \cdot & \\ & & M_I \end{bmatrix}, \quad [\Omega^2] = \begin{bmatrix} \omega_1 & & \\ & \cdot & \\ & & \omega_I^2 \end{bmatrix}$$

Note that this yields I equations, where I is the number of linear modes in the system, which can be large for a complex system. One might therefore seek a method to reduce the number of equations in a manner similar to that used for steady state vibrations. This reduction can be accomplished in the following manner:

One forms a convolution integral from equation (7):

$$M_i a_i(t) = \frac{1}{\omega_i M_i} \int_0^t \sin\ \omega_i(t-\tau)\Big[\sum_{j=1}^{J} \beta_j(\tau)\phi_i(x_j) + \sum_{b=1}^{B} F_b(\tau)\phi_i(x_b)\Big] d\tau \tag{17}$$

Equations (8), (9), and (17) then yield:

$$z_j(t) = \sum_{i=1}^{I} \frac{\phi_i(x_j)}{\omega_i M_i} \int_0^t \sin\omega_i(t-\tau)\Big[\sum_{b=1}^{B} F_b(\tau)\phi_i(x_b) - \sum_{j=1}^{J} \phi_i(x_j)[\tilde{M}_j \ddot{z}_j(\tau) + \tilde{M}_j \omega_{z_j}{}^2 z_j(\tau) + 2\xi_j \omega_{z_j} \dot{z}_j(\tau) + \epsilon_j(z_j(\tau))^3 + \sigma_j(\dot{z}_j(\tau))^3]\Big] \tag{18}$$

By differentiating twice one obtains:

$$\ddot{z}_j(t) + \sum_{i=1}^{I} \frac{\phi_i(x_j)}{M_i} \sum_{k=1}^{J} \phi_i(x_k)\tilde{M}_k \ddot{z}_k(\tau) = \Sigma \frac{\phi_i(x_j)}{M_i} \times \begin{bmatrix} \omega_i \cos\omega_i t \int_0^t \sin\omega_i \tau\ G(\tau)\, d\tau \\ -\omega_i \sin\omega_i t \int_0^t \cos\omega_i \tau\ G(\tau)\, d\tau \\ +G(t) \end{bmatrix} \tag{19}$$

where

$$G(\tau) = \sum_{b=1}^{B} F_b(\tau)\phi_i(x_b) - \sum_{j=1}^{J} \phi_i(x_j)[\tilde{M}_j z_j(\tau)[\omega_{z_j}{}^2 - \omega_i^2] + 2\xi_j \tilde{M}_j \omega_{z_j} \dot{z}_j(\tau) + \epsilon_j(z_j(\tau))^3 + \sigma_j(\dot{z}_j(\tau))^3]$$

This will be called the reduced mode method. Using either method, one would take the newly calculated acceleration terms along with the known velocities and displacements to form a new displacement at time $= t+\Delta t$. The velocities at $t+\Delta t$ can be formed from the displacements at t and $t+\Delta t$ and the procedure can then be repeated.

The reduced mode method involves a group of equations equal to the number of nonlinear components as opposed to the number of linear modes. The integral in equation (19) is in such a form that it can be incremental for each new time step and the result added to the previous calculation. If it had been left in a form such as equation (17), one would have to recalculate from 0 to $t+\Delta t$ for each new incremental time step. This would make the procedure quite inefficient for the determination of long time histories.

Results

Steady State, Free Vibration. By setting σ_j to zero and varying ϵ_j one can reproduce the typical results for a stiffening spring [9]. By altering parameters of the system, a new phenomenon can be observed. If the beam is treated as pinned (by suitably defining ϕ_i) and the position of the two SMD's are taken as $\tilde{x}_1 = 0.50$, $\tilde{x}_2 = 0.60$, with $\epsilon_j = 1.00$ then Figs. 2 and 3 are obtained. $\tilde{z}_1$ represents the nondimensionalized oscillation amplitude of the SMD at midbeam ($\tilde{x}_1 = 0.5$). The ratio of the second SMD's oscillation amplitude to the first is given by A. Other choices of $\tilde{x}_1$, $\tilde{x}_2$, and ϵ_j lead to qualitatively similar results. Figure 2 represents A versus $\tilde{z}_1$, the ratio of the second to first SMD amplitudes versus the first SMD amplitude. Figure 3 presents the nondimensional frequency of oscillation, $\tilde{\omega}$, versus $\tilde{z}_1$. Results are shown for the first two system modes, although a total of eight modes were retained in the numerical calculation and the method readily permits higher mode results to be obtained.

An interesting result occurs at point B in Fig. 2. If the amplitude $\tilde{z}_1$ is steadily increased then A will suddenly jump to a different value (point C). The phenomenon can be understood by examining the solution space. A solution point is formed by the intersection of two surfaces of the form $g_i(\tilde{z}_1, \tilde{\omega}, A)$ for two SMD's. If one picks a specific $\tilde{z}_1$ then the problem reduces to the intersection of two curves of the form $f_i(\tilde{\omega}, A)$. This is illustrated in Fig. 4. Figure 4(a) shows a typical solution. f_1 and f_2 intersect at two points, E and F, which define solutions to the equations of motion. As $\tilde{z}_1$ is

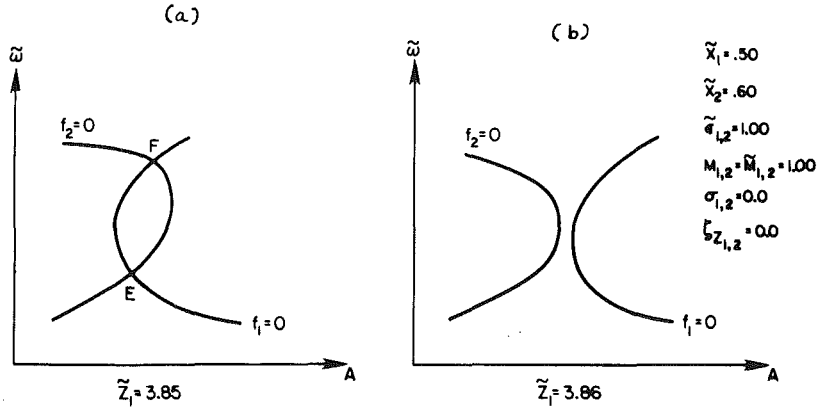

Fig. 4 Nondimensionalized frequency of oscillation ($\tilde{\omega}$) versus ratio of second SMD's vibration amplitude to first SMD's vibration amplitude (A), for first SMD amplitude (z_1)

Downloaded 02 May 2010 to 171.66.16.246. Redistribution subject to ASME license or copyright; see http://www.asme.org/terms/Terms_Use.cfm

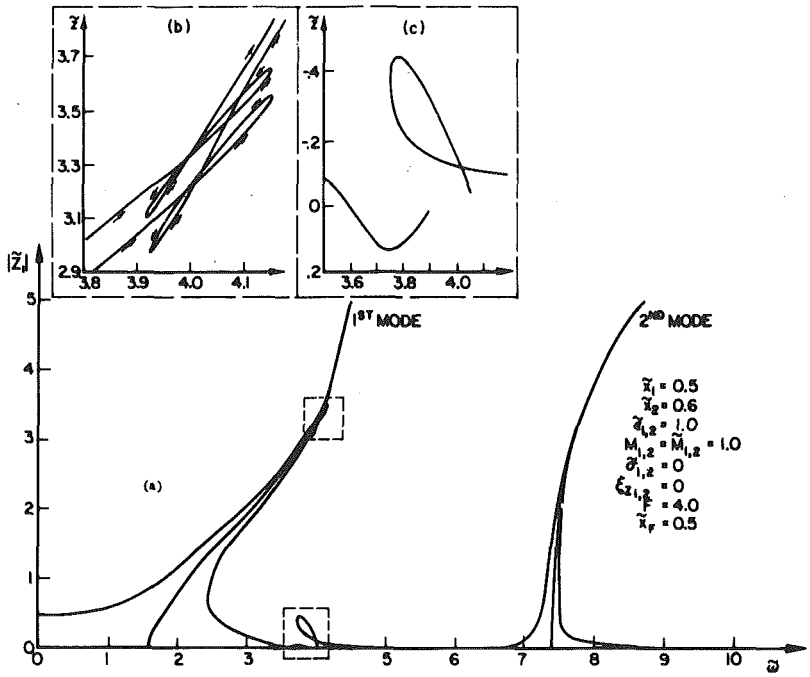

Fig. 5 Amplitude of forced vibrations of SMD with stiffening springs $\tilde{x}_1 = 0.5$ ($\tilde{z}_1$) versus nondimensionalized frequency of vibration ($\tilde{\omega}$) for first two modes of system

Table 1 Ratio of time required by primitive mode method to calculate new position versus time required by reduced mode method

# SMD's \ # MODES	1	2	4	8	16	32	64	128
1	.29	.32	.36	.42	.55	.81	1.3	2.3
2	.30	.33	.37	.42	.52	.70	1.1	1.8
4	.25	.28	.31	.34	.39	.49	.68	1.1
8	.16	.18	.20	.21	.23	.27	.34	.48
16	.09	.10	.11	.13	.17	.21	.27	.39

increased, f_1 moves to the right and f_2 moves to the left. Therefore the points E and F approach each other, coalesce, and finally disappear due to the separation of the curves (Fig. 4(*b*)). One would expect that under the case of increasing $\tilde{z}_1$ the amplitude of $\tilde{z}_2$ would suddenly change. Note that this condition corresponds to a looping of the frequency locus (Fig. 3). Although the change in amplitude of $\tilde{z}_2$ is highly discontinuous, the change in the frequency of oscillation is not large.

Steady State, Forced Vibration. One would expect the forced response to resemble an envelope with upper and lower frequency branches surrounding the free response, as occurs in linear systems and similar nonlinear systems. To verify this, plots were generated for an input force applied at midbeam, $F_b = 4.0$. Figure 5(*a*) shows that the overall response does form an envelope. Moreover, the response has several additional interesting features. Figure 5(*b*) illustrates that the driven response has the same character at $|\tilde{z}| \approx 3.3$ and $\tilde{\omega} \approx 4.0$ as the free vibration case. Both the upper and lower branches form a "bow tie." Furthermore, at low amplitude the response forms a loop, as shown in Fig. 5(*c*). Also, the phase for the forced nonlinear case changes more than in the linear case. In a linear system, the phase will change by 180 deg after each eigenfrequency is passed. One can see from Fig. 5(*c*) that the phase is changing sign more rapidly with frequency than this for the lower branch of the nonlinear response. This unexpected behavior for the lower branch is especially interesting since one would expect a more linear response due to the small amplitude of the vibration. The reasons for this behavior is that at the frequencies where this behavior occurs, z_2 is at least an order of magnitude greater than z_1. Thus the nonlinear behavior of z_2 causes the looping of the response for small z_1.

Transient Response. For transient vibration the principal question is that of computational efficiency. Therefore, detailed results are omitted and only this question is addressed.

At first glance it may appear that equation (19) is generally computationally superior to equation (17) because of the smaller number of equations to be solved. However, the terms used to evaluate z at each step are rather lengthy. One can determine the amount of computer time needed for each calculation and by forming the ratio of the number of seconds needed for the primitive mode method versus the number of seconds needed for the reduced mode method, for different numbers of modes and SMD's, one can decide which method is more efficient. The results of such a calculation are displayed in Table 1. Note that only for a small number of SMD's and a large number of linear component modes does the reduced method outperform the primitive mode method. Thus, in spite of the elegance of the reduced mode method, the primitive mode method may prove superior from a calculation point of view for transient motion unless the number of linear modes is very large and the number of nonlinear components is small.

Conclusions

The method of component mode analysis offers a convenient method for generating the equations of motion for

Downloaded 02 May 2010 to 171.66.16.246. Redistribution subject to ASME license or copyright; see http://www.asme.org/terms/Terms_Use.cfm

coupled linear-nonlinear systems, and the formulation facilitates the investigation of various nonlinear phenomena. The use of Lagrange multipliers allows a separation of the linear and nonlinear portion of the problem and yields a number of equations that is proportional to the number of nonlinear constraints rather than to the number of modes in the linear components of the system. This greatly simplifies the solution procedure for a system with a large number of linear modes, but a small number of nonlinear components. Computational cost advantages are also obtained for steady state variations, but are generally less for transient vibrations.

References

1 Dowell, E. H., "Component Mode Analysis of a Simple Nonlinear, Nonconservative System," ASME JOURNAL OF APPLIED MECHANICS, Vol. 47, 1980, pp. 172–176.

2 Saczalski, R. S., and Juang, T. C., "Coupled Response of Spatial Vibratory Structures Mounted to Isotropic Plate Elements," ASME *Journal of Engineering for Industry*, Vol. 94, 1972, pp. 15–22.

3 Yang, W. H., "Vibrations of a Plate With Internal Constraints," ASME JOURNAL OF APPLIED MECHANICS, Vol. 41, 1974, pp. 1072–1074.

4 Bishop, R. E. D., and Johnson, D. C., *The Mechanics of Vibration*, Cambridge University Press, 1960.

5 Jacquot, R. G., and Soedel, W., "Vibrations of Elastic Surface Systems Carrying Dynamic Elements," *Journal of the Acoustical Society of America*, Vol. 47, 1970, pp. 1354–1358.

6 Dowell, E. H., "Free Vibrations of a Linear Structure With Arbitrary Support Conditions," ASME JOURNAL OF APPLIED MECHANICS, Vol. 38, 1971, pp. 595–600.

7 Hallquist, J., and Snyder, V. W., "Linear Damped Vibrating Structures With Arbitrary Support Conditions," ASME JOURNAL OF APPLIED MECHANICS, Vol. 40, 1973, pp. 312–313.

8 Klein, L., "Vibrations of Constrained Plates by a Rayleigh-Ritz Method Using Lagrange Multipliers," *Quarterly Journal of Mechanics and Applied Mathematics*, Vol. 30, 1977, pp. 51–70.

9 Meirovitch, L., *Elements of Vibration Analysis*, McGraw-Hill, New York, 1975, pp. 373–380.

Downloaded 02 May 2010 to 171.66.16.246. Redistribution subject to ASME license or copyright; see http://www.asme.org/terms/Terms_Use.cfm

Journal of Applied Mechanics

Brief Notes

A Brief Note is a short paper that presents a specific solution of technical interest in mechanics but which does not necessarily contain new general methods or results. A Brief Note should not exceed 1500 words *or equivalent* (a typical one-column figure or table is equivalent to 250 words; a one line equation to 30 words). Brief Notes will be subject to the usual review procedures prior to publication. After approval such Notes will be published as soon as possible. The Notes should be submitted to the Technical Editor of the JOURNAL OF APPLIED MECHANICS. Discussions on the Brief Notes should be addressed to the Editorial Department, ASME, United Engineering Center, 345 East 47th Street, New York, N. Y. 10017, or to the Technical Editor of the JOURNAL OF APPLIED MECHANICS. Discussions on Brief Notes appearing in this issue will be accepted until two months after publication. Readers who need more time to prepare a Discussion should request an extension of the deadline from the Editorial Department.

Stability of Nonparallel Developing Flow in a Pipe to Nonaxisymmetric Disturbances

V. K. Garg[1]

Linear spatial stability of the nonparallel developing flow in a rigid circular pipe has been studied at several axial locations for nonaxisymmetric disturbances. The main flow velocity profile is obtained by Hornbeck's finite-difference method assuming uniform flow at entry to the pipe. The method of multiple scales is used to account for all the nonparallel effects. It is found that the nonparallel developing flow is most unstable to nonaxisymmetric disturbances with azimuthal wave number n equal to unity. Axisymmetric disturbances are, however, more unstable than nonaxisymmetric disturbances with $n \geq 2$ except in the near-entry region. The results show that the parallel flow theory overpredicts the critical Reynolds number by as much as 136.5 percent in the near entry region for the $n = 1$ disturbance. The present results compare well with the available experimental data.

Introduction

It is well known that while the Hagen-Poiseuille flow is stable to all infinitesimal disturbances [1, 2], the developing flow in a circular pipe is unstable [3, 4]. However, both the aforementioned studies treated the developing flow as parallel which is not really true. Shen et al. [5] did consider the effect of the radial component of velocity on the otherwise parallel flow stability of the Sparrow et al. profile [6] but found that the minimum critical Reynolds number dropped only to 19,670 from the value of 19,900 for the parallel flow theory. In contrast, Garg and Gupta [7] considered all nonparallel effects while studying the stability of the Hornbeck profile [8], considered to be superior to the Sparrow et al. profile [9], and found that the minimum critical Reynolds number dropped to only 9700 from the value of 11,700 for the parallel flow theory. However, all these studies assumed the disturbance to be axisymmetric.

Spielberg and Timan [10] have shown that Squire's theorem [11] is not applicable to axisymmetric flows, and it is known [1] that the Hagen-Poiseuille flow is least stable to nonaxisymmetric disturbances with azimuthal wave number equal to unity. Even though the developing flow in a pipe, taken as parallel flow, is found to be more unstable to axisymmetric disturbances in the near-entry region [12, 13], there is no apriori reason to believe that the actual nonparallel developing flow would also show a similar behavior. We, therefore, consider the spatial stability of the nonparallel developing flow in a pipe to infinitesimal nonaxisymmetric disturbances.

Analysis

For the flow of an incompressible, Newtonian fluid in the inlet region of a rigid circular pipe of radius a, we define the following nondimensional variables

$$X = \frac{x}{a}, r = \frac{\hat{r}}{a}, T = \frac{tu_a}{a}, \mathrm{Re} = \frac{u_a a}{\nu},$$

where x and $\hat{r}$ are the axial and radial coordinates measured from the inlet section and the pipe axis, respectively, u_a is the average velocity of the flow, ν is the kinematic viscosity of the fluid, and Re is the Reynolds number of the flow. Considering an infinitesimal nonaxisymmetric disturbance with dimensionless velocity components $u(X, r, \theta, T)$, $v(X, r, \theta, T)$, and $w(X, r, \theta, T)$ in the axial, radial, and tangential directions, respectively, and dimensionless pressure $p(X,r,\theta,T)$ superimposed on the main flow, where θ is the azimuthal coordinate of the cylindrical coordinate system, we follow the analysis described in [14] for the annular flow. The difference is that r varies from 0 to 1, and the boundary conditions at $r = 0$ for the regular problem are

$$p = u = v + iw = 0 \quad \text{for} \quad n = 1,$$
$$p = u = v = w = 0 \quad \text{for} \quad n \neq 1,$$

and for the adjoint problem are

$$u^* = 0, \quad rp^* \to nv^* \quad \text{for all} \quad n,$$
$$v^* + iw^* = 0 \quad \text{for} \quad n = 1,$$

and

$$v^* = w^* = 0 \quad \text{for} \quad n \neq 1,$$

where n is the azimuthal wave number of the disturbance, and the superscript * is for the adjoint variables. The boundary conditions at the pipe wall ($r = 1$) require that the disturbance velocity components vanish for both the regular and the adjoint problems.

[1] Professor, Department of Mechanical Engineering, Indian Institute of Technology, Kanpur, India. Presently, Adjunct Professor, Department of Mechanical Engineering, Naval Postgraduate School, Monterey, Calif. 93940. Mem. ASME.

Manuscript received by ASME Applied Mechanics Division, January, 1982; final revision, July, 1982.

Copyright © 1983 by ASME
Downloaded 02 May 2010 to 171.66.16.246. Redistribution subject to ASME license or copyright; see http://www.asme.org/terms/Terms_Use.cfm

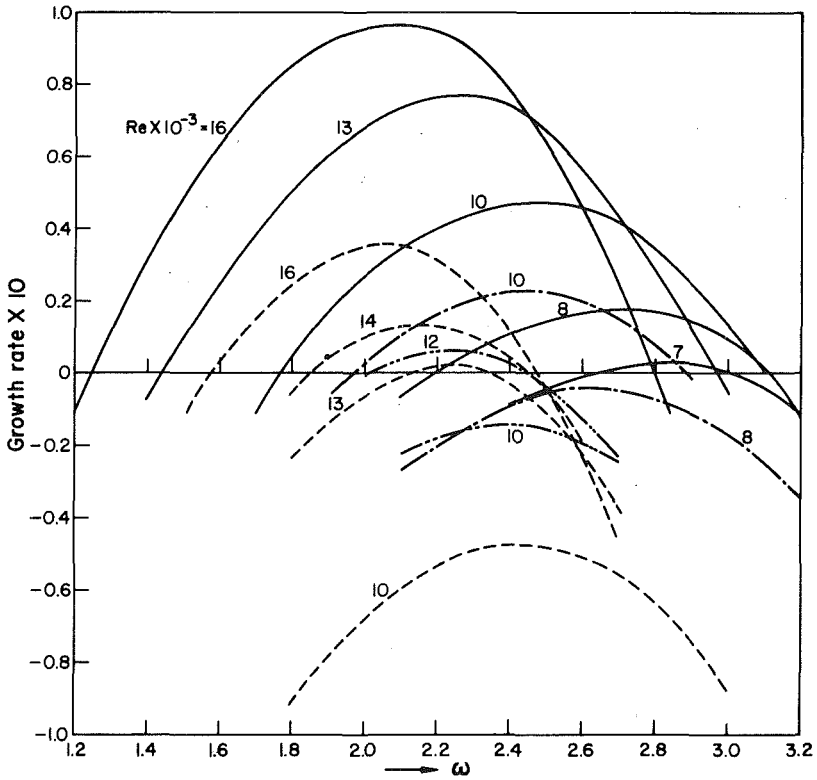

Fig. 1 Various growth rates at $\bar{X} = 0.001$.
——, $g_w(\bar{X}, r_w)$; – – –, $g_v(\bar{X}, 0)$ for $n = 1$. —— · ——, $g_w(\bar{X}, r_w)$ for $n = 2$.
—— · · ——, $g_w(\bar{X}, r_w)$ for $n = 3$.

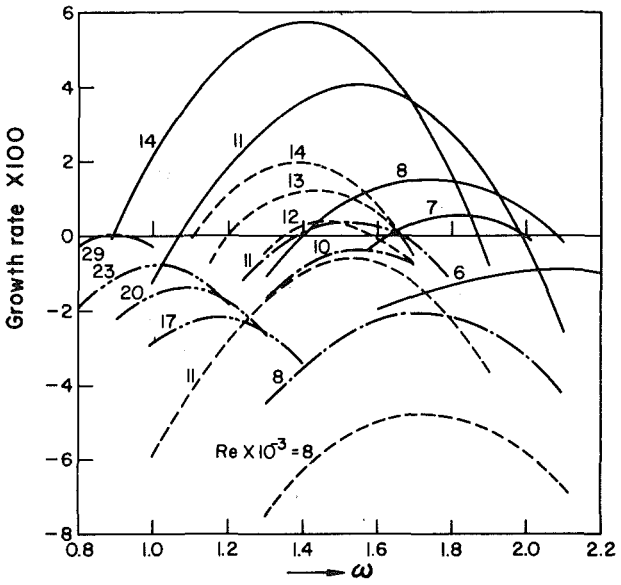

Fig. 2 Various growth rates at $\bar{X} = 0.002$.
——, $g_w(\bar{X}, r_w)$; – – –, $g_v(\bar{X}, 0)$ for $n = 1$. —— · ——, $g_w(\bar{X}, r_w)$ for $n = 2$.
—— · · ——, $g_w(\bar{X}, r_w)$ for $n = 3$.

It is instructive to note the solution of the adjoint problem is *singular* at $r = 0$ for $n = 1$. It is perhaps this singularity that makes the $n = 1$ disturbances so different from those for which $n = 0$, 2, or 3 (see the next section).

Results

Growth rates $g_v(X, r)$ and $g_w(X, r)$, based, respectively, on the radial and tangential components of disturbance velocity, and $g_E(X)$, based on the energy density E of the disturbance following Shen [15], were obtained at several axial locations. Expressions for the growth rates are available in [14]. Since the main flow velocity field was obtained at a given $\bar{X} = X/\mathrm{Re}$ instead of X, all growth rates have been obtained for a given $\bar{X}$ value, and are, hereafter, referred to as functions of $\bar{X}$. Also, u vanishes within $0 < r < 1$ so that its relative change would become infinite there. We should not therefore consider the growth rate based on u. Amongst $g_E(\bar{X})$, $g_v(\bar{X}, r)$, and $g_w(\bar{X}, r)$, it was found that the maximum value of g_w is the largest at a given $\bar{X}$. It is also known that for the non-parallel flow stability, one gets different wave numbers for different disturbance properties. It was found, however, that the modified wave numbers are little different from the parallel-flow wave numbers given elsewhere [12]. Therefore, the modified wave numbers, although computed, are not reported here.

Table 1 Values of r_w for various $\bar{X}$

$\bar{X}$	r_w^a		
	$(n=1)$	$(n=2)$	$(n=3)$
0.001	0.9200–0.9425	0.9200–0.9300	0.9250–0.9325
0.002	0.8925–0.9200	0.9000–0.9250	0.9125–0.9275
0.0035	0.8725–0.9050	0.8950–0.9125	–
0.005	0.8625–0.9025	–	–
0.007	0.8525–0.8925	–	–

[a] r_w varies slightly with Re and ω.

Figures 1–5 show the variation of $g_w(\bar{X}, r_w)$ and $g_v(\bar{X}, 0)$ with the dimensionless disturbance frequency ω at $\bar{X} = 0.001$, 0.002, 0.0035, 0.005, and 0.007. Whereas $g_v(\bar{X}, r)$ is found to be maximum at the pipe axis, g_w is maximum at the radial position r_w. The value of r_w is close to that corresponding to the boundary layer edge in the developing flow. Actual values of r_w are listed in Table 1. Results for $n = 2$ and 3 are shown only for $\bar{X} \leq 0.0035$ since critical Reynolds number for such disturbances increases rapidly with $\bar{X}$ (cf. Fig. 7). From these

Downloaded 02 May 2010 to 171.66.16.246. Redistribution subject to ASME license or copyright; see http://www.asme.org/terms/Terms_Use.cfm

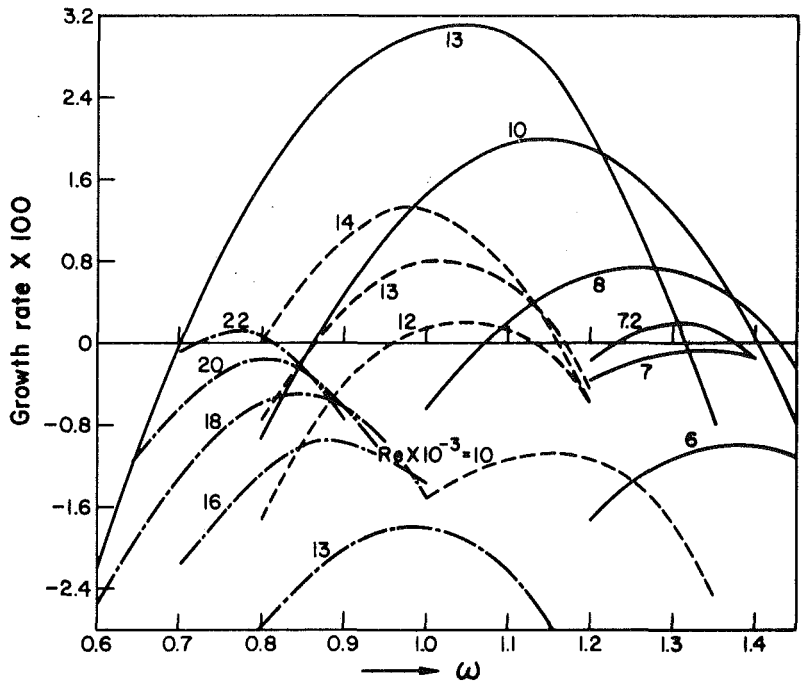

Fig. 3 Various growth rates at $\bar{X} = 0.0035$.
—, g_w $(\bar{X}, r_w)$; – – –, g_v $(\bar{X}, 0)$ for $n = 1$. — · —, g_w $(\bar{X}, r_w)$ for $n = 2$.

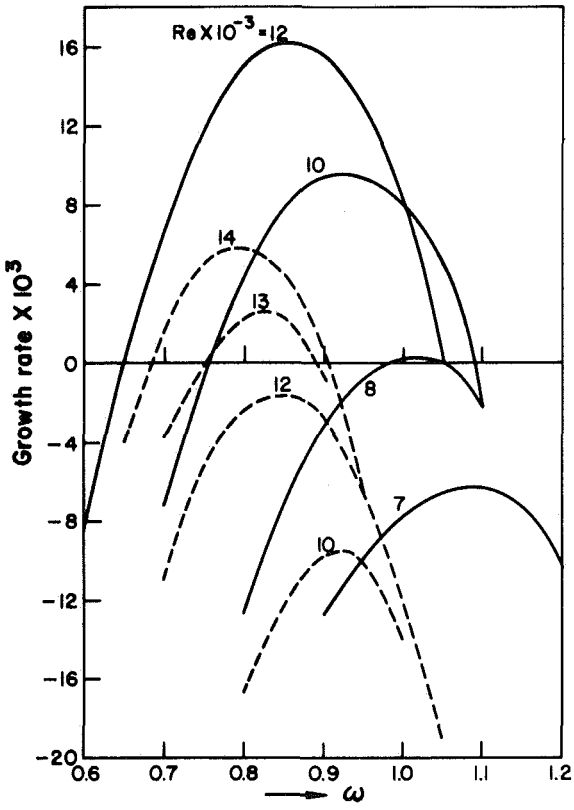

Fig. 4 Various growth rates at $\bar{X} = 0.005$ for $n = 1$.
—, g_w $(\bar{X}, r_w)$; – – –, g_v $(\bar{X}, 0)$.

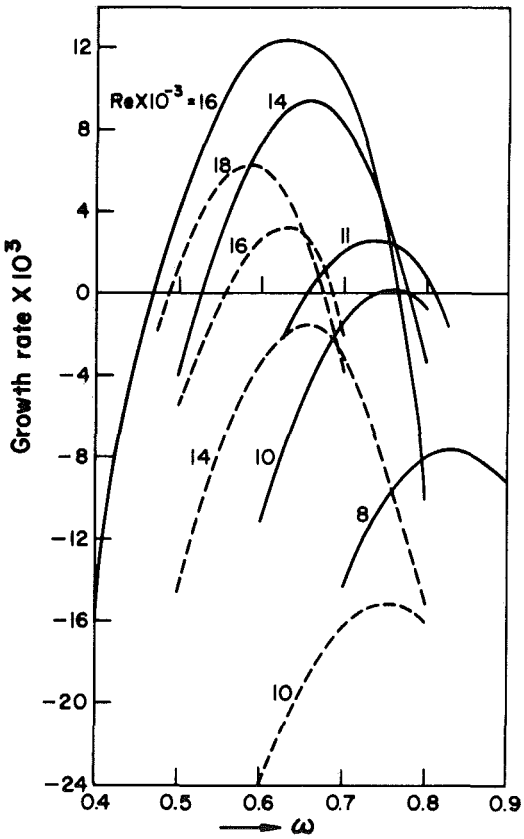

Fig. 5 Various growth rates at $\bar{X} = 0.007$ for $n = 1$.
—, g_w $(\bar{X}, r_w)$; – – –, g_v $(\bar{X}, 0)$.

figures, one can obtain the neutral curves corresponding to g_w $(\bar{X}, r_w)$ and g_v $(\bar{X}, 0)$. Figure 6 shows these neutral curves for $n = 1$ at different $\bar{X}$. Also included in this figure are the neutral curves for $n = 1$ based on the parallel flow theory [12]. In comparison to the results for the parallel flow theory, the nonparallel effects make the flow unstable at lower Reynolds numbers and for a wider range of ω. The actual amount of such an effect depends on the choice of growth rate used for determining the neutral curve. The growth rate g_w $(\bar{X}, r_w)$ gives the minimum critical Reynolds number at all $\bar{X}$.

Figure 7 shows the variation of critical Reynolds number

Downloaded 02 May 2010 to 171.66.16.246. Redistribution subject to ASME license or copyright; see http://www.asme.org/terms/Terms_Use.cfm

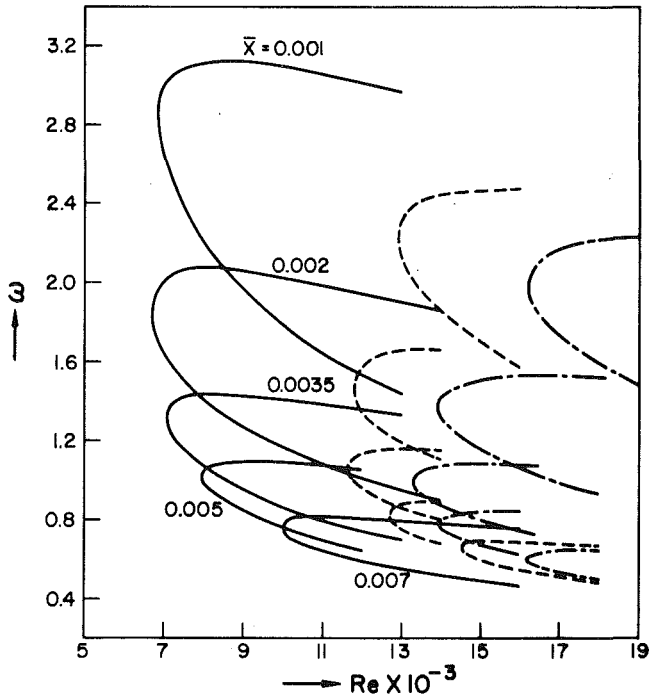

Fig. 6 Neutral curves at various axial locations for $n = 1$. ___, based on g_w $(\bar{X}, r_w)$; – – –, based on g_v $(\bar{X}, 0)$; ——– ——, based on parallel flow theory.

Re_c and critical frequency ω_c based on g_w $(\bar{X}, r_w)$, g_v $(\bar{X}, 0)$, and the parallel flow theory against $\bar{X}$. It is observed that while critical frequency decreases first sharply and then gradually with increasing $\bar{X}$ in the entry region, the critical Reynolds number versus $\bar{X}$ curves pass through a minimum except those for $n \geq 2$. The minimum critical Reynolds number for $n = 1$ corresponding to g_w $(\bar{X}, r_w)$, g_v $(\bar{X}, 0)$, and parallel flow theory are 6700, 11,600, and 13,250 occurring at $\bar{X} = 0.002$, 0.0035, and 0.0032, respectively. In comparison to the results based on g_w $(\bar{X}, r_w)$ the parallel flow theory over predicts the critical Reynolds number by 136.5 percent at $\bar{X} = 0.001$, by 107.5 percent at $\bar{X} = 0.002$, by 88.7 percent at $\bar{X} = 0.0035$, by 74.8 percent at $\bar{X} = 0.005$, and by 60.5 percent at $\bar{X} = 0.007$ for the $n = 1$ disturbance.

Also shown on Fig. 7 are the critical Reynolds number and frequency values obtained experimentally by Sarpkaya [16] for the nonaxisymmetric disturbance with azimuthal wave number equal to unity. It is obvious that the present results for $n = 1$ disturbance are very close to the experimental data for both critical Reynolds numbers and frequencies. Any discrepancy between the present theoretical results and Sarpkaya's experimental data may be attributed to the fact that Sarpkaya himself considered his initial disturbance level to be larger than that warranted by the linear theory used here. We may point out that our earlier attempt [7] with the stability of the nonparallel developing flow in a pipe to axisymmetric disturbances resulted in the minimum critical Reynolds number of 9700 at $\bar{X} = 0.0035$ for g_ψ $(\bar{X}, 0)$ where ψ is the disturbance stream function, and in fact the minimum

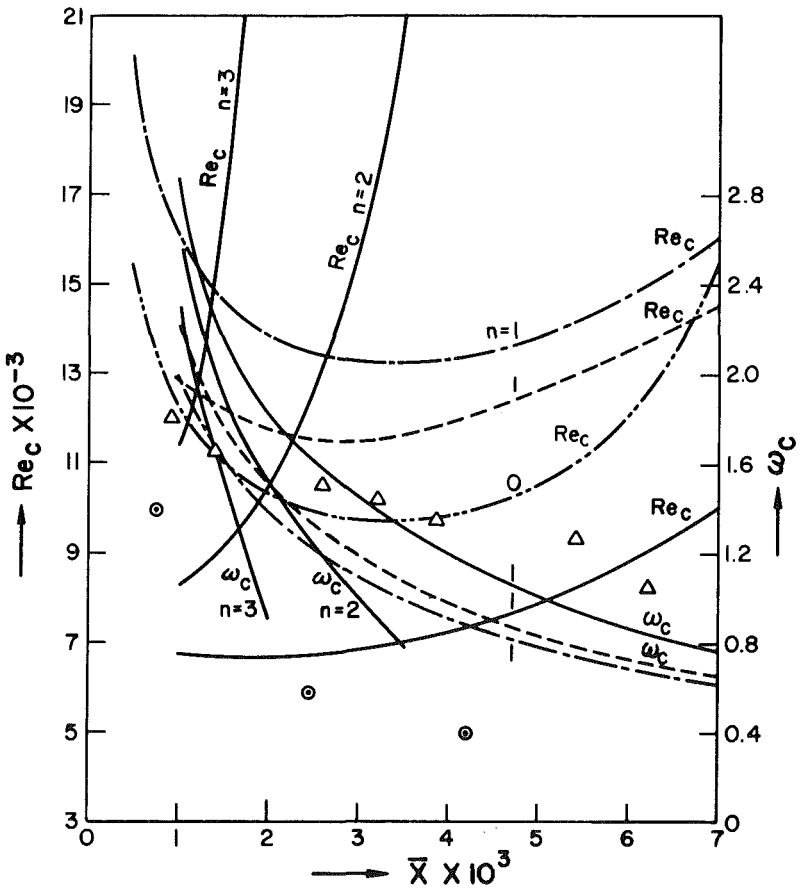

Fig. 7 Re_c and ω_c versus $\bar{X}$. ___, based on g_w $(\bar{X}, r_w)$; – – –, based on g_v $(\bar{X}, 0)$; ——– ——, based on parallel flow theory; ⊙, experimental Re_c; △, experimental ω_c; ——– – – ——, based on g_ψ $(\bar{X}, 0)$.

Downloaded 02 May 2010 to 171.66.16.246. Redistribution subject to ASME license or copyright; see http://www.asme.org/terms/Terms_Use.cfm

critical Reynolds number corresponding to g_v ($\bar{X}$, 0) was somewhat higher. The critical Reynolds number curve corresponding to g_ψ ($\bar{X}$, 0) for the axisymmetric disturbance ($n = 0$) is included in Fig. 7. Thus the real nonparallel developing flow in a pipe is more unstable to nonaxisymmetric disturbance with azimuthal wave number equal to unity than to the axisymmetric disturbances. In the near-entry region, this is in direct contrast to the results obtained when the developing flow is assumed to be parallel [12]. Nonaxisymmetric disturbances with azimuthal wave number greater than unity are, however, less unstable than the axisymmetric disturbance except in the near-entry region. For such disturbances the critical Reynolds number increases rapidly with $\bar{X}$.

Conclusions

The actual nonparallel developing flow in a rigid circular pipe is found to be most unstable to nonaxisymmetric disturbances with azimuthal wave number equal to unity. Axisymmetric disturbances are, however, more unstable than nonaxisymmetric disturbances with $n \geq 2$ except in the near-entry region. The present results compare well with the experimental data of Sarpkaya and show that for disturbances with $n = 1$, the parallel flow theory overpredicts the critical Reynolds number by as much as 136.5 percent at $\bar{X} = 0.001$. Thus considering the developing flow in ducts to be parallel for stability analysis is highly improper, a conclusion drawn also by Smith and Bodonyi [17].

Acknowledgment

The assistance of Dr. S. C. Gupta in carrying out some computations is gratefully acknowledged.

References

1 Garg, V. K., and Rouleau, W. T., "Linear Spatial Stability of Pipe Poiseuille Flow," *Journal of Fluid Mechanics*, Vol. 54, 1972, pp. 113-127

2 Gill, A. E., "The Least Damped Disturbance to Poiseuille Flow in a Circular Pipe," *Journal of Fluid Mechanics*, Vol. 61, 1973, pp. 97-107.

3 Huang, L. M., and Chen, T. S., "Stability of the Developing Laminar Pipe Flow," *Physics of Fluids*, Vol. 17, 1974, pp. 245-247.

4 Gupta, S. C., and Garg, V. K., "Effect of Velocity Distribution on the Stability of Developing Flow in a Pipe," *Physics of Fluids*, Vol. 24, 1981, pp. 576-578.

5 Shen, F. C. T., Chen, T. S., and Huang, L. M., "The Effect of Mainflow Radial Velocity on the Stability of Developing Laminar Pipe Flow," ASME *Journal of Applied Mechanics*, Vol. 43, 1976, pp. 209-212.

6 Sparrow, E. M., Lin, S. H., and Lundgren, T. S., "Flow Development in the Hydrodynamic Entrance Region of Tubes and Ducts," *Physics of Fluids*, Vol. 7, 1964, pp. 338-347.

7 Garg, V. K., and Gupta, S. C., "Stability of Developing Flow in a Pipe-Nonparallel Effects," ASME *Journal of Applied Mechanics*, Vol. 48, 1981, pp. 243-248.

8 Hornbeck, R. W., "Laminar Flow in Entrance Region of a Pipe," *Applied Science Research*, Section A, Vol. 13, 1963, pp. 224-232.

9 Shah, R. K., "A Correlation for Laminar Hydrodynamic Entry Length Solutions for Circular and Noncircular Ducts," *Journal of Fluids Engineering*, Vol. 100, 1978, pp. 177-179.

10 Spielberg, K., and Timan, H., "On Three and Two-Dimensional Disturbances of Pipe Flow," *Journal of Applied Mechanics*, Vol. 27, 1960, pp. 381-389.

11 Squire, H. B., "On the Stability for Three-Dimensional Disturbances of Viscous Fluid Flow Between Parallel Walls," *Proceedings of the Royal Society*, London, Series A, Vol. 142, 1933, pp. 621-628.

12 Garg, V. K., "Stability of Developing Flow in a Pipe: Nonaxisymmetric Disturbances," *Journal of Fluid Mechanics*, Vol. 110, 1981, pp. 209-216.

13 Huang, L. M., and Chen, T. S., "Stability of Developing Pipe Flow Subjected to Nonaxisymmetric Disturbances," *Journal of Fluid Mechanics*, Vol. 63, 1974, pp. 183-193.

14 Garg, V. K., "Stability of Nonparallel Developing Flow in an Annulus to Asymmetric Disturbances," ASME *Journal of Applied Mechanics*, Vol. 49, 1982, pp. 436-439.

15 Shen, S. F., "Some Considerations on the Laminar Stability of Time-Dependent Basic Flow," *Journal of Aeronautical Sciences*, Vol. 28, 1961, pp. 397-404.

16 Sarpkaya, T., "A Note on the Stability of Developing Laminar Pipe Flow Subjected to Axisymmetric and Nonaxisymmetric Disturbances," *Journal of Fluid Mechanics*, Vol. 68, 1975, pp. 345-351.

17 Smith, F. T., and Bodonyi, R. J., "On the Stability of the Developing Flow in a Channel or Circular Pipe," *Quarterly Journal of Mechanics and Applied Mathematics*, Vol. XXXIII, 1980, pp. 293-320.

Stability Analysis of Systems With Finite Displacements by Means of Extremum Curves

R. Parnes[1]

1 Introduction

The study of the stability of elastic systems subjected to compressive forces usually falls within the realm of bifurcation theory where the critical load, evaluated at a bifurcation point, corresponds to a neutral equilibrium position of the system.[2] In simple struts and other one-dimensional structures, *stable-symmetric* bifurcation points are usually encountered [1] and the equilibrium paths emanating from such points are described by a post-buckling behavior in which displacements increase with increasing loads. In the case of *unstable-symmetric* bifurcation points, the post-buckling behavior is characterized by increasing displacements with decreasing loads. If we consider finite displacements for systems with *unstable-symmetric* bifurcation points, it is recognized that several equilibrium positions may occur for forces below the classical "critical load," and indeed more than one of these positions may be stable.

In the following discussion, we consider the stability of systems subjected to large displacements and develop a general method, based on an extremum curve, to establish regions of stability and instability of a configuration space without invoking the second derivatives of the potential of the system. For mathematical simplicity, we develop the method using a simple asymmetric model, that of a rigid bar simply supported at one end and supported at the other by a linear elastic spring.

2 Basic Equations of the Model

We consider a rigid bar of length L, hinged at one end and supported at the other by means of a linear elastic spring of stiffness k which is attached at a fixed point a distance a from the bar and which is constrained to remain straight. The

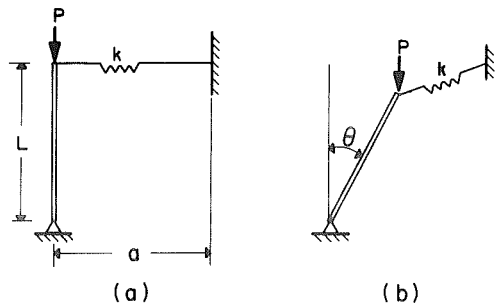

Fig. 1 Geometry of problem

[1]Department of Solid Mechanics, Materials and Structures, School of Engineering, Tel-Aviv University, Ramat-Aviv, Israel.

[2]Some investigators, e.g. [1-3], use the term "critical equilibrium" in place of "neutral equilibrium."

Manuscript received by ASME Applied Mechanics Division, July, 1979; final revision, January, 1982.

Downloaded 02 May 2010 to 171.66.16.246. Redistribution subject to ASME license or copyright; see http://www.asme.org/terms/Terms_Use.cfm

critical Reynolds number corresponding to g_v ($\bar{X}$, 0) was somewhat higher. The critical Reynolds number curve corresponding to g_ψ ($\bar{X}$, 0) for the axisymmetric disturbance ($n = 0$) is included in Fig. 7. Thus the real nonparallel developing flow in a pipe is more unstable to nonaxisymmetric disturbance with azimuthal wave number equal to unity than to the axisymmetric disturbances. In the near-entry region, this is in direct contrast to the results obtained when the developing flow is assumed to be parallel [12]. Nonaxisymmetric disturbances with azimuthal wave number greater than unity are, however, less unstable than the axisymmetric disturbance except in the near-entry region. For such disturbances the critical Reynolds number increases rapidly with $\bar{X}$.

Conclusions

The actual nonparallel developing flow in a rigid circular pipe is found to be most unstable to nonaxisymmetric disturbances with azimuthal wave number equal to unity. Axisymmetric disturbances are, however, more unstable than nonaxisymmetric disturbances with $n \geq 2$ except in the near-entry region. The present results compare well with the experimental data of Sarpkaya and show that for disturbances with $n = 1$, the parallel flow theory overpredicts the critical Reynolds number by as much as 136.5 percent at $\bar{X} = 0.001$. Thus considering the developing flow in ducts to be parallel for stability analysis is highly improper, a conclusion drawn also by Smith and Bodonyi [17].

Acknowledgment

The assistance of Dr. S. C. Gupta in carrying out some computations is gratefully acknowledged.

References

1 Garg, V. K., and Rouleau, W. T., "Linear Spatial Stability of Pipe Poiseuille Flow," *Journal of Fluid Mechanics*, Vol. 54, 1972, pp. 113-127

2 Gill, A. E., "The Least Damped Disturbance to Poiseuille Flow in a Circular Pipe," *Journal of Fluid Mechanics*, Vol. 61, 1973, pp. 97-107.

3 Huang, L. M., and Chen, T. S., "Stability of the Developing Laminar Pipe Flow," *Physics of Fluids*, Vol. 17, 1974, pp. 245-247.

4 Gupta, S. C., and Garg, V. K., "Effect of Velocity Distribution on the Stability of Developing Flow in a Pipe," *Physics of Fluids*, Vol. 24, 1981, pp. 576-578.

5 Shen, F. C. T., Chen, T. S., and Huang, L. M., "The Effect of Mainflow Radial Velocity on the Stability of Developing Laminar Pipe Flow," ASME *Journal of Applied Mechanics*, Vol. 43, 1976, pp. 209-212.

6 Sparrow, E. M., Lin, S. H., and Lundgren, T. S., "Flow Development in the Hydrodynamic Entrance Region of Tubes and Ducts," *Physics of Fluids*, Vol. 7, 1964, pp. 338-347.

7 Garg, V. K., and Gupta, S. C., "Stability of Developing Flow in a Pipe-Nonparallel Effects," ASME *Journal of Applied Mechanics*, Vol. 48, 1981, pp. 243-248.

8 Hornbeck, R. W., "Laminar Flow in Entrance Region of a Pipe," *Applied Science Research*, Section A, Vol. 13, 1963, pp. 224-232.

9 Shah, R. K., "A Correlation for Laminar Hydrodynamic Entry Length Solutions for Circular and Noncircular Ducts," *Journal of Fluids Engineering*, Vol. 100, 1978, pp. 177-179.

10 Spielberg, K., and Timan, H., "On Three and Two-Dimensional Disturbances of Pipe Flow," *Journal of Applied Mechanics*, Vol. 27, 1960, pp. 381-389.

11 Squire, H. B., "On the Stability for Three-Dimensional Disturbances of Viscous Fluid Flow Between Parallel Walls," *Proceedings of the Royal Society*, London, Series A, Vol. 142, 1933, pp. 621-628.

12 Garg, V. K., "Stability of Developing Flow in a Pipe: Nonaxisymmetric Disturbances," *Journal of Fluid Mechanics*, Vol. 110, 1981, pp. 209-216.

13 Huang, L. M., and Chen, T. S., "Stability of Developing Pipe Flow Subjected to Nonaxisymmetric Disturbances," *Journal of Fluid Mechanics*, Vol. 63, 1974, pp. 183-193.

14 Garg, V. K., "Stability of Nonparallel Developing Flow in an Annulus to Asymmetric Disturbances," ASME *Journal of Applied Mechanics*, Vol. 49, 1982, pp. 436-439.

15 Shen, S. F., "Some Considerations on the Laminar Stability of Time-Dependent Basic Flow," *Journal of Aeronautical Sciences*, Vol. 28, 1961, pp. 397-404.

16 Sarpkaya, T., "A Note on the Stability of Developing Laminar Pipe Flow Subjected to Axisymmetric and Nonaxisymmetric Disturbances," *Journal of Fluid Mechanics*, Vol. 68, 1975, pp. 345-351.

17 Smith, F. T., and Bodonyi, R. J., "On the Stability of the Developing Flow in a Channel or Circular Pipe," *Quarterly Journal of Mechanics and Applied Mathematics*, Vol. XXXIII, 1980, pp. 293-320.

Stability Analysis of Systems With Finite Displacements by Means of Extremum Curves

R. Parnes[1]

1 Introduction

The study of the stability of elastic systems subjected to compressive forces usually falls within the realm of bifurcation theory where the critical load, evaluated at a bifurcation point, corresponds to a neutral equilibrium position of the system.[2] In simple struts and other one-dimensional structures, *stable-symmetric* bifurcation points are usually encountered [1] and the equilibrium paths emanating from such points are described by a post-buckling behavior in which displacements increase with increasing loads. In the case of *unstable-symmetric* bifurcation points, the post-buckling behavior is characterized by increasing displacements with decreasing loads. If we consider finite displacements for systems with *unstable-symmetric* bifurcation points, it is recognized that several equilibrium positions may occur for forces below the classical "critical load," and indeed more than one of these positions may be stable.

In the following discussion, we consider the stability of systems subjected to large displacements and develop a general method, based on an extremum curve, to establish regions of stability and instability of a configuration space without invoking the second derivatives of the potential of the system. For mathematical simplicity, we develop the method using a simple asymmetric model, that of a rigid bar simply supported at one end and supported at the other by a linear elastic spring.

2 Basic Equations of the Model

We consider a rigid bar of length L, hinged at one end and supported at the other by means of a linear elastic spring of stiffness k which is attached at a fixed point a distance a from the bar and which is constrained to remain straight. The

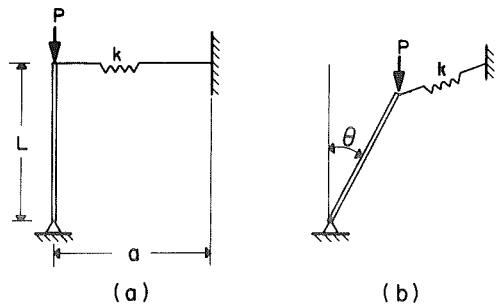

Fig. 1 Geometry of problem

[1]Department of Solid Mechanics, Materials and Structures, School of Engineering, Tel-Aviv University, Ramat-Aviv, Israel.

[2]Some investigators, e.g. [1-3], use the term "critical equilibrium" in place of "neutral equilibrium."

Manuscript received by ASME Applied Mechanics Division, July, 1979; final revision, January, 1982.

Copyright © 1983 by ASME
Downloaded 02 May 2010 to 171.66.16.246. Redistribution subject to ASME license or copyright; see http://www.asme.org/terms/Terms_Use.cfm

system is subject to a vertical force P as shown in Fig. 1(a). Denoting the deflected position by the angle θ (taken positive in the clockwise direction) (Fig. 1b), the elongation of the spring Δ is given by

$$\Delta = a[\psi(\theta) - 1] \tag{1a}$$

where

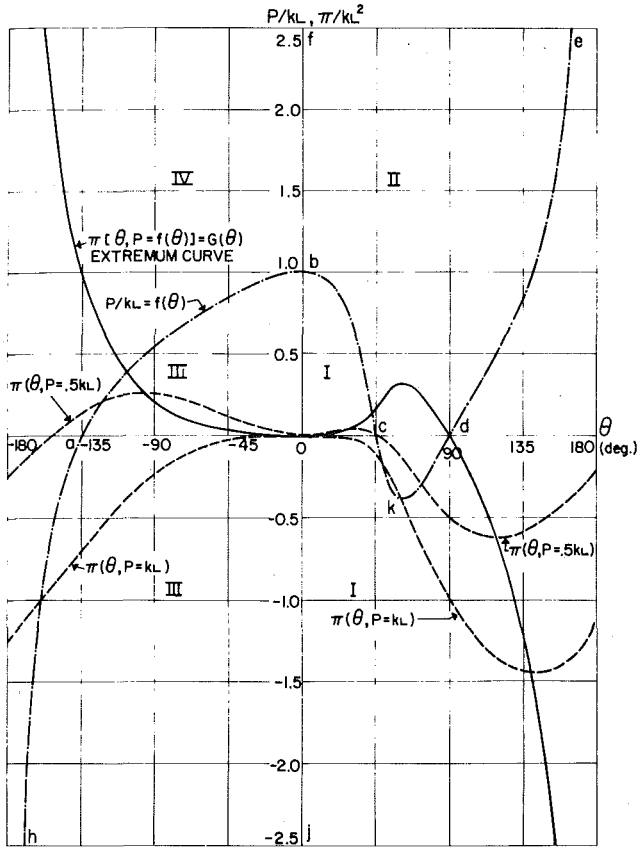

Fig. 2 Configuration space $\theta - P$

$$\psi(\theta) = \left[1 + \frac{2L}{a}\chi(\theta)\right]^{1/2} \tag{1b}$$

and

$$\chi(\theta) = \frac{L}{a}(1 - \cos\theta) - \sin\theta. \tag{1c}$$

The elastic strain energy of the spring is then

$$U = \frac{k\Delta^2}{2} = ka^2\left[1 - \psi(\theta) + \frac{L}{a}\chi(\theta)\right] \tag{2}$$

while the potential energy of the force P is

$$V = -PL(1 - \cos\theta). \tag{3}$$

For an equilibrium state to exist, the total potential of the system

$$\pi(\theta, P) = U + V \tag{4}$$

must satisfy $\delta\pi = (\partial\pi/\partial\theta)\,\delta\theta = 0$ and since $\delta\theta$ is an arbitrary variation, the equilibrium condition becomes

$$\frac{\partial\pi}{\partial\theta} = 0, \tag{5}$$

from which we obtain equilibrium loads for various values of θ:

$$P = f(\theta) = \frac{kL}{\sin\theta}(a/L)(1 - \psi^{-1})\left(\frac{L}{a}\sin\theta - \cos\theta\right) \tag{6}$$

The type of equilibrium is then usually determined according to the sign of the second derivative, given here by

$$\frac{\partial^2\pi}{\partial\theta^2} = kaL\left[(1 - \psi^{-1})\left(\frac{L}{a}\cos\theta + \sin\theta\right) + L/a\psi^{-3}\left(\frac{L}{a}\sin\theta - \cos\theta\right)^2\right] - PL\cos\theta \tag{7}$$

3 Analysis of the Model. The Extremum Curve Method

To analyze the model in detail, we consider the particular case $a = L$. Equations (4), (6), and (7) then become, respectively,

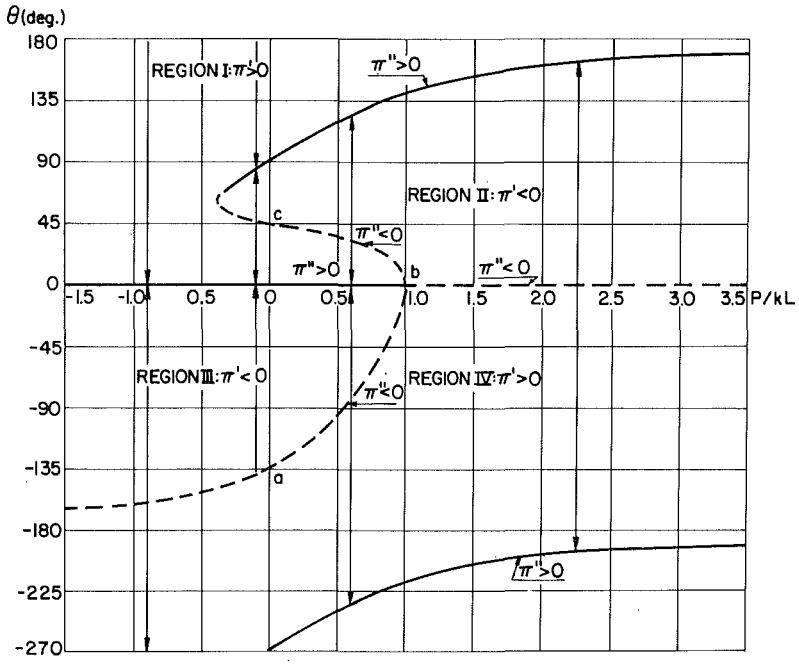

Fig. 3 Regions of $P - \theta$ space showing stable and unstable equilibrium paths, $a = L$

Downloaded 02 May 2010 to 171.66.16.246. Redistribution subject to ASME license or copyright; see http://www.asme.org/terms/Terms_Use.cfm

$$\pi = kL^2\left[2 - \sin\theta - \cos\theta - \phi^{-1} - \frac{P}{kL}(1-\cos\theta)\right] \tag{8}$$

$$P = \frac{kL}{\sin\theta}(1-\phi)(\sin\theta - \cos\theta) \tag{9}$$

$$\frac{\partial^2\pi}{\partial\theta^2}(\theta,P) = kL^2[(1-\phi)(\cos\theta+\sin\theta) + \phi^3(\sin\theta-\cos\theta)^2] - PL\cos\theta \tag{10}$$

where

$$\phi(\theta) = [3 - 2(\sin\theta + \cos\theta)]^{-1/2} \tag{11}$$

In Fig. 2, the force P is plotted as a function of θ for -180 deg $< \theta <$ 180 deg,[3] and the $P-\theta$ space is called a "configuration space" [3].

Values of π are superimposed on the configuration space of Fig. 2 for two typical cases, $P = 0.5kL$ and $P = kL$. From the first curve, we observe that the values $\theta = 0$ and $\theta = 125$ deg correspond to stable equilibrium positions. For the second case, $P = kL$, π is always negative (except at $\theta = 0$), reaching a minimum value at $\theta = 140$ deg which again corresponds to a stable position.

In summary, we conclude that when the system is subjected to a force P such that a stable equilibrium position exists at some value $\theta = \theta_s$, then if the system is given an initial finite displacement $\theta = \theta_0$, the system will move to the equilibrium position θ_s if

$$\frac{\partial\pi(\theta,P)}{\partial\theta} > 0 \quad \text{for all} \quad \theta_s < \theta \le \theta_0 \tag{12a}$$

$$\frac{\partial\pi(\theta,P)}{\partial\theta} < 0 \quad \text{for all} \quad \theta_0 \le \theta < \theta_s \tag{12b}$$

We observe that it is possible, according to the criteria of the spatial derivative to determine the stable equilibrium position that the system will assume if acted on by a prescribed force and if given a specified initial displacement; regions of behavior are thus characterized by the sign of these derivatives.

To this end, we first note the following properties of the load-displacement configuration space which we state in the following form:

Lemma 1. The configuration space can always be divided into fundamental open regions (defined by the sign of the first spatial derivative) which are separated by equilibrium paths (represented by the vanishing of these derivatives).[4]

Lemma 2. If the equilibrium path is of a stable or unstable nature, the first spatial derivatives in regions adjacent to the equilibrium path are of opposite sign.

Lemma 3. Since the character of an arbitrary region cannot change unless intersected by an equilibrium path, it follows that the sign of the spatial derivative along any arbitrary line segment (of constant force) within the fundamental region determines the character of the fundamental region.

With regard to the $P-\theta$ space of Fig. 2, for example (recalling that $\partial\pi/\partial\theta = 0$ along the line $\theta = 0$), we note that it contains four fundamental regions in -180 deg $< \theta <$ 180 deg, which are labeled Regions I–IV. Thus, in effect, each equilibrium path $P = f(\theta)$ constitutes a "separatrix" of the $\theta - P$ configuration space which plays a role analogous to the phase plane of oscillating systems.

Having found that the motion of a system undergoing large displacements is dependent on the sign of the spatial derivtive, we now develop a method, using an extremum curve, which permits together with the use of the foregoing lemmas, an immediate determination of the character of the fundamental regions of the configuration space. The method is based on the following theorem and its corollary.

Theorem. Let $\pi = \pi(\theta,P)$ and its derivatives be continuous and single-valued functions of θ and P in the region $\theta_1 \le \theta \le \theta_2$ and let $P = f(\theta)$ be a function that uniquely satisfies the condition

$$\frac{\partial\pi[\theta,f(\theta)]}{\partial\theta} = 0 \tag{13}$$

in this region. Furthermore, let $G(\theta) = \pi[\theta,f(\theta)]$ be a continuous function of θ representing the locus of extrema of π such that $G(\theta_1) \ne G(\theta_2)$.

If (a) $P = f(\theta)$ is single-valued and continuous in $\theta_1 \le \theta \le \theta_2$ and (b) $f(\theta) = P_0$ at $\theta = \theta_1$ and θ_2 but at no other point in $\theta_1 \le \theta \le \theta_2$, then

$$\frac{\partial\pi(\theta,P_0)}{\partial\theta} = K\,\mathrm{sgn}[G(\theta_2) - G(\theta_1)] \quad \text{for all} \quad \theta_1 < \theta < \theta_2 \tag{14}$$[5]

where K is a positive number.

Corollary. If $\pi(\theta,P)$ is of the form

$$\pi(\theta,P) = F(\theta) + g(\theta)P \tag{15}$$

where $F(\theta)$ and $g(\theta)$ and its derivatives are continuous single-valued functions of θ in $\theta_1 \le \theta \le \theta_2$ with $g(\theta_i) = 0$, ($i = 1$ or 2), then the property given by equation (14) remains valid even if $P = f(\theta)$ fails to be single-valued at one of the corresponding end points θ_i.

The proofs of the preceding theorem and its corollary are given in [4].

On the application of the Theorem and its Corollary in the context of stability analysis, we note that values of θ for which $P = f(\theta)$ fails to be single-valued will always define a position corresponding to a bifurcation point and the value of P will generally correspond to forces in the undeflected state. We note too that the end points (θ_1, θ_2) may be chosen arbitrarily and at convenience provided they conform to the conditions of the Theorem or its Corollary. Thus θ_1 and θ_2 can never be chosen such that a basic (undeflected) state exists between them.

To apply the method now to the analysis of the model under discussion, we first obtain the *extremum curve* $G(\theta)$ which represents the locus of stationary values of π for varying displacement positions θ. Substitution of equation (9) in equation (8) yields

$$G(\theta) = \pi[\theta, P = f(\theta)] = \frac{kL^2}{\sin\theta}[\sin\theta + \cos\theta - 1][1 + \phi(\sin\theta - 1)] \tag{16}$$

From this curve it is first noted that the total potentials reach a relative maximum with respect to the position $\theta = 0$ in the range -180 deg $< \theta <$ 60 deg. Thus within this range, the only possible stable equilibrium position is $\theta = 0$.

Having established the extremum curve $G(\theta)$, the character of the four fundamental regions of $\theta - P$ space of Fig. 2 is determined as follows:

[3] In addition, it is noted that for $\theta = 0$, all finite values of P satisfy the equilibrium condition $\partial\pi/\partial\theta = 0$.

[4] It is assumed that the spatial derivative is continuous throughout the configuration space.

[5] $\mathrm{sgn}(x)$ is defined as $\begin{cases} \mathrm{sgn}(x) > 0 \text{ for } 0 < x \\ \mathrm{sgn}(x) < 0 \text{ for } 0 > x \end{cases}$

Downloaded 02 May 2010 to 171.66.16.246. Redistribution subject to ASME license or copyright; see http://www.asme.org/terms/Terms_Use.cfm

(*a*) Choosing θ_1 and θ_2 as 0 deg and 45 deg, respectively, we observe that $G(45 \text{ deg}) > G(0 \text{ deg})$. Therefore, according to the corollary, along line segment *oc*, $\partial\pi/\partial\theta > 0$ and consequently by Lemma 3, $\partial\pi/\partial\theta > 0$ throughout Region I.

(*b*) Choosing θ_1 and θ_2 as 45 deg and 90 deg, respectively, we observe that $G(45 \text{ deg}) > G(90 \text{ deg})$. Therefore according to the Theorem, along line segment *cd*, $\partial\pi/\partial\theta < 0$ and consequently by Lemma 3, $\partial\pi/\partial\theta < 0$ throughout Region II.

The characters of Region III and IV are determined similarly; details are given in [4].

Equilibrium positions, as defined by the curves shown and by the abscissa, are plotted in Fig. 3 for varying loads and the four regions of the $P-\theta$ space are labeled according to the sign of $\partial\pi/\partial\theta$.[6] The criterion of equation (12), which governs the subsequent motion of the system when given an initial displacement, is applied, and these motions are indicated in each respective region by means of vertical arrows that terminate at the appropriate stable equilibrium positions. (The curves representing stable or unstable portions of the equilibrium states are sometimes referred to as *attractors* and *repellors*, respectively.)

Thus, for example, we conclude that for $P/kL < 1$, points along the abscissa represent stable equilibrium positions while for $P/kL > 1$, points along the abscissa represent unstable equilibrium positions.[7] Similarly, the upper and lower paths of Fig. 3 are seen to represent stable equilibrium paths. (It is noted that these last two paths in $P-\theta$ space represent, in fact, identical physical positions).

It is observed that within the context of the method, the stable or unstable character of the equilibrium paths has been established without invoking the second derivative. The results may, however, be verified by examining $\partial^2\pi/\partial\theta$ given in equation (10).

If we now define a stable system in the classical sense as one which returns to its original $\theta=0$ configuration when given a specified displacement, it is possible to make the following remarks on the nature of the regions: (1) If the bar, subjected to a force P, is given an initial displacement θ_0 such that the initial point $(P-\theta_0)$ lies in Region III, the member will snap back to its original $\theta=0$ position; hence this region is defined as "stable." (2) If the bar is given an initial displacement such that the $(P-\theta_0)$ point lies in either Regions II or IV, the member will snap to stable equilibrium positions described by the upper and low paths; hence these regions are defined as "unstable." (3) If the system is displaced such that its initial $(P-\theta_0)$ point lies in Region I, the bar will only return to the $\theta=0$ position provided that, for the given P, *all* points θ, $0 \le \theta \le \theta_0$, lie within the region; hence we shall call this region "conditionally stable.[8]

As illustrated by the model, the method presented provides a simple means of establishing regions of stability and instability. In particular the method leads to the direct identification of equilibrium paths as stable and unstable and thus obviates the need for calculating the second variation of the total potential of the system.

References

1 Thompson, J. M. T., and Hunt, G. W., *A General Theory of Elastic Stability*, Wiley, New York, 1973.

2 Roorda, J., "Concepts in Elastic Structural Satbility," *Mechanics Today*, Vol. 1, 1972, pp. 322-372.

3 Huseyin, K., *Nonlinear Theory of Elastic Stability*, Noordhoff, Leyden, 1975.

4 Parnes, R., "A Method of Stability Analysis Using Extremum Curves for Systems With Fnite Displacements," Tel-Aviv Univ. Report SOE 544/79, Ramat-Aviv, Israel.

[6] Stable and unstable equilibrium paths are indicated in Fig. 3 by solid and broken lines, respectively.

[7] Note that the bifurcation point ($P/kL=1$, $\theta=0$) represents a neutral equilibrium position and corresponds to the classical critical load obtained by considering only infinitesimal displacements.

[8] This definition is, in effect, a generalization of the usual statement that a stable system will return to its original position if given an infinitesimal displacement.

Nonaxially Symmetric Thermal Stresses in Thick Cylindrical Shells

D. Gamby[1] and H. Bourdillon[1]

Introduction

The thick shell theory proposed here is primarily intended to describe the behavior of solar boiler tubes. For the sake of simplicity our investigation is restricted to a long cylindrical tube with annular cross section, prevented from expanding axially and bending. The tube state will be assumed to be a plane strain one, in which stresses and deformations do not vary along the axis.

In the tube with mean radius R and thickness h, a temperature distribution symmetrical about the $\theta = 0(\pi)$ line is assumed to exist, where θ denotes the circumferential angular coordinate. In order to fix ideas, this distribution $T(\theta, z)$ is supposed to be linear with respect to the radial coordinate z such that $z = 0$ on the tube mean surface:

$$T(\theta,z) = T_0(\theta) + zT_1(\theta) \quad -h/2 \le z \le +h/2$$

where T_0 and T_1 are the mean temperature and through-the-wall thermal gradient, respectively. Let us point out that this assumption is not essential and does not preclude a greater generality.

As is well known, the thermoelastic constitutive equations contradict the classical Kirchoff's assumptions, valid for thin shells; this situation causes accuracy to decrease rapidly when the shell is no longer "very thin" and when the thermal gradient through the thickness becomes noticeable [1, 2].

Even for thick plates or shells subjected to pure mechanical loads, few results are available [3, 4]. Moreover these approaches cannot readily be extended to nonisothermal problems.

Kinematical Assumptions

As a starting point, we generalize Reiss's theory [5] for elastic cylindrical shells, in order to account for thermoelastic behavior. An asymptotic expansion in powers of the parameter $\epsilon = (h/2R)^{1/2}$ shows that the higher order theory immediately following the classical thin shell approach should be based on a displacement field whose dependence with respect to the "thickness variable" z is necessarily as follows:

$$u_z(z,\theta) = w(\theta) + z\psi_z(\theta) + z^2\chi_z(\theta)$$
$$u_\theta(z,\theta) = v(\theta) + z\psi_\theta(\theta) + z^2\chi_\theta(\theta) + z^3\rho(\theta) \qquad (1)$$

u_z and u_θ are the radial and circumferential displacement components associated with a polar coordinate system in the tube cross section. w, ψ_z, χ_z, v, ψ_θ, χ_θ, and ρ are the seven generalized displacements. The only nonzero strains are ϵ_θ, ϵ_z and $\gamma_{z\theta}$, using classical notation.

In order to reduce the number of independent generalized displacements, we satisfy one of the two stress boundary conditions on each of the inner and outer tube surfaces, i.e.,

$$\tau_{z\theta} = 0 \text{ at } z = \pm h/2$$

[1] Laboratoire de Mécanique des Solides, Université de Poitiers, 40, Avenue du Recteur Pineau, 86022 Poitiers Cedex, France.

Manuscript received by ASME Applied Mechanics Division, March, 1982; final revision, July, 1982.

Downloaded 02 May 2010 to 171.66.16.246. Redistribution subject to ASME license or copyright; see http://www.asme.org/terms/Terms_Use.cfm

(*a*) Choosing θ_1 and θ_2 as 0 deg and 45 deg, respectively, we observe that $G(45 \text{ deg}) > G(0 \text{ deg})$. Therefore, according to the corollary, along line segment *oc*, $\partial\pi/\partial\theta > 0$ and consequently by Lemma 3, $\partial\pi/\partial\theta > 0$ throughout Region I.

(*b*) Choosing θ_1 and θ_2 as 45 deg and 90 deg, respectively, we observe that $G(45 \text{ deg}) > G(90 \text{ deg})$. Therefore according to the Theorem, along line segment *cd*, $\partial\pi/\partial\theta < 0$ and consequently by Lemma 3, $\partial\pi/\partial\theta < 0$ throughout Region II.

The characters of Region III and IV are determined similarly; details are given in [4].

Equilibrium positions, as defined by the curves shown and by the abscissa, are plotted in Fig. 3 for varying loads and the four regions of the $P-\theta$ space are labeled according to the sign of $\partial\pi/\partial\theta$.[6] The criterion of equation (12), which governs the subsequent motion of the system when given an initial displacement, is applied, and these motions are indicated in each respective region by means of vertical arrows that terminate at the appropriate stable equilibrium positions. (The curves representing stable or unstable portions of the equilibrium states are sometimes referred to as *attractors* and *repellors*, respectively.)

Thus, for example, we conclude that for $P/kL < 1$, points along the abscissa represent stable equilibrium positions while for $P/kL > 1$, points along the abscissa represent unstable equilibrium positions.[7] Similarly, the upper and lower paths of Fig. 3 are seen to represent stable equilibrium paths. (It is noted that these last two paths in $P-\theta$ space represent, in fact, identical physical positions).

It is observed that within the context of the method, the stable or unstable character of the equilibrium paths has been established without invoking the second derivative. The results may, however, be verified by examining $\partial^2\pi/\partial\theta$ given in equation (10).

If we now define a stable system in the classical sense as one which returns to its original $\theta=0$ configuration when given a specified displacement, it is possible to make the following remarks on the nature of the regions: (1) If the bar, subjected to a force P, is given an initial displacement θ_0 such that the initial point $(P-\theta_0)$ lies in Region III, the member will snap back to its original $\theta=0$ position; hence this region is defined as "stable." (2) If the bar is given an initial displacement such that the $(P-\theta_0)$ point lies in either Regions II or IV, the member will snap to stable equilibrium positions described by the upper and low paths; hence these regions are defined as "unstable." (3) If the system is displaced such that its initial $(P-\theta_0)$ point lies in Region I, the bar will only return to the $\theta=0$ position provided that, for the given P, *all* points θ, $0 \le \theta \le \theta_0$, lie within the region; hence we shall call this region "conditionally stable.[8]

As illustrated by the model, the method presented provides a simple means of establishing regions of stability and instability. In particular the method leads to the direct identification of equilibrium paths as stable and unstable and thus obviates the need for calculating the second variation of the total potential of the system.

References

1 Thompson, J. M. T., and Hunt, G. W., *A General Theory of Elastic Stability*, Wiley, New York, 1973.

2 Roorda, J., "Concepts in Elastic Structural Satbility," *Mechanics Today*, Vol. 1, 1972, pp. 322-372.

3 Huseyin, K., *Nonlinear Theory of Elastic Stability*, Noordhoff, Leyden, 1975.

4 Parnes, R., "A Method of Stability Analysis Using Extremum Curves for Systems With Fnite Displacements," Tel-Aviv Univ. Report SOE 544/79, Ramat-Aviv, Israel.

[6] Stable and unstable equilibrium paths are indicated in Fig. 3 by solid and broken lines, respectively.

[7] Note that the bifurcation point ($P/kL=1$, $\theta=0$) represents a neutral equilibrium position and corresponds to the classical critical load obtained by considering only infinitesimal displacements.

[8] This definition is, in effect, a generalization of the usual statement that a stable system will return to its original position if given an infinitesimal displacement.

Nonaxially Symmetric Thermal Stresses in Thick Cylindrical Shells

D. Gamby[1] and H. Bourdillon[1]

Introduction

The thick shell theory proposed here is primarily intended to describe the behavior of solar boiler tubes. For the sake of simplicity our investigation is restricted to a long cylindrical tube with annular cross section, prevented from expanding axially and bending. The tube state will be assumed to be a plane strain one, in which stresses and deformations do not vary along the axis.

In the tube with mean radius R and thickness h, a temperature distribution symmetrical about the $\theta = 0(\pi)$ line is assumed to exist, where θ denotes the circumferential angular coordinate. In order to fix ideas, this distribution $T(\theta, z)$ is supposed to be linear with respect to the radial coordinate z such that $z = 0$ on the tube mean surface:

$$T(\theta,z) = T_0(\theta) + zT_1(\theta) \quad -h/2 \le z \le +h/2$$

where T_0 and T_1 are the mean temperature and through-the-wall thermal gradient, respectively. Let us point out that this assumption is not essential and does not preclude a greater generality.

As is well known, the thermoelastic constitutive equations contradict the classical Kirchoff's assumptions, valid for thin shells; this situation causes accuracy to decrease rapidly when the shell is no longer "very thin" and when the thermal gradient through the thickness becomes noticeable [1, 2].

Even for thick plates or shells subjected to pure mechanical loads, few results are available [3, 4]. Moreover these approaches cannot readily be extended to nonisothermal problems.

Kinematical Assumptions

As a starting point, we generalize Reiss's theory [5] for elastic cylindrical shells, in order to account for thermoelastic behavior. An asymptotic expansion in powers of the parameter $\epsilon = (h/2R)^{1/2}$ shows that the higher order theory immediately following the classical thin shell approach should be based on a displacement field whose dependence with respect to the "thickness variable" z is necessarily as follows:

$$u_z(z,\theta) = w(\theta) + z\psi_z(\theta) + z^2\chi_z(\theta)$$
$$u_\theta(z,\theta) = v(\theta) + z\psi_\theta(\theta) + z^2\chi_\theta(\theta) + z^3\rho(\theta) \qquad (1)$$

u_z and u_θ are the radial and circumferential displacement components associated with a polar coordinate system in the tube cross section. w, ψ_z, χ_z, v, ψ_θ, χ_θ, and ρ are the seven generalized displacements. The only nonzero strains are ϵ_θ, ϵ_z and $\gamma_{z\theta}$, using classical notation.

In order to reduce the number of independent generalized displacements, we satisfy one of the two stress boundary conditions on each of the inner and outer tube surfaces, i.e.,

$$\tau_{z\theta} = 0 \text{ at } z = \pm h/2$$

[1] Laboratoire de Mécanique des Solides, Université de Poitiers, 40, Avenue du Recteur Pineau, 86022 Poitiers Cedex, France.

Manuscript received by ASME Applied Mechanics Division, March, 1982; final revision, July, 1982.

Copyright © 1983 by ASME
Downloaded 02 May 2010 to 171.66.16.246. Redistribution subject to ASME license or copyright; see http://www.asme.org/terms/Terms_Use.cfm

where $\tau_{z\theta}$ is the shear in the circumferential direction, which amounts to the purely kinematical conditions:

$$\gamma_{z\theta}=0 \text{ at } z=\pm h/2$$

Then χ_θ and ψ_θ can be expressed in terms of the five other generalized displacements as:

$$\chi_\theta(\theta)=\frac{-1}{2R}\frac{d}{d\theta}\psi_z(\theta)-\frac{h^2}{4R}\rho(\theta)$$

$$\psi_\theta(\theta)=\frac{v(\theta)}{R}+\frac{h^2}{8R^2}\frac{d}{d\theta}\psi_z(\theta)-\frac{1}{R}\frac{d}{d\theta}w(\theta)$$
$$-\frac{h^2}{4R}\frac{d}{d\theta}\chi_z(\theta)+\left(\frac{h^4}{16R^2}-\frac{3h^2}{4}\right)\rho(\theta) \quad (2)$$

These conditions act as a generalized Kirchhoff hypothesis; the corresponding theory can accommodate some warping of the fibers normal to the mean surface. The classical thin shell theory together with its usual Kirchhoff hypothesis can be retrieved as a special case by taking:

$$\psi_z=0,\ \chi_z=0,\ \chi_\theta=0,\ \rho=0$$

The other stress boundary conditions bearing upon normal stress in the radial direction, $\sigma_z = 0$ at $z = \pm h/2$, are not used, as they would involve the temperature field and material properties; moreover they would not be appropriate for tubes subjected to noticeable internal or external pressure.

We want to point out that we could not obtain a consistent theory by using other displacement distributions between the preceding proposed field and that of the classical thin shell theory.

To our knowledge, the foregoing displacement distribution has never been proposed before; Levinson [3] uses a similar generalized Kirchhoff hypothesis for isothermal plates, but the displacement distribution he relies on is quite different and would be inappropriate for thermoelastic problems.

Equilibrium Equations

Here the density of virtual power of internal forces reduces to

$$p=\sigma_\theta\epsilon_\theta^*+\sigma_z\epsilon_z^*+\tau_{z\theta}\gamma_{z\theta}^*$$

where σ_θ denotes the normal stress in the circumferential direction, and the virtual deformation rates are related to the five independent generalized virtual velocities through expressions similar to (1), (2), and the usual strain-displacement relationships.

Integration through the tube thickness leads one to introduce generalized stresses, which are moments of order zero, one, two, or three of stresses defined by:

$$\{N_\theta,M_\theta,V_\theta,R_\theta\}=\int_{-h/2}^{+h/2}\{1,z,z^2,z^3\}\sigma_\theta dz$$

$$\{N_z,V_z\}=\int_{-h/2}^{+h/2}\{1,z\}\sigma_z(1+z/R)dz$$

$$\{N_{z\theta},R_{z\theta},K_{z\theta},V_{z\theta}\}=\int_{-h/2}^{+h/2}\{1,z,z^2,z^3\}\sigma_{z\theta}dz \quad (3)$$

After integrating by parts over the tube's half-circumference, the principle of virtual power yields the equilibrium equations (and the associated boundary conditions at $\theta = 0$ or $\theta = \pi$, which will be omitted to save space):

$$\frac{d^2}{d\theta^2}M_\theta-R\,N_\theta=0$$

$$\frac{d}{d\theta}N_\theta+\frac{1}{R}\frac{d}{d\theta}M_\theta=0$$

$$M_\theta+\frac{h^2}{8R^2}\frac{d^2}{d\theta^2}M_\theta-\frac{1}{2R}\frac{d^2}{d\theta^2}V_\theta+R\,N_z+\frac{1}{2R}\left(\frac{d}{d\theta}K_{z\theta}-\frac{h^2}{4}\frac{d}{d\theta}N_{z\theta}\right)=0$$

$$V_\theta+2R\,V_z-\frac{h^2}{4R}\frac{d^2}{d\theta^2}M_\theta-\left(\frac{d}{d\theta}K_{z\theta}-\frac{h^2}{4}\frac{d}{d\theta}N_{z\theta}\right)=0$$

$$\left(\frac{3h^2}{4}-\frac{h^4}{16R^2}\right)\frac{d}{d\theta}M_\theta+\frac{h^2}{4R}\frac{d}{d\theta}V_\theta-\frac{d}{d\theta}R_\theta$$
$$+\left(3R-\frac{h^2}{4R}\right)\left(K_{z\theta}-\frac{h^2}{4}N_{z\theta}\right)+2\left(V_{z\theta}-\frac{h^2}{4}R_{z\theta}\right)=0 \quad (4)$$

Shell Constitutive Equations

The expressions of generalized stresses in terms of generalized displacements are obtained by integrating the plane strain thermoelastic relations over the tube thickness, using (1), (2), (3), and the strain-displacement relations. In order to save place, we do not display here these cumbersome formulas; they can be found in [6].

Numerical Results

To assess the accuracy and the usefulness of the theory, several sorts of verifications were carried out; one of them involves a very thick tube (thickness over radius ratio of about 0.4) used in a steam solar boiler now under development.

The value of the axial stress at the most heated point is obtained by the present theory within 2 percent of that given by the exact theory: even in this borderline case, the theory we propose is still applicable and renders it unnecessary to resort to the complicated exact thermoelastic solution.

References

1 Chern J. M., and Pai, D. H., "Inelastic Analysis of a Straight Tube Under Combined Bending, Pressure, and Thermal Loads," ASME *Journal of Pressure Vessel Technology*, Vol. 97, 1975, pp. 155–162.

2 Wergeland J. H., "Temperature Load on Thick Curved Shell Elements," *International Journal for Numerical Methods in Engineering*, Vol. 11, 1977, pp. 1329–1342.

3 Levinson M., "An Accurate, Simple Theory of the Statics and Dynamics of Elastic Plates," *Mechanics Research Communications*, Vol. 7, No. 6, 1980, pp. 343–350.

4 Kienzler R., "A Consistent Linear Theory of Thin Elastic Shells," *Transactions of the 6th International Conference on Structural Mechanics in Reactor Technology*, Paris, France, Aug. 17–21, 1981, Paper M 11/5.

5 Reiss E. L., "On the Theory of Cylindrical Shells," *Quarterly Journal of Mechanics and Applied Mathematics*, Vol. 15, No. 3, 1962, pp. 325–338.

6 Bourdillon H., "Contribution à l'Étude du Comportement non Élastique des tubes de Chaudières des Centrales Électro-Solaires," Thèse de Docteur-Ingénieur, Poitiers, France, 1981.

Cylindrical Inclusion With Constant Transverse Eigenstrains in an Infinite Elastic Body

Y. Takao[1]

Introduction and Formulation

In this Note, the inclusion is defined as the subdomain in

[1] Assistant Professor, Research Institute of Applied Mechanics, Kyushu University, Higashi-Ku, Fukuoka, Japan.

Manuscript received by the Applied Mechanics Division, June, 1982.

Downloaded 02 May 2010 to 171.66.16.246. Redistribution subject to ASME license or copyright; see http://www.asme.org/terms/Terms_Use.cfm

where $\tau_{z\theta}$ is the shear in the circumferential direction, which amounts to the purely kinematical conditions:

$$\gamma_{z\theta}=0 \text{ at } z=\pm h/2$$

Then χ_θ and ψ_θ can be expressed in terms of the five other generalized displacements as:

$$\chi_\theta(\theta)=\frac{-1}{2R}\frac{d}{d\theta}\psi_z(\theta)-\frac{h^2}{4R}\rho(\theta)$$

$$\psi_\theta(\theta)=\frac{v(\theta)}{R}+\frac{h^2}{8R^2}\frac{d}{d\theta}\psi_z(\theta)-\frac{1}{R}\frac{d}{d\theta}w(\theta)$$
$$-\frac{h^2}{4R}\frac{d}{d\theta}\chi_z(\theta)+\left(\frac{h^4}{16R^2}-\frac{3h^2}{4}\right)\rho(\theta) \quad (2)$$

These conditions act as a generalized Kirchhoff hypothesis; the corresponding theory can accommodate some warping of the fibers normal to the mean surface. The classical thin shell theory together with its usual Kirchhoff hypothesis can be retrieved as a special case by taking:

$$\psi_z=0,\ \chi_z=0,\ \chi_\theta=0,\ \rho=0$$

The other stress boundary conditions bearing upon normal stress in the radial direction, $\sigma_z = 0$ at $z = \pm h/2$, are not used, as they would involve the temperature field and material properties; moreover they would not be appropriate for tubes subjected to noticeable internal or external pressure.

We want to point out that we could not obtain a consistent theory by using other displacement distributions between the preceding proposed field and that of the classical thin shell theory.

To our knowledge, the foregoing displacement distribution has never been proposed before; Levinson [3] uses a similar generalized Kirchhoff hypothesis for isothermal plates, but the displacement distribution he relies on is quite different and would be inappropriate for thermoelastic problems.

Equilibrium Equations

Here the density of virtual power of internal forces reduces to

$$p=\sigma_\theta\epsilon_\theta^*+\sigma_z\epsilon_z^*+\tau_{z\theta}\gamma_{z\theta}^*$$

where σ_θ denotes the normal stress in the circumferential direction, and the virtual deformation rates are related to the five independent generalized virtual velocities through expressions similar to (1), (2), and the usual strain-displacement relationships.

Integration through the tube thickness leads one to introduce generalized stresses, which are moments of order zero, one, two, or three of stresses defined by:

$$\{N_\theta,M_\theta,V_\theta,R_\theta\}=\int_{-h/2}^{+h/2}\{1,z,z^2,z^3\}\sigma_\theta dz$$

$$\{N_z,V_z\}=\int_{-h/2}^{+h/2}\{1,z\}\sigma_z(1+z/R)dz$$

$$\{N_{z\theta},R_{z\theta},K_{z\theta},V_{z\theta}\}=\int_{-h/2}^{+h/2}\{1,z,z^2,z^3\}\sigma_{z\theta}dz \quad (3)$$

After integrating by parts over the tube's half-circumference, the principle of virtual power yields the equilibrium equations (and the associated boundary conditions at $\theta = 0$ or $\theta = \pi$, which will be omitted to save space):

$$\frac{d^2}{d\theta^2}M_\theta-R\,N_\theta=0$$

$$\frac{d}{d\theta}N_\theta+\frac{1}{R}\frac{d}{d\theta}M_\theta=0$$

$$M_\theta+\frac{h^2}{8R^2}\frac{d^2}{d\theta^2}M_\theta-\frac{1}{2R}\frac{d^2}{d\theta^2}V_\theta+R\,N_z+\frac{1}{2R}\left(\frac{d}{d\theta}K_{z\theta}-\frac{h^2}{4}\frac{d}{d\theta}N_{z\theta}\right)=0$$

$$V_\theta+2R\,V_z-\frac{h^2}{4R}\frac{d^2}{d\theta^2}M_\theta-\left(\frac{d}{d\theta}K_{z\theta}-\frac{h^2}{4}\frac{d}{d\theta}N_{z\theta}\right)=0$$

$$\left(\frac{3h^2}{4}-\frac{h^4}{16R^2}\right)\frac{d}{d\theta}M_\theta+\frac{h^2}{4R}\frac{d}{d\theta}V_\theta-\frac{d}{d\theta}R_\theta$$
$$+\left(3R-\frac{h^2}{4R}\right)\left(K_{z\theta}-\frac{h^2}{4}N_{z\theta}\right)+2\left(V_{z\theta}-\frac{h^2}{4}R_{z\theta}\right)=0 \quad (4)$$

Shell Constitutive Equations

The expressions of generalized stresses in terms of generalized displacements are obtained by integrating the plane strain thermoelastic relations over the tube thickness, using (1), (2), (3), and the strain-displacement relations. In order to save place, we do not display here these cumbersome formulas; they can be found in [6].

Numerical Results

To assess the accuracy and the usefulness of the theory, several sorts of verifications were carried out; one of them involves a very thick tube (thickness over radius ratio of about 0.4) used in a steam solar boiler now under development.

The value of the axial stress at the most heated point is obtained by the present theory within 2 percent of that given by the exact theory: even in this borderline case, the theory we propose is still applicable and renders it unnecessary to resort to the complicated exact thermoelastic solution.

References

1 Chern J. M., and Pai, D. H., "Inelastic Analysis of a Straight Tube Under Combined Bending, Pressure, and Thermal Loads," ASME *Journal of Pressure Vessel Technology*, Vol. 97, 1975, pp. 155–162.

2 Wergeland J. H., "Temperature Load on Thick Curved Shell Elements," *International Journal for Numerical Methods in Engineering*, Vol. 11, 1977, pp. 1329–1342.

3 Levinson M., "An Accurate, Simple Theory of the Statics and Dynamics of Elastic Plates," *Mechanics Research Communications*, Vol. 7, No. 6, 1980, pp. 343–350.

4 Kienzler R., "A Consistent Linear Theory of Thin Elastic Shells," *Transactions of the 6th International Conference on Structural Mechanics in Reactor Technology*, Paris, France, Aug. 17–21, 1981, Paper M 11/5.

5 Reiss E. L., "On the Theory of Cylindrical Shells," *Quarterly Journal of Mechanics and Applied Mathematics*, Vol. 15, No. 3, 1962, pp. 325–338.

6 Bourdillon H., "Contribution à l'Étude du Comportement non Élastique des tubes de Chaudières des Centrales Électro-Solaires," Thèse de Docteur-Ingénieur, Poitiers, France, 1981.

Cylindrical Inclusion With Constant Transverse Eigenstrains in an Infinite Elastic Body

Y. Takao[1]

Introduction and Formulation

In this Note, the inclusion is defined as the subdomain in

[1] Assistant Professor, Research Institute of Applied Mechanics, Kyushu University, Higashi-Ku, Fukuoka, Japan.

Manuscript received by the Applied Mechanics Division, June, 1982.

Copyright © 1983 by ASME
Downloaded 02 May 2010 to 171.66.16.246. Redistribution subject to ASME license or copyright; see http://www.asme.org/terms/Terms_Use.cfm

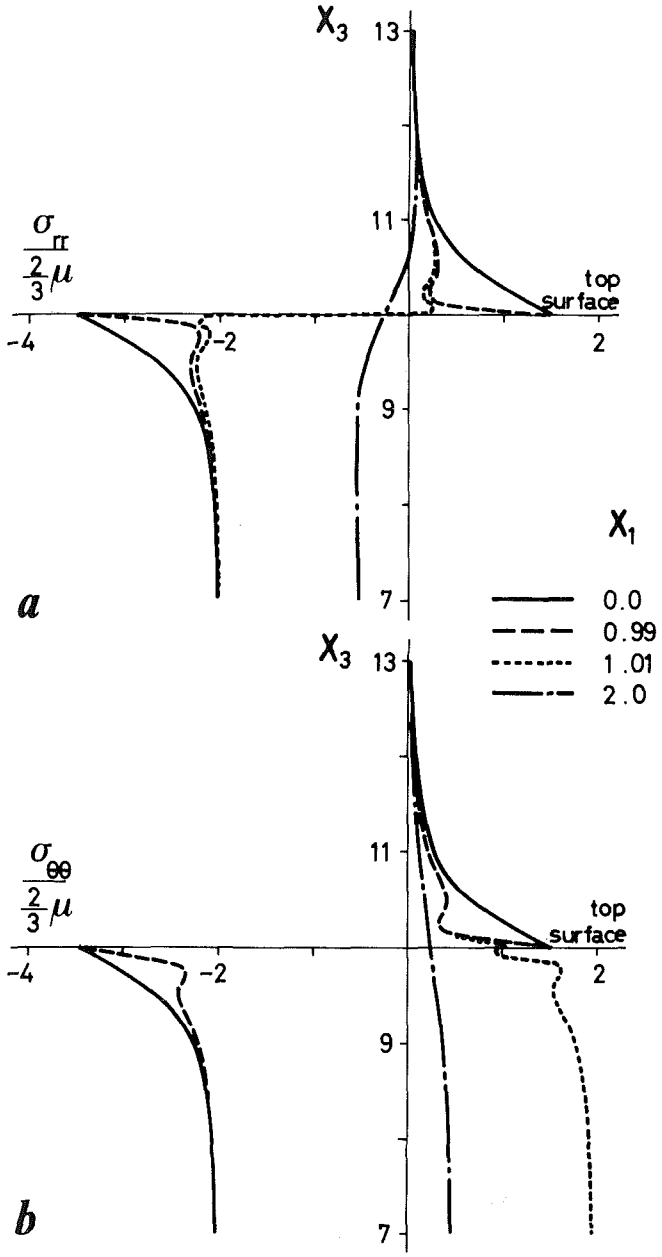

Fig. 1 The distributions of stresses normalized by $2\mu/3$ along the lognitudinal direction; *(a)* σ_{rr} and *(b)* $\sigma_{\theta\theta}$

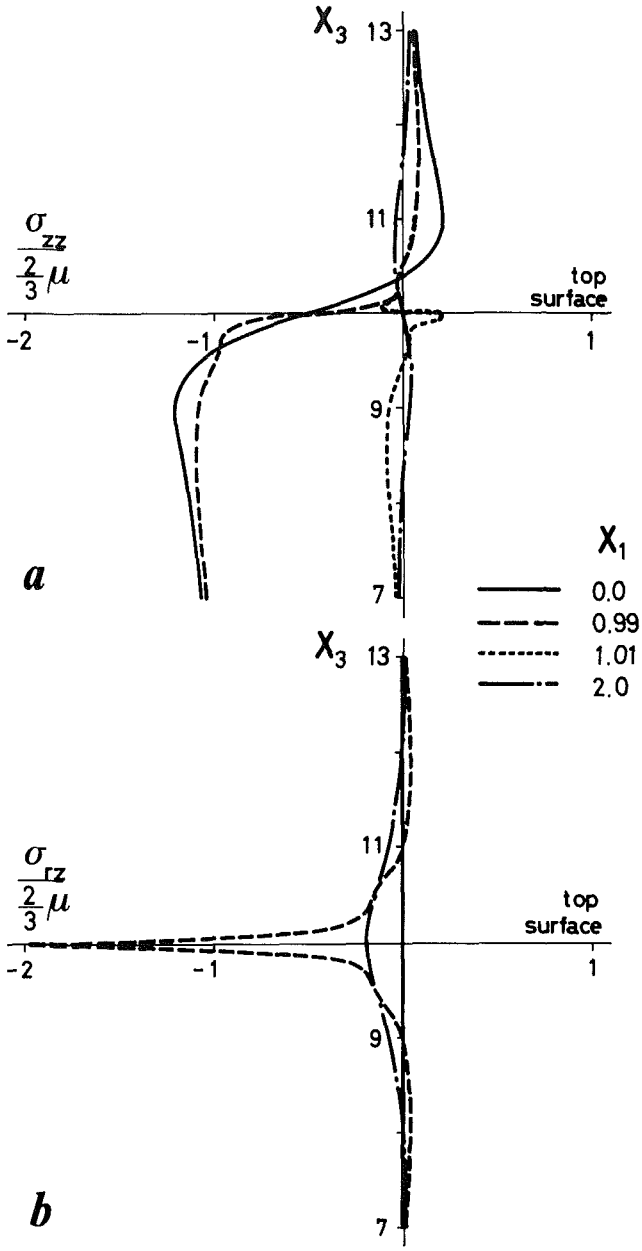

Fig. 2 The distributions of stresses normalized by $2\mu/3$ along the longitudinal direction; *(a)* σ_{zz} and *(b)* σ_{rz}

which the eigenstrains (transformation strains) are different from zero. The elastic moduli are identical in the subdomain and the matrix. Previously solutions have been obtained for the case of ellipsoid, cuboid, and rectangular sheets (see reference [1]). In the present paper we will show the stress field due to a finite cylindrical inclusion with constant transverse eigenstrains. Then this paper is a companion to reference [1]. The combination of both results yields solutions for the more practical problem, for example, thermal stress in an infinite body where thermal coefficients within cylinders are different from those of the surrounding body.

It is assumed that radial and circumferential components of eigenstrain, $\epsilon_{rr}{}^*$ and $\epsilon_{\theta\theta}{}^*$, are 1.0 within a cylinder and other components are zero in the cylindrical coordinate system (r,θ,z), taking the z axis along the cylinder. The aforementioned conditions mean that $\epsilon_{11}{}^* = \epsilon_{22}{}^* = 1.0$ in the Cartesian coordinate system (x_1, x_2, x_2) with the x_3 direction along the cylindrical axis.

Generally the strains $\epsilon_{mn}(\mathbf{x})$ induced by the eigenstrain $\epsilon_{ij}{}^*(\mathbf{x}')$, which is defined within Ω in the infinite elastic body are [2]

$$\epsilon_{mn}(\mathbf{x}) = (2\pi)^{-3} \int_{\Omega} \int \cdot \int_{-\infty}^{+\infty} \frac{1}{2} C_{ijkl} \epsilon^*{}_{ij}(\mathbf{x}') [\xi_1 \{ \xi_n M_{km}(\xi) + \xi_m M_{kn}(\xi) \}] \cdot e^{-i\xi(\mathbf{x}'-\mathbf{x})} d\xi d\mathbf{x}' \tag{1}$$

where

$$M_{ij}(\xi) = \frac{\delta_{ij}}{\mu\xi^2} - \left(\frac{\lambda+\mu}{\mu+2\mu} \right) \frac{\xi_i \xi_j}{\mu\xi^4} \tag{2}$$

C_{ijkl} are the elastic moduli, λ and μ are Lame constants, $d\mathbf{x}' = dx_1' dx_2' dx_3'$, $d\xi = d\xi_1 d\xi_2 d\xi_3$, and $\xi^2 = \xi_k \xi_k$. Here the variable $\mathbf{x}'$ is defined in the cylinder Ω which has the length 21_0 and radius 1.0. It is assumed that $\epsilon_{11}{}^* = \epsilon_{22}{}^* = 1.0$ within Ω and other components are zero in equation (1). Using the same type of mathematical formulas for integral as in reference [1], we have

Downloaded 02 May 2010 to 171.66.16.246. Redistribution subject to ASME license or copyright; see http://www.asme.org/terms/Terms_Use.cfm

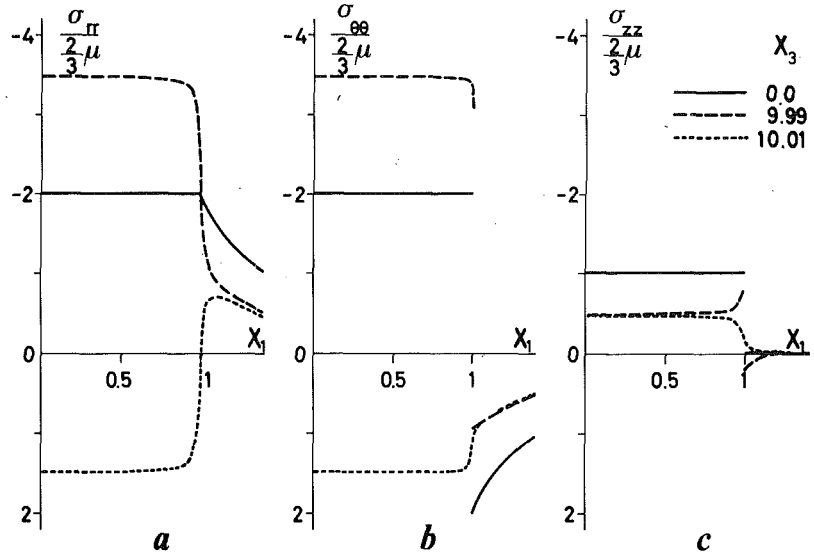

Fig. 3 The distributions of stresses normalized by $2\mu/3$ along the radial direction; (a)σ_{rr}, (b)$\sigma_{\theta\theta}$, and (c)σ_{zz}

$$\epsilon_{\substack{rr \\ (\theta\theta)}} = \int_0^\infty J_1(R)\{J_0(x_1R)_{(\mp)}J_2(x_1R)\}\frac{\lambda+\mu}{2(\lambda+2\mu)}$$
$$\{(-1+e^{-|x_3-1_0|R}-\frac{1}{2}|x_3-1_0|Re^{-|x_3-1_0|R})$$
$$\text{sign}(x_3-1_0)-(-1+e^{-|x_3+1_0|R}-\frac{1}{2}|x_3+1_0|$$
$$Re^{-|x_3+1_0|R})\text{sign}(x_3+1_0)\}dR$$

$$\epsilon_{zz} = \int_0^\infty J_1(R)J_0(x_1R) \tag{3}$$
$$\left\{\left(\frac{-\lambda}{\lambda+2\mu}e^{-|x_3-1_0|R}+\frac{\lambda+\mu}{2(\lambda+2\mu)}|x_3-1_0|\right.\right.$$
$$Re^{-|x_3-1_0|R})\text{sign}(x_3-1_0)-\left(\frac{-\lambda}{\lambda+2\mu}e^{-|x_3+1_0|R}\right.$$
$$\left.\left.+\frac{\lambda+\mu}{2(\lambda+2\mu)}|x_3+1_0|Re^{-|x_3+1_0R|})\text{sign}(x_3+1_0)\right\}dR$$

$$\epsilon_{rz} = \int_0^\infty J_1(R)J_1(x_1R)\frac{1}{2}\left\{\left(-\frac{2\lambda+\mu}{\lambda+2\mu}e^{-|x_3-1_0|R}\right.\right.$$
$$+\frac{\lambda+\mu}{\lambda+2\mu}|x_3-1_0|Re^{-|x_3-1_0|R})$$
$$-\left(-\frac{2\lambda+\mu}{\lambda+2\mu}e^{-|x_3+1_0|R}\right.$$
$$\left.\left.+\frac{\lambda+\mu}{\lambda+2\mu}|x_3+1_0|Re^{-|x_3+1_0|R})\right\}dR$$

where $\epsilon_{\theta\theta}$ is equal to ϵ_{rr} except for the sign in front of J_2, J_i is the first kind of Bessel function of the ith order, and the function sign(x) is 1 for $x>0$, 0 for $x=0$, or -1 for $x<0$. Equation (3) can be simplified by the gamma and hypergeometric functions for $x_3 \neq \pm 1_0$. But those functions show the slow convergence when $x_3 \simeq \pm 1_0$ or $x_1 >> 1$. Then the direct integration with the special numerical technique [1] is used. The strain field at $x_1 = 0$ can be obtained in closed form as

$$\epsilon_{\substack{rr \\ (\equiv\epsilon_{\theta\theta})}} = -\frac{\lambda+\mu}{4(\lambda+2\mu)}\left[\frac{(x_3-1_0)\{2(x_3-1_0)^2+1\}}{\{(x_3-1_0)^2+1\}^{3/2}}\right.$$
$$\left.-\frac{(x_3+1_0)\{2(x_3+1_0)^2+1\}}{\{(x_3+1_0)^2+1\}^{3/2}}\right]$$
$$\epsilon_{zz} = \frac{1}{2(\lambda+2\mu)}\left[\frac{(x_3-1_0)\{2\lambda(x_3-1_0)^2+3\lambda+\mu\}}{\{(x_3-1_0)^2+1\}^{3/2}}\right.$$
$$\left.-\frac{(x_3+1_0)\{2\lambda(x_3+1_0)^2+3\lambda+\mu\}}{\{(x_3+1_0)^2+1\}^{3/2}}\right]$$
$$+\frac{\lambda}{\lambda+2\mu}\{-\text{sign}(x_3-1_0)+\text{sign}(x_3+1_0)\}$$
$$\epsilon_{rz} = 0 \tag{4}$$

Numerical Results and Discussion

Figures 1 and 2 show the distribution of the stress σ_{ij} near the top surface for unit eigenstrain $\epsilon_{rr}{}^* = \epsilon_{\theta\theta}{}^* = 1.0$ in the cylindrical inclusion when $\lambda = \mu$: Poisson's ratio $\nu = 0.25$, and $1_0 = 10$. The stress is obtained through the relation $\sigma_{ij} = C_{ijkl}(\epsilon_{kl} - \epsilon_{kl}{}^*)$. Figure 3 shows the radial distribution of the stress.

The shear strain ϵ_{rz} (stress) shows the singularity at the point of $x_1 = 1$ and $x_3 = 1_0$ and following the discussion in reference [1] we can show that at $x_3 = 1_0$

$$\epsilon_{rz} \simeq \frac{2\lambda+\mu}{2(\lambda+2\mu)\pi}\ln|x_1-1| \tag{5}$$

The axial unit eigenstrain showed the singularity of $\epsilon_{rz} \simeq (\lambda+\mu)/\{2(\lambda+2\mu)\pi\}\ln|x_1-1|$[1]. Then the unit thermal expansion within Ω yields the shear singularity of $(3\lambda+2\mu)/\{2(\lambda+2\mu)\pi\}\cdot\ln|x_1-1|$.

Second, applying $\epsilon_{11}{}^* = \epsilon_{22}{}^* = 1.0$ and other components being zero to the general equation for stress jumps, $[\sigma_{ij}] \equiv \sigma_{ij,\text{outside}} - \sigma_{ij,\text{inside}}$, across the matrix-inclusion interface [3] we can show

$$[\sigma_{rr}]_A = 0$$
$$[\sigma_{\theta\theta}]_A = \frac{4(\lambda+\mu)\mu}{\mu+2\mu}$$

Downloaded 02 May 2010 to 171.66.16.246. Redistribution subject to ASME license or copyright; see http://www.asme.org/terms/Terms_Use.cfm

$$[\sigma_{zz}]_A = \frac{2\lambda\mu}{\lambda+2\mu}$$

$$[\sigma_{rr}]_B = [\sigma_{\theta\theta}]_B = \frac{2\mu(3\lambda+2\mu)}{\lambda+2\mu} \tag{6}$$

$$[\sigma_{zz}]_B = 0$$

$$[\sigma_{rz}]_A = [\sigma_{rz}]_B = 0$$

where A and B denote the side and top surfaces, respectively. Inputting $\lambda=\mu$ into equation (6) and normalizing the stresses by $2\mu/3$ yield

$$[\sigma_{\theta\theta}]_A = 4.0$$

$$[\sigma_{zz}]_A = 1.0 \tag{7}$$

$$[\sigma_{rr}]_B = [\sigma_{\theta\theta}]_B = 5.0$$

which agree well with our numerical results in Figs. 1 and 2. These jumps across the side surface are clearly shown in Fig. 3.

Acknowledgment

The author wishes to thank Profs. Taya and Chou of the University of Delaware for their helpful suggestion.

References

1 Takao, Y., Taya, M., and Chou, T. W., "Stress Field Due to a Cylindrical Inclusion With Constant Axial Eigenstrain in an Infinite Elastic Body," ASME JOURNAL OF APPLIED MECHANICS, Vol. 48, 1981, pp. 853–858.

2. Mura, T., *Micromechanics of Defects in Solids*, Martinus Nijhoff, 1982.

3. Walpole, L. J., "The Elastic Field of an Inclusion in an Anisotropic Medium," *Proceedings, Royal Society, London*, Series A, Vol. 300, 1967, pp. 270–289.

Circumferential Through-Crack in a Cylindrical Shell Under Combined Bending and Tension

J. L. Sanders, Jr.[1]

A formula for the energy release rate of an extending circumferential through-crack in a cylindrical shell subject to axial tension was given in [1]. Results were obtained according to elastic fracture mechanics and thin shell theory. A similar result obtained by the same methods is given here for the case of combined bending and tension.

Let the crack extend over a circumferential angle of 2α. Let F and M be the axial force and bending moment acting on the shell far from the crack. A positive M produces maximum tensile stress on the generator passing through the middle of the crack, and a positive F produces tension. Let other symbols be defined as follows: E = Young's modulus, ν = Poisson's ratio, R = shell radius, h = shell thickness, $\epsilon^2 = (h/R)[12(1-\nu^2)]^{-1/2}$. The energy release rate I (with respect to α) for the crack extending at both ends is given by

$$I = \frac{\sqrt{2}}{2\pi^2 E h \epsilon}\left(\lambda\alpha F + 2\mu \sin\alpha \frac{M}{R}\right)^2 \tag{1}$$

where

$$\lambda = 1 + \frac{\sqrt{2}}{2\alpha}\frac{1-\alpha\cot\alpha}{\cot[(\pi-\alpha)/\sqrt{2}]+\sqrt{2}\cot\alpha} \tag{2}$$

$$\mu = 1 + \frac{\sqrt{2}}{4}\frac{\alpha+\alpha\cot^2\alpha-\cot\alpha}{\cot[(\pi-\alpha)/\sqrt{2}]+\sqrt{2}\cot\alpha} \tag{3}$$

In the limit $\alpha\to 0$ both λ and μ approach unity, and a load $2M/R$ is equivalent to a load F. For such short cracks the result (1) matches the result from shallow shell analysis in the sense discussed in [1].

Acknowledgment

Support of the Office of Naval Research under contract N00014-81-K-0668 and the Division of Applied Sciences, Harvard University is gratefully acknowledged.

References

1 Sanders, J. Lyell, Jr., "Circumferential Through-Cracks in Cylindrical Shells under Tension," ASME JOURNAL OF APPLIED MECHANICS, Vol. 49, 1982, pp. 103–107.

Deformation of a Thin, Elastic Plate to a Deep Parabolic Cylinder[1]

R. C. Reuter Jr.[2] **and R. K. Wilson**[2]

Introduction

There exist uniform edge loads and a spatially varying surface pressure that will deform it to the shape of a deep parabolic cylinder when applied to a thin, elastic, rectangular plate [1–3]. The uniform edge loads consist of a shear force and bending moment applied only to that pair of opposing edges that become the rims of the parabola after deformation. Deep parabolas are obtained by elastically deforming the plate through large displacements. In [1] the solution for the forming loads was obtained for particular parabolas with an aperture equal to four times the focal length. The purpose of the present work is to generalize the solution for the forming loads by removing this restriction.

Problem Formulation and Solution

Symmetry about the focal plane allows consideration of only half of the deformed parabola, as shown in Fig. 1, where coordinates, geometric parameters, external loads $P_C(x)$, Q_R, and M_R, and internal reactions, N_V and M_V are defined. Since midplane extension is small enough to have negligible effect on equilibrium, the governing equation [4] for cylindrical bending of the plate [5, 6] is the familar Euler relationship

$$D\frac{d\phi(x)}{ds} = M(x), \tag{1}$$

where

$$\frac{d\phi}{ds} = \frac{\dfrac{d^2y}{dx^2}}{\left[1+\left(\dfrac{dy}{dx}\right)^2\right]^{3/2}}, \tag{2a}$$

[1]Professor, Division of Applied Sciences, Harvard University, Cambridge Mass. 02138. Fellow ASME.

Manuscript received by ASME Applied Mechanics Division, September, 1982.

[1]This work was performed at Sandia National Laboratories supported by the U.S. Department of Energy under contract number DE-ACO4-76DP00789 for the U. S. Department of Energy.

[2]Supervisor, Applied Mechanics Division, 1523, and Member, Technical Staff, Fluid Mechanics and Heat Transfer Division, 1511, respectively, Sandia National Laboratories, Albuquerque, N. Mex. 87185.

Manuscript received by ASME Applied Mechanics Division, March, 1982; final revision, August, 1982.

Downloaded 02 May 2010 to 171.66.16.246. Redistribution subject to ASME license or copyright; see http://www.asme.org/terms/Terms_Use.cfm

$$[\sigma_{zz}]_A = \frac{2\lambda\mu}{\lambda+2\mu}$$

$$[\sigma_{rr}]_B = [\sigma_{\theta\theta}]_B = \frac{2\mu(3\lambda+2\mu)}{\lambda+2\mu} \tag{6}$$

$$[\sigma_{zz}]_B = 0$$

$$[\sigma_{rz}]_A = [\sigma_{rz}]_B = 0$$

where A and B denote the side and top surfaces, respectively. Inputting $\lambda = \mu$ into equation (6) and normalizing the stresses by $2\mu/3$ yield

$$[\sigma_{\theta\theta}]_A = 4.0$$

$$[\sigma_{zz}]_A = 1.0 \tag{7}$$

$$[\sigma_{rr}]_B = [\sigma_{\theta\theta}]_B = 5.0$$

which agree well with our numerical results in Figs. 1 and 2. These jumps across the side surface are clearly shown in Fig. 3.

Acknowledgment

The author wishes to thank Profs. Taya and Chou of the University of Delaware for their helpful suggestion.

References

1 Takao, Y., Taya, M., and Chou, T. W., "Stress Field Due to a Cylindrical Inclusion With Constant Axial Eigenstrain in an Infinite Elastic Body," ASME JOURNAL OF APPLIED MECHANICS, Vol. 48, 1981, pp. 853–858.

2. Mura, T., *Micromechanics of Defects in Solids*, Martinus Nijhoff, 1982.

3. Walpole, L. J., "The Elastic Field of an Inclusion in an Anisotropic Medium," *Proceedings, Royal Society, London*, Series A, Vol. 300, 1967, pp. 270–289.

Circumferential Through-Crack in a Cylindrical Shell Under Combined Bending and Tension

J. L. Sanders, Jr.[1]

A formula for the energy release rate of an extending circumferential through-crack in a cylindrical shell subject to axial tension was given in [1]. Results were obtained according to elastic fracture mechanics and thin shell theory. A similar result obtained by the same methods is given here for the case of combined bending and tension.

Let the crack extend over a circumferential angle of 2α. Let F and M be the axial force and bending moment acting on the shell far from the crack. A positive M produces maximum tensile stress on the generator passing through the middle of the crack, and a positive F produces tension. Let other symbols be defined as follows: E = Young's modulus, ν = Poisson's ratio, R = shell radius, h = shell thickness, $\epsilon^2 = (h/R)[12(1-\nu^2)]^{-1/2}$. The energy release rate I (with respect to α) for the crack extending at both ends is given by

$$I = \frac{\sqrt{2}}{2\pi^2 E h \epsilon}\left(\lambda\alpha F + 2\mu \sin\alpha \frac{M}{R}\right)^2 \tag{1}$$

where

$$\lambda = 1 + \frac{\sqrt{2}}{2\alpha}\frac{1-\alpha\cot\alpha}{\cot[(\pi-\alpha)/\sqrt{2}]+\sqrt{2}\cot\alpha} \tag{2}$$

$$\mu = 1 + \frac{\sqrt{2}}{4}\frac{\alpha+\alpha\cot^2\alpha-\cot\alpha}{\cot[(\pi-\alpha)/\sqrt{2}]+\sqrt{2}\cot\alpha} \tag{3}$$

In the limit $\alpha \to 0$ both λ and μ approach unity, and a load $2M/R$ is equivalent to a load F. For such short cracks the result (1) matches the result from shallow shell analysis in the sense discussed in [1].

Acknowledgment

Support of the Office of Naval Research under contract N00014-81-K-0668 and the Division of Applied Sciences, Harvard University is gratefully acknowledged.

References

1 Sanders, J. Lyell, Jr., "Circumferential Through-Cracks in Cylindrical Shells under Tension," ASME JOURNAL OF APPLIED MECHANICS, Vol. 49, 1982, pp. 103–107.

Deformation of a Thin, Elastic Plate to a Deep Parabolic Cylinder[1]

R. C. Reuter Jr.[2] **and R. K. Wilson**[2]

Introduction

There exist uniform edge loads and a spatially varying surface pressure that will deform it to the shape of a deep parabolic cylinder when applied to a thin, elastic, rectangular plate [1–3]. The uniform edge loads consist of a shear force and bending moment applied only to that pair of opposing edges that become the rims of the parabola after deformation. Deep parabolas are obtained by elastically deforming the plate through large displacements. In [1] the solution for the forming loads was obtained for particular parabolas with an aperture equal to four times the focal length. The purpose of the present work is to generalize the solution for the forming loads by removing this restriction.

Problem Formulation and Solution

Symmetry about the focal plane allows consideration of only half of the deformed parabola, as shown in Fig. 1, where coordinates, geometric parameters, external loads $P_C(x)$, Q_R, and M_R, and internal reactions, N_V and M_V are defined. Since midplane extension is small enough to have negligible effect on equilibrium, the governing equation [4] for cylindrical bending of the plate [5, 6] is the familar Euler relationship

$$D\frac{d\phi(x)}{ds} = M(x), \tag{1}$$

where

$$\frac{d\phi}{ds} = \frac{\dfrac{d^2y}{dx^2}}{\left[1+\left(\dfrac{dy}{dx}\right)^2\right]^{3/2}}, \tag{2a}$$

[1] Professor, Division of Applied Sciences, Harvard University, Cambridge Mass. 02138. Fellow ASME.

Manuscript received by ASME Applied Mechanics Division, September, 1982.

[1] This work was performed at Sandia National Laboratories supported by the U.S. Department of Energy under contract number DE-ACO4-76DP00789 for the U. S. Department of Energy.

[2] Supervisor, Applied Mechanics Division, 1523, and Member, Technical Staff, Fluid Mechanics and Heat Transfer Division, 1511, respectively, Sandia National Laboratories, Albuquerque, N. Mex. 87185.

Manuscript received by ASME Applied Mechanics Division, March, 1982; final revision, August, 1982.

Copyright © 1983 by ASME
Downloaded 02 May 2010 to 171.66.16.246. Redistribution subject to ASME license or copyright; see http://www.asme.org/terms/Terms_Use.cfm

Dynamic Response of a Pulse-Loaded Ring Immersed in an Acoustic Medium

S. R. Reid[1] and S. R. Hendry[1]

Introduction

The deformation of structures immersed in a fluid when subjected to high-intensity transient loads has become important particularly in relation to estimating the residual deformation of reactor core structures exposed to high-pressure transients. Complex computer codes incorporating detailed treatments of fluid-structure interactions have been produced and accounts of their development can be found in the recent proceedings of the SMIRT conference [1].

The problem of a general structure interacting with a compressible fluid is very difficult but some insight can be gained by analyzing the response of a simple structure and quantifying the interactive effects. The purpose of this Note is to provide such an example. A ring immersed in an infinite volume of compressible fluid is subjected to a pressure pulse of general (temporal) shape applied uniformly to the inner surface of the ring. Imposing a pulse of general shape allows one to examine the form of correlation parameters sufficient to eliminate the effect of pulse shape on the final structural deformation. Youngdahl investigated this procedure in a number of papers [2–4] in which he demonstrated that the effect of pulse shape is virtually eliminated if the pulses have the same impulse and "effective" pressure or load.

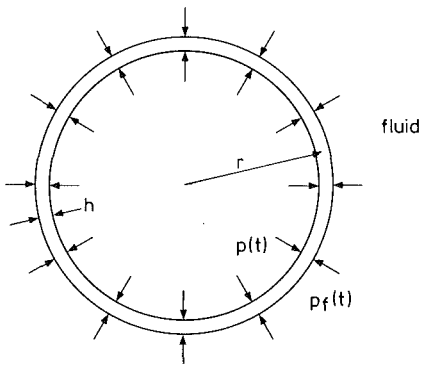

Fig. 1(*a*) Pulse loaded ring immersed in compressible fluid

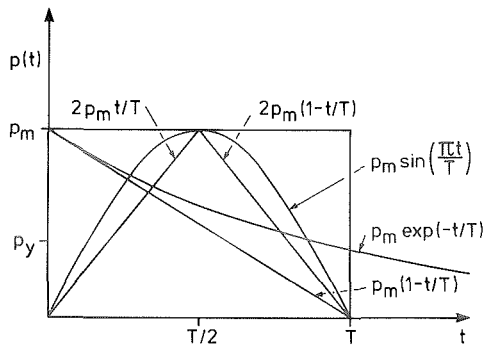

Fig. 1(*b*) Pulse shapes considered

Fig. 1

Equation of Motion

Let $p_f(t)$ represent the back-pressure exerted by the fluid on the ring as the ring expands. The equation of motion for the rigid perfectly-plastic ring shown in Fig. 1(*a*) is

$$\rho h\ddot{r} = [p(t) - p_f(t)] - Yh/r \tag{1}$$

where ρ and h are the density and thickness of the ring, respectively, r is its current radius, and Y is the yield stress of the material. It is assumed that $h/a << 1$, where a is the initial radius of the ring, and that the ring has unit depth.

The following assumptions are made:

(*i*) No deformation occurs until time, t_y, when $p(t)$ reaches the yield load, p_y, given by

$$p_y = Yh/a \tag{2}$$

(*ii*) The deformations are small. Hence $r = a + w$ and $w << a$ where w is the radial displacement of the ring.

(*iii*) The fluid behaves as an acoustic medium. Thus

$$p_f(t) = \rho_f c_f \dot{w}(t) = \rho_f c_f v(t) \tag{3}$$

where ρ_f and c_f are the density and sound speed of the fluid, respectively, and $v = \dot{w}$ is the radial velocity of the ring.

Incorporating these assumptions into equation (1) leads to

$$\frac{dv}{dt} + \alpha v = \frac{1}{\mu}[p(t) - p_y] \tag{4}$$

where $\alpha = \rho_f c_f/\rho h$ and $\mu = \rho h$. The solution of equation (4) is

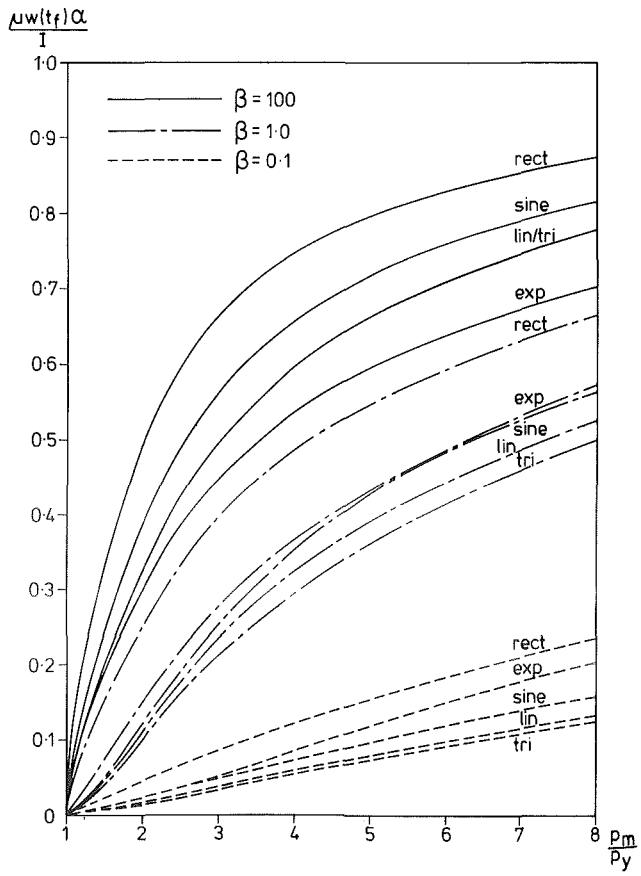

Fig. 2 Nondimension deflection, $\mu w(t_f)\alpha/I$ versus p_m/p_y produced by a variety of pulse shapes for $\beta = 0.1$, 1.0, and 100

[1] Jackson Professor of Engineering Science, Mem. ASME, and Research Student, respectively, Department of Engineering, University of Aberdeen, Marischal College, Aberdeen, Scotland.

Manuscript received by ASME Applied Mechanics Division, March, 1982; final revision, September 1982.

Copyright © 1983 by ASME
Downloaded 02 May 2010 to 171.66.16.246. Redistribution subject to ASME license or copyright; see http://www.asme.org/terms/Terms_Use.cfm

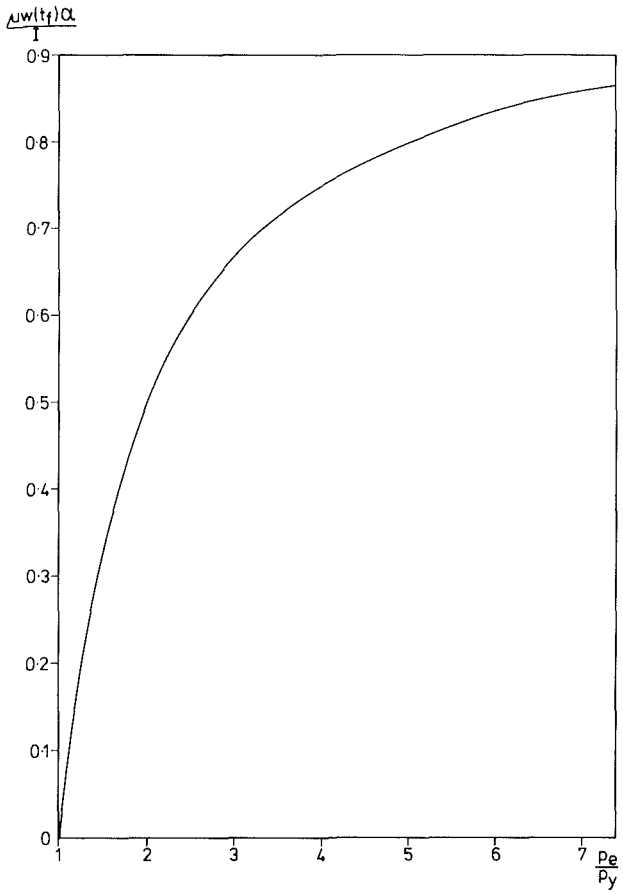

Fig. 3 Response expressed in terms of correlation parameters $\mu w(t_f)\alpha/I$ and p_e/p_y

$$v(t) = \frac{e^{-\alpha t}}{\mu} \int_{t_y}^{t} e^{\alpha\tau}[p(\tau) - p_y]d\tau, \tag{5}$$

and a further integration with respect to time leads to

$$w(t) = \frac{1}{\mu\alpha} \int_{t_y}^{t} [1 - e^{-\alpha(t-\tau)}][p(\tau) - p_y]d\tau \tag{6}$$

The time, t_f, at which the motion ceases is given from equation (5) as the solution of the equation

$$p_y[e^{\alpha t_f} - e^{\alpha t_y}]/\alpha = \int_{t_y}^{t_f} e^{\alpha\tau} p(\tau)\, d\tau. \tag{7}$$

Consequently the final deflection is given from equations (6) and (7) by

$$w(t_f) = \frac{1}{\mu\alpha} \int_{t_y}^{t_f} [p(\tau) - p_y]d\tau \tag{8}$$

Calculations have been performed for the rectangular, sinusoidal, triangular, linearly decaying, and exponentially decaying pulses shown in Fig. 1(*b*). The results in Fig. 2 show that there is a strong interaction between the final radial displacement and the pulse shape over a wide range of β even when attempts have been made to nondimensionalize the results by incorporating the impulse of the pressure pulse.

Correlation Parameters

For pulse-loaded structures in air, Youngdahl succeeded in taking account of the pulse shape by expressing the results as functions of an "effective" pressure rather than in terms of the peak pressure. A similar approach is adopted for the present problem except that the correlation parameters differ from those derived by Youngdahl in that they incorporate not only the properties of the structure and the pulse but also the acoustic properties of the fluid.

Defining the impulse, I, as

$$I = \int_{t_y}^{t_f} p(\tau)\, d\tau \tag{9}$$

and an effective pressure, p_e, as

$$p_e = \frac{I}{t_f - t_y}, \tag{10}$$

equation (8) can be reduced to

$$\frac{\mu w(t_f)\alpha}{I} = 1 - \frac{p_y}{p_e}. \tag{11}$$

Since the mode of deformation is the same for all pulse shapes the response can be represented by equation (11) and displayed in Fig. 3. It is suggested that these correlation parameters may prove useful in more complex situations.

Acknowledgments

The authors would like to thank the Science and Engineering Research Council for the award of a Research Grant (GR/B/74665) and a Research Studentship (SRH).

References

1 Transactions, 6th Int. Conf. on Structural Mechanics in Reactor Technology (SMIRT), North-Holland Publishing Company, Aug. 17-21, 1981.

2 Youngdahl, C. K., "Correlation Parameters for Eliminating the Effect of Pulse Shape on Dynamic Plastic Deformation," ASME JOURNAL OF APPLIED MECHANICS, Vol. 37, 1970, pp. 744-752.

3 Youngdahl, C. K., "Influence of Pulse Shape on the Final Plastic Deformation of a Circular Plate," *International Journal of Solids and Structures*, Vol. 7, 1971, pp. 1127-1142.

4 Youngdahl, C. K., "The Effect of Pulse Shape on the Dynamic Plastic Deformation of Reinforced Circular Cylindrical Shells," Paper No. 71-PVP-31, ASME, 1971.

On a One-Dimensional Formulation of the Problem of Torsion and Flexure of Shear Deformable Plates

E. Reissner[1]

Introduction

The following considerations are a complementation, and in one specific point an improvement, of a recent derivation of a system of one-dimensional beam equations from the equations of the linear theory of shear deformable plates [1]. The complementation of the earlier work depends on the use of the principle of minimum potential energy in place of a direct averaging procedure for the differential equations of plate theory. The improvement depends on the satisfaction of a requirement that the one-dimensional equations are exactly, rather than approximately, consistent with a solution of the St. Venant torsion problem within the framework of two-dimensional plate theory.

Derivation of Beam Equations

Our starting point are the expressions

[1] Department of Applied Mechanics and Engineering Sciences, University of California, San Diego, La Jolla, Calif. 92093

Manuscript received by ASME Applied Mechanics Division, May 1982.

Downloaded 02 May 2010 to 171.66.16.246. Redistribution subject to ASME license or copyright; see http://www.asme.org/terms/Terms_Use.cfm

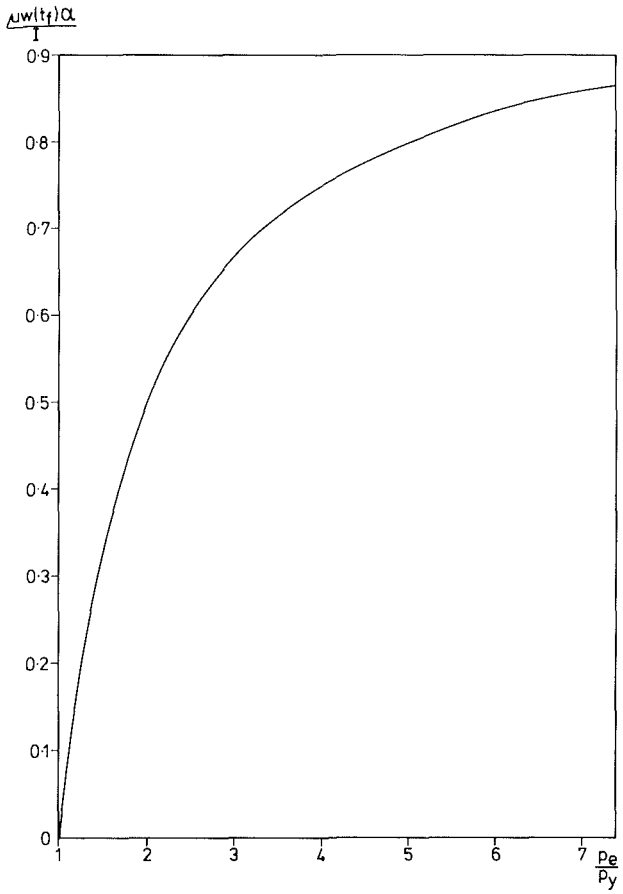

Fig. 3 Response expressed in terms of correlation parameters $\mu w(t_f)\alpha/I$ and p_e/p_y

$$v(t) = \frac{e^{-\alpha t}}{\mu} \int_{t_y}^{t} e^{\alpha\tau}[p(\tau) - p_y]d\tau, \tag{5}$$

and a further integration with respect to time leads to

$$w(t) = \frac{1}{\mu\alpha} \int_{t_y}^{t} [1 - e^{-\alpha(t-\tau)}][p(\tau) - p_y]d\tau \tag{6}$$

The time, t_f, at which the motion ceases is given from equation (5) as the solution of the equation

$$p_y[e^{\alpha t_f} - e^{\alpha t_y}]/\alpha = \int_{t_y}^{t_f} e^{\alpha\tau} p(\tau)\, d\tau. \tag{7}$$

Consequently the final deflection is given from equations (6) and (7) by

$$w(t_f) = \frac{1}{\mu\alpha} \int_{t_y}^{t_f} [p(\tau) - p_y]d\tau \tag{8}$$

Calculations have been performed for the rectangular, sinusoidal, triangular, linearly decaying, and exponentially decaying pulses shown in Fig. 1(*b*). The results in Fig. 2 show that there is a strong interaction between the final radial displacement and the pulse shape over a wide range of β even when attempts have been made to nondimensionalize the results by incorporating the impulse of the pressure pulse.

Correlation Parameters

For pulse-loaded structures in air, Youngdahl succeeded in taking account of the pulse shape by expressing the results as functions of an "effective" pressure rather than in terms of the peak pressure. A similar approach is adopted for the present problem except that the correlation parameters differ from those derived by Youngdahl in that they incorporate not only the properties of the structure and the pulse but also the acoustic properties of the fluid.

Defining the impulse, I, as

$$I = \int_{t_y}^{t_f} p(\tau)\, d\tau \tag{9}$$

and an effective pressure, p_e, as

$$p_e = \frac{I}{t_f - t_y}, \tag{10}$$

equation (8) can be reduced to

$$\frac{\mu w(t_f)\alpha}{I} = 1 - \frac{p_y}{p_e}. \tag{11}$$

Since the mode of deformation is the same for all pulse shapes the response can be represented by equation (11) and displayed in Fig. 3. It is suggested that these correlation parameters may prove useful in more complex situations.

Acknowledgments

The authors would like to thank the Science and Engineering Research Council for the award of a Research Grant (GR/B/74665) and a Research Studentship (SRH).

References

1 Transactions, 6th Int. Conf. on Structural Mechanics in Reactor Technology (SMIRT), North-Holland Publishing Company, Aug. 17-21, 1981.

2 Youngdahl, C. K., "Correlation Parameters for Eliminating the Effect of Pulse Shape on Dynamic Plastic Deformation," ASME JOURNAL OF APPLIED MECHANICS, Vol. 37, 1970, pp. 744-752.

3 Youngdahl, C. K., "Influence of Pulse Shape on the Final Plastic Deformation of a Circular Plate," *International Journal of Solids and Structures*, Vol. 7, 1971, pp. 1127-1142.

4 Youngdahl, C. K., "The Effect of Pulse Shape on the Dynamic Plastic Deformation of Reinforced Circular Cylindrical Shells," Paper No. 71-PVP-31, ASME, 1971.

On a One-Dimensional Formulation of the Problem of Torsion and Flexure of Shear Deformable Plates

E. Reissner[1]

Introduction

The following considerations are a complementation, and in one specific point an improvement, of a recent derivation of a system of one-dimensional beam equations from the equations of the linear theory of shear deformable plates [1]. The complementation of the earlier work depends on the use of the principle of minimum potential energy in place of a direct averaging procedure for the differential equations of plate theory. The improvement depends on the satisfaction of a requirement that the one-dimensional equations are exactly, rather than approximately, consistent with a solution of the St. Venant torsion problem within the framework of two-dimensional plate theory.

Derivation of Beam Equations

Our starting point are the expressions

[1] Department of Applied Mechanics and Engineering Sciences, University of California, San Diego, La Jolla, Calif. 92093

Manuscript received by ASME Applied Mechanics Division, May 1982.

Copyright © 1983 by ASME
Downloaded 02 May 2010 to 171.66.16.246. Redistribution subject to ASME license or copyright; see http://www.asme.org/terms/Terms_Use.cfm

$$\kappa_{xx} = \phi_{x,x}, \quad \kappa_{yy} = \phi_{y,y}, \quad \kappa_{xy} = \phi_{x,y} + \phi_{y,x}, \tag{1}$$

$$\gamma_x = \phi_x + w_{,x}, \quad \gamma_y = \phi_y + w_{,y}, \tag{2}$$

for transverse bending and shearing strains κ and γ in terms of rotational displacements ϕ, and a translational displacement w, for a plate with cartesian midplane coordinates x,y.

We assume that the direction of x is along the span of the beam for which a system of one-dimensional equations is to be derived, and we stipulate a plate strain energy functional of the form

$$U = \frac{1}{2}\int_0^L \int_{y_1}^{y_2} (D_x \kappa_{xx}^2 + D_y \kappa_{xy}^2 + C\gamma_x^2) dy\, dx, \tag{3}$$

consistent with the consequences $\kappa_{yy} = 0$ and $\gamma_y = 0$ of displacement assumptions

$$\phi_y = \theta(x), \quad w = v(x) - y\theta(x), \quad \phi_x = \phi(x) + g(y)\psi(x). \tag{4}$$

In this $g(y)$ is to be assumed suitably and $\theta(x)$, $v(x)$, $\phi(x)$, and $\psi(x)$ are to be determined through the variational equation

$$\delta\left\{U - \int (qv + m\phi + t\theta + r\psi)dx\right\} = 0. \tag{5}$$

The introduction of (4) into (3) makes it possible to write the variational equation (5) in the form

$$\int [Q\delta(\phi + v') + M\delta\phi' + T\delta\theta' + R\delta\psi' + S\delta\psi]dx - \int (q\delta v + m\delta\phi + t\delta\theta + r\delta\psi)dx = 0, \tag{6}$$

with the stress measures Q, M, T, R, and S depending on the displacement measures v, ϕ, θ, and ψ through constitutive equations

$$M = D_{B0}\phi' + D_{B1}\psi', \quad R = D_{B1}\phi' + D_{B2}\psi', \tag{7}$$

$$Q = C_0(\phi + v') - C_1\phi' + C_{0g}\psi, \tag{8a}$$

$$T = -C_1(\phi + v') + (D_{T0} + C_2)\theta' + (D_{T1} - C_{1g})\psi, \tag{8b}$$

$$S = C_{0g}(\phi + v') + (D_{T1} - C_{1g})\theta' + (D_{T2} + C_{gg})\psi, \tag{8c}$$

where

$$(D_{B0}, D_{B1}, D_{B2}) = \int_{y_1}^{y_2} (1, g, g^2) D_x\, dy, \tag{9a}$$

$$(D_{T0}, D_{T1}, D_{T2}) = \int_{y_1}^{y_2} (1, g', g'^2) D_y\, dy, \tag{9b}$$

$$(C_0, C_1, C_2, C_{0g}, C_{1g}, C_{gg}) = \int_{y_1}^{y_2} (1, y, y^2, g, yg, g^2) C\, dy, \tag{9c}$$

and with (6) implying the four equilibrium differential equations

$$Q' + q = 0, \quad M' - Q + m = 0, \quad T' + t = 0, \quad R' - S + r = 0. \tag{10}$$

Given the system (7) to (10) we may obtain the correponding results in [1] as a consequence of making the approximative assumption $g(y) = y$ in the constitutive coefficient defining relations (9). We then have, with D_i, D_T, and C_i as in [1], $D_{Bi} = D_i$, $D_{Ti} = D_T$, $C_{0g} = C_1$, $C_{1g} = C_{gg} = C_2$, and therewith (7) and (8a) directly as in [1] while at the same time (8b) and (8c) may be written in the form $T = T_M + T_Q$, $S = T_M - T_Q$, with T_M and T_Q as in [1].

Sequential Determination of Stresses and Displacements

We may determine the five functions Q, M, T, R, and S by means of the four equilibrium relations in (10) in conjunction with a compatibility equation involving R and M which may be derived through use of the inverted constitutive relations

$$\psi' = \frac{R}{D_R} - \frac{M}{D_{RM}}, \quad \psi = \frac{S}{C_S} - \frac{T}{C_{ST}} - \frac{Q}{C_{SQ}}, \tag{11}$$

in conjunction with the last equation in (10), in the form

$$\frac{R}{D_R} - \left(\frac{R'}{C_S}\right)' = \frac{M}{D_{MR}} + \left(\frac{r}{C_S} - \frac{T}{C_{ST}} - \frac{Q}{C_{SQ}}\right)'. \tag{12}$$

Having (10) and (12) we may then determine ϕ, θ, and v with the help of the additional inverted constitutive equations

$$\phi' = \frac{M}{D_M} - \frac{R}{D_{MR}}, \quad \phi' = \frac{T}{C_T} - \frac{Q}{C_{TQ}} - \frac{S}{C_{TS}}, \tag{13}$$

$$v' + \phi = \frac{Q}{C_Q} - \frac{T}{C_{QT}} - \frac{S}{C_{QS}}. \tag{14}$$

Asymptotic Considerations

The form of (12) shows the possibility of a warping constraint boundary layer effect, as a quantitative indication of the validity of St. Venant's principle. The existence of this effect depends on the satisfaction of the order of magnitude relation

$$D_R \ll C_S L^2, \tag{15}$$

where L is a representative spanwise linear dimension.

For cases for which (15) applies it is of advantage to write

$$R = R_e + R_i, \tag{16}$$

with R_e being the general solution of the homogeneous equation $R_e/D_R = (R_e'/C_S)'$ and with R_i being given, except for terms that are small of higher order, by

$$\frac{R_i}{D_R} = \frac{M}{D_{MR}} + \left(\frac{r}{C_S} - \frac{T}{C_{ST}} - \frac{Q}{C_{SQ}}\right)'. \tag{17}$$

With the decomposition (16), and with the observation that in the sense of (16) we will have $M = M_i$, $Q = Q_i$, $T = T_i$, while $S = S_e + S_i$, we may then further deduce from (13) and (14), with $R_e/D_{MR} = (D_R/D_{MR})(R_e'/C_S)' \approx D_R R_e''/D_{MR}C_S$,

$$\phi = \phi_i - \frac{D_R}{D_{MR}}\frac{R_e'}{C_S}, \quad \theta = \theta_i - \frac{R_e}{C_{TS}},$$

$$v = v_i + \frac{D_R}{D_{MR}}\frac{R_e}{C_S} - \frac{R_e}{C_{QS}}, \tag{18}$$

where $\phi_i = \int (M_i/D_M - R_i/D_{MR})dx$, etc., and where, in view of (11), $\psi = \psi_i + R_e'/C_S$. With these results, and with the order of magnitude relation

$$R_e = o(LR_e'), \tag{19}$$

which is implied by (15) and by the form of the differential equation for R_e we have then, in extension of a result stated in [1], that a system of *four* end-section boundary conditions $\phi = \bar{\phi}$, $\theta = \bar{\theta}$, $\psi = \bar{\psi}$, $v = \bar{v}$ will be asymptotically equivalent to a system of *three* conditions for the determination of the interior solution contributions ϕ_i, θ_i, ψ_i, v_i, consisting of one *contracted* boundary condition $D_{MR}\phi_i + D_R\psi_i = D_{MR}\bar{\phi} + D_R\bar{\psi}$, and two *reduced* boundary conditions $\theta_i = \bar{\theta}$, $v_i = \bar{v}$. At the same time we have, for the subsequent determination of the edge zone solution contribution R_e, the supplementary boundary condition $R_e' = C_S(\bar{\psi} - \psi_i)$.

Determination of Interior Solution Shear Center Coordinate

In order to obtain a shear center formula that is valid outside the warping constraint boundary layer we use the second relation in (13) for the case of a uniform beam and absent distributed loads, with $S_i = R_i'$ and $R_i' = (D_R/D_{RM})M'$, in the form

$$\theta_i' = \frac{T}{C_T} - \frac{Q}{C_{TQ}} - \frac{D_R}{D_{RM}}\frac{Q}{C_{TS}}. \tag{20}$$

Downloaded 02 May 2010 to 171.66.16.246. Redistribution subject to ASME license or copyright; see http://www.asme.org/terms/Terms_Use.cfm

The defining stipulation for the shear center coordinate y_s, that $\theta_i' = 0$ when $T = -Qy_s$, then gives

$$y_s = -\frac{C_T}{C_{TQ}} - \frac{C_T}{C_{TS}} \frac{D_R}{D_{RM}}. \tag{21}$$

An alternate form of this result in terms of the stiffness factors D and C in equations (7) and (8) is obtained upon writing $D_R/D_{RM} = D_{B1}/D_{B0}$ and by then setting in (8*a*) to (8*c*) $T = -Qy_s$, $\theta' = 0$ and $S = (D_{B1}/D_{B0})Q$. With this there follows

$$y_s = \frac{D_{B1}}{D_{B0}} \frac{C_0C_{1g} - C_1C_{0g} - C_0D_{T1}}{C_0C_{gg} - C_{0g}^2 + C_0D_{T2}} - \frac{C_1C_{gg} - C_{0g}C_{1g} + C_1D_{T2} + C_{0g}D_{T1}}{C_0C_{gg} - C_{0g}^2 + C_0D_{T2}}, \tag{22}$$

with (22) reducing to the previously obtained result [1],

$$y_s = \frac{D_1}{D_0} \frac{C_0(C_2 - D_T) - C_1^2}{C_0(C_2 + D_T) - C_1^2} - \frac{2C_1D_T}{C_0(C_2 + D_T) - C_1^2}, \tag{22'}$$

upon setting $g(y) = y$.

Consistency With St. Venant Torsion Theory

For the one-dimensional equations (7) to (10) to be such as to contain the torque-twist relation of the theory of St. Venant as a special case, it is necessary to stipulate that the function g in (4) be the warping function for St. Venant torsion, within the framework of shear-deformable plate theory.

Given the system of plate strain displacement relations (1) and (2) we have the conditions for St. Venant torsion upon setting

$$\phi_y = x, \quad w = -xy, \quad \phi_y = g(y), \tag{23}$$

and therewith $\kappa_{xx} = \kappa_{yy} = \gamma_y = 0$. The remaining strain components κ_{xy} and γ_y in conjunction with the strain energy expression (3) imply as plate stress strain relations for the problem of torsion

$$M_{xy} = D_y(g' + 1), \quad Q_x = C(g - y), \tag{24}$$

with the plate equilibrium equation $M_{xy,y} - Q_x = 0$ and the plate boundary conditions $M_{xy}(y_1) = M_{xy}(y_2) = 0$ leading to the boundary value problem

$$[D_y(g' + 1)]' - C(g - y) = 0, \quad g'(y_1) = g'(y_2) = -1. \tag{25}$$

For the use of the function g as defined by (25) it is of advantage to observe the two integral relations

$$\int_{y_1}^{y_2} C(g - y)dy = 0, \qquad \int_{y_1}^{y} D_y(g' + 1)g'dy + \int_{y_1}^{y_2} D_y(g - y)gdy = 0, \tag{26}$$

which imply the two one-dimensional constitutive coefficient formulas

$$C_{0g} = C_1, \quad C_{1g} - D_{T1} = D_{T2} + C_{gg}, \tag{27}$$

with these formulas being of obvious significance in relation to the form of equations (8).

Finally, an introduction of (27) into the shear center formula (22) leads to the unexpectedly simple result

$$y_s = D_{B1}/D_{B0}, \tag{22''}$$

with the effect of transverse shear deformability on the location of the center of shear now being implicit, rather than explict as in the approximate result (22'), upon introduction of the solution g as in (25) into the defining relations in (9*a*).

References

1 Reissner, E., "On Torsion and Transverse Flexure of Orthotropic Elastic Plates," ASME JOURNAL OF APPLIED MECHANICS, Vol. 47, 1980, pp. 855-860.

Cumulative Effect at the Soil Surface Due to Shear Wave Propagation

M. Zak[1]

A cumulation of the shear strain energy at the soil surface as a response to underground shear excitations is considered. It is shown that this effect is caused by the vanishing shear modulus at the soil surface. The corresponding mathematical model is presented by a linear hyperbolic equation with variable coefficients. The uniqueness and stability of the solutions are analyzed.

Introduction

Estimates of the shear strain energy release in earthquakes is one of the most important problems in the prediction of a bound of the hazard to be expected and in detection of underground nuclear explosions. A comprehensive review of both the theoretical and experimental efforts in this area is given in [1]. This Brief Note is devoted to the analysis of a special phenomenon associated with the cumulation of the shear strain energy at the soil surface as a response to underground shear excitations. These phenomena are caused by the vanishing shear modulus at the soil surface. Indeed, based on the results of the laboratory and field tests [2], it would appear that the shear strength versus depth relationship for the clay deposit can be reasonably represented as a uniform increase from an average value of 0.08 ton/ft^2 at elevation 0 to 0.52 ton/ft^2 at elevation -90 ft. The cumulative effect caused by such a property can be briefly explained in the following terms: Suppose that an isolated shear wave of small amplitude was generated somewhere underground. The speed of propagation of the leading front of the shear wave moving toward the surface will be smaller than the speed of the trailing front because the shear modulus decreased from the source of the disturbance to the surface. Hence, the length of the above wave will be decreasing and in some cases will tend to zero. Then the specific energy per unit of length will tend to infinity which leads to the cumulative effect. The similar situation associated with the snap of a weap was investigated in [3] and applied in [4] to some surface effects in elasticity.

Model Formulation

For better physical interpretation the simplest one-dimensional model of the shear wave propagation in a soil column of the height H is considered:

$$\rho \frac{\partial^2 u}{\partial t^2} = \frac{\partial}{\partial x}\left(G \frac{\partial u}{\partial x}\right) \tag{1}$$

where ρ is the density, u is the horizontal displacement, G is the shear modulus, t is time, and x is the vertical coordinate with the origin at the surface.

Ignoring the small shear stresses at the surface, the shear modulus will be taken in the following form [2]:

$$G = 0.5\rho gx \tag{2}$$

Equation (1) will be investigated subject to the initial and boundary conditions formulated below:

[1]Applied Mechanics Technology Section, Jet Propulsion Laboratory, California Institute of Technology, Pasadena, Calif. 91109.

Manuscript received by ASME Applied Mechanics Division, June, 1982; final revision, September, 1982.

Downloaded 02 May 2010 to 171.66.16.246. Redistribution subject to ASME license or copyright; see http://www.asme.org/terms/Terms_Use.cfm

The defining stipulation for the shear center coordinate y_s, that $\theta_i' = 0$ when $T = -Qy_s$, then gives

$$y_s = -\frac{C_T}{C_{TQ}} - \frac{C_T}{C_{TS}} \frac{D_R}{D_{RM}}. \tag{21}$$

An alternate form of this result in terms of the stiffness factors D and C in equations (7) and (8) is obtained upon writing $D_R/D_{RM} = D_{B1}/D_{B0}$ and by then setting in (8*a*) to (8*c*) $T = -Qy_s$, $\theta' = 0$ and $S = (D_{B1}/D_{B0})Q$. With this there follows

$$y_s = \frac{D_{B1}}{D_{B0}} \frac{C_0C_{1g} - C_1C_{0g} - C_0D_{T1}}{C_0C_{gg} - C_{0g}^2 + C_0D_{T2}} - \frac{C_1C_{gg} - C_{0g}C_{1g} + C_1D_{T2} + C_{0g}D_{T1}}{C_0C_{gg} - C_{0g}^2 + C_0D_{T2}}, \tag{22}$$

with (22) reducing to the previously obtained result [1],

$$y_s = \frac{D_1}{D_0} \frac{C_0(C_2 - D_T) - C_1^2}{C_0(C_2 + D_T) - C_1^2} - \frac{2C_1D_T}{C_0(C_2 + D_T) - C_1^2}, \tag{22'}$$

upon setting $g(y) = y$.

Consistency With St. Venant Torsion Theory

For the one-dimensional equations (7) to (10) to be such as to contain the torque-twist relation of the theory of St. Venant as a special case, it is necessary to stipulate that the function g in (4) be the warping function for St. Venant torsion, within the framework of shear-deformable plate theory.

Given the system of plate strain displacement relations (1) and (2) we have the conditions for St. Venant torsion upon setting

$$\phi_y = x, \quad w = -xy, \quad \phi_y = g(y), \tag{23}$$

and therewith $\kappa_{xx} = \kappa_{yy} = \gamma_y = 0$. The remaining strain components κ_{xy} and γ_y in conjunction with the strain energy expression (3) imply as plate stress strain relations for the problem of torsion

$$M_{xy} = D_y(g' + 1), \quad Q_x = C(g - y), \tag{24}$$

with the plate equilibrium equation $M_{xy,y} - Q_x = 0$ and the plate boundary conditions $M_{xy}(y_1) = M_{xy}(y_2) = 0$ leading to the boundary value problem

$$[D_y(g' + 1)]' - C(g - y) = 0, \quad g'(y_1) = g'(y_2) = -1. \tag{25}$$

For the use of the function g as defined by (25) it is of advantage to observe the two integral relations

$$\int_{y_1}^{y_2} C(g - y)dy = 0, \qquad \int_{y_1}^{y} D_y(g' + 1)g'dy + \int_{y_1}^{y_2} D_y(g - y)gdy = 0, \tag{26}$$

which imply the two one-dimensional constitutive coefficient formulas

$$C_{0g} = C_1, \quad C_{1g} - D_{T1} = D_{T2} + C_{gg}, \tag{27}$$

with these formulas being of obvious significance in relation to the form of equations (8).

Finally, an introduction of (27) into the shear center formula (22) leads to the unexpectedly simple result

$$y_s = D_{B1}/D_{B0}, \tag{22''}$$

with the effect of transverse shear deformability on the location of the center of shear now being implicit, rather than explict as in the approximate result (22'), upon introduction of the solution g as in (25) into the defining relations in (9*a*).

References

1 Reissner, E., "On Torsion and Transverse Flexure of Orthotropic Elastic Plates," ASME JOURNAL OF APPLIED MECHANICS, Vol. 47, 1980, pp. 855-860.

Cumulative Effect at the Soil Surface Due to Shear Wave Propagation

M. Zak[1]

A cumulation of the shear strain energy at the soil surface as a response to underground shear excitations is considered. It is shown that this effect is caused by the vanishing shear modulus at the soil surface. The corresponding mathematical model is presented by a linear hyperbolic equation with variable coefficients. The uniqueness and stability of the solutions are analyzed.

Introduction

Estimates of the shear strain energy release in earthquakes is one of the most important problems in the prediction of a bound of the hazard to be expected and in detection of underground nuclear explosions. A comprehensive review of both the theoretical and experimental efforts in this area is given in [1]. This Brief Note is devoted to the analysis of a special phenomenon associated with the cumulation of the shear strain energy at the soil surface as a response to underground shear excitations. These phenomena are caused by the vanishing shear modulus at the soil surface. Indeed, based on the results of the laboratory and field tests [2], it would appear that the shear strength versus depth relationship for the clay deposit can be reasonably represented as a uniform increase from an average value of 0.08 ton/ft^2 at elevation 0 to 0.52 ton/ft^2 at elevation -90 ft. The cumulative effect caused by such a property can be briefly explained in the following terms: Suppose that an isolated shear wave of small amplitude was generated somewhere underground. The speed of propagation of the leading front of the shear wave moving toward the surface will be smaller than the speed of the trailing front because the shear modulus decreased from the source of the disturbance to the surface. Hence, the length of the above wave will be decreasing and in some cases will tend to zero. Then the specific energy per unit of length will tend to infinity which leads to the cumulative effect. The similar situation associated with the snap of a weap was investigated in [3] and applied in [4] to some surface effects in elasticity.

Model Formulation

For better physical interpretation the simplest one-dimensional model of the shear wave propagation in a soil column of the height H is considered:

$$\rho \frac{\partial^2 u}{\partial t^2} = \frac{\partial}{\partial x}\left(G \frac{\partial u}{\partial x}\right) \tag{1}$$

where ρ is the density, u is the horizontal displacement, G is the shear modulus, t is time, and x is the vertical coordinate with the origin at the surface.

Ignoring the small shear stresses at the surface, the shear modulus will be taken in the following form [2]:

$$G = 0.5\rho gx \tag{2}$$

Equation (1) will be investigated subject to the initial and boundary conditions formulated below:

[1]Applied Mechanics Technology Section, Jet Propulsion Laboratory, California Institute of Technology, Pasadena, Calif. 91109.

Manuscript received by ASME Applied Mechanics Division, June, 1982; final revision, September, 1982.

Copyright © 1983 by ASME
Downloaded 02 May 2010 to 171.66.16.246. Redistribution subject to ASME license or copyright; see http://www.asme.org/terms/Terms_Use.cfm

$$u(x,0) = \varphi(x) \qquad 0 \le x \le H \tag{3}$$

$$\frac{\partial u}{\partial x}(x,0) = \psi(x)$$

$$u(H,t) = \alpha(t)$$

$$\frac{\partial u}{\partial x}(0,t) = 0 \tag{4}$$

Thus, it is assumed that the soil column is fixed at $x=H$ and there is no shear stress at the surface, i.e., at $x=0$.

One should notice that for simplicity in this model all the damping and creep effects are ignored.

Uniqueness of the Solution

Let us assume that there exist two solutions of the problem under consideration: $u'(x,t)$ and $u''(x,t)$ and let us examine the difference:

$$u^*(x,t) = u'(x,t) - u''(x,t) \tag{5}$$

The function $u^*(x,t)$ satisfied equation (1) with additional homogeneous conditions:

$$\rho \frac{\partial^2 u^*}{\partial t^2} = \frac{\partial}{\partial x}\left(G \frac{\partial u^*}{\partial x}\right) \tag{6}$$

$$u^*(x,0) = 0, \quad \frac{\partial u^*}{\partial t}(x,0) = 0 \tag{7}$$

$$u^*(H,t) = 0, \quad \frac{\partial u^*}{\partial x}(0,t) = 0 \tag{8}$$

For the total energy, one gets:

$$E(t) = E(0) = \frac{1}{2}\int_0^H \left\{ G\left(\frac{\partial u^*}{\partial x}\right)^2 + \rho\left(\frac{\partial u^*}{\partial t}\right)^2 \right\}\Big|_{t=0} dx = 0 \tag{9}$$

If the solution is sought in the open interval

$$0 < x \le H \tag{10}$$

which does not include the surface point $x=0$, then the uniqueness of the solution is obvious.

However, this proof cannot be applied to the closed interval

$$0 \le x \le H \tag{11}$$

which includes the surface point $x=0$. Indeed, in this case according to equation (2)

$$G = 0 \quad \text{at} \quad x = 0 \tag{12}$$

and any arbitrarily selected derivative $\partial u^*/\partial x$ at $x=0$ will satisfy the equality in (9).

Thus, for the closed interval (11), the uniqueness of the solution can be guaranteed only in the class of functions having continuous derivative $\partial u^*/\partial x$, otherwise the infinite number of different solutions can be offered to satisfy equation (1) with the conditions (3) and (4) in the interval (11). As will be shown in the following, the artificial mathematical restriction about the continuity of the derivative $\partial u^*/\partial x$ excludes such important physical phenomena as cumulative effect.

From the mathematical point of view the singularity at the point $x=0$ is associated with the fact that the original equation is hyperbolic in the open interval (10), but degenerates into a parabolic equation at the point $x=0$. The physical meaning of this singularity will be discussed in the following section.

Stability of the Solution

Starting with the initial conditions (3) let us assume that

$$\varphi(x) \begin{cases} > 0 & \text{for } 0 < \mathring{x}_1 < x < \mathring{x}_2 < H \\ = 0 & \text{for } x < x_1, \text{ and } x > x_2 \end{cases} \tag{13}$$

$$\psi(x)\,|_{0 \le x \le H} = 0 \tag{14}$$

$$\alpha(t) = 0, \quad t \ge 0 \tag{15}$$

i.e., we consider an initial disturbance in a local interval $[\mathring{x}_1, \mathring{x}_2]$ contained within the interval $[0,H]$.

From the differential equations of the characteristics one finds the equations of the characteristics passing through x_1 and x_2:

$$t' = \int_{x_1}^{\mathring{x}_1} \frac{d_\epsilon}{\sqrt{G(\epsilon)/\varphi}}, \quad t'' = \int_{x_2}^{\mathring{x}_2} \frac{d_\epsilon}{\sqrt{G(\epsilon)/\varphi}} \tag{16}$$

$$0 < x_1 < x_2 < H$$

Here x_1 and x_2 are the coordinates of the leading and trailing fronts of the discontinuity wave of derivatives $\partial^2 u/\partial t^2$ and $\partial^2 u/\partial x^2$, where

$$x_1 = \mathring{x}_1, \quad x_2 = \mathring{x}_2 \quad \text{at} \quad t = 0$$

A singular solution coincident for both characteristics holds for

$$x_1 = x_2 = 0$$

because

$$\frac{dx_1}{dt}\Big|_{x_1=0} = \frac{dx_2}{dt}\Big|_{x_2=0} = 0 \tag{17}$$

Two cases may arise:

(*A*) The improper integral

$$\int_x^{x_o} \frac{d\eta}{\sqrt{G(\eta)/\rho}} < \infty \quad \text{for} \quad x \to 0 \tag{18}$$

i.e., converges, which then means that coincidence of the characteristics (16) occurs for finite $t = t^*$.

Then

$$\left|\frac{\partial u}{\partial t}\right| \to \infty \quad \text{for} \quad t \to t^* < \infty \tag{19}$$

From the mathematical viewpoint this instability predicts a cumulation of the shear strain energy at the soil surface $x=0$. At the same time it illustrates the ambiguity in the solution which has been remarked in the investigation of equation (9).

(*B*) If the improper integral (18) diverges then the characteristics (16) coincide at $t^* \to \infty$ and the cumulation effect does not occur.

For the particular case of soil where the shear modulus is given in the form (2) the integral (18) converges and the time t^* defining the moment of the formation of the shear strain energy cumulation at the soil surface is

$$t^* = 2\sqrt{\frac{2\mathring{x}_2}{g}}$$

In the general case when the shear modulus is a more complicated function of the elevation the cumulative effect occurs if

$$G > \epsilon_1 x^{2+\epsilon_2}$$

where ϵ_1, ϵ_2 are arbitrarily small positive constants, because then the integral (18) converges.

References

1 Bath, M., "Earthquake Energy and Magnitude," in: *Physics and Chemistry of the Earth*, Pergamon Press, New York, 1966.

2 Weigel, R. L., *Earthquake Engineering*, Prentice-Hall, Englewood Cliffs, N.J., 1970.

Downloaded 02 May 2010 to 171.66.16.246. Redistribution subject to ASME license or copyright; see http://www.asme.org/terms/Terms_Use.cfm

3 Zak, M., "Uniqueness and Stability of the Solution of the Small Perturbation Problem of a Flexible Filament With a Free End," *J. Applied Math. and Mech.*, Vol. 34, No. 6, Moscow, 1970, pp. 1052–1098.
4 Zak, M., "Surface Phenomena in Elasticity," *Journal of Elasticity* Vol. 11, No. 2, Apr., 1981.

A Similarity Solution for a Rayleigh Flow of a Bingham Fluid

N. Phan-Thien[1]

Introduction

Many fluid commonly used in the food processing and in the oil drilling industries behave as if they have a yield stress. Below this yield stress, they do not deform, at least in the laboratory timescale; above this yield stress, they flow like a Newtonian fluid, viz, one with a constant viscosity. The simplest constitutive equation for such fluids is the Bingham model [1] where the shear stress in a simple shear flow is given by

$$\tau = \eta\dot{\gamma} + \tau_y \mathrm{sgn}(\dot{\gamma}). \tag{1}$$

In (1), η is the (constant) Newtonian viscosity, τ_y is the yield shear stress, $\dot{\gamma}$ is the shear rate, and sgn(•) is the generalized sign function. Generalization of (1) to account for three dimensionality has been done by Oldroyd [2]; however, we shall not be concerned with this aspect.

Because of the nonzero yield stress, the flow of any Bingham fluid involves two regions: a no-flow and a flow region, both separated by a yield surface whose position must be found as part of the solution. Not surprisingly there has not been found many nontrivial solutions for the Bingham fluid; a summary of known solutions is given in the book of Bird et al. [3]. In this short Note were present a similarity solution for the Bingham fluid. The flow we consider here is analogous to the Rayleigh flow (or Stokes' first problem), except that at time $t>0$ the fluid is given a constant shear stress τ_0 at the boundary $y=0$ instead of a constant velocity.

Analysis

We consider the flow of a Bingham body above the plane $y=0$ which is generated at time $t\geq 0+$ by imparting a constant shear stress

$$\tau = \tau_0 H(t) \quad \text{at} \quad y=0,$$

where $H(t)$ is the Heaviside function, x is the direction of the flow, and y is the direction normal to the boundary $y=0$. We assume that $\tau_0 > \tau_y > 0$. If $\tau_y > \tau_0 > 0$, there will be no motion. Body forces will be neglected. In this unidirectional flow, the constitutive relation (1) will be sufficient. However, to make the findings more general we shall assume that in a shear flow with shear rate $\dot{\gamma}$, the shear stress is given by

$$\tau = \begin{cases} \eta_2\dot{\gamma}, & |\tau| \leq \tau_y \\ \eta_1\dot{\gamma}, & |\tau| > \tau_y \end{cases} \tag{2}$$

The ratio $\alpha = \eta_2/\eta_1$ will be large for a "real" Bingham fluid ($\alpha = \infty$ for an ideal Bingham fluid). Denoting the shear stresses in the flow and no-flow[2] region by τ_1 and τ_2, respectively, then both τ_i are governed by the heat diffusion equation

$$\frac{\partial \tau_i}{\partial t} = \nu_i \frac{\partial^2 \tau_i}{\partial y^2}, \quad \nu_i = \frac{\eta_i}{\rho}, \tag{3}$$

where ρ is the common density of the fluid in both regions. The boundary conditions for τ_i are

$$\begin{aligned} &\text{at} \quad y=0, \quad \tau_1 = \tau_0 H(t), \\ &\text{at} \quad y=y_c(t), \quad \tau_1 = \tau_2 = \tau_y = \beta\tau_0; \quad u_1 = u_2, \\ &\text{at} \quad y=\infty, \quad \tau_2 = 0; \quad u_2 = 0. \end{aligned} \tag{4}$$

At the yield surface, $y = y_c(t)$, the shear stress τ_i are equal to the yield shear stress $\tau_y = \beta\tau_0$, $0<\beta<1$. Furthermore, we require that there is no discontinuity of velocity at the yield surface (u_i, $i=1,2$ are the velocities in the x-direction in the flow and no-flow region, respectively). The heat diffusion equation has been studied in detail in the book of Bluman and Cole [4]; it has a similarity solution of the type

$$\tau_i = \tau_0 f_i(\zeta), \quad \zeta = \frac{y}{2\sqrt{\nu_1 t}}, \tag{5}$$

where

$$f_1'' + 2\zeta f_1' = 0 \tag{6}$$

and

$$f_2'' + \frac{2}{\alpha}\zeta f_2' = 0 \tag{7}$$

In (6) and (7), the dash denotes a derivative with respect to the similarity variable ζ. The boundary conditions for f_i are

$$\begin{aligned} &f_1(0) = 1, \\ &f_1(\zeta_c) = f_2(\zeta_c) = \beta, \\ &f_2(\infty) = 0, \end{aligned} \tag{8}$$

where $\zeta_c = y_c(t)/2\sqrt{\nu_1 t}$. It will be seen that ζ_c is a constant; thus (5)–(8) indeed constitute a similarity solution to the present problem.

The solution to (6)–(8) are

$$f_1(\zeta) = 1 - (1-\beta)\frac{\mathrm{erf}(\zeta)}{\mathrm{erf}(\zeta_c)}, \quad \zeta \leq \zeta_c \tag{9}$$

and, for $\zeta \geq \zeta_c$,

$$f_2(\zeta) = \beta\left(1 - \frac{\left[\mathrm{erfc}\left(\frac{\zeta_c}{\sqrt{\alpha}}\right) - \mathrm{erfc}\left(\frac{\zeta}{\sqrt{\alpha}}\right)\right]}{\mathrm{erfc}\left(\frac{\zeta_c}{\sqrt{\alpha}}\right)}\right) \tag{10}$$

where $\mathrm{erf}(x)$ and $\mathrm{erfc}(x)$ are the error and the complementary error functions:

$$\mathrm{erf}(x) = 1 - \mathrm{erfc}(x) = \frac{2}{\sqrt{\pi}}\int_0^x e^{-t^2}\,dt.$$

Now, denoting the velocities u_i, $i=1,2$ by

$$u_i(y,t) = \frac{\tau_0}{\eta_i} 2\sqrt{\nu_1 t}\, U_i(\zeta), \tag{11}$$

it is found that

[1] Department of Chemical Engineering, California Institute of Technology, Pasadena, Calif. 91125. Permanent address: Mechanical Engineering Department, Sydney University, NSW 2006, Australia.
Manuscript received by ASME Applied Mechanics Division, August, 1982; final revision, October, 1982.

[2] The "no-flow" region is the region in which $|\tau_2| \leq \tau_y$. Since η_2 is finite, there will be some deformation in this region.

Downloaded 02 May 2010 to 171.66.16.246. Redistribution subject to ASME license or copyright; see http://www.asme.org/terms/Terms_Use.cfm

3 Zak, M., "Uniqueness and Stability of the Solution of the Small Perturbation Problem of a Flexible Filament With a Free End," *J. Applied Math. and Mech.*, Vol. 34, No. 6, Moscow, 1970, pp. 1052–1098.
4 Zak, M., "Surface Phenomena in Elasticity," *Journal of Elasticity* Vol. 11, No. 2, Apr., 1981.

A Similarity Solution for a Rayleigh Flow of a Bingham Fluid

N. Phan-Thien[1]

Introduction

Many fluid commonly used in the food processing and in the oil drilling industries behave as if they have a yield stress. Below this yield stress, they do not deform, at least in the laboratory timescale; above this yield stress, they flow like a Newtonian fluid, viz, one with a constant viscosity. The simplest constitutive equation for such fluids is the Bingham model [1] where the shear stress in a simple shear flow is given by

$$\tau = \eta\dot{\gamma} + \tau_y \mathrm{sgn}(\dot{\gamma}). \tag{1}$$

In (1), η is the (constant) Newtonian viscosity, τ_y is the yield shear stress, $\dot{\gamma}$ is the shear rate, and sgn(•) is the generalized sign function. Generalization of (1) to account for three dimensionality has been done by Oldroyd [2]; however, we shall not be concerned with this aspect.

Because of the nonzero yield stress, the flow of any Bingham fluid involves two regions: a no-flow and a flow region, both separated by a yield surface whose position must be found as part of the solution. Not surprisingly there has not been found many nontrivial solutions for the Bingham fluid; a summary of known solutions is given in the book of Bird et al. [3]. In this short Note were present a similarity solution for the Bingham fluid. The flow we consider here is analogous to the Rayleigh flow (or Stokes' first problem), except that at time $t>0$ the fluid is given a constant shear stress τ_0 at the boundary $y=0$ instead of a constant velocity.

Analysis

We consider the flow of a Bingham body above the plane $y=0$ which is generated at time $t\geq 0+$ by imparting a constant shear stress

$$\tau = \tau_0 H(t) \quad \text{at} \quad y=0,$$

where $H(t)$ is the Heaviside function, x is the direction of the flow, and y is the direction normal to the boundary $y=0$. We assume that $\tau_0 > \tau_y > 0$. If $\tau_y > \tau_0 > 0$, there will be no motion. Body forces will be neglected. In this unidirectional flow, the constitutive relation (1) will be sufficient. However, to make the findings more general we shall assume that in a shear flow with shear rate $\dot{\gamma}$, the shear stress is given by

$$\tau = \begin{cases} \eta_2\dot{\gamma}, & |\tau| \leq \tau_y \\ \eta_1\dot{\gamma}, & |\tau| > \tau_y \end{cases} \tag{2}$$

The ratio $\alpha = \eta_2/\eta_1$ will be large for a "real" Bingham fluid ($\alpha = \infty$ for an ideal Bingham fluid). Denoting the shear stresses in the flow and no-flow[2] region by τ_1 and τ_2, respectively, then both τ_i are governed by the heat diffusion equation

$$\frac{\partial \tau_i}{\partial t} = \nu_i \frac{\partial^2 \tau_i}{\partial y^2}, \quad \nu_i = \frac{\eta_i}{\rho}, \tag{3}$$

where ρ is the common density of the fluid in both regions. The boundary conditions for τ_i are

$$\begin{aligned} &\text{at} \quad y=0, \quad \tau_1 = \tau_0 H(t), \\ &\text{at} \quad y=y_c(t), \quad \tau_1 = \tau_2 = \tau_y = \beta\tau_0; \quad u_1 = u_2, \\ &\text{at} \quad y=\infty, \quad \tau_2 = 0; \quad u_2 = 0. \end{aligned} \tag{4}$$

At the yield surface, $y = y_c(t)$, the shear stress τ_i are equal to the yield shear stress $\tau_y = \beta\tau_0$, $0<\beta<1$. Furthermore, we require that there is no discontinuity of velocity at the yield surface (u_i, $i=1,2$ are the velocities in the x-direction in the flow and no-flow region, respectively). The heat diffusion equation has been studied in detail in the book of Bluman and Cole [4]; it has a similarity solution of the type

$$\tau_i = \tau_0 f_i(\zeta), \quad \zeta = \frac{y}{2\sqrt{\nu_1 t}}, \tag{5}$$

where

$$f_1'' + 2\zeta f_1' = 0 \tag{6}$$

and

$$f_2'' + \frac{2}{\alpha}\zeta f_2' = 0 \tag{7}$$

In (6) and (7), the dash denotes a derivative with respect to the similarity variable ζ. The boundary conditions for f_i are

$$\begin{aligned} &f_1(0) = 1, \\ &f_1(\zeta_c) = f_2(\zeta_c) = \beta, \\ &f_2(\infty) = 0, \end{aligned} \tag{8}$$

where $\zeta_c = y_c(t)/2\sqrt{\nu_1 t}$. It will be seen that ζ_c is a constant; thus (5)–(8) indeed constitute a similarity solution to the present problem.

The solution to (6)–(8) are

$$f_1(\zeta) = 1 - (1-\beta)\frac{\mathrm{erf}(\zeta)}{\mathrm{erf}(\zeta_c)}, \quad \zeta \leq \zeta_c \tag{9}$$

and, for $\zeta \geq \zeta_c$,

$$f_2(\zeta) = \beta\left(1 - \frac{\left[\mathrm{erfc}\left(\frac{\zeta_c}{\sqrt{\alpha}}\right) - \mathrm{erfc}\left(\frac{\zeta}{\sqrt{\alpha}}\right)\right]}{\mathrm{erfc}\left(\frac{\zeta_c}{\sqrt{\alpha}}\right)}\right) \tag{10}$$

where erf(x) and erfc(x) are the error and the complementary error functions:

$$\mathrm{erf}(x) = 1 - \mathrm{erfc}(x) = \frac{2}{\sqrt{\pi}}\int_0^x e^{-t^2}\,dt.$$

Now, denoting the velocities u_i, $i=1,2$ by

$$u_i(y,t) = \frac{\tau_0}{\eta_i} 2\sqrt{\nu_1 t}\, U_i(\zeta), \tag{11}$$

it is found that

[1] Department of Chemical Engineering, California Institute of Technology, Pasadena, Calif. 91125. Permanent address: Mechanical Engineering Department, Sydney University, NSW 2006, Australia.
Manuscript received by ASME Applied Mechanics Division, August, 1982; final revision, October, 1982.

[2] The "no-flow" region is the region in which $|\tau_2| \leq \tau_y$. Since η_2 is finite, there will be some deformation in this region.

Copyright © 1983 by ASME
Downloaded 02 May 2010 to 171.66.16.246. Redistribution subject to ASME license or copyright; see http://www.asme.org/terms/Terms_Use.cfm

$$U_1(\zeta) = \zeta - (1-\beta)\frac{\left[\zeta\int_0^{\zeta} e^{-x^2}dx + \frac{1}{2}e^{-\zeta^2}\right]}{\int_0^{\zeta_c} e^{-x^2}dx} \tag{12}$$

and

$$U_2(\zeta) = \beta\left\{\zeta - \frac{\left[\zeta\int_{\frac{\zeta_c}{\sqrt{\alpha}}}^{\frac{\zeta}{\sqrt{\alpha}}} e^{-x^2}dx + \frac{\sqrt{\alpha}}{2}e^{-\frac{\zeta^2}{\alpha}}\right]}{\int_{\frac{\zeta_c}{\sqrt{\alpha}}}^{\infty} e^{-x^2}dx}\right\} \tag{13}$$

In obtaining (12) and (13), we have used the constitutive law (2), where $\dot{\gamma} = \partial u_i/\partial y$ in each flow region i, and the conservation of linear momentum

$$\frac{\partial u_i}{\partial t} = \nu_i \frac{\partial^2 u_i}{\partial y^2}.$$

It should be noted that $U_2(\zeta) \to 0$ as $\zeta \to \infty$ as required. Finally, to find ζ_c we require that the velocity field is continuous at $y = y_c(t)$, that is

$$U_2(\zeta_c) = \alpha U_1(\zeta_c)$$

which leads to

$$\beta = \left(\sqrt{\pi}\frac{\alpha-1}{\alpha}\zeta_c \operatorname{erf}\zeta_c + e^{-\zeta_c^2} + \frac{1}{\sqrt{\alpha}}\frac{\operatorname{erf}\zeta_c}{\operatorname{erfc}\frac{\zeta_c}{\sqrt{\alpha}}}e^{-\frac{\zeta_c^2}{\alpha}}\right)^{-1} e^{-\zeta_c^2} \tag{14}$$

Given a value of $\beta = \tau_y/\tau_0$ and of $\alpha = \eta_2/\eta_1$, this equation is solvable for ζ_c and thus the claimed solution is indeed a similarity solution for the problem at hand.

At low value of $\zeta_c << 1$ (or, alternatively, $1-\beta << 1$), we have

$$y_c(t) \sim (1-\beta)\sqrt{\alpha\pi\nu_1 t}, \tag{15}$$

and at high value of $\zeta_c >> 1$ (or, at low value of $\beta << 1$), we have

$$y_c(t) \sim 2\sqrt{\frac{\nu_1 t}{\epsilon}\left(1 + \frac{\epsilon}{2}ln\epsilon\right)}, \tag{16}$$

where $\epsilon = \left(ln\frac{1}{\sqrt{\pi}\beta}\right)^{-1}$.

Table 1 displays some values of β for ζ_c ranges from 0.5 to 2 at two possible values of α: $\alpha = \infty$ and $\alpha = 100$.

Acknowledgment

This work was completed while the author was a visiting Fulbright Scholar at the Chemical Engineering Department at Caltech, Pasadena. Thanks are due to those agencies for providing a hospitable atmosphere.

Table 1 Some solutions of (14)

ζ_c	β	
	$\alpha = 100$	$\alpha = \infty$
0.5	0.60349	0.62802
1	0.18969	0.19762
1.5	0.038162	0.039417
2	0.0050395	0.0051642

References

1 Bingham, E. C., *Fluidity and Plasticity*, McGraw-Hill, New York, 1922, pp. 215–218.

2 Oldroyd, J. C., "A Rational Formulation of the Equations of Plastic Flow for a Bingham Solid," *Proc. Camb. Phil. Soc.*, Vol. 43, 1947, pp. 100–105.

3 Bird, R. B., Armstrong, R. C., and Hassager, O., *Dynamics of Polymeric Liquids*, Vol. 1, Wiley, New York, 1977.

4 Bluman, G. W., and Cole, J. D., *Similarity Methods for Differential Equations*, Springer-Verlag, New York, 1974.

On the Stability of Large Discrete Buckling Structures

A. Maher[1]

An approximate applicable method is presented for the computation of the critical buckling load of a moderately large complicated assembly in terms of traces of successive powers of the stability matrix. The method is based on the use of the bound approach of references [1, 2]. An illustrative example and comparison with known results are given.

1 Introduction

A variety of structural stability problems concerning buckling of large practical structures under axial compression, bending, torsion, or a combination of these are of the utmost importance in ensuring safe design of structures.

A reliable assessment of the critical buckling load is the basic step in the structural stability, since from a practical point of view an assembly will have failed with the load exceeds the lowest one. There are several alternative approaches to this problem, most of which are best suited for simple structures. Rayleigh and Timoshenko [5] developed their approaches through the use of various modes as a reasonable guess for the first buckled shape. The latter provided a means of obtaining both upper and lower bounds for the critical load. Vianello [4] presented an iterative technique based on the Stodola approach. The latter will be more effective by starting with a reasonable assessment of the buckled modes. None of the aforementioned methods can avoid the employment of the assumed modes in their applications. However the difficulty of selecting suitable buckled shapes increases rapidly with the number of dimensions of the system and the reliability of the result is reduced accordingly.

This paper attempts to offer a simple applicable procedure based on the use of the bound method [1, 2], for the calculation of the critical buckling load with a specified accuracy. The present method produces a monotonically increasing sequence of lower bounds and a monotonically decreasing sequence of upper bounds by the use of traces of successive powers for the stability matrix.

In contrast to the previous methods, the present procedure is equally applicable to simple systems as well as for complicated discrete systems with repeated and close eigenvalues [1] and even with unpredictable buckled shapes. These frequently arise in the analysis of moderately large practical structures.

As compared to the Vianello method, the present method is of known accuracy being bounded above and below as shown in the representation of an example from reference [4].

[1] Honorary Fellow in the Department of Engineering Mechanics, University of Wisconsin-Madison. On leave from Military Technical College, Cairo, Egypt.

Manuscript received by ASME Applied Mechanics Division, November, 1981; final revision, August 1982.

Downloaded 02 May 2010 to 171.66.16.246. Redistribution subject to ASME license or copyright; see http://www.asme.org/terms/Terms_Use.cfm

$$U_1(\zeta) = \zeta - (1-\beta)\frac{\left[\zeta\int_0^{\zeta} e^{-x^2}dx + \frac{1}{2}e^{-\zeta^2}\right]}{\int_0^{\zeta_c} e^{-x^2}dx} \tag{12}$$

and

$$U_2(\zeta) = \beta\left\{\zeta - \frac{\left[\zeta\int_{\frac{\zeta_c}{\sqrt{\alpha}}}^{\frac{\zeta}{\sqrt{\alpha}}} e^{-x^2}dx + \frac{\sqrt{\alpha}}{2}e^{-\frac{\zeta^2}{\alpha}}\right]}{\int_{\frac{\zeta_c}{\sqrt{\alpha}}}^{\infty} e^{-x^2}dx}\right\} \tag{13}$$

In obtaining (12) and (13), we have used the constitutive law (2), where $\dot{\gamma} = \partial u_i/\partial y$ in each flow region i, and the conservation of linear momentum

$$\frac{\partial u_i}{\partial t} = \nu_i \frac{\partial^2 u_i}{\partial y^2}.$$

It should be noted that $U_2(\zeta) \to 0$ as $\zeta \to \infty$ as required. Finally, to find ζ_c we require that the velocity field is continuous at $y = y_c(t)$, that is

$$U_2(\zeta_c) = \alpha U_1(\zeta_c)$$

which leads to

$$\beta = \left(\sqrt{\pi}\frac{\alpha-1}{\alpha}\zeta_c \operatorname{erf}\zeta_c + e^{-\zeta_c^2} + \frac{1}{\sqrt{\alpha}}\frac{\operatorname{erf}\zeta_c}{\operatorname{erfc}\frac{\zeta_c}{\sqrt{\alpha}}}e^{-\frac{\zeta_c^2}{\alpha}}\right)^{-1} e^{-\zeta_c^2} \tag{14}$$

Given a value of $\beta = \tau_y/\tau_0$ and of $\alpha = \eta_2/\eta_1$, this equation is solvable for ζ_c and thus the claimed solution is indeed a similarity solution for the problem at hand.

At low value of $\zeta_c << 1$ (or, alternatively, $1-\beta << 1$), we have

$$y_c(t) \sim (1-\beta)\sqrt{\alpha\pi\nu_1 t}, \tag{15}$$

and at high value of $\zeta_c >> 1$ (or, at low value of $\beta << 1$), we have

$$y_c(t) \sim 2\sqrt{\frac{\nu_1 t}{\epsilon}\left(1 + \frac{\epsilon}{2}ln\epsilon\right)}, \tag{16}$$

where $\epsilon = \left(ln\frac{1}{\sqrt{\pi}\beta}\right)^{-1}$.

Table 1 displays some values of β for ζ_c ranges from 0.5 to 2 at two possible values of α: $\alpha = \infty$ and $\alpha = 100$.

Acknowledgment

This work was completed while the author was a visiting Fulbright Scholar at the Chemical Engineering Department at Caltech, Pasadena. Thanks are due to those agencies for providing a hospitable atmosphere.

Table 1 Some solutions of (14)

ζ_c	β	
	$\alpha = 100$	$\alpha = \infty$
0.5	0.60349	0.62802
1	0.18969	0.19762
1.5	0.038162	0.039417
2	0.0050395	0.0051642

References

1 Bingham, E. C., *Fluidity and Plasticity*, McGraw-Hill, New York, 1922, pp. 215–218.

2 Oldroyd, J. C., "A Rational Formulation of the Equations of Plastic Flow for a Bingham Solid," *Proc. Camb. Phil. Soc.*, Vol. 43, 1947, pp. 100–105.

3 Bird, R. B., Armstrong, R. C., and Hassager, O., *Dynamics of Polymeric Liquids*, Vol. 1, Wiley, New York, 1977.

4 Bluman, G. W., and Cole, J. D., *Similarity Methods for Differential Equations*, Springer-Verlag, New York, 1974.

On the Stability of Large Discrete Buckling Structures

A. Maher[1]

An approximate applicable method is presented for the computation of the critical buckling load of a moderately large complicated assembly in terms of traces of successive powers of the stability matrix. The method is based on the use of the bound approach of references [1, 2]. An illustrative example and comparison with known results are given.

1 Introduction

A variety of structural stability problems concerning buckling of large practical structures under axial compression, bending, torsion, or a combination of these are of the utmost importance in ensuring safe design of structures.

A reliable assessment of the critical buckling load is the basic step in the structural stability, since from a practical point of view an assembly will have failed with the load exceeds the lowest one. There are several alternative approaches to this problem, most of which are best suited for simple structures. Rayleigh and Timoshenko [5] developed their approaches through the use of various modes as a reasonable guess for the first buckled shape. The latter provided a means of obtaining both upper and lower bounds for the critical load. Vianello [4] presented an iterative technique based on the Stodola approach. The latter will be more effective by starting with a reasonable assessment of the buckled modes. None of the aforementioned methods can avoid the employment of the assumed modes in their applications. However the difficulty of selecting suitable buckled shapes increases rapidly with the number of dimensions of the system and the reliability of the result is reduced accordingly.

This paper attempts to offer a simple applicable procedure based on the use of the bound method [1, 2], for the calculation of the critical buckling load with a specified accuracy. The present method produces a monotonically increasing sequence of lower bounds and a monotonically decreasing sequence of upper bounds by the use of traces of successive powers for the stability matrix.

In contrast to the previous methods, the present procedure is equally applicable to simple systems as well as for complicated discrete systems with repeated and close eigenvalues [1] and even with unpredictable buckled shapes. These frequently arise in the analysis of moderately large practical structures.

As compared to the Vianello method, the present method is of known accuracy being bounded above and below as shown in the representation of an example from reference [4].

[1] Honorary Fellow in the Department of Engineering Mechanics, University of Wisconsin-Madison. On leave from Military Technical College, Cairo, Egypt.

Manuscript received by ASME Applied Mechanics Division, November, 1981; final revision, August 1982.

Copyright © 1983 by ASME
Downloaded 02 May 2010 to 171.66.16.246. Redistribution subject to ASME license or copyright; see http://www.asme.org/terms/Terms_Use.cfm

Table 1 Comparison of results for present formulas (8) and (9) and that of reference [4]. All values are calculated relative to (G/EI). N and ϵ are the number of steps and the corresponding maximum permissible error, respectively.

N	Vianello Method [4]	Bound formula (8) (ϵ)	Bound formula (9) (ϵ)
1	1,391750	1,302812-1,508731 (0,205918)	1,302812-1,508731 (0,205918)
2	1,326780	1,312965-1,333506 (0,020541)	1,313720-1,324721 (0,011001)
3	1,313868	1,313720-1,315995 (0.002275)	1,313795-1,313869 (0,000074)

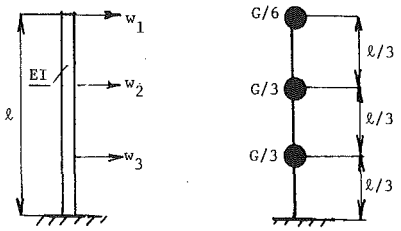

Fig. 1 Stability analysis for column buckling due to its own weight. The uniform column is modeled as a three degree-of-freedom discrete system as shown.

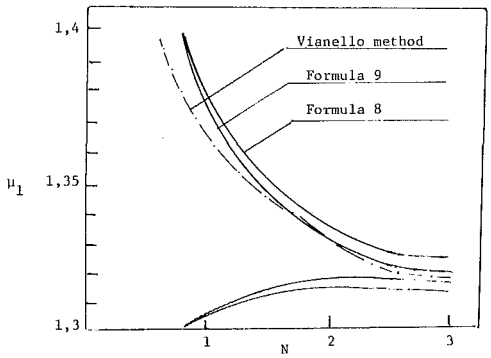

Fig. 2 Sketch of load factor μ_1 against number of steps N as given by Vianello method and several approximate expressions, showing the convergence of the successive upper and lower bound estimates of the formulas (8) and (9).

Although the example presented to illustrate the solution procedure is applied to a simple system with few degrees of freedom, the procedure can be readily applied to practical buckling structures involving any degree of repetition or closeness of eigenvalues and any possible combination of axial, torsional, and flexural degrees of freedom within the capacity of the available computer. In the case of too large structures, there are efficient reduction methods that render the generated matrices tackable by the available computer storage. These methods often include those associated with the employment of master and slave coordinate systems [10], and of substructure analysis [3, 11].

2 Statement of the Problem

In structural stability analysis [3], the static eigenvalue equation is characterized by the following matrix form

$$KW=\mu K_G w \tag{1}$$

where K = standard elastic stiffness matrix; K_G = geometrical (incremental) stiffness matrix, W = buckling mode vector; and, μ = load parameter (compressive stress factor), which gives the classical buckling load.
Equation (1) may be recast as

$$FW=\lambda W \tag{2}$$

where

$$F=K^{-1}K_G, \quad \lambda=1/\mu$$

If the inverse of large stiffness matrices with nonreducable sizes is required, then one could possibly avoid computational difficulties by using the partitioned technique [8], transformation in pairs [9], or Cholesky decomposition [11]. Fortunately for many large buckling structures, the flexibility matrices, K^{-1}, can be directly found by the utilization of the force method [3, 12], without the inverse processes. The successive premultiplication of equation (2) by the stability matrix F, $s-1$ times leads to

$$F^s W=\lambda^s W \tag{3}$$

If F is a matrix of order n, the trace of the matrix F^s is then given by

$$T_s=\sum_i^n \lambda_i^s=\lambda_1^s(p+\psi_s) \tag{4}$$

where p is the number of multiplicity of λ_1, T_s is the trace of the matrix F^s and ψ_s is the sth buckling ratio, defined here as

$$\psi_s=\sum_{i=p+1}^n (\lambda_i/\lambda_1)^s \tag{5}$$

3 Determination for Both Bounds of Classical Critical Load

With $\lambda_1 \geq \lambda_2 \ldots \geq \lambda_n$, the buckling ratio decreases monotonically as the power s increases and tends to zero as s tends to infinity [1]. Hereby a sequence of upper bounds for λ_1 may be recognized from equation (4), as

$$U_s=(T_s)^{1/s} \geqslant U_{s+1} \geqslant \ldots \geqslant \lambda_1 \tag{6}$$

Upon taking into account that $\psi_{s+1} \leq \psi_s$, a sequence of lower bounds is then given by

$$L_s=T_{s+1}/T_s \leqslant L_{s+1} \leqslant \ldots \leqslant \lambda_1 \tag{7}$$

Here, the critical load parameter is then bounded by

$$(T_s)^{-1/s} \leqslant \mu_1 \leqslant T_s/T_{s+1} \quad \text{for} \quad s=1,2,3,4, \ldots \tag{8}$$

Both bounds may rapidly converge to μ_1 if the power s is set equal to 2^s [2], and the form (8) will be converted to

$$(T_{2s})^{-1/2s} \leqslant \mu_1 \leqslant (T_s/T_{2s})^{1/s} \quad \text{for} \quad s=1, 2, 4, 8 \ldots \tag{9}$$

With the aid of the latter form, the computing time for obtaining a stability matrix raised to a power 2^s is proportional to $s+1$ as compared to 2^s for the bound formula (8). But, at a comparatively very high current value of s overflow may occur earlier in formula (9) compared with formula (8). Therefore in some cases it may be advantageous to start the calculations by using equation (9) and to finish by using equation (8). However the utilization of the formulae (8) and (9) or a combination of them depends on many factors such as the nature of the stability matrix, the required accuracy, and the computing time. In some other applications, the average value of μ_1 at an assigned value of s may be more convenient. From equations (8) and (9) it follows that

$$\mu_{av}=0.5[(T_s)^{-1/s}+(T_s/T_{s+1})], \tag{10}$$

$$\mu_{av}=0.5[(T_{2s})^{-1/2s}+(T_s/T_{2s})^{1/s}] \tag{11}$$

4 On the Applications of the Developed Formulas

The form (2) is frequently selected for its suitability for a wide class of practical discrete structural systems such as imperfect structural systems [7] and some types of combined

Downloaded 02 May 2010 to 171.66.16.246. Redistribution subject to ASME license or copyright; see http://www.asme.org/terms/Terms_Use.cfm

deformed structures with unpredictable modal shapes. However in some cases of partially constrained structures, there may be some restrictions in the formulation of the stability matrix. Such limitations can be avoided by modifying the stiffness matrix, using the eigenvalue shift [2, 6] to be

$$\bar{K} = (K + \alpha K_G) \tag{12}$$

where α is some constant. Consequently the form (2) may be recast as

$$\bar{F}^s W = \bar{\lambda}^s W \tag{13}$$

with

$$\bar{F} = \bar{K}^{-1} K_G$$

Here the critical load parameter is obtained from the shifted eigenvalue $\bar{\lambda}$ according to the formula

$$\mu = (1/\bar{\lambda}) - \alpha \tag{14}$$

Therefore the formulas (8) and (9) may be recast respectively, as

$$(\bar{T}_s)^{-1/s} - \alpha \leq \mu_1 \leq (\bar{T}_s/\bar{T}_{s+1}) - \alpha \tag{15}$$

where

$$(\bar{T}_{2s})^{-1/2s} - \alpha \leqslant \mu_1 \leqslant (\bar{T}_s/\bar{T}_{2s})^{1/s} - \alpha \tag{16}$$

where $\bar{T}_s$ is the trace of the modified stability matrix $\bar{F}^s$. In some applications of closely coupled systems it may be required to obtain the critical load parameter without inverting the stiffness matrix. In such case the form (1) may be rewritten as

$$K^* W = \delta W \tag{17}$$

with

$$K^* = \beta I - F^{-1} \tag{18}$$

$$\delta = \beta - \mu \tag{19}$$

Consequently the formulas (8) and (9) may be rewritten, respectively, as

$$\beta - (T_s^*)^{1/s} \leqslant \mu_1 \leqslant \beta - (T_{s+1}^*/T_s^*), \tag{20}$$

$$\beta - (T_{2s}^*)^{1/2s} \leqslant \mu_1 \leqslant \beta - (T_{2s}^*/T_s^*)^{1/s} \tag{21}$$

where β is the proper eigenvalue shift and T_s^* is the trace of the matrix K^{*s}. However for some cases of the nearly singular geometrical stiffness matrices, equation (18) may be modified as stated by equations (2) and (12).

5 Numerical Example

To illustrate the foregoing results, a uniform column with flexural rigidity EI and total length l loaded by its own weight G [4] was considered. The structure has been modeled as a three degree-of-freedom coupled system (see Fig. 1) and the results are shown in Fig. 2 and also in Table 1.

6 Conclusion

The method developed in this work is well suited to the stability analysis of a wide class of complicated discrete systems involving a moderately large number of degrees of freedom. The method allows repetition and closeness of eigenvalues and avoidance of selecting buckled modes. The utilization of the developed bound formulas or a combination of them is efficient for the computation of the critical buckling load with a determined accuracy and with a relatively short computer time, particularly for practical engineering systems.

References

1 Maher, A., "Bound Formula for Determining the Fundamental Frequency," *Journal of Sound and Vibration*, Vol. 63, 1979, pp. 459-462.

2 Maher, A., "Determination of the Lowest Frequency of an Unconstrained Discrete System," *Journal of Sound and Vibration*, Vol. 70, 1980, pp. 213-220.

3 Przeminiecki, J. S., *Theory of Matrix Structural Analysis*, McGraw-Hill, New York, 1968.

4 Clough, R. W., and Penzin, J., *Dynamics of Structures*, McGraw-Hill, New York, 1975.

5 Timoshenko, S. P., and Gere, J. M., *Theory of Elastic Stability*, McGraw-Hill, New York, 1961.

6 Parlett, B. N., *The Symmetric Eigenvalue Problem*, Prentice-Hall, Englewood Cliffs, N. J., 1980.

7 Ho, D. H., "Buckling Load of Nonlinear Systems With Multiple Eigenvalues," *Int. J. Solids and Structures*, Vol. 10. 1974, pp. 1315-1330.

8 Faddeeva, D. K., and Faddeeva, V. N., *Computational Methods of Linear Algebra*, W. H. Freeman, San Francisco, 1963.

9 Ayres, F., *Matrices*, McGraw-Hill, New York, 1962.

10 Guyan, R. J., "Reduction of Stiffness and Mass Matrices," *AIAA Journal*, Vol. 3, 1965, p. 380.

11 Meirovitch, L., *Computational Methods in Structural Dynamics*, Alphen can den Rijin, The Netherlands, 1980.

12 Hurty, W. C., and Rubinstein, M. F., *Dynamics of Structures*, Prentice-Hall, Englewood Cliffs, N. J., 1967.

Downloaded 02 May 2010 to 171.66.16.246. Redistribution subject to ASME license or copyright; see http://www.asme.org/terms/Terms_Use.cfm

Journal of Applied Mechanics Discussion

Unconventional Internal Cracks Part 1: Symmetric Variations of a Straight Crack, and Part 2: Methods of Generating Simple Cracks[1]

Z.-b-Kuang.[2] Professor Wu published two papers that are also of interest to me. In a scientific report of Xi'an Jiaotong University, 1976, in a Chinese journal *Acta Mechanica Sinica*, 1979, No. 2, and in the "Selected Papers of Scientific Research," 1978-1980 of Xi'an Jiaotong University, we published papers entitled "Stress Analysis For Plane Curved Polygonal Defects Containing Cusps Only," and so on. In those papers we modified the contour of Muskhelishvili's contour integral formulas as shown in Fig. 1.

Using the behavior of stresses near corner points, we prove that for any polygonal defects the formulas of complex stress functions $\varphi(\zeta), \phi(\zeta)$ can be expressed as follows:

$$\varphi_0(\zeta) - \frac{1}{2\pi i}\int_{c_1} \frac{\omega(\sigma)}{\overline{\omega'(\delta)}} \frac{\overline{\varphi_0'(\sigma)}\,d\sigma}{\sigma-\zeta} = -\frac{1}{2\pi i}\int_{C_1} \frac{f_0(\sigma)\,d\sigma}{\sigma-\zeta} \tag{1}$$

$$\psi_0(\zeta) - \frac{1}{2\pi i}\int_{C_2} \frac{\overline{\omega(\sigma)}}{\omega'(\sigma)} \frac{\overline{\varphi_0'(\sigma)}\,d\sigma}{\sigma-\zeta} = -\frac{1}{2\pi i}\int_{C_2} \frac{\overline{f_0(\sigma)}\,d\sigma}{\sigma-\zeta} \tag{2}$$

$$\varphi(\zeta) = \varphi_0(\zeta) + \Gamma R\zeta - \frac{X+iY}{2\pi(1+\kappa)} \ln\zeta \tag{3}$$

$$\psi(\zeta) = \psi_0(\zeta) + \Gamma' R\zeta + \frac{\kappa(X-iY)}{2\pi(1+\kappa)} \ln\zeta \tag{4}$$

$$f_0(\sigma) = i\int_{t_0}^{t} (X_n + iY_n)\,ds - \Gamma R\sigma - \bar{\Gamma}' R\frac{1}{\sigma} + \frac{X+iY}{2\pi} \ln\sigma + \frac{X-iY}{2\pi(1+\mathrm{K})} \frac{\sigma\omega(\sigma)}{\overline{\omega'(\sigma)}} - \Gamma\bar{R}\frac{\omega(\sigma)}{\overline{\omega'(\sigma)}} \tag{5}$$

where the meaning of the symbols $\varphi(\zeta), \omega(\zeta)$ . . . . . can be understood from the literature [1].

Because near a general corner point $\varphi(\zeta)$, $\psi(\zeta)$, and $\omega(\zeta)$ are nonrational functions, equations (1) and (2) can only be solved by numerical methods. But, in the neighborhood of a cusp $\varphi(\zeta)$, $\psi(\zeta)$, and $\omega(\zeta)$ are all rational functions and therefore the exact solution of equations (1) and (2) can be obtained.

In those papers we discussed some particular problems. The body is applied a uniform load at infinity and the faces of flaw are free. The tangent of cusp which is of interest to us is parallel to the axis OX. Therefore, the complex stress intensity factor can be expressed by

$$K = K_1 - iK_2 = 2\sqrt{\pi}\frac{\varphi'(\sigma_j)}{\sqrt{\omega''(\sigma_j)}} \tag{6}$$

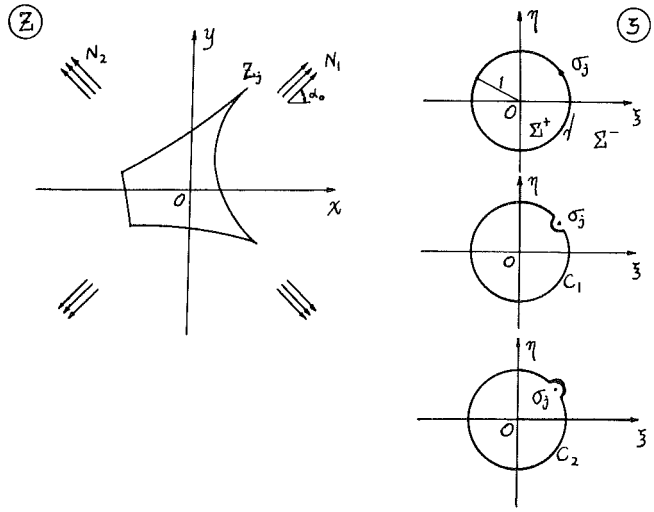

Fig. 1

1 Airfoil Flaw

The mapping function which is well known in hydrodynamics

$$Z = \omega(\zeta) = \frac{1}{2}e^{i\beta}[(\rho\zeta+\alpha) + (\rho\zeta+\alpha)^{-1}] \tag{7}$$

transforms the airfoil flaw in the Z-plane onto the unit circle γ in the ζ-plane, and transforms the exterior region of the flaw onto Σ^- (Fig. 2). In equation (7) ρ, α, and β are parameters, as shown in Fig. 2. By varying these parameters we can obtain various shapes of airfoil flaw. Substituting (7) into (1) and (2) we obtain

$$K = \sqrt{\pi}e^{\frac{i\beta}{2}}\left\{\Gamma + \bar{\Gamma}' e^{-i\beta} + \frac{(\rho^2-\alpha\bar{\alpha})^2}{[(\rho^2-\alpha\bar{\alpha})^2-\alpha^2]}\left[\Gamma + \frac{2}{\rho}e^{i\beta}\bar{\varphi}_0'\left(-\frac{\rho}{\alpha}\right)\right]\right\} \tag{8}$$

[1] By C. H. Wu, and published in the March and June issues of the ASME JOURNAL OF APPLIED MECHANICS, Vol. 49, pp. 67-68, and 383-388.

[2] Associate Professor, Department of Engineering Mechanics, Xi'an jiatong University, Xi'an, China.

Copyright © 1983 by ASME
Downloaded 02 May 2010 to 171.66.16.246. Redistribution subject to ASME license or copyright; see http://www.asme.org/terms/Terms_Use.cfm

$$\bar{\varphi}_0'\left(-\frac{\rho}{\alpha}\right)=\left\{1-\frac{\alpha^2\bar{\alpha}^2}{[(\rho^2-\alpha\bar{\alpha})^2-\alpha^2][(\rho^2-\alpha\bar{\alpha})^2-\bar{\alpha}^2]}\right\}^{-1}$$
$$\left\{\Gamma' R\frac{\alpha^2}{\rho^2}+\frac{\Gamma R e^{-2i\beta}\alpha^2}{(\rho^2-\alpha\bar{\alpha})^2-\bar{\alpha}^2}-\frac{\bar{\Gamma}'\bar{R}\alpha^2\bar{\alpha}^2 e^{-2i\beta}}{\rho^2[(\rho^2-\alpha\bar{\alpha})^2-\bar{\alpha}^2]}\right.$$
$$\left.+\frac{\Gamma\bar{R}\alpha^2\bar{\alpha}^2}{[(\rho^2-\alpha\bar{\alpha})^2-\alpha^2][(\rho^2-\alpha\bar{\alpha})^2-\bar{\alpha}^2]}\right\} \quad (9)$$

For the symmetrical airfoil flaw we have

$$\alpha=\bar{\alpha}=-a, \quad \beta=0, \quad \rho=1+a \quad (10)$$

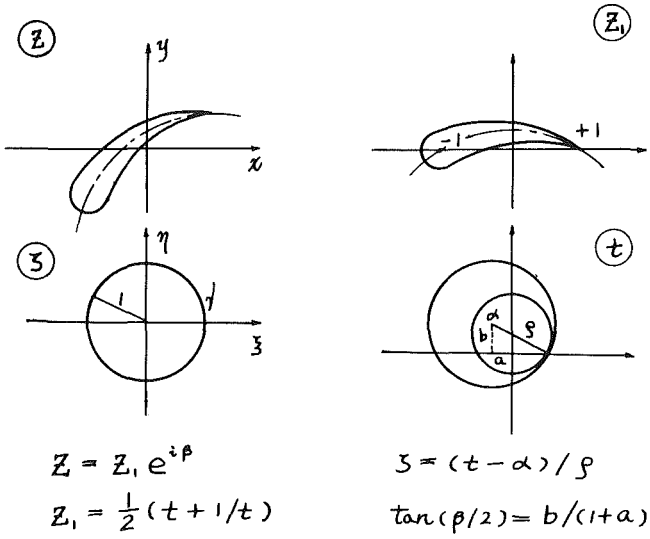

Fig. 2

2 Lip Flaw

The mapping function that transforms the lip flaw whose length is 2 in the Z-plane onto the unit circle in the ζ-plane is

$$Z=\omega(\zeta)=\frac{1}{2}\rho i\left[\zeta+\frac{m}{\zeta}-\frac{\zeta}{\rho^2(\zeta^2+m)}\right] \quad (11)$$

$$\rho(1+m)=a, \quad \rho(1-m)=1 \quad (12)$$

where ρ and m are parameters, as shown in Fig. 3. The stress intensity factor now takes the form

$$K=\frac{\sqrt{\pi}}{1+m}\left[\Gamma+\bar{\Gamma}'-m\Gamma+\frac{(1+m)^3}{(1+m^2)^2}(\Gamma+m\Gamma'-m^2\Gamma)\right.$$
$$\left.-\frac{m^2(1+m)}{(1+m^2)^2}(\Gamma'-\bar{\Gamma}')\right] \quad (13)$$

For any lip flaw with length 2 we can select the following approximate mapping function

$$Z=\frac{1}{2}\left(t+\frac{1}{t}\right), \quad t=i\rho\left(\zeta+\sum_{1,3}^{N}A_n\zeta^{-n}\right) \quad (14)$$

where

$$\rho\left(1+\sum_{1,3}^{N}A_n\right)=a, \quad \rho\left[1+\sum_{1,3}^{N}(-1)^{\frac{n+1}{2}}A_n\right]=1 \quad (15)$$

here a is a selected constant and ρ and A_n are two real coefficients that are determined in such a way so that the approximate configuration is as close as possible to the true configuration.

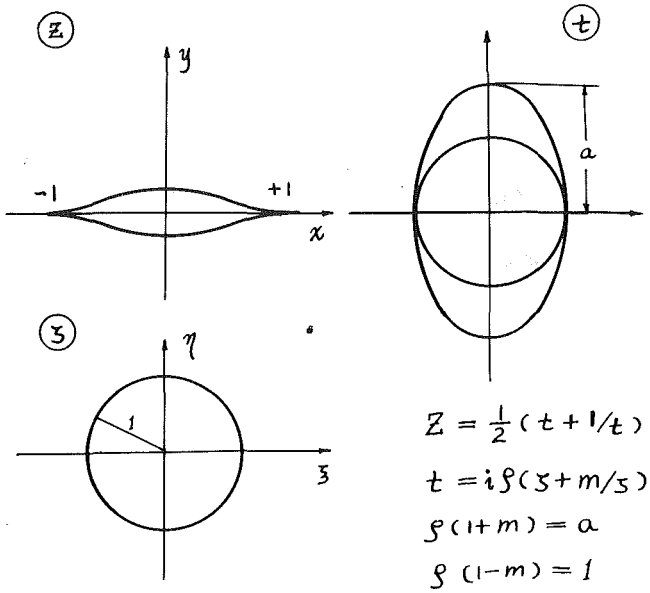

Fig. 3

3 Hypocycloidal Polygon Flaw With $n+1$ Cusps

The mapping function for this case is

$$Z=\omega(\zeta)=R\left(\zeta+\frac{1}{n\zeta^n}\right) \quad (16)$$

and the stress intensity factor is given by

$$K=\frac{2\sqrt{\pi R}}{\sqrt{n+1}}\left(2\Gamma+\frac{n^2\bar{\Gamma}'+n(n-2)\Gamma'}{n^2-n+2}\right) \quad (17)$$

The foregoing discussed flaw can be easily applied to solve some interesting elastic inclusion problems.

From this discussion we can conclude that the formulas (1) and (2) are quite general and useful, and can be applied to corner points that are not cusps.

Reference

[1] Muskhelishvili, N. I., *Some Basic Problems of the Mathematical Theory of Elasticity*, translated by J. R. M. Radokk, Groningen, P. Noordhoff Ltd., 1963.

A Further Examination on the Application of the Strain Energy Density Theory to the Angled Crack Problem[1]

G. C. Sih[2] and E. Madenci[3]. The paper is another one of the author's numerous attempts[4] on the angle crack and elliptical notch problem. Presumably, the objective is to help identify a realistic failure criterion. This, however, cannot be accomplished merely by comparing experimental data with theoretical predictions because the scatter on critical load measurements often overshadow the small differences between different failure criteria. The main purpose of this discussion is to clarify that the dilemmas of the S-theory as

[1] Chang, K. J., and published in the June 1982 issue of the ASME JOURNAL OF APPLIED MECHANICS, Vol. 49, pp. 377–385.

[2] Professor of Mechanics and Director of Institute of Fracture and Solid Mechanics, Lehigh University, Bethlehem, Pa. Fellow ASME.

[3] Research Assistant, Department of Mechanical Engineering, Lehigh University, Bethlehem, Pa.

[4] Refer to references [33–36] in the author's paper.

Downloaded 02 May 2010 to 171.66.16.246. Redistribution subject to ASME license or copyright; see http://www.asme.org/terms/Terms_Use.cfm

$$\varphi_0'\left(-\frac{\rho}{\alpha}\right)=\left\{1-\frac{\alpha^2\bar{\alpha}^2}{[(\rho^2-\alpha\bar{\alpha})^2-\alpha^2][(\rho^2-\alpha\bar{\alpha})^2-\bar{\alpha}^2]}\right\}^{-1}$$
$$\left\{\Gamma' R\frac{\alpha^2}{\rho^2}+\frac{\Gamma R e^{-2i\beta}\alpha^2}{(\rho^2-\alpha\bar{\alpha})^2-\bar{\alpha}^2}-\frac{\bar{\Gamma}'\bar{R}\alpha^2\bar{\alpha}^2 e^{-2i\beta}}{\rho^2[(\rho^2-\alpha\bar{\alpha})^2-\bar{\alpha}^2]}\right.$$
$$\left.+\frac{\Gamma\bar{R}\alpha^2\bar{\alpha}^2}{[(\rho^2-\alpha\bar{\alpha})^2-\alpha^2][(\rho^2-\alpha\bar{\alpha})^2-\bar{\alpha}^2]}\right\} \tag{9}$$

For the symmetrical airfoil flaw we have

$$\alpha=\bar{\alpha}=-a,\quad \beta=0,\quad \rho=1+a \tag{10}$$

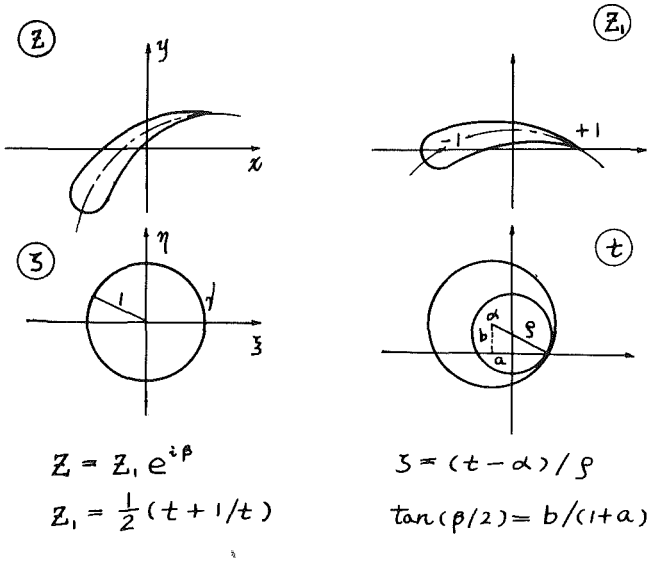

Fig. 2

2 Lip Flaw

The mapping function that transforms the lip flaw whose length is 2 in the Z-plane onto the unit circle in the ζ-plane is

$$Z=\omega(\zeta)=\frac{1}{2}\rho i\left[\zeta+\frac{m}{\zeta}-\frac{\zeta}{\rho^2(\zeta^2+m)}\right] \tag{11}$$

$$\rho(1+m)=a,\quad \rho(1-m)=1 \tag{12}$$

where ρ and m are parameters, as shown in Fig. 3. The stress intensity factor now takes the form

$$K=\frac{\sqrt{\pi}}{1+m}\left[\Gamma+\bar{\Gamma}'-m\Gamma+\frac{(1+m)^3}{(1+m^2)^2}(\Gamma+m\Gamma'-m^2\Gamma)\right.$$
$$\left.-\frac{m^2(1+m)}{(1+m^2)^2}(\Gamma'-\bar{\Gamma}')\right] \tag{13}$$

For any lip flaw with length 2 we can select the following approximate mapping function

$$Z=\frac{1}{2}\left(t+\frac{1}{t}\right),\quad t=i\rho\left(\zeta+\sum_{1,3}^{N}A_n\zeta^{-n}\right) \tag{14}$$

where

$$\rho\left(1+\sum_{1,3}^{N}A_n\right)=a,\quad \rho\left[1+\sum_{1,3}^{N}(-1)^{\frac{n+1}{2}}A_n\right]=1 \tag{15}$$

here a is a selected constant and ρ and A_n are two real coefficients that are determined in such a way so that the approximate configuration is as close as possible to the true configuration.

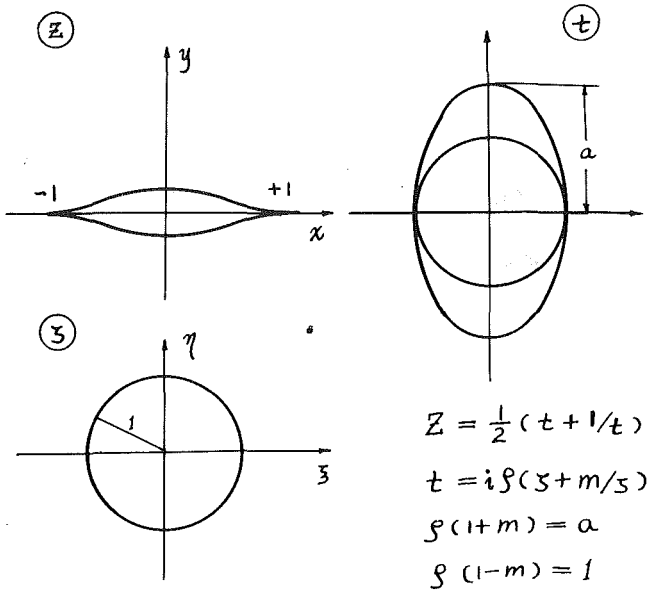

Fig. 3

3 Hypocycloidal Polygon Flaw With $n+1$ Cusps

The mapping function for this case is

$$Z=\omega(\zeta)=R\left(\zeta+\frac{1}{n\zeta^n}\right) \tag{16}$$

and the stress intensity factor is given by

$$K=\frac{2\sqrt{\pi R}}{\sqrt{n+1}}\left(2\Gamma+\frac{n^2\bar{\Gamma}'+n(n-2)\Gamma'}{n^2-n+2}\right) \tag{17}$$

The foregoing discussed flaw can be easily applied to solve some interesting elastic inclusion problems.

From this discussion we can conclude that the formulas (1) and (2) are quite general and useful, and can be applied to corner points that are not cusps.

Reference

[1] Muskhelishvili, N. I., *Some Basic Problems of the Mathematical Theory of Elasticity*, translated by J. R. M. Radokk, Groningen, P. Noordhoff Ltd., 1963.

A Further Examination on the Application of the Strain Energy Density Theory to the Angled Crack Problem[1]

G. C. Sih[2] and E. Madenci[3]. The paper is another one of the author's numerous attempts[4] on the angle crack and elliptical notch problem. Presumably, the objective is to help identify a realistic failure criterion. This, however, cannot be accomplished merely by comparing experimental data with theoretical predictions because the scatter on critical load measurements often overshadow the small differences between different failure criteria. The main purpose of this discussion is to clarify that the dilemmas of the S-theory as

[1] Chang, K. J., and published in the June 1982 issue of the ASME JOURNAL OF APPLIED MECHANICS, Vol. 49, pp. 377–385.

[2] Professor of Mechanics and Director of Institute of Fracture and Solid Mechanics, Lehigh University, Bethlehem, Pa. Fellow ASME.

[3] Research Assistant, Department of Mechanical Engineering, Lehigh University, Bethlehem, Pa.

[4] Refer to references [33–36] in the author's paper.

Copyright © 1983 by ASME
Downloaded 02 May 2010 to 171.66.16.246. Redistribution subject to ASME license or copyright; see http://www.asme.org/terms/Terms_Use.cfm

claimed by the author are due to inaccuracies in his numerical calculations even though the stress expressions may be exact.

First of all, it should be said that the selection of a suitable failure criterion cannot be based on the mere agreement of theory and experiment for a few special problems. Attention should be focused on the *generality* and *consistency* with which a single criterion can explain and predict a multitude of physical phenomena regardless of loading, geometry and material behavior. Failure criterion obviously cannot be responsible for errors and/or inaccuracies committed in the stress analysis. A case in point is the maximum stress [1] and maximum strain [2] criteria as proposed by the author that are known to be inadequate and lead to contradictions in many instances. It is well known that the elastodynamic[5] problem of a Mode *I* running crack where the maximum stress or strain occurs along the path of propagation rather than normal to it. This is contrary to the original assumption that crack spreads normal to the direction of maximum stress or strain. These criteria become even more inconsistent for nonlinear materials when the stress and strain no longer obey a one-to-one relation.

The superficially acclaimed dilemmas in the paper will be shown to be nonexistent. This can be done by first reviewing the basic assumptions of the strain energy density criterion that the author is apparently unaware of the past literature [3-6]. The basic assumptions of the strain energy density theory can be found in [6]. In contrast to what the author refers to as dilemma *A*, there are no difficulties in choosing $(dW/dV)_{\min}$ or $S_{\min}$ corresponding to fracture initiation under tensile or compressive loading. Moreover, the locations of yielding can also be easily identified from $(dW/dV)_{\max}$ or $S_{\max}$. It was pointed out as early as 1974 [7] that there can be many $S_{\min}$ in a given crack problem. The maximum of $S_{\min}$ or $S_{min}^{\max}$ obviously will first reach the critical value at which site fracture initiation is assumed. For nonself-similar crack growth in three dimensions [3-5], each point on the crack profile possess a $S_{\min}$ and growth is assumed to occur in accordance with the condition $S_j^k/r_j^k = \text{const.}$ where k stands for the number of points selected on the crack profile.

To be more specific, consider the example of an angle crack subjected to uniaxial tension or compression. The stress is $\sigma = \pm 100$ ksi while the other parameters are chosen as $\nu = 0.25$, $E = 30 \times 10^6$ psi, $\beta = 30$ deg, $a =$ lin., and $r_0/a = 0.01$. Indeed, two minima for $S_{\min}$ are obtained. The first occurs at $\theta_0 = -60$ deg with $S_{\min} = 29.2966$ lb/in. and the other at $\theta_0 = +130$ deg with $S_{\min} = 12.8932$ lb/in. Common experience tells us that it is easier to fracture material under tension than in compression. This is because more energy per unit volume is concentrated ahead of a crack in tension as compared to compression, i.e., $(S_{\min})_{\text{ten.}} > (S_{\min})_{\text{comp.}}$ Consequently, the compressive strength is usually higher than the tensile strength. For this example, $\sigma_{\text{comp}}/\sigma_{\text{ten.}} = 1.51$. The same conclusion applied to other values of β. One should be cognizant of the fact that even a quadratic equation possesses two roots, the physical interpretation of which must be supplied by the analyst. The corollary in [8] associated with the tensile hoop stress is not necessary and becomes problematic for complex and multiple crack systems. The recent work in [9] involving many complex crack systems showed convincingly that no additional conditions except common sense are needed for determining allowable tensile and compressive loads from the *S*-theory.

Referring to Figs. 4 to 6 in the paper, the author has carelessly attributed his inaccurate numerical calculations to shortcoming of the strain energy density criterion. Note how closely the $dS/d\theta$ versus θ curve comes to touching zero at $\theta_0 \simeq -40$ deg. The small gap is caused by numerical inaccuracy. Previous calculations performed at Lehigh University in 1973 [10] indicated that the locations of $S_{\min}$ are very sensitive to changes in ν, β, r_0/a, and b/a. Some of the results are outlined in Table 1. There is no doubt that there will be a $S_{\min}$ for θ_0 between -40 deg and -90 deg in the example quoted in Fig. 4 with $r_0/a = 0.15$, $\nu = 0.25$, and $\beta = 10$ deg even though Table 1 does not provide the answer for this particular case. Numerical calculations must be performed very carefully for small increments of θ otherwise the locations of of $S_{\min}$ can be overlooked. These comments also apply to the results in Figs. 5 and 6 where the absence of $S_{\min}$ is due to inaccurate numerical calculations even though the stress expressions may be exact.

Table 1 Fracture angles corresponding to $S_{\min}$ for $b/a = 0.2$ and different values of β, r_0/a, and ν

ν	β	r_0/a	θ_0
0.2	10 deg	0.3	−65.67 deg
	15 deg	0.1	−34.18 deg
		0.2	−60.24 deg
0.3	10 deg	0.2	−66.08 deg
	15 deg	0.1	−51.74 deg
		0.2	−69.77 deg
0.4	10 deg	0.1	−46.46 deg
		0.2	−74.67 deg
	15 deg	0.1	−60.67 deg
		0.2	−76.49 deg

The foregoing comments invalidate dilemma *B* in the paper. For the case of an elliptical notch, the surface layer concept should be adopted [11, 12] such that the influence of material microstructure within this layer must either be averaged or neglected. The site of fracture initiation is first located by having the strain energy per unit surface layer area reach some critical value. The $S_{\min}$ concept is then applied to the interior region excluding the notch boundary. The core region applies more readily to the line crack with its origin centered at the crack tip. Again, its introduction is necessitated to exclude the local material microstructure effects outside of which the continuum mechanics approach is assumed to be valid. The size of r_0 is certainly material dependent, a point that has been stressed by many previous investigators. What is not clear is that r_0 could also be influenced to a degree by stress or energy state. This involves a detail description of the conditions affecting crack initiation which is beyond the scope of this discussion.

In conclusion, the author is referred to [13] in which the inclined crack under biaxial load is treated by the *S*-theory. The results are shown to agree well with the available experimental data. No difficulties of the type mentioned by the author occurred. Agreement of theory with experiment should be regarded only as necessary but often may not be sufficient to validate any criterion. This is particularly true for the angle

[5] Even in the two-dimensional static case of a Mode *I* crack, the stress state is hydrostatic and there exists no distinct maximum of the stresses nor the strain component.

Downloaded 02 May 2010 to 171.66.16.246. Redistribution subject to ASME license or copyright; see http://www.asme.org/terms/Terms_Use.cfm

crack configuration where the specimen stiffness changes with the angle of load inclination β. The amount of overload that is not accounted for in the theory will change for each β. Generally speaking, it is not difficult to show that the results of several criteria will fall within the scatter of experimental data. Hence, the choice of a given criterion can only be judged by its usefulness and versatility in predicting physical phenomena free from any contradictions or inconsistencies. In this respect, the S-theory has already been demonstrated to predict crack growth under monotonic loading, fatigue [14], and gross yielding [15] in a consistent fashion based on the three assumptions stated earlier.

References

1 Chang, K. J., "Further Studies of the Maximum Stress Criterion on the Angled Crack Problem," *Int. J. of Eng. Fracture Mechanics*, Vol. 14, 1981, pp. 125-247.

2 Chang, K. J., "On the Maximum Strain Criterion—A New Approach to the Angles Crack Problem," *Int. J. of Eng. Fracture Mechanics*, Vol. 14, 1981, pp. 107-124.

3 Sih, G. C., "Mechanics of Crack Growth: Geometrical Size Effect in Fracture," *Proceedings of Fracture Mechanics in Engineering Application*, Sih, G. C., and Valluri, S. R., eds., Sijthoff and Noordhoff, The Netherlands, 1979, pp. 3-29.

4 Sih, G. C., and Kiefer, B. V., "Stable Growth of Surface Cracks," *Journal of the Engineering Mechanics Division*, ASCE, Vol. 106, No. EM2, 1980, pp. 245-253.

5 Sih, G. C., and Kiefer, B. V., "Nonlinear Response of Solids Due to Crack Growth and Plastic Deformation," *Nonlinear and Dynamic Fracture Mechanics*, Perrone, N., and Atluri, S. N., eds., ASME Applied Mechanics Division, Vol. 35, 1979, pp. 136-156.

6 Sih, G. C., "Experimental Fracture Mechanics: Strain Energy Density Criterion," *Mechanics of Fracture, Vol. VII Experimental Evaluation of Stress Concentration and Intensity Factors*, Sih, G. C., ed., Martinus Nijhoff, The Netherlands, 1981, pp. XVII-LVI.

7 Sih, G. C., and Cha, B. C. K., "A Fracture Criterion for Three-Dimensional Crack Problems," *International Journal of Fracture Mechanics*, Vol. 6, 1974, pp. 699-723.

8 Swedlow, J. L., "Criteria for Growth of the Angled Crack," *Cracks and Fracture*, ASTM STP 601, American Society of Testing and Materials, 1976, pp. 506-521.

9 Gdoutos, E. E., *Problems of Mixed Mode Crack Extension*, Martinus Nijhoff, The Netherlands (in press).

10 Sih, G. C., "Tables on Fracture Initiation Angles for Elliptical Notches: Strain Energy Density Criterion," Lehigh University Publication, Bethlehem, Pa., 1973.

11 Sih, G. C., "Surface Layer Energy and Strain Energy Density For a Blunted Crack or Notch," *Prospects of Fracture Mechanics*, Sih, G. C., van Elst, H. C., and Brock, D., eds., Noordhoff Int. Publishing, Leyden, 1974, pp. 85-102.

12 Sih, G. C., "Strain Energy Density and Surface Layer Energy for Blunt Crack or Notches," *Mechanics of Fracture V*, Sih, G. C., ed., Noordhoff Int. Publishing, Leyden, 1978, pp. XIII-CX.

13 Barthelemy, B., "Application of the Strain Energy Density Theory to the Inclined Crack Under Biaxial Load," *Proceedings of Absorbed Specific Energy and/or Strain Energy Density Criterion*, Sih, G. C., Czoboly, E., and Gillemot, F., eds., Akademiai Kiado, Budapest, 1982, pp. 57-65.

14 Sih, G. C., and Moyer, E. T., Jr., "Path Dependent Nature of Fatigue Crack Growth," *Int. J. of Eng. Fracture Mechanics*, Vol. 16, 1982 (in press).

15 Sih, G. C., and Madenci, E., "Failure by Crack Growth and Gross Yielding: Strain Energy Density Criterion," *Int. J. of Fracture Mechanics*, Vol. 16, 1982 (in press).

Finite Element Analysis of Vibration of Toroidal Field Coils Coupled With Laplace Transform[1]

B. S. Berger[2]. The authors have made an application of finite elements in spacial variables and numerical inversion of the Laplace transform in the temporal variable, to a problem of technical significance. In the Introduction the following statement is made: "As far as the authors know, examples of numerical analysis with the Laplace transform have been very few." They then cite two papers, leaving the reader with the impression that these two citations have exhausted the literature.

An extensive literature exists on the subject of the numerical inversion of the Laplace transform. A comprehensive bibliography is given in [1] and [2] of several hundred papers on the subject, published between 1934 and 1975. The recent application of the numerical inversion of the Laplace transform to the transformed time variable in connection with boundary element techniques is discussed in [3] and [4]. Numerical inversion of the Laplace transform has found application in transient fluid-solid interaction problem [5] and [6], viscoelasticity [7], and heat conduction [8]. These examples serve only to suggest the wide range of application of numerical inversion methods. It is hoped that the foregoing will assist in placing this paper in perspective.

References

1 Piessens, R., "A Bibliography on Numerical Inversion of the Laplace Transform and Its Applications," *Journal of Comp. and Applied Math.*, Vol. 1, 1975, pp. 115-128.

2 Piessens, R., and Dang, N. D. P., "A Bibliography on Numerical Inversion of the Laplace Transform and Its Application: A Supplement," *Journal of Comp. and Applied Math.*, Vol. 2, No. 3, 1976, pp. 225-228.

3 Cruse, T. A., and Rizzo, F. J., "A Direct Formulation and Numerical Solution of the General Transient Elastodynamic Problem," Part I and II, *Journal Math. Anal. Applic.*, Vol. 22, No. 1, 1968, pp. 244-254 and Vol. 22, No. 2, 1968, pp. 341-355.

4 Brebbia, C. A., and Walker, S., *Boundary Element Techniques in Engineering*, Newnes - Butterworths, London, 1980.

5 Berger, B. S., "Transient Motion of an Elastic Shell of Revolution in an Acoustic Medium," ASME JOURNAL OF APPLIED MECHANICS, Vol. 45, 1978, pp. 149-152.

6 Berger, B. S., and Palmer, M. E., "The Transient Motion of a Cylindrical Shell of Arbitrary Cross Section in an Acoustic Medium," ASME JOURNAL OF APPLIED MECHANICS, Vol. 44, 1977, pp. 482-486.

7 Longman, I. M., "Numerical Laplace Transform Inversion of a Function Arising in Viscoelasticity," *Journal Comp. Physics*, Vol. 10, 1972, pp. 224-231.

8 Norden, H. V., and Seppa, I., "A Problem on Heat Conduction in a Wire Enclosed by a Cylindrical Material Solved by Numerical Inverse Laplace Transforms," *BIT*, Vol. 4, 1964, pp. 224-242.

[1] By K. Miza, M. Uesaka, and F. C. Moon, and published in the September 1982 issue of ASME JOURNAL OF APPLIED MECHANICS, Vol. 49, pp. 594-600.

[2] Department of Mechanical Engineering, University of Maryland, College Park, Md. 20742.

Downloaded 02 May 2010 to 171.66.16.246. Redistribution subject to ASME license or copyright; see http://www.asme.org/terms/Terms_Use.cfm

crack configuration where the specimen stiffness changes with the angle of load inclination β. The amount of overload that is not accounted for in the theory will change for each β. Generally speaking, it is not difficult to show that the results of several criteria will fall within the scatter of experimental data. Hence, the choice of a given criterion can only be judged by its usefulness and versatility in predicting physical phenomena free from any contradictions or inconsistencies. In this respect, the S-theory has already been demonstrated to predict crack growth under monotonic loading, fatigue [14], and gross yielding [15] in a consistent fashion based on the three assumptions stated earlier.

References

1 Chang, K. J., "Further Studies of the Maximum Stress Criterion on the Angled Crack Problem," *Int. J. of Eng. Fracture Mechanics*, Vol. 14, 1981, pp. 125-247.

2 Chang, K. J., "On the Maximum Strain Criterion—A New Approach to the Angles Crack Problem," *Int. J. of Eng. Fracture Mechanics*, Vol. 14, 1981, pp. 107-124.

3 Sih, G. C., "Mechanics of Crack Growth: Geometrical Size Effect in Fracture," *Proceedings of Fracture Mechanics in Engineering Application*, Sih, G. C., and Valluri, S. R., eds., Sijthoff and Noordhoff, The Netherlands, 1979, pp. 3-29.

4 Sih, G. C., and Kiefer, B. V., "Stable Growth of Surface Cracks," *Journal of the Engineering Mechanics Division*, ASCE, Vol. 106, No. EM2, 1980, pp. 245-253.

5 Sih, G. C., and Kiefer, B. V., "Nonlinear Response of Solids Due to Crack Growth and Plastic Deformation," *Nonlinear and Dynamic Fracture Mechanics*, Perrone, N., and Atluri, S. N., eds., ASME Applied Mechanics Division, Vol. 35, 1979, pp. 136-156.

6 Sih, G. C., "Experimental Fracture Mechanics: Strain Energy Density Criterion," *Mechanics of Fracture, Vol. VII Experimental Evaluation of Stress Concentration and Intensity Factors*, Sih, G. C., ed., Martinus Nijhoff, The Netherlands, 1981, pp. XVII-LVI.

7 Sih, G. C., and Cha, B. C. K., "A Fracture Criterion for Three-Dimensional Crack Problems," *International Journal of Fracture Mechanics*, Vol. 6, 1974, pp. 699-723.

8 Swedlow, J. L., "Criteria for Growth of the Angled Crack," *Cracks and Fracture*, ASTM STP 601, American Society of Testing and Materials, 1976, pp. 506-521.

9 Gdoutos, E. E., *Problems of Mixed Mode Crack Extension*, Martinus Nijhoff, The Netherlands (in press).

10 Sih, G. C., "Tables on Fracture Initiation Angles for Elliptical Notches: Strain Energy Density Criterion," Lehigh University Publication, Bethlehem, Pa., 1973.

11 Sih, G. C., "Surface Layer Energy and Strain Energy Density For a Blunted Crack or Notch," *Prospects of Fracture Mechanics*, Sih, G. C., van Elst, H. C., and Brock, D., eds., Noordhoff Int. Publishing, Leyden, 1974, pp. 85-102.

12 Sih, G. C., "Strain Energy Density and Surface Layer Energy for Blunt Crack or Notches," *Mechanics of Fracture V*, Sih, G. C., ed., Noordhoff Int. Publishing, Leyden, 1978, pp. XIII-CX.

13 Barthelemy, B., "Application of the Strain Energy Density Theory to the Inclined Crack Under Biaxial Load," *Proceedings of Absorbed Specific Energy and/or Strain Energy Density Criterion*, Sih, G. C., Czoboly, E., and Gillemot, F., eds., Akademiai Kiado, Budapest, 1982, pp. 57-65.

14 Sih, G. C., and Moyer, E. T., Jr., "Path Dependent Nature of Fatigue Crack Growth," *Int. J. of Eng. Fracture Mechanics*, Vol. 16, 1982 (in press).

15 Sih, G. C., and Madenci, E., "Failure by Crack Growth and Gross Yielding: Strain Energy Density Criterion," *Int. J. of Fracture Mechanics*, Vol. 16, 1982 (in press).

Finite Element Analysis of Vibration of Toroidal Field Coils Coupled With Laplace Transform[1]

B. S. Berger[2]. The authors have made an application of finite elements in spacial variables and numerical inversion of the Laplace transform in the temporal variable, to a problem of technical significance. In the Introduction the following statement is made: "As far as the authors know, examples of numerical analysis with the Laplace transform have been very few." They then cite two papers, leaving the reader with the impression that these two citations have exhausted the literature.

An extensive literature exists on the subject of the numerical inversion of the Laplace transform. A comprehensive bibliography is given in [1] and [2] of several hundred papers on the subject, published between 1934 and 1975. The recent application of the numerical inversion of the Laplace transform to the transformed time variable in connection with boundary element techniques is discussed in [3] and [4]. Numerical inversion of the Laplace transform has found application in transient fluid-solid interaction problem [5] and [6], viscoelasticity [7], and heat conduction [8]. These examples serve only to suggest the wide range of application of numerical inversion methods. It is hoped that the foregoing will assist in placing this paper in perspective.

References

1 Piessens, R., "A Bibliography on Numerical Inversion of the Laplace Transform and Its Applications," *Journal of Comp. and Applied Math.*, Vol. 1, 1975, pp. 115-128.

2 Piessens, R., and Dang, N. D. P., "A Bibliography on Numerical Inversion of the Laplace Transform and Its Application: A Supplement," *Journal of Comp. and Applied Math.*, Vol. 2, No. 3, 1976, pp. 225-228.

3 Cruse, T. A., and Rizzo, F. J., "A Direct Formulation and Numerical Solution of the General Transient Elastodynamic Problem," Part I and II, *Journal Math. Anal. Applic.*, Vol. 22, No. 1, 1968, pp. 244-254 and Vol. 22, No. 2, 1968, pp. 341-355.

4 Brebbia, C. A., and Walker, S., *Boundary Element Techniques in Engineering*, Newnes - Butterworths, London, 1980.

5 Berger, B. S., "Transient Motion of an Elastic Shell of Revolution in an Acoustic Medium," ASME JOURNAL OF APPLIED MECHANICS, Vol. 45, 1978, pp. 149-152.

6 Berger, B. S., and Palmer, M. E., "The Transient Motion of a Cylindrical Shell of Arbitrary Cross Section in an Acoustic Medium," ASME JOURNAL OF APPLIED MECHANICS, Vol. 44, 1977, pp. 482-486.

7 Longman, I. M., "Numerical Laplace Transform Inversion of a Function Arising in Viscoelasticity," *Journal Comp. Physics*, Vol. 10, 1972, pp. 224-231.

8 Norden, H. V., and Seppa, I., "A Problem on Heat Conduction in a Wire Enclosed by a Cylindrical Material Solved by Numerical Inverse Laplace Transforms," *BIT*, Vol. 4, 1964, pp. 224-242.

[1] By K. Miza, M. Uesaka, and F. C. Moon, and published in the September 1982 issue of ASME JOURNAL OF APPLIED MECHANICS, Vol. 49, pp. 594-600.

[2] Department of Mechanical Engineering, University of Maryland, College Park, Md. 20742.

Copyright © 1983 by ASME
Downloaded 02 May 2010 to 171.66.16.246. Redistribution subject to ASME license or copyright; see http://www.asme.org/terms/Terms_Use.cfm

Journal of Applied Mechanics

Book Reviews

An Introduction to the Theory of Elasticity. By R. J. Atkin and N. Fox. Longman, London, 1980. 245 Pages. Price $14.95.

REVIEWED BY C. O. HORGAN[1]

This textbook is a companion text to that of A. J. M. Spencer (*Continuum Mechanics*, Longman, London, 1980), and is written in a similar concise style. It provides a self-contained brief introduction to the theory of elasticity (both infinitesimal and finite theory) suitable for undergraduates and beginning graduate students in applied mechanics, applied mathematics, and materials science. It is published in the series of *Longman Mathematical Texts* (edited by A. Jeffrey), a set of concisely written (and inexpensively produced) introductory textbooks used primarily in British universities.

The major novelty of this textbook on elasticity is that it begins with the *finite* (i.e., nonlinear) theory (covering the first half of the book) and then proceeds to the infinitesimal (linear) theory, which is shown to be a special case of the former. In this reviewer's opinion, such a treatment in the textbook literature on elasticity is long overdue and the authors are to be commended on their originality in this regard, especially in an introductory book.

The first chapter, entitled *Deformation and Stress*, summarizes those general principles of continuum mechanics that are necessary for the foundations of elasticity. Chapter 2, entitled *Finite Elasticity: Constitutive Theory* outlines the theory of constitutive equations in finite elasticity both for compressible and incompressible materials. The various forms of strain-energy functions which have been proposed in the literature are described, with citation of some original references. In Chapter 3, entitled *Exact Solutions*, some of the most important solutions of equilibrium problems in finite elasticity are discussed. Thus, homogeneous and nonhomogeneous deformations are described, together with associated experimental results. These first three chapters form a well-written, self-contained (but, of course, brief) introduction to finite elasticity.

The remainder of the book, in four chapters, is concerned with various topics in the classical linear theory of isotropic elasticity governing infinitesimal deformations. Chapter 4, entitled *Infinitesimal Theory* discusses the process of linearization as well as considerations of uniqueness. Other topics considered include problems involving spherical symmetry, displacement potentials, and solutions for some point force problems. Chapter 5, entitled *Antiplane Strain, Plane Strain, and Generalized Plane Stress* provides a brief account of the two-dimensional theories of elasticity governing the deformations of the chapter title, including a concise treatment of the complex variable approach for such problems. In Chapter 6, entitled *Extension, Torsion, and Bending*, the classical Saint-Venant problems of the chapter title are considered, with emphasis on the torsion problem. Curiously, the flexure problem (bending by terminal loads) is not mentioned. The book concludes with Chapter 7, entitled *Elastic Waves*, which contains a short summary of the most important results in linear isotropic elastodynamics.

The style of this book is, by its very nature, overly concise. This is a serious shortcoming in the second half of the book where the treatment of linear elasticity is uneven, with various topics included apparently at random. Those items that are covered are not distinguished by any originality in exposition. Thus, the present book is inferior to the standard textbooks on linear elasticity currently available. However, the first half of the book goes a long way toward remedying this. Here the authors have provided a readable condensed account of finite elasticity theory accessible to the beginner. In view of the current flourishing research activity in mechanical and mathematical aspects of this theory, the contribution of such an introduction for beginning students is a welcome addition to the textbook literature.

Hot-Wire Anemometry. By A. E. Perry. Clarendon Press, Oxford, 1982. 184 Pages. Price $47.00.

REVIEWED BY P. A. LIBBY[2]

The hot-wire anemometer is certainly the single most important instrument in experimental turbulence and is certainly the basis for most of the current knowledge of turbulent flows. Most experimental projects related to such flows start with the assembly of one or more hot-wire anemometers and the associated equipment for calibration, positioning, and output recording. This book summarizes ". . .those fundamental aspects of . . . (hot-wire anemometry) . . . .which will always be needed for successful hot-wire practice." It focuses on the sensor, the basis for its operation, and potential pitfalls in its use, and on its calibration. Unfortunately, other literature dealing with

[1] Professor, Department of Metallurgy, Mechanics, and Materials Science, and Department of Mathematics, Michigan State University, East Lansing, Mich. 48824.

[2] Professor, Department of Applied Mechanics and Engineering Science, Mail Code B-010, University of California, La Jolla, Cal. 92093.

Copyright © 1983 by ASME
Downloaded 02 May 2010 to 171.66.16.246. Redistribution subject to ASME license or copyright; see http://www.asme.org/terms/Terms_Use.cfm

ERRATA

Erratum on Discussion of "Characteristic Forms of Differential Equations for Wave Propagation in Nonlinear Media," by M. Ziv, and published in the December 1982 issue of the ASME JOURNAL OF APPLIED MECHANICS, Vol. 49, p. 929.

On page 929, third paragraph, last sentence, should read: With these simplifications, equation (35) of [1] now reads

$$\frac{d\sigma_{xx}}{dt} - \rho_0 c \frac{dv_x}{dt} = M_{xxqp} v_{q,p} - \rho_0 c^2 v_{x,x} - c\sigma_{xp,p} + c\sigma_{xx,x} \text{ along } dx/dt = c$$

where M_{kqdl} is the term $\frac{\partial^2 w}{\partial E_K^N \partial E_D^Q} x_{i,D}^{kd} x_{i,}^N + T_Q^K \delta_l^d$ in equation (25) of [1].

Copyright © 1983 by ASME
Downloaded 02 May 2010 to 171.66.16.246. Redistribution subject to ASME license or copyright; see http://www.asme.org/terms/Terms_Use.cfm